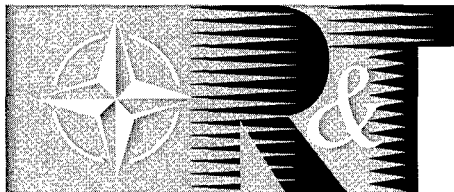NORTH ATLANTIC TREATY ORGANIZATION

RESEARCH AND TECHNOLOGY ORGANIZATION

BP 25, 7 RUE ANCELLE, F-92201 NEUILLY-SUR-SEINE CEDEX, FRANCE

RTO MEETING PROCEEDINGS 6

Non-Cooperative Air Target Identification Using Radar

(l'Identification radar des cibles aériennes non coopératives)

Papers presented at the Symposium of the RTO Systems Concepts and Integration Panel (SCI) held in Mannheim, Germany, 22-24 April 1998.

19990119 066

AQF99-04-0648

The Research and Technology Organization (RTO) of NATO

RTO is the single focus in NATO for Defence Research and Technology activities. Its mission is to conduct and promote cooperative research and information exchange. The objective is to support the development and effective use of national defence research and technology and to meet the military needs of the Alliance, to maintain a technological lead, and to provide advice to NATO and national decision makers. The RTO performs its mission with the support of an extensive network of national experts. It also ensures effective coordination with other NATO bodies involved in R&T activities.

RTO reports both to the Military Committee of NATO and to the Conference of National Armament Directors. It comprises a Research and Technology Board (RTB) as the highest level of national representation and the Research and Technology Agency (RTA), a dedicated staff with its headquarters in Neuilly, near Paris, France. In order to facilitate contacts with the military users and other NATO activities, a small part of the RTA staff is located in NATO Headquarters in Brussels. The Brussels staff also coordinates RTO's cooperation with nations in Middle and Eastern Europe, to which RTO attaches particular importance especially as working together in the field of research is one of the more promising areas of initial cooperation.

The total spectrum of R&T activities is covered by 6 Panels, dealing with:

- SAS Studies, Analysis and Simulation
- SCI Systems Concepts and Integration
- SET Sensors and Electronics Technology
- IST Information Systems Technology
- AVT Applied Vehicle Technology
- HFM Human Factors and Medicine

These Panels are made up of national representatives as well as generally recognised 'world class' scientists. The Panels also provide a communication link to military users and other NATO bodies. RTO's scientific and technological work is carried out by Technical Teams, created for specific activities and with a specific duration. Such Technical Teams can organise workshops, symposia, field trials, lecture series and training courses. An important function of these Technical Teams is to ensure the continuity of the expert networks.

RTO builds upon earlier cooperation in defence research and technology as set-up under the Advisory Group for Aerospace Research and Development (AGARD) and the Defence Research Group (DRG). AGARD and the DRG share common roots in that they were both established at the initiative of Dr Theodore von Kármán, a leading aerospace scientist, who early on recognised the importance of scientific support for the Allied Armed Forces. RTO is capitalising on these common roots in order to provide the Alliance and the NATO nations with a strong scientific and technological basis that will guarantee a solid base for the future.

Non-Cooperative Air Target Identification Using Radar

(RTO MP-6)

Executive Summary

The rapid and reliable identification of (air-) targets at maximum surveillance systems and weapon systems range is still a challenging problem which has a long history in NATO research studies. The different techniques that have been proposed to solve this problem may roughly be divided into two classes: cooperative and non-cooperative techniques. Cooperative techniques (often referred to as IFF - Identification Friend or Foe - techniques) are already operational in the radar domain, e.g. in airborne radars. NATO fighter aircraft are equipped with transponder systems answering on authorized interrogations by transmitting a predetermined coded signal. By this, friendly aircraft may be identified but positive identification of hostile or neutral aircraft is not possible.

This could in principle be achieved by the so-called non-cooperative identification techniques which rely on a comparison between the measured target signature with a reference data base. As one of the most promising techniques with long-range capability, radar based NCTI can be characterized. New developments in radar techniques should allow for major advances in radar based NCTI.

The symposium addressed many aspects of the topic "Non-Cooperative Air Target Identification using Radar". It started with a discussion on system requirements. The question of radar waveforms best suited for the NCTI problem was investigated. Evaluation of micro-Doppler effect and of acoustic signatures were discussed. Some emphasis was laid on the discussion of the benefits of fully polarimetric radar for the signature extraction and on the problems combined with calibration of fully polarimetric radars. The problem to establish and to interpret 2D-ISAR images was given some emphasis. Application of Time-Frequency Distributions in case of manoeuvering aircraft was proposed and different pre-processing steps investigated. Different algorithms and approaches for classification/identification of targets based on HRR or 2D-ISAR imagery were presented. The question which features should be derived from the radar signal information found a broad interest. Real time classification using optical processors was addressed and data fusion algorithms using simultaneous JEM and HRR information. The really challenging question of how to establish reference data bases for the classification/identification process was broadly discussed. There was the common understanding that this task can only be solved by the exploitation of modelling techniques. Besides other advantages this is the only practical way to get access to data of hostile aircraft. Many approaches are considered in different countries, relying on scale-model measurements or on CAD models plus computer prediction respectively. Implementation of the different techniques in real systems seems to be feasible at least as far as the JEM and HRR techniques are concerned. A technical demonstrator for the evaluation of the NCTI algorithms was presented and upgrades of fighter radars that will make the implementation of the above mentioned techniques into existing systems possible.

L'identification radar des cibles aériennes non coopératives

(RTO-MP-6)

Synthèse

L'identification rapide et fiable à distance maximale de cibles aériennes par les systèmes de surveillance et les systèmes d'armes demeure un problème délicat, qui a fait d'ailleurs l'objet de nombreuses études dans l'OTAN. Pour résoudre ce problème, deux grandes catégories existent : les techniques coopératives et non-coopératives. Les premières, souvent appelées IFF (identification ami-ennemi) sont déjà utilisées avec les radars, par exemple aéroportés. Les avions de combat de l'OTAN sont équipés de répondeurs qui, en cas d'interrogation envoient des signaux codés. Ces dispositifs ne permettent d'identifier que les avions amis, mais non les aéronefs ennemis ou neutres.

Ces derniers pourraient, en principe, être repérés avec ce qu'il est convenu d'appeler les techniques d'identification de cibles aériennes non-coopératives (NCTI) qui comparent la signature de la cible et une base de données de référence. La NCTI avec un support radar peut être considérée comme l'une des techniques très prometteuse pour la détection longue portée. Les progrès escomptés dans le domaine des techniques radar devraient amener des avancées importantes pour le principe NCTI.

Le symposium a examiné les aspects de l'identification radar des cibles aériennes non-cooperatives. Les spécifications du système ont d'abord été passées en revue avant d'étudier les formes d'onde les mieux adaptées au NCTI. L'évaluation de l'effet micro-Doppler et des signatures acoustiques a été, ensuite, discutée. Une place importante a été accordée à la discussion des avantages que pourraient apporter les radars entièrement polarimétriques pour l'extraction de la signature, sans oublier les problèmes soulevés par leur étalonnage. La conférence s'est penchée également sur la prise d'images et l'interprétation ISAR-2D. Une proposition d'attribution temps-fréquence aux aéronefs en évolution a été émise ainsi que les différentes étapes possibles pour un pré-traitement. Différents approches et algorithmes de la classification/identification des cibles, basés sur l'imagerie HRR et ISAR-2D, ont été présentés. La question de savoir quelles caractéristiques devaient être extraites des informations radar a été suivie avec grand intérêt. La classification en temps réel à l'aide de processeurs optiques ainsi que les algorithmes de fusionnement des données à base d'informations JEM et HRR simultanées a également fait l'objet de discussions.

Le délicat problème de l'établissement de bases de données de référence pour établir une classification/identification a été évoquée dans ses grandes lignes. Un consensus s'est dégagé sur le fait qu'il ne pouvait être résolu que par le biais des techniques de modélisation qui, seules permettent, de façon pratique, d'accéder aux données concernant des avions ennemis. De nombreuses études sont en cours à l'heure actuelle dans différents pays, basées sur des calculs à partir de modèles à l'échelle, de modèles CAO couplés à des prédictions de modèles informatiques. L'installation de ces techniques sur des systèmes existants semble possible, du moins en ce qui concerne les techniques JEM et HRR. Un démonstrateur technologique pour l'évaluation des algorithmes NCTI a été présenté, ainsi que des versions améliorées de radars d'avions de combat qui permettront l'installation de ces techniques.

Contents

_____

* Published in Classified Supplement

SESSION IV: TARGET CLASSIFICATION

SESSION V: SCATTERING TECHNIQUES, TARGET MODELLING AND VALIDATION

SESSION VI: CLASSIFIED SESSION

POSTER SESSION

---

* Published in Classified Supplement

Preface

Identification of aircraft is a critical function in both command and control (C 2) and weapon systems. Since many years work is going on in a variety of NATO countries to develop an identification system which will allow for reliable identification of friendly, hostile and neutral aircraft at maximum surveillance systems and weapon systems range. Different sources could in principle be exploited for the identification process, one of which is the so called "cooperative" component, often addressed as IFF (Identification Friend Foe) systems. This source relies on the response of an interrogated aircraft via a transponder and a predefined code, by this identifying an aircraft as a friendly one. Missing response is an indication for a hostile or neutral aircraft but there is no positive hostile/neutral aircraft identification. An incorrect identification can result in fratricide or engagement of civilian aircraft, both of which happened in recent conflicts.

Systems having the potential for identification of friendly, hostile and neutral aircraft are elements of the so-called "Non-Co-operative Target Identification (NCTI)" system class. These systems operate by comparing the received signatures (radar, infrared, acoustic, etc.) of an aircraft against a database of known signatures. As one of the most promising techniques with long-range capability, radar based NCTI can be characterized. Recent developments in radar techniques improving e.g. the resolution capabilities of the radar systems and new more advanced processing techniques should allow for major advances in radar based NCTI.

There is no doubt that a future identification system will be a "system of systems" where different entries will be used for the final declaration of a target as friend, foe or neutral. In this system the cooperative IFF mode and the non-co-operative mode together with auxiliary informations from other sources (ESM, intelligence, flight/mission plans, airspace control procedures, track by origin, flight profile and target behaviour, etc.) will form the input information in a data combining process (see proposed NATO Identification Data Combining Process (IDCP)).

This Symposium will concentrate on the discussion of the non-co-operative component. Its scope is to serve as a forum where experts from the whole alliance will be able to present and discuss novel technical solutions and novel processing techniques to the NCTI problem, and by that will help to explore current capabilities in all topics that are of relevance to the problem of non-co-operative air target identification using radar and even beyond this special application.

Dr. J. SCHILLER   Mr. R.L. CRANOS
Germany   USA

Co-Chairmen

Technical Programme Committee

Co-Chairman:

Dr. J. SCHILLER
Forschungsintitut für Hochfrequenzphysik
(FGAN/FHP)
Neuenahrer Str. 20
D-53343 Wachtberg-Werthhoven
GERMANY

Mr. R.L. CRANOS
US Air Force Research Laboratory
(AFRL/SNZ)
Wright-Patterson AFB
Ohio, 45433-7318
U.S.A.

Members

Dr. W.J. MICELI
Office of Naval Research
Surveillance, Communications &
   Electronic Combat Division, ONR
Code 313
Ballston Tower #1
800 North Quincy Street
Arlington, VA 22217
U.S.A.

Dr U. USCHKERAT
Forschungsinstitut für
   Hochfrequenzphysik
(FGAN-FHP)
Neuenahrer Str. 20
D-53343 Wachtberg-Werhhoven
GERMANY

Mr. P. ENERT
Office National d'Etudes
   et de Recherches Aérospatiales
(ONERA)
BP 72
F-92322 Châtillon Cedex
FRANCE

Mr. J.P. RIO
Service des Programmes
   Aéronautiques
26 Boulevard Victor
F-75731 Paris Cedex 15
FRANCE

Mr. R. VAN DER HEIDEN
TNO Physics and Electronics Laboratory
P.O. Box 96864
NL-2509 JG The Hague
NETHERLANDS

BEng. E.S. RISEBOROUGH
Centre de Recherche pour la Défense
3701 Av. Carling
Ottawa, Ont. K1A 0Z4
CANADA

NON-COOPERATIVE AIR TARGET IDENTIFICATION BY RADAR

Research Activities of the Panel 10, RSG.12 (DRG)
J. Schiller, Chairman RSG.12
Forschungsinstitut für Hochfrequenzphysik
Wachtberg-Werthoven, Germany

Background

In 1984 RSG.12 started its first working phase. In the first TOR you can read the following sentences:

" Probably the most serious defficiency in NATO's air defence capability... is the lack of a rapid and reliable means of identifiying all objects at max;mum weapon and surveillance system range. To improve identification capabilities and to ensure high confidence in positive air target identification, more advanced techniques and additional sources have been proposed (STANAG 4162 on the "Technical Characteristics of the NATO Identification System (NIS)). These include Non-Cooperative Target Identification (NCTI) by radar."

By that the focus of the RSG.12 activities was defined. What has been achieved in the meantime?

Overview on the different phases of work of RSG.12

Since 1984 RSG.12 has completed three phases of work:

Phase I 1984-1988

- The first phase was dedicated to elaboration of a survey and detailed discussion on candidate techniques applicable to Non-Co-operative Target Identification (NCTI) of air targets by radar.

Phase II 1988-1992

- As Jet Engine Modulation (JEM) was found to be the most promising and easiest implementable technique, the second phase focused on investigation of JEM-techniques for NCTI of aircraft.

Phase III 1992 - 1996

- While JEM-techniques were found to provide a powerful NCTI capability under certain prerequisites they showed some drawbacks as far as detection ranges and all aspect capabilities were concerned. For this reason the capabilities of Radar Imaging Techniques in the context of NCTI were investigated within this phase.

<u>Phase IV</u> 1997 - 1999

- Radar Imaging Techniques showed to be a very promising approach for non-cooperative air target identification. These techniques have the potential of overcoming at least some of the shortcomings of the JEM-techniques but the establishment of reference data bases is a challenging and still unsolved problem. So the present working phase focusses on investigations on the quality of reference data generated via modelling techniques. Besides that the improvement in identification performance using fully polarimetric data will be investigated.

More detailed description of the different working phases

<u>Phase I</u>: Survey of candidate techniques for NCTI of aircraft using radar

- Participating nations: Denmark, France, Germany, The Netherlands, Norway, United Kingdom, United States of America, SHAPE Technical Centre

- The following candidate techniques were discussed:

  High Range Resolution (HRR)
  High Cross Range Resolution by Inverse Synthetic Aperture Radar (ISAR)
  Combination of HRR and ISAR
  Jet Engine Modulation (JEM)
  Helicopter Rotor Modulation (HERM)
  Backscatter Modulation by Aircraft Vibration
  Target Backscatter Fluctuation
  Polarimetric Techniques
  Resonance Region Techniques
  Non-Linear Scattering Effect .

Most promising technique

As most promising technique applicable to NCTI of air targets JEM (or HERM) were identified.

- Extractable target (turbine) features should be independent of target aspect
- Relatively simple target data base

Promising techniques

Radar Imaging Techniques (HRR and 2-D-ISAR) were anticipated as promising techniques.

Problems:

- Features will be sensitive to target aspect changes
- Features will be sensitive to changes in external load configurations
- High demands on radar bandwith
- No simple reference data base

Beneficial to NCTI techniques

Adding polarimetric capabilities to other NCTI techniques

In principle useful

- Aircraft Vibrations. Restricted to mmW or shorter wavelengths

Hard to estimate

- NCTI techniques in the resonant region

Limited NCTI capability

- Target Backscatter Fluctuation

Most probably will only allow for discrimination between rather broad target classes (e.g. jet aircraft and propeller aircraft)

No NCTI capability

- Non-linear scattering techniques

Most probably only allows for discrimination between metallic objects and non-metallic objects

System considerations

- All techniques require relatively long dwell times and /or high prf modes

    ⇒ Severe problems for surveillance radar modes

- Candidates most suited to the incorporation of NCTI techniques will be tracking radars and multifunctional active phased array radar systems

Phase II 1988 - 1992: Radar Signal Modulation Techniques for NCTI

Participating nations: Canada, Denmark, France, Germany, The Netherlands, Norway, United Kingdom, United States of America, SHAPE Technical Centre

For phase II RSG.12 decided to investigate on the technique, that was identified as most promising technique for NCTI of aircraft using radar

Objective of the study

- To gain a better understanding of the capabilities and limitations of RSM/JEM techniques and to derive reliable estimates for achievable percentages of correct classification/identification and NCTI confidence factors in operational environment

Trials

- A prerequisit for further investigations was a common data base of real data

- RSG.12 initiated, organized and conducted a multinational cooperative field trial at WTD 81 Greding, Germany

- The name "TIME" (Target Identification by Modulation Exploitation) was assigned to this trial

- The trial TIME lasted from 3 - 28 April 1989

- Twenty-three aircraft from different member nations participated in the trial representing 16 different aircraft types

- Six different radar systems operating in the L, S, C, X and Ku bands were provided by the nations

The trial TIME turned out to be very effective in establishing a comprehensive common data base for the following investigations; data of trial TIME have been exchanged between the nations of RSG.12 and are still available

Main Conclusions of the study

- The Study showed that JEM techniques can provide a powerful tool for the non-cooperative identification of aircraft.

- Principal radar candidates for application of JEM techniques are lock-follow weapon system tracker/illuminator radars, multi-function phased array radars with high prf modes, and airborne interception radars.

Databases for JEM techniques are relatively simple but

- JEM techniques do not provide an all-aspect NCTI capability.

- They require a relatively high Signal-to-Noise ratio.

The Study ended with a Final Report on Radar Signal Modulation Techniques (NATO SECRET) (Technical Report AC/243 (Panel 10) TR/5.

Phase III 1992 - 1996: Radar Imaging Techniques for NCTI of Aircraft

Participating nations: Denmark, France, Germany, The Netherlands, Norway, United Kingdom, United States of America, NC3 A.

To overcome some of the shortcomings of the JEM techniques RSG.12 started in phase III the study on techniques having additional potential in NCTI of aircraft. The work focused on radar imaging techniques.

What do we understand by "radar imaging techniques" ?

The idea is having high resolved target RCS presentations in the slant-range and cross-range (2-DISAR techniques) dimensions.

Workshop

- In order to get a fast survey and a better understanding of the state of the art in the field of one- and two-dimensional radar imaging and data analysis RSG.12 organized a two days workshop on "Radar Imaging and Classification Techniques".

- The Workshop took place at FGAN, Werthhoven, Germany on 28-29 January 1993. Papers were published in the Technical Proceedings AC/243(Panel 10) TP/1.

- The Workshop was very succesful in giving an overview of the state of the art in radar imaging and in developing ideas on analysis of radar images with respect to target identification.

Trials

- Again a prerequisit for relevant investigations was a common data base of real, in-flight measured aircraft data. Because of the lack of any available data and to establish a common data base for the further investigations, RSG.12 conducted two multinational field trials in 1992 and 1993.

1992 Trials

- The trials of 1992 took place in autumn 1992 in the air spaces of the United Kingdom, of Germany and France.

- Two long-range radars participated,

    the BYSON radar of DERA, Great Malvern, UK and
    the TIRA radar of FGAN, Wachtberg-Werthhoven, GE.

BYSON-radar parameters: - S-Band
                                    - stepped frequency waveform
                                    - 400 MHz bandwith

TIRA system parameters: - Ku-Band
                                      - chirp
                                    - 800 MHz bandwith

- The BYSON radar collected HRR - profiles, the TIRA radar had the potential for both, HRR-profiles and 2-D-ISAR imagery.

- In the trials 9 different types of aircraft, provided by the RSG.12 member nations, participated.

- Total recording times were 9 hours for the BYSON and 8 hours for the TIRA system

1993 Trials

- In October 1993 the "AIDA" (Aircraft Imagery Data Acquisition) trials were conducted in the airspace of The Netherlands near Volkel.

- Its purpose was to build up a library of 2D-ISAR radar images of fighter aircraft.

- Four radar-systems participated in the measurements; two of these were long-range stationary systems (TIRA of FGAN, located at Werthhoven/GE and FELSTAR-radar of TNO/FEL, located at The Hague) and two were short-range mobile systems (MPR of DERA and RAMSES of ONERA).

FELSTAR parameters: - S-Band
                       - stepped frequency waveform
                       - 450 MHz bandwith

TIRA-system: - Ku-Band
                       - chirp waveform
                       - 800 MHz bandwith

MPR-system: - X-Band
                       - stepped frequency waveform
                       - 200 MHz bandwith

RAMSES system: - Band
                       - chirp waveform
                       - 200 MHz bandwith

- In the trials 15 different aircraft participated, respresenting 13 different aircraft types

- Total flight time was about 30 hours

The trials in 1992 and 1993 again were very successful, the recorded data showed to be of high quality according to the requirements for the following investigations

Data distribution

- All the data were distributed among the member nations of RSG.12 and are still available

- Two approaches were investigated:

  i) one dimensional High-Range-Resolution (HRR)- techniques for NCTI

  ii) two dimensional ISAR imaging techniques for NCTI

- The different nations developed their own approaches for solving the identification problem based on the HRR or 2D-ISAR aircraft data.

- The results of the classification processes were distributed and discussed among the group members and the structures of the different classifiers were illustrated. Classifier codes were not exchanged.

Main Conclusions

- The study showed that target identification based on HRR is a highly promising NCTI technique for fighter size or larger aircraft. It has an all aspect capability and moderate demands on signal-to-noise ratio and shows real time capability.

- A definite answer on the capabilities of 2D-ISAR based identification could not be given. It turned out that the existing database still is not broad enough for statistically relevant conclusions. The performance is less satisfactory than expected. Reasons may be found in problems in imaging algorithms or features used. In any case this technique presently is not real time capable in a fighter aircraft.

- A necessary prerequisit for identification techniques based on radar images of the targets is a database of HRR resp. 2D-ISAR signatures form the different aircraft types.

The study ended with a Final report on Radar Imaging Techniques for NCTI of Aircraft (Technical Report AC/243 (Panel 10)TR/14; NATO SECRET).

Phase IV 1997-1999 : Present working phase

Participating nations : Canada, Denmark, France, Germany, Greece, Italy, The Netherlands, Norway, Spain, United Kingdom, United States of America, NC3A

The focus of the present working phase is on the following topics :

- Further research in the area of 2D-ISAR imagery (autofocus methods, problem of manoeuvering targets) before the background of still not satisfying identification results

- Investigate on the applicability of radar signature modelling techniques for establishing a reference data base of HHR or 2D-ISAR data including hostile targets.

- Investigate on the improvement in identification rates under all aspects and for all targets if data fusion techniques are applied, combining specifically JEM, HRR and 2D-ISAR techniques.

- Investigate on possible improvements in identification performance, if fully polarimetric signature data is used.

Trials

For the question of model validation, to find out about the benefit of fully polarimetric data and for a better understanding of problems in 2D-ISAR imagery a (limited) number of fully instrumented aircraft field trials was necessary.

The trials under the name CARMINA (Correlated Attitude Radar Measurements of Images of Non-cooperative Aircraft) were conducted in the time frame November to February 1997/1998.

Six aircraft performed test flights under observation of the

- TIRA - system of FGAN/GE
- BYSON-radar of DERA/UK
- MERIC-system of ONERA/FR
- HYPERBRAHMS-system of DGA/FR
- FELSTAR-system of TNO-FEL/NL

in the Dutch, the UK and the French airspace

Partly the aircraft were instrumented with INS-systems. Four aircraft were fitted with an external attitude measurement system (ARDS - pod) .

MERIC radar system:	- X-band - stepped frequency waveform - 300 MHz bandwith - fully polarimetric system
HYPERBRAHMS:	- seven frequency bands from 500 MHz to 34 GHz - high prf mode - detection of JEM lines

The trials were succesfully finalized in February 1998. The radar data will be distributed in May/June.

In parallel the member nations started their work in scale-model measurements resp. computer modelling of those targets, that have participated in the CARMINA trials.

Expectations on this Symposium

This Symposium should act as a forum to bring together experts of the different disciplines that deal with problems related to the work in the fields of Automatic Target Recognition.

We hope that we will find a forum to discuss especially on the ideas of

- Target Characterization

- Target Classification

- Feature Extraction

- Modelling Techniques

in the area of air target identification and related areas.

At the end of this Symposium I hope we will leave with a lot of new, stimulating ideas, to go on in our different but related areas of research work for developing tools and methods for the Non-cooperative (air) target identification.

MILORD : a Technical Demonstrator for Long Range Radar Identification

Christian DELHOTE, Michel MORUZZIS
THOMSON-CSF/ AIRSYS
7 rue des Mathurins, BP 10, Bagneux, France

ABSTRACT

The objective of the MILORD project (Moyen d'Identification Longue portée d'Objectifs Radar Désignés) is to build a technical demonstrator for radar NCTR techniques in short, medium and long range, to assess the performance of these techniques in real environment, to bring out the conditions of their utilisation and to anticipate the recognition modes that may be embedded in the future surveillance and multifunction ground based and airborne radars.

The need for a technical demonstrator for identification radar techniques derives from a two-fold requirement :

- from an operational point of view, to prove that it is possible to fill an important gap of the air surveillance systems,
- from a technical point of view, to validate modes of target analysis that are adapted to the specificity and constraints of long range radar detection, and to play a federative role for all these techniques.

MILORD is a federative, multi-application project from the DGA (Délégation Générale à l'Armement) whose participants are THOMSON-CSF (AIRSYS and RCM) and the ONERA.

1. INTRODUCTION

The efficiency of the territory defence, projected forces, or Navy ships heavily depends on the available reaction time, after the identification of an hostile aircraft.

In order to increase this reaction time, it is necessary to add long identification capabilities to long range surveillance sensors. Depending on the detection system, these capabilities may be integrated into the present or future surveillance and multifunction radars through specific modes of target analysis, or supplied by a specialised auxiliary sensor.

Indeed, in present air defence systems, the operational need for target identification is only partially met by IFF-type systems. This need derives simultaneously from the requirement of knowing the air situation, and preparing possible ripostes, fit to the threat : jamming, interception, engagement of weapon systems. This need for identification is amplified by the recent improvement of threats that make attacks by stealthy platforms possible - even at a low degree -, using low altitude penetration techniques, radar discretion and

jamming, and therefore reducing the time available for air defence.

In this context, the techniques of echo radar analysis can bring a decisive benefit to the implementation of the following functions on non-cooperative air targets : numbering, classification of platform type, model recognition within the type.

Radar recognition techniques are numerous, bearing simultaneously on kinematics, rotating parts or target geometry, furthermore they can be coarse for a simple classification, or fine for model recognition within the class.

After a reminder in Chapter 2 of the issues linked to the NCTR (Non Cooperative Target Recognition) function, Chapter 3 describes the MILORD project in detail.

2. NCTR RADAR

2.1 INTRODUCTION

2.1.1 Objective

Air target recognition is conventionally split into two parts (see Figure 1) : the recognition of friendly targets by means of cooperative means (IFF, ...), and the recognition of unknown or hostile targets by different sensors, including the radar.

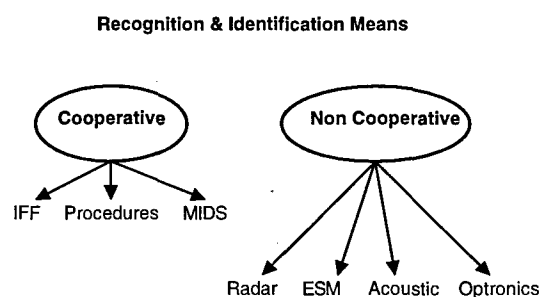**Recognition & Identification Means**

Figure 1

The main assets expected from the NCTR function are :

- a better understanding of the tactical situation,
- a more detailed assessment of threat (hierarchy of threats, priority in processing),
- a reduction of fratricide risk,

- a reduction in reaction time (for example for an interception by fighters),
- an optimisation of the riposte (interception, selection of appropriate weapon system),
- the selection and operation of protection means (for example, in a context of ARM threat),
- an optimisation of the surveillance means (adaptation of processing to target type in order to optimise detection and localisation quality, and adaptation of transmitted waveforms in order to optimise the discretion).

We discuss below the physical variables and the recognition methods that can be used in radar in order to reach the desired objective.

2.1.2 Physical features

The physical features accessible in radar, which can give information on the target type come mainly from three sources:

- target navigation:
data such as altitude, speed, acceleration or trajectory behaviour, can already provide information on rough target classes (helicopter, missile, combat fighter, ...)

- propulsion mode:
the analysis of the rotating parts allows, in a first stage ("coarse"), to distinguish the propulsion type (helicopter blade, propeller, jet engine, ...), then in a second stage ("fine"), to find detailed characteristics in the type of propulsion (frequency of blade occurrence, number of blades and rotation speed of a jet engine, ...)

- physical structure of the target:
as for the rotating parts, we can distinguish a "coarse" analysis (spatial resolution at the scale of the dimensions of small air targets), where macroscopic information on the target is indicated (size, length, width,...), and a "fine" analysis, where detailed information is given (position of air inlets, cockpit, wings, ...).

2.1.3 Recognition process

From the physical variables accessible to the radar, in order to obtain the desired recognition objectives, the NCTR process is typically split down in four broad steps (see Figure 2).

- Step 1:
using appropriate waveforms and processing (see Chapter 2.2), the radar carries out measurements on kinematics by tracking filtering or tracking, measurements on rotating parts by spectrum analysis, and measurements on the target spatial structure.

- Step 2:
from these measurements, the variables that are considered relevant for the NCTR function, along with their quality, are extracted so as to reduce data flow, to

simplify the database and the merging-recognition process.

- Step 3:
the set of values enters the merging-recognition process that elaborates the supposed class of the target with an associated confidence, after a comparison with a database. This merging-recognition process can be considered in two ways :
  * a recognition process elaborated for each characteristic variable, followed by a merging of the local decisions of recognition (symbolic fusion),
  * a merging-recognition process on the whole set of variables extracted for the different analysis modes (numerical fusion).

- Step 4:
this step consists in the making of the database itself. It is normally made before engaging the recognition process. This database is made up from existing knowledge (based on measurements and/or models).
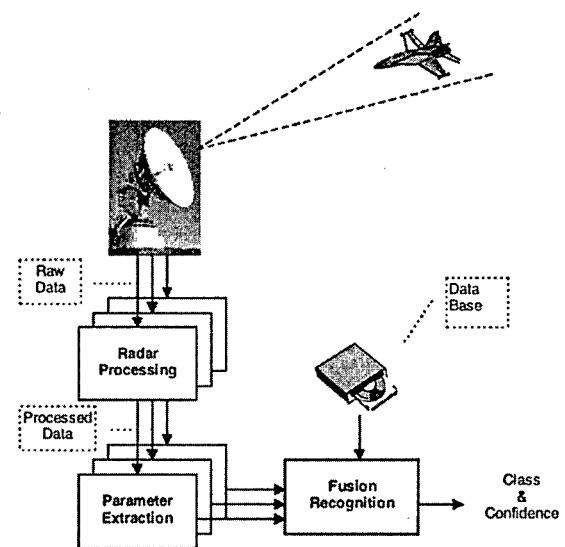
Figure 2

The performances of the NCTR function will depend on each steps :

- quality of radar measurements (resolution, measurement error, ...)
- relevance of extracted characteristic variables,
- efficient exploitation of measurement complementarities through the merging process,
- representativity of the database.

The following chapters discuss each of these steps in detail.

2.2 MEASUREMENTS AND RADAR PROCESSING

2.2.1 Kinematics

After plot extraction, an adaptive Kalman filter using a 3D state vector is able to provide the basic inputs (target

coordinates, velocity and acceleration and associated covariance matrix). From this basic inputs, discriminant parameters may be computed together with their accuracies.

2.2.2 Doppler processing

It is used to provide an estimate of the target short term spectrum which strongly depends on the fast moving parts of it (helicopter blades, jet engine rotors, propellers). The waveform parameters (PRF and duration) must be optimised in order to get the best estimate.

It may be necessary to add a rejection filter to eliminate the spurious components such as clutter which could otherwise strongly affect the spectrum and thus its analysis.

Furthermore, for moving targets, one must compensate the target velocity before extracting any spectrum parameter.

Finally one must take care of the possible spectrum foldover which may occur if the target spectrum bandwidth is larger than the PRF.

Figures 3 and 4 show respectively a typical helicopter and propeller aircraft spectrum.
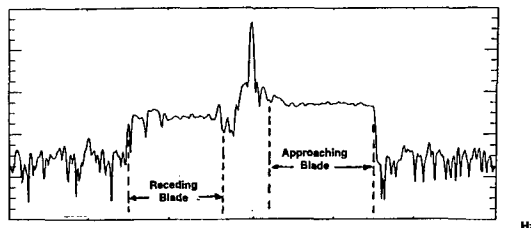
Figure 3
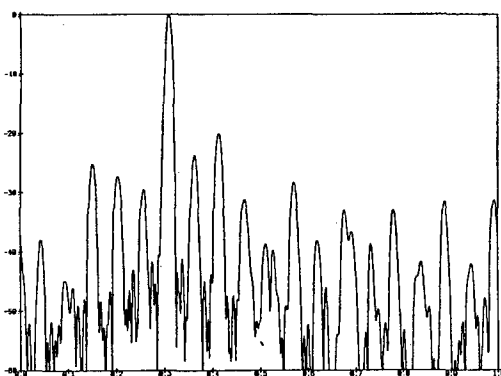
Figure 4

2.2.3 Down-Range Processing

High Range Resolution may be obtained through several radar techniques (short pulse, pulse compression, multifrequency, stepped frequency,...). If target range motion during the analysis time becomes comparable to

the desired resolution, then motion compensation is required; it can be performed with simple phase correction, but when accurate compensation is required it can be necessary to use autofocusing techniques.

Both coherent and non coherent range profiles can be generated; non coherent profiles are less informative but in general more resistant to target motion.

Doppler pre-processing may be required for removing spurious spectral components such as clutter echoes or JEM.

Figure 5 is an example of a range profile obtained with an operational S-Band Radar.
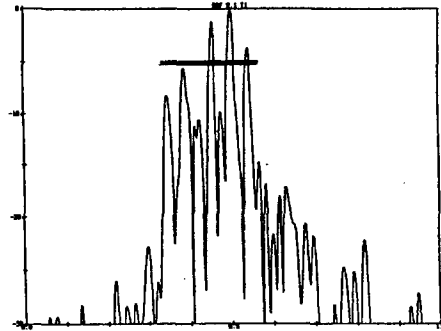
Figure 5

2.2.4 Cross-Range Processing

One-dimension target cross-range profiles (1D ISAR) may be obtained with simple fixed frequency waveforms. It is produced by the differences of radial velocities between the different target scatterers which are generated by the target rotation as seen by the radar. This effect may be due to an actual target rotation (such as roll/ pitch for a ship) and also to the variation of aspect angle which occurs during a simple translation (this is the case for an aircraft flying at a constant course on a non-radial trajectory).

Cross-range profiling is illustrated on Figure 6 obtained with the same S-band Radar as above.
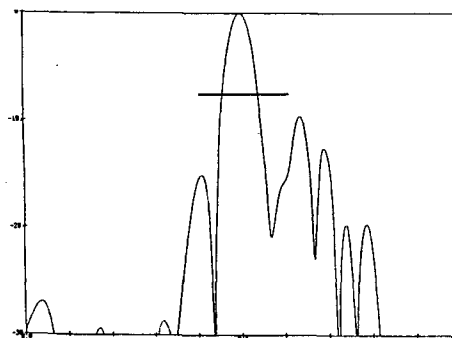
Figure 6

2.2.5 2D (nD) Processing

2D (or nD) target images can be obtained by the combination of elementary 1D processing, such as:

- Doppler and HRR which gives the target Doppler spectrum as a function of the target down-range dimension (such an image may be used to locate the mobile parts of the target); Figure 7 gives an example of such an image for a simulated helicopter,
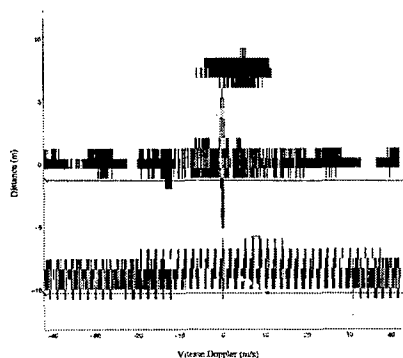
Figure 7

- ISAR and HRR which gives the distribution of target scattering centres in a 2D plane (such images are generated from holography for instance in measurement chambers); accurate target motion compensation is required for such a processing because long analysis time are often necessary. This method is illustrated on Figure 8 which shows a 2D representation of a simulated aircraft.
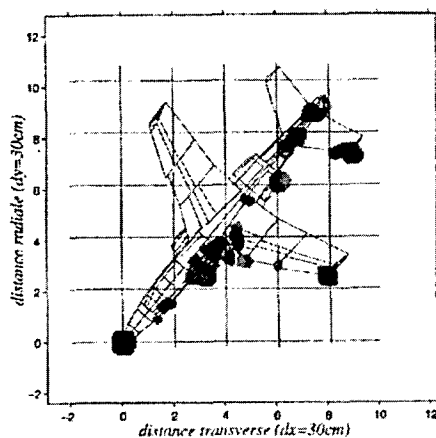
Figure 8

2.3 EXTRACTION OF CHARACTERISTIC PARAMETERS

This operation consists in keeping only relevant variables for recognition from radar measurements, through non-linear process :

- For kinematics, the variables kept are mainly the true speed vector of the target (possibly its acceleration), the position and orientation in space of the target (among others, its attitude and altitude). Indications on their uncertainty

(covariance matrix) are generally added to these values.

- For the rotating parts, two types of variables are extracted depending on the level of measurement resolution;
  * for the "coarse" level (short analysis time), the extracted variables are of the following types : spectrum width, flatness, purity, detection of isolated flashes for time processing. These information allow to decide on the existence and nature of the rotating parts (blades, propellers, jet engine)
 * for the "fine" level (long analysis time), the extracted variables are mainly the frequency or period steps. These information may allow to decide on the aircraft model in the aircraft class (Mirage, MiG, ...), or on the helicopter model in the helicopter class (Puma, Gazelle, ...)

- For the spatial structure, as for the rotating parts, two types of variables are extracted depending on the level of measurement resolution;
  * for the "coarse" level (resolution at the scale of target size), variables of the following type are extracted :
    – RCS of the target (the resolution may be much greater than the size of the target)
    – target dimensions (length, width, ...).
  * for the "fine" level (several "pixel" in the target), the measurements (responses or images) in high resolution allow the analysis of the localisation and properties of the scattering centres and diffraction edges. The characteristic variables for these measurements are less known, several are candidates :
    – the "N" first statistical moments of the spatial process (average, standard deviation,...),
    – the position (1D or 2D) of the scatterers, possibly with their associated diagram...,
    – a simple average in power of the measurements (1D or 2D) over an angular sector (typically several degrees)

Though the impact of the choice of these parameters onto the NCTR performance is still to be assessed, it is necessary to extract and to use their respective qualities (accuracies) in order to control the robustness of the decision (avoid false decisions).

Extracting and processing the quality of each parameters for target recognition is in fact equivalent to the CFAR method for target detection.

2.4 MERGING AND RECOGNITION

The merging-recognition process may be designed in two ways:

- a process of local recognition per variable, followed by a simple merging of the local recognition decisions,
- a global and complex process of merging - recognition on the whole set of variables.

The main merging techniques that can be considered are fuzzy logic, evidence theory, Bayesian inference, and expert systems. Depending on the chosen technique, the prerequisite knowledge required on the variables can vary, it may range from fine knowledge on statistical law to simple heuristic rules.

The quality of the merging process will play a very important role in the radar NCTR performances because the variables to be merged, though extracted from the same sensor, are :

- of very different nature (see Chapter 2.2), which makes the merging difficult,
- generally strongly complementary, precisely because they are very different, which makes merging more interesting in terms of performance improvement,
- of very variable quality (for example, depending on the distance of the target, of its angular presentation, of the presence of spurious signals - clutter, jamming, ...)

For example, the absence of jet engine lines alone is not strongly discriminating because even for a jet aircraft the JEM is only visible into a cone in the front view. On the other hand, the absence of jet engine lines for a fast flying incoming target indicates that it is more surely a missile than an airplane. Conversely, the presence of JEM, even without information on the target aspect angle, reveals that it is a plane.

2.5 DATABASE

2.5.1 Issue

Target recognition will be possible only with a catalogue containing the characteristics of the targets relative to the different recognition techniques.

Therefore, this database will have several inputs. Roughly, we shall have an input per recognition technique :

- Kinematics,
- Spectral analysis, coarse and fine,
- 1D or 2D spatial analysis, coarse and fine,
- Joint 1D or 2D spatial analysis and spectral analysis.

If for the attributes of the kinematics and for certain attributes of the spectral analysis the nature and structure of data are relatively simple (there are intrinsic data such as speed domain, number of blades, frequency of rotation of blades, ...), the case of attributes, relative to high 1D or 2D spatial resolution and/or associated to the spectrum, is more complex.

Indeed, in this last case, the database may simultaneously comprise intrinsic data relative to the structure of the target (length, width, ...), hybrid data (value and position of scatterers, ...), and upstream data (pulse responses or images).

An in-depth analysis, joint to the reflection on the extraction of characteristic parameters, must be made so as to define the nature of the data to be stored (reasonable memory size), and to elaborate the best possible structure for the database.

In a second step, it will be necessary to build this database. Here again, the case of the intrinsic data is relatively simple, because these ones are easily accessible (in specialised literature for example). On the opposite, the hybrid or upstream data are more difficult to obtain; they may come either from measurements, or from electromagnetic modelling.

The elaboration of the database from existing measurements poses two problems :

- completeness:
the measurements must be complete both in the number of representative targets, and also for a given target, in radar measurement parameters (sufficient frequency bandwidth, complete elevation and azimuth angular sectors, ...)

- representativity:
measurements are made in a particular context of environment, trajectory and sensor (waveform, signal/noise ratio), which must not particularise the database.

Generally, the two requirements above (completeness and representativity) are not met by existing measurements.

2.5.2 Modelling

The electromagnetic modelling of targets allows, from CAD models of the target and methods of digital computing (GO and PO asymptotic techniques, method of moments, or hybridisation techniques method), to obtain all the required radar data depending on the desired parameters (frequency, polarisation, angles, ...)

Provided that the corresponding CAD models are available, the electromagnetic modelling of targets allows to solve the completeness problem mentioned in the previous chapter.

But the problem of representativity remains, because there remains lacks in the modelling for instance for cockpits and air intakes, small details, and composite materials (helicopter blades, ULM, UAV,...). In the short term, the modelling of small air targets made up with composite materials (large glass panels, composite material, blade) does not appear to be representative enough to build up a database.

On the other hand, for airplanes, the problem of small cockpit may be addressed separately and solutions do exist to better address the air intake issue (these solutions use the method called "factorisation" which splits the object into different volumes, each one being processed by the more efficient electromagnetic. This modelling effort is planned in the MILORD project.

2.6 PERFORMANCES

The radar NCTR performances of the air targets will of course depend on the radar-target distance, and on the measurements accessible by the considered radar.

Two levels are generally distinguished :
- a level of classification of platform type,
- a level of recognition of the model in the type.

The "classification" level aims at separating targets in broad categories, it utilises rather "coarse" measurements (distance range of about a few meters, short Doppler analysis time).
If the whole set of kinematics measurements and "coarse" measurements can be obtained, six classes can be considered (not withstanding the "unknown" class corresponding to a non-decision):
- helicopter/ UAV,
- small turboprop,
- large turboprop,
- small jet,
- large jet,
- missile

The "recognition" level will define the type in the class (for example, Mirage 2000 in the "small jet" class). This level requires "fine" measurements (long Doppler analysis time, spatial resolution of about one meter, even some decimetres) -see Figure 9 below-
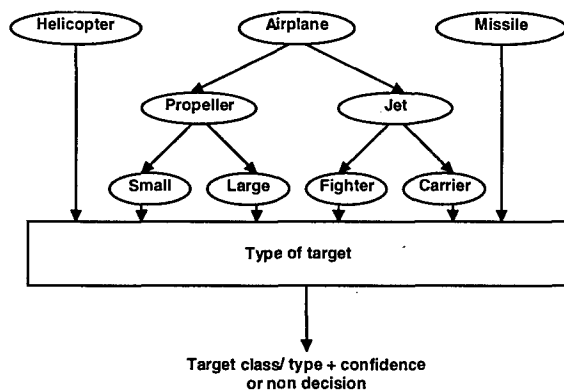
Figure 9

For each of these levels (classification and recognition of the model), one can define performance criteria in the form of probabilities :

- of good classification (recognition),
- of false classification (recognition),
- of non decision.

Some general remarks can be made on these last values:

a) for a given probability of good classification, the introduction of a "non decision" class allows a better control of the probability of false classification, which must remain small,

b) for a given range, the performances in classification are better than in recognition,

c) in order to obtain good recognition performances, the radar must be able to measure parameters whose signal/noise ratio may be lower than the one of the target cell (for example with a 5 to 10 dB loss). For the power budget the recognition range is then smaller than the detection range. However it can be improved by increasing the energy (specific waveforms).

3. MILORD

3.1 OBJECTIVE

The objective of the MILORD project is, by means of a radar sensor of sufficient performance, to be able to obtain all the relevant data for the radar NCTR function, that is :

- to go deeply into a fine NCTR algorithmic knowledge (elaboration of measurements, extraction of characteristic variables, databases, ...),
- to carry out a real-time demonstration of the NCTR function,
- to validate separately each of the techniques used, and to examine their complementarity depending on different applications (federative role),
- to assess NCTR performances (probability of good and false classification/ recognition) in real environment depending on techniques,
- to make recommendations for the implementation of a NCTR operational function for present and future radars, in the framework of various applications (multi-applicative role).

3.2 FUNCTIONAL ARCHITECTURE

Figure 10 describes the functional architecture of the recognition demonstrator, which comprises :

- a radar sensor able to transmit and receive the different waveforms required for recognition, with sufficient power level (in order to insure the signal/noise ratio),
- a recognition processor able to process the radar sensor data so as to achieve target recognition,

- a recording device allowing to store the data at different stages of the processing chain so as to build a database,
- a MMI (Man-Machine Interface) allowing to control the system and to display the results.

Figure 10

The operation of the system requires a surveillance function allowing to provide a designation to the recognition system wh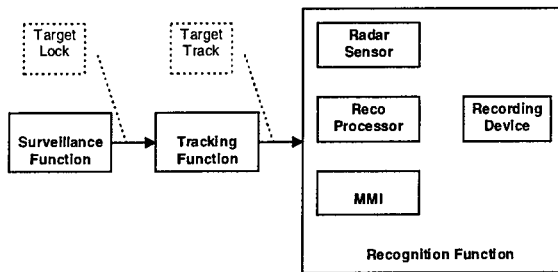ich furthermore comprises a tracking function. This tracking function is made either by inserting periodically a tracking waveform between its recognition waveforms, or by using a second radar used for trajectography and designation.

Figure 11 details the functional architecture of the recognition processor, which comprises :

- an input/output interface for the dialogue with the radar,
- a scheduler for the sequencing of the radar waveforms,
- a real time digital signal data processing for carrying out the High Resolution Range and Doppler processing,
- a recognition processing, used for extracting the attributes required for recognition, then for the carrying out of the final fusion in order to give the type of the target.
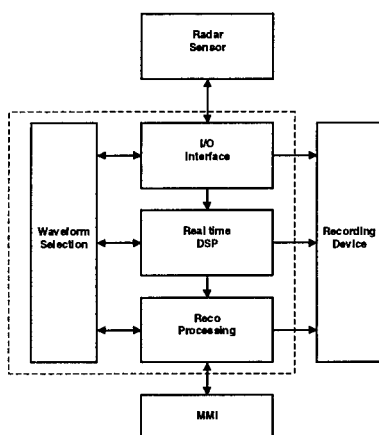
Figure 11

3.3 SPECIFICATIONS OF THE RADAR AND RECOGNITION PROCESSOR

Federative and multi-application aspect of the MILORD project puts important constraints on the radar :

- in C band operation, because its achieves a good trade-off between S band (long range air defence radars) and X band (airborne radars),
- very various waveforms capacities, especially :
  * tracking waveforms,
  * Low, Medium and High PRF (at least 40 kHz) so as to cover the different Doppler/ ISAR applications,
  * High Range Resolution waveforms (at least 300 MHz bandwidth) with different methods (chirp, stepped frequency,..) in order to compare their behaviour,
  * coherent analysis times for durations ranging from some tens of ms to several seconds (ISAR).
- for the antenna and data processing, a capacity to track the target in elevation/azimuth/range,
- a high power budget (range greater than 200 km on plane) so as to be able to test long range NCTR modes, and also to analyse the benefits for the NCTR of small scatterers or rotating parts of much lower level than the airframe one,
- a very comprehensive experiment logistic environment (mission preparation, calibration, target acquisition, communication and recording means,...), available and movable for carrying out various experiments,
- a reduced cost of the sensor so as to allocate the greatest part of the available budget to the study of the NCTR function itself.

For the recognition processor, two parts can be distinguished :

- the hardware and software tools which, from recorded data, allow, in non real time mode, the analysis and improvement of processing, along with the assessment of performances.
- the hardware and software tools which allow in real time on the site to insure the validity of the recorded measurements and to carry out a convincing demonstration of the recognition capacities.

For the recognition processor the "digital signal processing" part (pulse compression, coherent processing,...) is made in real time (at radar time scale), on the other hand the recognition processing part (extraction of characteristic variables, fusion, ...) can be made in quasi-real time (at the time scale of some seconds) without affecting the demonstrative aspect.

3.4 PHYSICAL DESCRIPTION

Within the framework of the MILORD project, the chosen approach is to use existing equipment as far as

possible, provided they meet the specifications presented in Chapter 3.3.

3.4.1 Radar

The ARMOR onboard the BEM (Bâtiment d'Essais et de Mesures) MONGE is the only radar that meets all the specifications at the price of minor modifications. Furthermore, the integration of the recognition processor in the sensor requires only software modifications of the time management and display console of the ARMOR.

ARMOR (see Figure 12) is a very long range tracking radar used for restoring target trajectories for test ranges applications. Its large instantaneous bandwidth is used to perform off-line analysis of target radar cross section. Multiple receiving channels allow Co and Cross polarisation analysis.

Figure 12

It uses a high gain C-Band monopulse antenna with a 10m diameter Cassegrain reflector. The transmitter has a first wideband TWT stage and a final high power Klystron (this last stage will not be required for the purpose of MILORD).

Various High Range and/or Doppler Resolution waveforms can be generated through the wideband channel, which is used for the measurement function:
- VHR [stretch waveform (ramp mode) using a long FM pulse], Low PRF
- HR [pulse compression], High PRF
- HR [short pulse], Very High PRF

For MILORD on plans to yet improve the current VHR waveform by using a multiple ramp mode.

Other waveforms can be generated through the narrowband channel, which is mainly used for the tracking function. For the purpose of MILORD it is planned to modify the frequency synthesiser in order to generate Stepped Frequency Waveforms for Synthetic Range Profiling through the existing narrowband channel.

The radar stability is compatible with ISAR processing; this characteristic has already been used to provide high resolution 2D images of distant targets.

The two ARMOR radars installed on the MONGE are interconnected with other onboard sensors (instrumentation radars SAVOIE and GASCOGNE, telemetry and optical means,..) -see Figure 13-.
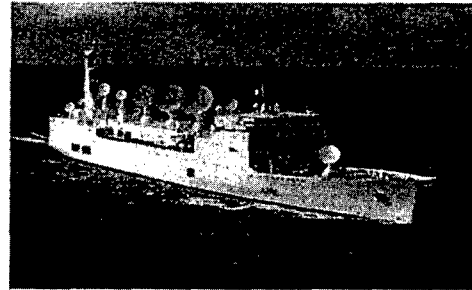
Figure 13

3.4.2 Recognition Processor

For the recognition processor, the digital signal processing part is made by existing boards based on DSP, the recognition processing part along with the MMI are carried out by a standard workstation. The recording means are dimensioned to record at least 30 mn of continuous measurements, that is a capacity of several Gb.

3.5 PROJECT SCHEDULE

The project extends over 4 years in four main phases :

- a definition study for defining the NCTR requirement objectives, the waveforms and modifications to carry out on the ARMOR, the recognition algorithms and the recognition processor,
- a realisation and integration phase,
- a "technical" trial phase for validating the overall performances of the radar, testing and tuning the NCTR processing, and for recording target signatures (of at least 8 different types),
- a "final" trial phase for completing the recorded signatures, demonstrating the recognition capacities in quasi real time, assessing the recognition performances with respect to the different analysis modes, and finally for extrapolating the previous results for the different applications, and bringing out recommendations for the implementation of a NCTR operational function.

4. ACKNOWLEDGEMENTS

POLARIMETRY - FOR THE FULL STORY

E. Krogager

Danish Defence Research Establishment
Ryvangs Allé 1, DK-2100 Copenhagen, Denmark
T: +45 39151736 F: +45 39291533 E-mail: ek@ddre.dk

1. SUMMARY

This paper is dealing with one of the special topics which have become important in modern radar, namely, polarimetric imaging techniques [1]. Although the fundamental capabilities of polarimetric radar, that is, radar utilizing the polarization of the transmitted and received waves, have been known since the early days of radar back in the fifties, it is only in recent years that such techniques have actually been implemented for practical utilization. There are a variety of reasons for that, some major reasons being the cost and complexity of polarimetric radars, and an apparent lack of appreciation of what polarization can actually be used for. Not least within the NATO community, as regards operational systems, the utilization of information carried with the polarization of electromagnetic waves, is virtually nonexistent. A main purpose of this paper is to try to point to the necessity of utilizing polarimetric information in order to optimize the use of radar for military as well as civilian applications.

2. TRADITIONAL RADAR IMAGING

Traditional radar may largely be understood in terms of amplitudes and phases of the involved plane waves which in the simplest form are just continuous waveforms. The parameters that can be measured with such a radar are the amplitude and the phase and/or frequency of the wave reflected from the target, relative to the amplitude and phase of the wave transmitted towards the target. For a moving target, the frequency of the reflected wave will be shifted according to the Doppler-effect, and the velocity of the target can thus be determined from the Doppler-shift. In more sophisticated systems, high resolution of Doppler-shift and high resolution of range propagation delay can be obtained by the use of long observation times and wide frequency bandwidths, respectively. Thus, if the target is rotating, as it effectively is when moving in such a way as to change aspect relative to the radar, then the different parts of the target will produce (slightly) different Doppler-shifts which form the basis for high resolution SAR and ISAR, where SAR stands for Synthetic Aperture Radar, referring to the fact that the technique may also be considered as one of synthesizing a very long array antenna by taking data samples corresponding to each element of the array. High Doppler-resolution, obtained by long observation times (in the order of 1-10 seconds), may thus be used to produce a one-dimensional signature of the target. Somehow similarly, a high range resolution profile of the target can be produced by illuminating the target with a waveform consisting of very narrow pulses, which is equivalent to using signals with frequency components within a quite wide bandwidth.

3. VECTOR FIELDS

When dealing with traditional single polarization data we look at the signals only in a scalar, i.e., an amplitude and phase description. However, as the electromagnetic field is by nature a vector field, this description is incomplete, even very incomplete. An electromagnetic field must be regarded in terms of two orthogonal components, e.g., linear basis components Horizontal and Vertical. The field may be thought of as being generated by transmitting a signal simultaneously via two different paths: One via a horizontally polarized antenna, another via a vertically polarized antenna, and with a certain amplitude and phase difference between the two components. The resulting total electric field is then described by a vector, i.e., direction and amplitude, which in general traces an ellipse as a function of time, or as a function of distance along the direction of propagation. Two main parameters characterizing the polarization ellipse are: 1. The orientation angle, θ, of the main axis of the ellipse relative to the first axis, the x-axis, of the reference basis, and 2. The ellipticity angle, τ. Two particularly important special cases are: 1. Linear polarization, for which τ is zero, and 2. Circular polarization, for which τ equals $\pm 45°$.

4. TRANSMIT/RECEIVE COMBINATIONS

Since both the transmitted and the received polarization states can thus be resolved into two mutually orthogonal polarization states, there are four combinations of transmit and receive polarizations that need to be measured in order to aquire the full amount of polarimetric target information for a given radar system. The four possible combinations are usually represented in the form of a 2x2 target scattering matrix with complex elements, i.e., each element has associated with it an amplitude and a phase. A main point here is, that no matter which particular polarization is transmitted towards a given target, the polarization of the reflected wave will in general be elliptically polarized. This means that when we use a radar which has the same, fixed polarization for transmission and reception, we will only measure a fraction of the potentially available information contained in the reflected signal, i.e., we will only measure one of the elements of the scattering matrix. Not least in military applications, this could mean a critical lack of information which could otherwise be available.

5. POLARIMETRIC CHARACTERISTICS OF ELEMENTARY SCATTERERS

To illustrate the basic power of polarimetry, Fig. 1 shows the scattering matrices for some important elementary scatterers. To the upper left, we have shown the so-called voltage equation for a polarimetric radar. This equation states the voltage at the output of the receiver for a given radar with the following key parameters: A given transmit polarization, characterized by the polarization vector, $\bar{p}_T$; a given receive polarization vector, characterized by the polarization vector, $\bar{p}_R$, and a given target scattering matrix, [S]. The propagation factor and some other system parameters can be ignored for the present discussion. By measuring the received voltage for the four combinations of transmit and receive polarization, we can thus measure the target scattering matrix. It is noted in passing, that for

monostatic radars with co-located transmit and receive antennas, the two off-diagonal terms, in this case, HV and VH, are normally identical, i.e., the scattering matrix is symmetrical, which of course simplifies matters considerably. Now, starting with the sphere, it has the identity matrix as its characteristic scattering matrix, with equal responses for HH and VV polarizations. This matrix is characteristic for any odd-bounce scatterer, like plates and tri-hedrals, i.e., three-sided corner reflectors. Next, the dipole has this characteristic scattering matrix which contains the orientation angle, θ, of the dipole around the line of sight, which means that this angle can actually be measured with a polarimetric radar. For this type of target, it makes a great deal of difference, whether HH or VV polarizations are used, while a polarimetric radar will always measure the same total power, independent of whether linear, circular, or any other reference polarizations are used. The diplane, i.e., the two-sided corner reflector, shown to the lower left, also contains the orientation angle around line of sight, and we note for this type of target a characteristic phase difference between the two co-polar responses, which is characteristic for any even-bounce reflector. We further note, that the combined response from a sphere plus a diplane yields the response from a dipole, which means that for more general, complex targets we must expect to see significant differences between the single polarization HH and VV components. The helix is shown here as a more peculiar type of target with the characteristics that it transforms incident linear polarization to reflected circular polarization. However, although the helix is a somehow artificial target, it should be observed that the helix scattering matrix can also be produced by two diplanes with a relative orientation of 45° and a relative displacement along line of sight of 1/8 wavelength. This means that for practical targets with two or several double-bounce scatterers in a resolution cell, helix-like scattering may also be found. It should be quite clear at this point, that a polarimetric radar is able to measure a great deal of target characteristics that would never be revealed by a single polarization radar. The single polarization radar may even happen to get zero or near zero response from a target which otherwise has a significant effective radar cross section.

6. COMBINED SCATTERING FROM SPHERE AND DIPLANE
The ability of a polarimetric radar to distinguish scatterers of different nature may be seen by considering the combined scattering from a sphere and a diplane. The combined response from a sphere and a (non-rotated) diplane with a certain range displacement relative to the sphere can be represented by the linear basis scattering matrix,

$$[S] = \frac{1}{2}\begin{bmatrix} a+b\,e^{-j2k\Delta r} & 0 \\ 0 & a-b\,e^{-j2k\Delta r} \end{bmatrix}$$

where a represents the sphere contribution, and b represents the diplane contribution. From this scattering matrix one can readily see that the two different scatterers can be completely separated, even if they are both located within the same resolution cell. Thus, by adding the HH and VV terms, the sphere (in general odd-bounce) contribution may be determined, while the diplane (in general even-bounce) contribution results from taking the difference between HH and VV. This property of fully polarimetric data is very important, because it reveals a way to separate - or decompose - scattering contributions of different nature. While even-bounce and odd-bounce contributions interfere in single polarization radar data, they

may be completely isolated by a polarimetric radar. The advantage of utilizing this property seems quite evident, not only for interpretation and classification of radar imagery, but also for the pre-processing of such data. Motion compensation for ISAR imaging of moving targets, for example, relies on estimating as accurately as possible the phase history of one or more reference points. The accuracy of such reference phase histories should be significantly improved by avoiding interference problems of the above nature.

7. FEATURE EXTRACTION
In relation to target identification problems, the issue of feature extraction is an important one, since any classification procedure relies on the selection of features that characterize the target. With single polarization data, only rather simple and rather arbitrary amplitude and phase related features can be extracted, and simple geometrical information, like overall size and relative position of distinct scattering contributions, can be estimated. However, with fully polarimetric data, much more well-defined and robust amplitude and phase related features can be extracted, related to physical scattering mechanisms and target orientation. Further, more detailed geometrical information, like type and orientation of distinct scatterers, can be estimated.

8. SPHERE, DIPLANE, HELIX DECOMPOSITION
The scattering matrix thus represents all the target characteristic information, and there are a wide variety of methods available for dealing with this information. We have already touched on the concept of decomposition in relation to separating even- and odd-bounce scatterers, as one example of polarimetric processing. Typical techniques deal with polarimetric data in terms of target characteristic parameters, scattering mechanisms, optimum polarizations, and so on. A recent review of target decomposition theorems in radar polarimetry may be found in [2]. Here, we shall confine ourselves to a particular decomposition method that was introduced by the author about eight years ago, based on the observation that any general scattering matrix can be resolved into the three elementary target components [3],[4],[5]: A sphere, a diplane, and a helix with some proper phase relations between them:

$$[S] = e^{j\varphi}\{e^{j\varphi_s} k_s [S]_{sphere}$$
$$+ k_d [S]_{diplane(\theta)} + k_h [S]_{helix(\theta)}\}$$

where

$$[S]_{sphere} = \begin{bmatrix} 1 & 0 \\ 0 & 1 \end{bmatrix}$$

$$[S]_{diplane(\theta)} = \begin{bmatrix} \cos2\theta & \sin2\theta \\ \sin2\theta & -\cos2\theta \end{bmatrix}$$

$$[S]_{helix(\theta)} = \frac{1}{2}e^{\mp j2\theta}\begin{bmatrix} 1 & \pm j \\ \pm j & -1 \end{bmatrix}$$

9. RESPONSES IN CIRCULAR BASIS
The relation between the sphere, diplane, helix decomposition and the actual scattering mechanisms, i.e., the actual physics, is particularly clear when considering the responses from these targets in a circular basis, as shown in this Table 1.

Table 1

	LL	RR	LR
Sphere	NO	NO	YES
Diplane	YES	YES	NO
Right helix	YES	NO	NO
Left helix	NO	YES	NO

Thus, the sphere is visible with the LR (or RL) term, but not with the two co-polar terms, while the opposite is the case for the diplane. A helix is visible with either the LL or the RR combination, depending on whether it is of right or left sense. Hence, the diplane component is represented by either the LL or the RR component, depending on whether the helix is of left or right sense, while the helix component is obtained as the difference between the magnitudes of the LL and RR elements. Therefore, this decomposition can be measured directly in the circular basis, independent of the incidental overall orientation angle of the target around the line of sight.

10. PARAMETERS OF ROLL INVARIANT SPHERE, DIPLANE, HELIX DECOMPOSITION

The relations between the components of the decomposition and the elements of the scattering matrix in a circular basis, mentioned above, are given as

$$k_s = |S_{RL}|$$

$$k_d^+ = |S_{LL}| \ ; \quad k_d^- = |S_{RR}|$$

$$k_h^+ = |S_{RR}| - |S_{LL}| \ ; \quad k_h^- = |S_{LL}| - |S_{RR}|$$

$$\varphi = \frac{1}{2}(\varphi_{RR} + \varphi_{LL} - \pi)$$

$$\theta = \frac{1}{4}(\varphi_{RR} - \varphi_{LL} + \pi)$$

$$\varphi_s = \varphi_{RL} - \frac{1}{2}(\varphi_{RR} + \varphi_{LL})$$

11. TRANSFORMATION FROM LINEAR TO CIRCULAR BASIS

Often, measurements are carried out using linearly polarized antennas, but transformation to the circular basis is quite simple,

$$S_{RR} = j S_{HV} + \frac{1}{2}(S_{HH} - S_{VV})$$

$$S_{LL} = j S_{HV} - \frac{1}{2}(S_{HH} - S_{VV})$$

$$S_{RL} = \frac{j}{2}(S_{HH} + S_{VV})$$

whereby quantities measured in the linear basis may be easily related to the sphere, diplane, helix decomposition.

More generally, once a full scattering matrix is given in one basis, it can be readily transformed to any other general elliptical basis. Thus, one can synthesize what the response would be using any other transmit and receive polarizations. With single polarization data, this would of course be impossible.

12. RGB COLOR MODULATION FOR VARIOUS DECOMPOSITIONS

To look at some actual applications of polarimetric techniques to high resolution imaging data, we shall consider some color images generated from an RGB color process, where three different component magnitudes are used to modulate each of the fundamental colors, red, green, and blue.

Table 2

	Red	Green	Blue
LIN	HV	HH	VV
CIRC	RL	RR	LL
SDH	k_s	k_d	k_h
SIGHEL	left k_h	right k_h	-

Four different types of modulation are shown Table 2. 1. LIN, obtained by using directly the magnitudes of the elements of the scattering matrix in the linear basis. 2. CIRC, similar to LIN, but in the circular basis. 3. SDH, the sphere, diplane, helix decomposition. 4. SIGHEL, where the sense of the helix component of SDH is considered. The latter is relevant, because it is interesting to see whether the sense of the helix component varies mostly randomly, or whether there are some more systematic, consistent variations between right and left sense.

13. MODEL TARGET FOR 2-D POL-ISAR SIMULATION

First, we shall consider some simulated polarimetric ISAR data, on which the decomposition technique was first tested during a stay at Georgia Tech Research Institute (GTRI) in 1990. For this purpose, a model target was defined as shown in Fig. 2, composed of a number of different single scatterers: spheres of different magnitudes, diplanes of different orientation angles, trihedrals of different orientation angles, and also some pairs of dihedrals to check the appearance of helix-like scattering. The socalled TRACK model of GTRI was used for computing data simulating measurements on a rotating platform.

Examples of the polarimetric images generated from the simulated data are shown in Fig. 3. Each of the single polarization images reveal only part of the total information available. The so-called maxpol image, on the other hand, reveals for each pixel the effective intensity. This parameter represents the maximum value of radar cross section that would be measured, if the optimum radar polarization had been used for each individual pixel. However, the maxpol image still doesn't reveal any phase or scattering mechanism related information. Such information appears from the decomposition components, and in particular the color-composite of all three components is a very useful representation of the data in just one image. It should be noted though, that only three out of the five available parameters are represented in such an image.

14. APPLICATION TO POLARIMETRIC SAR DATA

The data used for the results presented with this paper have been acquired with the Danish polarimetric SAR system which has been developed at the Electromagnetics Institute (EMI), Technical University of Denmark (TUD) [6],[7],[8]. This system, EMISAR, now makes up the key instrument for research at the Danish Center for Remote Sensing (DCRS) which was established at EMI in 1994.

The system, originally a C-band single polarization system, was upgraded to full polarimetric capability in 1993, and the performance has been demonstrated through numerous measurement campaigns. A remarkable feature of this civilian radar is its high resolution of 2 m in both range and cross-range together with the full-polarimetric, wide-swath capability, which makes it a powerful tool for many demanding applications, including classification and identification of natural and man-made targets.

A fully polarimetric L-band channel was added to the EMISAR system in 1995, and successfully tested during several missions in 1995. This has added significantly to the capabilities and the utility of the system, because the polarimetric scattering characteristics of a target are in general highly wavelength dependent [9].

Also, interferometric modes are presently implemented. A repeat-track mode in which the radar steers the aircraft enables the aircraft to fly a desired track with meter accuracy, and additional antennas are installed to provide for single pass across-track interferometry [10].

An important issue in connection with the use of fully polarimetric data is the quality of system calibration, since a correct interpretation of relative phases and amplitudes of the scattering matrix can only be made with a sufficiently accurate calibration. To ensure this, the present system accommodates unique features for internal calibration and for ensuring system stability. External calibration is carried out just before and after a mapping sequence, and calibration reflectors as well as distributed targets may be used to verify and improve the calibration [11].

The three sets of color-modulation parameters, denoted in Table 2 as LIN, CIRC, and SDH, all represent useful information for discrimination and contrast improvement in high resolution polarimetric SAR imaging. The ability of LIN to distinguish targets with predominant HH, HV, or VV returns provides an efficient way of revealing target characteristics which favor the generation (scattering) of a specific linear polarization, related to target geometry. On the other hand, the parameters of LIN are not directly related to a specific scattering mechanism, as are the parameters of SDH. For example, a horizontal or a vertical diplane (commonly found in areas with man-made targets) produces HH and VV components of equal magnitudes, which is also the case for an odd-bounce target like a sphere, a plate, or a trihedral. Hence, LIN will not discriminate between these two otherwise very different types of targets. To separate these targets, LIN must be used in conjunction with for example a plot of the phase difference between HH and VV. In the decomposition, this is already accomplished because the parameters of the decomposition incorporate the phases as well as the amplitudes of the elements of the linear basis matrix. The orientation angle, however, is hidden in the other two parameters in this approach and would have to be displayed in a different type of image.

It should be noted that only the three component magnitudes are used in these images. Additional information is actually present in the polarimetric data in the form of parameters like phases and orientation angles. For example, the phase difference between HH and VV returns may be utilized to generate images where certain types of scatterers stand out. Thus, a sphere has no phase difference between HH- and VV-components, while a diplane has a phase difference of π between these components.

The method denoted SIGHEL (signed helicity) aims at separating the helix-component of the sphere, diplane, helix decomposition into the two categories: left and right sense. Thereby it becomes possible to investigate the distribution between left and right sense of the helix-component. For distributed, natural targets with azimuthal symmetry, the correlation between co- and cross-polarized components in the linear basis is usually assumed to be zero, and helicity might be expected to be evenly distributed between left and right sense in such areas. However, it has been found that certain types of targets exhibit consistently one dominating sense of helicity, depending on carrier wavelength. This observation has for instance been made in agricultural areas, and is likely to be related to the fact that various crop types have distinct preferences and characteristics with regards to twine and composition [12],[13]. However, further investigations based on detailed ground truth studies is required before firm conclusions can be reached.

In order to keep this paper in grayscale print, examples of the images discussed above are included on the last pages in the form of a black and white print of an rgb image as well as the corresponding separated red, green, and blue component images. Although they do not provide the same overview of the data as a one-page color-composite image would do, some of the features provided by polarimetric processing are clearly seen. The scene is from the agricultural research center at Foulum, Denmark, with the research center located in the lower left corner of the images, and a variety of farm fields, woods, etc. are seen around the center.

15. IMPROVEMENT OF SAR AND ISAR IMAGES BY THE USE OF POLARIMETRIC DATA

Several problems are still identified in connection with the SAR and ISAR (Inverse SAR) imaging technique for general non-cooperative targets and scenarios. Two key elements of the ISAR principle are a motion compensation and a rotation compensation which are required to obtain a sufficiently high cross-range resolution. Both of these pose a major problem because the phase information required for carrying out these compensations is difficult to establish with sufficient reliability.

It is of interest to consider whether the use of fully polarimetric data could be advantageous in this connection. In the light of the decomposition of the scattering matrix presented above, it is apparent that the chance of localizing suited individual scatterers would increase significantly if fully polarimetric data were available for each resolution cell. Thus, instead of just searching for a resolution cell with a strong scatterer, one could then search for a resolution cell with a pure type of scattering, either of the odd-bounce or the even-bounce type. If such a resolution cell can be found, chances are much better that the corresponding back-scattering is due to a distinct single scatterer, which is required in order to obtain a well suited phase history for motion compensation. Similar considerations can be applied to the other data corrections that were mentioned above.

Although two-dimensional imaging of course provides a much better visualization of the radar reflectivity distribution of a

given target, there may be situations where it is only practical to implement either the cross-range resolution or the range resolution. The first requires only a CW radar while the latter avoids the long integration times. In such cases, polarization makes up a useful option for extending the capability of a given system so as to provide as much information about the target as possible.

16. CONCLUSIONS

The power of polarimetry in relation to high resolution radar applications were pointed out, followed by a presentation of a special three-component decomposition of the scattering matrix. By decomposing the scattering matrix into different components, it is possible to resolve different types of scatterers even if they are within the same resolution cell of the image. This allows for a better resolution of the target scattering properties as well as a better characterization of the type of scattering for the individual contributions. The usefulness of fully polarimetric data in connection with radar target imaging and identification was demonstrated by applying polarimetric techniques to fully polarimetric, well calibrated EMISAR data. The components of the decomposition may be imaged separately, and in combination by utilizing the three components to modulate a color-mixing process. Both representations are found to be powerful tools for handling and interpreting polarimetric imaging data. A particularly troublesome problem associated with dynamic radar imaging is the various phase compensations that must be carried out before the desired images are obtained. It was pointed out that polarimetric data should be used in such procedures and should be expected to greatly enhance this part of the processing, in addition to providing a lot of extra target related information as compared with single polarization data. Hence, fully polarimetric data should be expected to greatly improve the possibility of successful radar target discrimination in a wide variety of applications.

17. ACKNOWLEDGMENTS

18. REFERENCES

1. Boerner, W.-M., et al. eds., Inverse Methods in Electromagnetic Imaging Polarimetry, Proc. NATO-ARW-DIMRP (W.-M. Boerner, Director), 1988 Sept. 18-24, Bad Windsheim, FRG, NATO-ASI-Series C, (Math. & Phys. Sci.), Vol. 350, Part I (pp. 1-1064) and II (pp. 1065-1938), D. Reidel Publ. Co., Dordrecht/Boston, 1992.

2. Cloude, S.R., and E. Pottier, "A Review of Target Decomposition Theorems in Radar Polarimetry", *IEEE Transactions on Geoscience and Remote Sensing*, 34, 2, 498-518, Mar. 1996.

3. Krogager, E., *Aspects of Polarimetric Radar Imaging*, Doctoral Thesis, Technical University of Denmark, May 1993 (Danish Defence Research Establishment, P.O.Box 2715, DK-2100 Copenhagen, Denmark).

4. Czyż, Z.H., "Alternative Approaches to Polarimetric Signal and Image Processing", *Proc. 1994 Progress in Electromagnetics Research Symposium, PIERS'94*,

5. Krogager, E. and Z.H. Czyż, "Properties of the Sphere, Diplane, Helix Decomposition", *Proc. Journées Internationales de la Polarimétrie Radar*, JIPR'95, pp. 106-114, Nantes, France, 21-23 Mar., 1995.

6. Madsen, S.N., E.L. Christensen, N. Skou, and J. Dall, "The Danish SAR System: Design and Initial Tests", *IEEE Transactions on Geoscience and Remote Sensing*, 29, 3, 417-426, May 1991.

7. Christensen, E.L., S.N. Madsen, J. Dall, N. Skou, J.H. Jørgensen, K. Woelders, A. Netterstrøm, J. Granholm, and M. Dich, "The Danish Polarimetric SAR for Remote Sensing Applications", *Proc. IGARSS'94, 1994 International Geoscience and Remote Sensing Symposium*, pp. 1361-1364, Pasadena, CA, USA, 8-12 Aug., 1994.

8. Skou, N., J. Dall, S.N. Madsen, E.L. Christensen, K. Woelders, A. Netterstrøm, and J.H. Jørgensen, "EMISAR: An Airborne L & C-Band Polarimetric SAR for Future European Campaigns", *First International Airborne Remote Sensing Conference and Exhibition*, pp. III-711-722, Strasbourg, France, 11-15 Sep., 1994.

9. Freeman, A., "Classification of Multi-frequency, Multi-temporal Polarimetric SAR Images of Natural Vegetation", *Journées Internationales de la Polarimétrie Radar*, JIPR'92, Nantes, France, 8-11 Sep., 1992.

10. S.N. Madsen, N. Schou, J. Granholm, K. Woelders, and E. Lintz Christensen, "A System for Airborne SAR Interferometry", *European Conference on Synthetic Aperture Radar, EUSAR'96*, Königswinter, Germany, 171-176, Mar. 1996.

11. Skriver, H., J. Dall, and S.N. Madsen, "External Calibration of the Danish Polarimetric C-Band SAR", *Proc. IGARSS'94, 1994 International Geoscience and Remote Sensing Symposium*, Pasadena, CA, USA, 8-12 Aug., 1994.

12. Krogager, E. and S.N. Madsen, "Comparison of Various Decompositions for Analysis, Interpretation, and Classification of Polarimetric SAR Images", *European Conference on Synthetic Aperture Radar, EUSAR'96*, Königswinter, Germany, 105-108, Mar. 1996.

13. Krogager, E. and W.M. Boerner, "On the Importance of Utilizing Polarimetric Information in Radar Imaging and Classification", AGARD Conference Proceedings CP 582, pp.17-1 - 17-12, AGARD Symposium: Remote Sensing - A Valuable Source of Information, Toulouse, FRANCE, 22-25 April, 1996.

European Space Agency, Noordwijk, The Netherlands, Jul. 11–15, 1994.

$$V_r = A\,e^{j\varphi}\,\vec{p}_R^*\,[S]^*\,\vec{p}_T^*\,\frac{e^{-j2kr_0}}{4\pi r_0^2}$$

$$[S] = \begin{bmatrix} S_{11} & S_{12} \\ S_{21} & S_{22} \end{bmatrix}$$
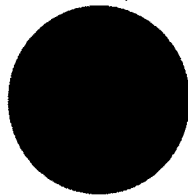
$$[S]_{sphere} = \begin{bmatrix} 1 & 0 \\ 0 & 1 \end{bmatrix}$$

$$[S]_{wire} = \begin{bmatrix} \cos^2\theta & \frac{1}{2}\sin 2\theta \\ \frac{1}{2}\sin 2\theta & \sin^2\theta \end{bmatrix}$$
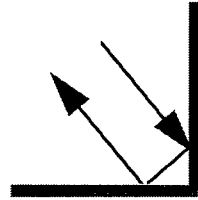
$$[S]_{diplane} = \begin{bmatrix} \cos 2\theta & \sin 2\theta \\ \sin 2\theta & -\cos 2\theta \end{bmatrix}$$

$$[S]_{helix} = \frac{1}{2}\begin{bmatrix} 1 & \pm j \\ \pm j & -1 \end{bmatrix}$$
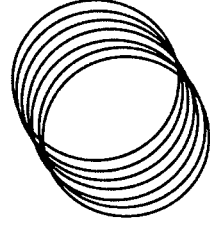
Figure 1 Voltage equation and scattering characteristics of some elementary scatterers

Figure 2 Definition of target model
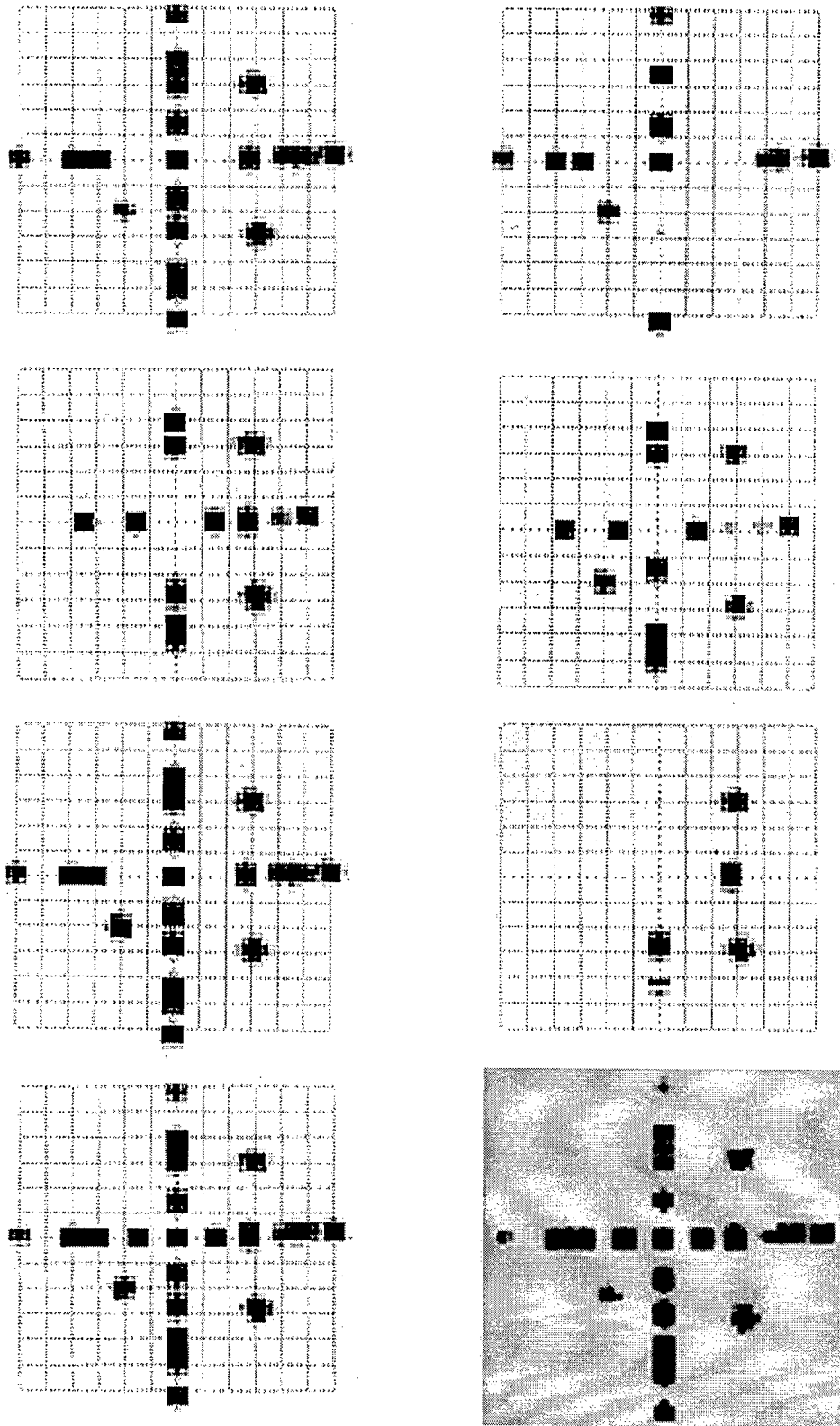
Images of model target. Left: HH, HV, VV, maxpol. Right: k_s, k_d, k_h, colmix.

Figure 3 Images of model target in Fig. 1. Left column from top: HH, HV, VV, maxpol.
Right column from top: k_s, k_d, k_h, colmix.

Foulum, Jutland, Denmark

Polarimetric SAR Images

Acquired:	June 8, 1995	
Processed:	June 20, 1995	
Latitude, center:	N 56°30.5'	
Longitude, center:	E 9°35.6'	

Platform:	RDAF, Gulfstream G-3	
Altitude:	12497	
Frequency:	1.25 GHz	
Incidence angle:	36.3° to 57.2°	

DCRS, Electromagnetics Institute, Technical University of Denmark
Danish Defence Research Establishment
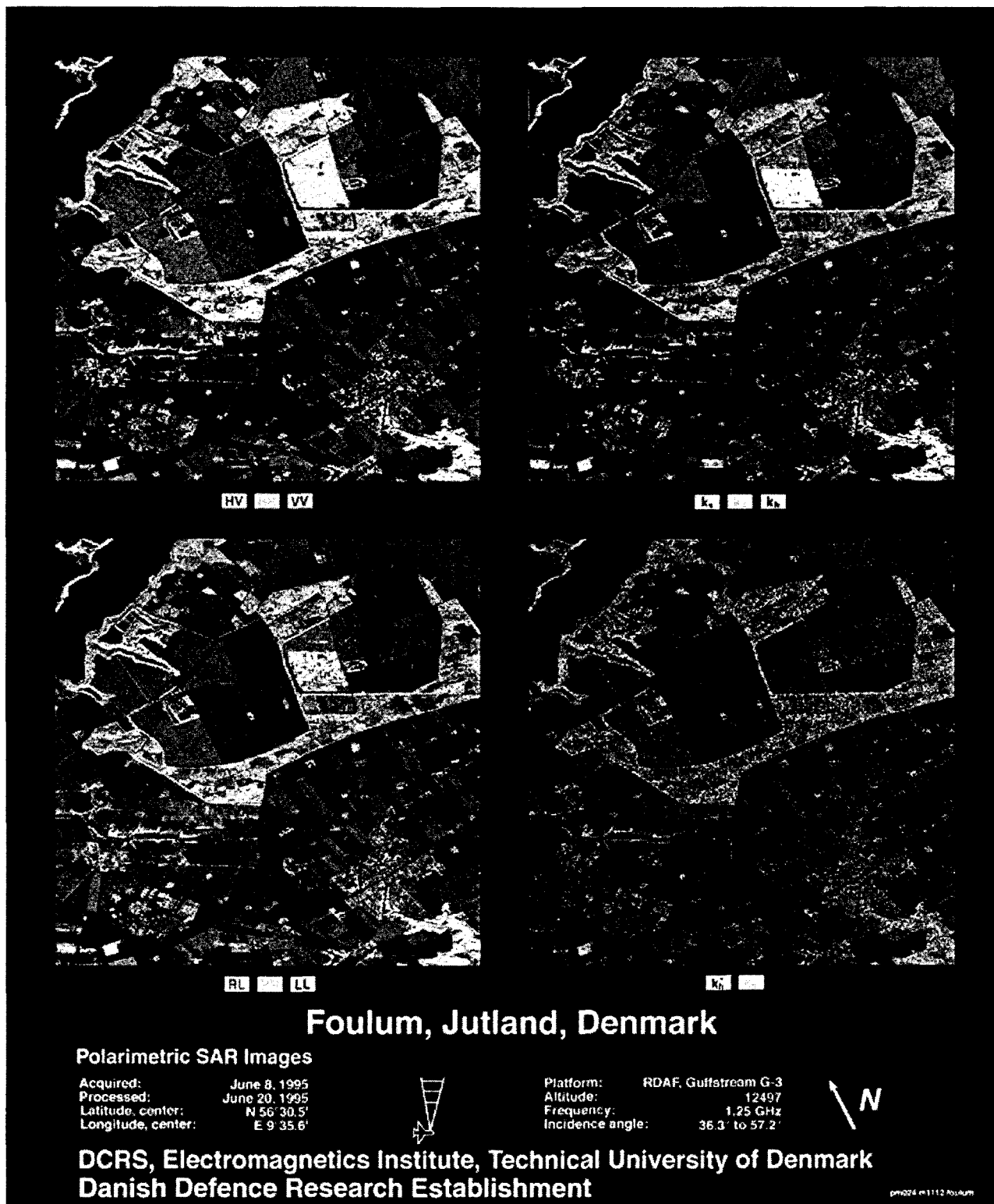
Figure 4. Grayscale print of example of color composite images according to Table 2.

Foulum, Jutland, Denmark

Polarimetric SAR Images

Acquired:	June 8, 1995	Platform:	RDAF, Gulfstream G 3
Processed:	June 20, 1995	Altitude:	12497
Latitude, center:	N 56 30.5'	Frequency:	1.25 GHz
Longitude, center:	E 9 35.6'	Incidence angle:	36.3° to 57.2

DCRS, Electromagnetics Institute, Technical University of Denmark
Danish Defence Research Establishment

Figure 5. Red channel of Figure 4.

Foulum, Jutland, Denmark

Polarimetric SAR Images

Acquired:	June 8, 1995
Processed:	June 20, 1995
Latitude, center:	N 56 30.5'
Longitude, center:	E 9 35.6'

Platform:	RDAF, Gulfstream G-3
Altitude:	12497
Frequency:	1.25 GHz
Incidence angle:	36.3 to 57.2

DCRS, Electromagnetics Institute, Technical University of Denmark
Danish Defence Research Establishment

Figure 6. Green channel of Figure 4.

Figure 7. Blue channel of Figure 4.

ISAR Image Interpretation

Peter N.R. Stoyle
Defence & Evaluation Research Agency (DERA)
St Andrews Road, MALVERN, Worcs WR14 3PS, U.K.
Tel: (44) 1684 894900 , Fax: (44) 1684 894504, Email: pnstoyle@dera.gov.uk

1. SUMMARY

This paper represents an early stage of the author's research into the Interpretation of ISAR. Necessarily Interpretation must proceed from an EM scattering theory viewpoint. As the author's past experience has not been in electromagnetics, the treatment at this stage is far from deep or comprehensive, but nonetheless attempts to surv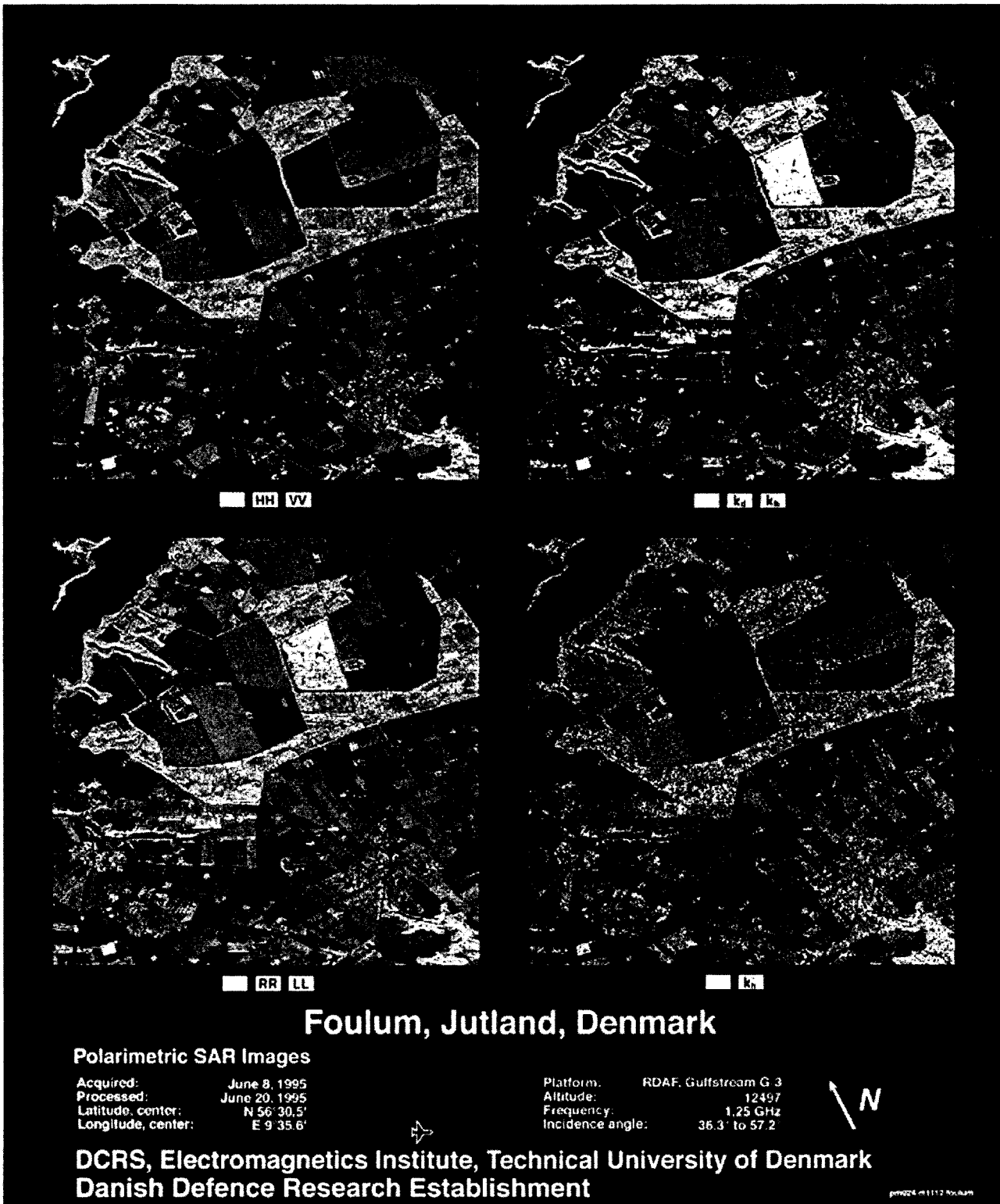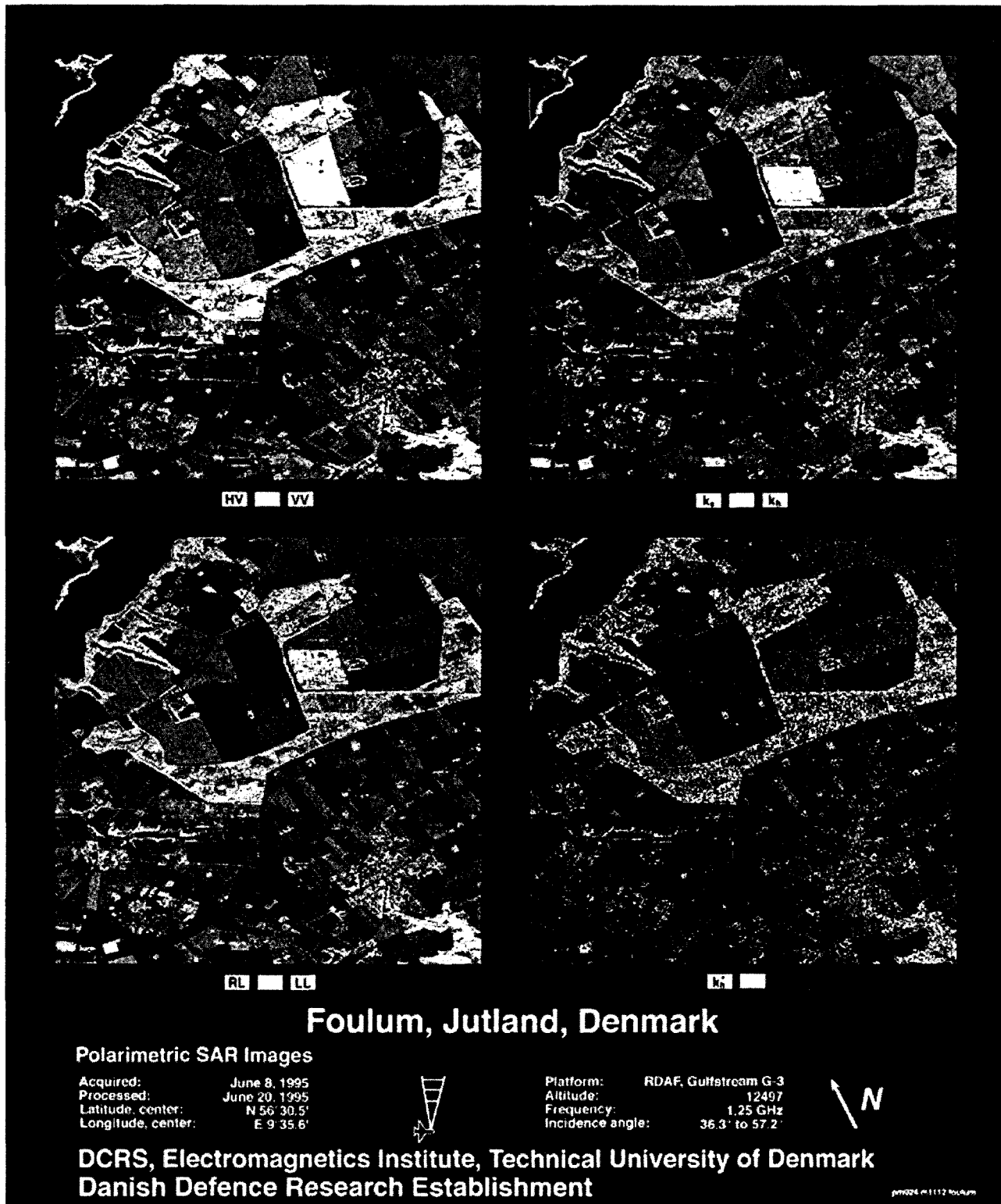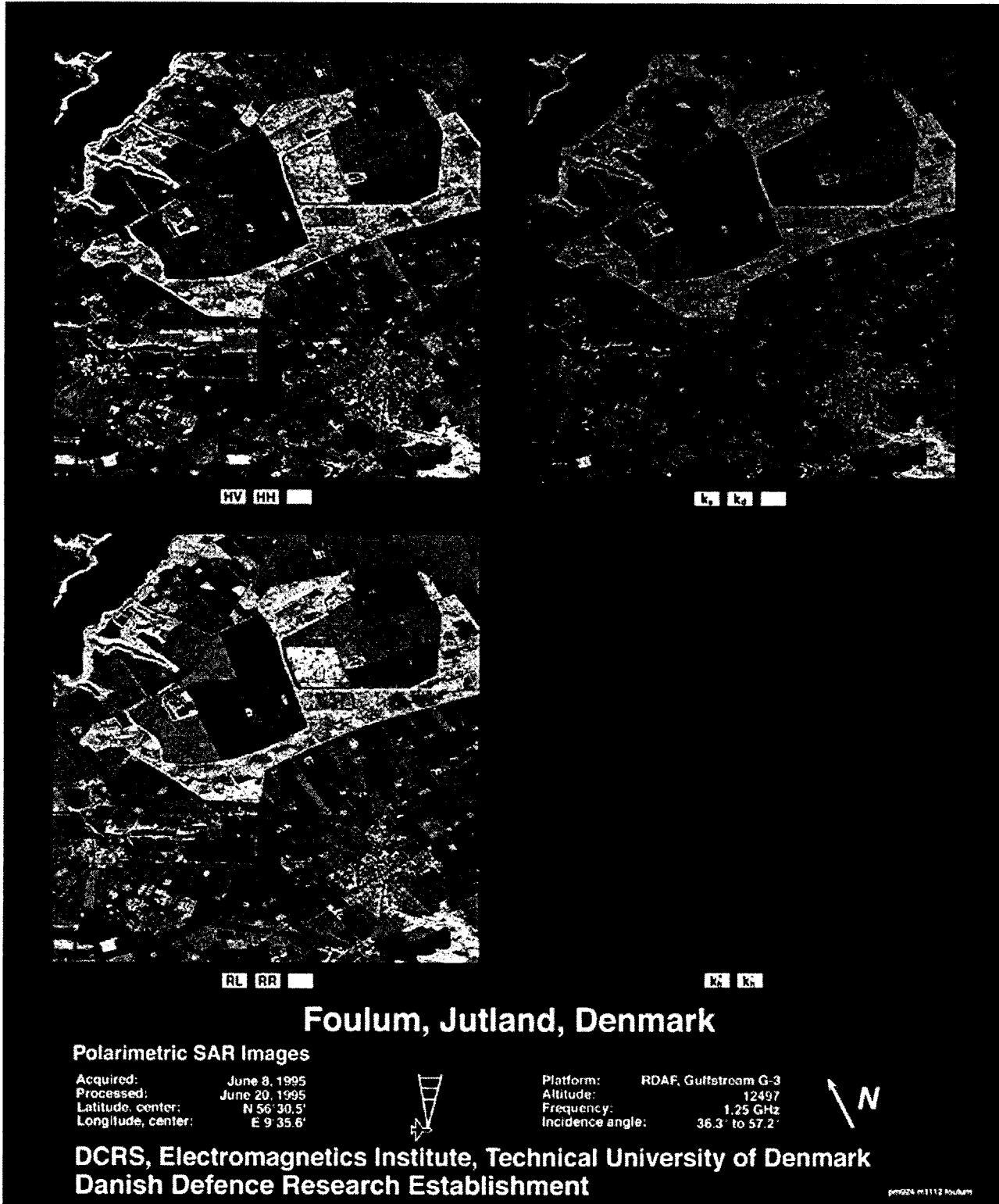ey how some typical scattering phenomena might manifest in an ISAR image. Also, some questions and techniques relating to Image Interpretation are raised and discussed. For example, pure monostatic measurements can sometimes fail to positively diagnose a particular scattering mechanism (even when including polarization information). It is then asked, can bistatic measurements provide such a diagnosis? Also the important question of the adequacy of point scatterer models (PSM) of air targets is raised. Where the PSM model fails, what simple extension can replace it?

Keywords:
Radar Imaging, ISAR, Electromagnetic Scattering, Travelling Waves, Radar Cross Section

Abbreviations used:

DE	Differential Equation
DFT	Discrete Fourier Transform
EM	ElectroMagnetic
FF	Far Field
FT	Fourier Transform
ISAR	Inverse Synthetic Aperture Radar
IsImI	ISAR Image Interpretation
LOS	Line of Sight
MoM	Method of Moments
NCTI	Non-Cooperative Target Identification
PO	Physical Optics
PTD	Physical Theory of Diffraction
PSM	Point Scatterer Model
RCS	Radar Cross Section
Rx	Receiver/Receive
TW	Travelling Wave(s)
Tx	Transmitter/Transmit
U/C	Unclassified
XR	Cross-Range

2. Introduction

It is an obvious point but it always interesting to know what we are seeing in an ISAR image, in terms of EM scattering mechanisms. A time-honored procedure is to take the scaled ISAR image and overlay an optical outline (preferably showing the features of the aircraft) having the same projection. The experienced interpreter can then make statements about each major 'blob' in the ISAR image based on their correspondence with the known features and geometry, and with his/her experience. For example, cavity returns usually appear in the R/XR neighbourhood of the engine, and also down-range of this.

ISAR Image Interpretation (abbrev. IsImI) is closely allied to various important areas for the EM, NCTI and radar modelling specialist. Firstly, ISAR imaging, both bistatic and monostatic, is a direct way of obtaining images of diffraction phenomena. As such 2-D ISAR (and possibly 3-D despite its current lack of practicality) should be of even greater interest to the pure EM researcher than zero dimensional RCS, which has been the traditional tool of interpretation in academic papers. This was doubtless partly due to cost, but now the cost of doing full ISAR imaging has come down. There is not very much in the open unclassified literature on IsImI specifically in relation to ISAR, although the recent book [1] contains very many pertinent observations, some of which are followed up here.

Secondly IsImI is important for understanding how to reduce RCS, and in understanding the main mechanisms involved in backscatter. This paper attempts to classify a few generic scattering mechanisms, with a view to finding simple ways to understand the main characteristics of each. For each scattering mechanism, some consideration is given to how it might be actually characterized by measurements, including bistatic measurements if fully polarimetric monostatic will not suffice.

Thirdly in the matter of prediction code and NCTI database validation, it is crucial to understand mechanisms in relation to target features, as much qualitatively as quantitatively. Do we have to model down to the level of rivets, plates and minor surface irregularities, or how important is it to model sensors etc.? The often-noted discrepancies between prediction codes, scale model measurements and full-scale measurements highlights the fact that certain key

elements of backscatter modelling are still far from perfectly understood, but ISAR imaging gives us a very good tool to investigate the sources of the discrepancies.

Finally, it is important to understand to what degree PSM's are adequate to model a target. For example many autofocus methods implicitly tend to assume that there are one or several scatterers which are well-behaved in the sense of looking like a resolved point scatterer. Synthetic models of targets for monostatic imaging radar simulations are often PSM's. A PSM (or equivalently a PO) assumption is made when making Near Field monostatic ISAR measurements and extrapolating them to the Far Field.

2. Scattering Mechanisms and Diagnosis Aids

A perfect conductor has been assumed in the following incomplete list of scattering types. Dielectrics and other materials will be examined later in the study.

List of Scatterer Classification Categories Examined

1. True point scatterer (Linear Phase in both frequency and aspect angle, over some aspect angle range)
2. Unresolved scatterers and continuous distributions of point scatterers
3. Sliding scatterers
4. Surface Discontinuities
5. Travelling and Creeping Waves
6. Edge Diffraction
7. Multiple Bounce Interactions
8. Dispersive Cavity Interactions

The above categories are not in all cases mutually exclusive, for example a multiple bounce return can look like a point scatterer. As well as the mechanisms, we need to consider what tools and general techniques are available to the Image interpreter, listed as follows:

Aids to Interpretation/Diagnosis of ISAR Images

1. Superposition of Aircraft Optical Outline and scaled ISAR image. Apply knowledge of likely scattering mechanisms in relation to the known geometry and disposition of sensors etc., to deduce or to guess what each image feature is.
2. Utilise image editing techniques to excise an area around a scattering centre, and to do a phase (Rihaczek-type) analysis on it to determine if it is resolved. For the details, consult [1].
3. Polarimetry can be a useful tool to gain more information on the type of scatterer. There are expert papers on this topic in this conference, see e.g. [2].
4. Specialist Signal Processing (such as wavelet transformations on raw ISAR data) can be useful when analysing cavity and other types of returns. Refs [9,10].
5. Bistatic measurements contain more information than monostatic. They can reveal some shape information and the presence of interaction between scatterers.

Method 1 will be assumed here as a baseline that one can always use, in conjunction with knowledge of the monostatic characteristics of the various scattering mechanisms to be examined in some more detail below. Occasionally monostatic ISAR measurements (in conjunction with polarimetry and the other techniques above) will perhaps give a strong suspicion or indication that a certain mechanism is in play. But they may not be sufficient to uniquely identify that mechanism beyond all doubt, in which case bistatic measurements may be considered for a more positive diagnosis. For a given angular traverse $\Delta\phi$ with mid aspect ϕ_0, as is well-known [4] a monostatic ISAR image will have a XR resolution $\lambda(2\Delta\phi)$, whereas a bistatic image has resolution $\lambda/\Delta\phi$. To be comparable on the same basis, the equivalent bistatic image should traverse angle $\pm\Delta\phi$ about the mid aspect ϕ_0 - we shall return to this shortly.

3. Point Scatterers

The signature of an isolated point scatterer is that it is largely non-dispersive with respect to frequency (i.e. has approximately linear phase in the raw data domain over the bandwidth used to form the ISAR image). Also that over some specified aspect angle range it has linear phase in the raw or range profile domain. These two properties guarantee that under FT, the scatterer transforms to a fixed R & XR position in the image domain, i.e. a point. Often rather than establishing linear phases in the raw data domain say, it is easier to reason that the scatterer must be localised in the image domain due to localisation of the radiating current, or from ray-tracing arguments. A typical example of a point scatterer might be a highly localised target feature such as a bump or facet on the target surface of dimensions less than a resolution cell size.

Let us next consider sampling the Far Field of a larger facet such as a rectangular metal strip or plate illuminated by a plane wave at near normal incidence. From Physical Optics (PO) the assumption is that the strip current is uniform (its magnitude is uniform) and given by $\mathbf{J} = 2\hat{n} \times H_{inc}$. It can readily shown that the PO assumption is equivalent to the strip acting as a re-radiating rectangular aperture antenna of width D say (a full derivation is quite lengthy, see e.g. [3]). [3] arrives at the expression (for the monostatic case)

$$E^s(u) = \int_{-D/2}^{D/2} p(x) . e^{4\pi j(x/\lambda).\tan(\alpha)} . dx$$

where α is the incidence or aspect angle relative to the normal, $p(x) = 1$ for $-D/2 \leq x \leq D/2$, $=0$ elsewhere, and $x = x'/\lambda$ where x' is cross-range. The integral is seen to be the Fourier transform of the pulse-type function $p(x)$, which is a sinc function. In ISAR measurements we are measuring complex samples from discrete points on this sinc function (of width λ/D for bistatic, $\lambda/(2D)$ for monostatic). The sinc function is of course modulated by the usual complex phase exponential due to the range rate of the strip phase centre. To form the ISAR image we just take the inverse DFT of these samples which around normal incidence include the main beam, take the

modulus and we retrieve a constant magnitude reflectivity over the XR width D of the strip. So the ISAR image of a strip at near-normal incidence gives an image of the strip. In effect we are imaging the 'specular flash' of the strip and it appears like a line source in XR, i.e. a continuous line distribution of point scatterers which are unresolvable. Clearly in the inverse domain we now have a non-linear phase which is the superposition of the linear phases of the original continuous distribution of scatterers.

If we now consider imaging the strip somewhat away from normal incidence (but not so obliquely that travelling waves -see later - are significant), we are now taking samples on just the sidelobes of the sinc function. Over small angles, to quite a good approximation these sidelobes are just a sinusoid of spatial frequency $2D/\lambda$, which on inverse DFT transforms to 2 points separated by a XR distance D. So what we see in this case is just the endpoints of the strip. One can also reason as below that seeing the endpoints is due to rapid truncation of the induced currents near those points. We are assuming of course in the above that the ISAR sample spacing is less than $\lambda/(2D)$, the usual Nyquist sampling condition.

Next we consider a current on a surface and suppose that this current has some discontinuity on the surface due to surface geometry (sharp bend or curvature say), or due to truncation at an edge. For a step-like discontinuity say, we can consider the current as being the sum of two currents on two contiguous strips like the above. When these are FT'ed, and subsequently Inverse DFT'ed to form the ISAR image (subject to Nyquist sampling being satisfied of course for the overall XR length D of the surface), we will image the step in reflectivity in the right position. when cutting across the specular region of the surface. For aspect angle ranges not including the specular region, we will see just the end-points of the steps, i.e just the locations of the discontinuities will be seen. In modelling terms, the most efficient way of storing the above information may be in terms of the XR directivity pattern of the strip or facet (the inverse Fourier domain to the image domain), rather than by enumeration of point scatterers.

Looking ahead a moment to travelling waves (TIW's), if there is a local surface impedance change, the current and in particular the TW current itself might be continuous, but due to there being reflected and transmitted TWs from the impedance inhomogeneity, the derivative of the current will be discontinuous, and again it can be shown that the discontinuities act like point scatterers.

Sliding Point Scatterers

For a curved surface, the set of surface patches reflecting specularly back to the Tx can move in R & XR in a way unlike a point attached to a rigid body. Such reflections will having a shifting, unstable Doppler or Cross-range, and will often therefore fail to focus up as a point with the standard ISAR FT processing. As Rihaczek [1] notes, such a scatterering centre will have a quadratic type of phase characteristic which should generally be sufficient to distinguish it from other scattering phenomena. A succession of stacked overlapping ISAR subimages, either bistatic or monostatic formed over smallish angles $\Delta\phi$, should show the migration of a sliding XR scatterer peak when seen as a 'movie'. This will be tested during this study as a diagnostic measure.

Edge Diffraction

Diffraction at a wedge-like edge is a non-PO phenomenon involving truncation of the current as we pass into the shadow region. A rigorous treatment of edge diffraction is afforded by Mitzner's Incremental Length Diffraction Coefficients (abbrev. ILDC) which is a PTD approach. The current at a finite length edge can be regarded as a sum of a PO current (which as already seen can give rise to line or point scatterers) and a fictitious equivalent edge current due to Michaeli, which by definition appears like a line source localised along the edge. From stationary phase considerations these edges will appear stronger when the backscatter direction is along Keller's GTD cone of specular diffraction directions. The conclusion here is that edges (like specular reflections from strip-like facets as we saw earlier) will look line or point scatterers.

No very specific diagnostics for edges are put forward here. The simple inspection of the ISAR image in relation to the superimposed optical outline will usually confirm the collocation of edge returns with the physical edges, with the strongest returns (for sharp leading edges) observed when the polarisation vector is such that the E-vector is parallel with the edge. In the opposite polarisation, travelling waves are set up and the strongest return tends to be from the trailing edge at oblique (i.e. near grazing) incidence angles. One could go further toward a positive diagnosis if full bistatic measurements were performed. This would resolve the surface currents, in principle to a $\lambda/2$ resolution, and thus allow diagnosis of the currents responsible for edge diffraction. However full bistatic measurements, even if just at a single frequency and Tx angle, represent a large number of measurements and the practicality issues are not straightforward. Full bistatic current imaging is mentioned in the literature as a viable and useful analytical procedure, for example in [5, Chapter 4], though principally for use as a visualisation tool with MoM3D Moments code outputs.

4. EM Interaction Phenomena

This section looks at some backscatter phenomena which are not purely local in origin but involve interaction at a distance.

Travelling Waves

Travelling waves are surface waves of freespace wavelength λ, which propagate over geodesics of the illuminated surface. Creeping waves are TW's which

have propagated into the shadow region, but which then radiate due to the curvature of the shadow face and are thus attenuated as they travel . There are a number of ways to gain a picture how travelling waves arise. One is via analysis of the case of a thin wire of length h. Hallen's equation for a thin z-axis directed wire is simply derived from Maxwell's equations in many antenna texts, see e.g. [6], as:

$$\frac{\partial^2 A_z}{\partial z^2} + k^2 . A_z = -j . \frac{k^2 . E_z^i}{\omega}$$

where $k = 2\pi/\lambda$, and $\omega = kc$. From this linear DE the solution for the vector potential A_z is given by a homogenous term + a forcing integral from the right hand side:

$$A_z = C_1.\cos(kz) + C_2.\sin(kz) + K\int_0^z E_z^i(z').\sin k(z-z').dz'$$

where $E_z^i = E.\sin\theta.e^{jkz\cos\theta}$ is the incident

field strength, θ is the angle the (assumed plane) incident wave makes to the negative z-direction on the wire, and K is a constant. The current I_z is related to A_z via the defining integral equation for vector potential:

$$A_z = \frac{\mu}{4\pi}\int_0^h J(z') . \frac{e^{-jkr}}{r}. dz$$

where $r = [a^2 + (z - z')^2]^{1/2}$.

When the wire radius a is $<< \lambda$, one can argue from this that except near the end points $A_z \approx c.I_z$ where c is a constant. Substituting we get:

$$I_z \approx C_1'.\cos(kz) + C_2'.\sin(kz) + K'.\int_0^z E_z^i(z').\sin k(z-z').dz'$$

whence the constants C_1 & C_2 can be determined from the boundary condition that current is zero at the ends of the wire, $z=0$ & $z=h$. On performing the integration the only terms remaining are terms in $cos(kz)$, $sin(kz)$ and $e^{jkz\cos\theta}$. The last term gives rise to the specular reflection and the first 2 terms can be regrouped as a term in e^{jkz} representing a forward travelling wave in the negative z direction and a backward (reflected) TW e^{-jkz} in the positive z direction. The reflected TW is what radiates back (in the manner of an endfire antenna, see e.g. [7]), in the monostatic backscatter direction when the angle θ is within a certain narrow range in the neighbourhood of the so-called Peter's angle, calculated from endfire antenna theory, typically about 15 or 20°.

If we have several wires, we get a set of DE's similar to the above, coupled through their forcing terms, as the incident wave now includes the near electric field produced by the current on each wire. But we may still expect TW terms to be present to force satisfaction of the boundary conditions on current. And in the general case of a surface, as is well-known this is electrically equivalent to a suitable grid of thin wires. The same kind of TW terms can be expected to be present as for the wire case.

An alternative way of viewing TW's is as a phenomenon of surface waves generated by edge diffraction, see e.g. [6, Chapter 12]. Consider a V-polarised wave impinging on a horizontal metal strip or plate near the Peters angle. In this viewpoint, there is a forward TW travelling just above the strip surface launched off the leading edge (the point of 'attachment'), it travels parallel to the surface and is diffracted off the trailing edge (so-called 2nd order diffraction) as the TW which gives the monostatic backscatter return. From edge diffraction theory [8] the TW current falls off as $\cong 1/\sqrt{x}$ as we go away from the trailing edge, i.e. as if from a line source. This current though decaying still launches a backward TW in the Peters angle direction, and in the ISAR image the TW will appear to emanate mainly from the location of the current close to the trailing edge (point of 'detachment').

Higher order diffractions (further 'reflections' of the TW off the ends of the strip) do occur, but their contributions are normally negligible. A conclusion here is that in VV polarisation the trailing edge will give a more significant return, whereas in HH polarisation, both edges will tend give returns though at a lower level. A TW return, like edge diffraction generally, can often be significant in magnitude, though they are typically well down on specular returns. PO-based EM codes do not normally include either effect unless they are incorporated as extras.

The TW is the first example of an interacting scattering mechanism, involving multiple reflections, cavity bounces or edge diffractions. The TW return as noted above will appear like a point-scatterer at the trailing edge of the strip, as just noted. Thus from a monostatic viewpoint it can be modelled as a point scatterer, but with an associated near-endfire directivity. If the strip is in fact a curved surface, the TW return will then have a range slightly down-range of the trailing edge (and at the same XR), because the curved path length over the surface is longer than the LOS range. TW's are often traversing a surface not only from front to back and to front again, but they can resonate in many directions, and will also radiate from any surface discontinuities encountered. Creeping waves are TW's traversing the back of an object whilst being continuously edge diffracted, and finally reappearing in the backscattering direction. But normally if the back of the object is more than just a few wavelengths long, these waves are very much attenuated in magnitude and their effects are unlikely to be seen.

We have already given some largely well-known diagnostic hints on how TW's manifest. Further diagnostics which could be made are as follows. One procedure would be to make full bistatic measurements in Azimuth and possibly Elevation to image the currents to near $\lambda/2$ resolution, for a given Tx illumination direction. The wavelength λ currents responsible for TW's and creeping waves may then be extractable. Another bistatic diagnostic tool is less costly in number of measurements and is tentatively suggested here,

although it largely remains to be investigated. At the end of Section 2 above, the bistatic image equivalent to a small to medium angle ISAR monostatic image was introduced. The conjecture here is that when ISAR mono- and equivalent bi-static images are compared, that the main differences noted in the magnitude and position of scatterers between the two images will be attributable to interaction phenomena. Genuine single bounce point scatterers should appear the same in both images, even if they are continuous distributions, or sliding scatterers. But for example a standard retroreflective Corner Reflector will be appear like a strong point scatterer to a wide range of monostatic aspect angles, but in the equivalent bistatic image it will give a strong return only very close to the monostatic backscatter directions, but away from these only a small return. Thus the return strength which is integrated will differ in the two cases. Similarly a cavity viewed monostatically will have different modes excited as the Tx angle changes, but bistatically the same modes are imaged as the illumination is fixed and the Rx probe angle varies - here again one can expect the images to differ. The edges of a sphere imaged monostatically will not be seen because the sphere always just looks like a point, but bistatically the creeping wave at the edge, or at least the current which gives rise to it, may become visible. In a similar way one might expect a general TW to look different in the bistatic image, but the details have not been sufficiently clarified at the time of writing.

Non-Dispersive Multiple Bounces

Retroreflective (abbrev. RR) specular reflection from a set of planar facets such as irregular corner or large (i.e. electrically large compared to λ) cavity will normally be a strong reflection and appear to come in XR from the average XR of the first and last facet involved in the RR chain. The range is the path length along any ray, and is the same for all rays associated with a given RR mechanism. All ray reflections appear then to emanate from the one point with the R & XR just discussed. Thus this type of RR will appear like a true point scatterer, with directivity pattern a function of aspect angle - since the projected facet area involved in the RR changes with aspect. There may be m different sets of facets involved in RR, each valid over possibly slightly different ranges of aspect angles - in this case up to m point scatterers at different ranges will be observed in the image of the facetted cavity.

More generally still, the cavity or corner will have curved surfaces, and we thus have a hybrid of the above and the sliding scatterer case. As the aspect changes the 'point scatterers' above will move about in XR and slightly in R too, leading to non-linear phase behaviour and some observed smearing.

The strength of RR returns and the likely presence of multiple delayed returns as a "down-range trail" are indicators of a cavity. Not all cavities are RR of course - for these, the facet angles are such that the strong returns go out in bistatic directions. Such a cavity may hardly

show up on monostatic measurements, but bistatic can give information such as the orientation of the facets. For a general cavity whose interior is curved, further investigation is required as to what bistatic measurements can yield in this important (as it occurs commonly) case. But it is likely again that, properly processed and interpreted, bistatic contains shape information about the cavity geometry.

Dispersive Cavities

If any dimension of a cavity is of wavelength order, then the cavity returns may become noticeably dispersive, i.e. non-linear with frequency. This means that the ISAR images of such cavities may be very smeared in range as well as possibly in XR. If just one 'waveguide-type' mode is excited across the range of aspects used to form the ISAR image, there is likely to be little XR smearing, but normally a mixture of modes will be excited in amounts depending on the aspect. Each mode will have a different phase centre to we can expect the return phase to be highly non-linear in general. To determine how exactly a cavity appears in an ISAR image, a modal analysis needs to be performed. It is hoped later in the study to perform simulations for regular cavities such as cylindrical or rectangular (in which the Helmholtz equation is separable and analytically solvable in these coordinate systems); for irregular cavities an analysis of the type put forward in [11] will numerically determine the modes. How does one determine what modes are excited? One way is, for each mode, to determine the tangential fields or equivalent currents at the aperture. From this the radiation pattern in the FF can easily be determined. If mode k contributes a proportion α_k to the FF in a certain direction φ, then by reciprocity this will be the proportion in which mode k is excited by an incident plane wave arriving from the aspect φ.

Related to the previous observations, if full bistatic measurements are made on a cavity at a single frequency, what is imaged at a given frequency and Tx illumination direction is the equivalent current over the aperture on a $\lambda/2$ grid. The appropriate spatial frequency component of that current will reradiate in the monostatic direction. This component will be seen to vary quite rapidly in magnitude and phase as the frequency is changed, due to the frequency dispersion. Moreover, the cavity can be economically modelled, not directly via a PSM of course, but by the magnitude and phase of this component, stored as a piecewise linear function of frequency.

Finally, the conjecture is made here, that if the aperture current has been estimated to within $\lambda/2$ accuracy via bistatic Rx measurements on a $\lambda/(2D)$ angle grid (where D is the aperture dimension) for all Tx positions on a similar grid, then the shape of the cavity can be determined from this information.

4-6

Observations on Interaction and Non-Interaction

We have reached from the foregoing the somewhat surprising conclusion that interacting scattering mechanisms can sometimes lead to well-behaved linear-phase point scatterers. Conversely, PO-type returns can sometimes give non-linear phase behaviour, e.g. if imaging a continuous distribution of scatterers such as a line source, or in the case of sliding scatterers, or even if imaging two or more XR unresolved scatterers in a given resolution cell [1].

The distinction between interacting and non-interacting can be particularly important in relation to Near to Far Field Transformations. For non-interacting scatterers monostatic measurements suffice, but for interacting it turns out that it is necessary to make the measurements in some measure bistatically [12].

Two different types of bistatic measurement have been mentioned so far, full bistatic of various resolutions in effect to image current, and small angle bistatic images, which are compared to 'equivalent' monostatic images. We can mention a third type, still just at the 'ideas' stage. In the above two, the Tx stayed fixed, but if we allow the Tx probe position to vary in addition to the Rx probe positions around the Tx, in principle we can form a narrow Tx beam on one part of the target, and we may also form a high resolution Rx beam on a different area of the target. If there is no interaction between the two XR resolution cells involved, nothing will be imaged, but where there is interaction, clearly it will be picked up in the appropriate Rx beam positions. Of course, there are difficulties of doing this in the Near Field, and questions relating to Tx beam sidelobe levels etc. The question of practicality of such a bistatic mode is currently being examined

CONCLUSIONS

These will be presented for clarity as a series of bullet points.

- Need to use existing codes such as NEC, and some specialist simulations and measurements, to confirm some of the above observations.
- The work has only looked at good conductors, and needs extension to cover other common materials such as dielectrics.
- Further investigation of the practicality of bistatic measurement modes as a diagnostic tool is indicated, also of their potential to yield shape information.
- The methodology needs to be integrated with existing techniques such as polarimetry and signal analysis.
- Bring any key insights to bear on the target modelling and NCTI database problem.

References

1. Rihaczek, A W & Hershkowitz, S J , "Radar Resolution and Compex-Image Analysis", Artech House 1996
2. Krogager, E. , "Polarimetry, the full story", this conference, Apr 1998
3. Birtcher C R and Balanis C A, "RCS Measurements, Transformations and Comparisons", IEEE Trans. AP-42, pp329-333, Mar 1994
4. Wehner D R, "High Resolution Radar (2nd Ed.)", Artech House, 1995
5. Knott E F, Shaeffer J F, & Tuley M T, "Radar Cross Section, 2nd Ed.", Artech House 1993
6. Balanis C A, "Antenna Theory", Wiley 1997
7. Stutzman W L and Thiele G A, "Antenna Theory and Design, 2nd Ed.", Wiley 1998
8. Brewitt-Taylor C, Private Communication, DERA Malvern
9. Moghaddar A, Walton E K, "Time-Frequency Distribution Analysis of Scattering from Waveguide Cavities", IEEE AP-41, No.5,pp. 677-680, May 1993
10. Kim H, Ling H, "Wavelet Analysis of Radar Echo from Finite-Size Targets", IEEE AP-41, No.2, pp. 200-207, Feb 1993
11. Harrington R F, and Mautz J R, "Theory of Characteristic Modes for Conducting Bodies", IEEE AP-19, No. 5, pp. 622-639, Sept 1973
12. Mensa D L & Vaccaro K, "Near Field to Far Field Transformation of RCS data, AMTA Conference 1995.

Time-Frequency Transforms for Radar Imaging of Maneuvering Targets*

Victor C. Chen
Naval Research Laboratory
Washington D.C. 20375, U.S.A.

William J. Miceli
Office of Naval Research
Arlington, VA 22217, U.S.A.

Abstract— Fourier transforms are the basis for conventional SAR and ISAR (range-Doppler) imaging. Target rotation during the coherent integration time results in a time-varying Doppler frequency shift that produces, after Fourier transform, a smeared Doppler spectrum and a blurred image. Sophisticated motion compensation algorithms must be applied to obtain focussed images using Fourier techniques.

However, image blurring can be mitigated without resorting to sophisticated focusing algorithms by using time-frequency transforms in place of the Fourier transform for Doppler processing. Various time-frequency transforms are described and compared. Range-Doppler images of maneuvering aircraft produced by conventional Fourier transform methods are compared with those produced produced by time-frequency transform methods. A set of NATO provided ISAR data illustrates the benefit of using the latter.
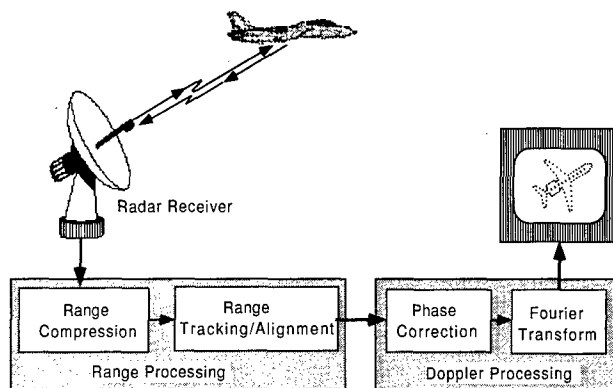
Fig. 1. Diagram of conventional radar image processing.

1. Introduction

The purpose of forming radar images is to reveal useful features of targets that can be used for target recognition and classification. The imaging process consists of a range processing followed by Doppler processing, as illustrated in Fig.1.

The algorithmic implementation of the range compression in the range processing generally depends on the radar waveform (e.g. step-frequency (SF) waveform or linear frequency modulation (LFM) waveform). For some waveform such as SF, the range compression is performed by the Fourier transform. However, in conventional radar imaging systems, the Doppler processing is always achieved by

applying the Fourier transform [1], [2].

These Doppler processing methods based on the Fourier transform work best when the Doppler spectrum of the radar phase history is stationary during the imaging time, which is sometimes referred to as the synthetic aperture time, coherent integration time, or coherent processing interval (CPI), etc.. If the target being imaged is maneuvering during this CPI, the Doppler spectrum becomes time-varying and the reconstructed image will be blurred. Sophisticated motion compensation algorithms that adjust the phase of each echo being processed must then be applied before application of the Fourier transform.

As defined, the Fourier transform is a method of global spectral analysis that only indicates what frequency components are contained in the analyzed signal; it does not indicate how these components vary with time. Because of the time-varying behavior of the Doppler frequency spectrum, the analysis is more effective by using time-frequency transforms. Short imaging time may minimize the effect of image blurring caused by time-varying Doppler spectrum. However, short time also reduces the Doppler resolution.

The use of time-frequency transform allows us to obtain the instantaneous Doppler spectrum. By optimally balancing between the resolution and the cross-term interferences, a high resolution instantaneous Doppler spectrum can be achieved and, thus, the image blurring problem caused by time-varying Doppler frequency shifts can be circumvented.
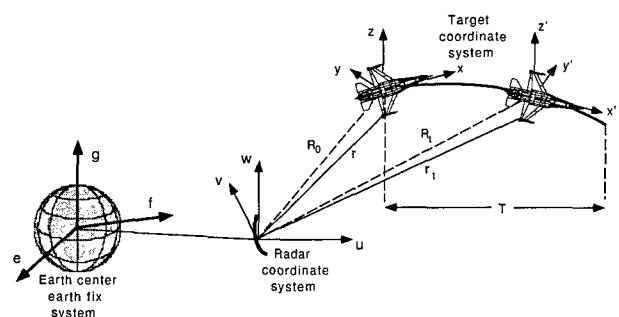

Fig. 2. Three coordinate systems: earth coordinate (e,f,g), radar coordinate (u,v,w) and target coordinate (x,y,z).

2. Dynamics of Maneuvering Targets

We define a maneuvering target as having translational and rotational, possibly nonuniform motions during the

CPI, which we define to be between time $t = 0$ and $t = T$. We also assume the radar sensor is located at the origin of the (u,v,w) frame of reference, as indicated in Fig.2 where the (e,f,g) frame is defined as the earth coordinate frame. The target's center of mass is denoted in (u,v,w) coordinates as a function of time at $t = 0$, $R(u, v, w, t = 0) = R_0$ and at any t, $R(u, v, w, t) = R_t$.

We presume a reference scatterer is located at $P(x, y, z)$ and has a distance d from the origin in an inertial (x,y,z) coordinate, as shown in Fig.3. We also define the heading of the target to be always aligned with the x-axis of the inertial frame. Thus, translation and rotational coordinate transformations can express the positions of this reference scatterer at any time during the CPI in terms of the radar's (u,v,w) coordinate system. The instantaneous position vector to the reference scatterer is the vector sum $\vec{r_t} = \vec{R_t} + \vec{d}$, or more precisely,

$$[u_t, v_t, w_t]^{-T} = Trans(T_u(t), T_v(t), T_w(t)) \cdot$$
$$Rot(\theta_u(t), \theta_v(t), \theta_w(t)) \cdot [x, y, z]^{-T}$$

where Trans(*) is the coordinate translation matrix that expresses the position vector $\vec{OS}$ in the (u,v,w) coordinate system and Rot(*) is the coordinate rotation matrix that expresses the vector $\vec{SP}$ in the (u,v,w) coordinate system.
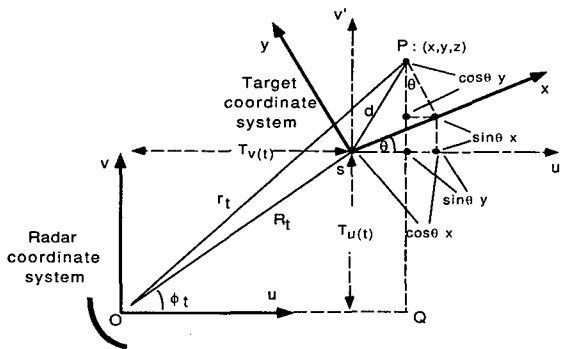

Fig. 3. Radar and target coordinates.

For simplicity, we only analyze 2-dimensional coordinate systems where the (x,y)-coordinate has a translation (T_u, T_v) from the (u,v)-coordinate and has a rotation θ about the (u',v')-coordinate. The (u',v')-coordinate has only translation from the (u,v)-coordinate but no translation from the (x,y)-coordinate. In this case, the translation matrix becomes

$$Trans(T_u(t), T_v(t)) = \begin{bmatrix} 1 & 0 & T_u(t) \\ 0 & 1 & T_v(t) \\ 0 & 0 & 1 \end{bmatrix},$$

where $T_u(t) = R_0 cos\phi_t$ and $T_v(t) = R_0 sin\phi_t$. The rotation matrix becomes

$$Rot(0, 0, \theta) = \begin{bmatrix} cos\theta & -sin\theta & 0 \\ sin\theta & cos\theta & 0 \\ 0 & 0 & 1 \end{bmatrix}$$

The instantaneous range to the reference scatterer from the origin of the radar coordinate (u,v) becomes

$$
\begin{aligned}
r_t &= (\overline{OQ}^2 + \overline{QP}^2)^{1/2} \\
&= \{R_0^2 + d^2 + 2R_0[xcos(\theta - \phi_t) - ysin(\theta - \phi_t)]\}^{1/2} \\
&\cong R_0 + xcos(\theta - \phi_t) - ysin(\theta - \phi_t)
\end{aligned}
\tag{1}
$$

A frequently used set of rotational motions is roll, pitch and yaw. As shown in Fig.4, for an aircraft heading along the x-axis, roll corresponds to a rotation θ_r about the x-axis, pitch corresponds to a rotation θ_p about y-axis, and yaw corresponds to a rotation θ_y about the z-axis. If the order of rotations is a roll, followed by a pitch, and finally, a yaw, then the composite roll, pitch and yaw motions can be represented by a rotation matrix

$$Rot(\theta_r, \theta_p, \theta_y) =$$
$$Roll(x, \theta_r)Pitch(y, \theta_p)Yaw(z, \theta_y) \tag{2}$$
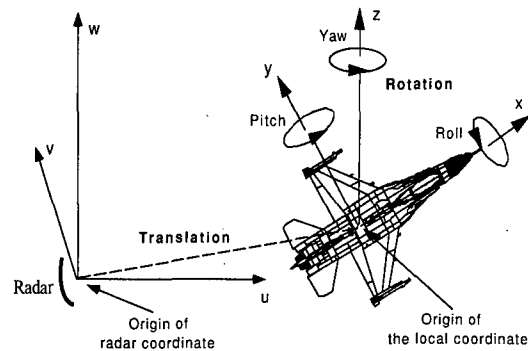

Fig. 4. Target rotation.

The roll matrix can be expressed as [3]

$$Roll(x, \theta_r) = \begin{bmatrix} 1 & 0 & 0 & 0 \\ 0 & cos\theta_y & -sin\theta_y & 0 \\ 0 & sin\theta_y & cos\theta_y & 0 \\ 0 & 0 & 0 & 1 \end{bmatrix}, \tag{3}$$

the pitch matrix is

$$Pitch(y, \theta_p) = \begin{bmatrix} cos\theta_p & 0 & sin\theta_p & 0 \\ 0 & 1 & 0 & 0 \\ -sin\theta_p & 0 & cos\theta_p & 0 \\ 0 & 0 & 0 & 1 \end{bmatrix}, \tag{4}$$

and the yaw matrix is

$$Yaw(z, \theta_y) = \begin{bmatrix} cos\theta_r & -sin\theta_r & 0 & 0 \\ sin\theta_r & cos\theta_r & 0 & 0 \\ 0 & 0 & 1 & 0 \\ 0 & 0 & 0 & 1 \end{bmatrix}. \tag{5}$$

Therefore, the rotation matrix can be expressed as

$$Rot(\theta_r, \theta_p, \theta_y) = \begin{bmatrix} a_{11} & a_{12} & a_{13} & 0 \\ a_{21} & a_{22} & a_{23} & 0 \\ a_{31} & a_{32} & a_{33} & 0 \\ 0 & 0 & 0 & 1 \end{bmatrix}, \tag{6}$$

where

$$a_{11} = cos\theta_p cos\theta_y;$$
$$a_{12} = -cos\theta_p sin\theta_y;$$
$$a_{13} = sin\theta_p;$$
$$a_{21} = sin\theta_r sin\theta_p cos\theta_y + cos\theta_r sin\theta_y;$$
$$a_{22} = sin\theta_r sin\theta_p sin\theta_y - cos\theta_r cos\theta_y;$$
$$a_{23} = -sin\theta_r cos\theta_p;$$
$$a_{31} = cos\theta_r sin\theta_p cos\theta_y - sin\theta_r sin\theta_y;$$
$$a_{32} = cos\theta_r sin\theta_p sin\theta_y + sin\theta_r cos\theta_y;$$
$$a_{33} = cos\theta_r cos\theta_p.$$

When there is a translational motion represented by a vector $[T_u, T_v, T_w]$, the translation matrix is

$$Trans(T_u, T_v, T_w) = \begin{bmatrix} 1 & 0 & 0 & T_u \\ 0 & 1 & 0 & T_v \\ 0 & 0 & 1 & T_w \\ 0 & 0 & 0 & 1 \end{bmatrix}$$

Thus, the composite translation and rotation matrix becomes

$$Trans(T_u, T_v, T_w)Rot(\theta_r, \theta_p, \theta_y) =$$
$$\begin{bmatrix} a_{11} & a_{12} & a_{13} & T_u \\ a_{21} & a_{22} & a_{23} & T_v \\ a_{31} & a_{32} & a_{33} & T_w \\ 0 & 0 & 0 & 1 \end{bmatrix} \qquad (7)$$

Any scatterer on the target will move from its initial location $[u_0, v_0, w_0]$ to a new location $[u_t, v_t, w_t]$:

$$\begin{bmatrix} u_t \\ v_t \\ w_t \\ 1 \end{bmatrix} = \begin{bmatrix} a_{11} & a_{12} & a_{13} & T_u \\ a_{21} & a_{22} & a_{23} & T_v \\ a_{31} & a_{32} & a_{33} & T_w \\ 0 & 0 & 0 & 1 \end{bmatrix} \begin{bmatrix} u_0 \\ v_0 \\ w_0 \\ 1 \end{bmatrix}$$

or

$$\begin{bmatrix} u_t \\ v_t \\ w_t \\ 1 \end{bmatrix} = \begin{bmatrix} a_{11}u_0 + a_{12}v_0 + a_{13}w_0 + T_u \\ a_{21}u_0 + a_{22}v_0 + a_{23}w_0 + T_v \\ a_{31}u_0 + a_{32}v_0 + a_{33}w_0 + T_w \\ 1 \end{bmatrix} \qquad (8)$$

When the target is maneuvering, the Doppler frequency spectrum of the returned signal from the target becomes time-varying, and the reconstructed image becomes blurred. In the next section, we will discuss the time-varying Doppler spectrum induced by the target maneuvering.

3. Target Maneuvering Induced Time-Varying Doppler Spectrum

Target maneuvering is mainly caused by target's translational and fast rotational motions. Assume a target has translational and rotational motions only in the x-y plane as shown in Fig.5. At a time t, the target coordinate system (x,y) becomes (x',y') by a translational motion and a rotational motion. Thus, the range of the reference scatterer from the radar becomes

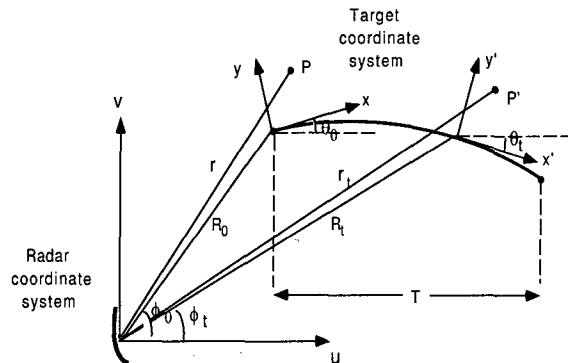$$r_t = r(t) \cong R_t + x cos(\theta_t - \phi_t) - y sin(\theta_t - \phi_t), \qquad (9)$$

Fig. 5. Maneuvering target.

where
$$R_t = R(t) = R_0 + v_R t + a_R t^2/2$$
and
$$\theta_t = \theta(t) = \theta_0 + \Omega t + \alpha t^2/2.$$

We can assume the angle of the reference scatterer in the radar coordinate system is also a function of time:

$$\phi_t = \phi(t) = \phi_0 + \Delta\phi t$$

where $\Delta\phi$ is determined by the target's trajectory as well as the rotation of the target.

The phase of the returned signal from the reference scatterer is

$$\phi_R(t) = 2\pi f \frac{2r_t}{c}$$
$$\cong 2\pi f \frac{2[R_t + x cos(\theta_t - \phi_t) - y sin(\theta_t - \phi_t)]}{c}.$$
$$(10)$$

Since the time-derivative of the phase is frequency, by taking time-derivative of the phase function, the Doppler frequency shift can be derived as

$$f_D \cong \frac{2f}{c}v_R$$
$$+ \frac{2f}{c}x[-\sin(\Theta_0 - \phi_0)(\Omega - \Delta\phi)$$
$$- \cos(\Theta_0 - \phi_0)(\Omega - \Delta\phi)^2 t]$$
$$- \frac{2f}{c}y[\cos(\Theta_0 - \phi_0)(\Omega - \Delta\phi)$$
$$- \sin(\Theta_0 - \phi_0)(\Omega - \Delta\phi)^2 t] \qquad (11)$$

For simplicity, we take a look at the following two cases and examine target rotating induced time-varying spectra.

The first case is a target with yaw motion only, i.e., $\theta_r = \theta_p = 0$ and $\theta_y = \Omega_y t$, where Ω_y is the yaw rate as shown in Fig.6, the rotation matrix becomes

$$Rot(\theta_r, \theta_p, \theta_y) = \begin{bmatrix} cos\theta_y & -sin\theta_y & 0 & 0 \\ sin\theta_y & cos\theta_y & 0 & 0 \\ 0 & 0 & 1 & 0 \\ 0 & 0 & 0 & 1 \end{bmatrix}. \qquad (12)$$

Assuming the initial range from the radar to the center of rotation R_0 is much larger than the dimension of the target, the range from the radar to the scatterer at (x, y) can be approximately expressed as

$$R = R_0 + cos\Theta_0 x - sin\Theta_0 y \qquad (13)$$

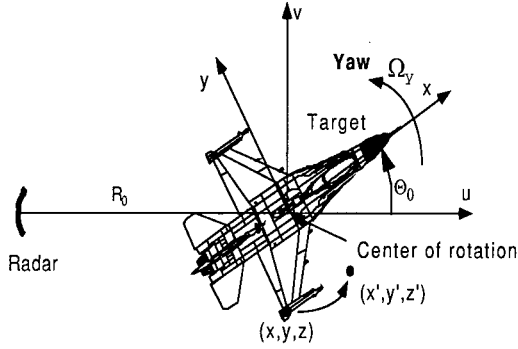where Θ_0 is the initial yaw angle as shown in Fig.6.

Fig. 6. A target with yaw motion.

Because of the yaw motion, a scatterer at (x, y, z) will transform to a new location (x', y', z'), where

$$
\begin{aligned}
x' &= cos\theta_y x - sin\theta_y y & (14) \\
y' &= sin\theta_y x + cos\theta_y y & (15) \\
z' &= z & (16)
\end{aligned}
$$

and the new range becomes

$$
\begin{aligned}
R'(t) &= R_0 + cos\Theta_0 x' - sin\Theta_0 y' \\
&= R_0 + cos(\theta_y + \Theta_0)x - sin(\theta_y + \Theta_0)y \\
&= R_0 + cos(\Omega_y t + \Theta_0)x \\
&\quad - sin(\Omega_y t + \Theta_0)y. \qquad (17)
\end{aligned}
$$

Thus, the phase of the returned signal from the target becomes

$$
\begin{aligned}
\phi_R(t) &= 2\pi f \frac{2R'(t)}{c} \\
&= 2\pi f \frac{2[R_0 + cos(\Omega_y t + \Theta_0)x - sin(\Omega_y t + \Theta_0)y]}{c}. \\
&\qquad (18)
\end{aligned}
$$

By taking the time-derivative of the phase function, the Doppler frequency shift can be derived as

$$
\begin{aligned}
f_{D_{yaw}} &= \frac{2f}{c}[x(-\Omega_y \sin\Theta_0 - \Omega_y^2 t \cos\Theta_0) \\
&\quad - y(\Omega_y \cos\Theta_0 - \Omega_y^2 t \sin\Theta_0)] \qquad (19)
\end{aligned}
$$

We can see that even if the rotation rate Ω_y is a constant, the yaw motion-induced Doppler frequency shift $f_{D_{yaw}}$ can still be time-varying.
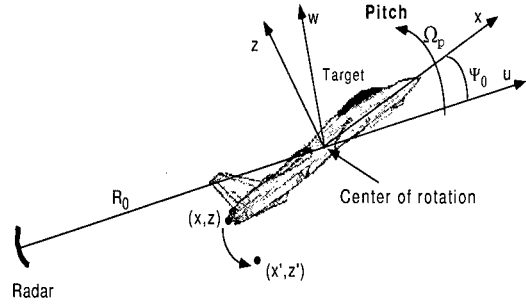

Fig. 7. A target with pitch motion.

The second case is a target with pitch motion only, *i.e.*, $\theta_r = \theta_y = 0$ and $\theta_p = \Omega_p t$, where Ω_p is the pitch rate as shown in Fig.7, the rotation matrix becomes

$$
Rot(\theta_r, \theta_p, \theta_y) = \begin{bmatrix} cos\theta_p & 0 & sin\theta_p & 0 \\ 0 & 1 & 0 & 0 \\ -sin\theta_p & 0 & cos\theta_p & 0 \\ 0 & 0 & 0 & 1 \end{bmatrix}. \qquad (20)
$$

A scatterer at (x, y, z) will transform to a new location (x', y', z'), where

$$
\begin{aligned}
x' &= cos\theta_p x + sin\theta_p z & (21) \\
y' &= y & (22) \\
z' &= -sin\theta_p x + cos\theta_p z. & (23)
\end{aligned}
$$

The new range becomes

$$
\begin{aligned}
R'(t) &= R_0 + cos\Psi_0 x' + sin\Psi_0 z' \\
&= R_0 + cos(\theta_p + \Psi_0)x + sin(\theta_p + \Psi_0)z \\
&= R_0 + cos(\Omega_p t + \Psi_0)x + sin(\Omega_p t + \Psi_0)z, \\
&\qquad (24)
\end{aligned}
$$

where Ψ_0 is the initial pitch angle.

Thus, the phase of the returned signal from the target becomes

$$
\begin{aligned}
\phi_R(t) &= 2\pi f \frac{2R'(t)}{c} \\
&= 2\pi f \frac{2[R_0 + cos(\Omega_p t + \Psi_0)x + sin(\Omega_p t + \Psi_0)z]}{c}; \\
&\qquad (25)
\end{aligned}
$$

and the Doppler frequency shift becomes

$$
\begin{aligned}
f_{D_{pitch}} &= \frac{2f}{c}[x(-\Omega_p \sin\Psi_0 - \Omega_p^2 t \cos\Psi_0) \\
&\quad + z(\Omega_p \cos\Psi_0 - \Omega_p^2 t \sin\Psi_0)]. \qquad (26)
\end{aligned}
$$

Even if the pitch rate Ω_p is a constant, the motion-induced Doppler frequency shift $f_{D_{pitch}}$ is still time-varying.

Fig.8 shows the rotational motion induced time-varying Doppler spectrum for a given rotation rate ($\Omega_p = 0.2$ rad/s) and different initial rotation angles. To represent the
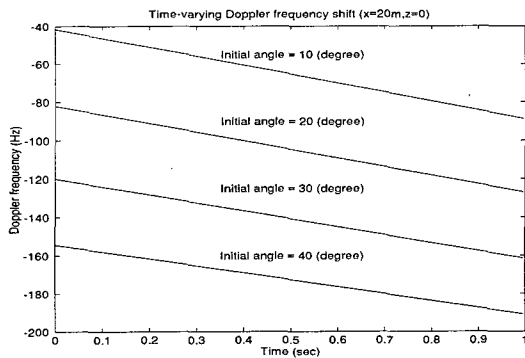
Fig. 8. Rotational motion-induced time-varying Doppler spectrum.

time-varying spectrum accurately, time-frequency transforms should be used.

4. Time-Frequency Transforms

Because of the time-varying behavior of the Doppler frequency shift, an efficient method to solve the problem of the smeared Fourier frequency spectrum and, hence, the blurred image is to apply a high-resolution time-frequency transform to the Doppler processing.

By replacing the Fourier transform with a high resolution time-frequency transform, the image blurring caused by the time-varying Doppler frequency shifts can be mitigated without applying sophisticated motion compensation algorithms. The time-frequency transform actually decomposes the phase function into instantaneous time slices. At each time slice, the Doppler frequency components are fixed, possessing the Doppler resolution provided by the time-frequency transform.

In principle, any time-frequency transform can be used to replace the Fourier transform for radar image reconstruction. However, a desired time-frequency transform should have high resolution in both the time and frequency domains, and should accurately reflect the instantaneous frequencies of the analyzed signal.

Time-frequency transforms include linear transforms, such as the short-time Fourier transform (STFT), and bi-linear transforms, such as the Wigner-Ville distribution (WVD) and the time-frequency distribution series (TFDS). In the following sub-sections, we will review each of these methods in terms of their respective time-frequency resolutions.

4.1 Short-Time Fourier Transform (STFT)

The STFT is the simplest way for time-varying spectral analysis and defined as

$$STFT(t,\omega) = \int_{-\infty}^{+\infty} s(\tau)w(\tau - t)exp\{-j\omega\tau\}d\tau \quad (27)$$

where $s(t)$ is a signal and $w(t)$ is a short-time window function.

The joint time-frequency resolution of the STFT is limited by the uncertainty principle. With a time-limited window function, the frequency resolution of the STFT is determined by the window size. There is a trade-off between the time-resolution and the frequency resolution. A larger window has higher frequency resolution but lower time resolution.

4.2 Wigner-Ville Distribution

The power spectrum $P(\omega)$ of a non-stationary signal $s(t)$ is the Fourier transform of the auto-correlation function $R(\tau)$ of the signal. One approach for achieving high energy concentration in both the time and frequency domains is to use the auto-correlation function and make it time-dependent.

The Fourier transform of a time-dependent auto-correlation function $R(t, \tau)$ is a time-dependent power spectrum of the signal, which is a function of time and frequency, i.e.,

$$P(t,\omega) = \int_{-\infty}^{\infty} R(t,\tau)exp\{-j\omega\tau\}d\tau \quad (28)$$

When the time-dependent auto-correlation function is defined as

$$R(t,\tau) = s(t + \frac{\tau}{2})s^*(t - \frac{\tau}{2}) \quad (29)$$

The time-dependent power spectrum becomes

$$WVD(t,\omega) = \int s(t + \frac{\tau}{2})s^*(t - \frac{\tau}{2})exp\{-j\omega\tau\}d\tau \quad (30)$$

which is the Wigner-Ville distribution (WVD) [6].

Because of the high resolution and the accuracy of the time-frequency representation, the WVD can be the candidate for time-varying spectral analysis. However, there is a problem of cross-term interference associated with it. When the signal contains more than one component, the WVD will generate cross-term interference that occurs at spurious locations of the time-frequency plane and often obscures the useful time-varying spectrum patterns. To reduce the cross-term interference, the filtered WVD can be used to preserve the useful properties of the time-varying spectrum with slightly reduced time-frequency resolution and largely reduced cross-term interference. The WVD with a linear low-pass filter is characterized as a Cohen's class, such as Choi-Williams distribution [5], and the distribution with a non-linear low-pass filter is the time-frequency distribution series [7].

4.3 Time-Frequency Distribution Series

Since the cross-term is localized at the mid-point of two signal components and its magnitude is oscillatory in the time-frequency domain [4], [5], we could first decompose the WVD as the sum of 2-D localized functions, such as 2-D Gabor expansion,

$$WVD(t,\omega) = \sum_{m,n}\sum_{p,q} D_{m,n,p,q}H_{m,n,p,q}(t,\omega) \quad (31)$$

where $\{D_{m,n,p,q}\}$ are the coefficients of the expansion, and $H_{m,n,p,q}(t,\omega)$ is a 2-D Gaussian function given by

$$H_{m,n,p,q}(t,\omega) = exp\{-\frac{(t - m\Delta T)^2}{\sigma^2} + jn\Delta Wt\}$$

$$\times exp\{-\sigma^2(\omega - p\Delta W)^2 + jq\Delta T\omega\} \qquad (32)$$

where the parameters m and p are the time index and the frequency index, respectively, n and q characterize the rate of oscillation of the 2D Gaussian functions, and ΔT and ΔW are the time sampling step and the frequency sampling step, respectively.

The instantaneous frequency is mainly determined by those $H_{m,n,p,q}(t,\omega)$ which possess low oscillation. The highly oscillatory $H_{m,n,p,q}(t,\omega)$ has a smaller average, hence has negligible influence to the instantaneous frequency. Since the highly oscillatory terms $H_{m,n,p,q}(t,\omega)$ are directly associated with cross-terms [4], [5], if we use the leading terms (with small n and q) to represent the time-varying spectrum, the resulting presentation is expected to well delineate the time-varying spectrum with limited cross-term interference. This is the time-frequency distribution series (TFDS) [7]

$$TFDS^d(t,\omega) = \sum_{m,p} \sum_{|n|+|q|\leq d} D_{m,n,p,q} H_{m,n,p,q}(t,\omega) \qquad (33)$$

where d denotes the order of TFDS, which balances the resolution and cross-term interference. When d is small, $TFDS^d(t,\omega)$ has low cross-term interference but poor resolution; when d is large, $TFDS^d(t,\omega)$ has good resolution but strong cross-term interference.
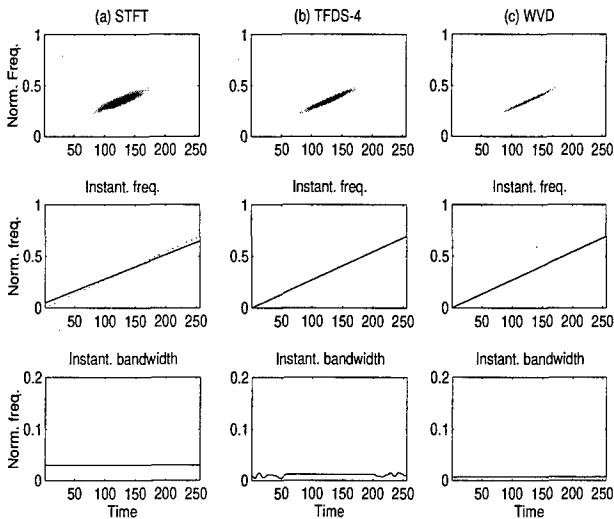

Fig. 9. Performance comparison in terms of the instantaneous frequency (dotted line: true instantaneous frequency) and the instantaneous bandwidth using a linear chirp signal with a Gaussian envelope: (a) STFT, (b) 4th-order TFDS and (c) WVD.

Fig.9 shows a comparison of the energy concentration, and the instantaneous bandwidth for the STFT, the TFDS and the WVD. The WVD has highest time-frequency concentration or lowest instantaneous bandwidth, and the instantaneous frequency accurately reflects the true instantaneous frequency of the signal. Depending on the order of the distribution, the TFDS has slightly lower time-frequency concentration than the WVD, but can accurately

reflect the true instantaneous frequencies of the signal. The STFT has lower time-frequency concentration and a deviation from the true instantaneous frequencies.

In this example, the instantaneous bandwidth in normalized frequency is 0.007 for the WVD, 0.012 for the 4th-order TFDS, and 0.03 for the STFT. Thus, the time-frequency concentration of the STFT is about 4.3 times lower than that of the WVD and about 2.4 times lower than that of the 4th-order TFDS.

Because of the flexibility and adaptability of the TFDS, we will use this method to illustrate the benefits of the time-varying spectral analysis for radar imaging.

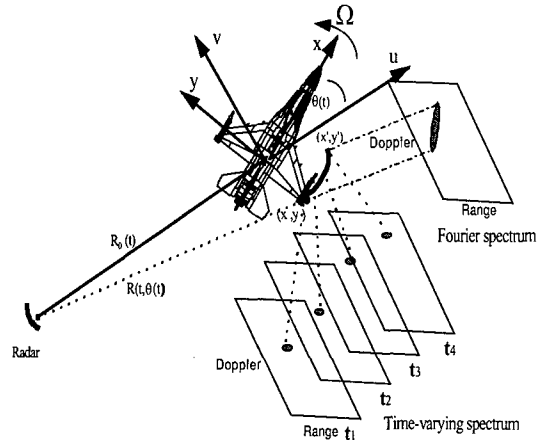## 5. Radar Imaging of Maneuvering Targets

Fig. 10. Time-varying spectral analysis of radar range-Doppler image.

Fig.10 shows a rotating aircraft about the z-axis with a constant rotation rate of Ω. Let us examine a scatterer at the wing-tip of the aircraft (x,y). Because of target rotation, at the end of image frame time the scatterer at the wing-tip will move to x',y'.

If the Fourier transform is taken from $t = 0$ to $t = t'$, the reconstructed range-Doppler image of the wing-tip is smeared as illustrated in Fig.10. However, if a time-frequency transform is used, at time instants t_1, t_2, t_3, and t_4, each time-sampling image of the wing-tip becomes a clear dot and, thus, the image blurring problem can be circumvented [8].
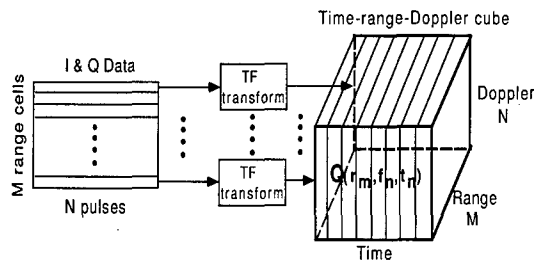

Fig. 11. The time-frequency transform based image formation.

The Fourier transform generates only one image frame from an $M \times N$ I & Q data, where the data consists of M time history series, each having the length of N. However, the time-frequency transform is applied to each time history series and generates an $N \times N$ time-Doppler distribution. By combining the M time-Doppler distributions at M range cells, the $N \times M \times N$ time-range-Doppler cube $Q(r_m, f_n, t_n)$ can be formed. At a particular time instant t_i, only one range-Doppler image frame $Q(r_m, f_n, t_n = t_i)$ can be extracted from the cube as shown in Fig.11. There are a total of N image frames available, and every one represents a full range-Doppler image at a particular time instant.

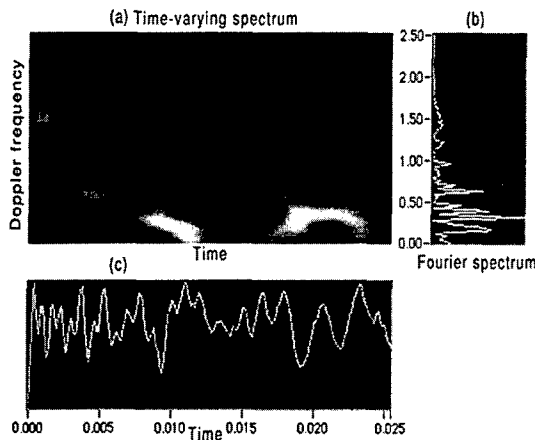## 5.1 Simulated Maneuvering Aircraft F-16

Fig. 12. Time-varying spectral analysis of the time history series at a range cell: (a) the time-varying spectrum; (b) the Fourier spectrum, and (c) the analyzed time history series at a range cell.
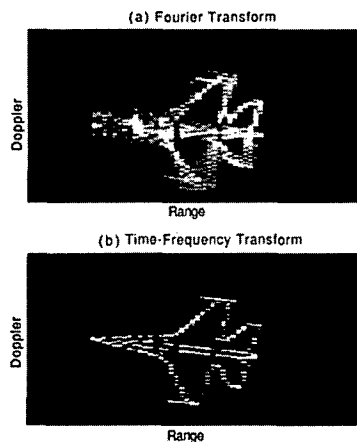

Fig. 13. Radar image of the simulated aircraft with maneuvering by using (a) the Fourier transform, and (b) the time-frequency transform.

Returned data from an Aircraft F-16 is simulated with a X-band step-frequency radar. The aircraft has only fast

rotational motion that makes image blurring. After standard motion compensation processing, the uncompensated phase error still causes the Doppler spectrum to be time-varying as shown in Fig.12(a). If we use the Fourier transform to this time-varying Doppler spectrum, we obtain a blurred image in the Doppler domain (Fig.13(a)). By replacing the Fourier analysis with the time-varying spectral analysis, the single Fourier image frame becomes a sequence of time-varying image frames. Each of them represents a full radar range-Doppler image at a particular time instant. Fig.13(b) shows one of the image frames from the sequence of frames. We can easily see that by using the time-frequency transform, the smeared Fourier image in Fig.13(a) is resolved into a sequence of cleared time-frequency images.
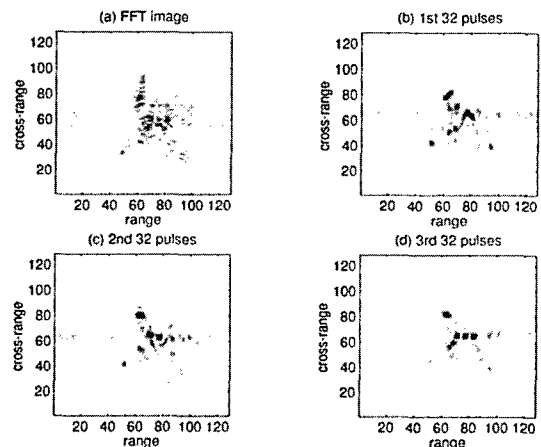
5.2 MPR AIDA Data

Fig. 14. ISAR images of MPR AIDA data (a) the FFT image; (b) the 2-D super-resolution image from the 1st 32 pulses, (c) the 2-D super-resolution image from the 2nd 32 pulses, and (d) the 2-D super-resolution image from the 3rd 32 pulses.

The radar parameters for the MPR AIDA data are: (1) center frequency $f_0 = 9.605$(GHz), (2) frequency step $df = 6.0$(MHz), (3) number of frequency steps $N = 35$, (4) number of pulses $M = 128$, and (5) pulse repetition frequency (PRF) $PRF = 20$(KHz). Fig.14 shows the FFT image of the MPR-130 data compared with a super-resolution ISAR image reconstructed only from the first 32 pulses of the same data (Fig.14(b)), the second 32 pulses (Fig.14(c)), and the third 32 pulses (Fig.14(d)). The 2-D super-resolution processing expanded the 35x32 raw data to a 128x128 image.

However, the time-frequency transform takes the whole 35x128 raw data and generates a stack of time-frequency images. Compared with the super-resolution method, the time-frequency transform has better cross-range resolution. Fig.15 shows 5 frames (frame no.4 to frame no.8) extracted from the sequence of 16 time-varying image frames. We can easily see that by using the time-frequency transform, the time-varying spectrum can be represented very well and, as a result, the smeared Fourier image is resolved into
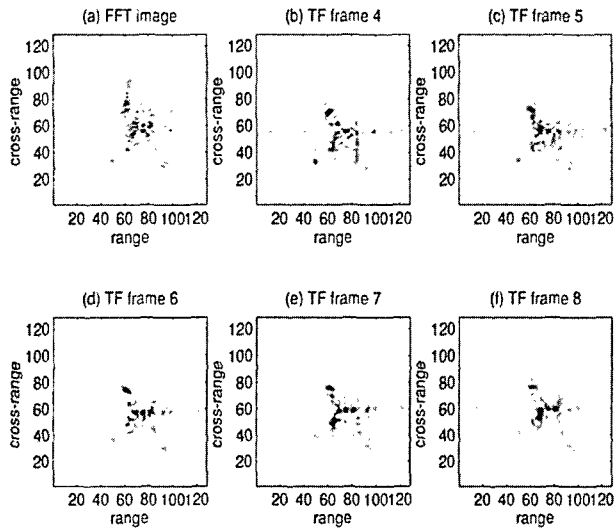
Fig. 15. A sequence of image frame of the MPR130 aircraft generated by time-frequency transform.

Fig. 17. ISAR images of FGAN data (a) the FFT image; (b)-(f) the time-frequency frames.

a sequence of time-varying images, which not only have superior resolution, but also shows the Doppler change and range walk in time.

5.3 NATO TIRA and ARDS Data

The NATO TIRA and ARDS data was collected by FGAN using a Ku-band radar operating at 16.7GHz wih a bandwidth of 800MHz to achieve 0.1875m range resolution. The total number of range cells is 1024. A set of ARDS data is also available to generate trajectories, angular positions and rotation rates.

We only take a small portion of the data (y97b1f15) where the target is located. 128 pulses (from pulse no.100 to no.227) and 128 range cells are used to generate the image of the target. Fig.16 shows the aligned range profiles after the range processing. The range-Doppler image generated by FFT after applying the phase correction is shown in Fig.17(a), and five selected range-Doppler image frames generated by the time-frequency image formation are shown in Fig.17(b)-(f).
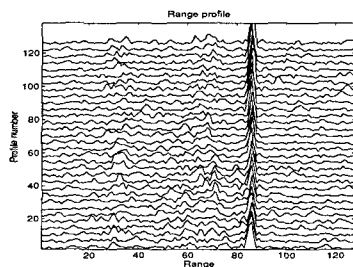

Fig. 16. Range profiles of the FGAN data.

6. Conclusion

We have examined the relationship between target motion and time-varying spectra in radar imaging of maneu-
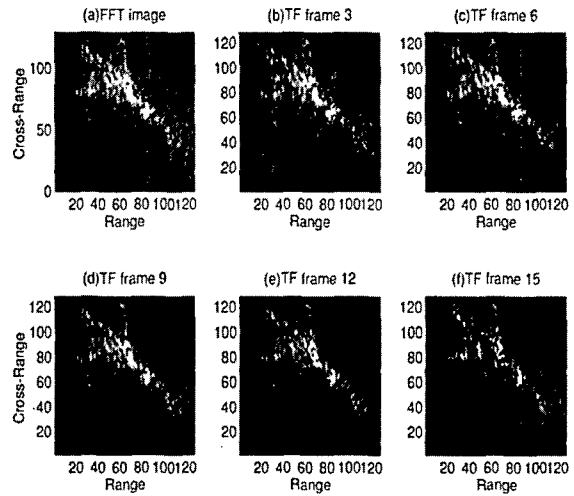
vering targets, and provided an insight into the blurring problem of radar images. We discussed the restriction of the Fourier analysis for radar image reconstruction and proposed a time-frequency approach to replace the Fourier analysis.

To represent time-varying spectra, a high resolution time-frequency analysis is desirable. We compared the time-frequency concentration and the instantaneous frequency of the commonly used algorithms (the STFT and the WVD) and the TFDS. We applied the TFDS to our time-varying analysis for radar imaging.

We used simulated data as well as real data to demonstrate the capability of the time-frequency transform to radar imaging of maneuvering targets. The result clearly shows that the time-frequency transform can be used to replace the Fourier analysis as a means of radar image formation that eliminates the image blurring problem.

REFERENCES

[1] D.R. Wehner (1994) *High-Resolution Radar* (2nd edition), Chapter 6 and 7, Artech House, Boston, 1994.
[2] W.G.Carrara, R.S.Goodman and R.M.Majewski (1995) *Spotlight Synthetic Aperture Radar - signal processing algorithms* Chapter 4, Artech House, Boston, 1995.
[3] R.P.Paul (1986) *Robot Manipulators: Mathematics, Programming, and Control* Chapter 2: Kinematic Equations, The MIT Press, Cambridge, MA, 1986.
[4] S.Qian and D.Chen (1996) *Joint Time-Frequency Analysis - methods and applications* Chapter 3, 5, and 7, Prentice-Hall, Upper Saddle River, New Jersey, 1996.
[5] L.Cohen (1995) *Time-frequency Analysis* Prentice-Hall, Englewood Cliffs, New Jersey, 1995.
[6] T.A.C.M. Claasen and W.F.G. Mecklenbrauker (1980) The Wigner distribution - A tool for time-frequency signal analysis *Phillips J. Res.*, **35**, (1980) pp.217-250, pp.276-300, pp.1067-1072.
[7] S.Qian and D.Chen (1994) Decomposition of Wigner-Ville distribution and time-frequency distribution series *IEEE Trans. on Signal Processing*, **42**, (1994) pp.2836-2842.
[8] V.C.Chen and S.Qian(1998) Joint time-frequency transform for radar range-Doppler imaging *IEEE Trans. on Aerospace and Electronic Systems*, **34(2)**, (1998) (to appear).

COHERENT RANDOM NOISE RADAR TECHNOLOGY FOR COVERT SURVEILLANCE OF NON-COOPERATIVE TARGETS

Ram M. Narayanan
Department of Electrical Engineering
Center for Electro-Optics
University of Nebraska-Lincoln
Lincoln, NE 68588-0511, U.S.A.

1. SUMMARY

An ultrawideband random noise radar system operating over the 1-2 GHz frequency range has been developed and tested at the University of Nebraska. A unique signal processing scheme is used to inject coherence in the system by performing heterodyne correlation of the reflected signal with a time-delayed replica of the transmit waveform. Heterodyne correlation preserves the phase of the reflected signal during the downconversion process, thereby permitting the extraction of the ultrawideband polarimetric scattering properties of the target for enhancing target identification. The phase coherence can also be exploited to obtain azimuthal tracking of targets using principles of interferometry, while the wide instantaneous bandwidth of the system can be used to achieve fine range resolution. The system can also be used to obtain linear as well as rotational Doppler information on non-stationary targets. Simulation results and experimental measurements confirm the ability of the ultrawideband random noise radar system to be usable for polarimetry, interferometry, and Doppler estimation.

The advantage of the random noise radar system is its covertness feature, i.e., its immunity for detection and jamming. Furthermore, the ultrawideband signal has the ability to provide high-resolution images on non-cooperative targets, while system phase coherence can be exploited to enhance target detection and reduce clutter. This paper will summarize the results obtained using this unique radar system, and address the extension of this technique for tracking position and velocity of non-cooperative targets in a covert manner.

Keywords: random noise radar, covert, polarimetry, interferometry, Doppler estimation

2. RANDOM NOISE RADAR POLARIMETRY

2.1 Description of Polarimetric Random Noise Radar System

A block diagram of the polarimetric random noise radar system is shown in Figure 1. This system was designed to detect and identify shallow buried objects, such as landmines. The noise signal is generated by OSC1 which provides a wideband noise signal with a Gaussian amplitude distribution and a constant power spectral density in the 1-2 GHz frequency range, with a power output of 0 dBm. This output is split
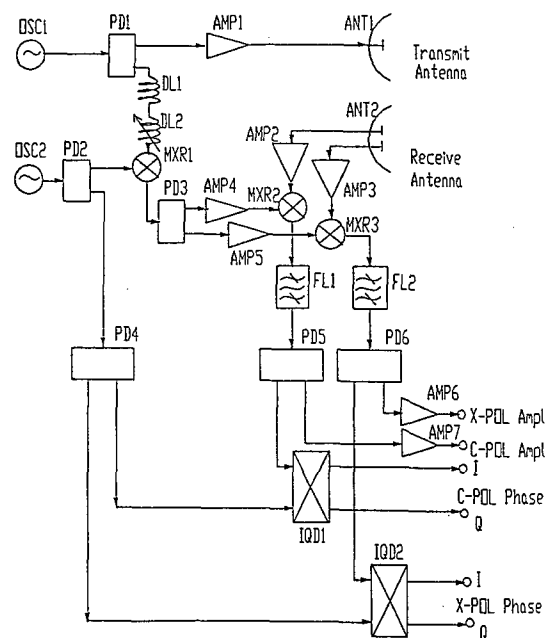
Figure 1: *Block diagram of ultrawideband polarimetric random noise radar system.*

into two in-phase components in power divider PD1. One of these outputs is amplified in a 34 dB gain power amplifier AMP1, which has a 1 dB gain compression point greater than +40 dBm. Thus, the average power output of AMP1 is +30 dBm (1 W), but the amplifier is capable of faithfully amplifying noise spikes that can be as high as 10 dB above the mean noise power. The output of the amplifier is connected to a dual-polarized broadband (1-2 GHz) log-periodic transmit antenna ANT1. The log-periodic antenna, in addition to being broadband, has desirable features such as a constant gain of 7.5 dB with frequency, and superior cross-polar isolation of greater than 20 dB.

The other output arm of the power divider PD1 is connected to a combination of a fixed and variable delay lines DL1 and DL2 respectively. These delay lines are used to provide the necessary time delay for the sampled transmit signal so that it can be correlated with the received signal scattered from objects or interfaces at the appropriate depth corresponding to the delay. Since the total probing depths are of the order of

1 m maximum, the delay lines are relatively short with maximum losses of not more than 1 dB. The variable delay line can be rapidly programmed to step through the entire range of available delays, so that various probing depths can be obtained.

In order to perform coherent processing of the noise signals, a unique frequency translation scheme is proposed. The primary component of this technique is a 160 MHz phase-locked oscillator OSC2. This is connected via a power divider PD2 to the IF input terminal of MXR1. The output of MXR1 is the lower sideband of the mixing process, which lies within the 0.84-1.84 GHz frequency range. This coherent noise signal is split by power divider PD3 into two channels: the co-polarized and the cross-polarized channels. Also the second output of the power divider PD2 is again split into two 160 MHz signals in power divider PD4.

We will now discuss the signal processing of the co-polarized channel. The cross- polarized channel operation is essentially identical, so it will not be repeated. One of the outputs of PD3 is amplified in a 19 dB gain amplifier AMP4. Since this signal is noiselike, the amplifier AMP4 is chosen so as to provide a linear output of +10 dBm minimum. This signal is used as the local oscillator (LO) input to a biasable mixer MXR2, whose RF input is obtained from the co-polarized channel of the receive antenna ANT2 and a 20 dB gain low noise amplifier AMP2. The receive antenna is identical to the transmit antenna. Amplifier AMP2 is used to improve the noise figure at the receiver input. Mixer MXR2 is DC-biased in the square-law region which ensures that the mixing process is efficient for low LO drive levels. In general, the RF input signal to the mixer MXR2 consists of transmitted noise at 1-2 GHz scattered and reflected from various objects/interfaces. However, since the LO signal has a unique delay associated with it, only the signal scattered from the appropriate depth (i.e., range) bin will mix with the LO to yield a IF signal at a frequency of exactly 160 MHz. Signals scattered or reflected from other depth bins, will not provide a constant frequency of 160 MHz. The output of the mixer MXR2 is connected to a narrowband bandpass filter FL1 of center frequency 160 MHz and bandwidth 5 MHz, ensuring that only 160 MHz signals get through. The output of filter FL1 at 160 MHz is split into two outputs in power divider PD5. One of these outputs is amplified and detected in a 70 dB dynamic range 160 MHz logarithmic amplifier AMP6. The other output of the power divider PD5 is connected to one of the inputs of an I/Q detector IQD1, whose reference input is one of the outputs from PD4. Both of the signals are exactly at 160 MHz; thus the I/Q detector provides the in-phase (I) and quadrature (Q) components of the phase difference between the two signals. Since frequency translation preserves phase differences, the I and Q outputs can be related to the polarimetric co-polarized scattering characteristics of the buried object or interface.

In a similar fashion, the cross-polarized channel is simultaneously processed using amplifier AMP5 (equivalent to AMP4), biasable mixer MXR3 (equivalent to MXR2), 160 MHz bandpass filter FL1 (equivalent to FL2), power divider PD5 (equivalent to PD6), logarithmic amplifier AMP7 (equivalent to AMP6) and I/Q detector IQD2 (equivalent to IQD1).

The system therefore produces the following outputs at various depths as set by the delay lines: (a) Co-polarized amplitude, (b) Co-polarized phase angle, (c) Cross-polarized amplitude, and (d) Cross-polarized phase angle.

Thus, the system outputs can be related to the polarimetric scattering characteristics of the target.

2.2 Theory of Random Noise Polarimetry

Since the transmitted signal has a random amplitude distribution and a uniform power spectral density, we model the transmit voltage wave $v_t(t)$ as

$$v_t(t) = a(t) \cos(\omega_o + \delta\omega)t \qquad (1)$$

where $a(t)$ takes into account the amplitude distribution, and $\delta\omega(t)$ takes into account the frequency spectrum of $v_t(t)$. ω_o is the center frequency of transmission. We assume that $a(t)$ follows a Gaussian distribution while $\delta\omega(t)$ follows a uniform distribution, and that both $a(t)$ and $\delta\omega(t)$ are ergodic processes. Furthermore, we assume that $a(t)$ and $\delta\omega(t)$ are uncorrelated and statistically independent.

The average power transmitted P_t, is given by

$$P_t = \frac{\overline{v_t^2(t)}}{R_o} \qquad (2)$$

where R_o is the characteristic system impedance, and a bar over a variable denotes its time average value. Since $a(t)$ and $\delta\omega(t)$ are independent, we can write

$$\begin{aligned}
\overline{v_t^2(t)} &= \overline{a^2(t)\cos^2\{(\omega_o + \delta\omega)t\}} \\
&= \overline{a^2(t)} \cdot \overline{\cos^2\{(\omega_o + \delta\omega(t))t\}} \\
&= \frac{1}{2}\overline{a^2(t)} \qquad (3)
\end{aligned}$$

since the average value of $\cos^2(\cdot)$ is $\frac{1}{2}$. Thus,

$$P_t = \frac{1}{2R_o}\overline{a^2(t)} \qquad (4)$$

Consider an object of complex reflectivity $R\,exp\{j\phi_o\}$ buried at a depth d. To simplify the analysis, we assume that both the magnitude R and the phase angle ϕ_o of the object reflectivity are invariant with frequency. If the dielectric constant of soil is $\epsilon_r(= \epsilon_r' - j\epsilon_r'')$, the phase velocity of the electromagnetic wave is

$$v_p = \frac{c}{\sqrt{\epsilon_r'}} \qquad (5)$$

if we assume that the soil medium is lossless, i.e., $\epsilon_r'' \ll \epsilon_r'$. Thus, the two-way delay for a signal that is transmitted, reflected and arriving at the receive antenna, τ, is

$$\tau = \frac{2d}{v_p} = \frac{2d\sqrt{\epsilon_r'}}{c} \qquad (6)$$

For lossy media, the phase velocity v_p is slower than the lossless case, thereby increasing the two-way signal delay τ.

Let the propagation constant in soil, γ, be given by

$$\gamma = \alpha + j\beta \qquad (7)$$

where α is the attenuation constant and β is the phase constant. In general, α and β both increase with frequency. Thus, the two-way propagation factor is given by

$$\begin{aligned} A(d) &= exp\{-2\gamma d\} \\ &= exp\{-2\alpha d\}exp\{-2j\beta d\} \end{aligned} \qquad (8)$$

The time varying expression for the received voltage $v_r(t)$ can now be obtained as the time-delayed version of $v_t(t)$ modified to include the effects of scattering and two-way propagation. Thus,

$$\begin{aligned} v_r(t) &= a(t - \tau) \, R \, exp\{-2\alpha d\} \cdot \\ &\quad cos\{(\omega_o + \delta\omega)(t - \tau) + \phi_o - 2\beta d\} \end{aligned} \qquad (9)$$

The time-delayed sample of the transmit signal is

$$v_t(t - \tau) = a(t - \tau)cos\{(\omega_o + \delta\omega)(t - \tau)\} \qquad (10)$$

When this signal is passed through a double sideband upconverter whose IF frequency is ω', the lower sideband output $v_t'(t - \tau)$ is

$$v_t'(t - \tau) = a(t - \tau)cos\{(\omega_o - \omega' + \delta\omega)(t - \tau)\} \qquad (11)$$

The difference frequency from the mixing process of $v_r(t)$ and $v_t'(t - \tau)$ yields a voltage $v_d(t)$ given by

$$\begin{aligned} v_d(t) &= K_1 R a^2(t - \tau)exp\{-2\alpha d\} \\ &\quad cos\{\omega'(t - \tau) + \phi_o - 2\beta d\} \end{aligned} \qquad (12)$$

where K_1 is some constant. Note that this signal is always centered around ω'. The average amplitude of this signal, $\overline{V_d}$, is given by

$$\begin{aligned} \overline{V_d} &= K_1 \overline{Ra^2(t - \tau)}exp\{-2\alpha_o d\} \\ &= 2K_1 RR_o P_t \, exp\{-2\alpha_o d\} \end{aligned} \qquad (13)$$

where α_o is the value of α at $\omega = \omega_o$. The average power in this signal, P_r, is given by

$$\begin{aligned} P_r &= \frac{\overline{V_d}^2}{2R_o} = 2K_1^2 R_o P_t^2 exp\{-4\alpha_o d\}R^2 \\ &= K_2 R^2 \end{aligned} \qquad (14)$$

where K_2 is a constant. Thus measurement of the power P_r yields the square of the reflection coefficient magnitude.

In order to measure the phase ϕ_o, consider the output of the I/Q detector fed by $v_d(t)$ and $v_1(t)$, where $v_1(t)$ is given by

$$v_1(t) = cos \, \omega' t \qquad (15)$$

Since both of these signals are at the same frequency ω', the I/Q detector can unambiguously measure the phase difference, θ, given by

$$\theta(t) = -\omega'\tau + \phi_o - 2\beta d \qquad (16)$$

The average value of θ as measured by the I/Q detector is

$$\overline{\theta} = -\omega'\tau + \phi_o - \overline{2\beta d} \qquad (17)$$

Note that $\overline{\beta}$ is simply the value of β at $\omega = \omega_o$, which is

$$\overline{\beta} = \frac{\omega_o\sqrt{\epsilon_r'}}{c} \qquad (18)$$

We therefore obtain

$$\overline{\theta} = \phi_o - \omega'\tau - \frac{2\omega_o\sqrt{\epsilon_r'}d}{c} \qquad (19)$$

Thus, a measurement of the average value of θ yields the phase angle ϕ_o.

Until this point, we have not considered the effects of polarization. If the antenna can simultaneously measure both the co-polarized and the cross-polarized scattered power, and if the hardware for both co-polarized and cross-polarized channels are identical, then we can measure $P_{rc}, P_{rx}, \overline{\theta_c}$ and $\overline{\theta_x}$ where the subscripts "c" and "x" refer to the co-polarized and the cross-polarized channels respectively.

Thus

$$P_{rc} = K_2 R_c^2 \qquad (20)$$
$$P_{rx} = K_2 R_x^2 \qquad (21)$$

Thus the ratio of P_{rx} to P_{rc} yields the power depolarization ratio, D, which is seen to be independent of the system transfer function, i.e.,

$$\frac{P_{rx}}{P_{rc}} = \frac{R_x^2}{R_c^2} = D \qquad (22)$$

Furthermore, we have

$$\overline{\theta_c} = \phi_{oc} - \omega'\tau - \overline{2\beta d} \qquad (23)$$

and

$$\overline{\theta_x} = \phi_{ox} - \omega'\tau - \overline{2\beta d} \qquad (24)$$

Thus the difference between $\overline{\theta_x}$ and $\overline{\theta_c}$ yields the phase angle between the cross-polarized and co-polarized channels, again seen to be independent of the system.

$$\overline{\theta_x} - \overline{\theta_c} = \phi_{ox} - \phi_{oc} \qquad (25)$$

The resolution properties of the system can be easily observed by considering a received signal from another range (or depth) bin whose delay is different from τ. Let the delay from the buried object be τ', but the delay within the system be τ. In this case, $v_r(t)$ is now modified and expressed as $v_r'(t)$ as follows:

$$\begin{aligned} v_r'(t) &= a(t - \tau') \, exp\{-2\alpha d\} \cdot \\ &\quad cos\{(\omega_o + \delta\omega')(t - \tau') + \phi_o - 2\beta d\} \end{aligned} \qquad (26)$$

When this signal is mixed with $v_t'(t - \tau)$, we get $v_d'(t)$ given by

$$\begin{aligned} v_d'(t) &= Ra(t - \tau)a(t - \tau')exp\{-2\alpha d\} \cdot \\ &\quad cos\{\omega'(t - \tau) - \omega_o(t - \tau') + \delta\omega'(t - \tau') \\ &\quad - \delta\omega(t - \tau) + \phi_o - 2\beta d\} \end{aligned} \qquad (27)$$

Since the noise voltage $a(t)$ has an impulse-like function of the form $\sin x/x$, for its temporal correlation function, we have the result

$$\overline{a(t_1)a(t_2)} = 0 \qquad (28)$$

for $|t_1 - t_2| >> 1/B$, where B is the system bandwidth. Thus, the average power in the signal $v'_d(t)$ can be shown to be equal to zero.

We see, therefore, that unless the internal time delay is exactly matched to the expected time delay, the output of the detector is zero. As we step the internal time delay τ from zero to the maximum expected value, the depth profile of scattering can be built up by the system, so that not only can targets be identified, but they can also be localized.

In practice, the practical system will suffer from drawbacks such as system non-linearities in amplitude and phase that can degrade the detection efficiency and resolution. In an ideal case, the resolution is determined by the system bandwidth B. The resolution Δd is given by

$$\Delta d = \frac{v_p}{2B} = \frac{c}{2\sqrt{\epsilon'_r}B} . \qquad (29)$$

For $c = 3 \times 10^8$ m/sec and $B = 1$ GHz, we get

$$\Delta d = \frac{15}{\sqrt{\epsilon'_r}} \, cm . \qquad (30)$$

For dry soil, $\epsilon'_r \simeq 3$ and for wet soil, $\epsilon'_r \simeq 25$. Thus the resolution varies from 8.6 cm in dry soil to 3 cm in wet soil, with an intermediate value of about 5 cm.

From the raw data collected by the radar system, we generate images based on the Stokes matrix formulation for facilitating the detection and recognition of targets using the polarimetric information on the buried target. The Stokes vector is a convenient method for representing the polarization state of an electromagnetic wave, and is denoted as $[S]$, given by

$$[S] = \begin{bmatrix} S_0 \\ S_1 \\ S_2 \\ S_3 \end{bmatrix} \qquad (31)$$

whose individual elements are defined as follows:

$$S_0 = |E_H|^2 + |E_V|^2 \qquad (32)$$
$$S_1 = |E_H|^2 - |E_V|^2 \qquad (33)$$
$$S_2 = 2|E_H||E_V| \cos\theta_d \qquad (34)$$
$$S_3 = 2|E_H||E_V| \sin\theta_d \qquad (35)$$

In the above equations, θ_d is the polarimetric phase angle, i.e, the difference between the phase angle of the horizontally received signal and the vertically received signal. Also, $|E_H|$ and $|E_V|$ are the electric field amplitudes of the horizontally and vertically polarized received signals, whose squared values represent the co-polarized reflected power and cross-polarized reflected power respectively (assuming the transmit polarization is horizontal). We recognize S_0 as the total reflected power (sum of the co-polarized and cross-polarized reflected power). S_1 is recognized as the difference between the co-polarized and cross-polarized reflected power. S_2 is proportional to the cosine of the polarimetric phase angle, while S_3 is proportional to the sine of the polarimetric phase angle θ_d. Both S_2 and S_3 are weighted by the absolute electric field amplitudes of the reflected co-polarized and cross-polarized signals, as can be seen from their definitions. It is also to be noted that

$$S_0^2 = S_1^2 + S_2^2 + S_3^2 . \qquad (36)$$

The use of S_2 and S_3 is very helpful in detecting targets, since these parameters move in opposite directions and thereby provide additional information about the reflected signal. When S_2 is high, S_3 is low, and vice versa. Thus, no matter what the polarimetric phase angle is, the target image is bound to show up in either S_2 or S_3, or sometimes in both.

2.3 Simulation Results

Various computer simulations were performed to evaluate the performance of the radar system design. These simulations were performed for various combinations of soil type, soil moisture, depth of target burial, as well as polarimetric response of the buried target. Ground reflections as well as uncorrelated system noise were added to the received signal to simulate realistic field conditions. Results of simulations using random noise as the probing signal are shown in Figures 2 and 3. In Figure 2, the reflectivity of the buried object is assumed to be $1 \exp\{j0°\}$, while in Figure 3, the reflectivity of the buried object is assumed to be $1 \exp\{j90°\}$. The objects are assumed to be located at a depth of 5 cm in clayey soil (48% clay, 40% silt) with 10% volumetric moisture whose dielectric constant was computed as $\epsilon_r = 4.56 - j1.32$. The following plots are shown in the figures: (a) Transmitted signal amplitude vs. time, (b) Transmitted signal shifted by $\pm \omega'$ to simulate the double sideband upconversion, (c) Received signal amplitude vs. time after two-way propagation and reflection, (d) Multiplied output of signals in (b) and (c) above vs. time, (e) Spectrum of filtered output in (d) showing the peak at ω', and (f) Multiplied output in (d) filtered at ω', showing the input signal at the I/Q detector vs. time (solid line). As can be seen, the polarimetric phase of the reflection from the buried object is clearly evident in Figures 2(f) and 3(f). These signals are 90° out of phase, consistent with the 90° phase difference in their assumed reflectivity.

2.4 Experimental Results

The radar system was used to gather data from an assortment of different buried objects in a specially designed sand box, 3.5 m long, 1.5 m wide and 1 m deep. Metallic as well as non-metallic objects were buried at different depths and orientations. The radar antennas were scanned over the surface as data were collected continuously.

A typical raw image obtained using the polarimetric random noise radar is shown in Figure 4. The figure contains four images from one radar scan over various buried objects. The top image is the co-polarized received power. The second image is the cross-polarized received power. The third image
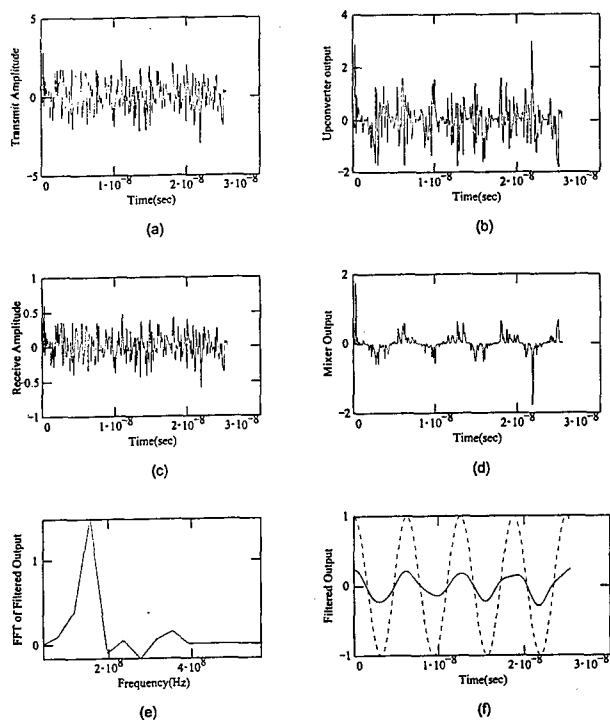
Figure 2: *Simulated waveforms for target reflectivity of* $1 \exp\{j0°\}$: *(a) Transmit waveform, (b) Upconverter output waveform, (c) Received waveform, (d) Mixer output waveform, (e) Spectrum of mixer output, and (f) Filtered mixer output waveform - solid line.*

Figure 3: *Simulated waveforms for target reflectivity of* $1 \exp\{j0°\}$: *(a) Transmit waveform, (b) Upconverter output waveform, (c) Received waveform, (d) Mixer output waveform, (e) Spectrum of mixer output, and (f) Filtered mixer output waveform - solid line.*

is the depolarization ratio, and the fourth image is the absolute phase difference between the co-polarized and the cross-polarized received channels.

The image pertains to a metal plate, 23 cm in diameter and 2 cm thick, and an identical wooden plate. Both plates were buried at a depth of 23 cm below the surface, with a lateral separation of 23 cm. In this image, it is easy to detect the metal plate, but the wooden plate is not clearly observable on account of its low dielectric contrast with respect to the soil medium. Further data processing using the polarimetric phase information may make this object more visible, and one such technique based on Stokes matrix processing is discussed below.

Stokes matrix images were generated and combined with simple image processing operations to improve target detectability and clutter rejection. The smoothing filter is used for reduction of radar clutter and noise. It was found from the original raw data that high-frequency tonal variations were prevalent in regions without targets, and these grainy variations were attributed to the fact that the soil volume was inhomogeneous, and contained voids and rocks. The smoothing operation, when performed, results in low pass filtering and eliminates the high-frequency noise components. The thresholding operation is applied on the global scale to the entire smoothed
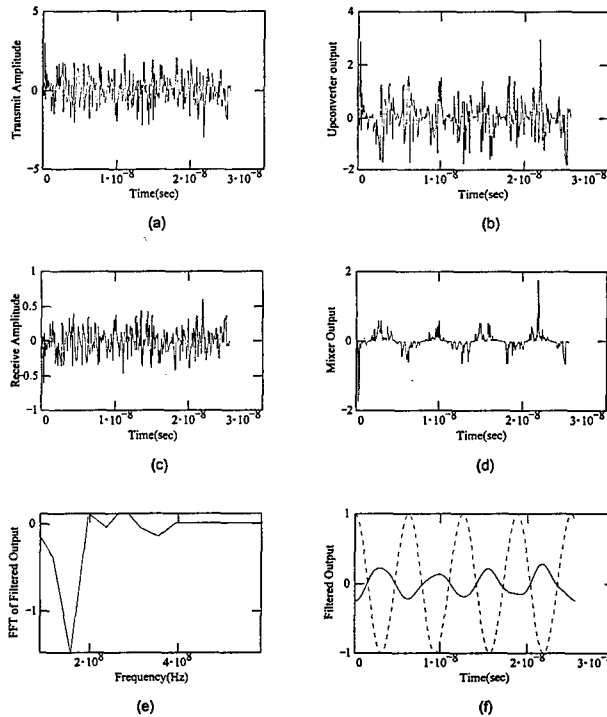
image. It enhances image intensities above the mean intensity of the entire image, thereby enhancing target detectability, while simultaneously eliminating clutter, identified as low intensity areas, by setting these to zero digital number. As will be shown, these post-processing operations are successful in reducing clutter and enhancing target detectability. The smoothing and thresholding operations were performed on all four Stokes matrix images.

The corresponding post-processed image of Figure 5 shows S_0 (top left), S_1 (bottom left), S_2 (top right), and S_3 (bottom right). Both objects, especially the wooden plate (right object) are detectable in the S_1 image, thereby demonstrating the advantage of polarimetric processing.

3. RANDOM NOISE INTERFEROMETRY

3.1 Description of Random Noise Interferometer

A simplified block diagram of the random noise radar interferometer is shown in Figure 6. The noise source OSC1 produces a signal with a Gaussian amplitude distribution and a constant power spectral density in the 1-2 GHz frequency range at an average output power level of 0 dBm (1 mW). The noise source output is split into two equal in-phase components in power divider PD1. One of the outputs is amplified in a broadband 34 dB gain medium power amplifier AMP1,
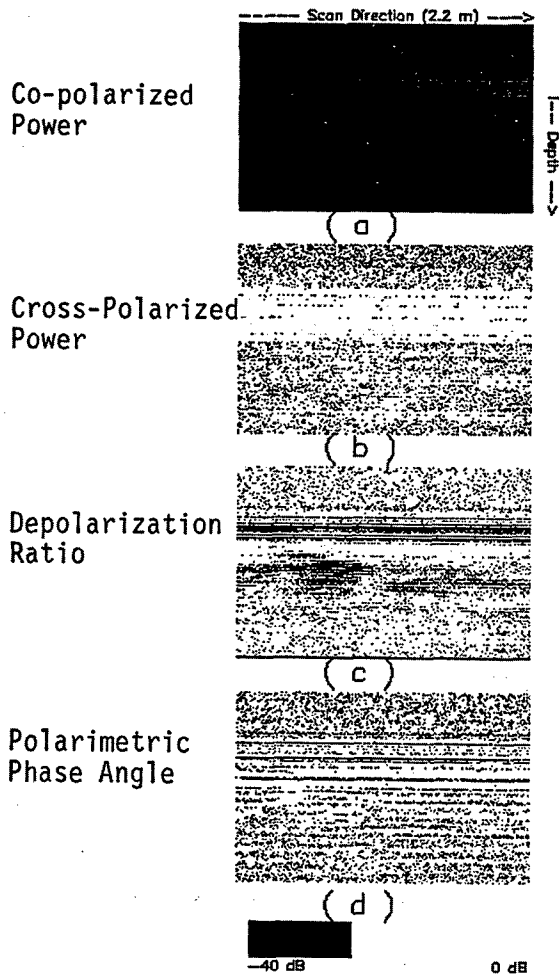
Figure 4: *Raw image of a metal plate and a wooden plate buried at same depth: (a) co-polarized received power, (b) cross-polarized received power, (c) depolarization ratio, and (d) polarimetric phase difference.*

Figure 5: *Post-processed image of a metal plate and a wooden plate buried at same depth: (a) S_0-image smoothed and thresholded, (b) S_1-image, smoothed and thresholded, (c) S_2-image, smoothed and thresholded, and (d) S_3-image, smoothed and thresholded.*

and transmitted via a horn antenna ANT1, whose E/H plane beamwidths and gain at 1.5 GHz are 23°, 34°, and 17 dB, respectively. The other output is connected to a combination of a fixed delay line DL1 and a digitally controlled variable delay line DL2. The fixed delay line is used to set the minimum range to the target, while the variable delay line can be programmed for delays from 0 to 19.968 nsec in 0.156 nsec steps. The delay line output is mixed with the output of a 160 MHz phase-locked oscillator OSC2 (through a power divider PD2) in a lower sideband upconverter MXR1. The upconverter output, in the 0.84-1.84 GHz frequency range, feeds a power divider PD3, whose two outputs feed each receive chain.

One of the outputs is amplified in AMP4 and fed to a mixer MXR2. The other input to this mixer is the signal received by one of the receive antennas ANT2 in the 1-2 GHz range, subsequently amplified in a low noise amplifier AMP2. The output of mixer MXR2 is thus always at 160 MHz, since the two inputs to the mixer are shifted by 160 MHz. However, the phase of the receive signal at the input to the antenna ANT2
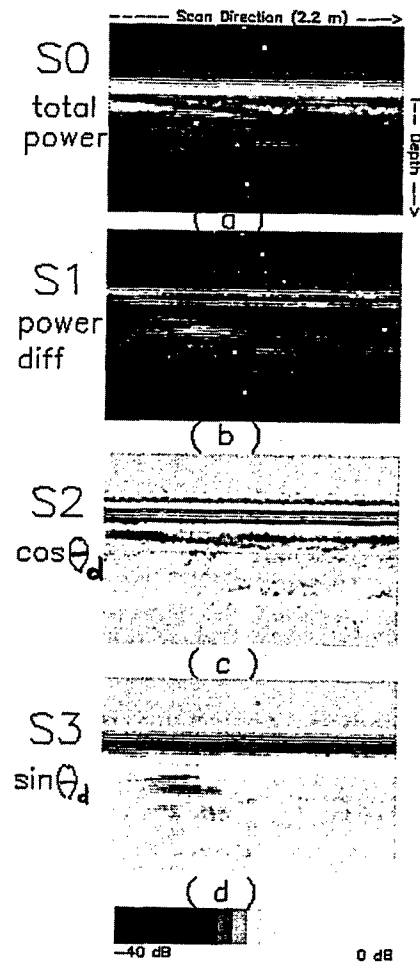
is preserved in the mixing operation. This 160 MHz signal is filtered in a 160 MHz bandpass filter FL1, and split in a power divider PD5, one of which is amplified in a logarithmic amplifier AMP7 to yield the signal amplitude, while the other is fed to the I/Q detector IQD1 fed by the 160 MHz master oscillator to yield the in-phase (I) and quadrature (Q) components of the signal phase. A similar receiver is used for the second receive chain that is received by the antenna ANT3. Receive antennas ANT2 and ANT3 are broadband constant 7.5 dB gain log-periodic antennas with E/H plane beamwidths of 65° and 100° respectively. Knowledge of the instantaneous phase of the receive signal at each antenna can yield the azimuthal angle at which the scattered signal from the target arrives at the receiver.

3.2 Theory of Random Noise Interferometry

Consider a simple interferometer shown in Figure 7. The spacing between the two receive antennas is $2d$, while the
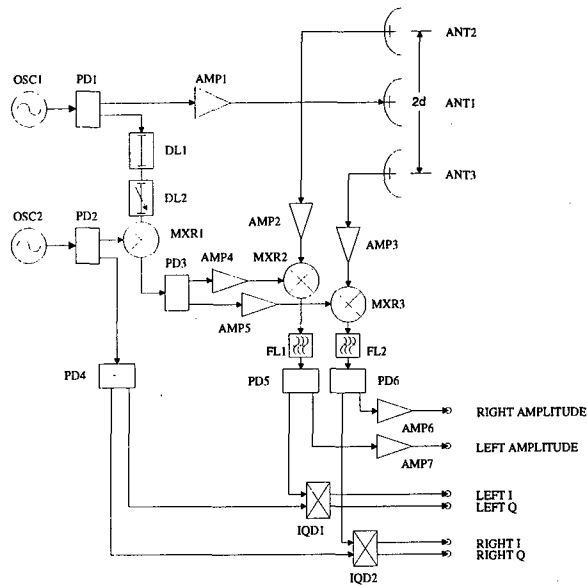
Figure 6: *Block diagram of the random noise radar interferometer.*

Figure 7: *Geometry of simple interferometer.*

transmit antenna is located at the center of the baseline. Let the range to the target, measured from the center of the baseline, be R. We assume that $R \gg 2d$. Also, we assume that the transmit and receive antenna patterns are broad compared to the angle subtended at the target by the two receive antennas.

We assume that the transmit waveform, $\hat{V}_t$, can be represented in phasor form as

$$\hat{V}_t = A \, \exp\{j(\omega_0 + \delta\omega)t\} \tag{37}$$

where A is the Gaussian distributed amplitude, ω_0 is the center frequency of transmission and $\delta\omega$ is the uniformly distributed frequency variation.

Let R_1 and R_2 be the distance from the target to each receive antenna, as shown. We can show that

$$R_1 \simeq R - d\sin\theta \tag{38}$$

and

$$R_2 \simeq R + d\sin\theta \tag{39}$$

where θ is the target's azimuthal location with respect to the boresight direction. θ is positive for targets located towards the right side of the boresight axis, and negative for targets located towards the left side of the boresight axis.

The phasor representation for the voltage at the left receive antenna, $\hat{V}_{r1}$, is given by

$$\hat{V}_{r1} = A\rho \cdot \tag{40}$$
$$\exp\left\{ j \left[(\omega_0 + \delta\omega)t + \phi_0 - \frac{(\omega_0 + \delta\omega)}{c}(2R + d\sin\theta) \right] \right\}$$

where ρ and ϕ_0 are the magnitude and phase of the target's reflection coefficient, respectively.

Similarly, the phasor representation for the voltage at the right receive antenna, $\hat{V}_{r2}$, is
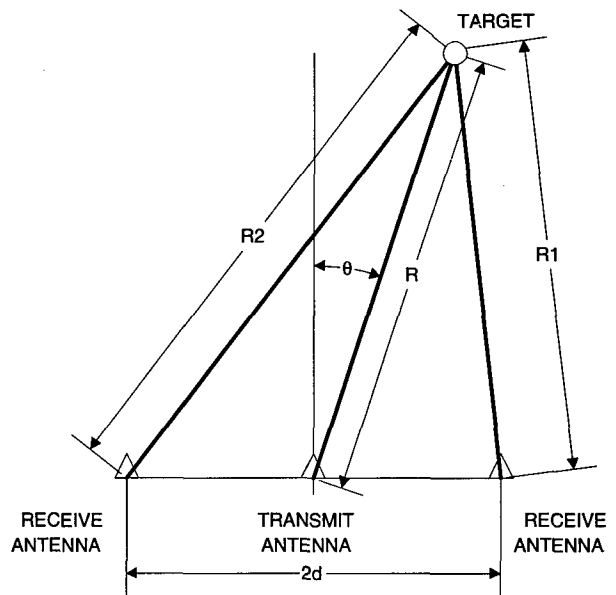
$$\hat{V}_{r2} = A\rho \cdot \tag{41}$$

$$\exp\left\{ j \left[(\omega_0 + \delta\omega)t + \phi_0 - \right.\right.$$
$$\left.\left. \frac{(\omega_0 + \delta\omega)}{c}(2R - d\sin\theta) \right] \right\}$$

Let a phase shift of $\Delta\phi$ (positive or negative) be added to $\hat{V}_{r2}$. We have

$$\hat{V}'_{r2} = \hat{V}_{r2} \cdot \exp\{j\Delta\phi\} = A\rho \cdot \tag{42}$$

$$\exp\left\{ j \left[(\omega_0 + \delta\omega)t + \phi_0 - \frac{(\omega_0 + \delta\omega)}{c} \right.\right.$$
$$\left.\left. (2R - d\sin\theta) + \Delta\phi \right] \right\}.$$

The cross-correlation of the signal received by the left antenna and the phase-shifted signal received by the right antenna is given by

$$\langle \hat{V}_{r1}\hat{V}'^*_{r2} \rangle = \rho^2 \langle A^2 \rangle \cdot \tag{43}$$

$$\left\langle \exp\left\{ j \left[\frac{-2(\omega_0 + \delta\omega)}{c} d\sin\theta + \Delta\phi \right] \right\} \right\rangle$$

$$= \rho^2 \langle A^2 \rangle \exp\left\{ j \left[\frac{-2\omega_0 d\sin\theta}{c} + \Delta\phi \right] \right\} \cdot \tag{44}$$

$$\left\langle \exp\left\{ -j\frac{2\delta\omega \, d\sin\theta}{c} \right\} \right\rangle,$$

where the expectation operator $\langle \cdot \rangle$ denotes the time average, and the random variables A and $\delta\omega$ are assumed to be uncorrelated.

The total power received by either receive antenna is given by

$$\langle \hat{V}_r\hat{V}^*_r \rangle = \langle \hat{V}_{r1}\hat{V}^*_{r1} \rangle = \langle \hat{V}_{r2}\hat{V}^*_{r2} \rangle = \rho^2 \langle A^2 \rangle. \tag{45}$$

The ratio of the cross-correlated power to the total power received, as a function of the phase shift $\Delta\phi$ introduced, is de-

noted by $\hat{C}(\Delta\phi)$, and is given by

$$\hat{C}(\Delta\phi) = \exp\left\{ j\left[\frac{-2\omega_0\, d\sin\theta}{c} + \Delta\phi\right] \right\} \cdot \qquad (46)$$

$$\left\langle \exp\left\{ -j\frac{2\delta\omega\, d\sin\theta}{c} \right\} \right\rangle.$$

In (46), we recognize the term within the expectation operator as the instantaneous phase shift introduced due to the varying instantaneous frequency. Since this frequency variation is a zero-mean uniformly distributed random variable, we assume that the average phase shift introduced by the frequency excursion around the center frequency, ω_0, is zero, thus making the second term reduce to unity. We have, therefore,

$$\hat{C}(\Delta\phi) = \exp\left\{ j\left[\frac{-2\omega_0\, d\sin\theta}{c} + \Delta\phi\right] \right\}. \qquad (47)$$

As $\Delta\phi$ is varied, the value of $\hat{C}(\Delta\phi)$ varies, and its maximum value occurs at $\Delta\phi = \Delta\phi_{max}$ when

$$\Delta\phi_{max} = \frac{2\omega_0 d\sin\theta}{c}. \qquad (48)$$

Thus, we have

$$\theta = \sin^{-1}\left[\frac{c\Delta\phi_{max}}{2\omega_0 d}\right]. \qquad (49)$$

Knowledge of ω_0 and d, and measurement of $\Delta\phi$, the correct amount of phase shift (positive or negative) to be added to $\hat{V}_{r2}$ to maximize $\hat{C}$, will yield θ, the azimuth angle at which the target is located.

3.3 Experimental Results

The results of measurements made using the random noise interferometer system are shown in this section. The transmit antenna was located at the center of a 40-cm long baseline, which was chosen to optimize the azimuthal scanning accuracy. The receive antennas were located at each end of the baseline. The angle θ is measured from the normal to the baseline, with positive angles to the right, and negative angles to the left. The polarization used was vertical.

The first experiment was performed to check if the interferometer could correctly locate a target placed along the boresight direction, i.e., $\theta = 0°$. At this location, the phase at each receive antenna is the same. The target used was a large corner reflector of side 45.72 cm, whose radar cross section (RCS) at 1.5 GHz was computed as 4.576 sq.m (+6.6 dBsm). The target was placed at a range of 2.134 m from the center of the baseline. The range-angle map, shown in Figure 8, correctly places the target in range and in azimuth. The amplitude of the reflected signal is indicated by the height of the spike.

In the second experiment, the same corner reflector was moved 0.61 m to the right. It was thus located at a range of 2.219 m and an azimuth angle of +15.95°. This caused a phase difference between the signals received by each receive antenna, which was processed to locate the target in azimuth. The range determination was made by stepping the
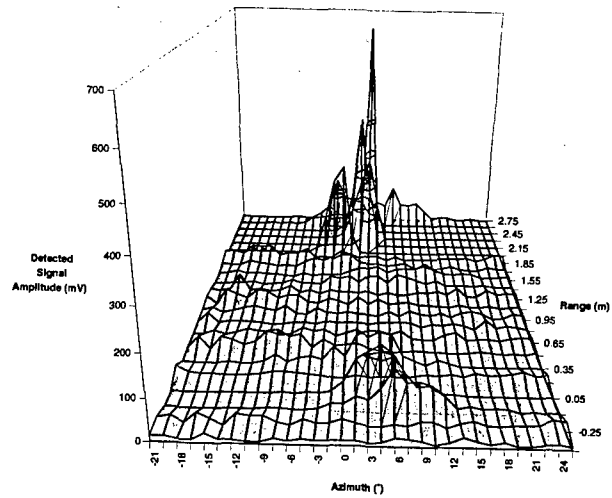
Figure 8: *Range-angle map of target located on boresight axis.*
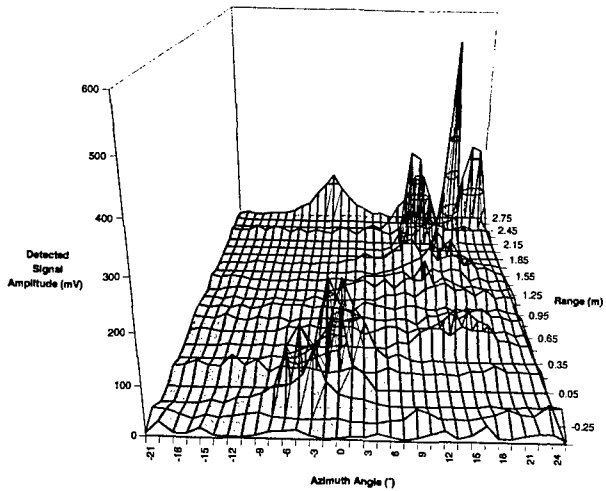
Figure 9: *Range-angle map of target located at an angle of 15.95° to right of boresight axis.*

variable delay line, as in the previous case. The range-angle map, shown in Figure 9, correctly locates the target in range and in azimuth. The slight reduction in the signal amplitude is attributed to the slightly increased range to the target as compared to the previous case.

4. DOPPLER ESTIMATION USING COHERENT RANDOM NOISE RADAR

4.1 Configuration of Random Noise Doppler Estimation System

A simplified block diagram of the random noise Doppler radar is shown in Fig. 10. The noise source OSC1 produces a sig-

Figure 10: *Block diagram of random noise Doppler radar system.*

nal with a Gaussian amplitude distribution, constant PSD, and average output level of 0 dBm (1 mW) in the 1-2 GHz frequency range. The noise source output is split into two equal in-phase components in power divider PD1.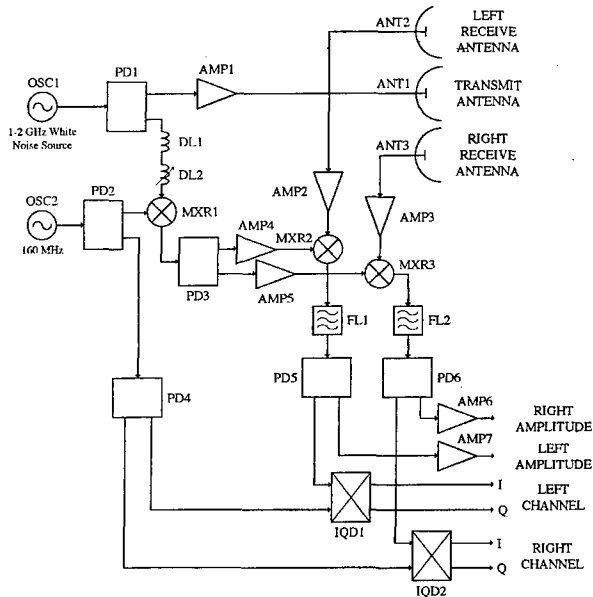 One of the outputs is amplified in a broadband 34 dB gain medium power amplifier AMP1 and transmitted via a horn antenna ANT1. The E/H plane beamwidths and gain of ANT1 at 1.5 GHz are 23°, 34°, and 17 dB respectively. The second output of PD1 is connected to a combination of a fixed delay line DL1 and a digitally controlled variable delay line DL2. The fixed delay line is used to set the minimum range to the target, while the variable delay line can be programmed for delays from 0 to 19.968 ns in 0.156 ns steps. The delay line output is mixed with the output of a 160 MHz phase-locked oscillator OSC2 (through power divider PD2) in a lower sideband upconverter MXR1. The upconverter output, in the 0.84-1.84 GHz frequency range, feeds power divider PD3, whose outputs feed each receive chain.

One of the outputs of PD3 is amplified in AMP4 and fed to mixer MXR2. A 1-2 GHz signal received by antenna ANT2 and amplified through low noise amplifier AMP2 provides the second input to mixer MXR2. Thus, the output of mixer MXR2 is always at 160 MHz, since the two mixer inputs are shifted by 160 MHz. However, the phase of the received signal at the input to antenna ANT2 is preserved in the mixing operation.

The 160 MHz output of MXR2 is filtered in a 160 MHz bandpass filter FL1 and split in power divider PD5. One of the outputs of PD5 is amplified in logarithmic amplifier AMP7 to yield the signal amplitude, and the other output is fed to I/Q detector IQD1. The 160 MHz master oscillator OSC2 also feeds IQD1. Thus, IQD1 yields the in-phase (I) and quadrature (Q) components of the received signal. A similar receiver is used for the second receive chain connected to antenna

ANT3. Receive antennas ANT2 and ANT3 are broadband constant 7.5 dB gain log-periodic antennas with E/H plane beamwidths of 65° and 100°, respectively.

4.2 Theory of Doppler Estimation Using Coherent Random Noise Radar

Since the transmitted amplitude has a Gaussian amplitude distribution and uniform power spectral density, it can be modeled as:

$$v_t(t) = a(t)\cos\left\{(\omega_0 + \delta\omega)\,t + \psi_t\right\} \qquad (50)$$

where $a(t)$ represents the Gaussian amplitude distribution, ω_0 is the center frequency at 1.5 GHz, $\delta\omega$ is uniformly distributed over the 0.5 GHz frequency range, and ψ_t is the arbitrary transmitter phase.

The time delayed version of the transmitted signal, $v_t(t)$, is mixed in MXR1 with the reference frequency ω_{ref} at 160 MHz to produce the lower side band output, $v_{m1}(t)$, given by:

$$v_{m1}(t) = k_1 a(t - \tau)\cos\left\{(\omega_0 + \delta\omega - \omega_{ref})\,(t - \tau)\right\} \quad (51)$$

where k_1 is some constant and τ is the delay.

The echo from the target is expressed as

$$v_r(t) = k_2 a(t)\rho\cos\left\{(\omega_0 + \delta\omega)\left(t - \frac{2R}{c}\right) + \psi_t + \psi_s\right\} \quad (52)$$

where c is the velocity of light, ρ and ψ_s are the amplitude and phase of the target reflectivity, and the term $2R/c$ represents the time taken by the transmitted wave to return to the receiver from the target, at range R.

The instantaneous phase of the echo voltage can be defined as:

$$\psi_r = \left(\frac{-4\pi R}{\lambda}\right) + \psi_t + \psi_s \qquad (53)$$

where

$$\lambda = \frac{c}{f_o + \delta f} \qquad (54)$$

is the instantaneous wavelength.

If the target is in motion, ψ_r will change with time, and equation (52) can be written as

$$v_r(t) = k_2 a(t)\rho\cos\left\{(\omega_o + \delta\omega - \frac{4\pi V}{\lambda})t + \psi_t + \psi_s\right\} \quad (55)$$

where V is the target velocity given by dR/dt and k_2 is a constant.

This received echo is mixed with the output of MXR1 at a delay time set equal to $2R/c$, yielding

$$v_{m2}(t) = k_3\rho a^2(t)\cos\left\{(\omega_{ref} - \frac{4\pi V}{\lambda})t + \psi_s\right\} \qquad (56)$$

where k_3 is some constant.

The output of MXR2 and ω_{ref} are fed to the I/Q detector producing inphase and quadrature components that are proportional to the cosine and sine of the phase difference respectively,

$$I = k_I \cos\left\{-\frac{4\pi V}{\lambda}t + \psi_s\right\} \qquad (57)$$

$$Q = k_Q \sin\left\{-\frac{4\pi V}{\lambda}t + \psi_s\right\} \qquad (58)$$

where k_I and k_Q represent the amplitudes of the I and Q components, respectively. We note that the I and Q outputs are time-varying functions depending upon the target velocity V. The Doppler frequency f_d, is given by $(1/2\pi)$ times the total phase, and can be shown to be equal to:

$$f_d = -\frac{2V}{\lambda} \qquad (59)$$

In the above equation, the negative sign appears due to the fact that a positive radial velocity generates a negative Doppler shift and is associated with an outward moving target. Note that Doppler frequency is not a constant but varies due to the varying nature of the instantaneous wavelength λ. Since, λ varies between 0.15 m and 0.3 m corresponding to a frequency variation between 1-2 GHz, the Doppler frequencies vary from f_{dl} to f_{dh}. The relationship between f_{dl}, f_{dh}, and f_{do}, the mean Doppler corresponding to transmit frequency of 1.5 GHz, can be shown to be :

$$f_{dl} = \frac{2}{3}f_{do} \quad \text{and} \quad f_{dh} = \frac{4}{3}f_{do} \qquad (60)$$

Knowing either the upper or lower Doppler frequency, the target velocity V can be computed as

$$V = \frac{3}{20}f_{dl} = \frac{3}{40}f_{dh} \qquad (61)$$

However, in practice, all random frequencies in the range of 1-2 GHz are not always present. Therefore, it is required that the frequency components be averaged over longer intervals. Since samples are uncorrelated and statistically independent of each other, an average power spectral density, $\overline{S(\omega)}$ from N trials can be computed as

$$\overline{S(\omega)} = \frac{1}{N}\sum_{i=1}^{i=N} S_i(\omega) \qquad (62)$$

where $S_i(\omega)$ is the PSD estimate at each frequency per trial, and N is the total number of trials.

This averaging results in a peak Doppler spectra corresponding to

$$f_{d0} = \frac{-2V}{\lambda_0} \qquad (63)$$

where $\lambda_0 = 0.2$ m, corresponding to the mean transmit frequency of 1.5 GHz.

4.3 Simulation Results

Various simulations were performed to evaluate the performance of the radar system. Results of these simulations are shown in Figures 11 and 12.

In Figure 11, the simulated Doppler spectra of linear motion are presented. The target is assumed to be moving along the boresight direction towards the radar with constant velocities of (a) 1.1 m/s, (b) 1.8 m/s, (c) 2.3 m/s, and (d) 2.3 ± 1 m/s. From these figures, it is seen that as the target velocity increases, the Doppler center frequency and spread increase. The spread is symmetric around the center frequency, for a constant target velocity i.e. cases (a), (b) and (c), and the target velocity can be extracted using equations (60), (61) and (63). Figure 11(d) corresponds to a case with non-uniform velocity which shows that as the target velocity changes, the Doppler spread is asymmetric around the center frequency. The lower cutoff frequency yields information on the minimum speed, and the upper cutoff frequency yields information on the maximum speed.

In Figure 12, the Doppler spectra of a fixed rotating target are presented for 40 rpm and 75 rpm, respectively. The radius of rotation is assumed to be 0.15 m. The spectrum contains all frequencies from - f_{dh} to + f_{dh}, including frequencies at and close to DC. The outer skirt of the spectra corresponds to the upper limit of the transmitted frequency and provides information on the target's rotational speed if its radius is known. Also, it is seen that as the rotational speed increases, the spectrum correspondingly widens.

4.4 Experimental Results

The results of Doppler measurements carried out using the random noise radar are shown in Figures 13 and 14. The target approached along boresight direction with approximate uniform velocities of 1.1 m/s, 1.8 m/s, and 2.3 m/s. These targets were small corner reflectors with side lengths of 10 cm. The total range of the radar is subdivided into 22 range bins, each having a resolution of 15 cm, and the radar was operated in the 20th range bin. Since a single target passes through a specific range bin very swiftly, the number of collected samples will be too small for meaningful observation. To overcome this, a linear array of 10 corner reflectors was fabricated on a 0.5 m long wooden strip. This wooden strip was then used as the target. For comparison purposes and to obtain a good reference, each experiment was also repeated at a fixed 1 GHz transmitted frequency. Furthermore, all experiments were repeated eight times, and their respective PSD's were averaged as shown in equation (62).

Figures 13 shows the Doppler spectra of linear motion using the fixed 1 GHz reference frequency at the abovementioned three velocities. The respective Doppler components corresponding to these velocities are (a) 7 Hz, (b) 12 Hz, and (c) 15-16 Hz and corresponding calculated target velocities are (d) 1.05 m/s, (e) 1.8 m/s and (f) 2.3 m/s, respectively. Figure 13 also depicts the average Doppler spectra of linear motion using the 1-2 GHz random noise signal at the same respective velocities. The central peaks of the Doppler spectra corresponding to mean transmit frequency of 1.5 GHz are at (d)
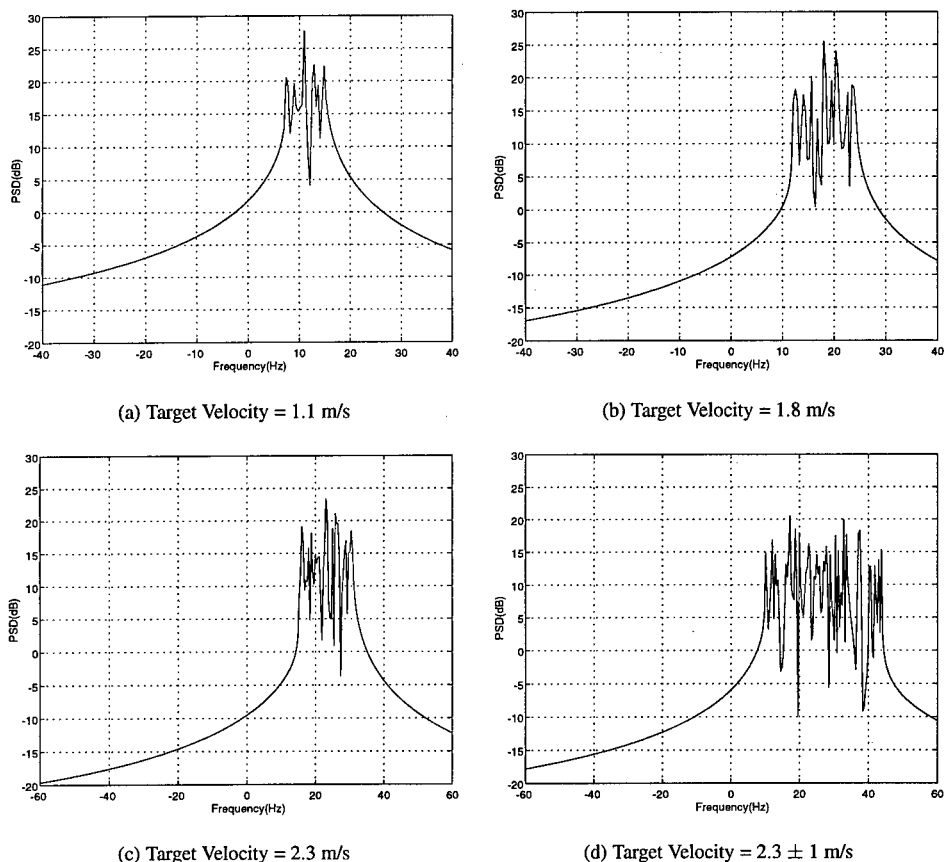
(a) Target Velocity = 1.1 m/s

(b) Target Velocity = 1.8 m/s

(c) Target Velocity = 2.3 m/s

(d) Target Velocity = 2.3 ± 1 m/s

Figure 11: *Simulated Doppler Spectra of Linear Motion*

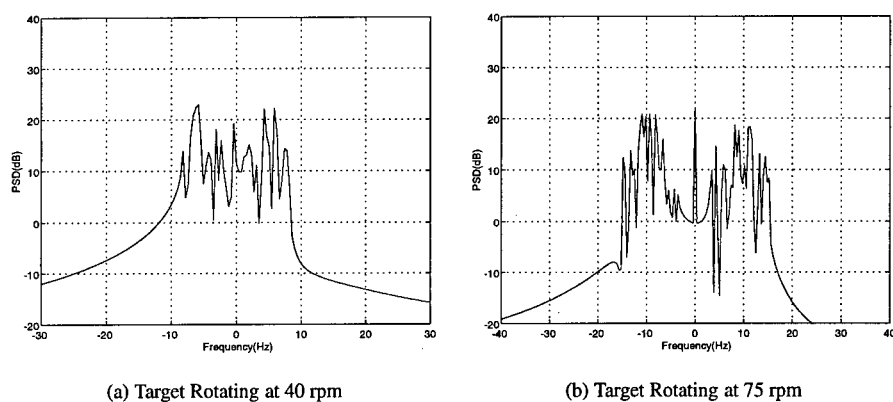(a) Target Rotating at 40 rpm

(b) Target Rotating at 75 rpm

Figure 12: *Simulated Doppler Spectra of Rotating Target*

11 Hz, (e) 17-18 Hz, and (f) 22-23 Hz. The estimated target velocities corresponding to these Doppler frequencies are 1.1 m/s, 1.8 m/s and 2.3 m/s, respectively. These velocities compare very well with the estimated velocities using fixed frequency transmission. It may also be noted that we have not suppressed the DC components in these figures. Figure 14 shows the Doppler spectra of a rotational target at (a) 40 rpm and (b) 75 rpm. The radius of rotation is 0.15 m, and the results were averaged over four experiments. The experimental results compare very favorably with the simulated results

shown in Figures 12(a) and 12(b). This again proves that the random noise radar is indeed capable of estimating Doppler frequencies, though for rotational Doppler further investigations are required.

5. CONCLUSIONS

This paper has described some unique applications of the coherent random noise radar concept. The concept synergistically combines the advantages of ultrawideband random noise radar transmission with the power of coherent signal process-
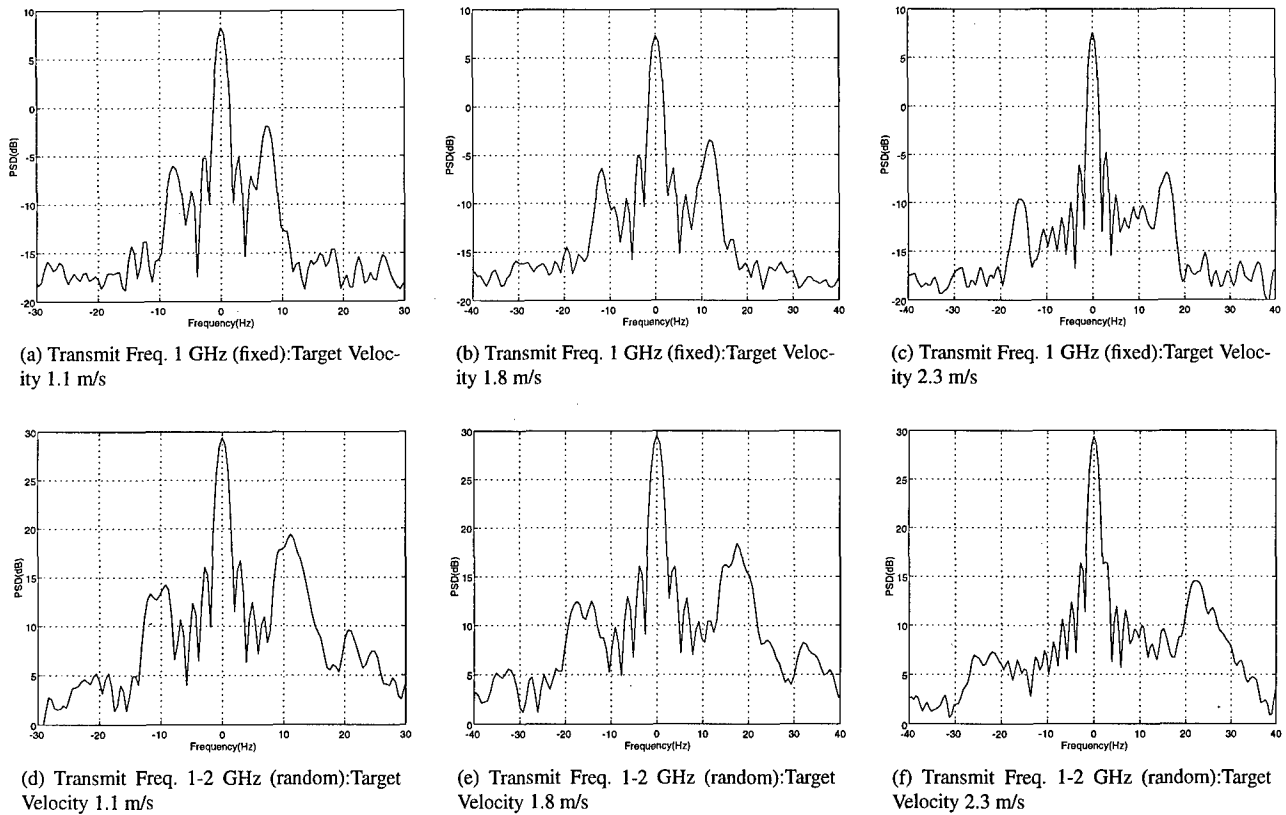
(a) Transmit Freq. 1 GHz (fixed):Target Velocity 1.1 m/s

(b) Transmit Freq. 1 GHz (fixed):Target Velocity 1.8 m/s

(c) Transmit Freq. 1 GHz (fixed):Target Velocity 2.3 m/s

(d) Transmit Freq. 1-2 GHz (random):Target Velocity 1.1 m/s

(e) Transmit Freq. 1-2 GHz (random):Target Velocity 1.8 m/s

(f) Transmit Freq. 1-2 GHz (random):Target Velocity 2.3 m/s

Figure 13: *Measured Doppler spectra of linear motion at different target velocities*

(a) Transmit Freq. 1-2 GHz (random):Target Rotating at 40 rpm

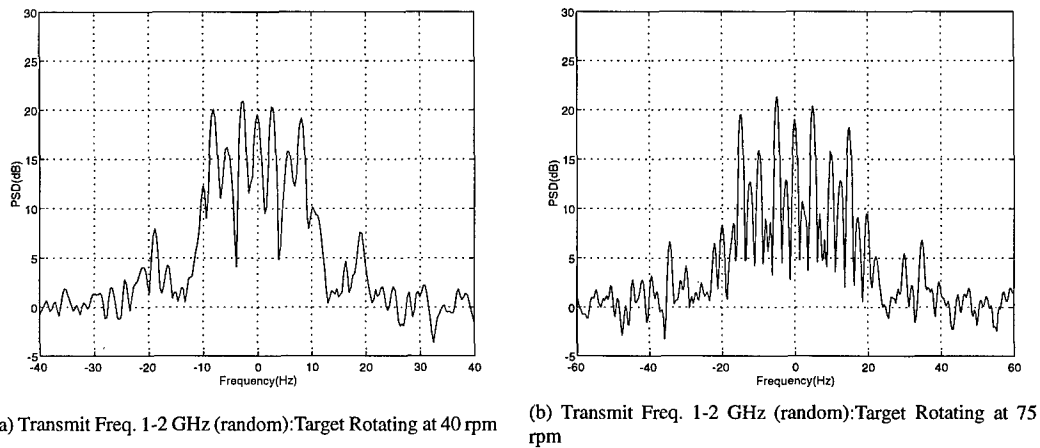(b) Transmit Freq. 1-2 GHz (random):Target Rotating at 75 rpm

Figure 14: *Measured Doppler spectra of rotational motion at different rotation speeds*

ing to yield powerful techniques for military applications. Other applications being currently explored are long-range surveillance of targets, ISAR and SAR imaging of targets and terrain, and phase-comparison monopulse configuration for target tracking. The primary advantage of the random noise radar sytem is its immunity from detection and jamming, and this feature makes such a system a promising candidate for covert surveiilance of non-cooperative targets.

6. ACKNOWLEDGMENTS

Spatial Spectra for Aircraft Identification

J. Willey, H. Faust
Doppler Techniques Section
Code 5344, Naval Research Laboratory
4555 Overlook Ave, Washington, DC 20375-5336, USA.
faust@radar.nrl.navy.mil

Abstract— Aircraft identification by RCS has several limitations. Estimates of RCS probability density functions are not independent of aspect angle. Furthermore, the RCS, modeled as a stochastic process, is neither stationary nor ergodic. These difficulties in the exploitation of RCS have led to the exploration of the aspect angle dependence of glint phenomenology from simple and complex targets.

The RCS amplitude as a function of aspect angle for simple targets can be predicted. The result is a complex periodic function of aspect dependent on target interscatterer distances. A Fourier transform of the aspect angle space yields spatial spectra suitable for use in a matched filter.

Perturbations of the target due to turbulence and/or flexing is treated as a noise in aspect angle. For targets that have different interscatterer spacing but similar target noise, the results are unique RCS probability distributions.

The spatial spectra for several targets of opportunity are shown. Successful classifier results using a linear correlator and a neural network (NN) indicate merit in the approach. For larger class sizes, several research opportunities present themselves. Discussions of these and recommendations for future directions of the work are presented.

I. INTRODUCTION

Modern RSM (Radar Signal Modulation) algorithms have several limitations: restricted aspect angle coverage and ambiguity between several target classes. Practical constraints favor subclass techniques that minimize radar modifications. In this paper, deterministic and stochastic discriminants of RCS (Radar Cross Section) are explored as mechanisms for subclass ID.

II. THE RCS DATA

The RCS measurements were provided by NRaD, San Diego, California, via NRL's colleagues at NAWC/AD. Coherent calibrated X-band radar data was collected using a stepped frequency RF waveform. Each frequency employed a pulse width of 1 usec. A detailed description of the data collection, the radar modes, and the flight profiles may be found in [1].

From this database, the analysis concentrated on

measurements obtained at approximately 9.01 GHz with a PRF of 8.2 or 11.2 kHz (see Table 1). The data were further culled to consider almost exclusively flight profiles exhibiting only a linear change in azimuth aspect angle.

III. SPATIAL SPECTRA OF SIMPLE TARGETS

Let $RCS(\theta)$ be the radar cross section as a function of θ; define the spatial spectra of a target as the Fourier transform of $RCS(\theta)$, $F\{RCS(\theta)\}$.

Consider Fig. 1, an idealization of two perfectly reflecting spheres separated by a distance d, rotated about an angle, θ, and illuminated by a RF carrier of wavelength λ. It is desired to determine the far field function $RCS(\theta)$.

Let the far field voltage in the receiver from the closer sphere, sphere 1, be

$$V_1 = A_1 e^{j\theta_1} \qquad (1)$$

where A_1 is proportional to the reflection coefficient magnitude and θ_1 is proportional to the reflection coefficient phase. Similarly, the far field signal from the more distant sphere, sphere 2, including the increased electrical path length, is

$$V_2 \approx A_2 e^{j(\theta_2 + \frac{2d}{\lambda} sin(\theta))} \qquad (2)$$

If it is assumed that the spheres have the same reflection coefficients, then the received signal has the form

$$V = V_1 + V_2 = A_1 e^{j\theta_1}(1 + e^{j\frac{2d}{\lambda} sin(\theta)}) \qquad (3)$$

and the RCS power is

$$RCS(\theta) \propto VV^* = 2A_1^2 e^{j2\theta_1}(1 + cos(\frac{2d}{\lambda} sin(\theta))) \qquad (4)$$

This may be simplified by using a trigonometric identity:

$$RCS(\theta) \propto 4A_1^2 e^{j2\theta_1} cos^2(\frac{d}{\lambda} sin(\theta)) \qquad (5)$$

Neglecting the amplitude coefficient in Eq. 5:

$$RCS(\theta) = cos^2(\frac{d}{\lambda} sin(\theta)) \qquad (6)$$

A plot of this function is shown in Fig. 2. Next, the Fourier spectrum of $RCS(\theta)$ may be calculated from the following expansion (Eq. 7):

$$RCS(\theta) = \sum_{-\infty}^{\infty} f_n e^{jn\theta} \qquad (7)$$

where the Fourier coefficients f_n are determined by

$$f_n = \frac{1}{2\pi} \int_0^{2\pi} RCS(\theta) e^{-jn\theta} d\theta \qquad (8)$$

where $RCS(\theta) = cos^2(\frac{d}{\lambda}sin(\theta))$. To solve Eq. 8 explicitly, $RCS(\theta)$ must first be expressed in terms of exponentials:

$$RCS(\theta) = \tfrac{1}{2} + \tfrac{1}{4}(e^{j\frac{2d}{\lambda}sin(\theta)} + e^{-j\frac{2d}{\lambda}sin(\theta)}) \qquad (9)$$

Thus Eq. 8 becomes

$$f_n = \tfrac{1}{4\pi}\int_0^{2\pi} e^{-jn\theta}d\theta +$$
$$\tfrac{1}{8\pi}\int_0^{2\pi}\left(e^{j[\frac{2d}{\lambda}sin(\theta)-n\theta]} + \right. \qquad (10)$$
$$\left. e^{-j[\frac{2d}{\lambda}sin(\theta)+n\theta]} \right) d\theta$$

A table of integrals [2] provides the solutions:

$$\int_0^{2\pi} e^{\pm j(\alpha sin(\theta)+n\theta)}d\theta = 2\pi(-1)^n J_n(\alpha) \qquad (11)$$

and

$$\int_0^{2\pi} e^{\pm j(\alpha sin(\theta)-n\theta)}d\theta = 2\pi J_n(\alpha) \qquad (12)$$

where $J_n(\alpha)$ is a Bessel function of the first kind of order n. Thus, Eq. 10 reduces to

$$f_n = \frac{\delta_{n,0}}{2} + \frac{1}{4}\left[J_n\left(\frac{2d}{\lambda}\right) + (-1)^n J_n\left(\frac{2d}{\lambda}\right) \right] \qquad (13)$$

where $\delta_{n,0}$ is the Kronecker delta function. Eq.13 indicates that the spectral characteristics are functions of d and λ. Thus, for the idealized two scatterer case, the spatial spectrum can serve as a discriminant.

Observe that the function $RCS(\theta)$ is not a bandlimited signal. Still, it is possible to estimate a sampling requirement if the Nyquist spatial sampling frequency is taken as $f_s = \frac{2}{\theta_{min}}$, where θ_{min} is the smallest change in aspect angle between minima (see the definition of θ_{min} in Fig. 2). The corresponding upper bound on the Nyquist spatial sampling interval in degrees azimuth as a function of carrier frequency and selected interscatterer distances is plotted in Fig 3.

The implications are significant. At X-band, a target composed of two scatterers separated by 70 meters requires measurements on the order of 10^{-2} degrees/sample. Since the actual spatial sampling interval is a function of both the flight dynamics $\frac{d\theta}{dt}$

and radar PRF

$$\text{Actual Sample Interval} = \frac{\frac{d\theta}{dt}}{PRF} \qquad (14)$$

the possibility of undersampling is real.

Next, consider obtaining an analytic function of $RCS(\theta)$ for real flying targets. The modeling must include the contribution due to multiple bounce, physical optics, creeping waves, polarization, propagation through the non-homogenous air medium, aspect angle dependency of the reflection coefficient magnitude and phase, true 3-d aspect angle relative to the radar, bounded dynamic range of the radar receiver, and so on.

In addition, there are dynamic effects that must be considered aside from the obvious gross changes in aspect angle of varying flight profiles. The airframe, a non-rigid body, has vibrational and flexing modes peculiar to the mechanical architecture of the specific airframe (see Fig. 4). The rotating blades inside the jet engines doppler modulate the signal, while the engines generate mechanical vibrations observed on the airframe skin. Air turbulence, another significant source of vibration of the airframe and its skin, is a function of the relative air speed and density (target altitude). (For example, see Fig. 5, the power spectral density of vibration in the cockpit of the F-14 [3].)

In the next section, perturbations of the target and/or flexing are considered jointly as a single noise in aspect angle. It is assumed that the underlying $RCS(\theta)$ is fixed. The RCS probability density function (PDF) dependency may then be explored as a function of the underlying spatial spectra.

IV. STATISTICS OF A SIMPLE TARGET

Consider the two simple scatterer idealization of Fig 1 and its corresponding spatial function, $RCS(\theta) = cos^2(\frac{d}{\lambda}sin(\theta))$. Now examine two local windows of this function shown in Fig 2. Clearly, the local windows have different spatial frequency contents. It is desired to determine the RCS PDFs within each window.

Let the first window be modeled as a fixed frequency spatial sinusoid of frequency n_1:

$$r_1 = RCS_1(\theta) = W(\theta)\ sin(n_1\theta) \qquad (15)$$

and, similarly, let the second window be modeled at another spatial frequency of n_2:

$$r_2 = RCS_2(\theta) = W(\theta)\ sin(n_2\theta) \qquad (16)$$

where $n_1 \neq n_2$, $W(\theta) = 1$ for $-\pi \leq \theta < \pi$, and $W(\theta) = 0$ elsewhere. Now if $f_\theta(\theta)$ is the PDF of the

aspect angle noise of the target, then the PDFs of the RCS for each window are obtained by a simple transformation of random variables [4]:

$$f_{r_1}(r_1) = \sum_{j=1}^{m_1} \frac{f_\theta(\theta_j)}{|n_1 cos(n_1\theta_j)|} \qquad (17)$$

$$f_{r_2}(r_2) = \sum_{k=1}^{m_2} \frac{f_\theta(\theta_k)}{|n_2 cos(n_2\theta_k)|} \qquad (18)$$

where θ_j are the m_1 roots of Eq. 15, and θ_k are the m_2 roots of Eq. 16.

Next, the conditions of equality between $f_{r_1}(r_1)$ and $f_{r_2}(r_2)$ may be examined. Equating Eq. 17 and Eq. 18:

$$\sum_{j=1}^{m_1} \frac{f_\theta(\theta_j)}{|n_1 cos(n_1\theta_j)|} = \sum_{k=1}^{m_2} \frac{f_\theta(\theta_k)}{|n_2 cos(n_2\theta_k)|} \qquad (19)$$

Eq. 19 is true if $f_\theta(\theta)$ is uniform and $n_1 = n_2$. If $n_1 \neq n_2$ and $f_\theta(\theta)$ is Gaussian with finite variance then Eq. 19 is not true. The transformation of $f_\theta(\theta)$ into $f_r(r)$ is illustrated graphically in Fig. 6.

Actual measurements of the variance for typical fighter perturbations [5] are shown in Table 2. Referring to Fig. 3, for two scatterers separated by 70 meters at W-band, the smallest minimum to minimum separation in $RCS(\theta)$ is on the order of 10^{-3} degrees. In this scenario the yaw variance of 0.02 degrees suggests that the RCS PDF would resemble Fig. 6b more than Fig. 6a.

Fly-by measurements of a single target's RCS PDF were examined over narrow ranges (0.5 degrees) of azimuth aspect angle. The Parzen approximation was used to estimate the RCS PDF [6]:

$$\hat{f}_r(r) = \frac{1}{n} \sum_{i=1}^{n} g(r - r_i) \qquad (20)$$

where g() is a Gaussian kernal of zero mean and unit variance, and r_i are the RCS samples in dBsm. The PDF estimates (Fig. 7) suggest that the narrow aspect angle PDF is non-stationary (and therefore non-ergodic) with respect to aspect angle. Indeed, the earlier analysis argues that $f_r(r)$ is a function of aspect angle.

V. Classification

Next, two classification methods motivated by the earlier analysis are presented. Both methods are applied to RCS measurements of live targets. The first method is spatial spectral correlation. The second method uses function approximation to map RCS and aspect angle into unique aircraft classes.

A. Spatial Spectral Correlation

The preprocessing necessary for spatial spectral correlation on live data is illustrated in Fig. 8. First the RCS function of time is converted into $RCS(\theta)$ by inverting the track history. Then the Fourier transform of the $RCS(\theta)$ yields the spatial spectra, $F\{RCS(\theta)\}$. Thus, the correlation between class j and class k is computed by treating the spectral density as deterministic vectors:

$$\begin{aligned} corr(F_j\{RCS(\theta)\}, F_k\{RCS(\theta)\}) &= \\ \frac{F_j\{RCS(\theta)\}}{|F_j\{RCS(\theta)\}|} \cdot \frac{F_k\{RCS(\theta)\}}{|F_k\{RCS(\theta)\}|} \end{aligned} \qquad (21)$$

The spatial spectra of four target classes (with the DC term removed) are shown in Fig. 9. Samples extracted from the data set were confined to 9.01-9.04 GHz and constant $\frac{d\theta}{dt}$ and restricted to the aspect angle range of 30.9-56.3 degrees. The four target confusion matrix is shown in Table 3.

A brief exploration was made of the intra-class correlation of

$$corr(F_j\{RCS(\theta)\}, F_j\{RCS(\Delta\theta)\})$$

where $F_j\{RCS(\theta)\}$ is taken over the entire range of 30.9 to 56.3 degrees for target class j; $F_j\{RCS(\Delta\theta)\}$ is also from target class j but over the range of 30.9 to $(30.9 + \Delta\theta)$ such that $2 \leq \Delta\theta \leq 25.4$ degrees. The results of the same four targets appear in Fig. 10.

The earlier analysis suggests that targets viewed as scatterers with different inter-scatterer distances will have different spatial spectra. The off-diagonal elements of the confusion matrix support this analysis, given some idealized assumptions. The assumptions include ideal measurements and sampling and noise-free observations. Note that if these assumptions are relaxed and it is further assumed that the spatial spectrum is corrupted with additive white Gaussian noise, the matched filter is still optimal.

Given the ideal assumptions, the intra-class observed decorrelation of

$$F_j\{RCS(\theta)\} \cdot F_j\{RCS(\Delta\theta)\}$$

also supports the argument that the spectral content is a function of the aspect angle. This phenomenon is implicit in the earlier analysis of two simple scatterers.

B. Target Function Approximation

The earlier analysis and Parzen estimates argue that the RCS PDF is a function of the local spatial frequency content, which is in turn a function of aspect angle. This suggests that a mapping of the RCS

PDF into class must necessarily include aspect angle. The rest of this section reports the results of an initial look using a NN as a function approximation tool.

Five two-layer feed-forward NNs were trained functionally to approximate target class from RCS measurements and aspect angle. The five NNs were chosen to span 10 degree azimuth increments from -25 to +25 degrees. The input of each network consisted of 33 elements, 32 of which were single frequency measurements of RCS from the radar's stepped frequency waveform starting at 9.01 GHz with each sample separated by 16 MHz. The aspect angle completed the 33rd element of the input vector. The output vector consisted of a two element vector forming a binary code respresent 4 target classes.

Training was implemented with a variation of the back error progation algorithm [7]. Each NN was trained with 200 randomly chosen samples. The test set came from another 1000 randomly chosen samples outside the training set. The cumulative ID performance for single looks only (no decision class voting) is shown in Fig. 11.

VI. DISCUSSION

This section opens with identification of the major sources of error; it concludes with a discussion of several research opportunities.

The analysis presented at the beginning of this paper assumed two highly idealized scatterers. The $RCS(\theta)$ function for real complex (many scatterers) targets must necessarily include contributions from multiple bounce, physical optics, creeping waves, polarization, propagation through the non-homogenous air medium, aspect angle dependency of the reflection coefficient magnitude and phase, true 3-d aspect angle relative to the radar, bounded dynamic range of the radar receiver, etc. Although these contributions have been omitted from the discussions herein, the authors maintain that the spectral content of $RCS(\theta)$ is still a function of aspect angle and target geometry.

The results presented within this article have several sources of error, some of which deserve specific enumeration. The spatial spectra were taken from flight trajectories in which the track history, $\frac{d\theta}{dt}$ was assumed constant. This small departure from constant $\frac{d\theta}{dt}$ results in non-uniform sampling. Cross-winds also contribute to aspect angle error. Throughout the analysis, aspect angle was assumed to vary only in azimuth, but true aspect angle is 3-d with azimuth, elevation, and roll components.

Several open problems must be addressed before attempting to scale these methods for larger class numbers. One problem is the representational basis of the spatial spectrum itself. The $RCS(\theta) = cos^2(\frac{d}{\lambda}sin(\theta))$ function for two simple scatterers yields a Fourier decomposition which is not band-limited. This is due to the frequency modulation in the spatial domain, clearly evident in Fig. 2. In light of this, the authors suggest that it may be fruitful to examine non-Fourier kernals and other transforms that exhibit locality (wavelets). The effects of stochastic sampling on ID performance also must be assessed.

VII. CONCLUSION

Aircraft identification by RCS has several limitations. Estimates of RCS probability density functions are not independent of aspect angle. It has been shown that fine aspect angle RCS, modeled as a stochastic process, is neither stationary nor ergodic.

The RCS amplitude as a function of aspect angle for simple targets can be predicted. The result is a complex periodic function of aspect dependent on target inter-scatterer distances. A Fourier transform of the aspect angle space yields spatial spectra that can form the basis of a matched filter.

Perturbations of the target due to turbulence and/or flexing is treated as a noise in aspect angle. For targets that have different interscatterer spacing but similar target noise, the results are unique RCS probability distributions.

The fly-by spatial spectra for four targets were calculated. Successful classifier results using a linear correlator and a neural network to map relatively narrow aspect angle RCS PDFs and aspect angle into class number supports the analysis. For larger class sizes several research opportunities present themselves, including the use of non-Fourier kernals, to more compactly represent the spatial frequency content.

REFERENCES

[1] Davis. D., W. Berger, R. Wohlers, J. Tannenbaum, and S. Hawk. Non-coopertive Target Identification and Airborne Target Classification Results using Stepped Frequency Radar Cross Section (U) **Proceedings of the 1992 Joint Service Combat Identification Systems Conference (CISC-92), pp 657-665.**, JHU APL, Laurel, Maryland. 28-31 July 1992.

[2] Hildebrand, F., **Advanced Calculus for Applications.** Prentice-Hall, Englewood Cliffs, New Jersey, 1976.

[3] Foley, T., E. Pasyanos., Aircraft Automatic Target Recognition (Secret), **F-14D Vibration and noise test reports, part 5, F-14D vibration,** Report No. LD-303D-89-002, A55-338-R-89-91. Grumman Aerospace Corporation, Bethpage, New York. (Obtained from NAVAIR 4.3.3.2)

[4] Papoulis, A., **Probability, Random Variables, and Stochastic Processes,** McGraw-Hill, New York, 1984.

[5] Inertial navigational data for a typical fighter size aircraft obtained from the Georgia Technical Research Institute, Summer, 1992.

[6] Fukunaga, K., **Introduction to Statistical Pattern Recognition,** Academic Press, Boston, 1990.

[7] Brown H., R. Gardner, H. Faust, and J. Willey, Aircraft Automatic Target Recognition (Secret), **Combat Identification Systems Conference** (CISC-90), Vol 1, Monterey, California, Dec 4-6, 1990.

Target Class	Base Freq (GHz)	Freq Step Size (MHz)	PRF (KHz)	Number of Freq Steps
GR60	9.01	3.7	8.2	128
GR61	9.04	3.7	8.2	128
GR62	9.04	3.7	8.1	128
GR65	9.01	3.7	11.1	128

Table 1. The 4 target classes used in this study came from a large database measured with a stepped frequency radar. The data was culled to look only at the base frequency and flight profiles with uniform aspect angle changes [1].

Parameter	0.1 sec	0.5 sec	1.0 sec
Roll	0.20	0.40	0.40
Pitch	0.06	0.07	0.07
Yaw	0.02	0.07	0.08

Table 2. Angle variance over time for a typical fighter [5].

Target Class	GR60	GR61	GR62	GR65
GR60	1.00	0.76	0.66	0.78
GR61	0.76	1.00	0.62	0.68
GR62	0.66	0.62	1.00	0.70
GR65	0.78	0.68	0.70	1.00

Table 3. Inter-class confusion matrix for the 4 target classes. The entries are the correlation values between spatial spectra. Specifics: Single trial. GR60 & GR61 from 56.3 to 30.3 degrees, GR62 & GR65 from 30.3 to 56.3 degrees. Straight line interpolation of track histories.
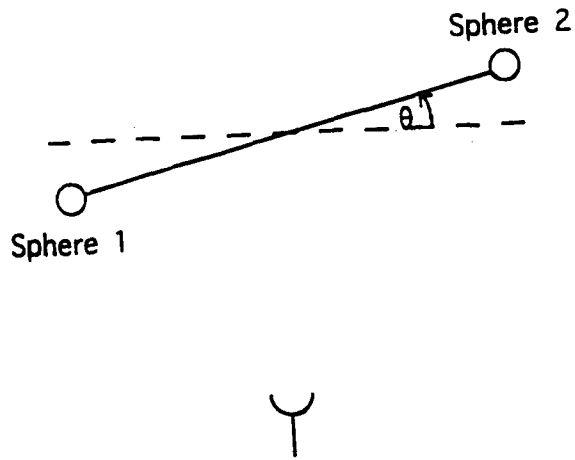
Figure 1. Two ideal scatterers rotating about an angle in the receiving antenna's far field.
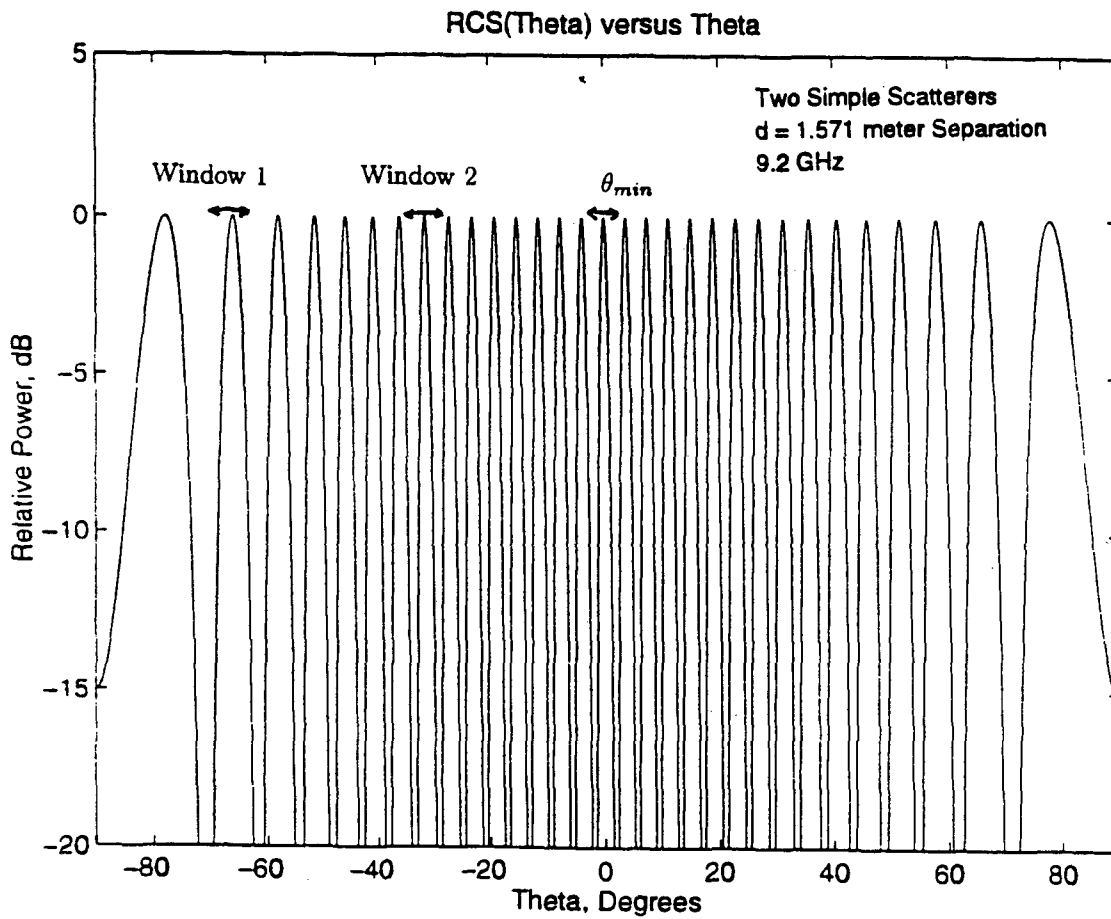
Figure 2. RCS as a function of aspect angle, for the two scatterers in Fig. 1.

Nyquist Sample Interval versus Carrier Frequency
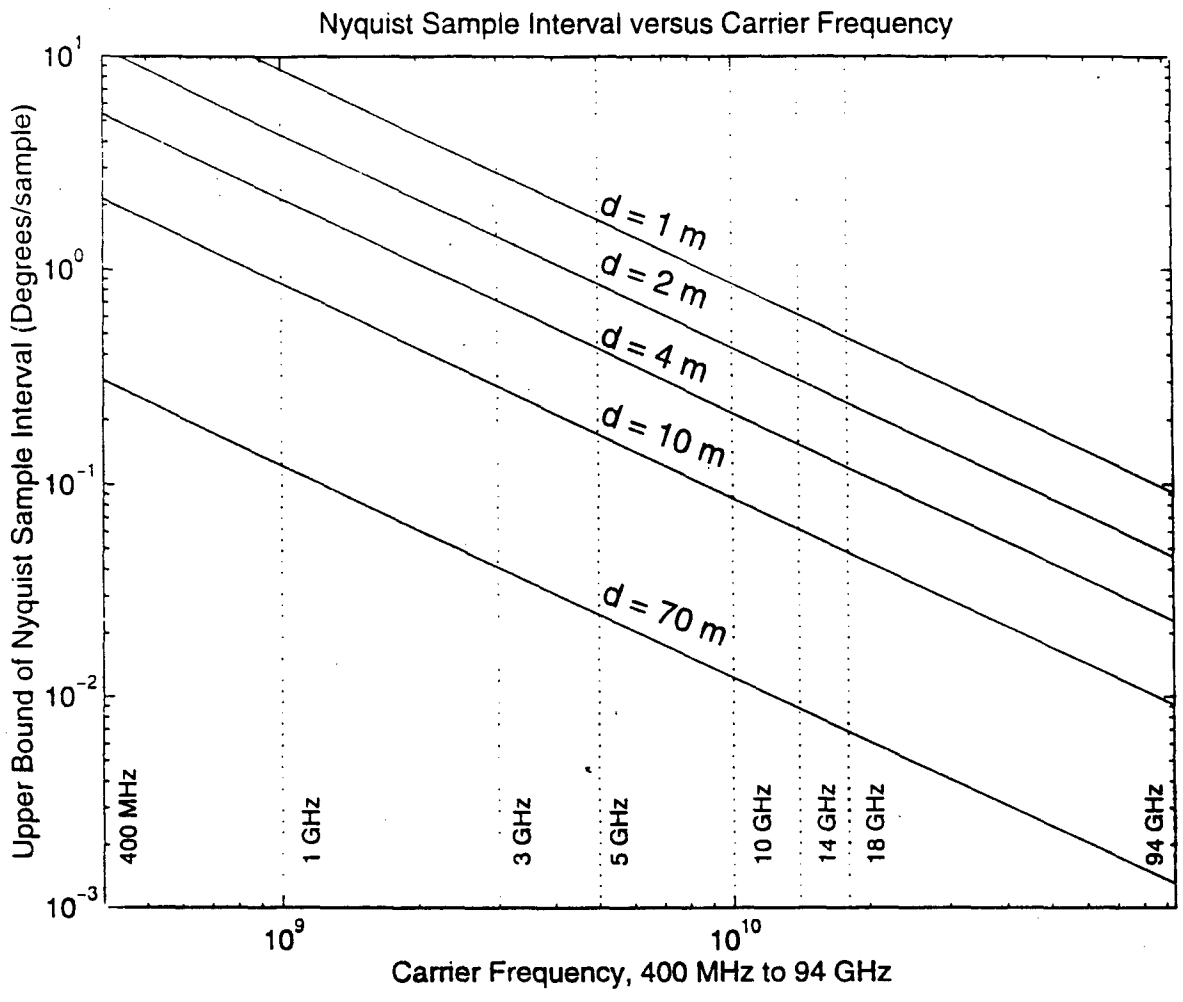
Figure 3. The upper bound of the Nyquist sample interval as a function of carrier frequency for the function shown in Figure 2.
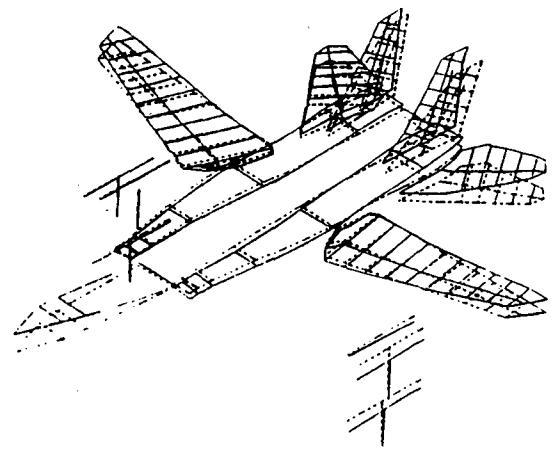
Figure 4. F-14 Fuselage vertical bending mode (from pg 30 of [3]).
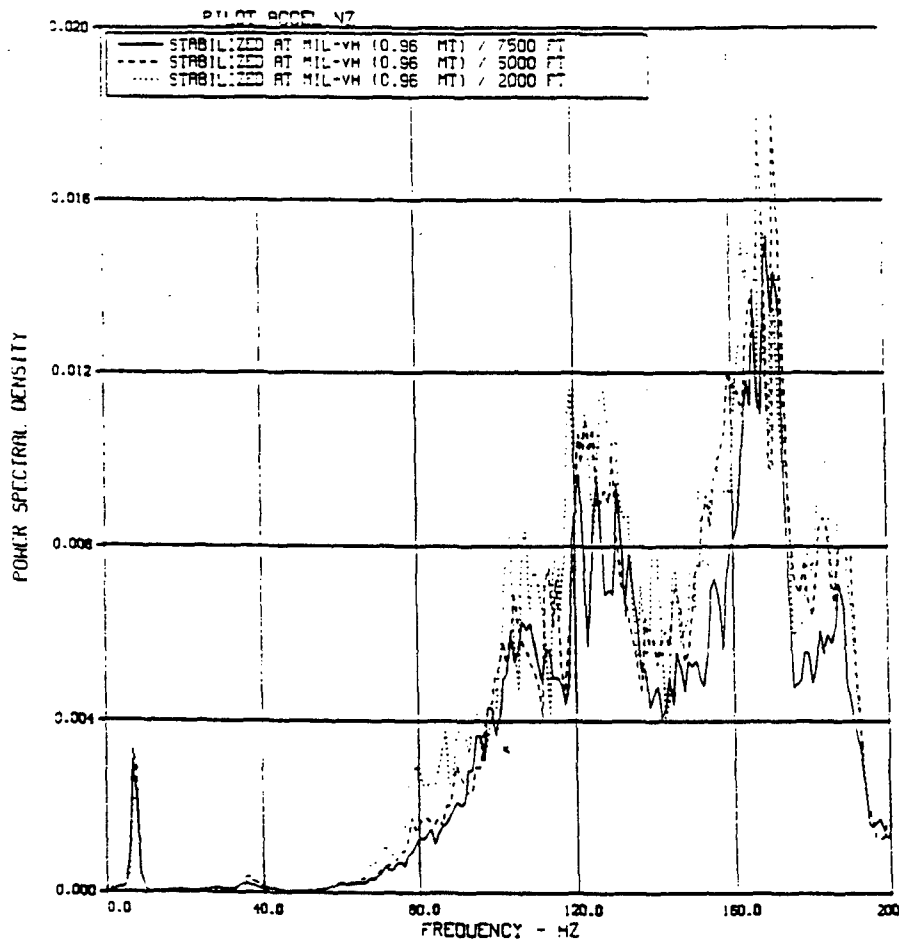
Figure 5. The power spectral density of a vibration sensor in the cockpit of an F-14, for three different altitudes at the same air speed (from pg 40 of [3]).
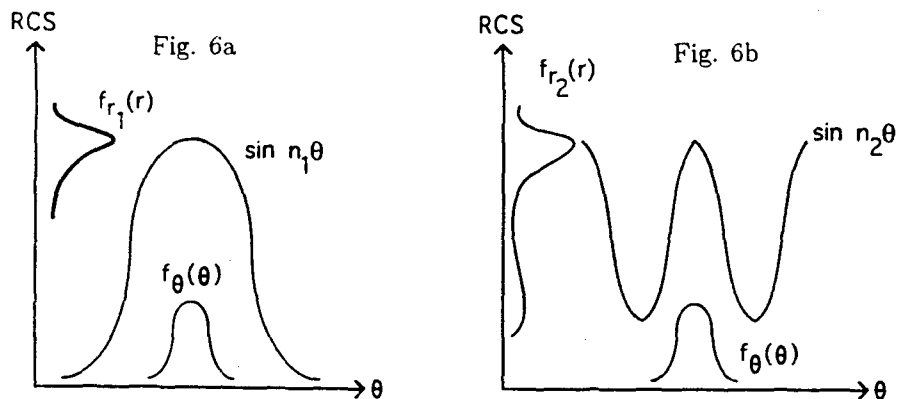
Figure 6. Graphical transformation of aspect angle PDF into RCS PDF for two different functions of RCS(theta).
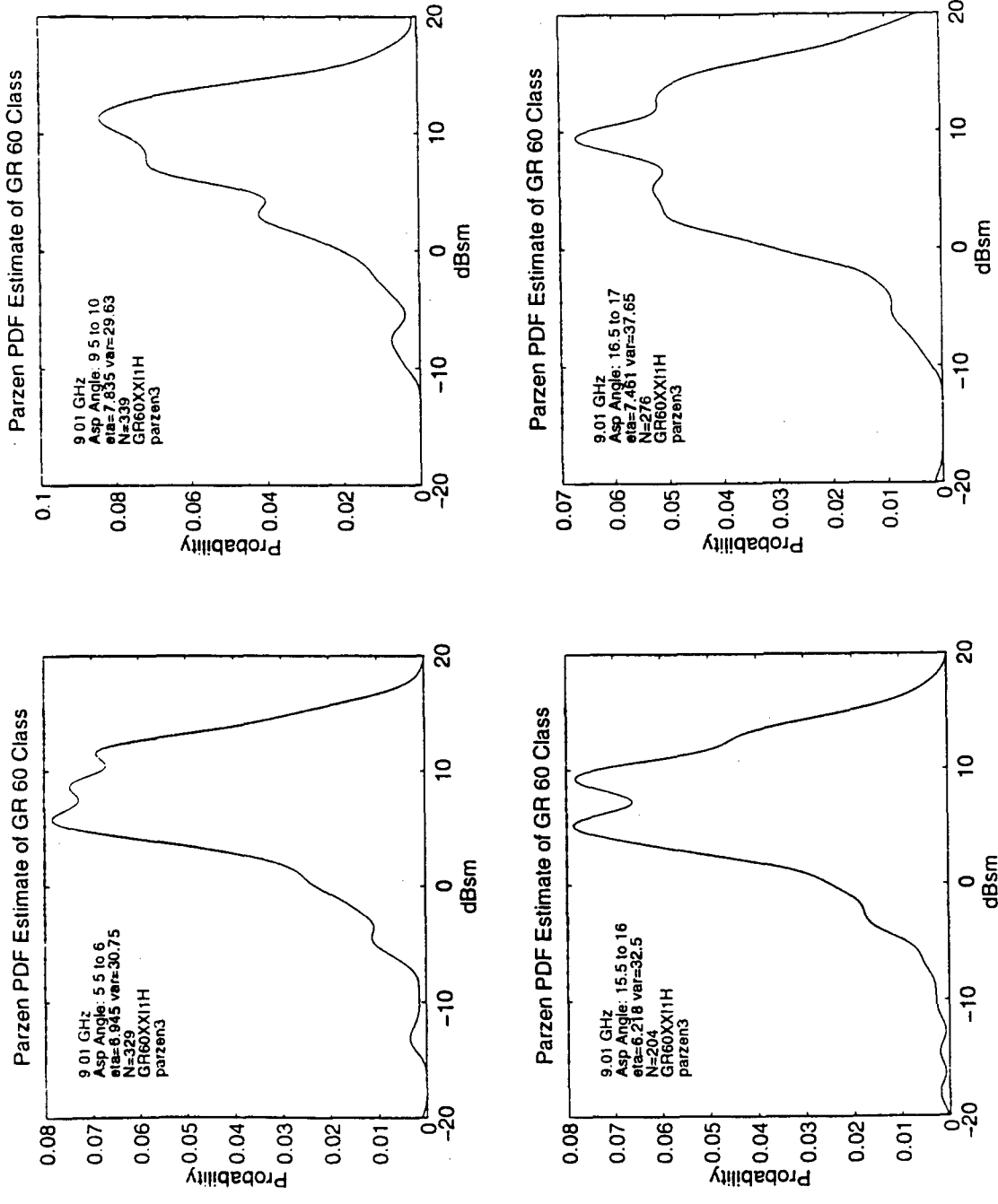
Figure 7. Parzen PDF estimates (from flight measurements) of RCS PDFs for fine ranges of aspect angle.
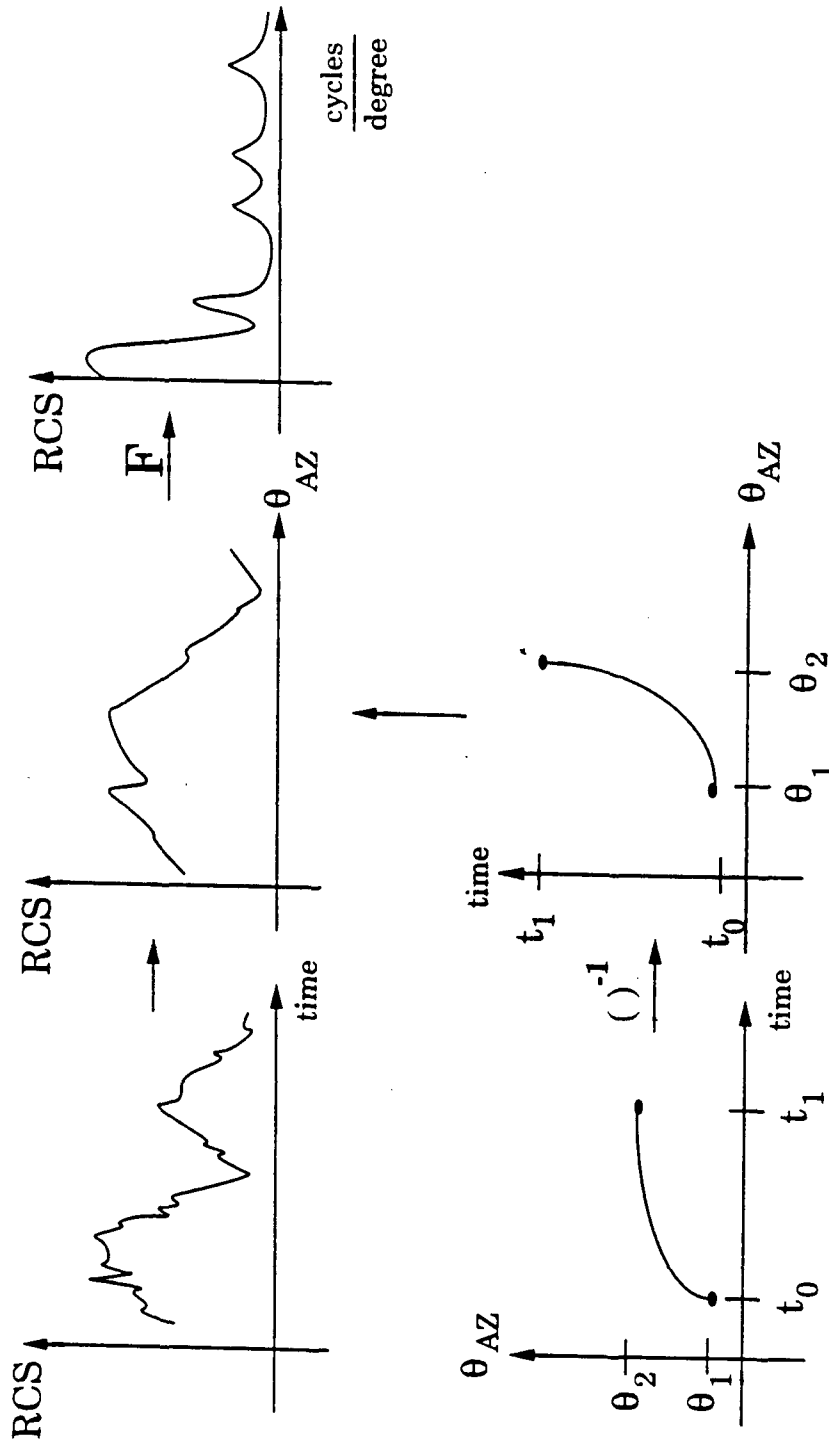
Figure 8. Graphical depiction of preprocessing necessary to generate a spatial spectrum.
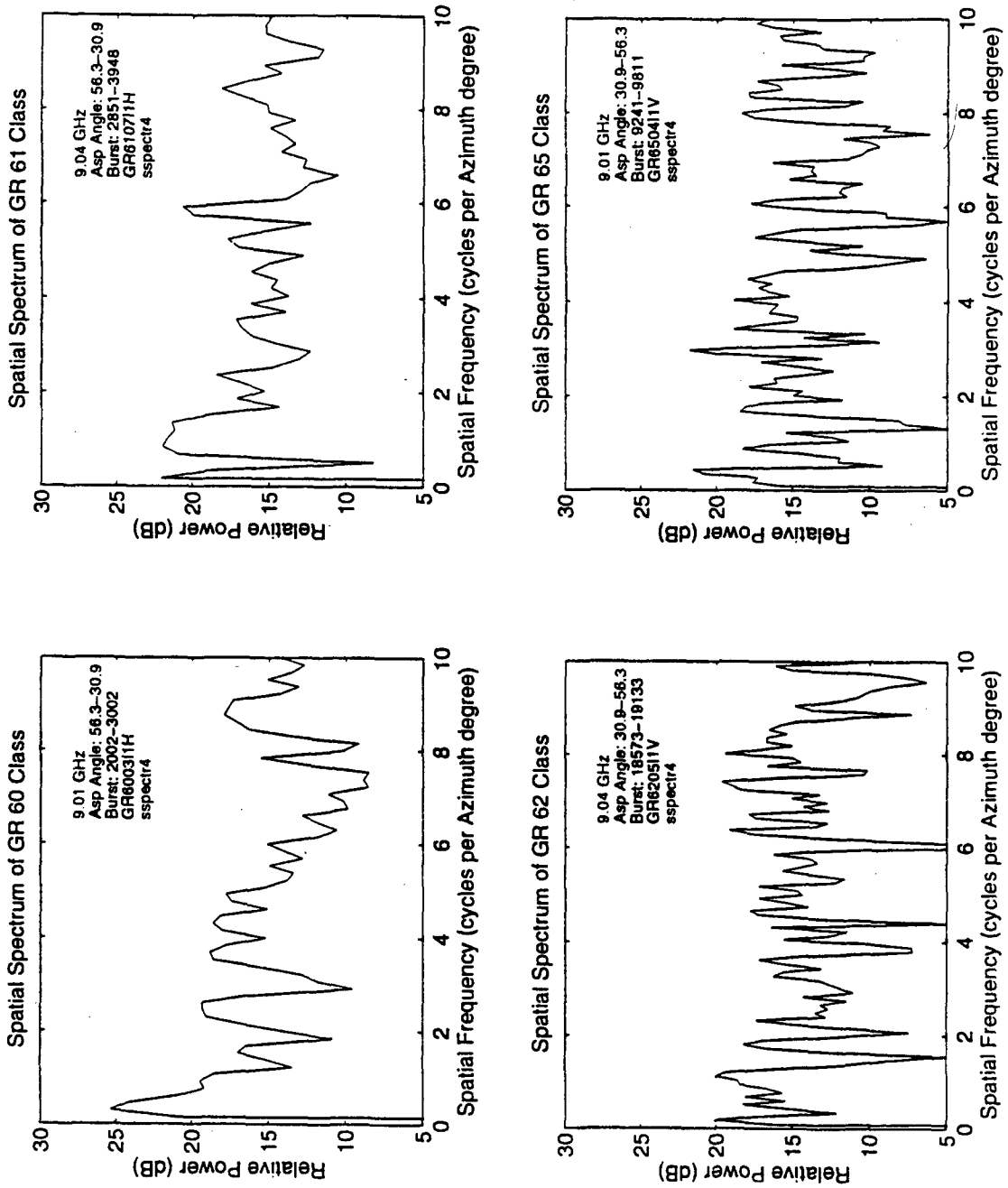
Figure 9. Spatial spectra (from flight measurements) for 4 different targets all over the same range of aspect angles.

Correlation of F(RCS(theta)) vs F(RCS(delta theta))
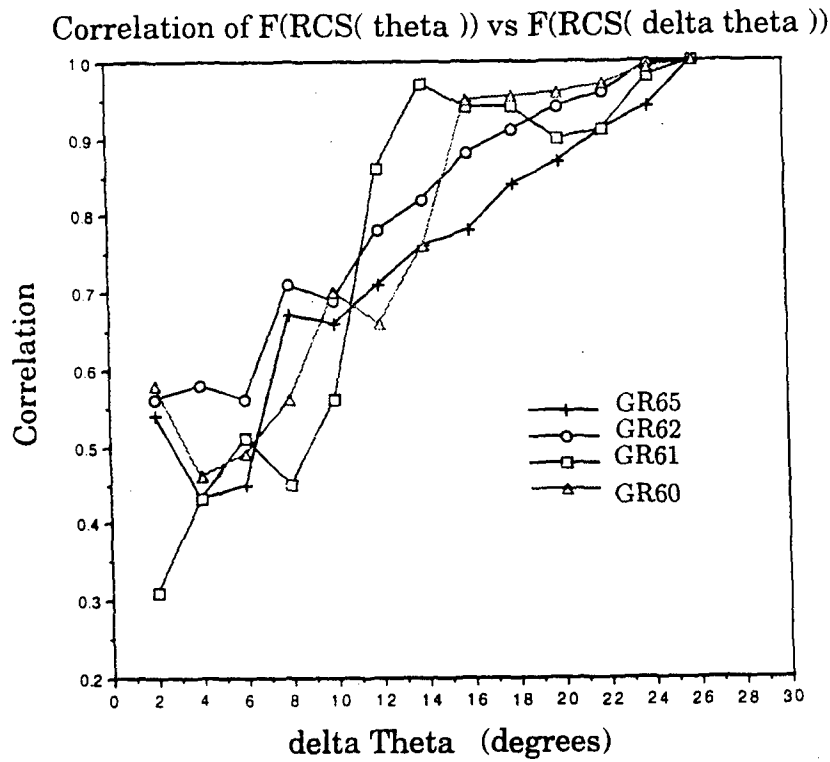
Figure 10. Intra-class correlation of the spatial spectra for 4 targets.

Cumulative ID Probability vs Class, Aspect Angle
NN 33.12:2, N Train=200, Single Look, 30 Sept 1992

Figure 11. Classification results on 4 targets by 5 different neural networks spanning -25 to +25 degrees of azimuth.

THE EFFECTS OF SMALL RANDOM AIRCRAFT ROTATIONAL MOTION ON THE TARGET SIGNATURES

S. K. Wong

Defence Research Establishment Ottawa
3701 Carling Ave.
Ottawa, Ontario
Canada K1A 0Z4

ABSTRACT

Small random rotational motion of an aircraft can affect the fidelity of the target's High Range Resolution range profile. A multiple scattering point source model has been developed to investigate the distorting effect on a simulated target. Results indicate that even when the target possesses a very small amount of random rotational motion during radar interrogation using a stepped frequency waveform scan, sizeable distortion can still occur, making target identification more difficult. The well known range walk effect of the target during the radar scan offers a partial explanation for the distortion of the target's range profile. A more interesting situation emerges when the rotational motion is time-varying; a more severe distortion can occur as a result, leading to dispersive and glint-like phenomena and spurious peaks appearing in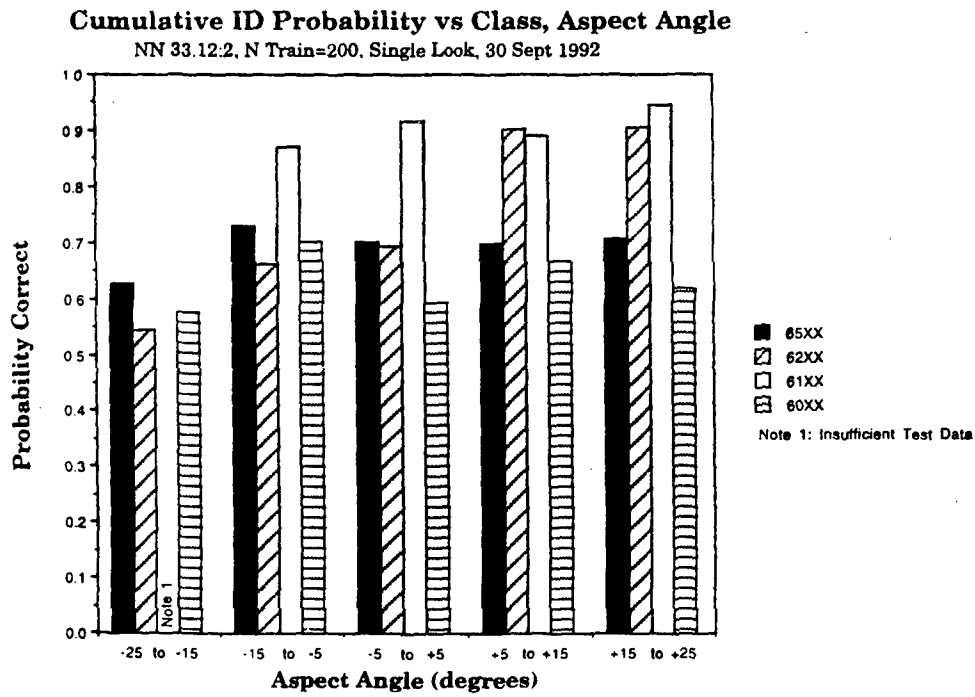 the target's range profile. These anomalies can be quantitatively explained by the creation of many side-bands in the phase of the rotating scatterers on the target.

1. INTRODUCTION

The problem of Non-Cooperative Target Recognition (NCTR) of air targets using High Range Resolution (HRR) range profile has been a subject of considerable interests in recent years. Target identification based on HRR is looked upon as a highly promising technique for NCTR. The HRR range profile is a simple one-dimensional image of an aircraft; it offers a rapid means to characterize an air target. HRR also has an all aspect capability; the signal to noise ratio (SNR) requirement is moderate. Moreover, this technique is applicable to a wide range of new generation of ground, naval and airborne radars.

Stepped Frequency Wave Form (SFWF) is a common technique for generating HRR range profile; in particular, it is well suited for phased array radar which has a narrow instantaneous bandwidth. SFWF consists of a sequence of narrow band radar pulses. However, over the duration of the SFWF scan, small random motion of the target due to air turbulence, aircraft control jitter and maneuvering of the aircraft could be sufficient enough to introduce distortion to the target's HRR range profile. This distorting effect would consequently have a detrimental effect on the target identification process, reducing the effectiveness of the NCTR system.

In this paper, a quantitative examination of the distorting effect on the target's range profile relating to the SFWF-HRR technique is given. In Section 2, a brief overview of the SFWF technique is given. In Section 3, the distorting effects on a simulated target resulting from random rotational motion of the target are illustrated. In Section 4, computational results illustrating quantitatively the distortion on the target's HRR range profile due to random rotational motions are presented; physical characterization of the distorting effect using

a simple model is given to provide some physical insight. In Section 5, prospective solution on how the distortion problem could be mitigated for NCTR identification processing is discussed.

2. STEPPED FREQUENCY WAVE FORM

Stepped Frequency Wave Form (SFWF) consists of a sequence of narrow bandwidth pulses (a few MHz) transmitted with fixed, uniform, pulse-to-pulse frequency change. The effective bandwidth β of the SFWF is determined by the frequency step size Δf and the number of frequency steps N; i.e.

$$\beta = N \Delta f \qquad (1)$$

The resulting range resolution ΔR of the target profile is

$$\Delta R = \frac{c}{2\beta} \qquad (2)$$

where c is the speed of light. For example, if the effective bandwidth β is 300 MHz, the range resolution of the target is 0.5 m. Hence most of the major scattering centers of the target can be resolved clearly in the HRR range profile to give a distinct signature of the target. However, the radar dwell time associated with using SFWF in generating a HRR profile could present a problem. The SFWF is transmitted on a pulse to pulse basis in order to measure the phase of the echo by comparing the received echo to the transmitted reference pulse (i.e. coherent detection). However, this coherent mode of operation restricts the maximum pulse repetition frequency (PRF) of the SFWF scan in order to achieve a desired operational radar detection range. As a result, a relatively long dwell time is required to transmit N number of pulses. The radar dwell time of the SFWF scan to acquire one HRR range profile is given by

$$t_D = \frac{N}{PRF} \qquad (3)$$

The PRF is mostly dictated by the radar operating range. For example, to detect and identify a target out to a range of 75 Km, the maximum PRF is restricted to 2 kHz or less. The number of transmitted pulses N in the SFWF depends on the stepped frequency size Δf and the range resolution ΔR. In order to view a target within an unambiguous range window of W=50 m, it requires a $\Delta f = c/2W = 3$MHz. From Equations (1) and (2), to acquire a range resolution $\Delta R = 0.5$ m, the number of pulses required is N = c/(2 ΔR Δf) = 100. The corresponding radar dwell time is thus t_D = N/PRF= 100/2000 = 50ms.

3. MODEL OF DISTORTION IN THE TARGET'S RANGE PROFILE

3.1 Multiple-Point Source Target

An aircraft can have turning, pitching, rolling and yawing motions along with translational motion. The yaw rotational motion is the most dominant motion in producing distortion in the target's range profile. To describe the distorting effect due to rotational motion, a complex target is represented by a large number of spatially separated scattering centers; this is applicable to the case when the target dimensions are significantly greater than the radar wavelength (Ref. 1). A multiple point source target simulating a F-16 is given in Figure 1. Each of the scattering centers is not any geometric point on the target, but it represents a combination of specular scattering sources which return a signal. A group of scatterers are statistically independent from one another; that is to say, the echo signal of the target is the sum of all the phase amplitude contributions from each of the scatterers. The total electric field of the radar echo from the target is given by

$$E = \sum_i \mathscr{E}_i \exp\left[j\left(2\pi f_c t + \frac{4\pi f_c}{c}(R_i - vt - X(t)) \right) \right] \qquad (4)$$

where $\mathscr{E}$ is the field amplitude, f_c is the transmitted radar carrier frequency, R is the radar's line of sight range, v is the radial velocity of the target along the radar's line of sight and X is the radial displacement along the radar's line of sight due to the rotational motion of the target. The subscript i denotes the i-th scatterer of the target.

To generate the HRR range profile, the I,Q in-phase and quadrature signals are measured; they are given by,

$$I = Re\left[\sum_i \mathscr{E}_i \exp(j\phi_i(t))\right]$$

$$Q = Im\left[\sum_i \mathscr{E}_i \exp(j\phi_i(t))\right] \qquad (5)$$

where

$$\phi_i = \frac{4\pi f_c}{c}\left(R_i - vt - X_i(t)\right) \qquad (6)$$

is the phase of the i-th scatterer. The first term in Equation (6) describes the time delay of the i-th scatterer which allows the forming of the target's range profile. The second term describes the Doppler effect due to the translational motion of the target; in general, this terms causes a shift in the target's range profile in the unambiguous window and broadens the range profile of the target (Ref.2). It is assumed in this paper that the radial velocity of the target will be perfectly compensated (i.e. $v = 0$); thus the second term is ignored. The third term describes the line-of-sight Doppler effect on the i-th scatterer due to the rotational motion of the target. Given that the i-th scatterer has a pair of coordinates (x_0, y_0) initially with respect to the center of rotation, the subsequent change to the pair of coordinates of the i-th scatterer due to angular rotation of the target is given by

$$\begin{pmatrix} x \\ y \end{pmatrix}_i = \begin{pmatrix} \cos(\omega(t)t) & -\sin(\omega(t)t) \\ \sin(\omega(t)t) & \cos(\omega(t)t) \end{pmatrix}\begin{pmatrix} x_0 \\ y_0 \end{pmatrix}_i \qquad (7)$$

$X_i(t)$ is hence given by

$$X_i(t) = \left(x_{0,i}\cos(\omega(t)t) - y_{0,i}\sin(\omega(t)t)\right) - x_{0,i} \qquad (8)$$

where $\omega(t)$ is a time-dependent angular rotational rate.

3.2 Random Rotational Motion of the Target

Small random yaw rotational motion can be described by stochastic process using the Markov Chain. Random variations in the angular orientation of a target as given by Niklasson and Nilsson (Ref.3) is employed here; a plot of angular orientation as a function of time is given in Figure 2. To study the distorting effect on the target's range profile due to random rotation, four 50ms intervals are selected from Figure 2 to simulate four different SFWF-HRR radar scans; these are indicated by the dashed line segments in Figure 2. It can be seen from Figure 2 that the angular variation of the target within a 50 ms duration can be very small, less than 0.05 degree. However, the rate of temporal change in the angular variation can be quite high in some of these temporal segments; for example, "segment 4" in Figure 2 corresponds to a frequency of about 30 Hz. This large rate of oscillation in the angular orientation of the target perhaps may not be realistic; but it may provide useful insight into the characteristics of a time-varying rotating target. This will be discussed in details in Section 4.

In general, the angular displacement of a target as a function of time as shown in Figure 2 can be described by,

$$\theta(t) = \sum_n \left(a_n \cos(\Omega_n t) + b_n \sin(\Omega_n t)\right) \qquad (9)$$

where a_n and b_n are amplitude coefficients and $\Omega_n = n\pi$, $n=1,2,3,\cdots$. To simplify the analysis and to get a clearer physical insight, $\theta(t)$ of interest is approximated by a simple single-frequency sinusoidal function. The corresponding rotational rate, $\omega(t)$ is derived

from the time-varying angular displacement given by,

$$\omega(t) = \frac{d\,\theta(t)}{dt} \qquad (10)$$

Hence, the rotational rate (in rad/s) of the four selected time segments in Figure 2 can be expressed as,

$$
\begin{aligned}
&1: \quad \omega_1 = 0.09 \\
&2: \quad \omega_2(t) = 0.07\sin(10\pi t + \Phi) \\
&3: \quad \omega_3(t) = 0.06\sin(20\pi t + \Phi) \\
&4: \quad \omega_4(t) = 0.16\sin(60\pi t + \Phi)
\end{aligned}
\qquad (11)
$$

where $0 < \Phi < 2\pi$ is an arbitrary value to give a non-zero initial rotational rate at time $t = 0$; $\Phi = \pi/2$ is used here.

3.3 Distortion of the Range Profile due to Rotation

When rotational motion is introduced to the target, the HRR range profile of the target can suffer considerable distortion. Figures 3 and 4 show the range profiles of a simulated F-16 target with different rotational motions given by Equation (11) at aspect angles of 0 degree (nose-on) and 60 degrees respectively. At nose-on aspect, the range profile suffers only a relatively minor distortion. Most of the distortion is coming from the scatterers in the wings area (see Figure 1). Since these scatterers are 20dB weaker than the ones located on the fuselage, they have a minor overall effect on the target's range profile. Nevertheless, the distortion is still clearly evident as shown in Figure 3. A Kaiser-Bessel weighting window is applied to the range profile processing to suppress the scatterer sidelobes so that the 20dB smaller scatterers show up in the range profiles.

As the target is viewed at a 60 degree aspect angle, the distortion in the target's range profile becomes more severe; this is shown in Figure 4. The more profound distortion in the range profile in this case is due to the fact that the stronger scatterers along the fuselage of the target are acquiring Doppler component along the radar's line of sight at this aspect orientation. Furthermore, it can be seen from Figure 4 that as the rotational motion becomes more rapidly time varying, the target's range profile exhibits increasing dispersive characteristics; this is shown by curves d and e in Figure 4. A more quantitative characterization of the distorting effect on the target profile will be given in the next section.

The amount of distortion in the target's range profile is also dependent on the radar cross-section (RCS) of the scatterers. Figures 5 and 6 show the target profiles of the F-16 simulated target when all the scattering centers have the same relative RCS for 0 degree and 60 degree aspect angles respectively. It is conceivable that, in reality, the RCS of the scatterers on the wings of the target can be larger due to the wing pylons and mounted bombs and missiles. It can be seen from Figures 5 and 6 that the distortion is considerably bigger in the target's range profile in this case. A more lightly weighted Kaiser-Bessel window is applied to Figures 5 and 6 since all scatterers on the target have identical RCS; hence the resolution of the range profiles appears to be sharper than those in Figures 3 and 4. With the sharper resolution of the target's range profile, it is more apparent that glint-like phenomenon where scatterers appear to wander beyond the physical extent of the target also occurs; this is illustrated by curve e in Figure 6.

4. CHARACTERIZATION OF THE DISTORTING EFFECT ON THE TARGET'S RANGE PROFILE

In order to better understand the underlying mechanism of the distorting effect on the target's range profile, it is useful to examine the behaviour of a single rotating scatterer. Given that a single scatterer is isolated from the target and that at a given instant of time t, the rotating scatterer has a geometry that is depicted in Figure 7, the instantaneous Doppler velocity of the scatterer along the radar's line of sight is given by,

$$v_D = \omega y_0 \qquad (12)$$

where ω is the target's instantaneous rotational rate and y_0 is the moment arm of the rotation. Assuming $\omega = 0.1$ rad/s and $y_0 = 15$ m, $v_D = 1.5$ m/s; this is a rather small Doppler velocity. Note that in the case of a F-16 aircraft, the distance between the wing tip and the fuselage is only 5 m; hence a scatterer at the wing tip would have a even smaller Doppler velocity of $v_D = 0.5$ m/s.

To characterize the range profile of a rotating scatterer, time dependent rotating rates $\omega(t)$ given by,

$$
\begin{aligned}
1: &\quad \omega_1 = 0.10 \\
2: &\quad \omega_2(t) = 0.10 \sin(10\pi t + \frac{\pi}{2}) \\
3: &\quad \omega_3(t) = 0.10 \sin(20\pi t + \frac{\pi}{2}) \qquad (13)\\
4: &\quad \omega_4(t) = 0.10 \sin(60\pi t + \frac{\pi}{2})
\end{aligned}
$$

are used; $\omega_2(t)$, $\omega_3(t)$ and $\omega_4(t)$ correspond to rotational motion with angular fluctuation frequency of 5 Hz, 10 Hz and 30 Hz respectively. In the case of a constant rotational rate (e.g., $\omega_1 = 0.1$ rad/s), the scatterer's range profile suffers a range walk during the SFWF scan; this is illustrated as curve b in Figure 8. The static range profile of the scatterer is shown as curve a in Figure 8 for reference. The number of range cell migrated along the unambiguous range window as a result of the Doppler velocity $v_D = \omega y_0$ of the scatterer is given by (Ref. 4),

$$M = \frac{2f_c}{c} \omega y_0 \frac{N}{PRF} \qquad (14)$$

where f_c is the carrier frequency and N/PRF is the duration of the SFWF scan. Given $N=100$, PRF=2 kHz, $\omega y_0 = 1.5$ m/s and $f_c = 10$ GHz , the number of range cell migrated M = 5. Since unambiguous range window is 50 m containing N = 100 points, each range cell, therefore, corresponds to 0.5 m. Hence the rotating scatterer has range walked 2.5 m as

shown in Figure 8 (i.e., the displacement between curves a and b). In comparison, the actual physical displacement of the scatterer during the SFWF scan is given by,

$$D = \omega y_0 \frac{N}{PRF} \qquad (15)$$

Thus the actual movement along the radar's line of sight, D = 1.5 x (100/2000) = 0.075 m, is only a fraction of one range cell. This range walk problem is a well known effect (Ref. 1) and partially explains the distorting effect of the target's range profile due to rotation.

A more interesting situation emerges when the rotating scatterer has an oscillating motion as given by $\omega(t)$ in Equation (13); range profiles of the scatterer with time-varying rotation are shown as curves c, d and e in Figure 8. In these instances, the range profile of the single scatterer exhibits considerable distortion. Dispersive behaviour and glint-like multiple peaks that span tens of meters occur (e.g., curve e in Figure 8). Thus a time-varying rotational motion provides a significant source of distortion to a complex target's range profile.

To reconcile with these anomalous dispersive and glint-like characteristics, it is more useful to analyze the phase of an oscillating scatterer in a slightly different manner. From Equation (8), the phase of the scatterer detected is given by,

$$
\begin{aligned}
\phi &= \exp\left(j\frac{4\pi f}{c} X(t) \right) \\
&= \exp\left(j\frac{4\pi f}{c} \left[x_0 \cos(\omega(t)t) - y_0 \sin(\omega(t)t) - x_0 \right] \right)
\end{aligned}
\qquad (16)
$$

Using the geometry given in Figure 7, the x-coordinate of the scatterer is $x_0 = 0$; moreover, since $\omega t = 0.1$ x $0.05 = 0.05 \ll 1$, $\sin(\omega(t)t)$ can be approximated by $\omega(t)t$. Thus Equation (16) can be rewritten as,

$$\phi = \exp\left(-j\frac{4\pi f_c}{c} y_0 t \, \omega(t) \right) \qquad (17)$$

Substituting $\omega(t)$ by $\omega_0\sin(\Omega t+\Phi)$, Equation (17) becomes,

$$\phi = \exp\left(-j\frac{4\pi f_c}{c}\omega_0 y_0 t\sin(\Omega t + \Phi)\right)$$
$$= \exp(-jx\sin(\gamma)) \qquad \textbf{(18)}$$

where $x = (4\pi f_c/c)\omega_0 y_0 t$ and $\gamma = \Omega t + \Phi$. Expanding Equation (18) using Bessel functions, it becomes,

$$\phi = \exp(-jx\sin(\gamma))$$
$$= \cos(x\sin(\gamma)) - j\sin(x\sin(\gamma))$$
$$= (J_0(x) + 2J_2(x)\cos(2\gamma) + 2J_4(x)\cos(4\gamma) + \cdots) \qquad \textbf{(19)}$$
$$-j(2J_1(x)\sin(\gamma) + 2J_3(x)\sin(3\gamma)$$
$$+ 2J_5(x)\sin(5\gamma) + \cdots)$$

It can be seen from Equation (19) that the range profile of a time dependent rotating scatterer consist of many side-band components. The existence of the side-bands offers an explanation of the dispersive-like multiple peaks and glint-like character of the single scatterer's range profile; this is illustrated quantitatively in Figure 9. The range profile of a single scatterer given by curve d in Figure 8 is used as an example in the illustration; it has a time-oscillating rotational motion given by $\omega_3(t)$ in Equation (13). When 12 Bessel function components are used to represent the phase ϕ in Equation (19), the resulting profile is narrower than the actual profile; this is shown as the dashed curve in b of Figure 9. As more Bessel function components are added to the phase expression, the resulting profile is approaching the actual profile; this is shown as the dashed curve in c of Figure 9 using 18 components. When 22 Bessel function components are applied, the resulting profile is almost an exact replica of the actual profile; this is shown as a dashed curve in d of Figure 9. In summary, when a scatterer experiences time-varying rotational motion, its range profile could display dispersive characteristic and could exhibit many spurious peaks; this is a consequence of the multiple side-band characteristics in the phase of a time-varying rotating scatterer. The analysis given in this section has demonstrated quantitatively how these anomalous behaviours could have arisen, resulting in profound distortion in the range profile of a complex target.

5. DISCUSSION ON THE PROBLEM OF REMOVING THE DISTORTION FROM THE TARGET'S RANGE PROFILE

In non-cooperative target recognition (NCTR), a detected unknown target is compared with a set of target signatures or signature parameters that are stored in a library database for identification. In an operational NCTR system, the library database is likely generated by computer model computations of static targets (Ref. 5); any distortion in the unknown target's range profile could, therefore, be quite problematic to the target identification process. Thus the removal of distortion in the detected target's signature could be an essential part of the NCTR process.

Intuitively, it is obvious that if the stepped frequency waveform (SFWF) scan can be performed quickly, the target's HRR range profile would have much less distortion due to rotational motion. One prospective solution would be increasing the PRF of the SFWF scan. Figures 10 and 11 show that by increasing the PRF to a high enough value, the intrinsic range profile of the target can be captured without any noticeable distortion. Figure 10 corresponds to the constant rotational motion case as given by curve b of Figure 6 and Figure 11 corresponds to the time-varying rotational motion case as given by curve e of Figure 6. In both cases, at PRF = 20 kHz or higher, the target's HRR range profile approaches that of a static target. However, although increasing the PRF seems to offer a simple solution to the distortion problem, there is difficulty in arbitrarily increasing the PRF in practice. The SFWF technique requires coherent detection to generate the HRR range profile. In a coherent radar system, the phase of the echo signal is measured by comparing the received signal to a reference sample of the transmitted signal. In order to measure the phase, the received signal must be compared with the transmitted signal on a pulse to pulse basis. As a result, the maximum effective operational radar

range of the SFWF-HRR technique will be shortened if the PRF is increased; i.e.,

$$R_{max} = \frac{c}{2\,PRF} \qquad (20)$$

For example, if the PRF is 2 kHz, the maximum radar range R_{max} is 75 km. However, if the PRF is increased to 20 kHz, R_{max} is only 7.5 km, and when PRF = 50 kHz, R_{max} is just 3 km. Thus, it is not hard to see that a high PRF would not offer an useful operational radar range. Techniques for working around the limited PRF problem such as having many synthesizers to sort the pulses in the air or measure the transmitted pulse and store it for processing on each pulse have been proposed (Ref.2,4). But these are complex and expensive solutions that are still remained to be tried and proven.

6. CONCLUSION

NCTR techniques for identifying air targets using the HRR range profiles can be subjected to distortion due to small random perturbing motion of the target. Rotational motion, in particular, can be quite problematic in introducing distortion to the HRR range profile. It has been shown in this paper that even a very small rotational motion induced in the target is sufficient to generate sizeable distortion; this could potentially create difficulty in the target identification process. SFWF techniques are especially susceptible to the distortion problem because of the relatively long dwell time of the radar waveform.

7. REFERENCES

1. R. V. Ostrovityanvo and F. A. Basalov, "Statistical Theory of Extended Radar Targets", Artech House, Boston, 1985.

2. D. R. Wehner, "High Resolution Radar", Artech House, 1987.

3. L. Niklasson and J. E. Nilsson, "Radar Imaging of Air Targets using HRR and Time Filtering at High Radar Frequencies", Proceedings of the International Conference on Radar, p.582, 3-6 May, Paris, France 1994.

4. A. Scheer and J. L. Kurtz, "Coherent Radar Performance Estimation", Artech House, Boston, 1993.

5. S. Wong, S. Kashyap, A. Louie, S. Gauthier and E. Riseborough, "Target Identification in the Frequency Domain", NATO Symposium on Non-Cooperative Air Target Identification using Radar", Paper 19, Mannheim, Germany, April 22-24, 1998.
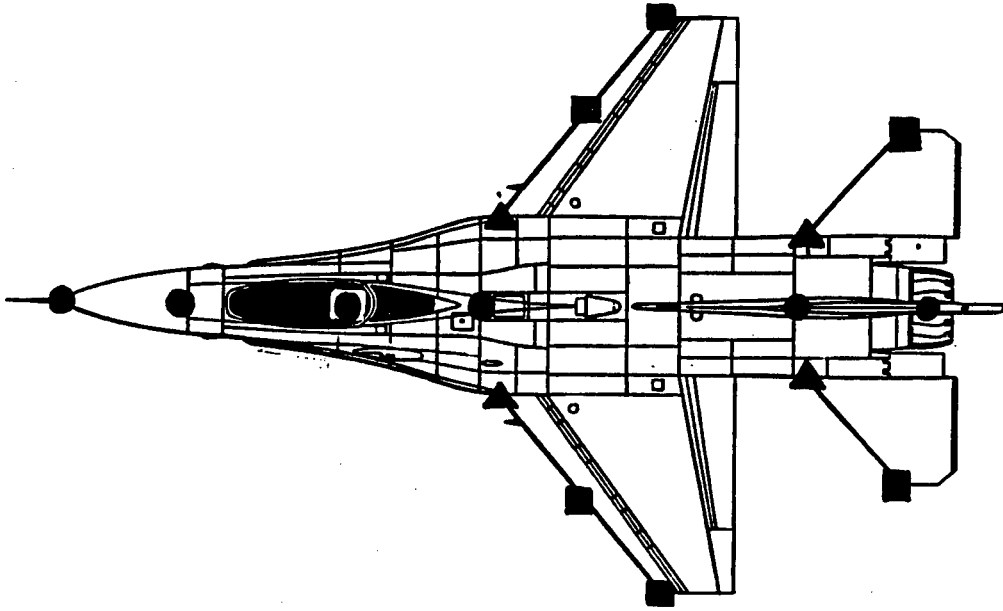
Figure 1   A multiple scattering point source model of a simulated F-16 target.
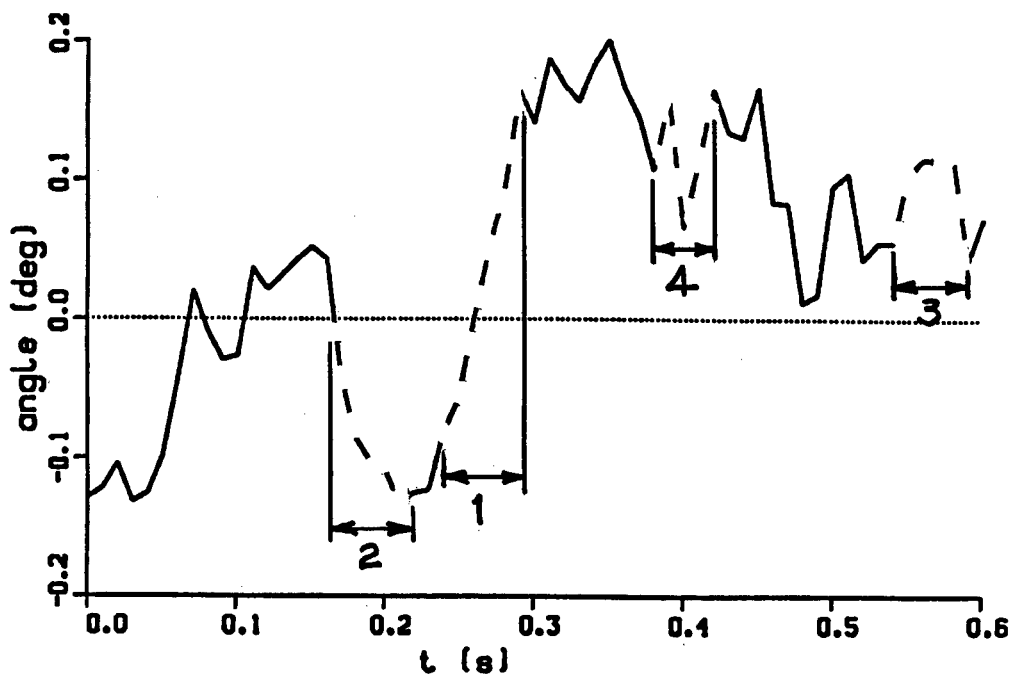Relative RCS: circle = 0 dB, triangle = -10 dB, square = -20 dB.

Figure 2   Random angular variations of a target as a function of time (Ref. 3)
The four selected time segments are shown as dashed lines. Temporal oscillating
frequency : 1) 0 Hz, 2) 5 Hz, 3) 10 Hz, 4) 30 Hz.

Figure 3   HRR range profile of a simulated F-16 target for different target rotational motions at 0 degree aspect. Target has scatterers of different relative RCS as given in Figure 1. a) static, b) ω_1, c) $\omega_2(t)$, d) $\omega_3(t)$, e) $\omega_4(t)$. Kaiser-Bessel weighting window parameter $\pi\alpha = 0.6$.
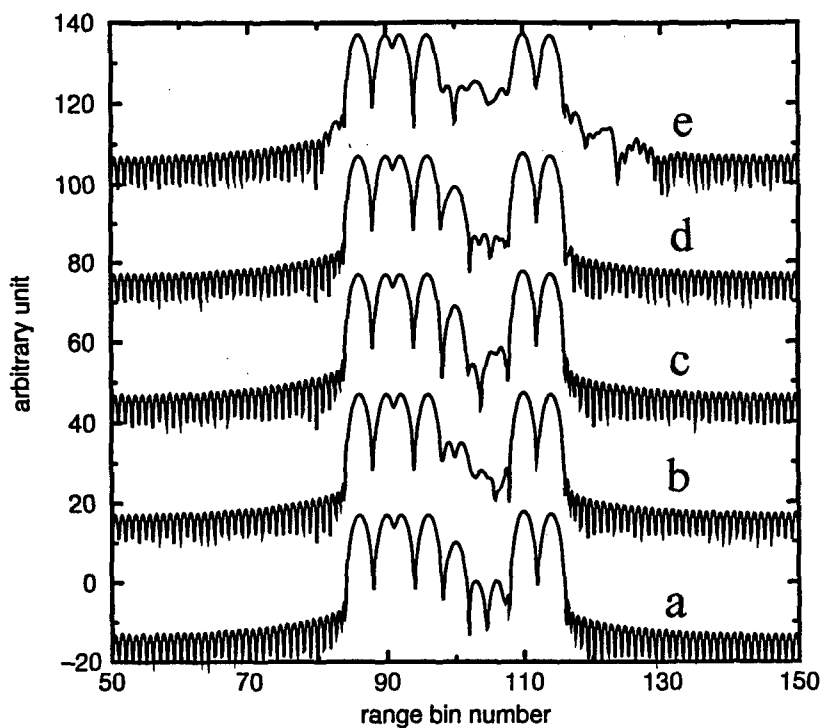

Figure 4   HRR range profile of a simulated F-16 target for different target rotational motions at 60 degree aspect. Target has scatterers of different relative RCS as given in Figure 1. a) static, b) ω_1, c) $\omega_2(t)$, d) $\omega_3(t)$, e) $\omega_4(t)$. Kaiser-Bessel weighting window parameter $\pi\alpha = 0.6$.

Figure 5   HRR range profile of a simulated F-16 target for different target rotational motions at 0 degree aspect. All scatterers on the target have the same relative RCS. a) static, b) ω_1, c) $\omega_2(t)$, d) $\omega_3(t)$, e) $\omega_4(t)$. Kaiser-Bessel weighting window parameter $\pi\alpha = 0.2$.
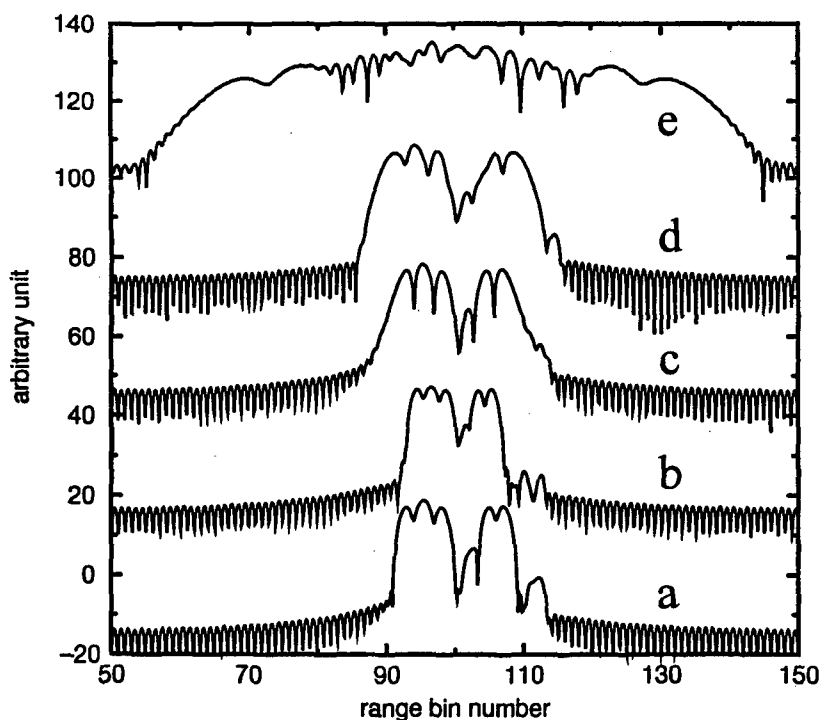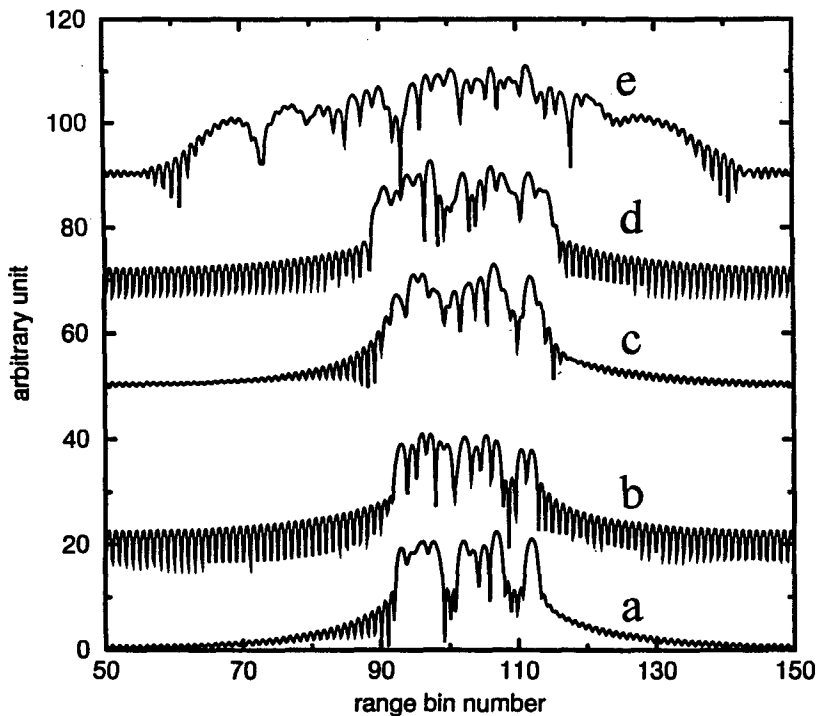
Figure 6   HRR range profile of a simulated F-16 target for different target rotational motions at 60 degree aspect. All scatterers on the target have the same relative RCS. a) static, b) ω_1, c) $\omega_2(t)$, d) $\omega_3(t)$, e) $\omega_4(t)$. Kaiser-Bessel weighting window parameter $\pi\alpha = 0.2$.

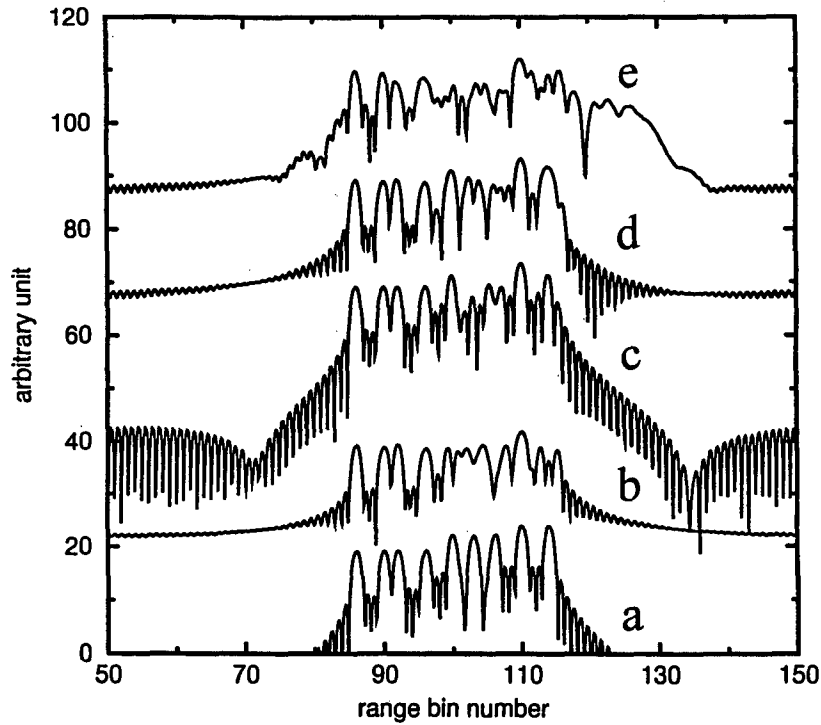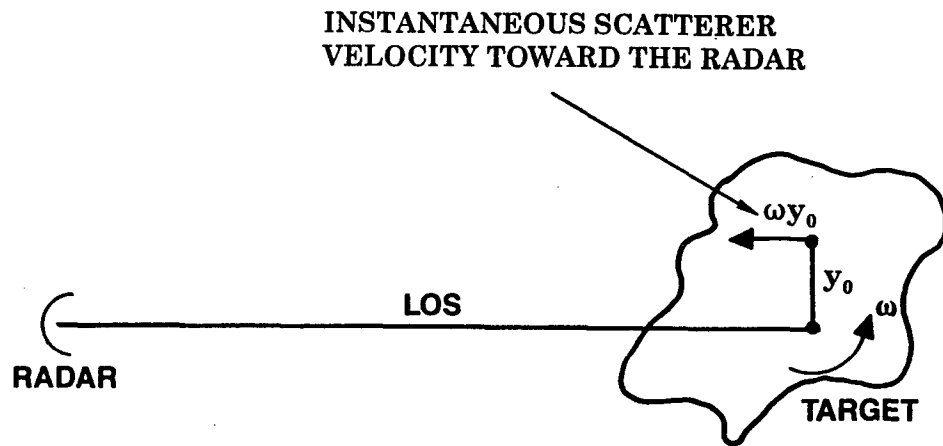Figure 7   Schematic of a single rotating scatterer.
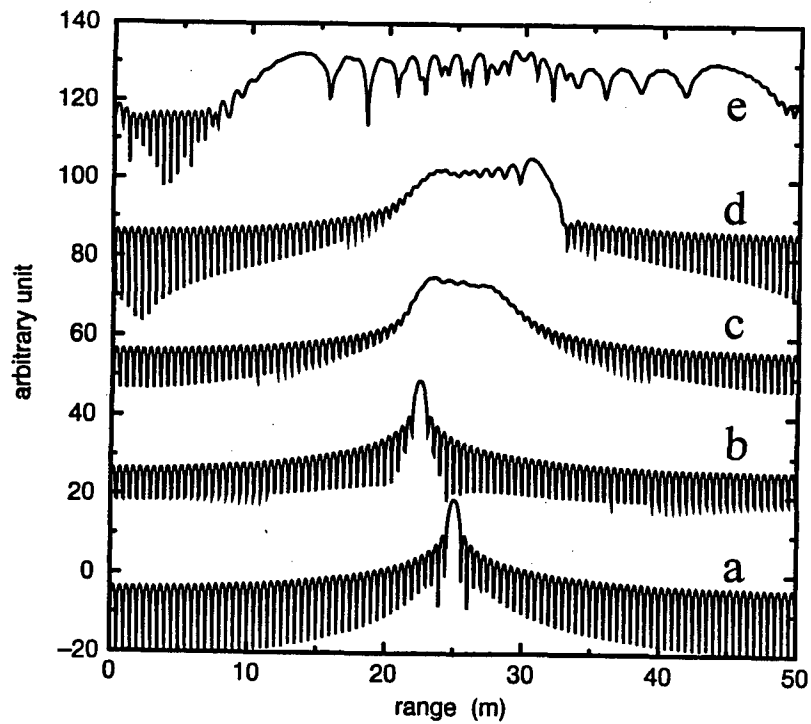
Figure 8   The range profile of a single scatterer. Target's rotational motion : a) static, b) ω_1, c) $\omega_2(t)$, d) $\omega_3(t)$, e) $\omega_4(t)$.
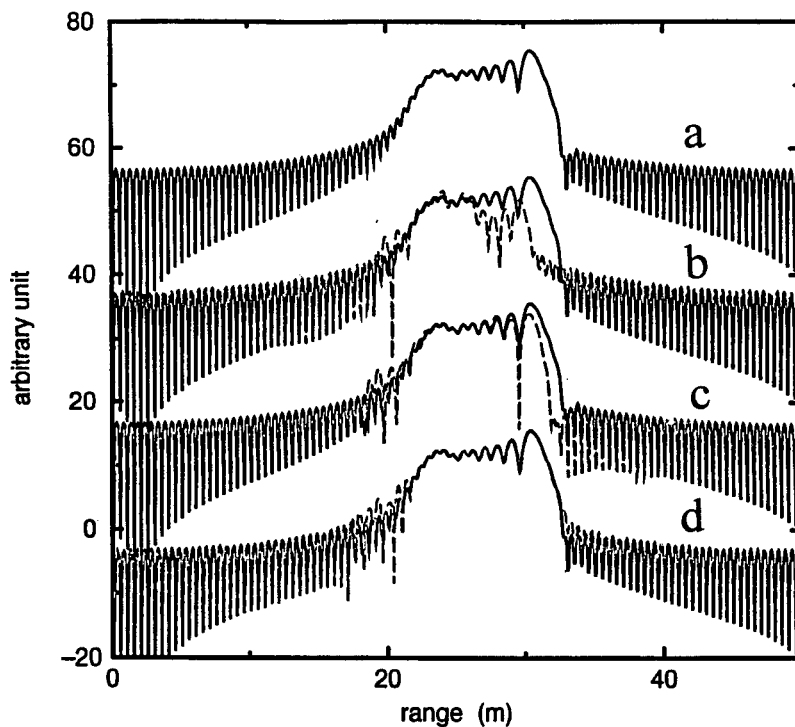
Figure 9   The effects of multiple side-bands of an oscillating scatterer on its range profile.
$\omega_1(t) = 0.1 \sin(60\pi t + \pi/2)$. a) actual profile, b) profile containing 12 Bessel
function components (light dashed), c) profile containing 18 Bessel function
components (light dashed), d) profile containing 22 Bessel function components
(light dashed).
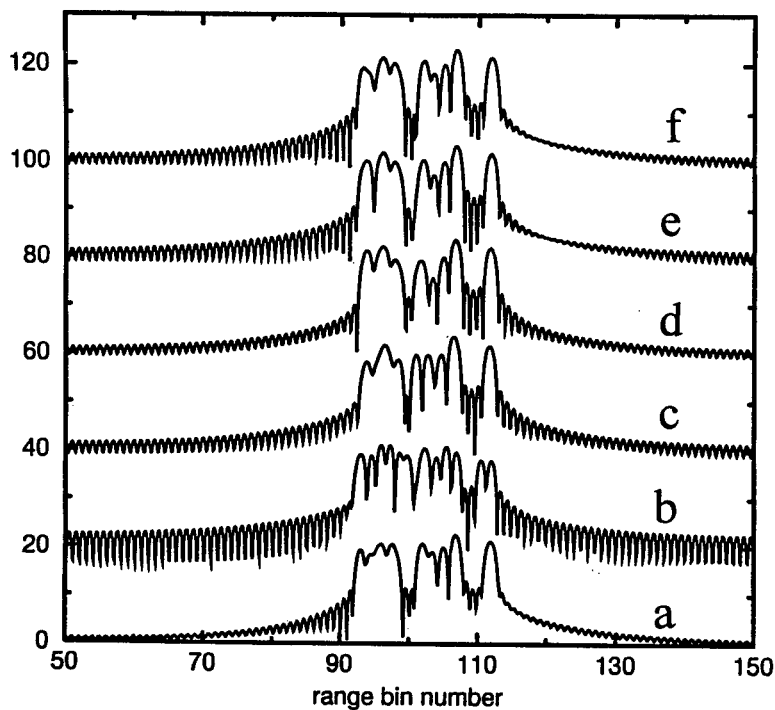
Figure 10   HRR range profile of a simulated F-16 target at various PRFs.
Target rotational motion, $\omega = 0.09$ rad/s: a) static reference (ω=0)
PRF= b) 2 kHz, c) 5 kHz, d) 10 kHz, e) 20 kHz, f) 50 kHz.

Figure 11   HRR range profile of a simulated F-16 target at various PRFs.
Target rotational motion, $\omega = 0.16 \sin(60\pi t + \pi/2)$ rad/s: a) static reference ($\omega=0$)
PRF= b) 2 kHz, c) 5 kHz, d) 10 kHz, e) 20 kHz, f) 50 kHz.

MERIC* - Recent developments

(*Moyen Experimental pour la Reconnaissance et l'Identification des Cibles)

P. Brouard, S. Attia, R. Guern

Office National d'Etudes et de Recherches Aérospatiales
B.P. 72   92322 Châtillon Cedex , France

RESUME

In this paper we present some recent technological developments in a ground based radar station named MERIC. We describe the X band polarimetric radar and some of its applications :

- Simultaneous measurement of the four terms of the polarimetric backscattering matrix ;
- Study of wide band coherent waveform (up to 300 MHz) ;
- HRR measurements and 2 D Imaging.

Some results obtained on cooperative aircrafts are presented. We also describe the "state of the art" in the development of a bistatic Ku band radar which should be operationnal in the mid of 1998.

1.- Introduction

La station radar sol MERIC (Figure 1) est un système expérimental fonctionnant en bande X (mesures polarimétriques) et en bande Ku (mesures bistatiques sur une seule polarisation).
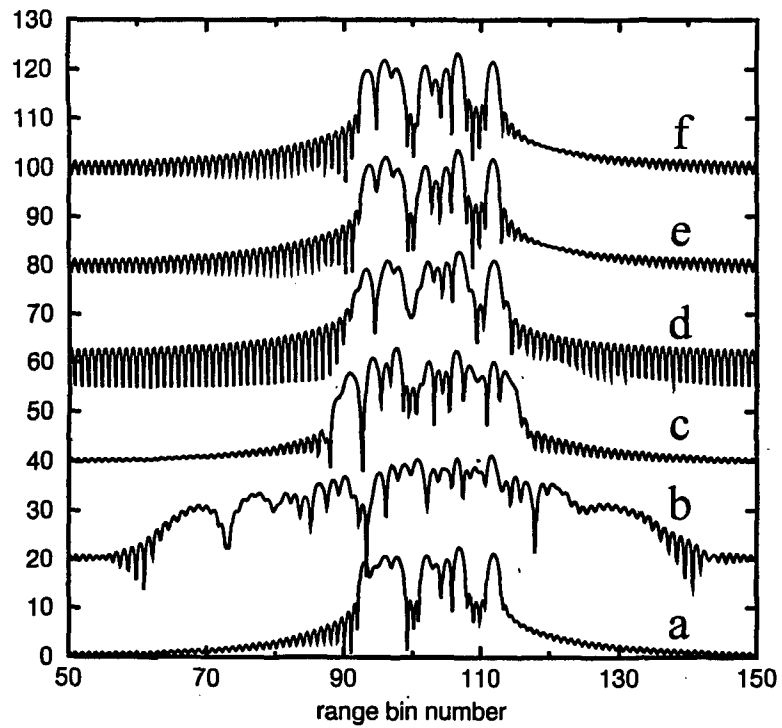
Une grande modularité lui permet d'effectuer des relevés sur des cibles fixes, des cibles mobiles ou du fouillis de sol. Sa vocation première est d'enrichir les banques de données existantes et de servir de base aux études menées actuellement à l'ONERA sur les thèmes suivants :
- Haute résolution distance ;
- Polarimétrie ;
- Imagerie ISAR (Inverse Synthetic Aperture Radar) ;
- Bistatisme.

Ce moyen, mis en oeuvre par l'ONERA, a été financé par la Délégation Générale à l'Armement.

Ses applications principales concernent la furtivité radar en configuration monostatique et bistatique (Surface Equivalente Radar et analyse des fluctuations dues aux moteurs et compresseurs) ainsi que la mise au point de méthodes de reconnaissance et d'identification de cibles aériennes.

Cet article propose une description des composantes du moyen de mesure avec le radar bande X polarimétrique et la base bistatique bande Ku.

Il décrit les étapes de traitement du signal et illustre les capacités d'analyses par des résultats de mesures effectuées sur des avions coopératifs.
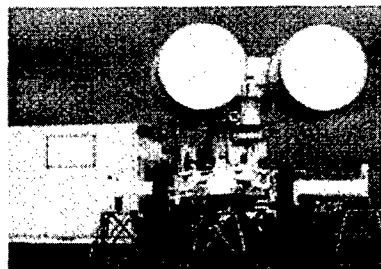
2.- Les moyens d'essais

Le moyen de mesures comprend un radar polarimétrique en bande X et un système bistatique en bande Ku.

L'infrastructure commune à ces radars est constituée de deux affûts Bofors, motorisés, équipés chacun d'une poutre sur laquelle sont fixées les antennes ainsi qu'une caméra vidéo.

Des logements aux dos des antennes ainsi qu'un caisson étanche placé en retrait de la poutre reçoivent une partie de l'électronique hyperfréquence (ATOP, amplificateurs faible bruit, oscillateurs...).

Deux shelters complètent l'infrastructure.
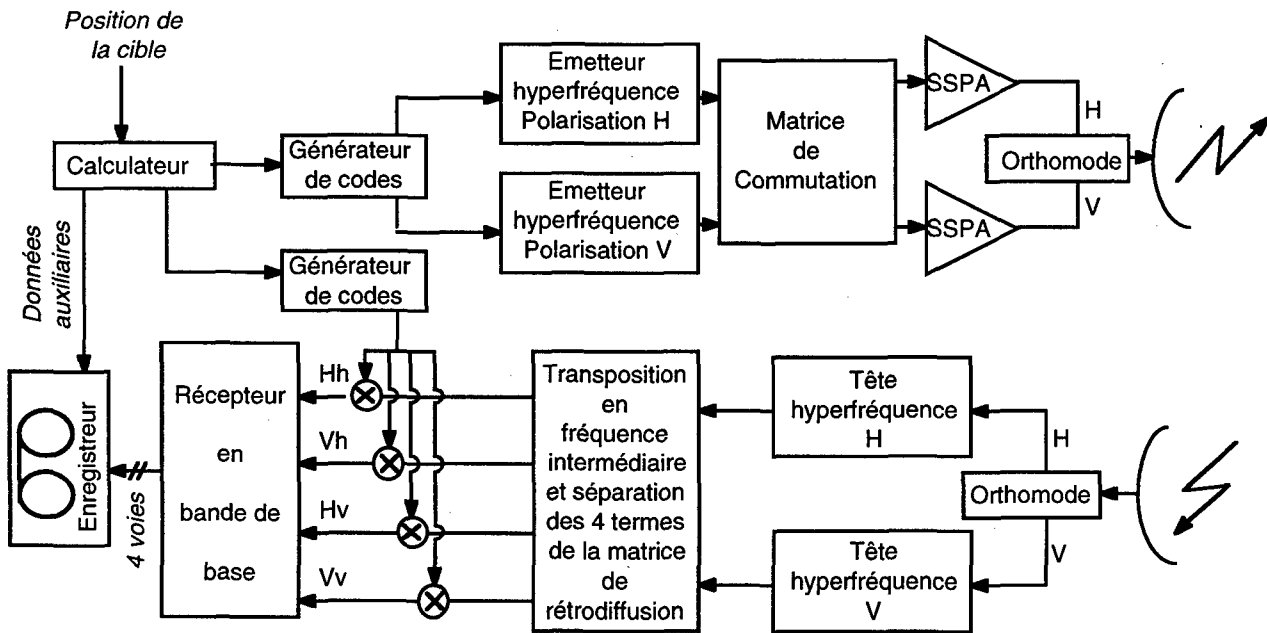
figure 2: synoptique du radar bande X

2.1 - Radar bande X polarimétrique.

Le fonctionnement du radar repose sur la corrélation analogique des signaux reçus avec un signal réplique représentant une cible unitaire dont la position et la vitesse sont choisies.

Cette opération permet de réduire considérablement la bande passante des données qui seront numérisées puis stockées.

Les formes d'onde utilisées sont des rampes linéaires de fréquence choisies pour leur tolérance vis-à-vis d'une désadaptation en distance et en vitesse de la réplique de la cible.

Le radar, dont l'architecture est présentée en figure 2, se décompose en quatre sous-ensembles :

• Synthèse des formes d'onde ;

• Chaînes hyperfréquences et antennes ;

• Numérisation et enregistrement des signaux ;

• Pilotage temps réel de l'installation.

2.1.1 - Synthèse de formes d'onde

La station MERIC utilise deux générateurs numériques constitués chacun d'une mémoire programmable de 2 Mega-octets contenant les échantillons temporels de la forme d'onde radar codés sur 8 bits.

Un convertisseur numérique-analogique, fonctionnant avec une horloge de 450 MHz, élabore des signaux dont la bande passante peut atteindre 150 MHz. Pour des bandes supérieures, et jusqu'à 300 MHz, un module de doublement de fréquence est associé à chaque générateur.

Les codes radars sont calculés au moyen d'une station de travail SUN SPARC SS10 et télé-chargés dans la mémoire des générateurs.

Un séquentiel temps réel permet de sélectionner, selon des critères pré-définis, la forme d'onde la mieux adaptée à la mission du radar.

La commutation temps réel de forme d'onde est utilisée pour adapter les paramètres du code tels que la période de récurrence, la bande passante, à la phase de mesure.

Les codes mis en oeuvre sont des rampes linéaires de fréquence avec en général un rapport cyclique unité. Ces choix sont motivés par les éléments suivants :

- Simplification de l'architecture de la chaîne de réception (mélange avec un signal réplique unique) ;

- Traitements par analyse spectrale ;

- Bilan de liaison.

2.1.2 - Chaînes hyperfréquences et antennes

Les chaînes hyperfréquences comprennent un premier étage capable d'émettre simultanément sur deux canaux radar des rampes linéaires de fréquence de pentes inverses.

La figure 3 montre une représentation temps-fréquence de ces formes d'ondes.

Fo: fréquence de début de la rampe
Bp: bande passante du code
Tr: période de récurrence du code
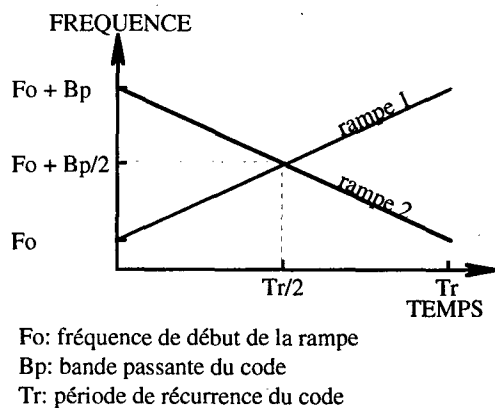
Figure 3: codes orthogonaux.

Placée entre ce premier ensemble et les amplificateurs de puissance, une matrice de commutation (figure 4) permet de choisir entre :

- l'émission simultanée de codes orthogonaux sur les polarisations horizontale (H) et verticale (V) ;

- l'émission alternée, d'une récurrence à l'autre, sur les polarisations H et V soit d'un code identique soit de codes orthogonaux. Le temps de commutation peut être réduit à quelques nano-secondes.

Le tableau 1 rassemble les caractéristiques principales de la station MERIC.

2.1.3 - Numérisation et stockage des signaux

La chaîne d'acquisition numérique est celle du système RAMSES (Radar Aéroporté Multi-Spectral d'Etude de Signatures).
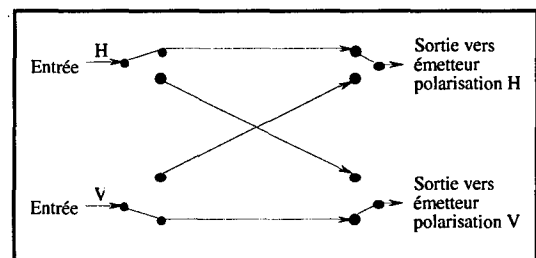
Figure 4: Matrice de commutation.

Elle comporte deux numériseurs RTD 710 A pouvant échantillonner quatre voies réelles à 100 Mech/s sur 10 bits, un "concentrateur" et un enregistreur numérique AMPEX DCRsi.

PARAMETRES	CARACTERISTIQUES
BANDE	X
BANDE DE MODULATION	300 MHz
EMETTEURS	AMPLI. ETAT SOLIDE
PUISSANCE	10 W
POLARISATIONS	LINEAIRES
EMISSION POLAR.	SIMULTANEE ou ALTERNEE
ANTENNES	PARABOLES
GAIN	37 dB
LARGEUR LOBE 3 dB	2°
ISOLATION POL.	20 dB

Tableau 1: Caractéristiques principales de la station MERIC.

Le concentrateur effectue le multiplexage des signaux numérisés avec des données auxiliaires (temps IRIG, coordonnées de la cible, position de la réplique,...) destinées aux traitements en temps différé.

L'enregistreur AMPEX a une capacité de stockage de 48 Giga-octets et un débit d'entrée de 107 Mb/s.

2.1.4 - Gestion temps réel de l'installation

Durant un essai, le séquencement temps réel des mesures est réparti en deux phases. La première est utilisée pour contrôler le radar et intègre une autocalibration par réinjection.

La seconde correspond à la mesure sur cible. Les opérations suivantes y sont effectuées au rythme de la désignation d'objectif :
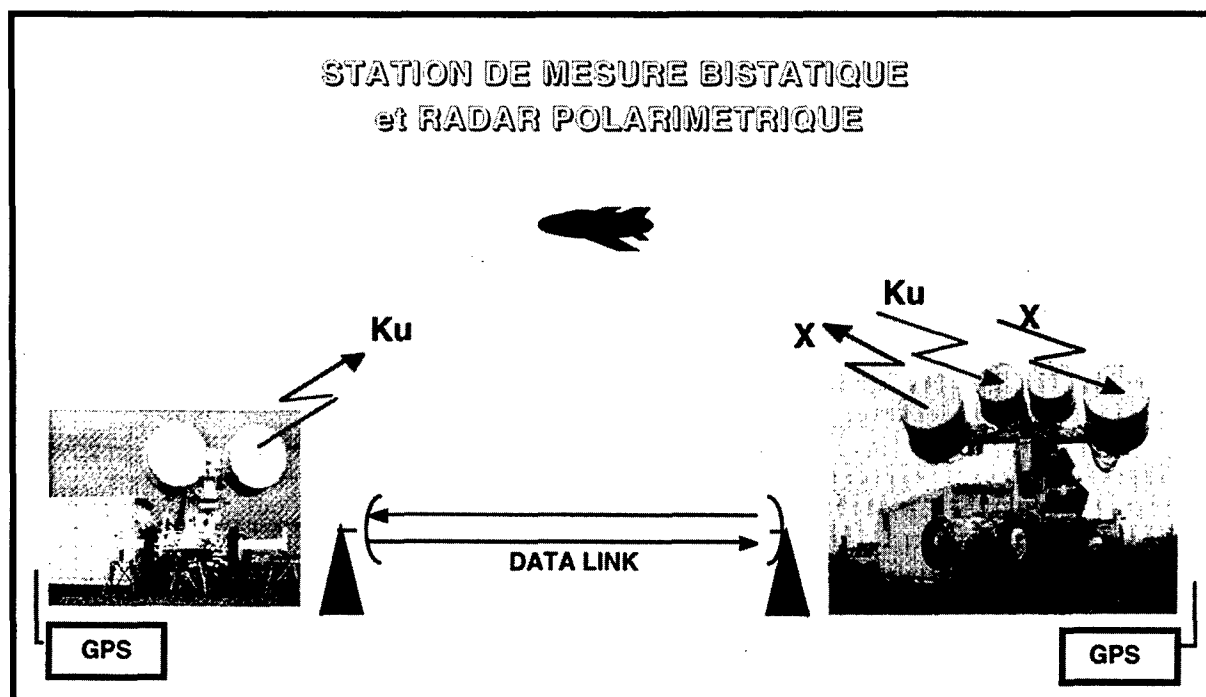
figure 5: synoptique du radar bande Ku

• Estimation de la distance et de la vitesse de la cible ;

• Sélection de la forme d'onde ;

• Asservissement de la réplique à la distance estimée de la cible ;

• Transmission à l'enregistreur des données auxiliaires.

2.2 - Base bistatique bande Ku

Cette configuration est en cours de développement et permettra à moyen terme d'étudier :

• Les signatures bistatiques ;

• Le guidage semi-actif ;

• Les trajets multiples.

La base sera composée de deux sous-ensembles (émission et réception), distants de 5 à 30 km, fonctionnant en bande Ku. La figure 5 illustre l'architecture générale de ce système de mesures.

Des récepteurs GPS assureront la synchronisation temps-fréquence des deux sites et une liaison data-link permettra l'échange bidirectionnel de données numériques et analogiques.

Dans le tableau 2 sont rassemblées les principales caractéristiques de cette station.

2.3 - Étalons

Les moyens d'essais comprennent également un trièdre, un dièdre et un répondeur actif (PARC) en bande X qui sont utilisés dans les phases d'étalonnage polarimétrique. Une sphère ou un PARC en bande Ku seront utilisés pour l'étalonnage de la base bistatique.

PARAMETRES	CARACTERISTIQUES
BANDE	Ku
BANDE DE MODULATION	150 MHz
EMETTEURS	ATOP
PUISSANCE	200 W
POLARISATIONS	LINEAIRES
émission	H ou V
réception	H ou V
ANTENNES	PARABOLIQUES
GAIN	37 dB
LARGEUR LOBE 3 dB	2°
ISOLATION POL.	20 dB

Tableau 2: Caractéristiques principales de la station bistatique

3 - TRAITEMENT DU SIGNAL

Les traitements assurent l'exploitation des enregistrements effectués en bande X mais certains de leurs modules seront utilisables pour les mesures bistatiques.

Plusieurs parties composent ces traitements :

- Mise en forme et étalonnage des données ;

- Calcul des niveaux de SER ;

- Analyse des modulations liées aux parties tournantes ;

- Calcul des images ISAR (utilisation de la technique du radar à synthèse d'ouverture).

3.1 - Mise en forme et étalonnage des données

Ce module extrait les données enregistrées et les "démultiplexe" pour constituer quatre fichiers associés aux polarisations directes et croisées. Un cinquième fichier rassemble les paramètres d'essais (coordonnées de la cible, position du code réplique, ...) pour chaque récurrence du code émis.

Les réponses impulsionnelles (figure 6 en annexe) de la cible sont obtenues par analyse spectrale du signal de mélange pondéré par une fenêtre de Hamming. Elles sont ensuite étalonnées en amplitude à partir des éléments suivants :

- Distance de la cible ;

- Réinjections incluant les émetteurs de puissance (opération répétée pour chaque enregistrement) ;

- Relevés sur des objets étalons statiques (Trièdres, dièdre, PARC) ou mobiles (sphère tractée ou larguée).

Les réponses impulsionnelles sont alors alignées par une méthode utilisant une corrélation amplitude. Cette opération est effectuée sur les deux voies copolaires à partir de la totalité ou d'une partie seulement de la réponse impulsionnelle centrée sur la cible.

3.2 - Exploitation des mesures

Un moyen d'exploiter les réponses impulsionnelles consiste à calculer la SER de la cible observée et à l'associer à un profil distance moyen.

On peut également effectuer un traitement Doppler pour l'analyse des parties tournantes ou la formation d'images ISAR.

3.2.1- Profils distances et niveaux de SER

Le calcul consiste à moyenner en puissance des réponses impulsionnelles alignées correspondant à un secteur de présentation de la cible et parallèlement à analyser statistiquement leurs fluctuations.

Une même planche (Figure 7) regroupe la réponse impulsionnelle moyenne et un profil d'intégration permettant de déterminer rapidement la SER de chaque portion de la cible.

Les valeurs ainsi obtenues correspondent à une SER moyenne pour un domaine de fréquence (bande passante du code utilisé) et un secteur angulaire (variation d'attitude de la cible entre la première et la dernière réponse impulsionnelle utilisée).

Ce type d'analyse est effectué sur les quatre canaux polarimétriques.
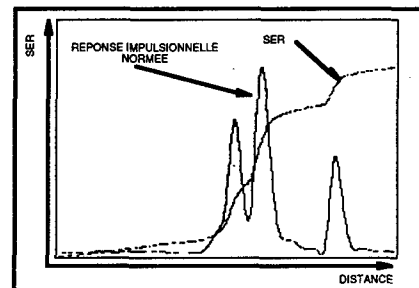
Figure 7: Présentation des niveaux de SER

3.2.2 Analyse Doppler

Le traitement Doppler des réponses impulsionnelles est effectué pour deux types d'analyse :

- l'identification des parties tournantes ;
- l'imagerie ISAR.

L'identification d'un avion ou d'un hélicoptère peut se faire à partir de la signature de ses parties tournantes (pales, hélice, aubes de compresseur ou de turbines,...).

Un traitement Doppler, sur des réponses impulsionnelles contiguës, permet de dissocier en vitesse chacune de ces composantes.

Le spectre obtenu occupe une bande de fréquence de largeur 1/Tr avec une résolution Doppler de $\frac{1}{\text{NTr}}$ où :

- Tr : période de récurrence du code ;
- N : Nombre de récurrences utilisées.

Une autre manière d'exploiter la vitesse des cibles consiste à former des images ISAR.

Cette technique combine la haute résolution distance (découpe de la cible suivant l'axe de visée radar) à une analyse transverse pour extraire les vitesses différentielles radiales affectant les points brillants et former des images 3D (distance radiale, distance tranverse et niveau de SER).

Le calcul des images ISAR comprend deux étapes :

• Compensation des migrations Doppler sur un ensemble de réponses impulsionnelles ré-alignées (méthode de focalisation de type DSA: Dominant Scaterrer Algorithm, MSA: Multiple Scaterrers Algorithm ou autre) ;

• CZT (Chirp Z Transform) pour obtenir les réponses transverses.

Pour la compensation Doppler, la technique retenue dépend du type de présentation mais en général, pour des avions, la méthode DSA fournit des résultats satisfaisants.

4.- Présentation de résultats

Pour illustrer les capacités de mesure et d'analyse de cette station radar, des images ISAR (figures 8 et 9) obtenues sur des avions sont présentées.

Les résolutions spatiales sont inférieures au mètre et les dynamiques d'affichage supérieures à 20 dB .

Associée à la planche, une silhouette d'avion rend compte de l'attitude de la cible au moment de la mesure.

Sur ces images, en vue quasi latérale, les niveaux de SER sont sensiblement plus faibles sur les polarisations croisées que sur les polarisations directes.

Ce n'est généralement pas le cas pour des profils avant ou arrière où l'écart d'amplitude est réduit à quelques décibels.

5. Conclusion

Les mesures effectuées avec la station MERIC sur différentes cibles ont permis de valider une configuration d'essai où les quatre termes de la matrice de rétrodiffusion sont obtenus simultanément grâce à l'utilisation de codes orthogonaux.

Cette méthode semble bien adaptée à des mesures sur des cibles rapides mais elle complexifie les chaînes radar (deux canaux à l'émission et quatre à la réception).

Aujourd'hui un travail d'investigation est mené dans le domaine de l'étalonnage [1] de manière à définir de nouvelles procédures reposant sur :

• Des étalons dont la matrice de rétrodiffusion est parfaitement connue théoriquement ou mesurée en chambre anechoïque ;

• Des méthodes de calibration peu sensibles à l'environnement (bruit de mesure, fouillis de sol, et au positionnement des étalons).

D'autre part, des travaux sont conduits pour permettre l'autonomie de la station radar en matière de trajectographie de cibles non coopératives.

Enfin, des premiers essais en configuration bistatique devraient bientôt être conduits.

REFERENCE:

[1] : "The Polarimetric Calibration Trade-Off" Mme C. Titin-Schnaider - NATO-symposium 22 - 24 April 1998 - Mannheim
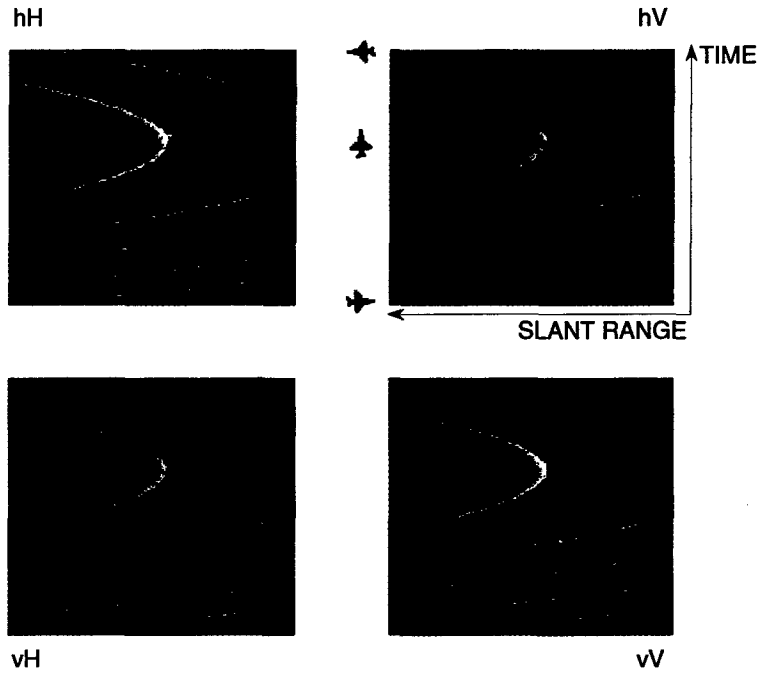
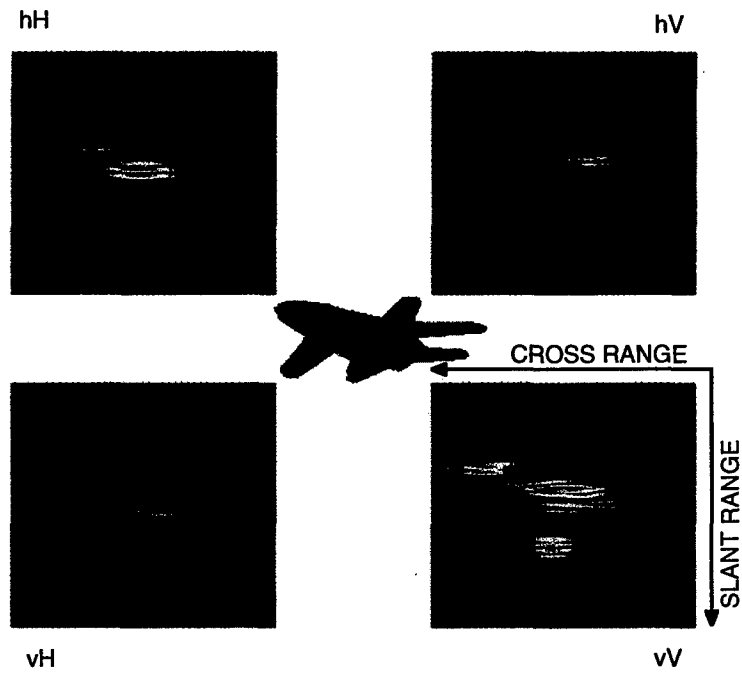figure 6: Evolution temporelle de réponses impulsionnelles
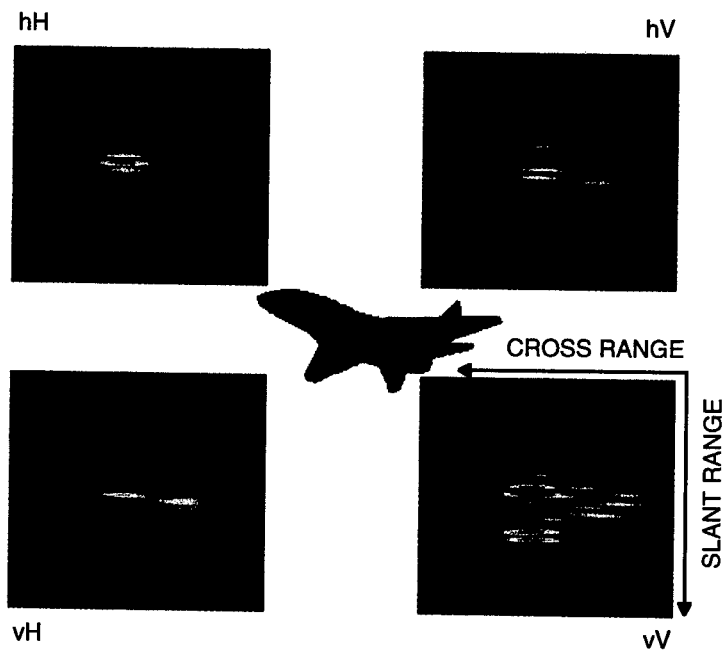

Figure 8: image ISAR - cible 1

Figure 9: image ISAR - cible 2

HRR Identification and Imaging of Air Targets
with a MultiMode Tactical Radar System

Dr. Marshall Greenspan
Director of Technology
Northrop Grumman Norden Systems
10 Norden Place
Norwalk, Connecticut 06856-5300
USA

1. SUMMARY

This paper describes how a slightly modified version of the AN/APG-76 radar was recently used to automatically collect high range resolution (HRR) Ku-band airborne target signatures from a variety of commercial aircraft flying past Norden's roof-top test facility*. The radar modifications included both enhanced range resolution and changes to the radar modal control. Quality of the collected signature data was confirmed by processing sets of contiguously-collected coherent HRR profiles into well-focused and scaled two-dimensional range-Doppler images of the target aircraft. Compatibility of the signature data with HRR target identification algorithms was verified by passing the data through a basic HRR-based Bayesian classifier and comparing the classification results and normalized distance scores to predictions based on the statistics of the training data.

2. INTRODUCTION

Advances in both the capabilities of new wide-bandwidth coherent multi-mode strike radar systems and breakthroughs in the computational power available in emerging airborne digital signal processors has made it feasible to incorporate a tactically useful airborne target classification capability into modern low-cost multi-mission fighter aircraft. Such modern multi-mode strike radars typically contain the capability to perform a variety of air search, acquisition, and precision track functions in an air-defense role as well as to generate wide bandwidth high resolution SAR images in a tactical surface target identification or strike role. Thus, it should be possible to interleave or otherwise combine these two inherent radar capabilities to allow non-cooperative airborne target identification to be accomplished as a normal part of the platform's air defense mission role. In such an advanced system configuration, HRR target signatures collected during airborne search frames would aid in prioritizing detected threats and enhanced quality HRR profiles supplemented with 2-D air target images would confirm threat identification decisions during longer target tracking dwells.

3. RADAR DESCRIPTION

The HRR signatures described in this paper were collected with slightly modified versions of the Ku-band AN/APG-76 radar originally developed in the mid-1980's by Norden Systems under contract to the Government of Israel for use in

the Israel Air Force F-4 Super Phantom 2000 aircraft[1]. These production radar variants had been modified for enhanced range resolution and had been subsequently used in several US government-funded data collection activities[2,3].

3.1 Baseline ANAPG-76 System

The AN/APG-76 radar was originally designed to provide high resolution synthetic aperture radar (SAR) ground maps with simultaneous overlays showing the location of all-speed surface moving vehicles within the SAR image frame.

In addition to its extensive high resolution air-to-surface target modes, the AN/APG-76 includes many air-target modes such as wide sector, multi-bar search and precision 3-axis single target track (STT) modes. These modes, coupled to an integral 9 state Kalman filter, provides the system with the ability to rapidly detect, acquire, and track highly maneuvering air target vehicles and to extract precision estimates of the target's 3 axis position, velocity, and acceleration.

Using a classical medium PRF pulse Doppler waveform set modeled after the AN/APG-68 radar in the F-16 aircraft, the AN/APG-76 reliably achieves medium range all-aspect look-up or look-down acquisition and track of fighter-sized targets under a wide variety of background clutter conditions. Target data supplied by the radar in these air targeting modes is presented to the pilot as symbology on the multi-function display (MFD) and is simultaneously passed to the weapon fire control system.

Figure 1. Baseline AN/APG-76 in F-4 Super Phantom

The current air target modes of the AN/APG-76 radar use only narrow band waveforms and are functionally separate from the air to surface modes. However, since both are implemented within the same common radar elements, there is no physical reason why wider-bandwidth SAR-type waveforms could not have been interspersed with the narrow band waveforms to enable the automatic capture of coherent wide bandwidth signatures from the airborne targets virtually simultaneously with the air-to-air search or track functions.

3.2 HRR Modifications

Following the design and delivery of the first production AN/APG-76 radars, Norden embarked on a series of enhancements to the radar to increase its capabilities and its utility to a variety of new missions. Among these enhancements was the addition of a wide bandwidth stretch waveform generator and associated RF deramping circuitry to provide enhanced range resolution for target identification. This enhanced bandwidth high range resolution capability was initially applied to the air-to-surface modes and enabled the in-flight generation and display of both 1.0 and 0.3 meter resolution SAR imagery as well as the post-flight generation of high resolution 3-D SAR topographic images[4].

The utility of high resolution SAR for the recognition of ships and surface vehicles has been well documented and, in many situations, provides the level of detail needed for positive target identification. Furthermore, such high resolution SAR images are compatible with automatic target detection and cueing algorithms that can be added to the in-flight image processor to significantly reduce operator workload and compensate for operator fatigue[5].

Although initially implemented to enhance the ground targeting capabilities of the AN/APG-76, this same HRR waveform modification can also be employed to enhance the extraction of information from airborne targets detected and tracked by the current air-to-air modes. To verify this assertion, Norden Systems, under sponsorship of the Office of Naval Research, undertook the collection of 1.0 and 0.3 meter HRR data on air targets using these same resolution waveforms operating in conjunction with the existing built-in air target search and air target track modes of this high performance radar system - i.e., detecting and tracking air targets of opportunity with the air target waveforms and subsequently locking the new wide bandwidth stretch waveform HRR target profiling mode to the target's dynamically changing range location. The high accuracy 3-D target tracking data, available simultaneously from the precision air target track modes, was used to both control the radar antenna azimuth and elevation angle steering as well as for subsequent signal processing and establishment of proper Doppler to cross-range image scaling.

3.3. Rooftop Experimental Setup

Although the modified AN-APG-76 radar had the capability of operating in both classical low RF bandwidth air-target modes and significantly higher bandwidth SAR-type modes, there was no mode control software included in the radar to automatically intersperse these two waveforms to enable simultaneous 3-D air target tracking and HRR signature extraction. Thus, to avoid the need to develop new radar control software, we decided to utilize two separate
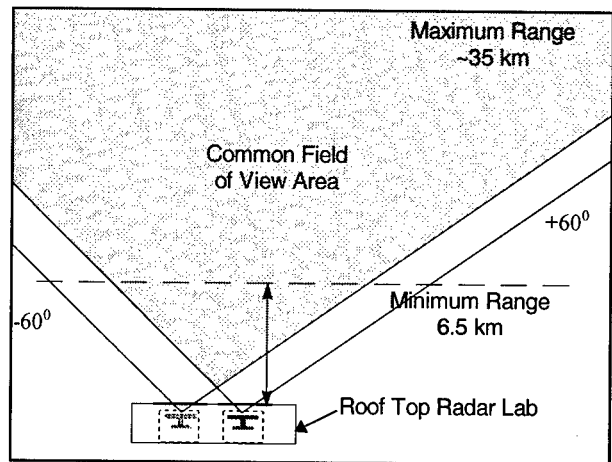
Figure 2. Rooftop Signature Collection Geometry

AN/APG-76 radars operating side-by-side to accomplish our objective. This side-by-side rooftop air target signature collection configuration is illustrated in Figure 2. One of the two radars was designated as the air target tracking radar and was used to acquire and track any selected airborne target entering it's field of view.

Three dimensional tracking data from this first sensor was then used to slave the second identical AN/APG-76 radar that was maintained in a high resolution SAR mode of operation. Since the lateral separation of the two radars was in the order of 23 meters and targets could be acquired and tracked anywhere within their mutual +/- 60 degree azimuth coverage region, the target track data from the first radar was on-the-fly parallax and range corrected by a small interface data processing unit operating at the common 20 Hz data rate on the interconnecting MIL-STD-1553B serial interface. Range and angle rate were also simultaneously corrected by the same method to enable smooth angular pointing of the second radar as well as correct dynamic positioning of its rather limited HRR range swath on the selected airborne target.

4. AIRBORNE TARGET DATA COLLECTION

The Norden Systems Norwalk, Connecticut, facility is conveniently located on the Eastern coast of the United States along the New York to Boston commercial air traffic corridor. Since funds for the project were limited, it was decided to utilize the large number of commercial aircraft traveling in the corridor as targets of opportunity for the data collection effort. Using this approach, over a period of only a few days, we were able to capture extended sequences of high quality radar signatures from 32 different aircraft flying by the laboratory facility at ranges between 6.5 and 30 km using both 1.0 and 0.3 meter resolution radar waveforms. Twenty four of the target aircraft were seen in various crossing geometries, six were in nominally nose-on geometries, and two were tracked at 0.3 meter resolution in a virtually direct fly-over configuration. The air target flight profile collection geometry for two typical track sequences are illustrated in Figure 3.

Figure 3. Two Air Target Profile Collections

A typical data collection sequence on a selected airborne target lasted from several seconds to nearly a minute depending upon its range and crossing rate. During this collection period the target aspect an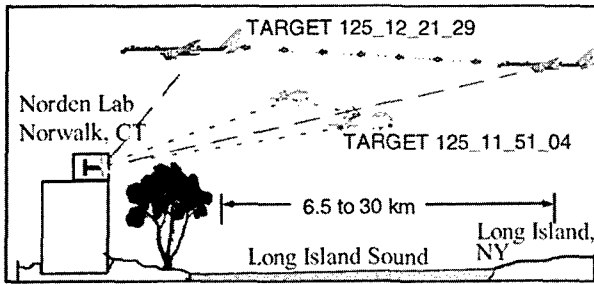gle as seen from the radar typically varied through several 10's of degrees and, with the nominal wide-band radar PRF in the area of 2 kHz, there were usually more than enough pulse samples available on any specific target to support processing of the coherent slant range vs aspect angle data array in any of several desirable ways. This high PRF also ensured that the target Doppler spectrum was fully un-aliased so that a valid Doppler spectrum of each range cell could be reconstructed from the radar-sampled data.

Since the tracking data from the air target tracker Kalman filter provided full 6 degree-of-freedom tracking information on the target throughout the data collection sequence, it was also a relatively simple task to both tag the data with a reasonably good estimate of the target aspect angle as well as to range and range-rate compensate the wideband coherent signature data for range walk and Doppler drift effects.

5. AIR TARGET IMAGING
To validate the quality of the aircraft data collected during the program, sets of complex-valued target range profiles contiguously-collected over nominal 2.5 degree aspect angle segments of the two flight trajectories illustrated in Figure 3 were range-Doppler processed to form 2-dimensional range-Doppler images of the airborne targets with nominally equal (1.0 or 0.3 m) range and cross-range resolutions. The results of this 2-D range-Doppler image processing are shown in Figure 4 and Figure 5.

- Civilian aircraft from NYC airport ... type unknown
- IRIG time 125:11:51:04 - May 5, 1997 EST
- East to West Approaching at Range of ~10.4 km
- Range & cross range resolution ~0.3 m
- Dwell time of 3.15 seconds
- Overlapping images with 2.6 seconds overlap
- Bright Spot autofocus

Figure 4. Time-Sequential Images of a Civilian Aircraft

- Civilian aircraft, likely deHavilland Dash 8 turbo prop
- IRIG TME 125_12_21_29 May 5,1997 EDT
- Closing at Range ~9.3 km
- Range & cross range resolution ~0.3 m
- Dwell time 1.04 secs
- Bright Spot autofocus processing
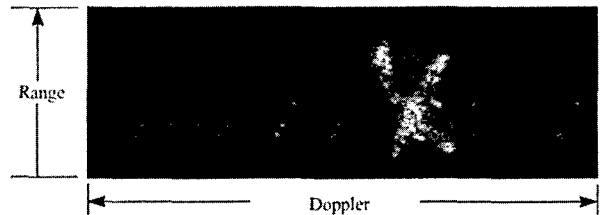
Figure 5. Civilian TurboProp Aircraft at 9.3 km

As illustrated, the images were sharply focused in both dimensions and, with the exception of significant Doppler sidebands at the ranges containing the engines, were extremely free of range or Doppler sidelobe artifacts. A set of outline drawings of the deHavilland Dash 8 Turboprop aircraft is shown in Figure 6 for comparison with the scaled range-Doppler radar image shown in Figure 5.

Wing span	25.91m
Height - overall	7.49 m
Length - overall	22.25m
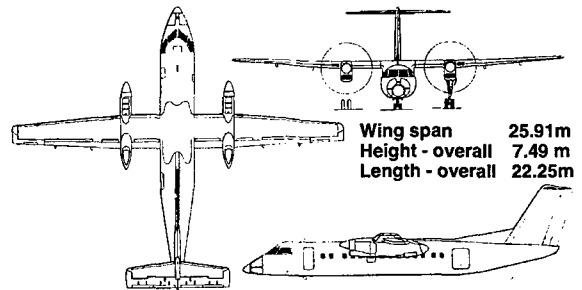
Figure 6. deHavilland DHC 8 Series 300 TurboProp

The algorithms used for this air target imaging demonstration were adapted from a set of Moving Target Imaging (MTIm) algorithms originally developed under Office of Naval Research sponsorship for the imaging of surface moving vehicles in SAR imagery. Of key importance to the formation of properly scaled (range & cross-range) imagery from the nominal range and Doppler imagery is the quality of the precision 9 degree-of-freedom target track data provided by the baseline AN/APG-76 radar.

6. HRR TARGET IDENTIFICATION
To evaluate the suitability of the collected HRR data for target identification purposes, a simple M-class HRR profile identification system as illustrated in Figure 7 was constructed. The implementation, based on mature pattern recognition technology, represented the target signature by a one dimensional feature vector and based its classification decision on well developed detection theory of hypotheses testing using a Bayes minimum error distance criterion[6].

In this HRR target identification process, successive wide bandwidth radar returns are passed into the Feature Extractor where they are range aligned, and then non-coherently combined to improve the signal to noise ratio. The combined returns define the radar high resolution range profiles from which the target magnitude feature vectors are extracted. For

training, these feature vectors are sent to the training algorithm for target structure evaluation and exploitation. For testing, these feature vectors are sent to the Minimum Error Bayesian Classifier for target decision declaration.

The Training Algorithm estimates statistical properties of the target feature vectors using an assumption of statistical independence among feature elements. Outputs of the training algorithm are sorted and stored in the Target Templates Library. A mean feature vector and a variance feature vector are kept in the library for each of the target classes.

During the testing phase, the M class Minimum Error Bayesian Classifier takes a feature vector from the Feature Extractor, measures normalized distances of the feature vector to all target templates in the library, and assigns a target class based on the minimum of these distances.

The performance of the HRR Target Identification Process is measured by inserting previously sequestered target data samples into the process and comparing classifier declarations with apriori known target truth data. Probabilities of correct versus incorrect classification decisions are then estimated by repeating this process with a large number of test data samples.
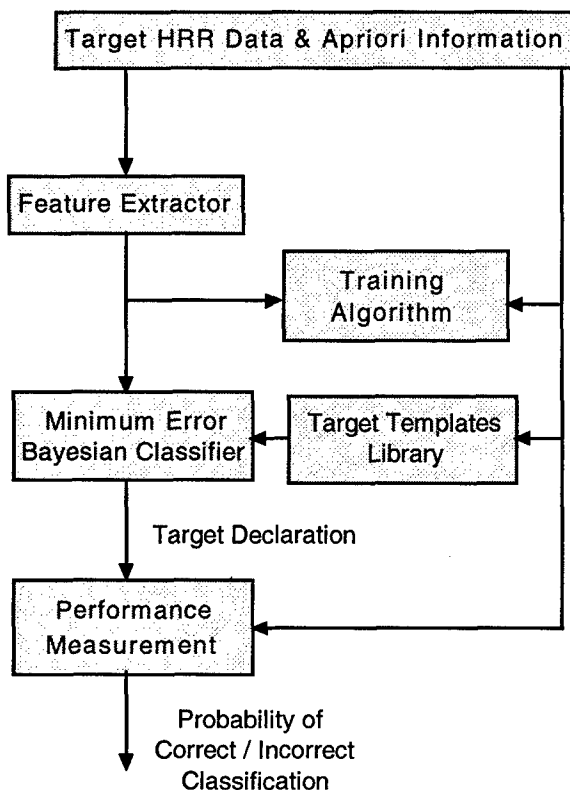
Figure 7. HRR Target Identification Process

To validate both the HRR identification process as well as the consistency of the collected HRR air target profiles, several segments of the collected data were passed through the training and testing portions of the process. Classification results and distributions of normalized distance scores were found to be consistent with theoretical expectations based on the statistical characteristics of the training samples. As expected, the HRR target identification process performed best when the candidate targets subtended a large number of range cells, the number of unique classes were small, and the inter-class profile differences were large compared to the intra-class variations. Conversely, poorer performance was seen when the number of range cells subtended by the target was small or when the candidate target classes had HRR profiles with a significant amount of statistical overlap.

7. SUMMARY AND CONCLUSIONS

The AN/APG-76 multi-mode tactical strike radar sensor was designed from the bottom up as both a capable all-aspect, look-up and look-down air-to-air search and track radar as well as a high resolution SAR imaging and targeting sensor. The combination of these two capabilities provides the means to add airframe-based target identification capabilities to its already impressive suite of capabilities that support both air and surface target missions.

8. REFERENCES

1. Tobin,M.E., "Real Time Simultaneous SAR/GMTI in a Tactical Airborne Environment" in "EUSAR'96 European Conference on Synthetic Aperture Radar" conference proceedings; Königswinter, Germany.; VDE-VERLAG GMBH, Berlin, Offenbach, ISBN 3-8007-2162-7, pp 63-66.

2. Tobin,M.E. and Greenspan,M.; "Adaptation of an AN/APG-76 Multimode Radar to the Smuggling Interdiction Mission", in "Proceedings of the IEEE 1996 National Radar Conference", Ann Arbor, MI, 13-16 May 1996, IEEE Pub. 96CH35891, pp 13-18.

3. Tobin,M.E. & Greenspan,M., "Smuggling Interdiction using an Adaptation of the AN/APG-76 Multimode Radar", IEEE AES Systems Magazine, vol. 11, n.11, pp 19-24; ISSN 0885-8985, November 1996

4. O'Brien,J., Holt,H., et.al., "Interferometric Radar Imaging Using the AN/APG-76 Radar", Radar Sensor Technology Conference, SPIE AeroSense Symposium, Orlando, Florida, April 1995.

5. Greenspan,M., Pham,L., et. al., "Development and Evaluation of a Real Time SAR ATR System" IEEE 1996 Radar Conference, Dallas, Texas, May 12-13, 1998.

6. VanTrees,H.L., "Detection, Estimation, and Modulation Theory", Part I, John Wiley & Sons Inc., New York, 1968.

The polarimetric calibration best trade-offs

Titin-Schnaider Cecile
ONERA
Chemin de la Hunière et des Joncherettes
91120 Palaiseau, France
email : titin@onera.fr

1. INTRODUCTION

A polarimetric radar must be able to measure the four terms (magnitude and phase) of the observed targets scattering matrices. The phase calibration of measurements is a critical step, because it determines the degree of validity in using polarimetric parameters (Huynen theory ...) for discrimining and identifying the targets. Simulations have shown that a phase control better than ±5 degrees in radar channels is desirable to derive significant calculation of polarimetric parameters.

The aim of full polarimetric radar calibration is to compensate the distortions of waves propagating in the four T/R radar channels: hH, vH, hV, vV. Measurements are altered by two types of distortions: unbalanced propagation delays in the four channels and polarization coupling between channels.

For each radar, a strategy of calibration must be designed to find a trade-off between accuracy and reliability of the results, in operational conditions: the number of standard targets must be as reduced as possible, the degree of realism of standard targets theoretical scattering matrix versus frequency variations and positioning errors must be carefully controlled .

This article shows the importance of taking into account the transmit waveform, the radar architecture and the phase distortions in channels. Investigations about calibration of the ONERA experimental radars are made: RAMSES (airborne based radar providing SAR images) and MERIC [4] (ground based radar designed for air target signature analysis and ISAR imaging).

Two concepts of fully polarimetric radar may be considered, depending on the way the two orthogonally polarized signals (H and V) are transmitted: alternately or simultaneously. The present work devoted to phase calibration problems and solutions may complete the Guili's papers [2] which widely discuss the advantages and drawbacks of the two concepts.

2. PHASE ANALYSIS

The phase behaviour through the radar channels for several designs of polarimetric radar transmitting

linearly frequency modulated pulses is analyzed, with the aim of defining the best suited phase calibration method in each case. Only one period of the signal is considered.

2.1 Linear FM phase analysis

- A linear FM signal with slope p and center frequency f_{em} is transmitted:

$$Z_{em}(T) = e^{j2\pi f_{em}T} e^{j\pi p T^2}$$

The signal travels to a punctual scattering center (scattering coefficient S) located at range d and back again, during the time $T_d = \dfrac{2d}{c}$. The received signal is:

$$Z_{rec1}(T) = S \ Z_{em}(T - T_d)$$

The received signal is mixed with a replica of the transmitted signal generated on the carrier frequency f_{rep} :

$$Z_{rep}(T) = e^{j2\pi f_{rep}T} e^{j\pi p T^2}$$

giving the demodulated signal:

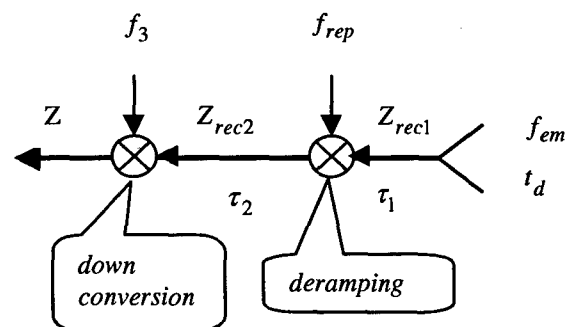$$Z_{rec2}(T) = Z_{rec1}(T) \ Z_{rep}^*(T - T_{rep})$$

Figure 1 : A theoretical receiving channel

- The starting time of the replica sets the time origin of the returned pulse (defining the reference range).

The change of variable: $t = T - T_{rep}$ allows to define: $t_d = T_d - T_{rep}$

The demodulated signal can therefore be written:

$$Z_{rec2}(t) = S \, Z_{em}(t - t_d) \, Z_{rep}^*(t) \qquad (1)$$
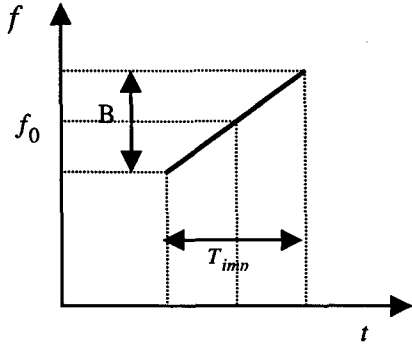

Figure 2 : A positive linear FM with carrier frequency f_0, pulse bandwidth B and pulse duration T_{imp}

● To clarify the notations, let us separate the pure carrier frequency terms as :

$$W(f_0, t) = e^{j2\pi f_0 t}$$

and the linear FM terms of given slope p (respectively positive and negative) as:

$$C_+(t) = e^{j\pi p t^2} \qquad C_-(t) = e^{-j\pi p t^2} = C_+^*(t)$$

In this way, the signal (1) after mixing can be written:

$$Z_{rec2}(t) = S \, W(f_2 - pt_d, t) W^*(f_{em}, t_d) C_+(t_d)$$

where : $f_2 = f_{em} - f_{rep}$

● Finaly, the value of the carrier frequency is reduced through a mixing with a pure wave. The signal at the end of the channel i e the measured signal is :

$$Z(t) = Z_{rec2}(t - \tau_2) W^*(f_3, t)$$

τ_2 being the duration of the wave propagation from the mixing.

$$Z(t) = S \, W(F - pt_d, t) W^*(f_2 - pt_d, \tau_2)$$
$$W^*(f_{em}, t_d) C_+(t_d)$$

The carrier frequency $F = f_2 - f_3$ of the resulting signals is generally low.

● The propagation delay τ_1^{xY} (duration of the wave propagation in the T/R radar channel xY before the mixing) changes the round trip duration t_d of the wave

travel radar-target-radar from a punctual scatterer to give :

$$t_d^{xY} = t_d + \tau_1^{xY} \qquad (2)$$

The resulting mesured signal in channel xY is:

$$Z^{xY} = S^{xY} W^*(F - p(t_d + \tau_1^{xY}), t)$$
$$W^*(f_{em}, t_d + \tau_1^{xY}) W^*(f_2, \tau_2^{xY}) \qquad (3)$$
$$W(pt_d, \tau_1^{xY} + \tau_2^{xY}) C_+(t_d)$$

The terms $C_+(\tau_1^{xY})$ and $W(p\tau_1^{xY}, \tau_2^{xY})$, being of second order with respect to channels delays will be neglected when delays are small enough.

2.2 Linear FM with positive slope

● In case of a radar transmitting a linear FM with positive slope p towards a punctual target, the FFT applied to the measured signal (3) gives a peak for the frequency:

$$v^{xY} = F - p(t_d + \tau_1^{xY}) \qquad (4)$$

The phase associated to the peak is deduced from (3):

$$\{\Phi_{xY}\} = \varphi_{xY} - 2\pi f_{em}(t_d + \tau_1^{xY}) - 2\pi f_2 \tau_2^{xY}$$
$$+ 2\pi p t_d \tau_{tot}^{xY} + \pi p(t_d)^2 + \Psi_{xY} \qquad (5)$$

This relation shows that the target phase φ_{xY} (the wanted information) is distorted by several types of undesired phase terms:

- a) The propagating phase terms:

before mixing : $2\pi f_{em}(t_d + \tau_1^{xY})$

after mixing : $2\pi f_2 (\tau_2^{xY})$ ......

-b) The residual video phase (RVP) $\pi p t_d^2$ is a deterministic phase term.

-c) A phase term resulting from the coupling between the residual video phase and the various channels propagation delays

It depends on the round trip duration t_d and on the total delay in channel xY:

$$\tau_{tot}^{xY} = \tau_1^{xY} + \tau_2^{xY} + ...$$

The total delay may include also other contributions like the delay before the beginning of sampling

-d) The residual unknown constant phase Ψ_{xY} which must not be forgotten.

● The above calculations enable us to conclude that the measured phase can be written in the following general form:

$$\left\{ \Phi_{xY} \right\}_+ = \varphi_{xY} - 2\pi f_1 \, t_d - 2\pi \sum_{i=1}^{I} f_i \, \tau_i^{xY}$$

$$+ 2\pi p t_d \sum_{i=1}^{I} \tau_i^{xY} + \pi p \left(t_d \right)^2 + \Psi_{xY}$$

(6)

The T/R channel xY is divided in I elements. Each element i is characterized by its carrier frequency f_i and its propagation duration τ_i^{xY}.

• Polarimetry is only concerned with relative phases. The methods of relative calibration are exclusively using ratios of channels measurements on the same target, in order to eliminate the absolute phase terms and to generate differential phase terms.

The phase of measured signals ratios $\left\{ Z_{xY} \right\}_+ / \left\{ Z_{aB} \right\}_+$ corresponding to linear FM with same (positive) slope are:

$$\left\{ \Phi_{xY} \right\}_+ - \left\{ \Phi_{aB} \right\}_+ = \left(\varphi_{xY} - \varphi_{aB} \right)$$

$$- 2\pi f_{em} \left(\tau_1^{xY} - \tau_1^{aB} \right) - 2\pi f_2 \left(\tau_2^{xY} - \tau_2^{aB} \right)$$

(7)

$$+ 2\pi p t_d \left(\tau_{tot}^{xY} - \tau_{tot}^{aB} \right) + \left(\Psi_{xY} - \Psi_{aB} \right)$$

It depends only on differential delays between the radar T/R channels xY and aB.

• The channels delays before deramping shift in range the peaks of punctual scattering centers.

The differential frequency shift between channels xY and aB is :

$$v^{xY} - v^{aB} = p \left(\tau_1^{xY} - \tau_1^{aB} \right)$$

In the SAR case, the four images hH, hV, vH and vV are slightly translated in range between them.

An estimate of the relative frequency shift $\Delta v = p \Delta \tau$ with respect to the frequency resolution cell $\delta v = 1/T_{imp}$ is given by:

$$\frac{\Delta v}{\delta v} = B \, \Delta \tau$$

$\Delta \tau$ being an estimate of the mean differential delay between any two channels

It is less than the resolution cell, when : $B \, \Delta \tau \ll 1$

2.3 Linear FM with negative slope

The measured signal corresponding to a transmit chirp with negative slope, is obtained by changing the slope p into $-p$. Thus, the same scattering center gives a peak for a frequency symetric about F :

$$v^{xY} = F + p(t_d + \tau_1^{xY})$$

(8)

The phase associated to the peak is:

$$\left\{ \Phi_{xY} \right\}_- = \varphi_{xY} - 2\pi f_{em} \left(t_d + \tau_1^{xY} \right) - 2\pi f_2 \, \tau_2^{xY}$$

$$- 2\pi p t_d \tau_{tot}^{xY} - \pi p \left(t_d \right)^2 + \Psi_{xY}$$

(9)

The sign of the two phase terms depending on range is thus changed.

The phase of the ratio of measured signals resulting from the transmission of two linear FM with the same negative slope $-p$, verifies the relation (7) for which p is changed into $-p$.

The phase of measured signals ratio corresponding to linear FM with opposite slope, for instance $\left\{ Z_{xY} \right\}_+ / \left\{ Z_{aB} \right\}_-$ may be written as:

$$\left\{ \Phi_{xY} \right\}_+ - \left\{ \Phi_{aB} \right\}_- = \left(\varphi_{xY} - \varphi_{aB} \right) + 2\pi p \left(t_d \right)^2$$

$$- 2\pi f_{em} \left(\tau_1^{xY} - \tau_1^{aB} \right) - 2\pi f_2 \left(\tau_2^{xY} - \tau_2^{aB} \right)$$

(10)

$$+ 2\pi p t_d \left(\tau_{tot}^{xY} + \tau_{tot}^{aB} \right) + \left(\Psi_{xY} - \Psi_{aB} \right)$$

Unlike the linear FM with same slope, the phase terms in this case depending on range are not substracted but added. The calibration has to take into account some phase terms depending on absolute delays instead of relative ones.

3. METHODS OF CALIBRATION

In a first step, channel cross-polarization is assumed to be sufficient low. Therefore, only channel inbalance has to be corrected.

The target c measurement Z_{xY}^c in channel xY is directly proportional to the theoretical scattering coefficient S_{xY}^c :

$$Z_{xY}^c = D_{xY} \, S_{xY}^c$$

(11)

the distortions being represented by D_{xY} .

The aim of the relative calibration is to estimate as accurately as possible the relative value of the distortion coefficients.

3.1 Single standard target method

If there were an ideal target 'o' whose scattering matrix is perfectly known, and which does not require precise positionning and orientation adjustement, the calibration formula of any target 'c' would be very simple:

$$\frac{S_{xY}^c}{S_{hH}^c} = \left(\frac{Z_{hH}^o \quad S_{xY}^o}{Z_{xY}^o \quad S_{hH}^o} \right) \frac{Z_{xY}^c}{Z_{hH}^c}$$

(12)

with xY = {hV, vH or vV}.

Moreover, to fulfil a good signal to noise ratio, the four terms of the standard target scattering matrix must be sufficiently high (in particular, they must not be theoretically zero)

A PARC could be used as a single standard target, provided that its theoretical scattering matrix is known

well enough and that all positionning problems are solved.

3.2 Sarabandi methods

To perform reliable mesurements in realistic conditions, it is preferable to make a minimum of assumptions on standard target theoretical scattering matrices and to consider calibration laws with low sensitivity to standard target positionning.

Copolar measurements on a trihedral corner 't' ($S_{hH}^t = S_{vV}^t$, $S_{vH}^t = S_{hV}^t = 0$) gives:

$$\frac{D_{hH}}{D_{vV}} = \frac{Z_{hH}^t}{Z_{vV}^t} \quad (13)$$

and consequently the first calibration formula:

$$\frac{S_{vV}^c}{S_{hH}^c} = \left(\frac{Z_{hH}^t}{Z_{vV}^t}\right)\frac{Z_{vV}^c}{Z_{hH}^c} \quad (14)$$

The reciprocity principle applied to a dihedral corner 'd' ($S_{hV}^d = S_{vH}^d, S_{vV}^d = S_{hH}^d = 0$) whose vertex is tilted by 45 degrees about the line of sight from the local horizontal, gives:

$$\frac{D_{vH}}{D_{hV}} = \frac{Z_{vH}^d}{Z_{hV}^d} \quad (15)$$

At this point two cases have to be examined, according to the validity of the relation:

$$D_{hH}\,D_{vV} = D_{hV}\,D_{vH} \quad (16)$$

3.2.1 Classical Sarabandi method

The distortions in radar channels are supposed to satisfy the condition (16). In the case of a switched transmit radar (only two receive channels v and h) distortions in receive and transmit channels are independant :

$$D_{xY} = D_x\,D_Y$$

and consequently verify (16).
The distortion ratio hv/hH may be written in the form :

$$\frac{D_{hV}}{D_{hH}} = \left(\frac{D_{hV}}{D_{hH}}\frac{D_{hV}}{D_{hH}}\right)^{1/2} = \left(\frac{D_{hV}}{D_{vH}}\frac{D_{vV}}{D_{vH}}\right)^{1/2}$$

$$= \left(\frac{Z_{hV}^d}{Z_{vH}^d}\frac{Z_{vV}^t}{Z_{hH}^t}\right)^{1/2}$$

which yield the second calibration formula:

$$\frac{S_{hV}^c}{S_{hH}^c} = \left(\frac{Z_{vH}^d}{Z_{hV}^d}\frac{Z_{hH}^t}{Z_{vV}^t}\right)^{1/2}\frac{Z_{hV}^c}{Z_{hH}^c} \quad (17)$$

In the same way, the third formula can be deduced,

$$\frac{S_{vH}^c}{S_{hH}^c} = \left(\frac{Z_{hV}^d}{Z_{vH}^d}\frac{Z_{hH}^t}{Z_{vV}^t}\right)^{1/2}\frac{Z_{vH}^c}{Z_{hH}^c} \quad (18)$$

Equations (14,17,18) were first proposed [1] by Sarabandi.
The advantages of the Sarabandi method are:
-a) If a trihedral and a dihedral (whose vertex is tilted in the radar wave plane, by about 45 degrees relatively to the local horizontal) are used as standard targets, it is shown that the method has little sensitivity to channel cross-polarization coupling.
-b) Any target with high cross-polar RCS , may be used instead of a dihedral (if the radar cross-coupling is negligible), because we are only applying the reciprocity principle.

The drawbacks of the Sarabandi method are:
-a) the sign ambiguity of cross-polarized terms,
-b) the dihedral alignement problems, to get a good signal to clutter ratio.

3.2.2 Generalized Sarabandi method

In the simultaneous transmit radar case (four receive channels), relation (16) is not true.
A new parameter γ has to be introduced :

$$\gamma = \left(\frac{D_{hV}}{D_{vV}}\frac{D_{vH}}{D_{hH}}\right)^{1/2} \quad (19)$$

giving the relations :

$$\frac{D_{hV}}{D_{hH}} = \left(\frac{D_{hV}}{D_{vH}}\frac{D_{vV}}{D_{hH}}\right)^{1/2}\gamma$$

$$\frac{D_{vH}}{D_{hH}} = \left(\frac{D_{vH}}{D_{hV}}\frac{D_{vV}}{D_{hH}}\right)^{1/2}\gamma$$

The calibration formula (17) and (18) become :

$$\frac{S_{hV}^c}{S_{hH}^c} = \gamma\left(\frac{Z_{vH}^d}{Z_{hV}^d}\frac{Z_{hH}^t}{Z_{vV}^t}\right)^{1/2}\frac{Z_{hV}^c}{Z_{hH}^c} \quad (20)$$

$$\frac{S_{vH}^c}{S_{hH}^c} = \gamma\left(\frac{Z_{hV}^d}{Z_{vH}^d}\frac{Z_{hH}^t}{Z_{vV}^t}\right)^{1/2}\frac{Z_{vH}^c}{Z_{hH}^c} \quad (21)$$

The parameter γ can be estimated from measurements on a PARC (Polarimetric Active Radar Calibrator) [3] with orthogonal antennas.
Its theoretical scattering matrix is known as being:

$$[S^P](\theta) = K(\theta)\begin{pmatrix} 1 & tg\theta \\ \cot g\theta & -1 \end{pmatrix} \quad (22)$$

The PARC gives an estimate of γ independant of its orientation angle θ.

$$\gamma = \left(\frac{Z_{vV}^{p}(\theta) Z_{hH}^{p}(\theta)}{Z_{hV}^{p}(\theta) Z_{vH}^{p}(\theta)} \right)^{1/2}$$ (23)

It can be easily demonstrated that the estimate of γ is also independant of the polarization coupling.

4. CALIBRATION IMPLEMENTATION

4. 1 The switched transmit radar

• The switched transmit radar (figure 3) provides the entire scattering matrix through two successive (pulse to pulse) transmission of linear FM waveforms of same slope on the two orthogonally polarized transmit channels (H and V), while receiving the target return through the two orthogonally polarized receive channels v and h .
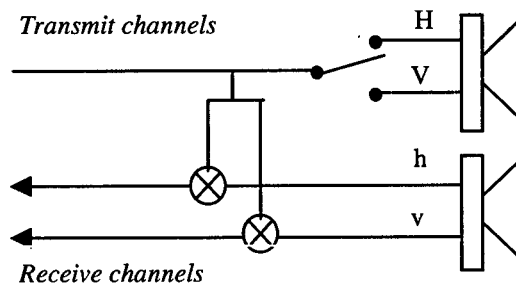

Figure 3: Simplified scheme of a switched transmit radar

The polarization switching technique leads to a complete retrieval of the target scattering matrix in a time $2T_r$ (T_r being the pulse repetition period). Therefore the Doppler sampling frequency is halved with respect to a conventional non polarimetric radar.

A delay of T_r is introduced between the measurement of the couples of elements $\left(S_{hH}, S_{vH} \right)$ and $\left(S_{hV}, S_{vV} \right)$, and may generate some decorrelation between them.

This radar type fulfills property (16) because the receiving and the transmitting channels are independant: $D_{xY} = D_x D_Y$

As, there are only two receiving channels (h and v), the delays in transmit channels can be separated from the delays in receive channels:

- before deramping: $\tau_1^{xY} = \tau^Y + \tau^x$

- after deramping: τ_2^x

Therefore, the classical Sarabandi method is well suited to calibrate the measurements of a switched transmit radar.

• This type of polarimetric radar transmits only linear FM of same slope (for instance positive).

Any calibration method uses only measurements ratios of linear FM with same slope, giving phase term like (7). In each waveform parameters case, the contribution of the term depending linearly on range has to be estimated. It can be written in the form :

$$\Phi_1 = 2\pi p \Delta\tau t_d$$

where $\Delta\tau$ denotes the mean differential delay between any two channels.

Let consider a typical case of the RAMSES radar SAR waveform:

Linear FM slope : $p = 5 \, 10^{12} \, Hz / \sec$

Pulse bandwidth: $B = 100 \, MHz$

Pulse duration: $T_{imp} = 33 \, \mu\sec$

Estimate of the mean differential delay: $\Delta\tau = 1 \, n\sec$

Swath: $d^{max} = 1500 \, m$ (i. e. $t_d^{max} = 10 \, \mu\sec$)

The variation of Φ_1 on the total swath is not negligible being:

$$\Delta\Phi_1 = 2\pi p \Delta\tau t_d^{max} = 18 \deg rees$$

Its variation on the temporal resolution cell $\delta t_d = (\delta v / p) = 1/\left(p T_{imp} \right)$:

$$\delta\Phi_1 = 2\pi p \Delta\tau \delta t_d = 2\pi \left(\Delta\tau / T_{imp} \right) = 0,01 \deg rees$$

is negligible.

• In the RAMSES case, the calibrating process has to take into account the linear variation of measurements ratio as a function of range.
The classical Sarabandi method (14, 16, 18) needs to know two linear phase laws $\varphi_{vV} - \varphi_{hH}$ and $\varphi_{hV} - \varphi_{vH}$. The linear law $\varphi_{vV} - \varphi_{hH}$ is provided by several trihedral corner reflectors deployed in range on the calibration area (x on figure 4).

The linear law $\varphi_{hV} - \varphi_{vH}$ is estimated by averaging the field clutter in each range cell (averaged clutter being supposed to satisfy the reciprocity principle). The use of clutter properties allows to avoid using an array of diagonal corner dihedrals. Moreover the clutter solution allows to escape from the corner dihedrals positionning problems: their very assymetric scattering lobe, making it very difficult to reach a good signal to noise ratio.

On figure 4, it can be seen that four areas returning a very poor signal to noise ratio (beginning and end of the swath, runways) are not taken into account (dashed lines) in the calculation of the least square line.

The calibration coefficients deduced from the calibration area may be used on any other area, if the radar parameters have not changed.
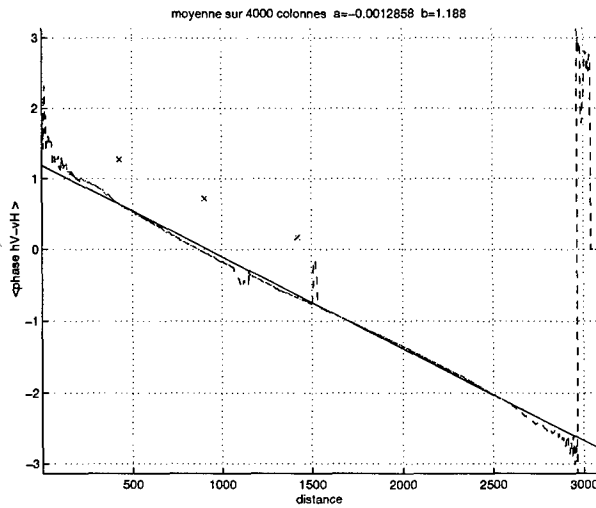

Figure 4 : cross-polar hV-vH and copolar hH-vV differential phases before calibration as function of range cell number

The slope of these two lines can be theoretically deduced from (7):

$$\frac{\partial(\Phi_{xY} - \Phi_{aB})}{\partial t_d} = 2\pi p\left(\tau_{tot}^{xY} - \tau_{tot}^{aB}\right)$$

(the slope p being an algebric number).

In any switched transmit radar, the delays τ_{em}^H and τ_{em}^V in the transmit channels can be separated from the delays τ_{rec}^h and τ_{rec}^v in the receive channels :

$$\tau_{tot}^{xY} = \tau_1^{xY} + \tau_2^{xY} + \ldots = \tau_{em}^Y + \tau_{rec}^x$$

Therefore :

$$\tau_{tot}^{vV} - \tau_{tot}^{hH} = \Delta\tau_{em} + \Delta\tau_{rec}$$

$$\tau_{tot}^{hV} - \tau_{tot}^{vH} = \Delta\tau_{em} - \Delta\tau_{rec}$$

where:

$\Delta\tau_{em}$ is the differential delay between the two transmit channels ($\Delta\tau_{em} = \tau_{em}^V - \tau_{em}^H$)

$\Delta\tau_{rec}$ is the differential delay between the two receive channels ($\Delta\tau_{rec} = \tau_{rec}^v - \tau_{rec}^h$)

From the slopes of lines $\varphi_{vV} - \varphi_{hH}$ and $\varphi_{hV} - \varphi_{vH}$, the differential delays $\Delta\tau_{em}$ end $\Delta\tau_{rec}$ can be estimated. On Figure 4, it can be seen that the slopes of the two lines $\varphi_{hH} - \varphi_{vV}$ and $\varphi_{hV} - \varphi_{vH}$ are very similar. Therefore, the delays between the receive channels seems to be dominant.

4. 2 The simultaneous transmit radar

Two linear FM signals of inverse slope are transmitted simultaneously. The returned signal is first separated according to its horizontal (h) and vertical (v) components. The four measurements Z_{hH} Z_{hV} Z_{vH} Z_{vV} are simultaneously collected at the end of the four receiving channels after deramping with the appropriate replicas of the transmitted signals (figure 5).
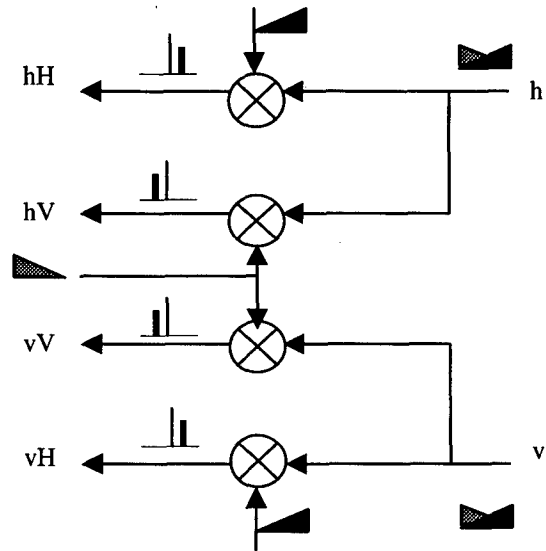
Figure 5: Receiver simplified scheme of a simultaneous transmit radar

The radar complexity is increased by the need of two transmitters and four receive channels, in particular.

- The measurement ratios may be divided into two classes according to whether they contain measurements belonging to the same (same slope linear FM) transmit polarizations (for instance Z_{xH}/Z_{aH}) or to different (inverse slope linear FM) transmit polarizations (for instance Z_{xV}/Z_{aH}).

The first case leads to the same measurement ratios than in the switched radar.

The second case causes the appearance of two different phase terms depending on range :

$$\Phi_2 = 4\pi\, p\, \bar{\tau}\, t_d$$

$$\Phi_3 = 2\pi\, p\, \left(t_d\right)^2$$

where $\bar{\tau}$ denotes the estimate of the mean total delay in a T/R channel.

The RVP which is eliminated in the switched radar case is doubled, giving the deterministic phase term Φ_3.

Let consider a typical case of the MERIC radar ISAR waveform parameters :

$$p = 5\,10^{12}\,Hz/\sec \quad B = 100\,MHz \quad T_{imp} = 33\,\mu\sec$$

$$\Delta\tau = 1\,n\sec \qquad \bar{\tau} = 33\,n\sec \quad (10\,m)$$

and swath: $d^{max} = 20\,m$ (i.e. $t_d^{max} = 133\,n\sec$)

The variations on the total swath are not negligible :

$$\Delta\Phi_2 = 4\pi\, p\, \bar{\tau}\, t_d^{max} = 14\,\deg rees$$

$$\Delta\Phi_3 = 2\pi\, p\left(t_d^{max}\right)^2 = 32\,\deg rees$$

The variations on the temporal resolution cell is:

$$\delta\Phi_2 = 4\pi\, p\, \bar{\tau}\,\delta t_d = 4\pi\left(\bar{\tau}/T_{imp}\right) = 0{,}65\,\deg rees$$

$$\delta\Phi_3 = 4\pi\, p\, t_d\,\delta t_d < 4\pi\, p\, t_d^{max}\,\delta t_d = 3\,\deg rees$$

Some care must be taken to correct the deterministic RVP phase term in large range windows case.

Therefore, a calibration range by range must be undertaken using the generalized Sarabandi method.

Given that it is not possible to deploy arrays of trihedrals, dihedrals and PARCS on the limited extend of the calibrating area, the only solution to vary $t_d = T_d - T_{rep}$ is to change T_{rep} (the starting time of the replicas).

In a tracking radar case (like MERIC) calibration is made on range profiles. In fact, the two radar designs must be tested:
- the simultaneous transmit technique implying the correction of RVP and a calibration being function of range by the generalized Sarabandi method, using three standard targets : a trihedral, a dihedral and a PARC deployed on a field area (measurements are distorted by the field clutter)

- the switched transmit technique allowing a range independant calibration, the phase variation being negligible :

$$\Delta\Phi_1 = 2\pi\, p\,\Delta\tau\, t_d^{max} = 0{,}24\,\deg rees$$

The classical Sarabandi method using two standard targets (a trihedral and a dihedral) is appropriate.

The price to be paid is the compensation for time delay between the two pairs of elements $\left(S_{hH}, S_{vH}\right)$ and $\left(S_{hV}, S_{vV}\right)$ of the calibrated scattering matrix.

5. CONCLUSION

The present paper, shows in the RAMSES and MERIC case that:
- the phase calibration problem must be taken into account at the radar design and waveform definition steps,
- the distortions of signals propagating in the radar channels must be theoretically known to be able to define a suited calibration strategy,
- the calibration process results in a trade-off between accuracy, practical conditions of measurements and costs requirements

6. REFERENCES

1. Sarabandi K.,Ulaby F.T., Tassoudji M.A., "Calibration od polarimetric radar system with good polarization isolation", IEEE Trans. Geosci. Remote Sensing, vol. 28, n° 1, Jan 1990.

2. Guili D., Facheris L., "SAR application of a signal coding technique for single-hit measurement of the target scattering matrix", European Trans. on Telecommunications, vol. 2, n° 6, 1991.

3. Freeman A., "A new system model for radar polarimeters", IEEE Trans. Geosci. Remote Sensing, vol. 29, n°5, Sept 1991.

4. Brouard P, Attia S., Guern R., "MERIC, Recent developments", AGARD 22-24 April 1998, Mannheim

FORME D'ONDE OPTIMISÉE POUR L'IMAGERIE ET L'IDENTIFICATION DE CIBLES

M. DINNICHERT

Office National d'Etudes et de Recherches Aérospatiales (ONERA),
29, Av. de la Division Leclerc, B.P. 72, 92322 Châtillon Cedex, France

1. INTRODUCTION

Les contraintes opérationnelles d'un radar dépendent bien évidemment des missions qu'on lui attribue. Un radar dédié à l'identification de cibles non coopératives doit exploiter au maximum les informations dont il dispose, à savoir :

- la cinématique de la cible,
- son spectre Doppler,
- sa réponse impulsionnelle obtenue par haute résolution distance (HRD),
- sa réponse transverse obtenue par ISAR,
- l'imagerie 2D
- sa réponse polarimétrique,
- les associations possibles de ces informations.

Une des caractéristiques prépondérantes du radar pour réussir sa mission est la haute résolution distance. Cette composante est nécessaire et son association avec d'autres analyses (spectrale, polarimétrique) est la clé de l'identification radar. Plusieurs analyses (confortées par des mesures expérimentales) ont montré qu'une résolution de 0,5 m (radiale et transverse) ainsi qu'une dynamique d'analyse de 30 dB sont nécessaires. La bande spectrale à émettre se déduit directement de la résolution radiale requise, soit 300 Mhz.

Deux familles distinctes de forme d'onde sont candidates pour émettre cette bande :

- la bande "instantanée", utilisant la voie large bande du radar et générée à l'aide d'une rampe de fréquence dans l'impulsion.
- la bande "synthétique", utilisant la voie bande étroite du radar et générée par une excursion de la fréquence d'émission d'impulsion à impulsion (ou de rafale à rafale).

L'objet de ce papier est de présenter les caractéristiques intrinsèques de formes d'onde opérant sur 300 Mhz de bande et susceptibles d'être intégrées dans un radar imageur.

Certaines d'entre elles ont été mises en oeuvre au centre de Palaiseau pour imager des avions civils en approche de l'aéroport de Paris-Orly.

2. DESCRIPTION DES FORMES D'ONDE

2.1 La bande instantanée

Cette forme d'onde utilise le principe du "deramping" en réception. Une onde hyperfréquence d'amplitude constante est modulée linéairement dans le temps pendant une durée T sur une bande de fréquence ΔF. L'onde reçue, retardée par le trajet aller retour sur la cible, est démodulée par une réplique de l'onde émise, elle même retardée d'un temps τ'. Le signal résultant de ce mélange fournit un ensemble de composantes spectrales qui est l'image du profil distance de la cible visée, figure 14. Ce profil est obtenu par FFT du signal de mélange.

L'intérêt majeur du "deramping" est de réaliser l'échantillonnage du signal sur une bande vidéo largement inférieure à la bande spectrale émise par le radar. En contrepartie, la difficulté de mise en oeuvre de cette forme d'onde réside dans l'élaboration des circuits large bande à l'émission et à la réception.

Le rapprochement (ou l'éloignement) de la cible introduit un décalage général du profil de la cible dans la fenêtre d'analyse mais introduit aussi un terme de phase quadratique qui dégrade la réponse impulsionnelle de la cible.

On admet que le terme $v.\Delta F.T/c$ ne doit pas excéder 1 pour un traitement par FFT pondérée (fenêtre de Hamming). Pour une forme d'onde caractérisée par $\Delta F = 300$ Mhz et $T = 100$ µs, la valeur limite de vitesse cible ne nécessitant pas de compensation est de 10 km/s. Les cibles aérobies ne sont pas concernées par cette

contrainte. Cette forme d'onde peut être aussi utilisée dans le contexte de défense de théâtre contre des missiles balistiques tactiques (phases de poursuite et engagement).

2.2 La bande synthétique

Sans modulation dans l'impulsion

Les séquencements de formes d'onde de type bande synthétique peuvent être relativement variés suivant les applications et les missions que l'on attribue au radar. Le séquencement le plus simple consiste à émettre une série d'impulsions, décalées les unes par rapport aux autres d'un pas constant en fréquence ΔF, figure 1. Cette forme d'onde, très prédictible, peut être utilisée par des radars bande étroite ne disposant pas de modulation dans l'impulsion.
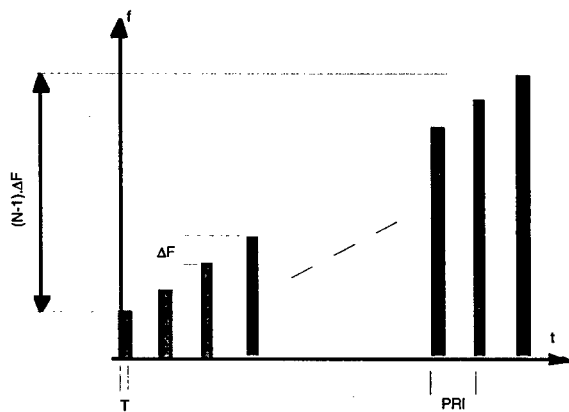

Figure 1 - Séquencement d'une forme d'onde bande synthétique sans modulation dans l'impulsion

Le traitement se réalise en deux étapes distinctes, figure 15 :

* la première étape est le filtrage adapté bande étroite à chaque impulsion de la rafale. Le traitement récupère donc un ensemble de profils basse résolution qu'il enregistre pour l'étape suivante.
* la seconde étape consiste en une FFT sur chaque case distance basse résolution pour accéder au profil haute résolution.

On montre que le mouvement de la cible induit un terme de phase quadratique qui dégrade la réponse impulsionnelle de la cible. Ce terme quadratique est proportionnel au produit B.T de la forme d'onde, T étant le temps de la rafale, $T=(Ni-1).PRI$.

Le terme v.B.T/c ne doit pas excéder 0,25 pour limiter la migration de la cible à une demi cellule de résolution pendant le temps d'émission de la rafale. L'erreur d'estimation de

$v_r, \Delta v_r = |v_r - \tilde{v}_r|$ ne devra donc pas dépasser

$$\Delta v_{r\ max} = \frac{c}{4BT}.$$

Pour l'identification d'une cible à longue distance (200 km par exemple) qui nécessite une PRI de l'ordre de 1,5 ms et pour N=128 et ΔF=2,5 Mhz, l'erreur d'estimation vitesse ne devra pas excéder 1,2 m/s. Outre la durée de la rafale synthétique, ce type de forme d'onde nécessite une ou des formes d'onde d'appoint pour recaler la vitesse de la cible à identifier.

De plus, la fonction d'ambiguïté de cette forme d'onde est plutôt appropriée à l'analyse d'une cible unique en environnement clair à cause de la présence de lobes de périodicité importants. La figure 2 illustre la réponse impulsionnelle d'une telle forme d'onde avec les caractéristiques suivantes :

* T=5 μs
* B=1/T=0,2 Mhz
* N=128
* ΔF=2,5 Mhz
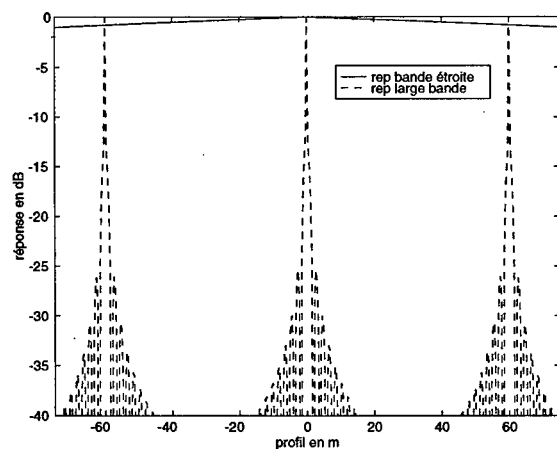
Figure 2- Réponse impulsionnelle pour une forme d'onde à BT=1

On note la présence de nombreuses remontées de FFT (pics de périodicité), pondérées seulement par l'enveloppe du filtre adapté bande étroite. Cette forme d'onde est dimensionnée pour imager des cibles de longueur inférieure à 60 m. Par contre, une analyse de raid devient délicate avec cette forme d'onde à cause de cette périodicité de la réponse synthétique et de la largeur de la réponse de l'impulsion, dite « réponse large bande ». En effet, si plusieurs cibles se trouvent dans la même case distance basse résolution, leurs profils (issus de l'analyse large bande) vont se superposer et l'analyse haute résolution de chaque cible sera brouillée. Une tendance est donc de réduire la taille de la case distance, soit par réduction de la durée de l'impulsion, soit par modulation de l'impulsion.

Avec modulation dans l'impulsion

Une manière de contrôler ces remontées de lobes de FFT est de moduler les impulsions de la rafale synthétique pour réduire la taille de la case distance. Une façon simple d'obtenir cette réduction de case distance est de réaliser une modulation linéaire de fréquence dans l'impulsion (chirp) , figure 3.
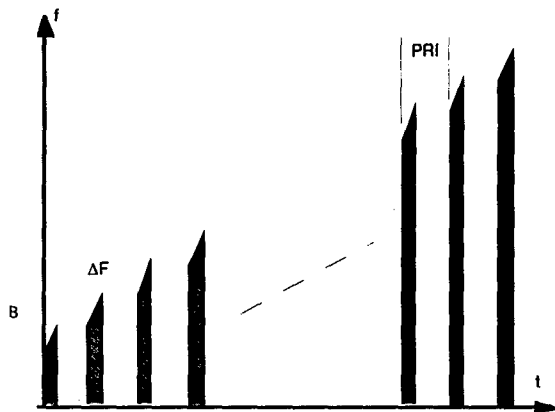
Figure 3 - Séquencement d'une forme d'onde bande synthétique avec modulation dans l'impulsion

En fait, la cible a un profil qui s'étale dans la case distance basse résolution et il est important de vérifier qu'une cible hors de cette case distance n'ait pas d'influence sur la cible en cours d'analyse. Le critère choisi est d'identifier le niveau des lobes de périodicité sur quelques cases distance basse résolution. La figure 4 permet de visualiser les réponses de plusieurs filtres FFT de l'analyse synthétique. Ces filtres ont été choisis pour couvrir la taille de la case distance basse résolution à 3 dB. La forme d'onde simulée est la suivante :

- T=50 µs
- BT=250 (B=5 MHz)
- N=128
- ∆F=3 MHz

Le chirp est pondéré en amplitude (Hamming) et les lobes de périodicité n'excèdent pas -28 dB car ils sont pondérés par l'enveloppe de la réponse basse résolution. Dans ce cas précis, 384 Mhz de bande sont nécessaires pour garantir 0,5 m de résolution (la FFT 128 points est elle aussi pondérée). La bande passante de chaque impulsion est supérieure au saut de fréquence ∆F.
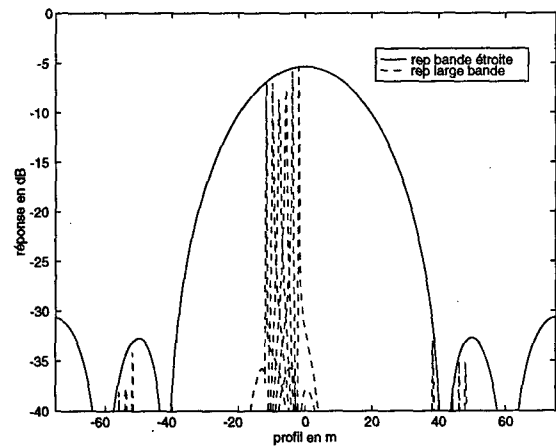
Figure 4 - Réponse impulsionnelle pour une forme d'onde à BT=250

Modulation pseudo-aléatoire de la rafale

Une autre manière de réduire les lobes parasites de la réponse synthétique est de rendre les paramètres de la forme d'onde pseudo-aléatoires. La figure 5 montre un séquencement extrême, où la durée de l'impulsion, la bande de chaque impulsion et chaque PRI varient dans la rafale.
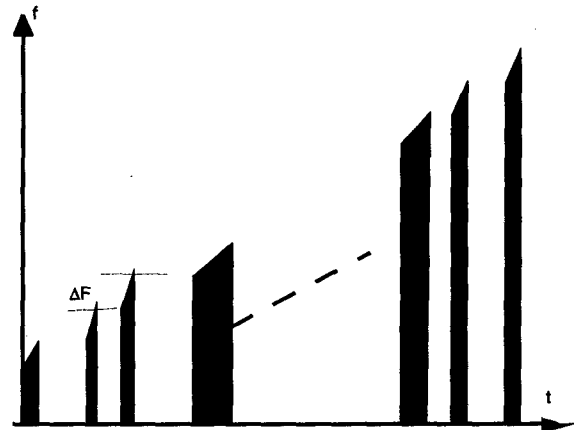
Figure 5- Séquencement d'une forme d'onde bande synthétique à modulation pseudo aléatoire

Bien que toutes les combinaisons de séquence aléatoire soient possibles, certaines présentent des spécificités difficilement acceptables du point de vue traitement radar :

- Si la durée des impulsions n'est pas constante, le traitement radar doit mettre en oeuvre un filtre égaliseur puisque l'énergie contenue dans chaque impulsion n'est pas constante.
- Si la PRI n'est pas constante dans la rafale, un traitement à base de FFT classique ne convient plus pour la reconstitution du profil de la cible. Un filtrage adapté à chaque cellule haute résolution doit être effectué pour reconstituer le profil. Ce type de séquencement nécessite plus de charge

de calcul mais a des performances de CCME non négligeables.

- Il reste donc la possibilité de moduler la bande de chaque impulsion pour conserver un traitement haute résolution le plus simple possible.

Nous avons simulé une forme d'onde où B est aléatoire avec les paramètres suivant :

- T=5 μs
- 4 MHz < B < 6 MHz
- N=128
- ΔF=2 MHz

La figure 6 illustre la réponse large bande. Le niveau des lobes de périodicité est à -28 dB environ. Ce niveau est du même ordre de grandeur que celui de la forme d'onde avec modulation dans l'impulsion. Par contre, la résolution synthétique est légèrement dégradée dans le cas présent à cause de la réduction du saut de fréquence ΔF.

La modulation aléatoire dans les impulsions d'une rafale de type bande synthétique n'apporte pas d'amélioration majeure ni en terme de résolution radiale ni en terme de dynamique d'analyse (niveau des pics de périodicité). Par contre, ce type de forme d'onde a des qualités de faible probabilité d'interception (LPI : low probability of Intercept) vis-à-vis d'un récepteur ESM dans un contexte de guerre électronique intense.
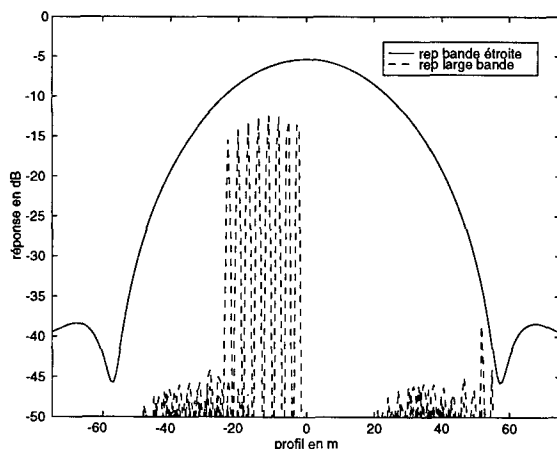
Figure 6 - Faisceau de réponses bande étroite et réponses large bande

Séquencement pseudo aléatoire de la rafale

La particularité de cette forme d'onde est d'avoir un séquencement non ordonné des porteuses de chaque impulsion, figure 7. Ceci a pour conséquence de briser le couplage distance-Doppler classique des lois linéaires en fréquence.
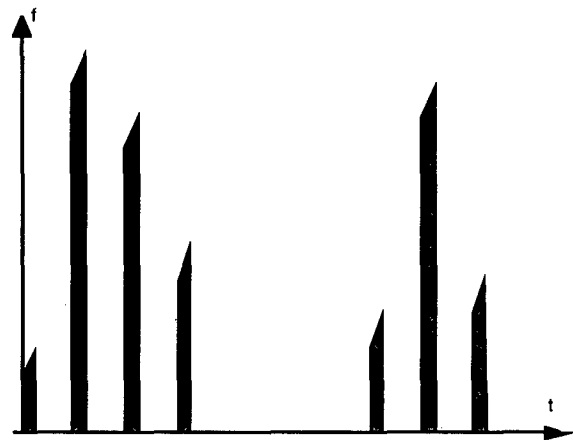
Figure 7 - Séquencement pseudo aléatoire d'une forme d'onde bande synthétique

Ce type de forme d'onde est beaucoup plus sensible au Doppler que les formes d'onde à loi monotone (en fréquence). Le caractère non prédictible de cette forme d'onde la rend moins sensible aux techniques de brouillage. Un brouilleur à bruit doit être large bande pour espérer couvrir toute la bande synthétique.

2.3 Recherche de la forme d'onde optimum

Quand le radar ne dispose pas de la bande instantanée nécessaire pour réaliser convenablement la fonction identification, nous avons vu qu'une solution est d'émettre un train d'impulsions décalées en fréquence et couvrant la bande désirée. Cette méthode présente des inconvénients opérationnels important, surtout la durée d'émission de la rafale. L'objet de ce chapitre est d'évaluer le meilleur compromis en terme de correction de mouvement (liée à la durée d'impulsion) et de dynamique d'analyse.

Rafale à deux impulsions

Dans un premier temps, nous considérons que la bande totale n'est couverte que par deux impulsions. Le traitement de réception envisagé est de type "deramping". La pente de modulation des chirp peut être du signe du saut de fréquence, soit du signe opposé. Le saut de fréquence entre les deux impulsions est inférieur ou égal à la bande de modulation d'une impulsion pour éviter l'apparition de "lobes de réseaux" dans la réponse impulsionnelle.

La figure 8 montre la réponse impulsionnelle de la forme d'onde suivante :

- T=100 μs
- B=150 MHz
- N=2

- ΔF=150 MHz

La pondération du chirp permet naturellement d'abaisser le niveau des lobes de la réponse "large bande", mais les lobes de la réponse synthétique sont inchangés. Le niveau de ces lobes ne peut être abaissé car il n'est pas envisageable de pondérer une FFT 2 points.
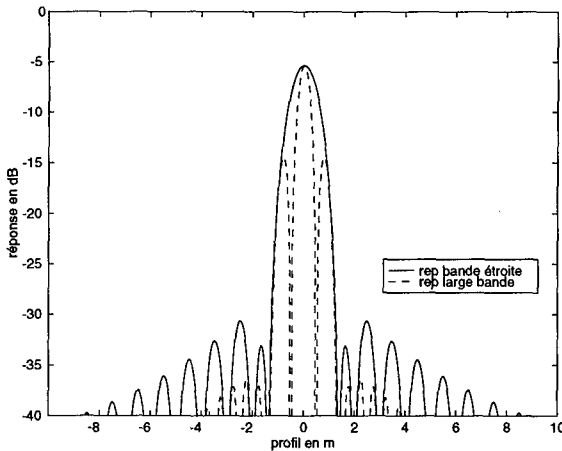
Figure 8 - Réponses impulsionnelles d'une double rampe pondérée

Un traitement synthétique sur deux impulsions permet d'accéder en théorie à une résolution double de celle de l'impulsion unique, mais le traitement associé induit des lobes secondaires forts qui dégradent le profil distance d'une cible et la dynamique d'analyse.

Rafale à plusieurs impulsions

Le dimensionnement de cette forme d'onde découle des conclusions précédentes. Le dimensionnement optimum doit garantir un temps d'émission de la rafale le plus court possible tout en maintenant une résolution finale de l'ordre de 0,5 m et des lobes secondaires faibles. Le problème revient à définir le nombre d'impulsions dans la rafale et leur composition spectrale. La première forme d'onde examinée est la suivante :

- T=100 μs
- B=50 MHz
- N=16
- ΔF=25 MHz

La figure 9 montre la réponse large bande et plusieurs filtres de FFT résultant de l'analyse synthétique. Les chirp et la FFT sont pondérés par une loi de Hamming. Le niveau des lobes secondaires reste inférieur à -25 dB pour tous les filtres de la case distance. La bande totale est de 400 Mhz. Compte tenu des pondérations qui élargissent la réponse synthétique, la résolution finale est de 0,5 m.
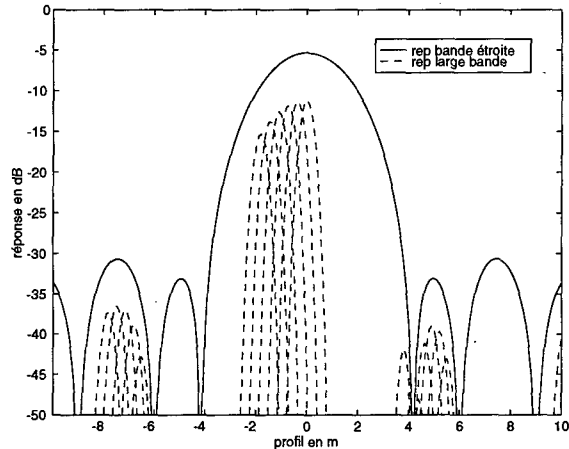
Figure 9 - Réponse impulsionnelle de la forme d'onde à 16 impulsions

En considérant le critère selon lequel l'estimation de la vitesse radiale de la cible doit être inférieure à $\Delta vr_{max} < c/(4 B_{tot} T)$, B_{tot} étant la bande totale d'excursion et T le temps total pour émettre B_{tot}, on en déduit le tableau ci-dessous. La PRF de 750 Hz est dimensionné pour réaliser l'identification de cibles à 200 km et B_{tot}=300 MHz.

N=4, B=150 Mhz, ΔF=75 MHz	Δv=47 m/s
N=8, B=100 Mhz, ΔF=50 MHz	Δv=23 m/s
N=16, B=50 Mhz, ΔF=25 MHz	Δv=12 m/s

On retiendra que pour des cibles en rapprochement et pour les formes d'onde présentées ici, il est nécessaire d'effectuer une correction du mouvement des cibles sur les profils basse résolution avant de réaliser le profil haute résolution de ces cibles.

3. IMAGES SUR DONNEES REELLES

Nous présentons ici quelques images radar obtenues sur données réelles. Compte tenu de la configuration du site, les formes mises en oeuvre sont destinées à de l'identification courte portée.

3.1 Forme d'onde 1

Les caractéristiques principales de cette forme d'onde sont les suivantes :

- T=12,8 μs
- PRI=132 μs
- B=150 MHz
- N=2

- ΔF=150 MHz

La cible est un Airbus de moyenne taille enregistrée en polarisation VV. L'image est floue et on constate un dédoublement des points brillants de la cible sur l'axe distance. Cet effet était prédictible à partir des simulations et plus particulièrement en observant la figure 8. La résolution de cette image n'est pas supérieure à celle obtenue sur une demi-bande de 150 MHz.
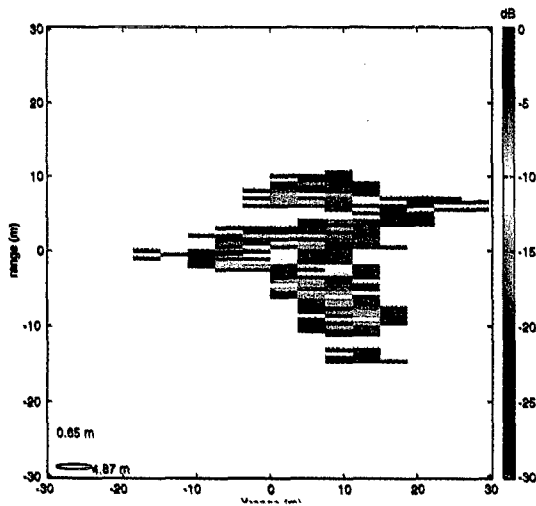
Figure 10

3.2 Forme d'onde 2

Les caractéristiques principales de cette forme d'onde sont les suivantes :

- T=12,8 μs
- PRI=132 μs
- B=36 MHz
- N=16
- ΔF=18 MHz

Ces enregistrements concernent un Boeing 747 en polarisation VV. Les images radar de la figure 11 ont été réalisées avec 128 profils haute résolution. La résolution transverse est donc d'environ 2,5 m, compte tenu de la fréquence porteuse et de la présentation de l'appareil.
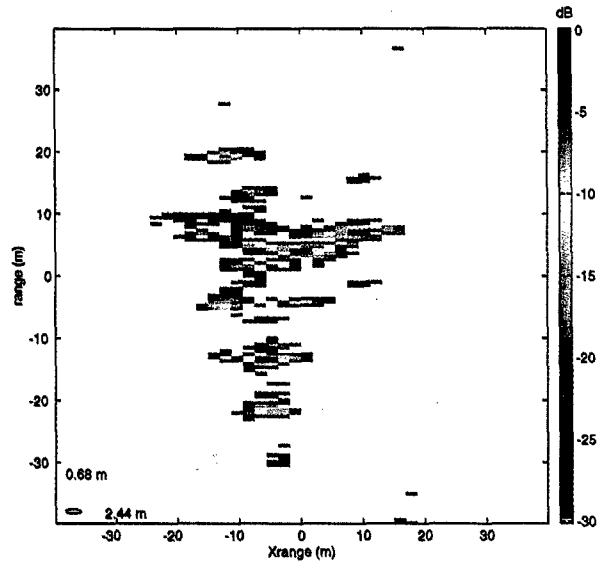
Figure 11 - Images radar d'un 747 en polarisation VV

Sur ce fichier de mesures, nous avons évalué le temps de cohérence d'une telle cible sur une passe de 1,1 s comportant 8192 profils. On s'aperçoit que dans les conditions de la mesure (fréquence, polarisation, type de cible, attitude, etc...) le temps de cohérence de la cible est de l'ordre de 0,3 s (seuil à 0,8). Ceci montre bien l'importance de limiter le temps nécessaire pour former une image.

La dimension polarimétrique peut être ajoutée à l'imagerie radar. La figure 12 illustre la signature d'un Airbus en polarisation VV tandis que la figure 13 montre sa signature en polarisation VH. On constate que la transition aile/carlingue signe plus sur la voie VH que sur la voie VV. Ceci est probablement dû aux réflexions multiples (effet dièdre). Les compensations de mouvement ont été effectuées séparément sur chaque voie. Une compensation de mouvement globale doit permettre d'améliorer la focalisation de l'image et l'analyse du comportement polarimétrique de chaque point brillant.
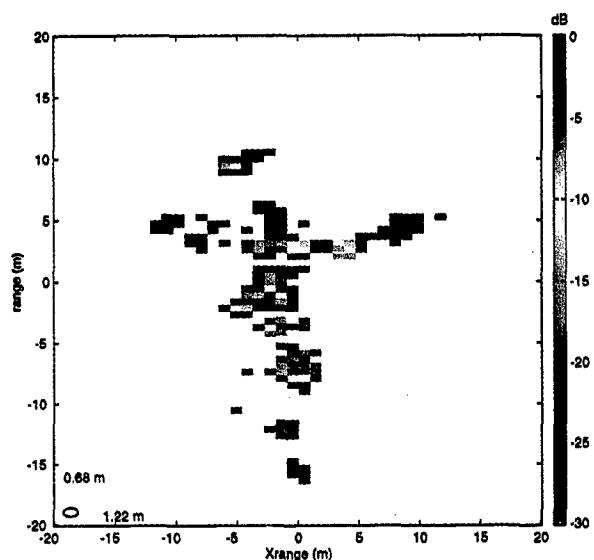
Figure 12 - Image radar d'un Airbus en polarisation VV

Figure 13 - Image radar d'un Airbus en polarisation VH

chaînes d'émission et de réception. Ces réflexions ont pour arrière plan la modification de L'ARMOR sur le bâtiment Monge pour augmenter sa bande de traitement de 150 MHz à 300 Mhz dans le cadre d'un futur développement exploratoire. Mais les formes d'onde présentées ici sont directement transposables pour un radar aéroporté opérant en mode SAR.

Le dimensionnement de ces formes d'onde est influencé par les objectifs de la mission opérationnelle du radar. Certaines de ces formes d'onde présentent en outre des qualités de CME intéressantes. Nous avons démontré sur des mesures la validité du concept. Pour couvrir 300 MHz, une rampe de 8 impulsions modulées portant chacune 75 Mhz et recouvrantes à 50% paraît être un choix intéressant.

4. CONCLUSION

Ce document passe en revue différentes formes d'onde pouvant être mises en oeuvre dans un traitement radar à haute résolution. L'effort porte surtout sur les formes d'onde dites « hybrides », dans lesquelles chaque impulsion d'une rafale porte une fraction de la bande totale. Ces impulsions ont la particularité d'être modulées, à l'inverse de la bande synthétique généralement abordée dans la littérature. L'intérêt premier de ces formes d'onde est d'augmenter la résolution radiale du radar sans modifier les composants hyperfréquence des
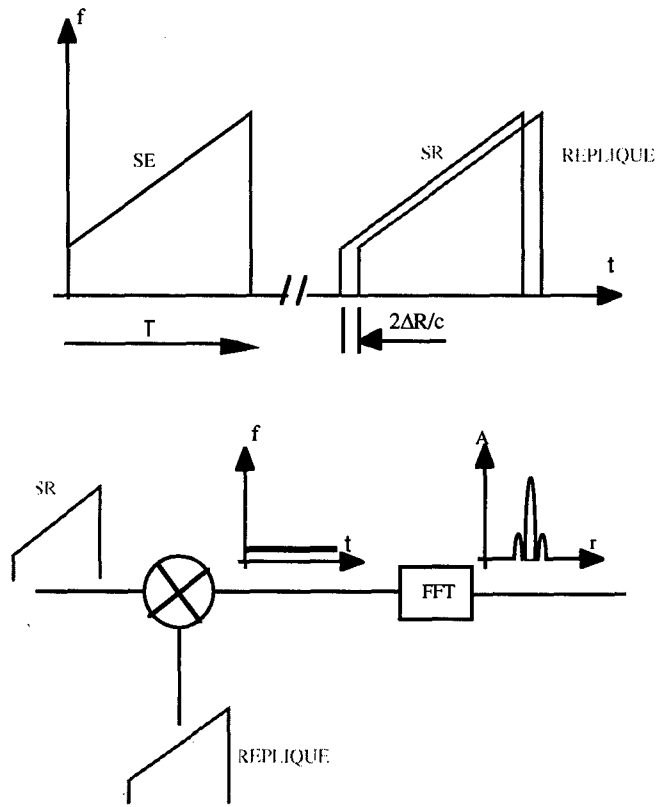
Figure 14 - Illustration du type de réception par "deramping"
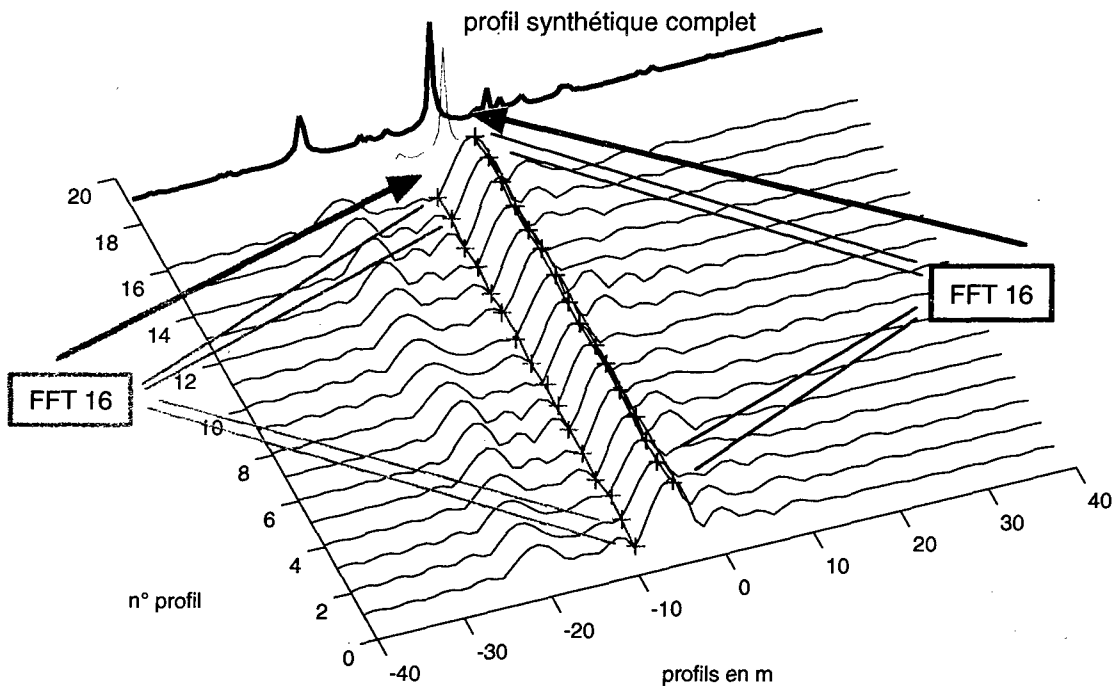
Figure 15 - Illustration de la reconstitution du profil synthétique

AIRCRAFT IDENTIFICATION VIA TWO-DIMENSIONAL IMAGING

A. W. Rihaczek
S. J. Hershkowitz
MARK Resources, Inc.
3878 Carson Street, Suite 210
Torrance, CA 90503 USA

B. I. Hauss
T. K. Samec
TRW, Inc.
One Space Park
Redondo Beach, CA 90278 USA

1. INTRODUCTION

We have developed a workable technology for noncooperative aircraft identification, based on the theory of Complex-Image Analysis [1] and implemented in an expert system. For the final adjustment of the algorithms and large-scale testing to determine performance, we need suitable data on a variety of aircraft under different conditions of flight. Unfortunately, such data do not exist within NATO. Until suitable data become available, the development of the identification system cannot be finished. In this paper we discuss how we identify aircraft, and what considerations have led to the chosen approach.

2. WHY TWO-DIMENSIONAL IMAGING IS NEEDED

Two-dimensional imaging has disadvantages in that it requires a motion compensation and dwell time on the target. Although a system based on one-dimensional range resolution would be much simpler, one problem is that wing responses are folded onto the fuselage responses, in a different way for different aspect angles. A more serious problem is that range resolution becomes very ineffective in resolving scatterers on the fuselage as the aspect angle approaches broadside. However, the most serious problem, which by itself would force one to go to two-dimensional resolution, is the need to resolve the delayed duct returns of fighter aircraft from the fuselage returns. Figure 1 shows the ISAR image of an aircraft in peaks plot form, where each local maximum in the intensity image is indicated by a dot, the size of which is proportional to the peak amplitude. Crossrange Gate 9 contains the delayed duct returns. Without crossrange resolution all dots will be translated onto a vertical line, with obvious consequences from the delayed duct returns. The problem is particularly serious for small aspect angles. We need the most efficient method for their suppression, which is Doppler resolution, and hence, two-dimensional imaging.

3. HOW WE UTILIZE A TWO-DIMENSIONAL IMAGE

Because we are accustomed to identifying targets by eye from photographs, the obvious approach is to attempt to do the same with radar images. Figure 2 shows the conventional ISAR image of the aircraft. It is clear that this obvious approach has a problem for the image in Figure 2. The solution would appear to be to process the image further. We can attempt to find a way of removing the duct returns, and in some fashion cleaning the image to bring out the shape of the aircraft. One might be successful in some cases, but not in most others.

The backscattering of man-made targets at radar wavelengths is rather different from that at optical wavelengths. At radar wavelengths, the return is dominated by the backscattering from such features as corners, cavities, and electronic devices. The most important features are on the fuselage, and most of them are near the centerline. There is little shape information to be extracted. Although the wings seems to give shape information, there are the problems of banking, rolling, and flexing. The conclusion is that identification must be based on measuring the positions of observable features and, when possible, their characteristics. We may add such information as a capability for carrying wing tip missiles, number of engines, and similar recognizable features, but most of the information on which identification can be based is in the positions of features on the fuselage.

4. THE CONSISTENCY OF FEATURES

Identification via feature detection evidently is practical only if the observable features persist over relatively large aspect angle sectors. This will be the case if the above statement as to the sources of observable backscattering is true. In this case we will also be able to use diagrams, photographs, and models to predict the feature positions of the aircraft to be identified. We will illustrate the consistency of features via turntable measurements, for which we have ground truth.

Figure 3 shows the match via a deformable template between the measured feature positions extracted from an image at 5° off nose-on and the feature positions obtained from a diagram of the aircraft. Range resolution is 0.30 m, and crossrange resolution is 1 m. The important part of the match is the match in range, because for low crossrange resolution we weight the match more heavily in range than in crossrange.

Figure 4 gives the analogous positional match for an aspect angle of 45°, which is 40° larger than in Figure 3. Crossrange resolution is somewhat worse at 1.35 m. The feature database is the same as for the small aspect angle, except that we have added one feature which would be visible only at a large
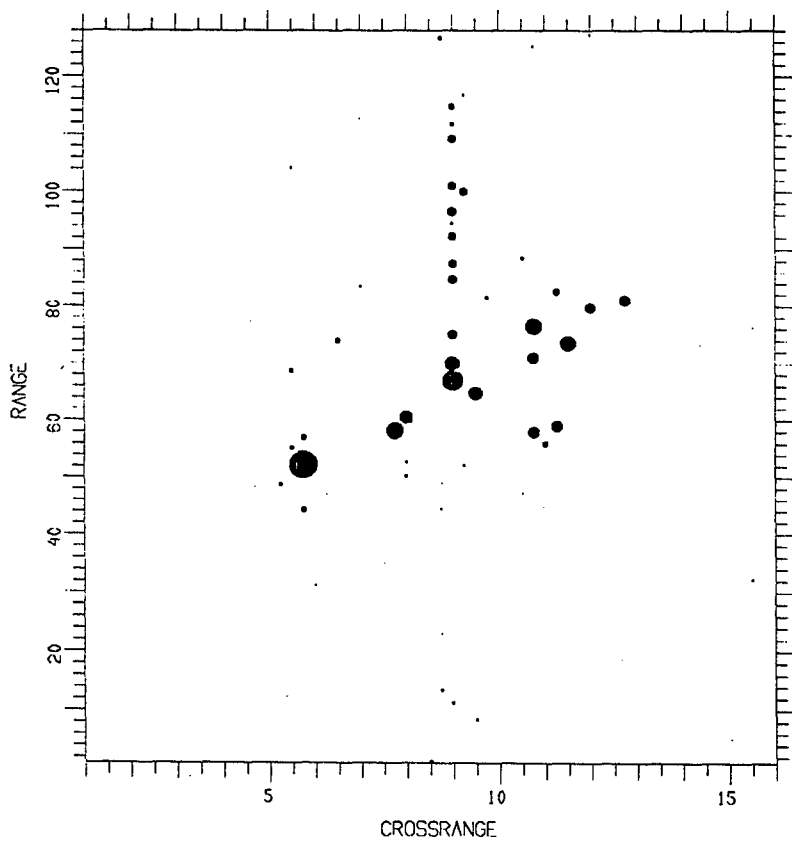
Figure 1. ISAR Image of an Aircraft in Peaks Plot Form.
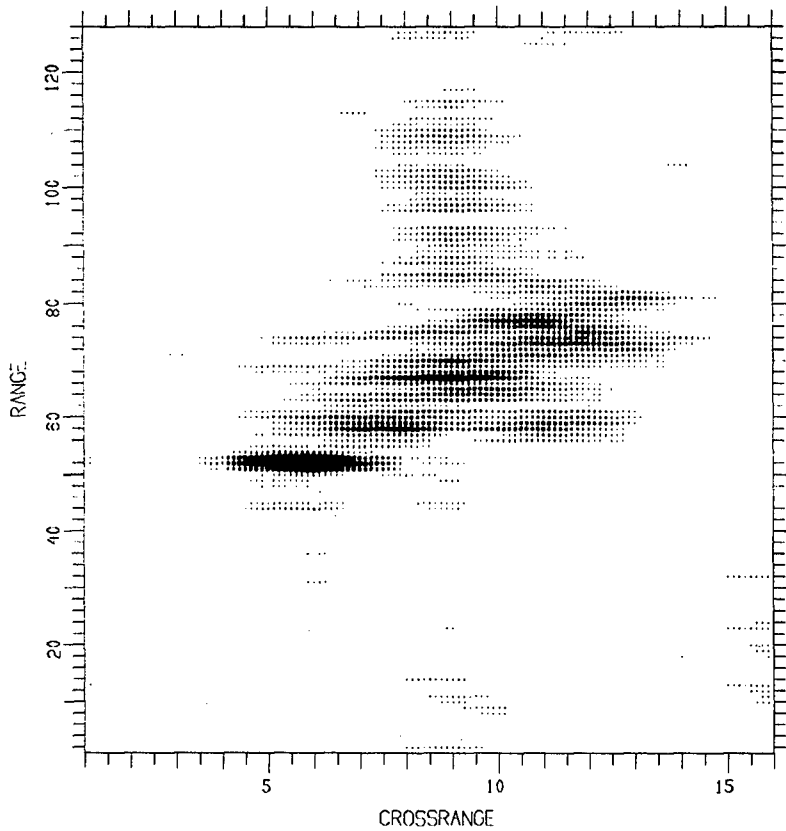
Figure 2. ISAR Image of the Aircraft.

RANGE

CROSSRANGE

G +

H

p

+ k

d l

O

O

+ c

B

+ M

+ E

V+

K +

l+

Asp Ang   4.86

Bank Ang 0.00

Pitch Ang 0.00

C Res   0.96

Roll Shr 0.00
Flex Shr 0.00
Pitch Shr 0.00

a Radar
c tacon
d Vhf(am/fm)
G ECM/RWR
k antenna
l instr panel
M Start Seat 2
p tailfin rootsep
V Intake
O Refuel Opening
O Refuel Opening
K Intake Plate
h ecm/rwr
B End Cockpit
E Instr Panel Dis
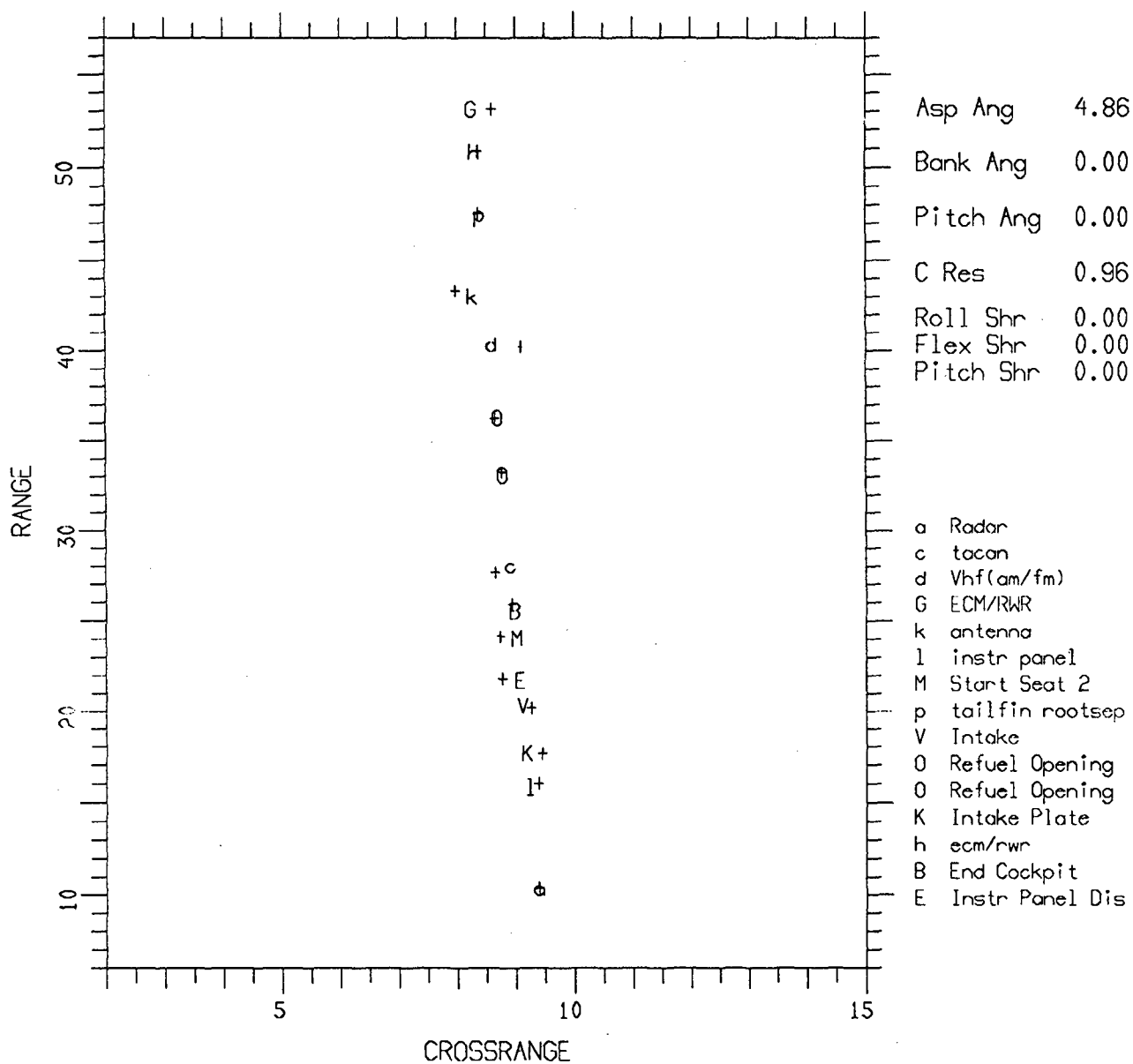
Figure 3. Feature Position Match for an Aspect
Angle of 5° off Nose-on.
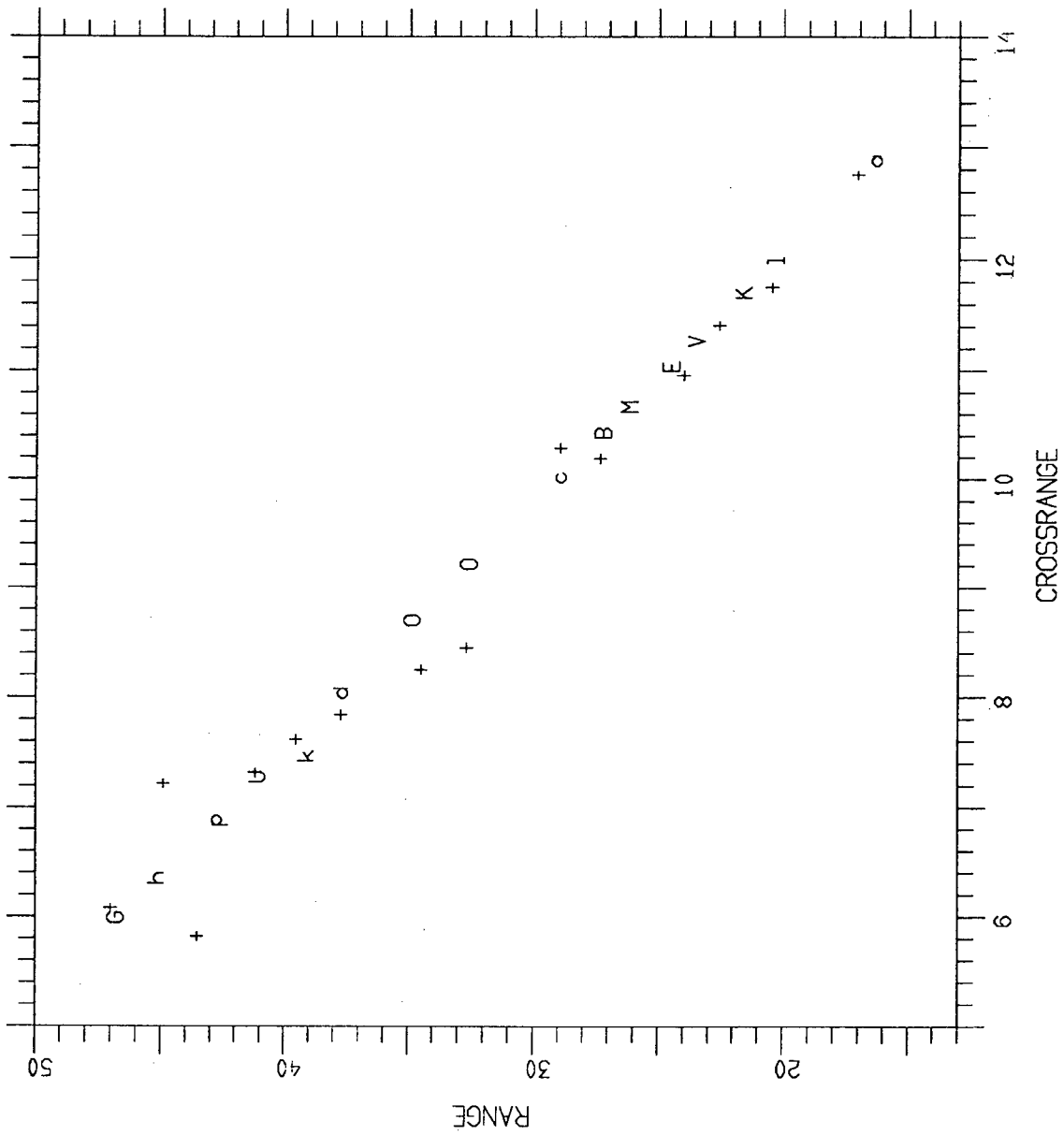
Figure 4. Match of Positions Measured at 45° Aspect
Angle with Database from 5° Aspect Angle.

aspect angle. Examination of Figure 4 shows that Features E and M are missing in the new image, and Features K and p are shifted along the fuselage. At a much larger angle, in particular if crossrange resolution is worse rather than better, we would expect one or the other response to disappear. For some scatterers we would also expect some changes in positions over such a large change in aspect angle. With some experience, they should be predictable. Nevertheless, it is remarkable how little has changed despite an aspect angle increase by 40°.

5. HOW MUCH CROSSRANGE RESOLUTION IS NEEDED

When we consider the need for crossrange resolution, we must keep in mind that the objective is to measure scatterer positions rather than to determine the shape of the aircraft. Here we must distinguish between measurement accuracy and resolution. Resolution refers to the width of a response, whereas measurement accuracy refers to how well the position of the response peak can be defined. Depending on the background interference, measurement accuracy for a resolved scatterer varies from less than 10% of the response width to perhaps 3%. Thus, even when crossrange resolution is, say, 2 m, we can measure the peak position to a few centimeters. Moreover, in the process of measuring the positions of interfering responses we can automatically estimate the interference level and thus estimate the measurement errors. The practical policy is to let the choice of crossrange resolution be governed by the need to resolve the delayed duct returns. In cases where there are no delayed duct returns, we can choose the crossrange resolution so that wing tip missiles do not interfere with measurements on the fuselage features.

6. THE NEED FOR ADAPTIVE PROCESSING

The crossrange resolution requirements will sometimes be governed by the need to suppress the delayed duct returns, and sometimes by the need to resolve the wing tips. This implies, also, that the required crossrange resolution depends on the aspect angle. Moreover, if an aircraft flies steadily and dwell time is available, it is easy to achieve high crossrange resolution if it is needed. On the other hand, if an aircraft is maneuvering it may not be possible to achieve a good enough motion compensation to allow measurement of the feature positions in an image formed from the entire dwell. Because of this large variability of conditions, the processing must be adaptive. The processor must measure the existing conditions (based on imaging) and choose the correct procedure.

7. THE NEED FOR UTILIZING THE COMPLEX IMAGE

It has been customary to treat radar images like photographs, that is, to utilize only the intensity image and discard the underlying phase. This is totally unacceptable in practice, for two reasons.

First, suppose that it is acceptable to model an aircraft by a set of point scatterers in fixed positions on the aircraft. Even in this idealized situation the use of the intensity image will degrade resolution performance by a factor of two. In practice, we cannot afford to degrade resolution to such a degree. We must utilize the complex image, intensity and phase, in order to realize the inherent resolution performance of radar.

Second, as already stated, the observable features in a radar image are corner-like features, cavities, electronic devices, and other devices that "trap" the radar signal. The phase centers of such features often shift with aspect angle or frequency, and the associated phase modulation will cause a spreading of responses and the generation of spurious responses which cannot be handled in an intensity image. It is the phase of the image that contains the information needed to deal with these effects.

8. PROCESSING ALGORITHMS BASED ON MATHEMATICAL TARGET MODELS

If a man-made target could be modeled by a set of point scatterers in fixed positions, one could write mathematical equations to be implemented as the processing algorithm. But an aircraft (or even worse, a ground vehicle) cannot be modeled in such a fashion. As a consequence, all algorithms based on the concept of a fixed point scatterer must fail in the sense that they cannot be the basis for an operational system with acceptable performance. To overcome this problem the complexity of the mathematical models has been increased to a considerable degree to attempt to account for a variety of effects. However, we have analyzed real data on countless targets under a variety of conditions, using the Complex-Image Analysis technology. Based on this experience, which goes back to the early 1980s, we claim that man-made targets of such complexity as aircraft and ground vehicles cannot be modeled mathematically with sufficient realism for identification. The approaches based on mathematical target models have not led to a workable operational system in the past 30 years, and we predict they will not lead to such a system in the next 30 years.

9. THE EXPERT SYSTEM APPROACH

If mathematical equations cannot be the basis of the processing, how can suitable processing algorithms be developed? The answer is that one has to study the characteristics of each response in the complex image, and determine whether the associated backscattering is from a stable phase center or from a shifting phase center. One must understand how to realize the inherent resolution capability of radar. One must learn how to deal with interference when the resolution is inadequate. One must learn to distinguish between the spreading of a response caused by interference between two scatterers and the phase center wander of a single scatterer. Real data pose a whole range of such problems, and one must gain the necessary knowledge and insight by analyzing a large variety of data.

After one has gained sufficient experience to be able to solve the problem at hand, the entire procedure must be automated. This will generally require a series of iterations until the automated system achieves the same performance as a trained analyst. By the definition of the term, one must develop an expert system. It is far more difficult, cumbersome, and time consuming than implementing mathematical equations in accordance with some target model, but for complicated man-made targets there is no alternative. Just as an expert never reaches the point where he knows everything, such an expert system is never likely to completely solve a complicated practical problem. However, the development of the system is deemed to be finished when the performance is acceptable.

10. AUTOMATION RESULTS

We have been handicapped by not having problem-free aircraft data, and this makes it difficult to perfect a method. We have recently been able to realistically test our manual algorithms by using turntable data with ground truth. As illustrated by Figures 3 and 4, these algorithms work rather well.

The turntable data also permit us to meaningfully test the automated algorithms, and improve them if needed. We have not finished this task as of the time this paper was written. Nevertheless, the results obtained so far are satisfactory, although they will be further improved. In Figure 5 we show a comparison of the feature measurement performed on turntable data manually and with automated algorithms. The Xs designate the scatterer positions derived with manual processing, and the Os give the positions obtained with fully automated processing. The automated processing missed several scatterers, but these are weak ones. Nevertheless, we have found in the past that the results from manual processing can be duplicated, and we expect to do this again. Slight differences in the measured positions do not matter, in particular in crossrange, because they will not prevent aircraft identification. In Figure 6 we show analogous results for flight test data. The automated processing missed four weak responses. Otherwise the agreement is excellent, with some less important crossrange differences.

11. THE PROBLEMS WITH FLIGHT TEST DATA

Since it is not possible to develop an aircraft identification system based on mathematical models of aircraft, we need flight test data. We have good data available for stationary and moving ground vehicles, and also for ships. No suitable data are available for aircraft. Every set of available data has serious problems. They range from the use of an unsuitable waveform that makes jet engine returns an unsolvable problem, to radars that work but have too low a bandwidth for small fighter aircraft, to radars that are too unstable, and to radars that operate at too low a carrier frequency. These problems are NATO-wide. Unless suitable data are collected, there will be no operational aircraft identification system.

12. CONCLUSIONS

Aircraft identification is a difficult problem, as is the identification of ground vehicles, ships, and other targets. In fact, all problems involving high resolution of man-made targets are difficult. In an operational sense, they cannot be solved with the conventional technology, because the phase of the processor output must be utilized and done so without any mathematical target models. We are confident that the approach discussed in this paper is the basis for an operational identification system, but finishing its development requires suitable data.

REFERENCE

1. Rihaczek, A. W., and S. J. Hershkowitz, *Radar Resolution and Complex-Image Analysis* (Artech House, 1996).
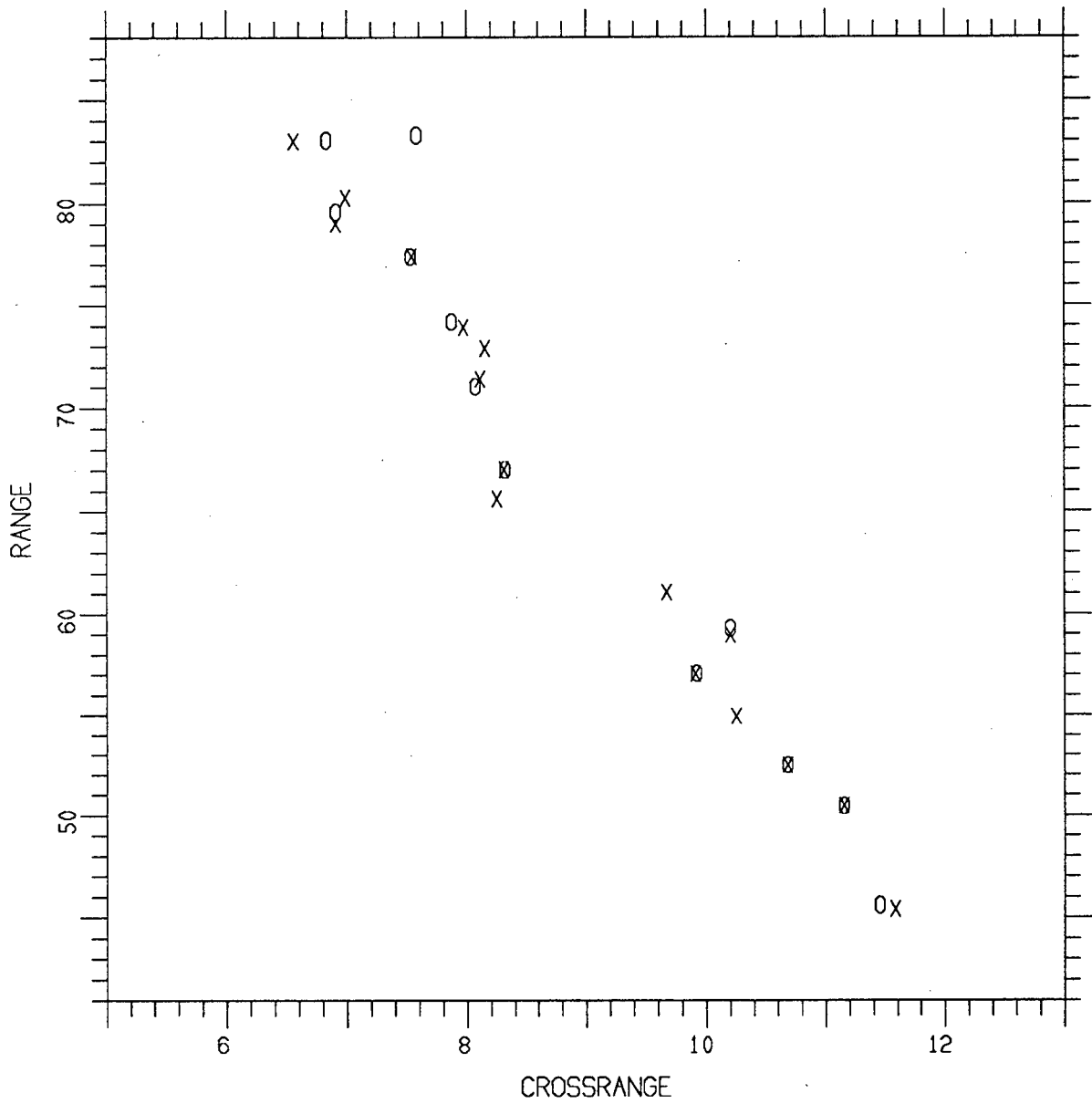
Figure 5. Comparison of Manual with Automated
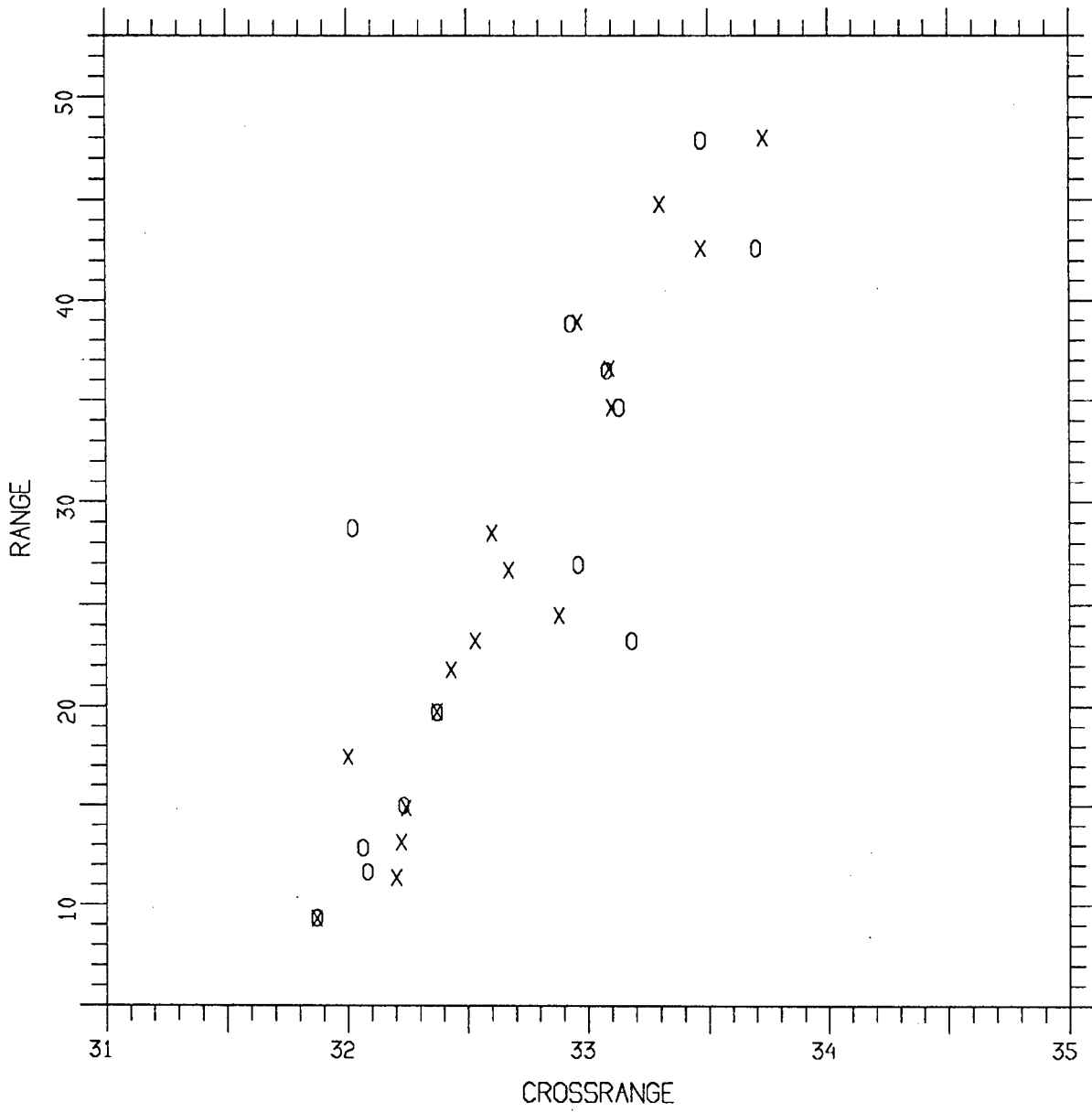Algorithms, Turntable Data.

Figure 6. Comparison of Manual with Automated
Processing, Flight Test Data.

Dispersive Scattering for Radar-Based Target Classification and Duct-Induced Image Artifact Mitigation

Brett Borden
Research and Technology Group
Naval Air Warfare Center Weapons Division
China Lake, CA 93555-6100
USA

Summary. The standard radar high-frequency weak-scatterer model is inappropriate to targets with inlets and cavities, and range-resolved images created under this model assumption often display artifacts associated with these structures. Since inlets and cavities (typically) make a strong contribution to the radar field scattered from aircraft targets, these artifacts often confound the image interpretation process and considerable effort has been spent in recent years to model, isolate, and remove these sources of error. Many of the more complete and accurate scattering models require extensive knowledge about the cavity/inlet shape and size and, moreover, are numerically intensive—features that make them unsuitable for many imaging applications. We examine an older (first order) model based on a weak-scattering modal expansion of the structure which appears to be well-suited to radar imaging. In addition, the analysis shows how cavity/inlet shape-specific information may be estimated from an ordinary radar image.

List of Symbols.

$\rho(x)$: target object function.

$E(k)$: radar scattered field (measured data).

ω: angular frequency of harmonic field component.

c: wave speed (free space).

$k = \omega/c$: wave number.

$W(x, x')$: spatially-varying point-spread function accounting for image artifacts (see equation (3)).

(k_1, k_2): wavenumber support of the data.

$S(x, k)$: strength of image artifact.

$\beta(x, k)$: phase off-set of image artifact.

S_m and β_m: strength and phase of waveguide mode expansion terms (see equation (4)).

x_{inlet}: location of the duct/cavity entrance.

$\omega_{c,m}$: cutoff frequency of m-th mode.

L: effective length of waveguide.

$\hat{\rho}(x)$: windowed Fourier estimate of ρ.

$\text{sinc}(x) \equiv x^{-1} \sin x$.

$\overline{k} \equiv (k_1 + k_2)/2$.

$\Delta k \equiv k_2 - k_1$.

$I_m(x)$: see equation (7).

$J_n(x)$: Bessel function of the first kind of order n.

$\overline{k}_{(1,c)} \equiv (\max\{k_1, k_{c,m}\} + k_2)/2$.

$\Delta k_{(1,c)} \equiv k_2 - \max\{k_1, k_{c,m}\}$.

$Y_n(x)$: Bessel function of the second kind of order n.

$K_n(x)$: modified Bessel function of order n.

$\mathcal{Y}_\nu\{f\}(\kappa) \equiv \int_0^\infty f(x)\sqrt{\kappa x}\, Y_\nu(\kappa x)\, dx$: $\mathcal{Y}_\nu$-transform of the function f.

$\mathcal{P}_n\{f\}$: see equation (12).

$\mathcal{F}\{f\}$: Fourier transform of f.

$\mathcal{H}_\nu\{f\}$: Struve transform of f, see equation (13).

$\mathbf{H}_\nu(x)$: Struve function of order ν.

$L^2(0, \infty)$: set of functions square-integrable over $\mathbb{R}^+$.

τ: threshold parameter used in truncation filter.

1. Introduction.

Radar imaging systems usually exploit the properties of a linear, non-dispersive model to recover an object function $\rho(x)$ from measured data $E(k)$ [1,2]—although it has been recognized that this so-called 'weak, point-scatterer' model is invalid for many practical scattering situations [3–5]. Despite this acknowledged limitation, the resulting analytical convenience of this traditional approach remains quite compelling and algorithm designers are loath to abandon it altogether. While there are many scattering situations that are well-approximated as non-interacting point subtargets, scattering bodies consisting of ducts or cavities can significantly deviate from the point-scatterer assumption. Typically, these re-entrant structures are dispersive in the sense that $\rho(x)$ has a strong dependence on the frequency of the interrogating radar signal. Reconstructing such a $\rho(x)$ under a non-dispersive assumption results in unwanted image artifacts which are sometimes difficult to associate with specific target features and which may obscure other (correctly modeled) image elements. Figure 1 is an example ISAR image displaying the kind of artifacts that are associated with re-entrant target structures.
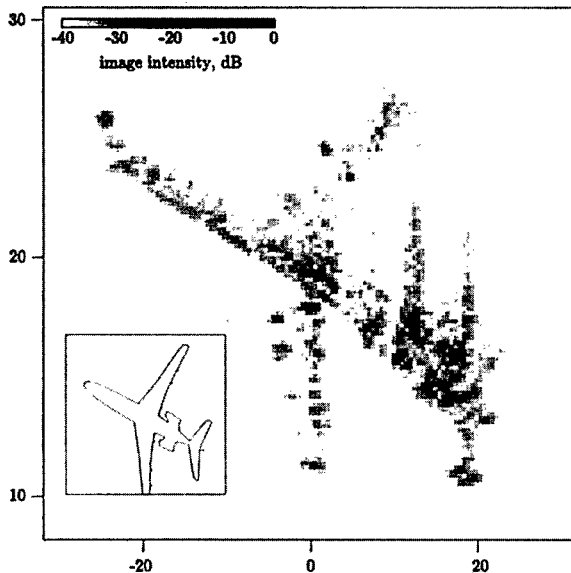
Figure 1 Example of duct dispersion in ISAR image.

Owing to the importance of ducts and cavities in airborne target image reconstruction—they often contribute the strongest part of the radar return—a significant effort has been made to accurately model and predict their scattering behavior. Much of this work has concentrated on accurately calculating the radar cross-section of known structures, and the devised methods are (typically) numerically intensive and require extensive a priori size and shape information [6-14]. Such direct scattering approaches are often inappropriate to the problem of identification of unknown targets because their complexity, which is required for predictive accuracy, makes them computationally unwieldy.

Below, we will examine an old and relatively simple model for duct and cavity scattering. We will demonstrate how this model leads to a very simple interpretation of the first-order properties of radar scattering from cavities and inlets while maintaining much of the complexity seen in actual radar data. We begin by establishing notation. Following this, we present the weak modal expansion model and its consequences to image interpretation. This model characterizes an inlet/cavity by a set of shape-dependent parameters and, in section 3, we present a simple method for extracting this information from complex radar images and filtering-out their effects. Our approach is related to recent dispersive-scatterer identification methods [15-17] but is easily extended to target parameter identification and (may) prove useful in target recognition problems.

2. A Modified Scattering Model. In a monostatic scattering situation (in which the transmitter and receiver are co-located) it can be shown [1,2] that the weak scatterer far-field response $E(k)$ due to an harmonic excitation of a target can be written:

$$E(k) \approx \int_{\mathbb{R}^2} \rho(x') \ e^{i2kx'} \ dx' . \tag{1}$$

This is a linear superposition of waves radiating from locations in the support of the target with local scatterer strength proportional to $\rho(x)$. The incident interrogating wave has: angular frequency ω; speed c; wave number $k = \omega/c$; and the factor of 2 accounts for the 2-way travel distance from the radar to the target and back again.

Equation (1) is basically a Fourier transform relationship between the target object function ρ and the measured data E. Because of this, frequency domain filtering is a sometimes suggested approach to eliminating cavity- and duct-dispersion artifacts. The idea is simple to understand: in the image domain, 'ordinary' scattering centers behave as point targets while dispersive scatterers display a distributed structure. Consequently, in the *Fourier transform domain* the point-like scatterers will be distributed while the dispersion artifacts will be localized. Filtering the peaks out of the transform domain data, followed by inverse transformation, should (in principle) mitigate duct dispersion image artifacts.

While this Fourier domain filtering approach is sometimes successful, there are many situations for which it fails—typically, by removing legitimate (i.e., non-dispersive) target structures from the filtered image. To help understand this, we will use a more 'complete' target model which retains much of the 'fixed, point-scatterer' nature of ρ. This is accomplished by fixing an effective phase-center to a single location on the target and describing the variations in ρ by including a dispersive phase term in the radar signal. In this way, any position shifts β are accounted for by a general dispersion relation. With this modification, equation (1) can be written

$$E(k) \approx \int_{\mathbb{R}^2} \rho(x') \ W(x', x'')$$
$$\times \ e^{-i2kx'} \ dx' \ dx'' , \tag{2}$$

where

$$W(x', x'') = \int_{k_1}^{k_2} S(x', k') \ e^{i(2k'x' - 2\beta(x', k'))}$$
$$\times \ e^{i2k'(x'' - x')} \ dk' , \tag{3}$$

$S(x', k') \leq 1$ accounts for varying strength and the interval (k_1, k_2) represents the data (bandwidth) limits. Equations (2) and (3) demonstrate how the effects of

complex scattering centers can be interpreted as being due to a spatially varying point-spread function $W(x, x')$ acting on an object function consisting of weak, isotropic, and frequency-*independent* scatterers fixed at effective phase-center locations on the target.

If we treat a target duct or cavity as a waveguide, then the point-spread function (3) associated with terminated waveguides of effective length L, with entrance located at x_{inlet} (which we shall take as the phase center associated with this structure), can be expressed in a modal expansion by:

$$S(x, k) \, e^{i(2kx - 2\beta(x,k))} \rightarrow$$
$$\frac{1}{k} \sum_{m=1}^{M} S_m(k) \, e^{i(2kx - 2\beta_m(x,k))}. \quad (4)$$

The phase term β_m depends upon the so-called 'cutoff' frequencies $\omega_{c,m} = c \, k_{c,m}$ which are labeled by the mode indices m [18]. The cutoff frequencies also allow us to limit the terms in the modal sum to $M = \max\{m | k_{c,m} \leq k_2\}$. The weak-scatterer approximation yields

$$2\beta_m(x, k) = \begin{cases} 2kx + 2L\sqrt{k^2 - k_{c,m}^2}, & \text{if } x = x_{inlet}; \\ 2kx, & \text{otherwise.} \end{cases} \quad (5)$$

(This approximation neglects multiple scattering between the open and closed ends of the waveguide but is otherwise known to be quite good [9].) If we assume that S_m is a slowly varying function of k (in comparison to the phase term) then applying this result and 'inverting' (2) yields

$$\hat{\rho}(x) \approx \int_{\mathbb{R}^2} dx' \, \rho(x')$$
$$\times \begin{cases} \left[\sum_{m=1}^{M} S_m \int_{k_1}^{k_2} k^{-1} \, e^{i2kx} \right. \\ \qquad \left. \times \, e^{-i2L\sqrt{k^2 - k_{c,m}^2}} \, dk \right], & \text{if } x' = x_{inlet}; \quad (6) \\ \left[\text{sinc}(\Delta k(x - x')) \right. \\ \qquad \left. \times \, e^{i2\overline{k}(x-x')} \right], & \text{otherwise} \end{cases}$$

where $\overline{k} = (k_1 + k_2)/2$ and $\Delta k = k_2 - k_1$.

The image $\hat{\rho}(x)$ can be understood in terms of the object $\rho(x)$ by examining the integral

$$I_m(x) = \int_{k_1}^{k_2} k^{-1} \, e^{-i2L\sqrt{k^2 - k_{c,m}^2}} \, e^{i2kx} \, dk. \quad (7)$$

If we substitute [19]

$$e^{-i2L\sqrt{k^2 - k_{c,m}^2}} = 2i\sqrt{k^2 - k_{c,m}^2}$$
$$\times \int_{L}^{\infty} J_0\left(2k_{c,m}\sqrt{x''^2 - L^2}\right) \, e^{-i2kx''} \, dx'', \quad (8)$$

where $J_0(\xi)$ is the Bessel function of the first kind, then we can write

$$I_m(x) = 2i \int_{L}^{\infty} dx'' \, J_0\left(2k_{c,m}\sqrt{x''^2 - L^2}\right)$$
$$\times \int_{\max(k_1, k_{c,m})}^{k_2} dk \sqrt{1 - (k_{c,m}/k)^2} \, e^{i2k(x-x'')}. \quad (9)$$

Equation (9) is somewhat easier to interpret than (7): $I_m(x)$ is a convolution of $J_0(2k_{c,m}\sqrt{x^2 - L^2})$ and $\int_{\max(k_1, k_{c,m})}^{k_2} \sqrt{1 - (k_{c,m}/k)^2} \, e^{i2kx} \, dk$. If we use the approximation

$$\int_{\max(k_1, k_{c,m})}^{k_2} \sqrt{1 - (k_{c,m}/k)^2} \, e^{i2k(x-x'')} \, dk \approx$$
$$\alpha \, \Delta k_{(1,c)} \, \text{sinc}(\Delta k_{(1,c)}(x - x'')) \, e^{i2\overline{k}_{(1,c)}(x-x'')}, \quad (10)$$

where $\overline{k}_{(1,c)} = (\max(k_1, k_{c,m}) + k_2)/2$ and $\Delta k_{(1,c)} = k_2 - \max(k_1, k_{c,m})$, then it is easy to see that the down-range effects of the inlet will appear as the function $J_0(x)$, shifted according to $x \to \sqrt{x^2 - L^2}$, dilated by $x \to 2k_{c,m}x$, and 'blurred' by the function $\text{sinc}(\Delta k_{(1,c)}x)$.

The approximation (10) is discussed in [20, 21] where it is shown that when $k_{c,m} \ll k_1$ the approximation is very good. When $k_{c,m} \sim k_1$, the general effect is to scale the $\text{sinc}(\Delta k_{(1,c)}x)$ function by a factor $\alpha < 1$ while closely retaining its general shape. Since $k_{c,m}$ typically increases with increasing m, this means that higher modes will contribute proportionally less to the image $\hat{\rho}(x)$ and that modes for which $k_{c,m} \geq k_1$ will be reduced by $\alpha \approx .5$. In addition, the scale factor $\Delta k_{(1,c)} = k_2 - \max(k_1, k_{c,m})$ means that when $k_{c,m} > k_1$ the $\text{sinc}(\Delta k_{(1,c)}x)$ blurring function will cause the associated image elements to be less sharply defined.

3. Modified Frequency-Domain Filtering.
The results of equations (9) and (10) imply that we should treat the model parameters L and $\{k_{c,m}\}$ within the context of the Bessel function approximation. Moreover, this model demonstrates why Fourier domain filtering will not be generally correct: the form of the argument of $J_0(2k_{c,m}\sqrt{x^2 - L^2})$ means that the frequency components will be blurred and shifted under Fourier transformation. While it is possible to correct for this analytically, such a procedure would introduce distortion in the non-dispersive scattering elements. An alternate approach rejects the Fourier

transform in favor of the $\mathcal{Y}_\nu$-transform which can be employed to show that [19]

$$- 2\kappa \int_L^\infty J_0 \left(2k_{c,m}\sqrt{x^2 - L^2} \right) x^n Y_{-1}\left(2\kappa x \right) \, dx$$

$$= \begin{cases} -\frac{2}{\pi} K_0 \left(2L\sqrt{k_{c,m}^2 - \kappa^2} \right) & \text{if } k_{c,m} > \kappa, \\ (-1)^n Y_0 \left(2L\sqrt{\kappa^2 - k_{c,m}^2} \right) & \text{if } \kappa > k_{c,m}, \end{cases}$$

$$(11)$$

where $Y_\nu(\xi)$ is the Bessel function of the second kind (of order ν), $K_0(\xi)$ is the modified Bessel function of order 0, and $n = 0, 1, \ldots, \infty$. Since $K_0(\xi)$ and $-Y_0(\xi)$ both rise sharply to ∞ as $\xi \to 0$, this result suggests a method for isolating the parameters $k_{c,m}$ from the image $\hat{\rho}(x) \sim s_L(x) J_0(2k_{c,m}\sqrt{x^2 - L^2})$ where $s_L(x)$ denotes the unit step at $x = L$.

Define the transformation

$$\mathcal{P}_n\{\rho\}(\kappa) = \pi\kappa \int_0^\infty \hat{\rho}(x) \, x^n \, Y_{-1}(2\kappa x) \, dx, \qquad (12)$$

for $\kappa > 0$. Then it is easy to see from equations (6–11) that $\mathcal{P}_n(\kappa)$ will be sharply peaked when $\kappa = k_{c,m}$, $k_1 \leq \kappa \leq k_2$. (Conveniently, the $\mathcal{P}_n$-transform of a point scatterer will have strength proportional to $Y_{-1}(2\kappa x)$ which, for large radar frequencies, will generally be very small in comparison to $|Y_0(\epsilon)|$ and $|K_0(\epsilon)|$ for ϵ small.)

Figure 2 compares and contrasts the $\mathcal{P}_0$-transform with the Fourier transform. These data are time-domain range profile measurements of the B272 used to create the ISAR image displayed in figure 1. Note that while there is a rough correspondence between the Fourier domain and the $\mathcal{P}_0$ representation, there is not a one-to-one mapping and identical filters applied to each will generally be expected to lead to different results.

The *reciprocal* transform to (12) is not quite as well defined. It can be shown [22], however, that

$$\mathcal{H}_\nu\{f\}(x) = \int_0^\infty f(\kappa) \, \mathbf{H}_\nu(x\kappa) \, (x\kappa)^{1/2} \, d\kappa, \qquad (13)$$

where $\mathbf{H}_\nu(x)$ is the Struve function, obeys $\mathcal{H}_\nu \mathcal{Y}_\nu = \mathcal{Y}_\nu \mathcal{H}_\nu = \mathcal{I}$ for functions in $L^2(0, \infty)$ when $-1 < \nu < 0$.

4. Some Experimental Results.

The simplest illustration is based on anechoic chamber measurements of a truncated waveguide. We launched a (stepped-frequency) pulse at the open end of a terminated 103 cm length of $WR284$ rectangular waveguide.
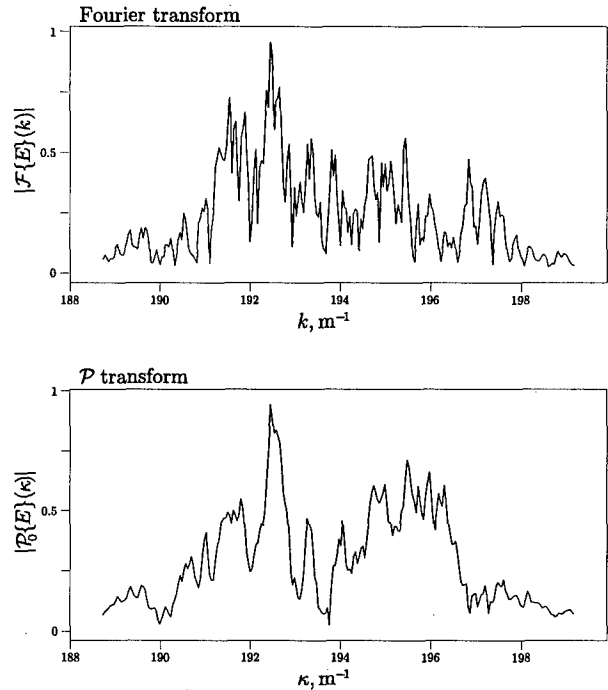
Figure 2 Comparison between Fourier and $\mathcal{P}_0$ domain representations of a measured range profile (from the data used in figure 1). The imperfect match between these two representations means that filtering will affect the final (artifact-mitigated) image in different ways.

Figure 3 shows the scattered return from the waveguide when the frequency band was 12.16–13.26 GHz and aspect angle $\theta \approx \pi/6$. Plotted is the magnitude of the Fourier transform of the scattered field data (in dBsm with range increasing to the right). The duct-related artifacts can be seen extending for many multiples of the length of the target. For test purposes we introduced an additional artificial signal into the measured data. This signal was generated (in the frequency domain) by simply adding the complex array generated by $0.02 \exp(i2k_j * 10)$ and corresponds to a point scatterer located at $x = 10$ m with strength less than that of the duct artifacts (so that it cannot be seen in figure 3).
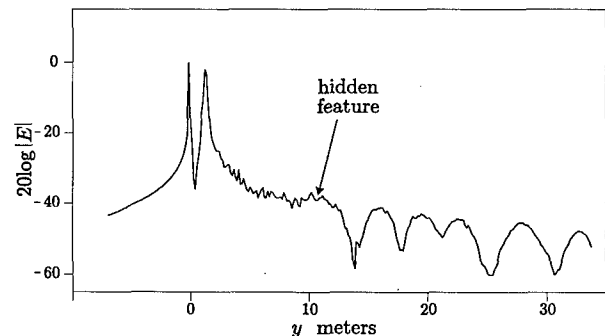
Figure 3 Intensity of the field scattered from an open ended waveguide terminated after 103 cm.

The image artifacts in figure 3 are to be reduced by filtering in the $\mathcal{P}_n$-transform domain. As part of our initial investigation, we applied a simple truncation filter: $\{\mathcal{P}_n(\kappa) : |\mathcal{P}_n(\kappa)| > \tau\} \to 0$ where τ is a user defined threshold. Figure 4 is the 'cleaned' reconstruction formed by inverting the filtered results with $\tau = .3 \times \max\{|\mathcal{P}_2|\}_\kappa$. Note that the point scatterer at $x = 10\,\text{m}$ is now clearly visible and that the duct-related artifacts have indeed been reduced.
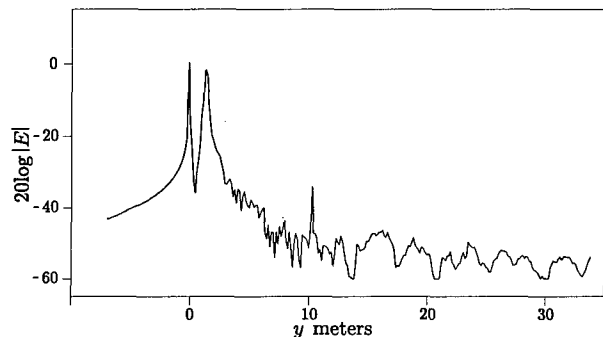
Figure 4 'Cleaned' image corresponding to figure 3. To remove the dispersion-induced artifacts, the filter $\{\mathcal{P}_n(\kappa) : |\mathcal{P}_n(\kappa)| > .3 \times \max\{|\mathcal{P}_2|\}_\kappa\} \to 0$ was applied in the $\mathcal{P}_2$ domain and the result was inverted using the Struve transform.

A more tantalizing example is based on the ISAR image of figure 1. Applying the truncation filter (with $\tau = .4 \times \max\{|\mathcal{P}_2(\kappa)|\}_\kappa$) to the $\mathcal{P}_2$-transform of each of the down-range cuts in the right half of figure 1, and inverting results in the filtered image shown in figure 5.
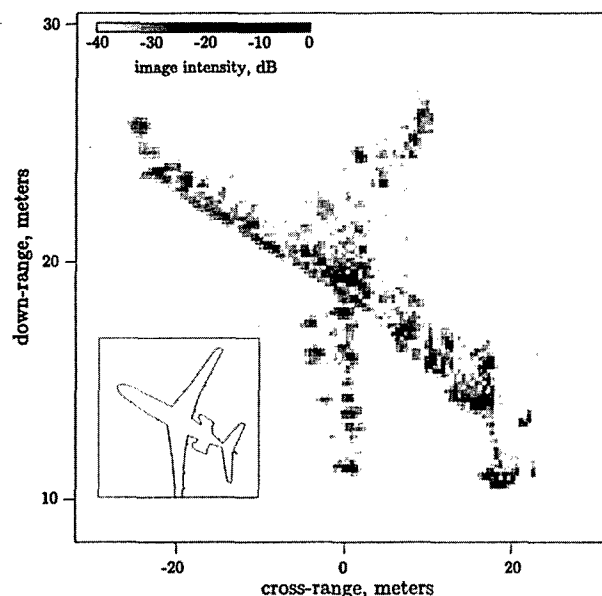
Figure 5 'Cleaned' version of figure 1.

For comparison purposes, the data of figure 1 were also filtered using Fourier domain methods. The ac-

tual filter applied was identical to that applied in the $\mathcal{P}_2$ transform domain used to generate figure 5. Note the significant differences in the resultant 'cleaned' images of figures 5 and 6. (Of course, this choice of filter is almost certainly not optimal to both transform domains and was chosen to illustrate the different results.)
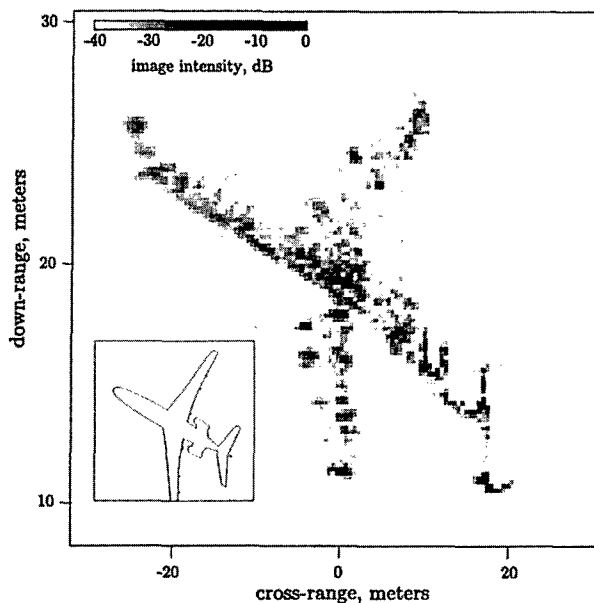
Figure 6 Fourier-based 'clean' version of figure 1.

The example of figure 5 is intended to demonstrate the applicability of this $\mathcal{P}_n$-transform based filtering technique to ISAR images. Moreover, the example of figure 3 shows that the filtering method can be applied to HRR range profiles—at least when the target is very simple. Range profiles of more complex targets cannot be expected to display such promising results, however, because the images are comprised of cross-range integrated target components. (So that the HRR image may consist of multiple ducts and cavities that will all be 'lumped together' and it may be difficult to select a phase center (origin) for the calculation of equation (12).) Nevertheless, when the target contains only one significant dispersive feature, the method may be appropriate. Figure 7 shows the (modest) 'improvement' that can occur in HRR profiles of aircraft targets. (Note, however, that without a clear baseline against which to compare this result, the actual improvement may be illusory.)

5. Discussion and Conclusion. The reader should be cautioned against drawing too optimistic of conclusions from the results of figure 5 and a truly convincing test of the algorithm would be one which reduces artifacts while leaving underlying target images elements unaltered. For such a test to be performed, of

course, such underlying image elements must be independently established—as was done in the example of figures 3 and 4.

Because of the one-sided nature of the $\mathcal{P}_n$-transform (equation (12)), origin placement is important. Our choice in all of these examples has been to place this origin at the 'mouth' of the re-entrant structure. This choice presupposes that x_{inlet} can be determined from the unmitigated image and this may not always be possible. To a lesser extent, accurate representation of the portion the object function in the region near the mouth requires that the effective length L of the dispersive structure also be estimated but, in practice, the algorithm has not shown great sensitivity to variations in this estimate. (Possible methods for estimating both the origin and L are discussed in [21].)
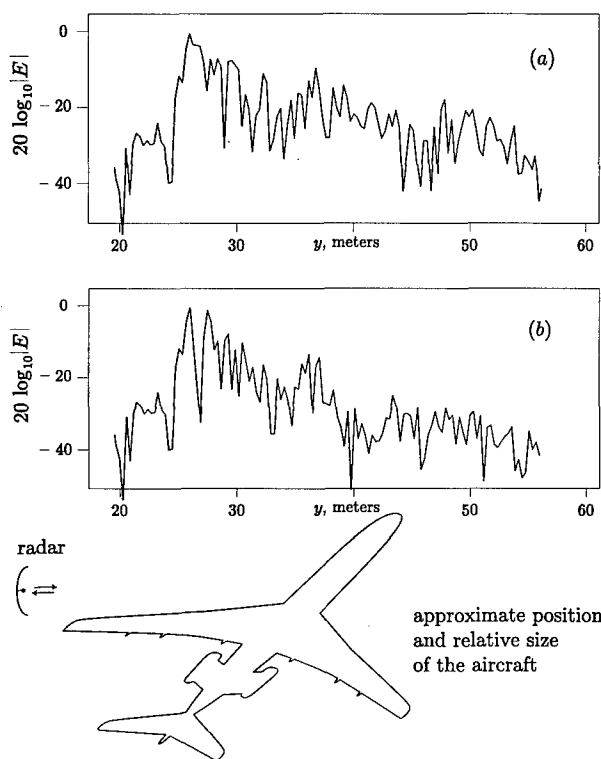
Figure 7 'Usual' (a) and 'cleaned' (b) versions of HRR profiles of a B727 aircraft target. Figure 7(b) was formed by applying the truncation filter (with $\tau = .4 \times \max\{|\mathcal{P}_2(\kappa)|\}_\kappa$) to the $\mathcal{P}_2$-transform of figure 7(a) and inverting the result.

In addition to artifact mitigation, the question naturally arises: is it possible to use the estimated 'spectrum' $\{k_{c,m}\}$, determined by the $\mathcal{P}_n$-transform, to classify targets by their characteristic ducts and cavities? A possible advantage to this approach lies in the observation that the scattered field returned from re-entrant structures is often quite strong (and may dominate the overall field scattered from the entire target). Moreover, unlike artifact mitigation, this

kind of spectral estimation does not require estimation of x_{inlet} or L. The down-side is that the mode strength S_m associated with the $k_{c,m}$ depends on target aspect [18] and so the spectral peak strength (as opposed to spectral peak position) can significantly affect correlation-based library search schemes. This idea is a current area of research.

References.

[1]   B. Borden, 'Problems in airborne radar target recognition,' *Inverse Problems*, **10**, 1009, 1994

[2]   B. Borden, 'Some issues in inverse synthetic aperture radar image reconstruction,' *Inverse Problems*, **13**, 571, 1997

[3]   A. Jain and I. Patel, 'Simulations of ISAR image errors,' *IEEE Trans. on Instrumentation and Meas.*, **39**, 212, 1990

[4]   G. Dural and D.L. Moffatt, 'ISAR Imaging to identify basic scattering mechanisms,' *IEEE Trans. on Antennas and Prop.*, **42**, 99, 1994

[5]   A.W. Rihaczek and S.J. Hershkowitz, *Radar Resolution and Complex-Image Analysis*, (Dedham MA: Artech), 1996

[6]   H.R. Witt and E.L. Price, 'Scattering from hollow conducting cylinders,' *Proc. Inst. Elec. Eng.*, **115**, 94, 1968

[7]   J.W. Moll and R.G. Seecamp, 'Calculation of radar reflecting properties of jet engine intakes using a waveguide model,' *IEEE Trans. on Aerospace and Elect. Syst.*, **6**(5), 675, 1969

[8]   T.W. Johnson and D.L. Moffatt, 'Electromagnetic scattering by open circular waveguides,' *Radio Science*, **17**(6), 1547, 1982

[9]   C-C. Huang, 'Simple formula for the RCS of a finite hollow circular cylinder,' *Electronics Letters*, **19**, 854, 1983

[10]   H. Ling, R-C. Chou, and S.W. Lee, 'Shooting and bouncing rays: calculating the RCS of an arbitrary cavity,' *IEEE Trans. on Antennas and Prop.*, **37**, 194, 1989

[11]   T.M. Wang and H. Ling, 'Electromagnetic scattering from three-dimensional cavities via a connection scheme,' *IEEE Trans. on Antennas and Prop.*, **39**, 1501, 1991

[12]   P.H. Pathak and R.J. Burkholder, 'High-frequency electromagnetic scattering by open-ended waveguide cavities,' *Radio Science*, **26**(1), 211, 1991

[13]   D.C. Ross, J.L. Volakis, and T.A. Hristos, 'Hybrid finite element analysis of jet engine inlet scattering,' *IEEE Trans. on Antennas and Prop.*, **43**(3), 277, 1995

[14]   J.L. Karty and J.M. Roedder, 'Application of modal and plane wave expansions to modeling large jet engine cavities,' *Applied Computational Electromagnetics Conference Proceedings: March 1995*, 1103, 1995

[15]   A. Moghaddar and E.K. Walton, 'Time-frequency distribution analysis of scattering from waveguides,' *IEEE Trans. on Antennas and Prop.*, **41**, 677, 1993

[16]   L. Carin, L.B. Felsen, D. Kralj, S.U. Pillai, and W.C. Lee, 'Dispersive modes in the time domain: analysis and time-frequency representation,' *IEEE Microwave Guided Wave Letters*, **4**, 23, 1994

[17]   L.C. Trintinalia and H. Ling, 'Joint time-frequency ISAR using adaptive processing,' *IEEE Trans. on Antennas and Prop.*, **45**, 221, 1997

[18]   J.A. Stratton, *Electromagnetic Theory*, (New York: McGraw-Hill), 1941

[19]   A. Erdélyi, W. Magnus, F. Oberhettinger, and F.G. Tri-

comi, *Tables of integral transforms* volume II (New York: McGraw-Hill), 1954

[20] B. Borden, 'Reduction of ISAR image artifacts caused by re-entrant structures,' SPIE Proc., Radar Processing, Technology, and Applications II, Vol. 3161, 31 July–1 August, San Diego, 9–19, 1997

[21] B. Borden, 'An observation about radar imaging of re-entrant structures with implications for automatic target recognition,' *Inverse Problems* **13**, 1441, 1997

[22] P.G. Rooney, 'On the $\mathcal{Y}_\nu$ and $\mathcal{H}_\nu$ transformations,' *Can. J. Math.*, **32**(5), 1021, 1980

Performance of a Target Identification Algorithm as a Function of the Discriminant Post-Processing Techniques Utilized

M. N. Cohen and V. B. Sylvester

Georgia Tech Research Institute

7220 Richardson Road, Smyrna, Georgia 30080 USA

SUMMARY[1]

A target identification algorithm can be thought of as being comprised of a pre-processor, discriminant generator, and a post-processor. The pre-processor forms and otherwise conditions the target signatures. The discriminant generator forms scalar quantities that represent the closeness-of-fit of each signature to the target classes of interest. Finally, the post-processor utilizes those scalars to form a decision as to the target that the signature came from; i.e., the identity of the target being examined.

In this paper, we start with a full set of discriminants generated by a particular pre-processor and discriminant generator operating on high-range-resolution (HRR) signatures of aircraft, and we perform various experiments to determine the effect on algorithm performance of applying various post-processing techniques. The overall target identification algorithm is described, numerous post-processing techniques are introduced, and their effects on performance are tabulated. It is shown that optimal combined performance of these techniques does not necessarily follow from combining the individual best-performing techniques. That is, an optimal post-processing architecture cannot be derived from a simple search of the diagonal of the multi-dimensional set of post-processing options.

Keywords: Target Identification, Performance Evaluation, Quadratic Classifier, Discriminant Post-Processing, Radar, High Range Resolution

1. INTRODUCTION AND OVERVIEW

Target ID algorithms may be viewed as being comprised of three parts: the pre-processor, the discriminant generator, and the post-processor. The pre-processor forms and otherwise conditions signatures in preparation for discriminant generation in the on-line algorithm, and includes the process of template (or exemplar or model) formation in the training phase of the algorithm development effort. The discriminant generator is an on-line engine that utilizes each incoming signature, stored template (or exemplar or model), and a computation rule to generate scalar quantities (the discriminants) that represent the goodness-of-fit of the signature to the algorithm's stored information. The post-processor is a decision/declaration rule that utilizes the output discriminants to generate the overall algorithm's determination of the ID of the subject target and how that ID should be reported.

A number of different techniques for post-processing the discriminants from a template-based quadratic classifier as applied to measured high-range-resolution (HRR) profiles of air targets have been evaluated in an effort to improve upon the target identification (ID) algorithm's overall ID performance. The ID performance measures that are obtained by applying the techniques described in this document are given relative to the performance of the algorithm when it utilizes a particular 'baseline' post-processing technique.

This document has several sections. The background section, Section 2, generally describes : feature vectors, templates, objective ID performance metrics, and the computation of a quadratic metric. Section 3 describes the baseline algorithm as well as the test feature vectors and the templates that were utilized throughout, and Section 4 begins the analyses by describing and discussing two options available for restricting the utilization of discriminants to only those that come from specific template-related subsets. Section Five continues the discussion of the analyses by describing specific post-processing methods employed with the specified subsets of discriminants that we actually exercised and the ID performance derived from them individually and in Section 6 we introduce the option of utilizing different decision thresholds for each target class and illustrate the ID performance that can be obtained by combining a number of the discussed post-processing techniques in a single post-processing architecture. Finally, in Section 7, the results are summarized and conclusions are formed.

2. BACKGROUND

2.1. Feature vectors

The feature vectors utilized in these experiments are simply vectorizations of radar HRR profiles of air targets.

where the vectors are indexed by range bin number. As we do not attempt 'feature extraction' in the statistical pattern recognition sense, but rather utilize the entire signature as the target representation, for the purposes of this paper, feature vector, signature, and HRR profile are used interchangeably.

2.2. Templates

A template is a statistical representation of a number of feature vectors. It has two parts: the mean of the feature vectors and the standard deviation of the feature vectors. The amplitude for a particular feature component of the mean portion of the template is formed by averaging the values of each feature vector at the feature component. The amplitude for a particular feature component of the standard deviation portion of the template is similarly calculated.

Radar feature vectors can be highly dependent on the orientation of the target (or pose) with respect to the sensor. Therefore, the feature vectors that are used to form a template normally come from an appropriately sized angular sector around a specific target pose. This is called the pose sector corresponding to the template.

2.3 The quadratic metric

The quadratic metric, as used here, is a distance metric that is used as a measure of the distance between a feature vector and a template. If a feature vector is represented by the vector s_i and the mean and standard deviation portions of the template are represented by the vectors μ_i and σ_i, respectively, where i is an index to the feature components and where there are K feature components, then the quadratic metric between the feature vector and template is given by the discriminant

$$D = \sum_{i=1}^{k} \frac{(s_i - \mu_i)^2}{\sigma_i^2} + 2.0 \ell n(\sigma_i) \qquad (1)$$

2.4. One-look decisions and decision thresholds

For the tests reported in this paper the declared identity of a target is based on applying the quadratic metric to a number of feature vectors from the target. For the "baseline" algorithm, the algorithm against which all innovations are compared, an internal decision is made each time a feature vector is processed by the algorithm. After a specified number of internal decisions are made, they are processed to form a declaration. Declarations, also referred to as external decisions, are reported to the user of the ID algorithm.

The classifier will normally utilize one template for each target of interest at each pose sector of interest. Processing a feature vector entails comparing it to all or to some subset of the templates used by the classifier,

depending on the accuracy with which the radar can estimate target pose angle. A comparison is simply the application of the quadratic metric to a feature vector and a template resulting in a single discriminant.

After a comparison, the algorithm generally will make an internal decision as to the target type (or class) associated with the best discriminant. The "best" discriminant is the one that is closest to $-\infty$. The best discriminant is then compared to a decision threshold. There may be a single decision threshold that is utilized independent of the target class selected -- the single-threshold configuration -- or there may be a threshold chosen for each possible target class -- the multiple threshold algorithm configuration. In either case, if the discriminant is less than the subject threshold, then the feature vector will be associated with the identified target type. If not, the feature vector will be identified with the "unknown target" designation. If the algorithm is to base its declaration on a single one-look decision then the external decision and the one-look decision (or internal decision) are one and the same.

2.5 Multilook decisions and M/N decision logic

Multilook decisions are based on a number of internal decisions and, therefore, a number of feature vectors. If declarations are to be based on some fixed number of internal decisions (for example, N) then the target class declared by a multilook decision algorithm is the one that is declared more than some number M, M > N/2 times over N looks, (that is, over N feature vectors). This holds for both the known target classes and the unknown class. If none of the target classes are declared M times or more, then a "no decision" declaration is made.

Notice that one-look decisions have two possible outcomes: a declaration for one of the known target classes or a declaration for the unknown target. A multilook decision has an additional possibility: "no decision."

2.6 Confusion matrices

A standard way for reporting the performance of a target classifier is via a confusion matrix. One possible format for a confusion matrix is illustrated by Table 2 in Section 4. The table has one row for each target type represented by the test feature vectors and a column for each target type represented by the templates of the ID classifier. The probability of correctly identifying a target is shown along the diagonal that starts at the upper left corner of the matrix. For example, the probability of correctly identifying target class 3 feature vectors is p3,3. Other entries in the matrix indicate the probability of mis-identifying feature vectors, of declaring the feature vectors "UNKNOWN", or of making no decision declarations. Two columns of the confusion matrix

shown in Table 2 are the probability of decision, P_d, and the decision confidence, P_{conf}. For the feature vectors of any one class, the probability of decision is the probability that the algorithm will make a declaration for any of the known classes -- in this case, T1 through T10. This excludes the unknown target class and no decision declarations. The decision confidence for the target class of any one of the feature vectors indicates the probability of correct ID, given that a declaration for one of the known target classes has been made.

2.7 Averaged performance measures

A confusion matrix may contain a good deal of information about the performance of a target classifier and offers a way to compare the performance of one ID algorithm to another. Another way to compare the performance of one algorithm to another is to compare summaries of their confusion matricies. For this research, three numbers are used to summarize performance: the average probability of decision $\overline{P_d}$, the average decision confidence $\overline{P_{conf}}$, and the average probability of unknown target mis-identification $\overline{P_{mu}}$.

$\overline{P_d}$ is an average of all D entries in the confusion matrix that pertain to feature vectors from the known target classes. Likewise, $\overline{P_{conf}}$ is an average of all *Conf* entries in the confusion matrix that pertain to feature vectors from the known target classes: S1 through S10. These two performance values are entirely independent of the presence of feature vectors from the "unknown" target classes: S11 through S14. $\overline{P_{mu}}$, the average probability of unknown target mis-identification, is an average of all D entries in the probability of decision column of the matrix that pertain to feature vectors from the unknown target classes.

$\overline{P_d}$, $\overline{P_{conf}}$, and $\overline{P_{mu}}$, can be computed simply as an average over the target classes or as a weighted average, where the contribution from each class is weighted by the number of test feature vectors in that class. For reporting here, the former is used rather than the latter.

It is desirable for the algorithm to have $\overline{P_d}$ and $\overline{P_{conf}}$ that are as high as possible, and $\overline{P_{mu}}$ as low as possible. A perfect score for an algorithm would thus be $\overline{P_d} = 100$ %; $\overline{P_{conf}} = 100\%$; $\overline{P_{mu}} = 0\%$. Values for $\overline{P_d}$ or $\overline{P_{conf}}$ that are less than 100% and for $\overline{P_{mu}}$ that are greater than 0% are considered to be errors. The performance of the classifier that results from the application of the various post-processing techniques are given in terms of percentage reduction in the errors in $\overline{P_d}$, $\overline{P_{conf}}$, $\overline{P_{mu}}$ of the baseline configuration of the classifier. These errors will be denoted by $\overline{EP_d}$, $\overline{EP_{conf}}$, and $\overline{EP_{mu}}$. Positive values indicate a reduction in errors, negative values indicate an increase in errors, and zero indicates no change in errors when compared to the baseline. Thus, $\overline{EP_d} = 50\backslash\%$, for example, indicates that the subject innovation has resulted in moving $\overline{P_d}$ halfway up to 100% declaration from the $\overline{P_d}$ performance that the baseline algorithm achieved.

3. DESCRIPTION OF THE BASELINE ALGORITHM AND EXPERIMENT

The baseline configuration of the classifier is the one to which all other configurations of the classifier are compared. This configuration uses a 4/7 decision logic, compares each feature vector to all templates in the classifier, and uses a single, common pre-decision threshold for all of the target classes.

3.1 The measured test feature vectors

The feature vectors used to test the classifier in its various configurations represent 14 different target classes: 10 from targets that are "known" to the classifier and four from targets that are unknown to the classifier. All of the feature vectors were derived from radar data gathered by a ground-based radar.

Each feature vector has associated with it estimates of the target's azimuth and elevation pose angles, which represent the orientation of the target at the time the feature vector was obtained. The angular orientation of all targets can be expressed in terms of two angles of a spherical coordinate system. They will be referred to as azimuth and elevation angles and, by a specified convention, they define the orientation of the target from the point-of-view of the sensor.

The exact number of feature vectors used from each of the 14 target classes are displayed in Table 1. There are a total of 56,574 feature vectors of which 53,074 are from among the known target classes and 3,500 are from the among the unknown classes.

Table 1. The distribution of the test feature vectors over the fourteen target classes.

Target Class	Number of Feature Vectors	Known to Classifier?
1	4480	YES
2	3808	YES
3	3248	YES
4	4368	YES
5	7000	YES
6	7000	YES
7	2639	YES
8	7000	YES
9	6531	YES
10	7000	YES
11	875	NO
12	875	NO
13	875	NO
14	875	NO

3.2 The templates

The templates used by this classifier are based on measured radar information that was chosen as independent from the feature vectors used to test the algorithm. Each template is formed by obtaining statistics on feature vectors whose poses span some number of degrees in both azimuth and elevation. Each template, therefore, represents the target over some range of orientations over which the target feature vectors maintain some degree of stability.

For each target class known to the classifier, there are a set of templates that represent the target over the range in azimuth and elevation of pose angles of interest. In this implementation of the algorithm the templates for a given target do not overlap. The experiments described herein are conducted over 40 templates for each target. These 40 templates cover a rectangular region of pose space.

3.3. The discriminants

The baseline classifier processes each feature vector the same way: it determines the quadratic metric between the feature vector and each of the 400 templates employed by the classifier -- 40 for each of ten target classes. Each comparison results in a discriminant, therefore, for each test feature vector processed by the classifier there will be a set of 400 discriminants. The discriminants may be stored along with other descriptive information, such as the radar's target orientation estimate and, for performance scoring, the target's identity.

3.4. The baseline performance

The baseline performance is expressed in terms of a confusion matrix and is summarized by the performance parameter averages. Since the purpose of this paper is to compare the performance of the different post-processing techniques, it is not important for the absolute performance of the baseline to be reported here. Therefore, only the form of the baseline performance is given. Table 2 is used to represent the performance of the quadratic classifier in its baseline configuration. Here, feature vectors from a total of 14 target classes were classified by a ten-target classifier. There is one row for each of the 14 different target classes represented by the feature vectors and one column for each target class represented by the templates of the classifier. There are also five additional columns in the matrixes: one each for the unknown target type, no decision declarations, probability of decision, decision confidence, and probability of mis-identification.

Table 2. An example of a confusion matrix. The symbols in place represent performance in terms of percentage. Average $P_d = \overline{P_d}$; Average Conf $= \overline{P_{conf}}$; Average MU $= \overline{P_{mu}}$

S	T1	T2	T3	T4	T5	T6	T7	T8	T9	T10	UNK	ND	Pd	Pconf	MIS-ID
1	$p1,1$	$p1,2$	$p1,3$	$p1,4$	$p1,5$	$p1,6$	$p1,7$	$p1,8$	$p1,9$	$p1,10$	U_1	ND_1	D_1	$Conf_1$	MID_1
2	$p2,1$	$p2,2$	$p2,3$	$p2,4$	$p2,5$	$p2,6$	$p2,7$	$p2,8$	$p2,9$	$p2,10$	U_2	ND_2	D_2	$Conf_2$	MID_2
3	$p3,1$	$p3,2$	$p3,3$	$p3,4$	$p3,5$	$p3,6$	$p3,7$	$p3,8$	$p3,9$	$p3,10$	U_3	ND_3	D_3	$Conf_3$	MID_1
4	$p4,1$	$p4,2$	$p4,3$	$p4,4$	$p4,5$	$p4,6$	$p4,7$	$p4,8$	$p4,9$	$p4,10$	U_4	ND_4	D_4	$Conf_4$	MID_4
5	$p5,1$	$p5,2$	$p5,3$	$p5,4$	$p5,5$	$p5,6$	$p5,7$	$p5,8$	$p5,9$	$p5,10$	U_5	ND_5	D_5	$Conf_5$	MID_5
6	$p6,1$	$p6,2$	$p6,3$	$p6,4$	$p6,5$	$p6,6$	$p6,7$	$p6,8$	$p4,9$	$p6,10$	U_6	ND_6	D_6	$Conf_6$	MID_6
7	$p7,1$	$p7,2$	$p7,3$	$p7,4$	$p7,5$	$p7,6$	$p7,7$	$p7,8$	$p7,9$	$p7,10$	U_7	ND_7	D_7	$Conf_7$	MID_7
8	$p8,1$	$p8,2$	$p8,3$	$p8,4$	$p8,5$	$p8,6$	$p8,7$	$p8,8$	$p8,9$	$p8,10$	U_8	ND_8	D_8	$Conf_8$	MID_8
9	$p9,1$	$p9,2$	$p9,3$	$p9,4$	$p9,5$	$p9,6$	$p9,7$	$p9,8$	$p9,9$	$p9,10$	U_9	ND_9	D_9	$Conf_9$	MID_9
10	$p10,1$	$p10,2$	$p10,3$	$p10,4$	$p10,5$	$p10,6$	$p10,7$	$p10,8$	$p10,9$	$p10,10$	U_{10}	ND_{10}	D_{10}	$Conf_{10}$	MID_{10}
11	$p11,1$	$p11,2$	$p11,3$	$p11,4$	$p11,5$	$p11,6$	$p11,7$	$p11,8$	$p11,9$	$p11,10$	U_{11}	ND_{11}	D_{11}	$Conf_{11}$	MU_{11}
12	$p12,1$	$p12,2$	$p12,3$	$p12,4$	$p12,5$	$p12,6$	$p12,7$	$p12,8$	$p12,9$	$p12,10$	U_{12}	ND_{12}	D_{12}	$Conf_{12}$	MU_{12}
13	$p13,1$	$p13,2$	$p13,3$	$p13,4$	$p13,5$	$p13,6$	$p13,7$	$p13,8$	$p13,9$	$p13,10$	U_{13}	ND_{13}	D_{13}	$Conf_{13}$	MU_{13}
14	$p14,1$	$p14,2$	$p14,3$	$p14,4$	$p14,5$	$p14,6$	$p14,7$	$p14,8$	$p14,9$	$p14,10$	U_{14}	ND_{14}	D_{14}	$Conf_{14}$	MU_{14}

4. DESCRIPTION OF TEMPLATE-RELATED OPTIONS

In developing a template-based ID algorithm, it is incumbent upon the designer to create templates that best represent the targets of interest over the pose angles of interest. Once that is accomplished, there still remain options as to how the constellation of templates will be utilized in the algorithm.

4.1. Template utility analysis

While it is incumbent on the designer to create the full template representation of each target over all poses, it is not necessarily incumbent upon him to utilize all these templates in his algorithm. Whether based on measured or modeled data, it is possible that specific templates for specific targets at specific pose angles are simply bad. If one has the luxury to go back in the process and improve these poorly performing templates, then one should certainly do so. However, if one cannot go that far back into the process, there is another alternative.

4.1.1. Individual template performance

An analysis of the individual performance of each template was conducted to determine their quality and perhaps to help to focus efforts on performance improvement which might involve improving feature vector formation, improving template formation, or algorithm issues. To form this analysis the 400 discriminants from each feature vector of the known target classes were processed in a single-look manner. Among these discriminants, one from each of the 400 templates, the one corresponding to the best feature

vector-template match is determined. For the purpose of brevity, let us say that a template activates or is activated when it most closely matches a feature vector.

When a template is activated, a register assigned to the template is incremented by 1 to keep track of the number of times the template has activated during a test. Similarly, another register keeps track of the number of times the template has activated correctly. A template is said to activate correctly when the target class associated with the template is the same as the target class associated with the feature vector that caused the template to activate.

The performance of each template may be measured by first passing the test feature vectors from the ten known target classes through the classifier, then by comparing the number of correct activations to the total number of activations. The ratio of these two numbers for each template can be used to determine which templates are most useful and which are under performing.

4.1.2. The elimination of low-performing templates

Templates that incorrectly activate most of the time attract feature vectors from the "wrong" target classes most of the time. It may, therefore, be possible to increase overall algorithm performance by improving these specific templates or simply by eliminating these templates from the algorithm entirely.

In our experiments, the average performance of the algorithm in terms of the percentage reduction of error in the $\overline{P_d}$, $\overline{P_{conf}}$, and $\overline{P_{mu}}$ of the baseline case that is

obtained by eliminating all templates that have a correct activation rating of less than some specified percentage are as follows: $\overline{EP_d}$ = 0.52%, $\overline{EP_{conf}}$ = 2.83%, and $\overline{EP_{umid}}$ = 0.0%.

As can be seen, the elimination of the lower performing templates had the affect of reducing, although slightly, the error of the average probability of decision and, a bit more significantly, the error in the average decision confidence. The error in $\overline{P_{mu}}$ was not changed. One would conclude that such an approach, while slightly improving performance, does not significantly improve the algorithm's overall performance.

4.2. Sector search restriction

The baseline configuration of the post-processor compares each feature vector to all templates used by the classifier. However, the post processor has the capability of using the aspect angle information associated with each feature vector to limit feature vector-template comparisons to just those templates that match the estimated angle associated with the test feature vector or, to perhaps, neighboring templates. Limiting the number of templates in this way will reduce the number of calculations required by the classifier and, perhaps, will reduce the number of opportunities that the classifier has to mis-identify a feature vector. The "best" selection for this parameter for a given application will be a function of the accuracy of the pose estimate the sensor can supply.

4.2.1. Restricting search to 3X3 and 1X1

Recall that exactly 40 templates for each target class are required to cover the pose angle range of interest. The post processor algorithm used to process discriminants was set up to process three different pose searches for discriminants: ALL, 3X3 and 1X1. For the baseline test, the "ALL" search pattern was employed: that is, each feature vector was compared to all of the templates of the classifier, and this corresponds to the assumption that the pose angle estimate supplied by the radar is too coarse to discern poses within the pose region of interest.

When the 1X1 search pattern is applied to a test feature vector, the feature vector is compared to just the single templates from each target class that covers the reported pose of the test feature vector. When the 3X3 search pattern is used each feature vector is compared to the single templates from each target class that cover the reported pose of the test feature vector and all of the immediately neighboring templates. This forms a 3X3 configuration of templates.

These template restrictions have been applied to the baseline test with the results summarized by the performance parameters shown in Table 3. For these tests, the pre-decision threshold was adjusted so that $\overline{P_d}$ matched that of the baseline test.

These results show that by reducing the search to a 3X3 pattern both $\overline{P_{conf}}$ and $\overline{P_{mu}}$ errors are significantly reduced. Using the 1X1 search pattern to further reduce the search for best feature vector-template matches slightly reduces the $\overline{P_{mu}}$ error but at the cost of slightly increasing $\overline{P_{conf}}$ error. For this particular data set, the best choice seems clearly to be a 3X3 search.

Table 3. Reduction of average performance errors relative to the baseline case.

Template Search Restriction	$\overline{EP_d}$	$\overline{EP_{conf}}$	$\overline{EP_{mu}}$
3x3	0.0	35.19	37.04
1x1	0.0	-5.93	7.41

5. DESCRIPTION OF DISCRIMINANT-RELATED OPTIONS

5.1. Introduction

Once the pre-processing, discriminant generation, and pose-angle search strategies have been established, then decision logics must be considered. Herein we take the maximum number of looks available for a given decision to be 7, as dictated by the sensor mode that generated the data. We thus have options as to the type of logic and computations we implement to best utilize up to 7 HRR profiles per decision.

5.2. 5/7 and 6/7 Decision logics

The M/N = 4/7 decision logic was used to establish the baseline performance. This logic can be made more stringent by using 5/7 or 6/7. These more stringent decision logics were applied to the baseline test to determine their effect on performance.

For these tests, the single pre-decision threshold was adjusted so that the average probability of decision matched that of the baseline test whenever possible. The results of these tests are summarized by Table 4.

In going from the 4/7 decision logic used by the baseline to the 5/7 decision logic, $\overline{P_{conf}}$ error has been cut approximately in half with no change to either $\overline{P_d}$ or $\overline{P_{mu}}$. This, clearly, performs better than the baseline.

Use of the 6/7 decision logic, on the other hand, significantly decreased $\overline{P_{conf}}$ error but increased both the $\overline{P_d}$ error and the $\overline{P_{mu}}$ error. Of these choices for this application, it is clear that the 5/7 decision logic is best, as it induces no change in $\overline{P_d}$ and $\overline{P_{umiss-id}}$ while closing the gap between $\overline{P_{conf}}$ and 100% by almost half, 47.41%.

Table 4. Reduction of average performance errors relative to the baseline case for the cases where 5/7 and 6/7 decisions logics are used along with a single pre-decision threshold.

M/N Decision Logic	$\overline{EP_d}$	$\overline{EP_{conf}}$	$\overline{EP_{mu}}$
5/7	0.0	47.41	0.0
6/7	-29.99	70.37	-395.19

5.3. Decision scoring

Another variation on the 4/7 decision logic test is to use not just the best matching discriminant from each feature vector-template comparison but the best two, three or four discriminants. For this study this variation has been explored.

This technique utilizes one score for each target class represented by the templates and one for the unknown class. Initially the score assigned to each of these classes is 0. The value of 1 is added to the target class associated with the template providing the best match with a test feature vector. A score of 0.5, 0.25, and 0.125, respectively, are added to the target classes associated with the templates giving the second, third and fourth best matches. In all cases, whenever any of the discriminants are above the pre-decision thresholds they are compared to, the appropriate score is added to the unknown target class. After the scores for a number of feature vectors have been accumulated the largest of the scores is compared to a post-decision threshold. If the score is above the post-decision threshold then the declaration will be for the associated target class; otherwise, a "no decision" declaration is made.

The decision scoring technique using the best two through four discriminants per feature vector has been applied to the baseline case. In all of these cases the pre-decision threshold used is the same as that used for the

baseline case and the post-decision threshold was chosen to yield average probability of decisions that is as close to that of the baseline as possible. Results of these tests are reported in Table 5. The performance of all three of these cases are inferior to the baseline case.

5.4. Discriminant integration

Another method for processing discriminants is to locate the best one or more discriminants for each feature vector and from each of the target classes associated with the templates and to determine the difference between those discriminants and the pre-decision threshold. The differences are formulated so that the better a feature vector matches a template the more positive the difference will be. A register is maintained for all of the target classes represented by the templates of the classifier and the unknown class. Each time a difference is calculated (there will be one for each target class represented by the templates) it is added to the appropriate register. In addition, the best of the differences is added to the register for the unknown class.

If the largest of the sums corresponds to one of the known target classes then that class will be declared. If the preceding is not the case then if the sum corresponding to the "Unknown class" is less than 0.0 the unknown class is declared. Otherwise the "no decision" declaration is made.

The discriminant integration technique using the best one through four discriminants per feature vector has been applied to the baseline case. In all of these cases the pre-decision threshold used is the same as that used for the baseline case and the post-decision threshold was chosen to yield average probability of decisions that is as close to that of the baseline as possible.

A summary of the average performance measures from single pre-decision scoring tests and from the discriminant integration tests is given in Table 5. In all four cases the error in $\overline{P_{mu}}$ has been greatly increased with either very little reduction or significant increases in $\overline{P_{conf}}$. In this case, one would likely conclude that the baseline algorithm is superior to any of the variations investigated.

Table 5. The reduction in average performance errors relative to the baseline case for the cases where the single pre-decision threshold, scoring, and discriminant integration tests using one, two, three and four discriminants per feature vector are used.

Decision Method	Number of Discriminants	$\overline{EP_d}$	$\overline{EP_{conf}}$	$\overline{EP_{mu}}$
Scoring	2	-0.15	2.22	-14.81
Scoring	3	-1.93	-2.22	-11.11
Scoring	4	-0.45	-18.15	-37.04
Disc. Intg.	1	0.30	4.07	-18.52
Disc. Intg.	2	0.22	-5.93	-25.93
Disc. Intg.	3	0.22	-14.81	-29.63
Disc. Intg.	4	0.15	-22.96	-29.63

6. COMBINED TECHNIQUES

In the preceding section the alternate post-processing techniques were applied one at a time. In this section some combinations of these techniques have been applied and the results discussed. In all cases, whenever possible, the post-decision threshold was adjusted so that the performance parameter $\overline{P_d}$ of these tests match as nearly as possible that of the baseline case.

6.1. Multiple pre-decision thresholds

The baseline results are compared to the result of using the scoring decision technique and the discriminant integration technique with multiple pre-decision thresholds. For the scoring decision method the best two through best four discriminants are used for each test feature vector. For the soft integration method the best one through four best discriminants are used for each test feature vector and for each of ten target classes represented by the classifier's templates.

The results of all of these tests are summarized by Table 6. In comparing the baseline performance to the others it is clear that the baseline test, the test that uses a single pre-decision threshold for all ten target classes, is inferior to the multiple pre-decision threshold tests. These results show that there is some potential merit to using multiple pre-decision thresholds in conjunction with other techniques. For example, by combining multiple thresholds with three-discriminant integration, we are able to hold the declaration rate while reducing

confidence error by 16.67% and the error rate in the mis-identification of unknowns by 44.44%.

6.2 Multiple pre-decision thresholds and template elimination

The baseline results are compared to the result of using the scoring decision method and the discriminant integration method when eliminating poorly performing templates and utilizing multiple pre-decision thresholds. For the scoring decision technique, tests using the best two through the best four discriminants for each test feature vector have been performed. For the discriminant integration tests the best one through four discriminants for each test feature vector and for each of the classifier's ten target classes have been performed. The performance of each template was analyzed and all templates that activated correctly 40 percent of the time or less were excluded from the process.

The results of all of these tests are summarized by Table 7. In comparing the baseline performance to the other it is clear that the baseline test, the test that uses a single pre-decision threshold for all ten target classes, is inferior to the multiple predecision threshold tests. These results show that the addition of template elimination to this configuration of the algorithm seems to provide a perhaps insignificant improvement to the two-discriminant and three-discriminant decision integration options, similar to its affect on the 4/7 logic case.

Table 6. The reduction in average performance errors relative to the baseline case for the cases that use multiple pre-decision thresholds: three of the tests used the scoring technique and four used discriminant integration.

Decision Method	Number of Discriminants	$\overline{EP_d}$	$\overline{EP_{conf}}$	$\overline{EP_{mu}}$
Scoring	2	-3.05	25.99	33.33
Scoring	3	-2.01	18.15	51.85
Scoring	4	-8.18	20.74	51.85
Disc. Intg.	1	-0.22	0.00	40.74
Disc. Intg.	2	-0.22	10.74	51.85
Disc. Intg.	3	0.00	16.67	44.44
Disc. Intg.	4	0.15	8.89	44.44

Table 7. The reduction in average performance errors relative to the baseline case for the cases where the multiple pre-decision thresholds and template elimination are used.

Decision Method	Number of Discriminants	$\overline{EP_d}$	$\overline{EP_{conf}}$	$\overline{EP_{mu}}$
Scoring	2	-6.10	51.11	33.33
Scoring	3	-2.08	28.52	51.85
Scoring	4	-8.93	34.44	51.85
Disc. Intg.	1	-0.37	6.30	44.44
Disc. Intg.	2	0.15	13.33	51.85
Disc. Intg.	3	0.67	15.93	44.44
Disc. Intg.	4	-0.37	14.07	44.44

6.3. Single threshold and 3X3 search

The baseline results are compared to the results from the scoring decision method and the discriminant integration techniques utilizing a 3X3 search. For the scoring decision technique the best 2 through best 4 discriminants are utilized for each test feature vector. For the discriminant integration method the best one through three discriminants per feature vector and for each target class of the classifier are used. In all cases the same pre-decision threshold is used for all ten target classes.

The result of these tests are given in Table 8. In comparing the baseline performance to the other tests in this group it is clear that the baseline test was outperformed by the discriminant integration tests where the best one and two discriminants are used. Further analysis would be performed to determine how the 3-discriminant integration test listed compares to the baseline case for the requirement of the particular application. The loss in $\overline{P_{mu}}$ would likely be considered prohibitive for most applications.

6.4. Multiple thresholds, 3X3 search and template elimination

The baseline results are compared to the results of the scoring decision technique and the discriminant integration technique. For the scoring decision technique tests using the best two through four discriminants for each feature vector have been performed. For the discriminant integration technique tests for the best one and two discriminants (for each test feature vector and for each target class of the classifier), were performed. All templates with a performance of some specified percentage or below are eliminated and search is restricted to a 3X3 set of sectors.

The result of these tests are given in Table 9 below. Among the tests in this group it is clear that the decision integration techniques listed give results that are superior to the baseline and to all variations considered to this point. The scoring methods, however, for most applications would be considered inferior.

Table 8. The reduction in average performance errors relative to the baseline for cases utilizing the single pre-decision thresholds, the 3X3 search pattern, and either scoring or discriminant integration.

Decision Method	Number of Discriminants	$\overline{EP_d}$	$\overline{EP_{conf}}$	$\overline{EP_{mu}}$
Scoring	2	-28.05	24.44	37.04
Scoring	3	-44.49	28.52	44.44
Scoring	4	-52.01	28.89	51.85
Disc. Intg.	1	0.15	32.59	29.63
Disc. Intg.	2	0.07	29.26	14.81
Disc. Intg.	3	0.15	20.37	-11.11

Table 9. The reduction in average performance errors relative to the baseline for cases utilizing multiple pre-decision thresholds, the 3X3 search pattern, and the elimination of all templates performing under 40%.

Decision Method	Number of Discriminants	$\overline{EP_d}$	$\overline{EP_{conf}}$	$\overline{EP_{mu}}$
Scoring	2	-51.49	71.85	88.89
Scoring	3	-71.80	75.93	88.89
Scoring	4	-84.15	76.30	88.89
Disc. Intg.	1	-0.30	50.00	74.04
Disc. Intg.	2	0.22	50.37	59.26

7. SUMMARY AND CONCLUSIONS

A number of tests have been performed by post-processing the outputs of a quadratic HRR air-target algorithm in an effort to improve upon its overall ID performance. The results of one of the techniques, taken as a baseline case, was used as a reference to which all of the other techniques were compared by providing percent change in identification performance.

For the data used it is clear that the single modification to the baseline that offered the most significant increase in performance is the use of 5/7 vice 4/7 decision logic. However, among all of the modifications to the baseline reported here, the combination of techniques that offered the most significant increase in performance over the baseline was the one employing multiple pre-decision thresholds, a 3X3 template search pattern, template elimination and discriminant integration.

The conclusion is a cautionary one. In the overall algorithm development process, it has long been recognized that the dimensionality of parameter and techniques that one can employ in even a simple algorithmic structure is much too large for one to exhaustively test all combinations to find an optimum configuration. As a result, we often evaluate a single parameter or technique at a time. The sequence of experiments reported herein shows that not only can one not presume to find an optimal solution for the overall target ID algorithm instantiation by 'searching the diagonal,' but that 'searching the diagonal' does not suffice even for the restricted case of finding an optimal post-processing algorithm.

Applications of Unsupervised Clustering Algorithms to Aircraft Identification Using High Range Resolution Radar

Dzung Tri Pham

US Air Force Research Laboratory (AFRL/SNZ)
Wright Patterson AFB
Dayton, OH 45433-7318
U.S.A.

Abstract—
Identification of aircraft from high range resolution (HRR) radar range profiles requires a database of information capturing the variability of the individual range profiles as a function of viewing aspect. This database can be a collection of individual signatures or a collection of average signatures distributed over the region of viewing aspect of interest. An efficient database is one which captures the intrinsic variability of the HRR signatures without either excessive redundancy (over-characterization) typical of single-signature databases or without the loss of information (under-characterization) common when averaging arbitrary groups of signatures.
The identification of "natural" clustering of similar HRR signatures provides a means for creating efficient databases of either individual signatures or of signature templates. Using a k-means and the Kohonen self-organizing feature net, we identify the natural clustering of the HRR radar range profiles into groups of similar signatures based on the match quality metric (Euclidean distance) used within a Vector Quantizer (VQ) classification algorithm. This greatly reduces the redundancy in such databases while retaining classification performance.
Such clusters can be useful in template-based algorithms where groups of signatures are averaged to produce a template. Instead of basing the group of signatures to be averaged on arbitrary regions of viewing aspect, the averages are taken over the signatures contained in the natural clusters which have been identified.
The benefits of applying natural cluster identification to individual-signature HRR data preparation are decreased algorithm memory and computational requirements with a consequent decrease in the time required to perform identification calculations. When applied to template databases the benefits are improved identification performance.
This paper describes the techniques used for identifying HRR signature clusters and describes the statistical properties of such clusters.
Keywords: Automatic target recognition (ATR), Non-cooperative target recognition (NCTI), Combat Identification, High range resolution (HRR) radar, Clustering, K-means, Kohonen, and Pattern Recognition

I. INTRODUCTION

A. Background

Clustering analysis is one of the basic tools for identifying structure in data. Clustering tries to partition objects in N disjointed subsets using some sort of similarity metric. That is, if we had M objects, where $M > N$, we want to partition this set of M objects into N subsets. Where the members of each N subsets are said to belong to the same cluster and are more similar to each other than to members of different subsets or clusters. The objective is to automatically search a database containing a large number of different objects and to group them into subsets of similar objects called clusters. The ability to form such clusters has a number of applications in target recognition. Rather than just simply using the whole data set or simply choosing an arbitrary subset of the data points as a basis set, one can use clustering techniques to find a basis set which more accurately represents the distribution of the data points. We can find these basis sets, by finding the cluster centers which are the mean data points that can best represent all members of a single cluster. By finding the mean data point of each cluster, we can create templates that can reduce the amount of data that need to be stored with minimum loss of information. These templates are then used in a template matching algorithm.

B. Problem Statement

This paper investigates the use of clustering techniques to enhance NCTI algorithm performance with synthetic database range profiles and to reduce the total number of required templates per class that must be stored in the database. By evaluating the "natural" signature clusters in the synthetic database we will eliminate redundancy between individual signatures. We will also increase the accuracy in constructing signature templates by grouping like signatures during template construction. This promises improved performance in template matching algorithms.

C. Scope and Approach

Computer-synthesized range profiles of three aircraft, generated at 1 degree increments in a 31X36 degrees aspect angle window of interest (a total of 1116 signature profiles per aircraft) will be used as training data to create templates using several clustering techniques. These templates will then be used in template matching algorithms and tested using ground-to-air measured data on the same three classes of aircraft (over 15,000 signatures total). By the use of clustering techniques to create templates, this paper analyzes the ability to improve classification performance and the ability to reduce the number of templates required to maintain baseline performance.
The approach taken in this investigation is composed of two steps. The first step is to implement a batch K-means algorithm and the Kohonen clustering algorithm described by Rogers, et al. [7]. The second step is to apply these techniques to the HRR problem to determine if classification performance can be increased and to determine if the amount of data stored can be reduced while maintaining equivalent performance levels.

II. THEORY AND METHODOLOGY

A. Overall Methodology and System

This section presents the details of the system that was implemented to accomplish our investigation. First, we discuss the general approach followed in the batch k-means clustering algorithm with variations in the ways of initializing the algorithm. Next, we will describe the implementation of the general approach of the Kohonen Self-Organizing Features Maps (SOFM) algorithm. Finally, we will detail how to implement a Vector Quantizer (VQ) as our classifier using codebooks generated from our two clustering techniques. A flow chart of how to build the codebooks and to implement a VQ procedure is given in Figure 1. In the following sections we will go into the details of the different parts that will go into our system.

B. Clustering Techniques

Clustering algorithms attempt to find the underlying relationship of input patterns using the assumption that inputs of the same class will naturally cluster together. How effectively the algorithm clusters depends greatly on the similarity measures used. Ideally, when the algorithm is effective, we achieve an optimal number of clusters that have samples that are similar to each other based on our similarity metric, with small variance. Each cluster is represented by a single point called a cluster center or codeword. A full set of codewords is known as a codebook. This codebook, once created, can be used to classify new samples by comparing the input sample to each codeword. The codeword most
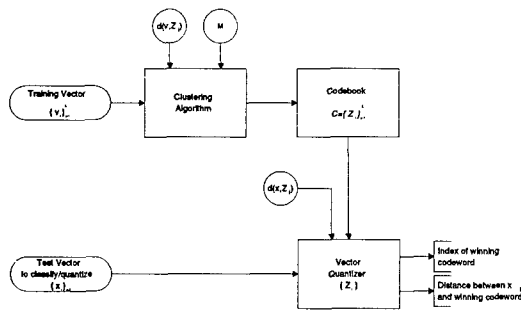
Fig. 1. Flow chart of how to build a codebook and to implement a VQ

5. Compute codebook membership by determining the closest codebook vector for each data point.
6. Update the location of each codebook vector to the centroid of all the data points that are members of each codebook vector's domain. Go to Step 2.
7. The algorithm has converged and the procedure is terminated.

Figure 2 is the basic flow diagram for the general approach taken for the k-means algorithm.
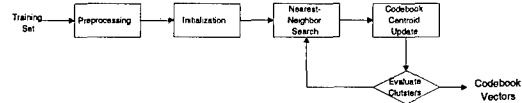

Fig. 2. Flow chart of k-mean algorithm

similar to the input, by use of the similarity metric, is the class where the input belongs [7].

In the following subsections, two well known unsupervised learning algorithms will be introduced. The two algorithms are k-means and Kohonen's self organizing maps algorithm.

B.1. K-Means Algorithm.   Linde, Buzo, and Gray [5] describe the General Lloyd Algorithm used to design a vector quantizer. The General Lloyd Algorithm is often referred to as the LBG Algorithm and when the distance function is chosen to be Euclidean, the algorithm is known as the k-means algorithm. The k-means algorithm attempts to minimize the euclidean distance from all members in a codebook vector to that of the input vector. This minimization is done through an iterative method which terminates when an average distortion metric stabilizes [8].

Specifically, the k-means algorithm starts with choosing the number of cluster centers k that will represent the distribution. The algorithm then involves the following simple iterative method: Assume we are given that there are N data samples x^n, and we wish to find a set of k clusters representative vector u_j where $j = 1,...,k$. The algorithm tries to cluster the data samples x^n into k disjoint subsets S_j containing N_j data samples, where each subset represents a cluster. The attempt is to make the samples in the same cluster be somehow more similar than samples in different clusters. One way to make this into a well defined problem is to select a criterion function that measures the clustering quality of any data partition. The most widely used criterion function for clustering is the sum-of-squared-error criterion given by [1]

$$J = \sum_{j=1}^{K} \sum_{n \in S_j} \| x^n - u_j \|^2 \qquad (1)$$

where u_j is the mean of the data sample in set S_j and is given by

$$u_j = \frac{1}{N_j} \sum_{n \in S_j} x^n. \qquad (2)$$

The following are the steps in the k-means algorithm [8]:
1. Select a stopping criterion which is defined as an acceptable level of total Euclidean distance.
2. Choose the number of codebook vectors k.
3. Using some initialization technique, select the initial locations for the k codebook vectors. It is acceptable to use the location of k samples randomly selected from the design set as the randomly selected initial locations.
4. Calculate the Euclidean distance between each data point and each codebook vector. If the total Euclidean distance is less than the stopping criterion, go to Step 7.

A major limitation of k-means clustering is the location of final codebook vectors may be influenced by how we set the initial positions of the codebook vectors and the order of presentation of the training samples, which will ultimately belong to different codebook vectors. The proper choice of codebook initialization scheme is key in avoiding this problem. A variety of codebook initialization schemes have been developed in hope of providing accelerated convergence, achieving better clusters that more accurately represent the distribution of the data points, and provide the flexibility in the number of cluster centers needed to represent the data. Linde, et al. [5] suggests a splitting method (LBG algorithm), whereby the k-means algorithm is applied at each power of two (giving codebook sizes of 1, 2, 4, 8, ...). Katsavounidis, et al. [3] proposed a maxi-min method, where the cluster centers are placed so that they are maximumly separated. This method is based on the idea that widely separated data points are likely members of different classes. While recently, DeSimio, et al. [2] proposed a Karhunen-Loeve initialization (KLI) scheme, whereby the cluster centers are placed along the principal component axis of the training data's covariance matrix. For this paper we will limit our study to the latter two techniques, the maxi-min and the KLI.

B.2. Kohonen's Self-Organizing Maps Algorithm.   One of the most obvious characteristics of the human brain's operation, and one of the most central problems in information sciences is the economic representation of data with all their interrelationships. In the subconscious information processing and in thinking there is a general tendency to compress information by forming reduced representations of the most relevant facts, without the loss of knowledge about their interrelationships. In this self-organizing process, we are aiming at mappings that will transform a signal pattern of arbitrary dimensionality onto a one- or two-dimensional array [4].

The Kohonen self-organizing features map, an unsupervised learning algorithm, will serve as an example of the self-organizing process. Since this is an unsupervised algorithm, the data is unlabeled. We will base our treatment of Kohonen self-organizing feature maps on a similar outline as found in Rogers, et al. [7]. The Kohonen network is shown in Figure 3.

Before we continue our development, it is assumed that the reader has a basic understanding of artificial neural networks. For the reader that has never encountered neural networks before or for a review of the topic, the reader is referred to Lippmann [6] or Rogers and Kabrisky [7].

Some basic characteristics of the Kohonen net is that it is feed-forward only and consists of an input layer and usually, a two-dimensional output or clustering layer. It mathematically transforms multidimensional input data vectors and maps it to the output vectors. The distribution of the output nodes is spread according to the pdf of the input data. If it is properly trained the nodes of the Kohonen output layer that are spatially close are sensitive to similar inputs. The similarity measure of the input is determined by the
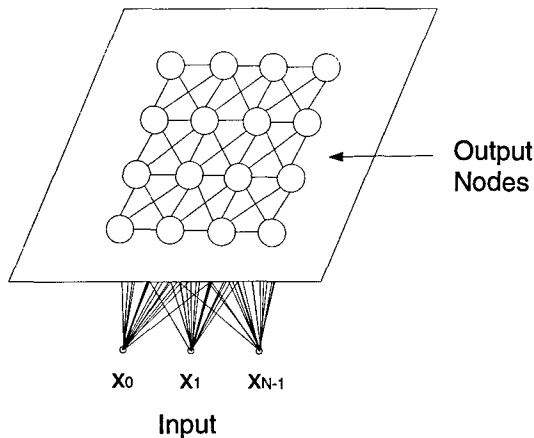
Fig. 3. Two-dimensional array of output nodes used to form feature maps. Every input is connected to every output node via a variable connection weight.

similarity metric used during the training phase and weight adjustments. A heuristic for a well trained Kohonen net is that every output node has an equal opportunity of winning or firing. The winning node is the one whose weights are closest or most similar to that of the unlabeled input.
The following are the steps in the Kohonen net [7]:

1. Select a learning rate of the Kohonen map for the stopping criterion. For example, the learning rate will be small if the distortion measure of the total map changes little between epoch/trial.
2. Choose the dimension of the output layer (m x n).
3. Initialize the weights to small random value and the neighborhood size. The weight can be initialized by using a uniform distribution from -0.5 to +0.5 or a potentially better method is to initialize to training exemplars.
4. Select both the learning rate by which to adjust the winning codebook vector and the codebook vector's neighbors (these can be the same).
5. Randomly select a normalized input vector and compute the distance to each codebook vector. The closest codebook vector to the input vector is the winning node.
6. Conscience (this is an optional step). Check to make sure the winning node has not already won its share of input vectors for this epoch through the data. If it has, pick the node with the second closest codebook vector to the input vector.
7. Using the learning rate, update the codebook vector of the winning node, moving it closer to the input vector. Similarly, update the nodes of the neighbors using the learning rate selected for neighborhood updates.
8. Repeat Steps 5 through 7 for all input vectors.
9. Change the learning rates and/or change the neighborhood size and run another epoch. Once the weights of networks are not changing significantly go to Step 10.
10. The algorithm has converged and the procedure is terminated.

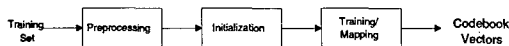Figure 4 is the basic flow diagram for the general approach taken for the Kohonen algorithm.

Fig. 4. Flow chart of Kohonen process

One problem commonly noted with the Kohonen algorithm is that it represents a compression of multidimensional data to just one or two dimensions. The goal is to compress information by forming reduced representations of the most

relevant facts without loss of knowledge about their interrelationships. The hope is that the projection onto the two dimensional space retains the interrelationships of what is close in the higher dimensional space. Sorry to say, but this projection is not unique and the multi-dimensional data representation may be too restrictive of a view. Roger, et al. propose a good analogy of this problem. They refer to it as the flattened-fauna analogy [7]. Suppose we came upon a once three dimensional animal that has been flattened along the road side. The projection of the three dimensional animal onto the two dimensional roadway is dependent on the position of the animal when it was flattened. You would hope that the foot and ankle would be close together on the flattened version and we could keep their basic physical interrelationships. Unfortunately, too often the ear of the creature, which is not close in physical relationship to the ankle, may end up next to the ankle in the two dimensional representation. This problem gets worse as the dimensionality of the original space increases. This implies that the order in which the input vectors are presented to the algorithm will determine the resulting end projection. Similarly Rogers, et al. have found that the result of the Kohonen learning algorithm will be different for different initial random weights.
But things are seldom as confused as they are depicted by the flattened-fauna analogy. The actual Kohonen weights are of the same dimensionality of the input data. Therefore, it is only when the weights are projected onto the Kohonen layer that the distortion of the high-dimensional distances occurs.

C. Classifier

The classifier we chose to use is a Vector Quantizer (VQ). In this section we will describe the actual implementation of a VQ for classification. The following are the steps to implement our VQ classifier:

1. Assume we have M classes. Create a codebook for each class $CB_1, ..., CB_M$.
2. For each input vector, x_i, compare each of its features with each codeword's features and find the distance metric d_{min} for all codewords in all codebooks. For instance, if we had a c dimensional input vector, we would have c distance metrics for each codeword comparison.
3. Accumulate or sum all the distance metrics for each codeword to compute the total distortion, D_i.
4. Choose the codeword with the minimum value of total distortion, D_i. The class j^* that owns the codebook with the winning codeword is declared as the class for that input vector. The VQ then outputs the winning codeword and associated minimum total distortion.

These steps are illustrated in Figure 5. This approach has been applied to the Speaker Identification problem with very good results. $P(error) \approx 2\%$ for 20 speakers using Mel-Frequency Cepstral Coefficient (MFCC) as features.

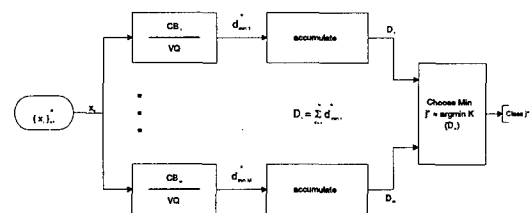Fig. 5. Flow Chart of the VQ

III. EXPERIMENTS AND RESULTS

Identification of aircraft from HRR radar range profiles requires a database of information capturing the variabilities of the individual range profiles as a function of viewing aspect. This database can be a collection of individual signatures or a collection of averaged signatures distributed

over the region of viewing aspects of interest. An efficient database is one which captures the intrinsic variabilities of the HRR signatures without either excessive redundancies typical of single-signature databases, or without loss of information common when averaging arbitrary groups of signatures into templates.

As mentioned before, there are two main thrusts in our investigation. First, we investigate the use of clustering techniques to increase the accuracy in constructing signature templates for improved performance in template matching algorithms. Second, we investigate the potential of reducing the total number of required templates per class that must be stored in the database.

A. Description of baseline experiment

One way to prevent over-characterization in our database is to use a template approach over that of single-signature databases. The easiest way to form templates is with grouping of range profiles in a certain azimuth/elevation. These signatures are grouped into small sets which span a specified azimuth and elevation area, see Figure 6. The azimuth/elevation windows are grouped in such a manner as to hopefully guarantee stationarity in the measured range profiles making up the window. For our investigation we will use 5 degrees by 5 degrees template regions to create each template for our baseline results with the VQ. Over our total aspect window of interests this would result in 42 total templates per class.
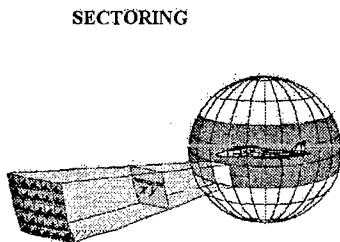
SECTORING

Fig. 6. Aircraft mxn window sectoring

B. K-Means Experiment

To avoid under-characterization in our database, where there is loss of information that is common when averaging arbitrary groups of signatures, we will cluster the signatures to get better representation. We will first try the k-means algorithm with three different initialization schemes.

B.1. 5x5 Averaging Initialization. Since we are using 5x5 degrees window templates for our baseline results, these templates might serve as good locations for initial codewords to use with our k-means algorithm. The results are shown in Figure 8. The figure shows the total aspect window of interest for all three classes. The different shading shows a particular cluster that each individual aspect would belong to. We have a total of 42 clusters since this is the amount of clusters used with a 5x5 azimuth/elevation window method.

B.2. Maxi-Min Initialization. The results of clustering with a k-means algorithm using the maxi-min initialization scheme is shown in Figure 9.

B.3. KLI Initialization. The results of clustering with a k-means algorithm using the KLI initialization scheme is shown in Figure 10.

C. Kohonen SOFM Experiment

As with k-means, to avoid under-characterization in our database, we will now try the Kohonen algorithm with two different output nodes structures.

C.1. Output Nodes Structures. The results of clustering with a Kohonen algorithm using a 6x7 output nodes structure is shown in Figure 11. The results of clustering with a Kohonen algorithm using a 1X42 output nodes structure is shown in Figure 12.

D. Analysis of Results

Several observations are immediately apparent upon inspection of the plots in Figures 7, 8, 9, 10, and 11. First, the clusters are not nicely grouped in 5x5 azimuth and elevation windows. Therefore, by averaging arbitrary groups of signatures like those done with the arbitrary 5x5 windows we have a good chance of under-characterization in our database. For instance, looking at aspect window 1 to 5 degrees in elevation by 0 to 5 in degrees azimuth in Figures 7 - 11. We see in this 5x5 degrees window that it contains aspects belonging to many different clusters. Grouping all these aspects into one template would be very undesirable and cause loss of information due to under-characterization. Another observation is that every clustering variation has different final clusters. We noted earlier that depending on how we initialize our set of initial parameters the final results would be different. But if we examine the clustering results closely we see that there are also some basic similarities in the final results. For instance, if we look at each Figure in the 11 to 12 degrees azimuth over -10 to -30 elevation we see that these signatures always group to the same cluster. Many other similar grouping exists and is consistent between the clustering techniques.

We must always keep in mind that good representation does not always mean good classification performance. In the next section we will look at the classification results of our three class problem using a VQ classifier. The classifier will use the templates created from our different clustering techniques.

E. Classification Performance

This section presents and summarizes the results obtained from applying the methodology and classifier described earlier. Results are presented in the form of confusion matrices for the full, three-class comparisons. To determine the variabilities of our results, a 97.5% confidence intervals are given for all estimates of the classification rates.

E.1. Baseline Results Using 5x5 Azimuth/Elevation Templates. We will take the classification results from using the 5x5 azimuth/elevation window templates for our baseline results. This is a good baseline to see if clustering can improve on our classification results, since this is the same technique for templates creation currently being employed by Wright Laboratory. See Table I.

E.2. Batch K-Means and Kohonen Performance Results. We now take the templates created from the K-means and Kohonen clustering techniques shown in Sections 5.4 and 5.5 and employing a VQ to the three class problem to give us our performance results. The classification results are given in Tables II, III, IV, V, and VI.

E.3. Integration. To further increase classification performance we could employ a couple of different integration schemes to improve our classifier. What we could do is take a 5 out of 8 or a full integration of the single-look performance and build confidence in our decision. What we mean by single-look performance, is that for every input vector we get, we will make a decision on its class. For a 5 out of 8 scheme we would take 8 single-look decisions and if at least 5 out of the eight single-look decisions are of the same class then we would classify the target as that class. If there are less than 5 out of 8 then we would make no declaration. In

the 5 out of 8 scheme, as we continue to get more inputs we would add this new input to our group of eight. Then we would throw away the oldest input and make a new decision with our new group of eight. In full integration we would not throw away the oldest input, but make a decision on the class if there are (5/8)% or 62.5% of all the decisions are of the same class.

The results are given for each templates creation techniques and both the 5 out of 8 and full integration results are shown. P_d stands for probability of declaration. Which means for every opportunity to declare, how often do we make a decision of the target class. P_c stands for probability of correct classification. Which means for every declaration, how often do we make the right decision of the target class.

See Tables VII, VIII, IX, X, XI, and XII for the integration results.

F. Discussion of Classification Results

The objective of this section was the investigation of clustering techniques to enhance algorithm's performance using a synthetic database range profiles and testing it on measured range profiles. Our results show that the algorithm's performance on templates created by clustering synthetic signatures was either enhanced or equivalent to the baseline in most cases. Up to a 15% increase in performance was achieved for Class A and up to a 10% increase in Class C depending on clustering techniques. Class B had no significant changes in performance but this is probably attributed to the high baseline performance of Class B. While improving performance overall, there was no significant instances of detriment to performance caused by clustering.

The integration performance showed that great improvement is attainable from using the techniques. The drawback is that computation time for a decision is also increased. This could be a major drawback if only a few seconds could determines an engagement outcome.

G. Data Reduction Study

In this section we investigated the potential of reducing the total number of required templates per class that must be stored in the database with minimum loss of information. In this experiment we chose the Kohonen clustering algorithm as the method to generate the required number of M codewords. We chose the Kohonen algorithm with a 1XM output layer since, from our performance results, the Kohonen with a 1X42 output achieved very good results. We chose M to be 1, 2, 3, 4, 5, 8, 10, 12, 15, 20, 25, 30, 35, and 42. We then graphed the total average distortions versus the number of M codewords. This plot is shown in Figure 7.

From Figure 7 we see that the average distortion falls as we increase the number of codewords, but at a certain point we ceased to lower the distortion. This break point is somewhere around 10 codewords for our aspect window of interests, any less than that and we have under-characterization, any more and we have over-characterization. The classification results with only 10 codewords per class is given in Figure XIII. These results are comparable to those results using 42 codewords per class.

IV. CONCLUSIONS AND RECOMMENDATIONS

A. Conclusions

The primary objectives of this research was to examine the use of clustering techniques to enhance algorithm performance with synthetic database range profiles, and to reduce the total number of required templates per class that must be stored in the database. Both objectives were met by applying two unsupervised algorithms (k-means and Kohonen) to the HRR problem. We have provided a brief description of the theoretical background for the two methods. We have presented the performance results for the clustering techniques using a Vector Quantizer classifier. The purpose of this chapter is to summarize the results of this research and to draw some general conclusions based on these results.
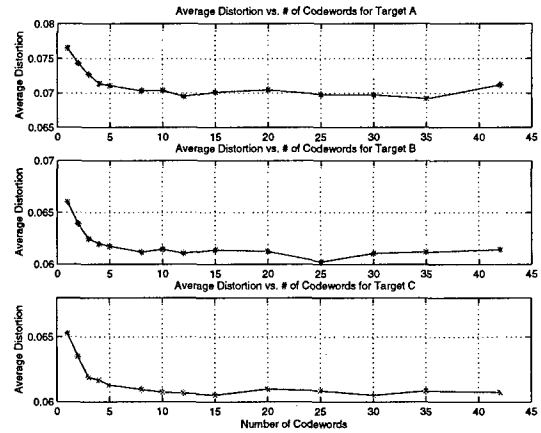

Fig. 7. Average Distortion versus Total Number of Codewords

B. Contributions

- This paper introduced a method for integrating clustering techniques into templates creation to improve algorithm performance and minimize database size. Instead of creating templates, basing the group of signatures to be averaged on arbitrary regions of viewing aspects, the averages are taken over the signatures contained in the natural clusters which can be identified.
- The analysis showed that the proper clustering of signatures into natural clusters can improve classification performance between 10% to 15% for some classes. It also showed that by clustering, the performance was not significantly lower in any of the cases.
- The analysis also showed that the proper clustering of signatures into natural clusters can reduce the database required by a factor of four. This would lead to decreased algorithm's memory and computational requirements, with a consequent decrease in the time required to perform the required identification calculations.
- This paper also applied a VQ classifier to the HRR identification problem with very good results. With the use of the VQ results we were able to explore the value of single look classification versus multi-look (integration) classification. The use of multi-look classification can prove crucial in maintaining high performance as the number of classes are increased to a usable size.

C. Summary of Results

The results of the experiments are summarized in Table XIV. The performance is reported for each experiment on all three targets and the Δ% is the value of increased or decreased performance as compared to the baseline performance. The results obtained in this paper lead to several interesting conclusions:

- Each clustering iteration did improve performance over the baseline results with a 5x5 window adhoc template formation, while not causing any significant detriment to performance.
- As we noted earlier, depending on how we initialized our clustering algorithms the final clusters will be somewhat unique. This representation even though different for each clustering iteration is a better method for template creation to improve data representation and classification.
- Our experiment at data reduction, using only 10 codewords rather than 42 codewords, also was quite successful. We were able to maintain the classification performance while reducing the amount of data stored in the database by a factor of four.

- All of the classification performances can be increased by the use of a multi-look or integration classifier schemes. In fact, for our three class problem we were able to attain 100% performance on all classes for all clustering schemes and the baseline.
- The use of k-means and Kohonen for clustering of the HRR data proved to significantly increase classification performances in most cases, while no significant detriment in performances was observed.
- The clustering of signatures can create an efficient database which capture the intrinsic variability of the HRR signatures without either loss of information or without excessive redundancy.
- The benefits of applying natural cluster to classification algorithms are increased performances, decreased algorithm's memory, and computational requirements with a consequent decrease in the time required to perform the required identification calculations.

D. Follow-on Research

The research discussed in this paper is by no means exhaustive. As with any large undertaking, there are many areas left for further research. Some possible enhancements are listed below:

- The number of classes in this investigation was limited to just three classes of fighter size aircraft. Further investigation on a more complex problem with a larger number of mixed size aircraft could be interesting. Clustering with a more complex problem could prove to have greater payoff on performance, database size, and computational complexity and time.
- The aspect window investigated was also very limited. Expansion of the aspect window to include the entire sphere of possible aspect angle should be done.
- Investigation needs to be done to see if integration classifiers can be operationally viable. Can we perform classification in a timely manner that will give the warfighter the necessary time to act on the information?
- The integration experiment showed that most of the input vectors gave correct classifications. There are a few out-lying input vectors that are somehow distorted and giveing us incorrect classifications. This distortion can be caused by misalignment, antenna flashes, EMI/RFI, atmospheric interference, clutter, radar calibration, low signal to noise, etc. Further investigation needs to look at either prescreening input signatures for these problems and eliminating the distortion or the input signatures itself.
- One of the main areas of possible improvement to the HRR problem is to lower the dimensionality of the problem by doing features selection and saliency. Using every range bin is not a very viable feature in that it is so dependent on alignment and the information is only located in a small subset of the range bins.
- We know that there are differences between the synthetic generated signatures and the measured signatures. Even though the synthetic signatures do not completly model every characteristic correctly there are many characteristics that are modeled well. Therefore we need to find the common information space between the synthetic and measure signatures and use this information to come up with good features for our classifiers or use this information to help improve the synthetic predictions.

REFERENCES

[1] Bishop, Christopher. *Neural Networks for Pattern Recognition.* Oxford University Press Inc., New York, 1995.

[2] DeSimio, Martin P., Dennis W. Ruck and Raymond E. Slyh. *Karhunen-Loeve Based Initialization for Generalized Lloyd Iteration.* Technical Report, Air Force Institute of Technology, 1996.

[3] Katsavounidis, Ioannis, C.-C. Jay Kuo and Zhen Zhang. "A New Initialization Technique for Generalized Lloyd Iteration," *IEEE Signal Processing Letters,* 1(10):144 – 146 (October 1994).

[4] Kohonen, Teuvo. *Self-Organization and Associative Memory* (Second Edition). Springer-Verlag, 1965.

[5] Linde, Y., A. Buzo and R. M. Gray. "An Algorithm for Vector Quantizer Design," *IEEE Transactions on Communication,* COM-28(1):84 – 95 (January 1980).

[6] Lippmann, Richard P. "An Introduction to Computing and Neural Nets," *IEEE ASSP Magazine, 4* (1987).

[7] Rogers, Steven K., Mathew Kabrisky Dennis W. Ruck and Gregory L. Tarr. *An Introduction to Biological and Artificial Neural Networks.* Bellingham, Washington: SPIE Optical Engineering Press, 1991.

[8] Rogers, Steven K. "Introduction to Perceptrons: Advanced Topics in Neural Networks." April 1996.
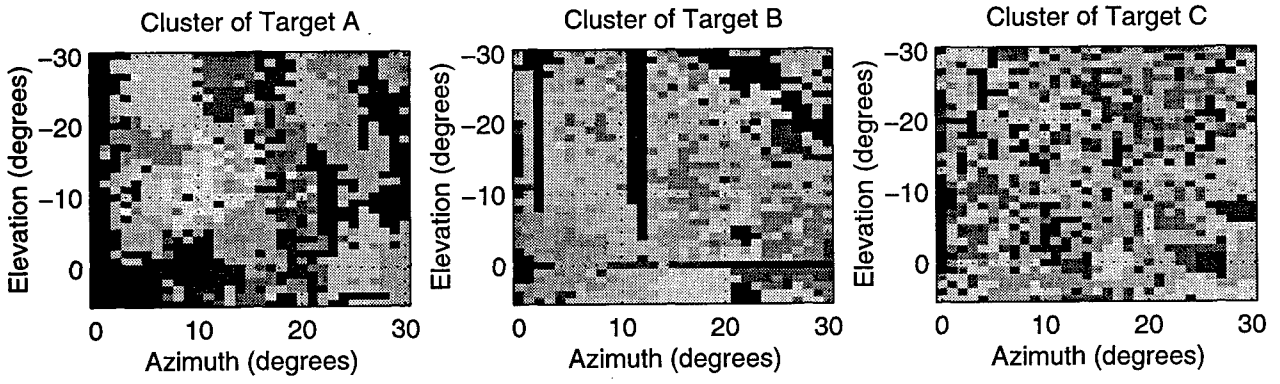
Fig. 8. Clustering results for 5x5 averaging initialization for total aspect window
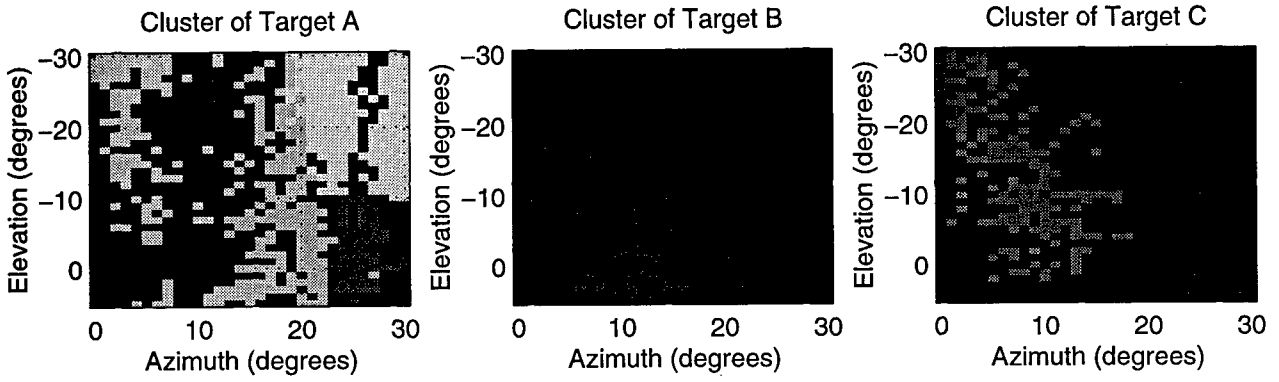

Fig. 9. Clustering results for Maxi-min initialization for total aspect window
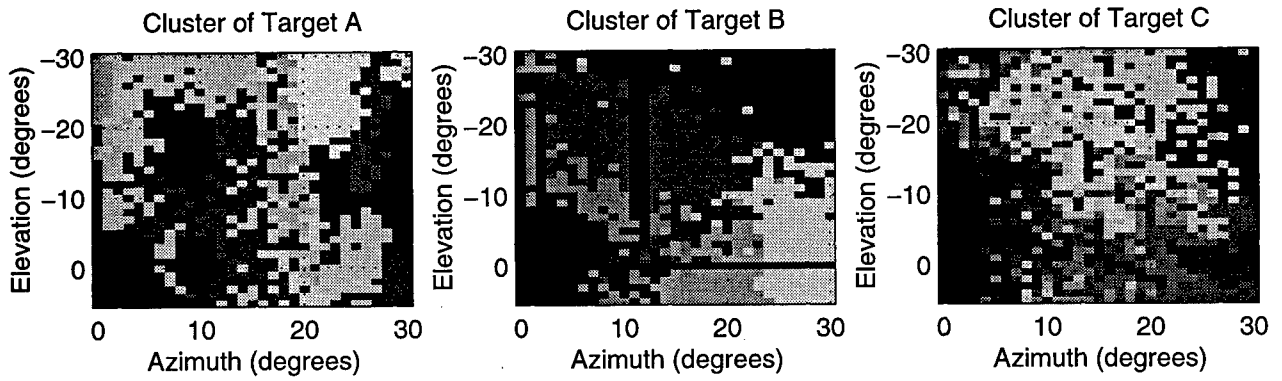

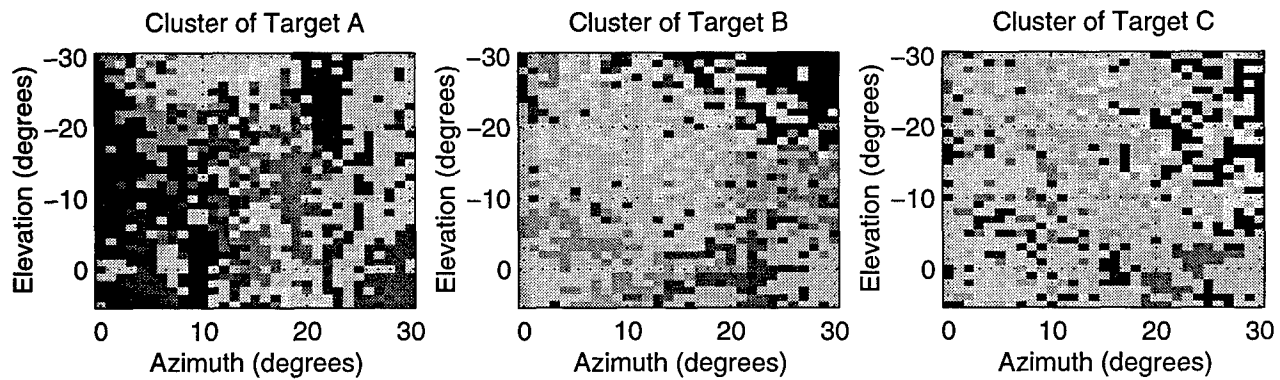Fig. 10. Clustering results for KLI initialization for total aspect window

Fig. 11. Clustering results for Kohonen with 6x7 output nodes for total aspect window
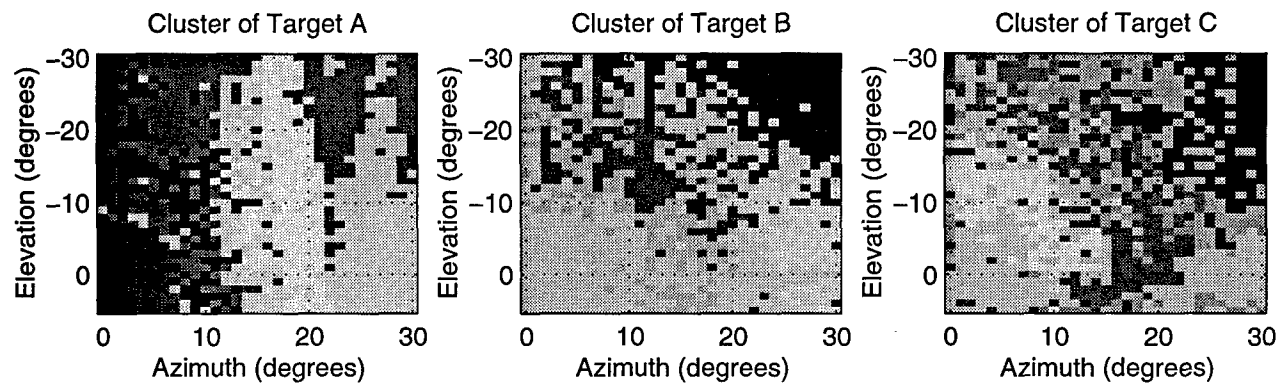

Fig. 12. Clustering results for Kohonen with 1x42 output nodes for total aspect window

Actual Class	Assigned Class			P_c (%)	97.5 % Confidence Interval (%)
	Target A	Target B	Target C		
Target A	5064	974	866	73.28	± 1.05
Target B	72	4367	276	92.62	± 0.75
Target C	10	1678	3121	64.90	± 1.35

TABLE I

BASELINE RESULTS WITH A VECTOR QUANTIZER USING 5X5 WINDOW TEMPLATES AND CONFUSION TABLE

Actual Class	Assigned Class			P_c (%)	97.5 % Confidence Interval (%)
	Target A	Target B	Target C		
Target A	5089	1047	768	73.71	± 1.04
Target B	25	4231	459	89.73	± 0.87
Target C	5	1379	3425	71.22	± 1.28

TABLE II

BATCH K-MEAN WITH 5X5 AVERAGE INITIALIZATION CLASSIFICATION RESULTS AND CONFUSION TABLE

Actual Class	Assigned Class			P_c (%)	97.5 % Confidence Interval (%)
	Target A	Target B	Target C		
Target A	6081	465	358	88.08	± 0.76
Target B	62	4519	134	95.84	± 0.57
Target C	80	1422	3307	68.77	± 1.31

TABLE III

BATCH K-MEAN WITH MAXI-MIN INITIALIZATION CLASSIFICATION RESULTS AND CONFUSION TABLE

Actual Class	Assigned Class			P_c (%)	97.5 % Confidence Interval (%)
	Target A	Target B	Target C		
Target A	5404	628	872	78.27	± 0.97
Target B	74	4253	388	90.20	± 0.85
Target C	14	1146	3649	75.88	± 1.21

TABLE IV

BATCH K-MEAN WITH KLI INITIALIZATION CLASSIFICATION RESULTS AND CONFUSION TABLE

Actual Class	Assigned Class			P_c (%)	97.5 % Confidence Interval (%)
	Target A	Target B	Target C		
Target A	6004	307	593	86.96	± 0.79
Target B	205	4206	304	89.20	± 0.89
Target C	43	1367	3399	70.68	± 1.29

TABLE V

KOHONEN WITH 6X7 OUTPUT LAYER NODES CLASSIFICATION RESULTS AND CONFUSION TABLE

Actual Class	Assigned Class			P_c (%)	97.5 % Confidence Interval (%)
	Target A	Target B	Target C		
Target A	6156	274	474	89.17	± 0.73
Target B	72	4437	206	94.10	± 0.67
Target C	43	1458	3308	68.79	± 1.31

TABLE VI

KOHONEN WITH 1X42 OUTPUT LAYER NODES CLASSIFICATION RESULTS AND CONFUSION TABLE

5x5 window templates				
Target Class	5 out of 8 results		full integration results	
	P_d (%)	P_c (%)	P_d (%)	P_c (%)
Target A	83.27	93.35	100	100
Target B	97.81	99.72	100	100
Target C	87.11	73.61	94.42	100

TABLE VII

5 OUT OF 8 AND FULL INTEGRATION PERFORMANCE RESULTS FOR 5X5 WINDOW TEMPLATES

5x5 Average Initialization				
Target Class	5 out of 8 results		full integration results	
	P_d (%)	P_c (%)	P_d (%)	P_c (%)
Target A	83.63	93.50	100	100
Target B	97.71	99.13	100	100
Target C	89.05	82.86	100	100

TABLE VIII

5 OUT OF 8 AND FULL INTEGRATION PERFORMANCE RESULTS FOR 5X5 AVERAGE INITIALIZATION

Maxi-min Initialization				
Target Class	5 out of 8 results		full integration results	
	P_d (%)	P_c (%)	P_d (%)	P_c (%)
Target A	95.66	99.15	99.94	100
Target B	99.70	100	100	100
Target C	86.88	79.31	100	100

TABLE IX

5 OUT OF 8 AND FULL INTEGRATION PERFORMANCE RESULTS FOR MAXI-MIN INITIALIZATION

KLI Initialization				
Target Class	5 out of 8 results		full integration results	
	P_d (%)	P_c (%)	P_d (%)	P_c (%)
Target A	87.81	97.06	100	100
Target B	97.58	99.50	100	100
Target C	91.27	87.22	100	100

TABLE X

5 OUT OF 8 AND FULL INTEGRATION PERFORMANCE RESULTS FOR KLI INITIALIZATION

6x7 Kohonen				
Target Class	5 out of 8 results		full integration results	
	P_d (%)	P_c (%)	P_d (%)	P_c (%)
Target A	94.49	98.37	100	100
Target B	96.43	99.23	100	100
Target C	88.09	81.63	100	100

TABLE XI

5 OUT OF 8 AND FULL INTEGRATION PERFORMANCE RESULTS FOR 6X7 KOHONEN

1x42 Kohonen				
Target Class	5 out of 8 results		full integration results	
	P_d (%)	P_c (%)	P_d (%)	P_c (%)
Target A	96.38	98.83	100	100
Target B	99.17	100	100	100
Target C	87.90	79.18	100	100

TABLE XII

5 OUT OF 8 AND FULL INTEGRATION PERFORMANCE RESULTS FOR 1X42 KOHONEN

Actual Class	Assigned Class			P_c (%)	97.5 % Confidence Interval (%)
	Target A	Target B	Target C		
Target A	5797	469	638	83.97	± 0.87
Target B	60	4445	210	94.25	± 0.66
Target C	41	1712	3056	63.55	± 1.36

TABLE XIII

RESULTS FOR KOHONEN WITH 1X10 OUTPUT LAYER

Summary of Results						
Target class	Target A		Target B		Target C	
	P_c (%)	Δ (%)	P_c (%)	Δ (%)	P_c (%)	Δ (%)
Baseline Result of VQ using 5x5 window templates	73.28		92.62		64.90	
Batch k-means with 5x5 Avg. Init.	73.71	0.43	89.73	-2.88	71.22	6.32
Batch k-means with Maxi-min Init.	88.08	14.80	95.84	3.22	68.77	3.87
Batch k-means with KLI Init.	78.27	4.99	90.20	-2.42	75.88	10.98
Kohonen with 6x7 output layer nodes	86.96	13.68	89.20	-3.41	70.68	5.78
Kohonen with 1x42 output layer nodes	89.17	15.89	94.10	1.48	68.79	3.89
Kohonen with 1x10 output layer nodes	83.97	10.69	94.25	1.63	63.55	-1.35

TABLE XIV

SUMMARY OF RESULTS

Statistical Feature Based HRR Radar Classification

Richard A. Mitchell and John J. Westerkamp[*]
Automatic Target Recognition Branch
USAF AFRL/SNAT, 2010 Fifth Street, Bldg 23
Wright Patterson AFB, OH 45433-7001, USA

SUMMARY

The statistical feature based (StaF) classifier is presented for robust high range resolution (HRR) radar aircraft identification which was originally developed in [1]. The target features used for classification are the amplitude and location of HRR signature peaks. These features are selected "on the fly" with no *a priori* assumptions about the number or location of the features. Therefore, the number of features extracted depends on the information content of the observed signature. This approach causes the number, location and amplitude of the extracted features to be random variables. Classification decisions and confidence levels are calculated at the feature level and fused over the observation to obtain overall target classifications. A primary goal for this research is to increase classifier robustness to maintain high performance known target identification while minimizing errors from unknown target. The StaF classifier performance is compared to a baseline quadratic classifier approach in two different unknown target tests. Results are presented demonstrating that the StaF classifier can significantly reduce errors associated with unknown targets while maintaining a high probability of correct classification.

1 INTRODUCTION

The goal of automatic target recognition (ATR) technology is to identify targets from observed sensor information. The need for this technology is evident from the numerous "friendly fire" incidents that have occurred over the past several years. One sensor technology used for ATR of aircraft is high range resolution (HRR) radar [1-4]. This sensor collects a "range profile" or "signature" of an aircraft. The information contained in this signature is the magnitude of the radar scattering as a function of range along the line of sight of the radar. The goal for HRR ATR is to use known information about specific aircraft to identify them when they are observed.

Analysis of HRR sensor data is very difficult because it collapses three dimensional information into a single
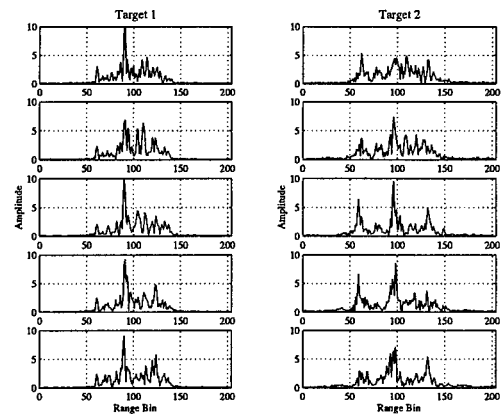

Figure 1: One Second Sequence of HRR for Two Aircraft

dimension. For this reason the signatures exhibit a large degree of variability over small changes in viewing aspect. An example of signature variability seen in figure 1, which shows sequential observations of two different aircraft over a period of 1 second (200ms between observations). In both cases the change in the angular view of the targets was less than 1 degree in azimuth and elevation. The degree of variability seen in these signatures is very typical. Because of this high degree of variability, most identification approaches for HRR are statistical in nature.

Using basic statistical pattern recognition techniques, the HRR target classes have been shown to be fairly separable for small sets of target classes [5]. The difficulties for the ATR primarily lie in the specified performance requirements. These requirements are high declaration probability (P_{dec}), high probability of correct identification of known targets (P_{cc}) and low probability of misidentifying unknown targets ($P_{mis-unk}$). Here the terms "known" and "unknown" refer to targets in the training database and those that are not.

P_{dec} specifies the probability that a target identification

---

[*]rmitchel@mbvlab.wpafb.af.mil, jwester@mbvlab.wpafb.af.mil

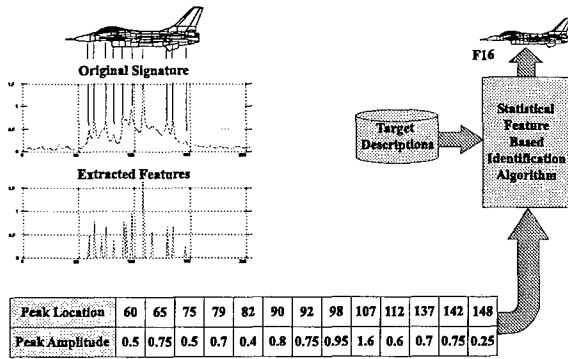| Peak Location	60	65	75	79	82	90	92	98	107	112	137	142	148
Peak Amplitude	0.5	0.75	0.5	0.7	0.4	0.8	0.75	0.95	1.6	0.6	0.7	0.75	0.25

Figure 2: Feature Based Target Identification Algorithm Concept

is declared if a known target is observed. P_{cc} specifies the probability of correctly classifying a target given that an identification declaration has been made. The last performance requirement, $P_{mis-unk}$, specifies the percentage of unknown target observations that are erroneously identified as some known target class. This unknown target identification requirement is especially difficult since it is not possible to train on an "unknown" target class. For this reason some measure of confidence must be included in the classification process. Then classifier decisions with low confidence can be rejected either because the target is unknown or because more information is required to make a decision.

To achieve these difficult performance goals, a classifier must be very robust. Part of achieving robustness is the selection of high quality features that compactly represent the target information while retaining target class separability. Through the understanding of the radar phenomenology, one useful set of features is the peaks in the radar signatures. This is because the peak information identifies the size and range location of scatterers on the target. Such a feature based classifier concept is shown in figure 2. How one statistically captures this information, given the data variability, and uses it for classification is the subject of this research.

2 STATISTICAL FEATURE BASED (StaF) CLASSIFIER

The StaF classification algorithm is based on the statistical behavior of extracted features. The features used are the location and amplitude of salient peaks in the HRR target signatures. The extracted peak information from an observation is determined on the fly with no restrictions being placed on number or location of features.

The basic statistical modeling concept is to estimate the probability that a peak occurs in a specific location l_j, given that the observation is from target ω_i. Further, the probability that the peak has amplitude a_j given that the peak is at the location l_j and that the observation is of target ω_i must be determined. The primary statistics required to determine these probabilities are the peak location probability function (PLPF) and the peak amplitude probability density function (PDF). The PLPF specifies the probability that a peak occurs in a specific location for each individual target. The peak amplitude PDF is based on the amplitude of the peaks given that a peak occurs in a given range bin for a specific target. The PLPF and peak amplitude PDF are discussed in section 2.1.

Given the PLPF and peak amplitude PDF, classification decisions can be made for individual features extracted from an observation. Section 2.2 discusses the calculations to determine the class likelihoods and class *a posteriori* probabilities for individual extracted features. The feature level classifications will then be fused using Dempster-Shafer (D-S) evidence theory. The reason for using D-S over Bayes is that D-S has the inherent ability to incorporate decision uncertainty. This is desirable since it allows one to assign confidence values to the classification decisions. The fusion of the features will be discussed further in section 2.2.3.

Confidence levels associated with a classification are assigned at the feature level. They are based on the joint likelihood of the peak locations and amplitudes. The goal of the confidence value is to determine the probability that the feature based classification is associated with a correct hypothesis. This information is accrued in the D-S algorithm, allowing the fused decision confidence to be assessed. This ability becomes extremely important when one needs to reject unknown target observations. Determination of these confidence levels will be discussed in section 2.2.1.

The notation used throughout this paper will be as follows. Target class hypotheses are defined as the set $\Omega = \{\omega_1, \omega_2, \ldots, \omega_n\}$ for an algorithm trained on n target classes. For the examples in this paper it is assumed that $n = 5$. The peak location data are represented by $L = \{l_1, l_2, \ldots, l_k\}$ and the peak amplitude data by $A = \{a_1, a_2, \ldots, a_k\}$ for k extracted peaks from an observed target signature.

2.1 Feature Statistics Estimation

The statistics models required for the StaF classifier are the peak location probability function (PLPF) and the feature amplitude PDF. Estimation of these distributions are discussed in sections 2.1.1 and 2.1.2
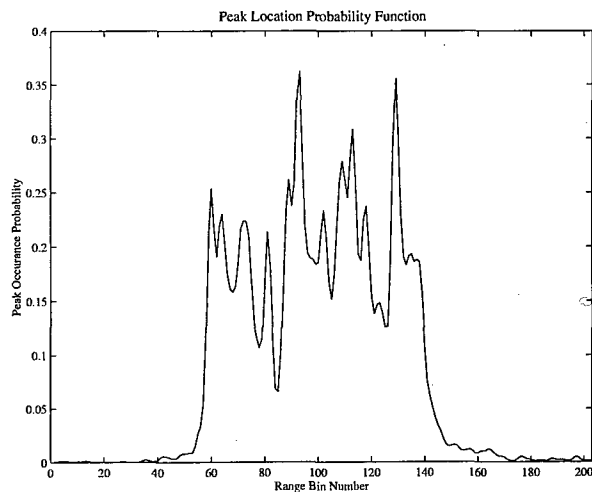
Figure 3: Parzen estimate of peak location probability function.

respectively.

2.1.1 PLPF Estimation

The role of the PLPF is to determine the probability that a peak will be observed in a specific range bin given that the observation was from some class ω_i. This probability is estimated from the peak locations of the training ensemble for each target class. A Parzen estimator with a normal kernel function along the range dimension is employed to estimate the PLPF [6]. An example of a Parzen estimated PLPF is shown in figure 3.

With this function, class probabilities are associated with peak locations. This information alone, however, is not enough to make robust class identification. The additional information will come from the conditional peak amplitude statistics. The next subsection will discuss how these statistics are generated.

2.1.2 Peak Amplitude Probability Density Function

The amplitude statistics are conditional on the occurrence of a peak in a specific location and for a given target class. This estimation approach ensures that the amplitude statistics are based only on the detected features rather than a specific range bin location.

The form of the amplitude statistical distribution is assumed to be Normal within a given range bin. While it is known that the magnitude of the signatures has a Rician distribution, the Gaussian assumption is reasonable if a "power transform" is performed [6]. Making this transformation significantly simplifies the problem since the normal PDF is completely specified

by two parameters, the mean and variance. These parameters are calculated for each range bin from the amplitudes of the extracted peaks of the training ensemble. The resulting mean and standard deviation for one target class are plotted in figure 4.

2.2 Target Class Likelihoods and Probabilities

Given the peak location probability functions (PLPF) and amplitude PDFs, class likelihoods and probabilities must be calculated for a set of features. The feature location likelihoods are found by evaluating the PLPF at a specific feature location. For example, assume a feature is found at location 60. For the target class associated with the PLPF in figure 3, the probability or likelihood that a feature is observed at that location is approximately $P(l_j = 60|\omega_i) = 0.25$.

The amplitude likelihoods are found in a similar way using a mathematical expression for the Gaussian PDF. The parameters of the Gaussian PDF are the estimated mean and variance terms as discussed in the previous section. The likelihood that the observed feature amplitude is the result of observing target class ω_i is found by evaluating

$$p(a_j|\omega_i l_j) = \frac{1}{\sqrt{2\pi}\sigma_{ij}} e^{-\frac{(a_j - \mu_{ij})^2}{2\sigma_{ij}^2}}, \qquad (1)$$

where μ_{ij} and σ_{ij} are the conditional mean and standard deviation for peak location l_j given class ω_i. Note that this likelihood is conditioned on both the target class and the feature location.

Figure 5 re-emphasizes that these likelihoods are based on a single peak feature . Additionally this figure demonstrates how the location and amplitude likelihoods are combined. The joint peak location and amplitude likelihood is calculated by multiplying the individual likelihoods,

$$p(a_j l_j|\omega_i) = p(a_j|\omega_i l_j)P(l_j|\omega_i). \qquad (2)$$

From the joint likelihoods a posteriori probabilities are calculated using Bayes rule,

$$P(\omega_i|l_j a_j) = \frac{p(l_j a_j|\omega_i)P(\omega_i)}{\sum_{m=1}^{n} p(l_j a_j|\omega_m)P(\omega_m)}. \qquad (3)$$

One problem associated with the Bayesian probability calculations is that only relative probabilistic information is considered rather than global information. This is because (3) normalizes the probabilities relative to the likelihoods of some set of target hypotheses. Therefore, only probabilistic
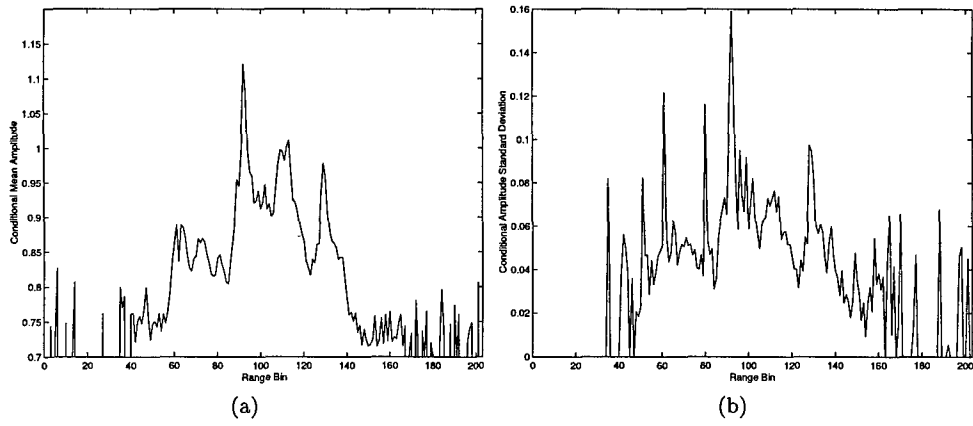
Figure 4: Conditional amplitude (a) mean and (b) standard deviation.

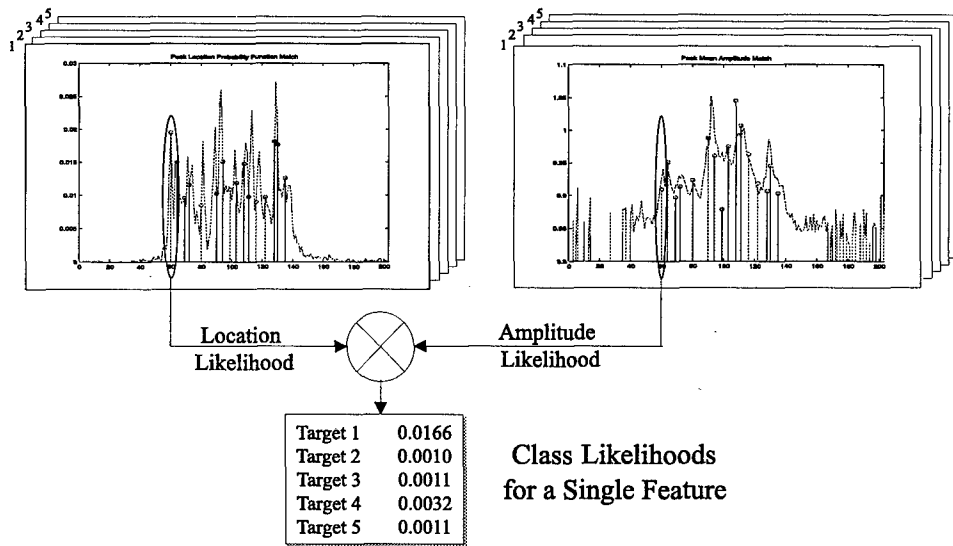| Target 1	0.0166
Target 2	0.0010
Target 3	0.0011
Target 4	0.0032
Target 5	0.0011

Class Likelihoods for a Single Feature

Figure 5: Feature level likelihood generation

information about a class relative to the probabilities of some set of other classes is given.

Consider the case that an observation is from a target for which no statistics are available. If that observation looks statistically more like one class, say class ω_1, than the other classes, the Bayesian probabilities would appear to be very confident that the observation belonged to class ω_1. In reality the likelihood, $p(a_j l_j | \omega_1)$, may be very low. This decision would result in an error. Therefore, if it is possible that unknown targets will be observed, then Bayes decision alone will not be able to reject incorrect decisions due to the unknown target. The information required to eliminate these errors can be obtained from the likelihood values.

The inclusion of likelihood information in this algorithm will be in the form of a confidence measure. The determination of the confidence will be discussed in section 2.2.1. Then how the individual peak confidence levels and *a posteriori* probabilities are used to determine class beliefs are discussed in section 2.2.2. Section 2.2.3 presents an approach to accrue the class beliefs to obtain an overall observation classification decision. Finally, the determination of the classification decision quality (or rejection of unknown target classes) will be discussed in section 2.2.4.

2.2.1 Confidence Measures

The most complicating requirement with HRR ID of aircraft is the rejection of unknown target classes. This problem occurs because it is impossible to train a classifier to recognize every possible aircraft. Therefore, the ID algorithm must only make classification decisions when the statistical confidence is very high.

The decision confidence measures are based on the class likelihoods. To do this, in-class likelihood PDFs are developed using equation (2) for each class. The likelihood statistics are obtained by comparing the training exemplars with their own statistical model. The actual likelihood PDFs are then estimated using a Parzen estimator with a normal kernel function.

Observing that the likelihoods are class-conditional probabilities, larger likelihood decisions should have higher confidence level. A function that mirrors this concept is the cumulative distribution function (CDF). For this reason the CDF of in-class likelihood PDFs is used to determine the decision confidence. An example of a likelihood CDF is shown in figure 6. At any likelihood x the CDF evaluates the probability $P(p(a, l | \omega_i) \leq x)$, which is represents the decision confidence. Note that both the likelihoods and the CDFs are probabilities and therefore their values are in the range $[0, 1]$. Additionally, $P(p(a, l | \omega_i) \leq 0.0) = 0$
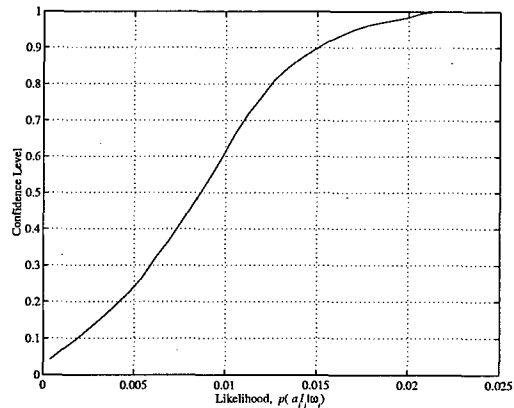

Figure 6: In-Class likelihood CDF used to determine decision confidence.

and $P(p(a, l | \omega_i) \leq 1.0) = 1$ represent the minimum and maximum confidence values.

To obtain the confidence measure a target class hypothesis, ω_{hyp}, must be made. It is therefore assumed that the observation belongs to class ω_{hyp}, resulting in the in-class likelihood $p(a_j l_j | \omega_{hyp})$. The ω_{hyp} decision confidence for peak j is calculated by evaluating the likelihood CDF at $p(a_j l_j | \omega_{hyp})$. This value represents the confidence that the observed peak is associated with class ω_{hyp}. To clarify, if $p(a_j l_j | \omega_{hyp}) = 0.015$, then the confidence level associated with the classification decision is approximately 0.9 when using the CDF in figure 6.

It should be noted that the confidence value is associated with a specific target class hypothesis, ω_{hyp}. Therefore, each target hypothesis of interest must have an associated confidence value for each of the k extracted peaks in an observation. Typically this corresponds to calculating a confidence value for each of the n target classes, ω_i. How these beliefs are used is the subject of the next section.

2.2.2 Multi-hypothesis Belief

In the beginning of this section the basic probabilistic information to perform classification was obtained for individual peak features. These data are the class likelihood, *a posteriori* probabilities and decision confidence. These are used to develop a set of beliefs for specific target hypotheses. This is graphically represented in figure 7.

Figure 7 shows that the confidences are obtained directly from the joint likelihoods, as discussed in the previous section. The confidences are then used to
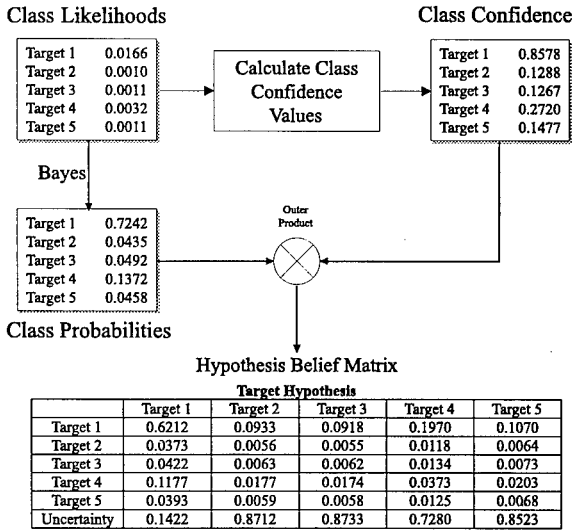
Class Likelihoods

Target 1	0.0166
Target 2	0.0010
Target 3	0.0011
Target 4	0.0032
Target 5	0.0011

Bayes

Calculate Class
Confidence
Values

Class Confidence

Target 1	0.8578
Target 2	0.1288
Target 3	0.1267
Target 4	0.2720
Target 5	0.1477

Target 1	0.7242
Target 2	0.0435
Target 3	0.0492
Target 4	0.1372
Target 5	0.0458

Class Probabilities

Outer
Product

$\bigotimes$

Hypothesis Belief Matrix

Target Hypothesis

	Target 1	Target 2	Target 3	Target 4	Target 5
Target 1	0.6212	0.0933	0.0918	0.1970	0.1070
Target 2	0.0373	0.0056	0.0055	0.0118	0.0064
Target 3	0.0422	0.0063	0.0062	0.0134	0.0073
Target 4	0.1177	0.0177	0.0174	0.0373	0.0203
Target 5	0.0393	0.0059	0.0058	0.0125	0.0068
Uncertainty	0.1422	0.8712	0.8733	0.7280	0.8523

Figure 7: Generation of the belief hypothesis matrix

weight the class *a posteriori* probabilities to create a belief in a specific target class. The beliefs are found using

$$b_{\omega_{hyp}}(\omega_i | l_j a_j) = C^j_{\omega_{hyp}} P(\omega_i | l_j a_j), \qquad (4)$$

where $C^j_{\omega_{hyp}}$ is the confidence that the jth peak is associated with the target hypothesis ω_{hyp}. Since the confidence is based on a class hypothesis the beliefs actually generate a table, each column of which is associated with a particular class hypothesis, as seen in figure 7. Additionally, an uncertainty value is calculated as $U^j_{\omega_{hyp}} = 1 - C^j_{\omega_{hyp}}$ and appended to the bottom of belief hypothesis matrix. Note that since the sum of the *a posteriori* probabilities is unity, the sum of the beliefs and uncertainty for any given hypothesis is also unity,

$$U^j_{\omega_{hyp}} + \sum_{i=1}^{n} b_{\omega_{hyp}}(\omega_i | l_j a_j) = 1. \qquad (5)$$

Generation of the beliefs and uncertainties in this way directly ties the confidence that an observed feature is associated with a target hypothesis. For this reason, a high uncertainty occurs when the likelihood that the observed feature is not associated with the hypothesized target. This is exactly the type of information that is needed to reject unknown target observations.

It is not expected, however, that the individual peak-based classifications and uncertainty values will result in robust classifier performance, rather they are bits of evidence that are accrued. Robustness and confidence are obtained through fusion of the individual

feature decisions. The manner in which these features are fused is presented in the next section.

2.2.3 Multi-Peak Evidence Accrual

For each feature extracted from an observation a belief hypothesis matrix is generated as seen in figure 8. Each of these matrices contain evidence that is accrued to aid in the acceptance or rejection of each target class hypothesis.

The beliefs are fused using Dempster's rule of combination [7]. This rule is actually very similar to Bayes rule as applied here. In fact the sum of the beliefs and uncertainties (5) equates to unity just as the Bayesian probabilities. For this application this rule is calculated as

$$b(a_1 a_2) = \frac{b(a_1)b(a_2) + U^1 b(a_2) + U^2 b(a_1)}{1 - \sum_{j=1}^{n} \sum_{\substack{k=1 \\ k \neq j}}^{n} b(a_1)b(a_2)}, \qquad (6)$$

where the denominator normalizes the beliefs. The fused uncertainty can be updated with the new beliefs using (5) or by

$$U^{1,2} = \frac{U^1 U^2}{1 - \sum_{j=1}^{n} \sum_{\substack{k=1 \\ k \neq j}}^{n} b(a_1)b(a_2)}. \qquad (7)$$

Equations (6) and (7) show the fusion of information for two different features. As demonstrated in figure 8, these equations are recursively applied to the entire set of extracted features to calculate the overall class beliefs and uncertainties for a specific class hypothesis. The calculations are performed for each combination of target class in the training set and for each target hypothesis. If a classifier is trained on five target classes and a hypothesis is made for each class, the resulting set of beliefs is shown at the bottom of figure 8.

This belief table consists of accrued belief for each target class given each target class hypothesis. Additionally, the last element of each column is the fused uncertainty associated with a specific target class hypothesis. The target classification decision is made by selecting the largest belief on the diagonal of this table. These are the belief values for a specific target class ω_i under the hypothesis that the correct class is indeed target class ω_i. The degree to which the classification decision is accepted depends on the uncertainty, U_{ω_i}. How the uncertainty is used in the decision process is the topic of the next section.
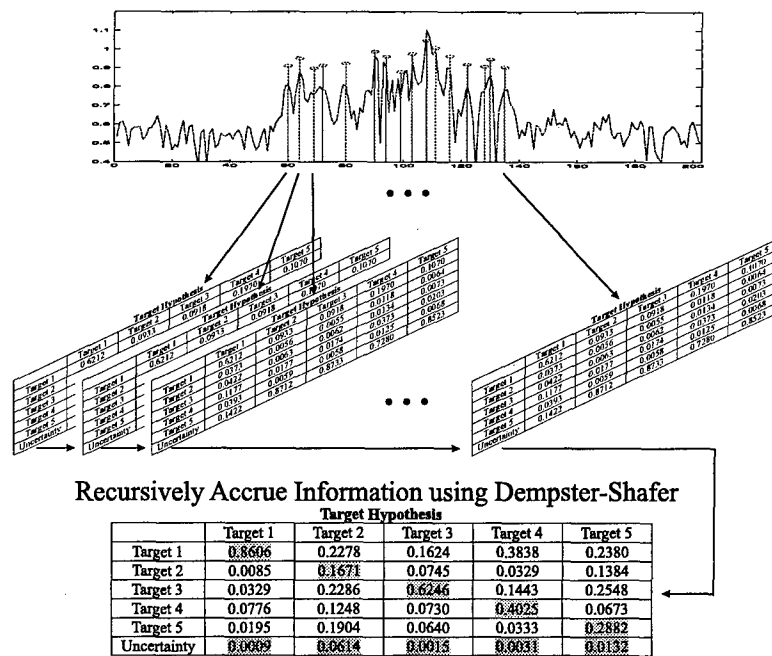
Recursively Accrue Information using Dempster-Shafer

Target Hypothesis

	Target 1	Target 2	Target 3	Target 4	Target 5
Target 1	0.8606	0.2278	0.1624	0.3838	0.2380
Target 2	0.0085	0.1671	0.0745	0.0329	0.1384
Target 3	0.0329	0.2286	0.6246	0.1443	0.2548
Target 4	0.0776	0.1248	0.0730	0.4025	0.0673
Target 5	0.0195	0.1904	0.0640	0.0333	0.2882
Uncertainty	0.0009	0.0614	0.0015	0.0031	0.0132

Figure 8: Belief hypothesis evidence accrual.

2.2.4 Decision Rejection Based on Low Confidence

Using the fusion techniques described above, one obtains a target class belief and uncertainty under some target class hypothesis. The decision uncertainty is used to determine the quality of the target classification. The specific interest is to determine when classification errors are made. The approach to rejecting incorrect decisions is identical for known and unknown targets.

The technique statistically models the uncertainty associated with a correct target class hypothesis. These data are generated by using in-class uncertainty statistics determined from the training ensemble. These "in-class" statistics are the uncertainties associated with classification of target class ω_i under the hypothesis that the target is from class ω_i. An example of an in-class and an out-of-class uncertainty CDF, with several thresholds, is shown in figure 9. The technique for setting classification thresholds is known as a Neyman-Pearson decision rule [6].

3 RESULTS

The StaF classification algorithm described in this paper and in [1, 2] has been used to generate classifier results for aircraft using HRR radar data. The primary purpose of the testing in this paper is to determine the capability of the StaF classifier to reject unknown targets while maintaining high known target
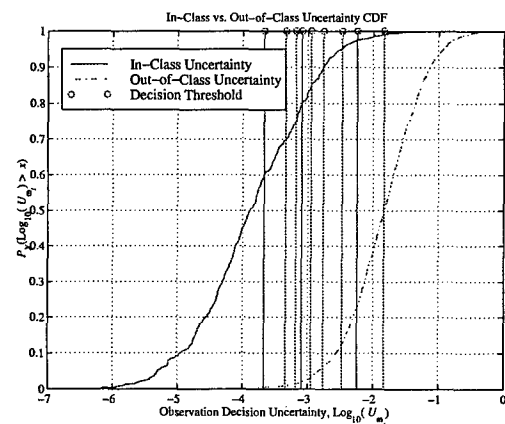
Figure 9: Uncertainty CDFs with decision thresholds.

identification rates. StaF classifier results are compared to baseline results from a constrained quadratic classifier [6].

To determine the classifier performance three classification parameters are calculated. These parameters are P_{dec}, P_{cc} and $P_{mis-unk}$, as defined in section 1. Both P_{cc} and $P_{mis-unk}$ are conditional probabilities, dependent on a target class identification declaration. For this reason P_{cc} and $P_{mis-unk}$ are plotted as a function of P_{dec}. Plots such as these are typically called receiver operator characteristic (ROC) curves. From these plots the classifier performance is totally specified once a P_{dec} value is selected.

For the StaF classifier the quality of classification decisions is based on the level of uncertainty associated with those decisions. Rejection of these uncertain decisions is performed by setting uncertainty thresholds as discussed in section 2.2.4. If the uncertainty is greater than the threshold, no decision will be made regarding the observation. The baseline classifier unknown rejection is essentially the same, only the rejection criteria is based on the likelihood values. Selection of a decision threshold directly effects the P_{dec} and indirectly effects P_{cc} and $P_{mis-unk}$.

Previous results have shown that the StaF classifier performs better than the baseline classifier when evidence is accumulated over multiple observations [2]. The results were based on classification of five target classes using a target class leave-one-out-method (LOOM) to simulate unknown target classes [6]. The new results presented in this paper are based on a true five known, five unknown target test. The five known targets are exactly the same five as used in the LOOM test. The five unknown targets are five totally different targets. In section 3.1 the LOOM results are presented. Then in section 3.2 the new true five known five unknown target test results are presented and compared with the LOOM results.

3.1 LOOM Unknown Target Test
Rejection of unknown target classes is typically a difficult problem in ATR. Adjusting the classifier to reject unknown targets requires the declaration rate to be severely reduced. Even then the performance is unreliable. To improve the performance it is often necessary to accrue evidence over multiple target observations. For the tests presented in this section performance results are generated for one, two and five observations. The benefit of this evidence accrual will be obvious when evaluating the performance.

The unknown target tests results are presented as two sets of curves. The first set of ROC curves relate P_{cc} as

a function of P_{dec}. The LOOM results are shown in figure 10 for both the baseline and StaF classifiers. It is found that the baseline classifier performs better than the StaF classifier for single-look decisions. However, the StaF classifier exceeds the baseline performance for multi-look decisions. However, the performance of both methods is so good that the difference in performance may be negligible. However, the interesting results involve the $P_{mis-unk}$ vs. P_{dec} ROC curves.

The $P_{mis-unk}$ vs. P_{dec} ROC curves are shown in figure 11 for both the baseline and StaF classifiers. For the single-look results the performance is fairly equivalent. However, the StaF classifier again begins to out perform the baseline classifier. In fact, for the five-look result at 0.95 declaration rate, the StaF classifier $P_{mis-unk}$ is approximately 44% lower than that of the baseline classifier. This is a significant improvement in performance. In general, the knee of the multi-look StaF ROC curves is approaching the lower right hand corner more quickly than the baseline classifier. This results in lower $P_{mis-unk}$ for a given P_{dec}, as desired.
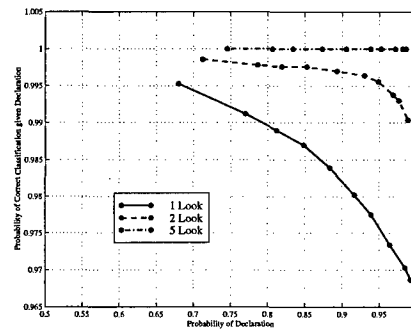
3.2 True Unknown Target Test
The results shown in the previous section show that the StaF classifier performs better than the baseline for multiple observation decisions. However, the results were limited to five target classes. In this section a similar test is performed only additional targets are introduced. The known target classes and data are exactly the same as those found in the LOOM test. However, the unknown targets are five totally different target classes. Therefore, this test has five true known and five true unknown targets in the test.

Since the known target classes are exactly the same as in the LOOM test it is expected that the P_{cc} should be very similar. The performance will not be identical because the LOOM test was really only a four target test. The five-look performance P_{cc} vs. P_{dec} ROC curve is shown in figure 12 for both the baseline and StaF classifier. As expected, when compared to the five-look results shown in figure 10 the performance is very similar. The one-look P_{cc} results do show a significant drop in performance but the multi-look results are very similar to the LOOM results.

While the known target performance was essentially known from the LOOM test, the unknown target rejection performance is not. The classifiers were trained with no information about the unknown targets. Any degredation in performance is due purely to the expansion of the known target set (from four to five) and the difference in similarity of the unknown targets to the known targets. The results are shown in figure 13.
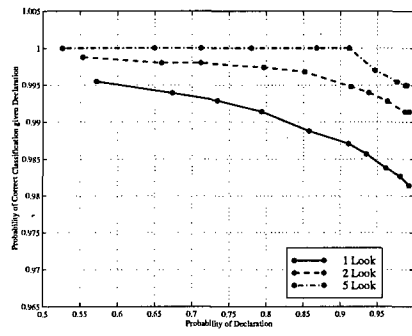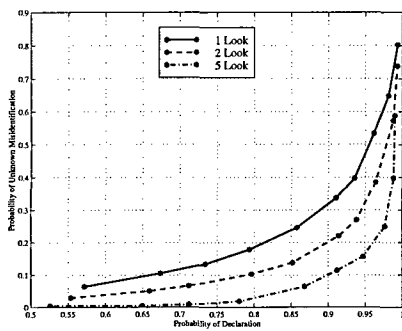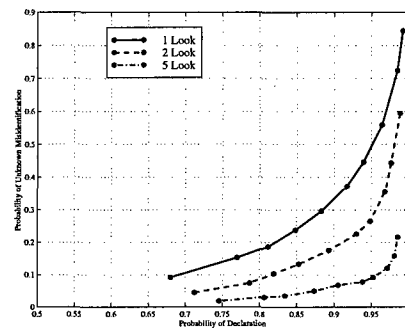
(a)　　　　　　　　　　　　　　　(b)

Figure 10: LOOM correct classification vs. declaration rate for the (a) baseline and (b) StaF classifiers.

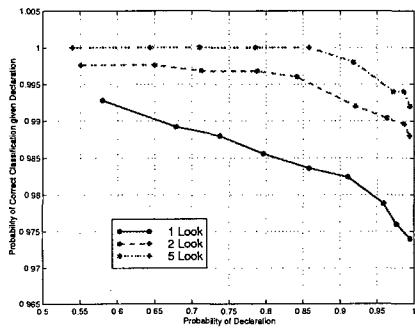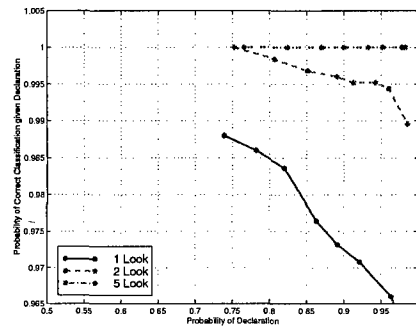
(a)　　　　　　　　　　　　　　　(b)

Figure 11: LOOM unknown target error vs. declaration rate for the (a) baseline and (b) StaF classifiers.

(a)　　　　　　　　　　　　　　　(b)

Figure 12: True unknown test correct classification vs. declaration rate for the (a) baseline and (b) StaF classifiers.
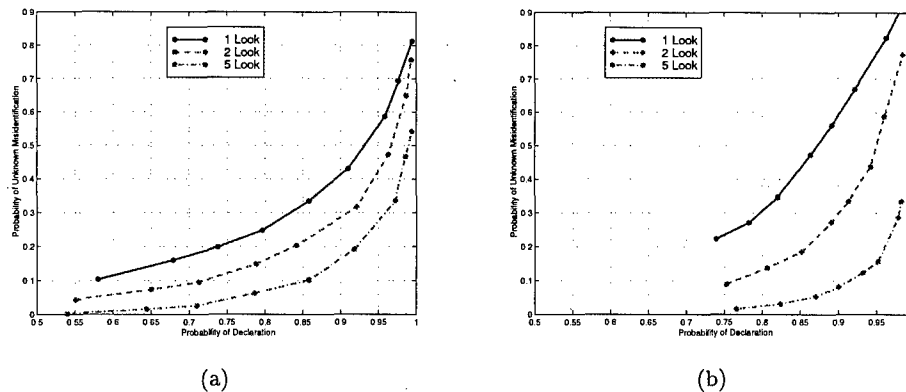
(a)   (b)

Figure 13: True unknown test probability of mis-identifying an unknown target vs. declaration rate for the (a) baseline and (b) StaF classifiers.

The unknown target error rates are found to be higher for this test configuration than for the LOOM test. However, the StaF classifier once again performed better than the baseline for the five-look decisions. At a declaration rate of 95% the baseline classifier misidentifies unknown targets at a rate of approximately 25% whereas the StaF only misidentifies at a rate of approximately 15%. This is a 60% reduction in unknown target errors when the StaF classifier is used.

While the two ROC curves characterize the overall performance, it is sometimes helpful to view the more detailed information associated with confusion matrices. For this reason a five-look StaF confusion matrix is included in table 1. Here an operating point is specified for five-looks decisions with $P_{dec} = 0.95$. The performance is then specified to have a $P_{cc} = 1.0$ and a $P_{mis-unk} = 0.15$.

Investigation of the unknown errors show that target Unknown 2 is the most difficult of the unknown targets to reject. Approximately 27% of Unknown 2 observations tested were classified as either Target 2 or Target 4. Additionally it is observed that target Unknown 5 was misidentified 14% of the time. More importantly, both Unknown 2 and Unknown 5 appeared to be misidentified as Target 4. This is of interest because it is also noted that Target 4 was correctly identified 100% of the time and declared with a probability of 99%. These two pieces of information indicate that the declaration threshold for Target 4 may be set too high, resulting in fewer rejections than desired. It is tempting to modify this threshold to reduce the unknown target misidentification errors but such modifications should not be made. Thresholds should never be changed based on test results because

one may be optimizing the classifier based on data that is not representative of the entire data space. For this reason the thresholds will not be changed based on this test information.

3.3 CONCLUSION

To date, most HRR ID algorithms have remained very basic [8], using the entire range profile as a feature vector. Often this approach was taken because the signatures were so random that reliable feature extraction was difficult. Even when features were extracted [4,9,10], effective classification techniques were not available.

The StaF classifier is a unique feature based approach for classification of HRR signals [1]. The classifier is based on the location and amplitude of signature peak features. One unique aspect is that the peak locations are not predefined in the classifier training. The features are instead extracted on the fly based only on information contained within the observed signature. Therefore, the number and locations of the features are variable from one observation to the next. Additionally, the classifier generates decision uncertainties which help to determine the quality of the classification decision.

Results were presented from two different tests. Both tests showed that the StaF classifier more effectively rejected unknown targets, relative to the baseline classifier. This unknown rejection performance was obtained while maintaining equal or better correct classification performance. These results are very encouraging but they may be optimistic for both classifiers because. This is because one complicating factor has not been factored into the results. This factor is the registration of the observation to the statistical model. In these test it was assumed that the

Table 1: Five-Look StaF Classifier Results, $P_{dec} = 0.95$

	Target 1	Target 2	Target 3	Target 4	Target 5	Reject
Target 1	0.89	0	0	0	0	0.11
Target 2	0	0.94	0	0	0	0.06
Target 3	0	0	0.99	0	0	0.01
Target 4	0	0	0	0.99	0	0.01
Target 5	0	0	0	0	0.95	0.05
Unknown 1	0.10	0	0	0	0.03	0.87
Unknown 2	0.01	0.13	0	0.14	0	0.73
Unknown 3	0	0.13	0	0	0	0.87
Unknown 4	0	0	0.03	0.02	0.06	0.90
Unknown 5	0.01	0	0	0.13	0	0.86

correct registration was known between the observations and the target statistics.

In a field test, the observations need to be registered such that the target signature is correctly aligned with the stored target statistics. The on-the-fly registration has been shown to be a difficult problem [11]. For this reason it is expected that the performance of both the baseline and the StaF classifiers will see a reduction in performance when signatures registration is required. Registration on-the-fly has been investigated for the baseline classifier but not for the StaF classifier. Note, however, that the registration was exactly the same for both classes throughout the classifier tests presented in this paper. The currently unanswered question is whether or not the StaF classifier will maintain its superior relative classification performance when registration is performed on-the-fly. Studies regarding the StaF registration are currently being investigated.

In closing, the StaF classifier has been shown to be superior in rejection of unknown target classes. Unknown target rejection is a problem that plagues not only HRR ID, but the entire ATR community. This is an area of research that has little attention in the literature, therefore advances in this area are drastically needed. The StaF classifier introduces some new concepts to handle this very difficult problem.

References

[1] Richard A. Mitchell, *Robust High Range Resolution Radar Target Identification using a Statistical Feature Based Classifier with Feature Level Fusion*, Ph.D. thesis, University of Dayton, Dayton, OH, December 1997.

[2] Richard A. Mitchell and John J. Westerkamp, "A statistical feature based classifier for robust high range resolution radar target identification," *IEEE Transactions on Aerospace and Electronic Systems*, Submitted December 1997.

[3] E. T. Jaynes and C. R. Smith, "Theory of radar target discrimination," Tech. Rep., U.S. Army Missile Command, 1991.

[4] Kie Eom and Rama Chellappa, "Non-cooperative target classification by hierarchical modeling of high range resolution radar signatures," Tech. Rep., Center for Automation Research, University of Maryland, 1995.

[5] Richard A. Mitchell and Robert DeWall, "Overview of high range resolution radar target identification," in *Automatic Target Recognition Working Group*, Monterey, CA, 1994.

[6] Keinosuke Fukunaga, *Introduction to Statistical Pattern Recognition*, Academic Press, Inc., second edition, 1990.

[7] E. Waltz and J. Llinas, *Multisensor Data Fusion*, Artech House, 1990.

[8] Edmund W. Libby, *Application of Sequence Comparison Methods to Multisensor Data Fusion and Target Recognition*, Ph.D. thesis, Air Force Institute of Technology, 1993.

[9] Mark R. DeWitt, "High range resolution target identification using the prony model and hidden markov models," M.S. thesis, Air Force Institute of Technology, 1992.

[10] Eric T. Kouba, "Recurrent neural networks for radar target identification," M.S. thesis, Air Force Institute of Technology, 1992.

[11] Pete Kosir, Robert DeWall, and Richard A. Mitchell, "A multiple measurement approach for feature alignment," in *National Aerospace and Electronics Conference*, Dayton, OH, 1995.

Non-cooperative target identification of isolated aircraft with real-time optical feature extraction and classification of high range resolution data

Charles Garvin* and Kelvin H. Wagner

Optoelectronic Computing Systems Center
Department of Electrical and Computer Engineering
University of Colorado, Boulder, CO 80309-0525

Abstract

Real-time non-cooperative target identification of wide bandwidth high resolution radar (HRR) returns is beyond the capabilities of many conventional digital signal processing approaches due to limitations on available computing resources, and is an appropriate task for a high-speed optical classifier. We have designed and constructed a feature-based adaptive multi-layer optical classifier for this task. The demonstrator consists of a feature extractor which computes a time-frequency representation of HRR returns cascaded into an adaptive linear machine utilizing multiplexed photorefractive volume holograms. Optical adaptation of stored weights enables the classifier to learn to identify a training set of aircraft radar range profiles. The trained optical system identifies aircraft with varying orientation and/or range from the radar using untrained HRR returns from the same aircraft. Single radar pulse classification of aircraft is demonstrated using labeled range profiles extracted from 1987 Paris Airshow data. Although trained on a single head-on aspect profile for each class, surprisingly good generalization performance has been demonstrated, and the optically trained weights generalize over limited aspect and unlimited range variations of the targets. These results demonstrate the power of adaptive optical connectionist systems for challenging real-world signal processing problems such as real-time non-cooperative classification of isolated aircraft targets using a single radar range profile.

* Current address: Lockheed Martin Sanders,
65 Spit Brook Rd, Nashua, NH, 03061-0868;
charles.g.garvin@lmco; (603) 885-6816.

1 Introduction

Target recognition using shape-, and position-dependent radar reflectivity was suggested as early as thirty years ago,[1] and has remained an area of active research throughout this time. As the variety of applications for wide bandwidth radar sensors increases, so too does the need for high-speed processing of radar data. In person-in-the-loop situations such as fire control and autonomous situations such as smart weapon guidance, the need for real-time pulse-to-pulse non-cooperative target identification (NTCI) is critical. NCTI on a pulse-to-pulse basis using HRR returns requires greater spatio-temporal processing resources than are typically available using general-purpose digital computing hardware. Optical signal processing architectures provide the spatial parallelism and computation speed that are necessary to meet the requirements of real-time high-bandwidth radar processing. NCTI is therefore an appropriate task for a high-speed optical classifier architecture. In this paper we review the design and operation of an optical signal processing architecture for adaptive spatio-temporal feature based signal processing that is well matched to a NCTI problem and we present experimental demonstration of single radar pulse classification of isolated aircraft.

In section 2, we describe the adaptive multi-layer optical architecture and discuss the training and operation of the classifier. In the third section we present experimental results of single-pulse non-cooperative radar target identification of isolated aircraft radar returns using a one-of-four class problem. We recommend future applications and additional research in the final section.

2 Adaptive optical classifier

The proper role of adaptive optical architectures is to leverage high operational speed and parallelism to provide timely solutions to otherwise intractable processing problems. This paper describes and demon-

strates an adaptive optical classifier consisting of an acousto-optic (AO) feature extractor cascaded through an optically addressed spatial light modulator (OASLM) into a volume holographic implementation of a trainable linear classifier. Using a multiple exposure error-driven learning scheme, the classifier interconnection weights adapt to classify the AO preprocessed features of wide-bandwidth temporal signal training sets. Error feedback for the learning procedure, along with device control for the different modules making up the classifier, is provided using a computer. The cascaded optical classifier in figure 1 demonstrates the unique applicability of optical computing components to problems of real-time wide-bandwidth temporal signal classification. The main subsystems of this cascaded optical classifier are described in detail in the following sections.

2.1 Acousto-optic triple product processor feature extractor

The feature extractor used in the cascaded classifier is a time-integrating (TI) triple product processor (TPP).[2] The TPP provides a high dimensional computational feature with range invariance[3] which is highly separable even with a single layer classifier. Previous implementations of the TI TPP,[4] used the processor output from the CCD detector and electronic postprocessing to classify the results. This serial processing acts to restrict the system throughput and the massive quantities of data produced seriously overburdens the electronic digital postprocessing. An optical classifier with a parallel interface that matches the data throughput can be used as a post-processor, thus avoiding the electronic bottleneck.

For rapid processing of high data rate temporal signals (such as radar returns), the TPP architecture is implemented using bulk acousto-optic devices, one AO device for each processed signal. The combined multiplicative and additive architecture is shown in figure 2. Expanded, collimated argon laser light (514.5 nm) is split into two arms of a Mach-Zehnder interferometer. In one arm of the interferometer, light in the first diffracted order of one $f_c = 50$ MHz center frequency TeO_2 AO device is passed through another $f_c = 50$ MHz TeO_2 AO device. A 1:1 telescope is used to reverse image the illuminated aperture of the first AO device onto the second AO device, and the intervening Fourier plane is used to spatially filter out the undiffracted light. The doubly-diffracted light from these two AO devices is similarly imaged and filtered with another

lens through a combiner cube to an output CCD array and onto the write side of an OASLM. Using this combiner cube, this light is added to light diffracted from a single $f_c = 100$ MHz TeO_2 AO device (similarly imaged and filtered) in the other arm of the interferometer. A Dove prism is used to orient the doubly-diffracted images of the AO devices in one arm orthogonal to the singly-diffracted light from the other arm to create a two-dimensional interference plane. A spherical lens system images the output light from one port of the combiner cube to a camera (or other time- integrating, square law detector), the other output port can be used simultaneously to illuminate the OASLM. The output of a square law, time-integrating detector results in the baseband cross term on a spatial carrier ($\cos(\vec{k} \cdot \vec{r})$ where $\vec{k}$ is determined by horizontal and vertical tilts of the combiner cube), all riding on a signal dependent bias

$$C(x,y) = \text{bias} + 2\cos(\vec{k} \cdot \vec{r}) \qquad (1)$$
$$\int S_1\left(t - \frac{y}{v_a}\right) S_2\left(t + \frac{y}{v_a}\right) S_3\left(t - \frac{x}{v_a}\right) \, dt$$

where x and y are shown in figure 2.[5] Different time-frequency transforms[6] can be implemented with the AO TPP by appropriately programmable input signals. Making the substitution $t - \frac{y}{v_a} = t'$, and assuming a single purely real signal as the modulation to all three AO devices results in the triple autocorrelation of the modulation $S(t)$ as the output of the AO TPP

$$C(S : \tau_x, \tau_y) = 2\cos(\delta'(\tau_y - \frac{\tau_x}{2})) \qquad (2)$$
$$\int S\left(t'\right) S\left(t' - \tau_x\right) S\left(t' - \tau_y\right) \, dt$$

The coordinates in this representation are mixed functions of the physical coordinates

$$\tau_x = -\frac{2y}{v_a} \; ; \; \tau_y = \frac{x - y}{v_a} \qquad (3)$$

An optically addressed spatial light modulator provides the necessary temporal integration in equation 3, along with an adjustable saturating intensity nonlinearity. In the cascaded optical system shown in figure 1, the read light illuminating the OASLM is modulated by the feature computed by the TPP and integrated on the OASLM, and the resulting schlieren filtered image is used as the input to the adaptive holographic classifier. Schlieren filtering removes the bias terms and demodulates a single sideband of the triple product integral from the spatial carrier. A Hughes homeotropically-aligned nematic

liquid crystal light valve (LCLV) is currently used as the OASLM, although ferroelectric liquid crystal SLMs have also been used in the same role to obtain faster response. Schlieren imaged AO TPP outputs for two low-pass filtered radar range profiles are shown in figures 4e and 4f.

2.2 Adaptive photorefractive classifier

The adaptive volume holographic classifier implements a bank of correlators in which the matched filter functions are represented by weights stored in a series of angularly-multiplexed volume holograms in a photorefractive crystal. In this implementation of a linear machine, the angle of a plane wave reference beam represents the output class. Volume holographic storage of the classifier weights using a photorefractive crystal provides the advantages of real-time adaptivity along with large weight capacity and fully parallel weight accessibility. Classifier weights W_{ij} are stored using the interference between the triple autocorrelation for exemplars of a specific signal class and the plane wave reference corresponding to that class. Using a dynamic holographic storage material allows the modification of the stored weights which permits the implementation of complex on-line learning algorithms. Photorefractive dynamics mimic weight decay, so an incremental recording scheme[7] is used to store multiple classifiers to equal diffraction efficiencies. When the stored weights are being read out, only the relatively low power signal beam (schlieren imaged output of the OASLM) illuminates the photorefractive crystal. This readout beam is diffracted by the stored gratings into plane wave reconstructions at the appropriate angles. When the diffracted plane waves are Fourier transformed onto a linear array of detectors using a lens, each class corresponds to a different spatial location on the detector array. The detector output is compared with the desired output using a digital computer. In what follows, we first describe the single-layer network and training algorithm. Next, the optical implementation of the training procedure using photorefractive weight storage is described.

With $\vec{x}$ representing the input feature vector (with $O[N^2]$ components lexicographically ordered in the two spatial dimensions computed by the AO TPP), $g(\ldots)$ representing the thresholding (activation) function, and θ_i representing the i-th threshold level, the i-th output (of L) of the linear machine is given by

$$O_i(\vec{x}) = g\left(\sum_{k=1}^{N^2} W_{ik}x_k - \theta_i\right)^T \qquad (4)$$

In a single-layer neural classifier, the classifier weights W_{ik} for a set of orthogonal vectors can be computed using a single pass of a learning rule such as the Hebb rule. In order to correctly classify non-orthogonal features, iterative error-driven learning algorithms can be used.[8] For each training epoch of the iterative procedure, the weights are modified by the outer product of the network error and the feature vector $\vec{x}$ for each exemplar randomly selected without replacement from the training set of P signals. In such a procedure, the weights after the first epoch of training are given by the outer product relation

$$W_{ik} = \sum_{\mu=1}^{P} D_i^\mu x_k^\mu \qquad (5)$$

where $\vec{D}^\mu$ is the desired output vector that corresponds to the μ-th input signal S^μ which is transformed by the AO TPP in equation 3 into the intermediate representation vector $\vec{x}^\mu = C(S^\mu)$. In a supervised error-driven learning algorithm, repetitive comparison of network outputs to the labeled training set inputs provides the corrections to modify the stored weights using the generic weight update of equation $W_{ik}^{new} = W_{ik}^{old} + \Delta W_{ik}$. The gradient descent least-mean-square learning procedur used here computes $\Delta W_{ik} = -\rho(D_i - O_i)x_k$ to modify the network input/output mapping. Network performance is monitored using the sum-of-squared-error metric: $SSE = \frac{1}{2}\sum_{i=1}^{L}\sum_{\mu=1}^{M}\|D_i - O_i\|^2$ computed after each epoch.

The feed forward optical training passes the acousto-optically computed TPP feature of each training signal through a thresholding square law nonlinearity and interferes the schlieren image of the modulated LCLV output in the photorefractive material with a corresponding coherent plane-wave reference. On the first pass through the training signals, one appropriately scheduled exposure is made for each schlieren-imaged AO TPP feature interfered with the desired reference beam at the predetermined Bragg resolved angles to store these features in the photorefractive material with equal diffraction efficiency.[9] Subsequent training epochs require more complex exposure sequences based on incremental pertubations to the existing weights. For each pattern on the OASLM, the error for all L outputs must be computed and all of the holograms will potentially need to be reexposed and the decay of the previously exposed holograms must be compensated. Using multiple volume hologram storage dynamics,[10] and assuming the reference beam is much stronger than the AO TPP pattern, the expression

for the weight evolution is

$$\frac{\partial W_{ik}}{\partial t} = \alpha R_i(t)x_k(t) - \beta(\|R_i\|^2 + \sum_k \|x_k\|^2)W_{ik} .$$

(6)

The parameter α represents learning gain and β represents decay or forgetting rate of the photorefractive material. For subsequent epochs, the photorefractive material is exposed using the AO TPP feature of each signal in the training set sequentially along with every reference beam thus $x_k(t)$ is held constant while each of the reference beams $R_i(t)$ is appropriately exposed. The exposure time for these updates is a small fraction of the photorefractive material time constant modified by the product of the magnitude of the corresponding error $(D_i - O_i)$ and a learning rate ρ. The error term $(D_i - O_i)$ in the weight update expression can be bipolar so that either selective enhancement or erasure of individual weights may be necessary. Each reference beam is used to enhance desired weights or is π-shifted to erase undesired weights, depending on the sign of the computed error. To account for their incoherent erasure during selective erasure of undesired weights, desired weights are given a small enhancement during each epoch. The connection weights incrementally approach the desired mapping until the measured performance exceeds a set threshold where training ceases.

Selective coherent erasure of photorefractively stored volume holograms is accomplished by inducing a π-radian phase-shift in the interference fringes produced by the signal and reference beams in the photorefractive material and then re-exposing the volume hologram. With the weights of a linear classifier stored as volume holograms in a photorefractive material, this process has been used to implement an error-driven training procedure. Modification of many stored holograms is accomplished by supplying a number of angularly multiplexed reference beams whose phase and amplitude are independently controlled by error-signals $E_i = (D_i - O_i)$ proportional to the difference between the detected reference beams reconstructed by the stored holograms and a desired target vector $\vec{D}$ during the training cycle described above. The bipolar error-signal is interpreted in the following manner: positive values represent the need to reinforce a hologram diffracting incident light to a given angle; negative values represent the need to reduce the efficiency of that hologram. To implement this bipolar error-signal, it is necessary to vary the phase and the exposure time of each reference beam in such a manner that they selectively reinforce or erase the appropriate recorded hologram. Exposure time or amplitude modulation encodes the magnitude of the error signal, and the sign of the error signal corresponds to the phase of the reference beam relative to the signal beam. To reinforce the stored hologram representing an interconnection weight between two vectors, the hologram is re-exposed with the original set of input/output vectors. To erase an existing stored hologram, the reference beam with phase delayed by π-radians and at the appropriate angle illuminates the photorefractive material along with a signal. In the cascaded systems discussed here, a voltage-controlled nematic liquid crystal variable waveplate shifts the reference phase by π-radians for selective, coherent erasure.

2.3 Computer control of the cascaded system

A laboratory computer is used for control and some operation functions of the classifier. For example, the signals for the classification demonstration exist in the computer disk archive and are supplied to the cascaded classifier using an arbitrary waveform generator. The computer controls all of the instruments necessary to implement the learning algorithm over a GPIB bus. This computer provides a user interface and accomplishes the gradient-based error driven learning algorithm to identify each of three radar range profile targets with the cascaded optical classifier. User modifiable control parameters (e.g. maximum number of epochs, minimum error threshold, etc.) permit tuning of the learning behaviour. The operation of the optical system can be monitored by the user during learning, and the computer tracks the initial classification performance after one training epoch, the current classifier performance on the training set and the overall training performance over the training time using a learning curve which reports the sum of squared classification error. After the optical system has learned the training data, the user interface provides for testing using untrained radar data from the disk archive.

3 Radar target classification

Classification speed is a critical factor in a radar target identification application. Single pulse classification of radar range returns is computationally intensive and may not be amenable to conventional DSP techniques, and so it is a valuable demonstration problem for the adaptive cascaded optical classifier architecture. What follows is a review of the

radar data used in the training and test sets and a summary of optical classification results.

3.1 Radar profile dataset

The dataset used in these classification experiments were made available to us by the USAF Rome Laboratories. The radar data were taken using a linear-FM radar in the S-band (2-4 GHz). The radar waveform consisted of linearly chirped 77 μsec pulses with a 320 MHz chirp bandwidth (range resolution $\doteq \frac{c}{2B} \approx 0.5$ m). Labeled 0.5 meter resolution range profiles were extracted from these data with the radar acquisition hardware during illumination (see figures 3a and 3b for examples). Varying numbers (ranging from 1 to 30) of individual pulse returns were reported together with range azimuth and elevation estimates extracted from radar antenna gimbal position, as well as target aspect angle estimate (± 10 deg) from radar tracking results. From the available data, 6 classes were sampled into independent training, validation, and test sets. Training data were randomly extracted from these available data; the results shown below use nominal head-on aspect training data only. The initial radar profile training sets for the adaptive classifier were low-pass filtered, resampled at a lower sampling rate (one tenth), and normalized to maximum value to construct two datasets which are used in the following experiments. Two range profiles in the 5 meter resolution training set are shown in figures 4a and 4b.

3.2 Isolated aircraft classification from radar range profiles

In figure 4c and 4d, a small window of the Schlieren-filtered outputs from the AO triple autocorrelator is shown for two of the radar range profiles used in training the adaptive classifier. The triple autocorrelation representation is not an orthogonalizing transformation for general radar range returns, however, it is reasonable to expect that this transformation provides more readily linearly separable representations of the exemplars of radar range returns. Digital simulations of the triple autocorrelation representation and the adaptive classifier have been used to motivate this assertion.

A typical optical classification experimental result of the cascaded system is shown in figure 5 for a one-of-four aircraft recognition problem using 5 meter resolution radar profiles. Optically-computed triple product features of single pulse returns were stored in the photorefractive crystal to equal diffraction efficiency using an incremental recording error-driven learning scheme. Figure 5a shows normalized linescans from the reconstructed plane wave references focussed onto a detector array when the trained classifier was tested using the training signals; these are the presynaptic outputs of the trained optical system. When each training signal was presented to the feature extractor the appropriate class was indicated by the strongest diffraction from the volume hologram, allowing simple threshold detection. Figure 5b shows the corresponding learning curve. Figure 6 shows representative normalized presynaptic outputs when the (5 meter data) trained classifier was tested using a test set of ten head-on ($\pm 10°$ estimated) aspect aircraft radar range profiles randomly selected from two different encounters for each of the four target classes. When each test profile was presented to the feature extractor, the appropriate class was indicated; 100 % correct classification of all profiles in the set of ten untrained radar range profiles was demonstrated for each of the four classes of aircraft.

For optical networks trained over a shorter number of epochs, good generalization is still observed. Figure 7 shows the generalization performance for two trained optical networks, one for 1 meter resolution data and another for 5 meter resolution data. In the case of these the 1 meter data, training was shut down after only three epochs to avoid overfitting, and this network demonstrated 95% correct generalization over fourty untrained profiles. For the 5 meter resolution data, 80% generalization over untrained profiles was observed for training as short as eight epochs.

Unfixed holograms stored in a photorefractive material can suffer "dark-intensity" mediated decay, slowly erasing due to thermal processes. Various techniques have been demonstrated to counter the effects of dark decay including thermal fixing,[11] electrical fixing,[12] amplification,[13] and periodic refreshing.[14] In order to characterize dark decay in the cascaded optical classifier, measurements of the classification performance on a test set were taken over a period of several days following training. The results of these measurements are shown in figure 8. Figure 8a documents that profiles in the test set are properly classified at the end of training. Three hours after training, untrained signals were correctly classified as shown in figure 8b. Figure 8c shows classification after 6 hours of dark decay. Even approximately two days after training, 100 % correct classification of all untrained exemplars is demonstrated. Although there is significant dark decay, the trained classifier correctly identifies the training set properly even after dark decay. Stored hologram

fixing using one of the aforementioned techniques would provide unlimited future classifications using these trained weights.

4 Summary

We have constructed an adaptive multi-layer optical classifier system consisting of an electronically reprogrammable AO triple product processor cascaded through an OASLM into a volume holographic implementation of a linear machine with adaptive weights stored in a photorefractive material. We have demonstrated that photorefractively stored weights can be adaptively modified implementing a gradient descent error-driven learning paradigm. We have shown that this optical connectionist system can be used for the classification of isolated aircraft targets using the triple autocorrelation representation of their radar range profiles. These results demonstrate the success of using the optical generalized linear classifier for real-time classification of isolated aircraft targets using a single radar range profile.

More extensive characterization of the training and generalization performance of this multi-layer adaptive optical classifier is warranted. We intend to examine the training and generalization performance of the alternate time-frequency representations which can be computed using the AO TPP. Using feature evaluation techniques such as relevance assessment and hierarchical clustering, other time-frequency feature sets (besides the triple autocorrelation) will be examined using a model of the multi-layer optical classifier before attempting to implement them optically. Additional radar training sets will be examined (including distributed radar targets) to explore the applicability of this optical system to other classification tasks.

5 Acknowledgements

References

[1] J.R. Copeland "Radar target classification by polarization properties," Proc. of the IRE, **48** (7), pp. 1290-1296, July, 1960.

[2] T. Turpin, "Time integrating optical processors," Proc. SPIE, vol. **154**, Real Time Signal Processing, pp. 196-203, 1978.

[3] A. Lohmann "Pattern recognition based on triple correlation," Optik, **78** (3), pp. 117, 1988.

[4] I.J. Abramovitz, N.J. Berg, and M.W. Casseday, "Coherent time-integration processors," in *Acousto-optic signal processing: Theory and implementation,* ed. N. J. Berg, and J.N. Lee, Marcel Dekker, NY. 1983.

[5] C. Garvin, and K. Wagner, "Real-time signal classification with an acousto-optic triple-product processor cascaded into a volume holographic classifier," Appl. Opt. 35(20), pp. 3937-3944, July 1996.

[6] L. Cohen, "Time-frequency distributions," Proc. IEEE, vol. **77** (7), pp. 941-981, 1989.

[7] Y. Taketomi, J. Ford, H. Sasaki, J. Ma, Y. Fainman, and S. H. Lee, "Incremental recording for photorefractive hologram multiplexing," Opt. Lett., **2** (16), pp. 2427-79, November 15, 1991.

[8] K. Wagner, and D. Psaltis, "Multilayer optical learning networks," Appl. Opt., **26** (23), pp. 5061-5076, December, 1987.

[9] A.C. Strasser, E.S. Maniloff, K.M. Johnson, and S. Goggin, "Procedure for recording multiple-exposure holograms with equal diffraction efficiency in photorefractive media," Opt. Lett., **14**, pp. 6-8, 1989.

[10] D. Psaltis, D. Brady, and K. Wagner, "Adaptive optical networks using photorefractive crystals," Applied Optics, **27**(9), pp. 1752-1759, 1 May 1988.

[11] J.J. Amodei, W. Phillips, and D.L. Staebler, "Improved electrooptic materials and fixing techniques for holographic materials," Appl. Opt. **11**, pp 390-396, (1972).

[12] Y. Qiao, S. Orlov, D. Psaltis, and R.R. Neurgaonkar, "Electrical fixing of photorefractive holograms in $Sr_{0.75}Ba_{0.25}Nb_2O_6$," Opt. Lett., **18**(12), pp 1004-1006, June 15, 1993.

[13] H. Rajenbach, S. Bann, and J-P Huignard, "Long-term readout of photorefractive memories by using a storage/amplification two-crystal configuration," Opt. Lett., **17**(23), pp 1712-1714, December 1, 1992.

[14] D. Brady, K. Hsu, and D. Psaltis, "Long-term readout of photorefractive memories by using a storage/amplification two-crystal configuration," Opt. Lett., **15**, pp 817-819, 1990.
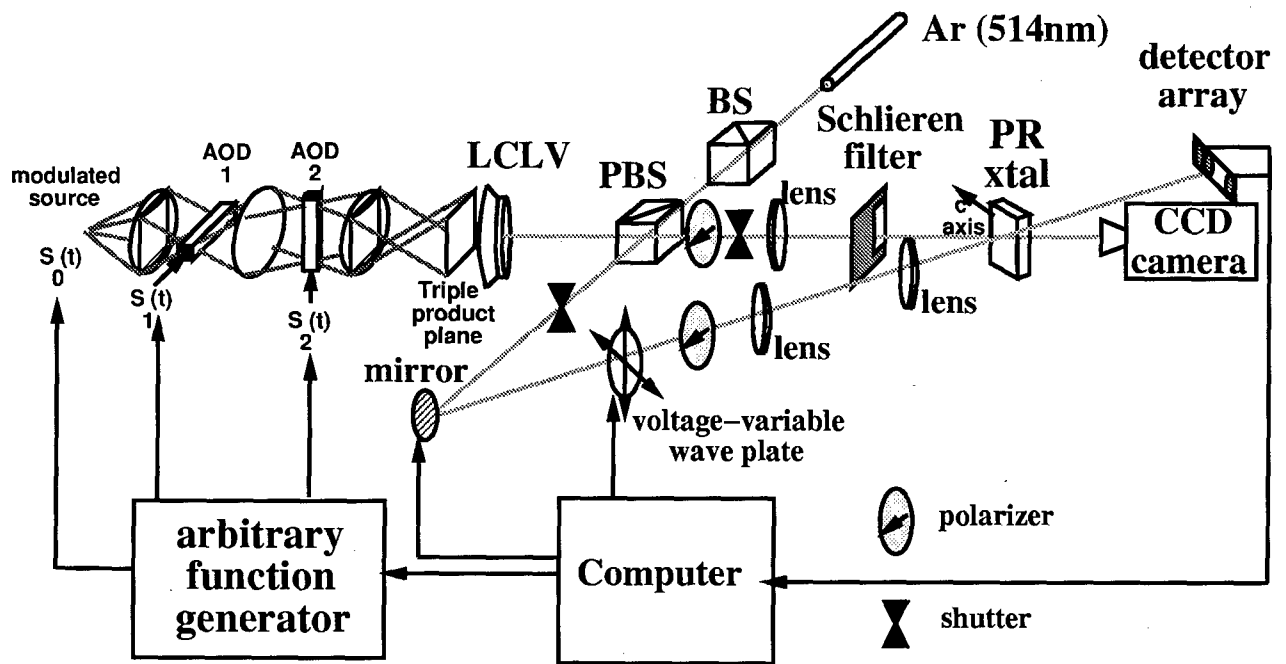
Figure 1: Cascaded optical classification network schematic: AO triple product processor cascaded through a liquid crystal light valve (LCLV) into a holographic classifier with weights stored in a photorefractive crystal (PR xtal).
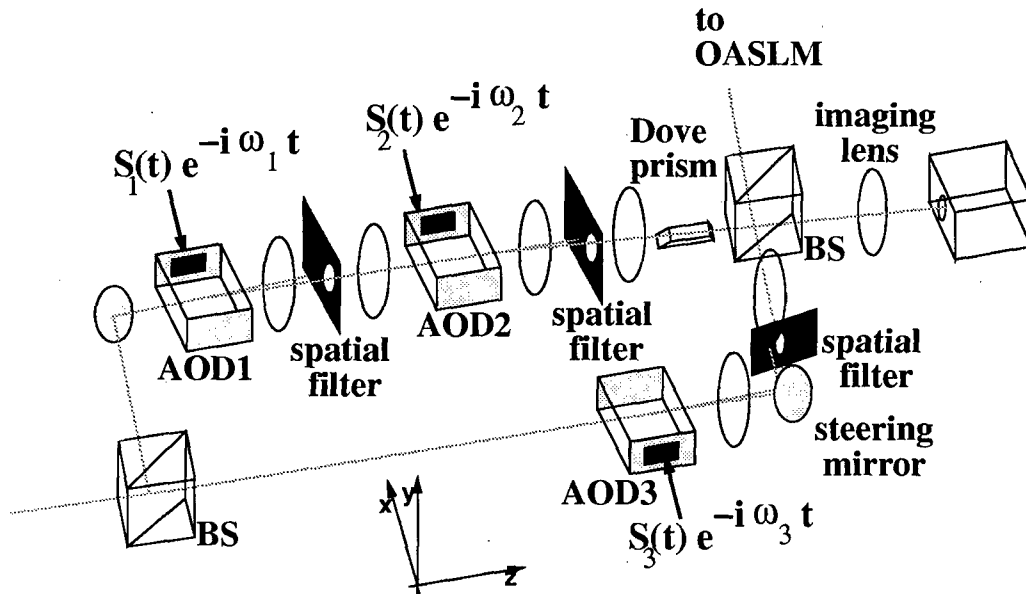

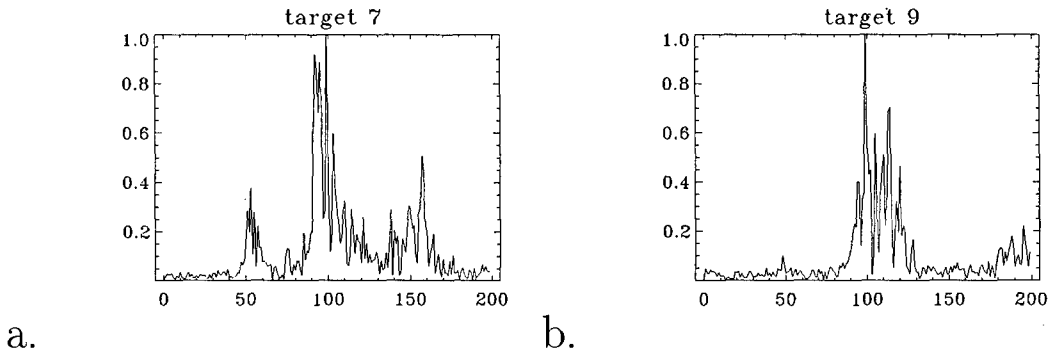Figure 2: Acousto-optic triple product processing architecture.

Figure 3: Two characteristic radar range profiles from 1987 Pairs airshow dataset; all profiles are all taken with head-on aspect ($\pm 10°$): a. type 7; b. type 9.
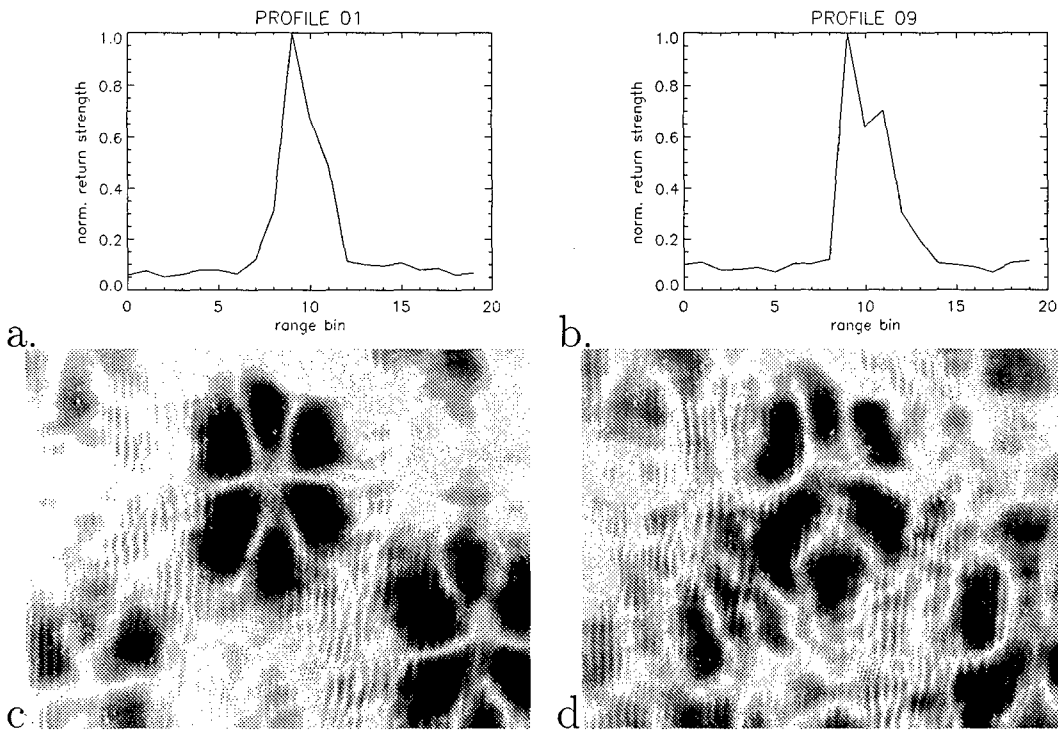

Figure 4: Low-passed radar range profiles of: a. type 1 aircraft; b. type 9 aircraft; and optically computed triple autocorrelation of: c. type 1 aircraft; d. type 9 aircraft.
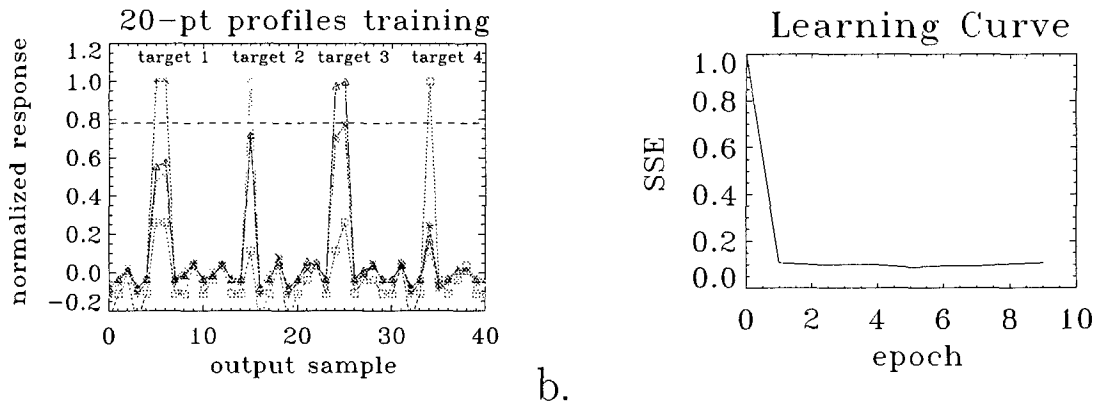
Figure 5: Training set performance for 5 meter data (single pulse return for each of four aircraft): a. typical presynaptic output; b. learning curve.
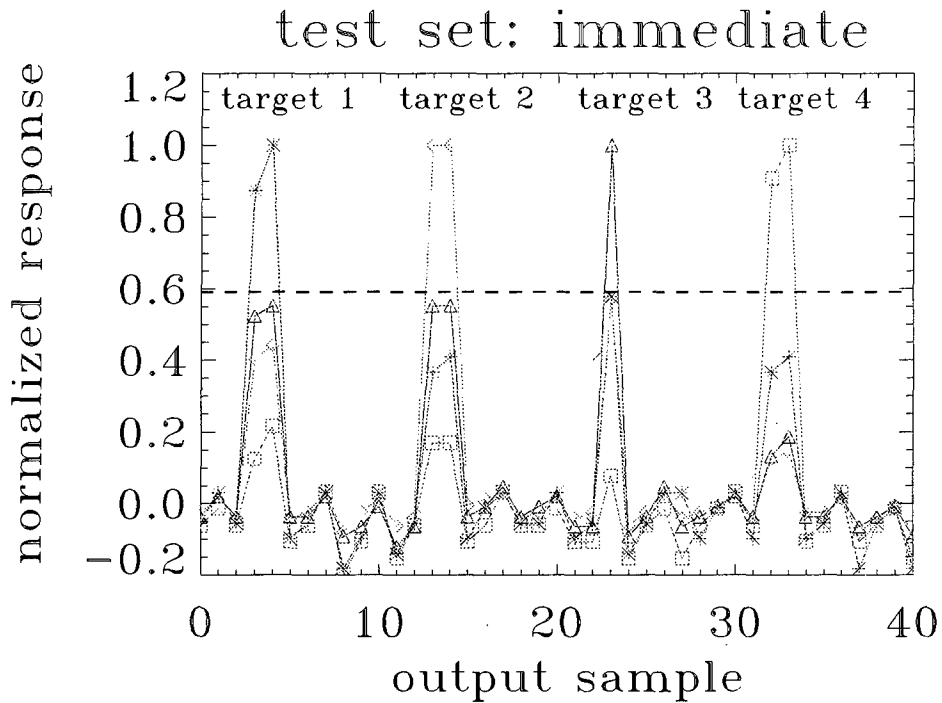
Figure 6: For all possible shifts of the input signals from the untrained testing set, 100 % correct optical classification of four radar range profiles from 1987 Pairs airshow dataset is demonstrated using the cascaded processor.

training sets: one head-on (1.0m and 5.0m) profile of each of four classes

test sets: ten head-on (1.0m and 5.0m) ($\pm 10°$) profiles of each of four classes

1.0m profiles				
	class 1	class 2	class 3	class 4
class 1	10	0	0	0
class 2	0	9	1	0
class 3	1	0	9	0
class 4	0	0	0	10

5.0m profiles				
	class 1	class 2	class 3	class 4
class 1	8	1	1	0
class 2	2	8	0	0
class 3	0	4	6	0
class 4	0	0	0	10

Figure 7: Confusion matricies for cascaded optical classifier trained using 1.0m and 5.0m resolution radar profiles and tested using ten untrained profiles for each class.
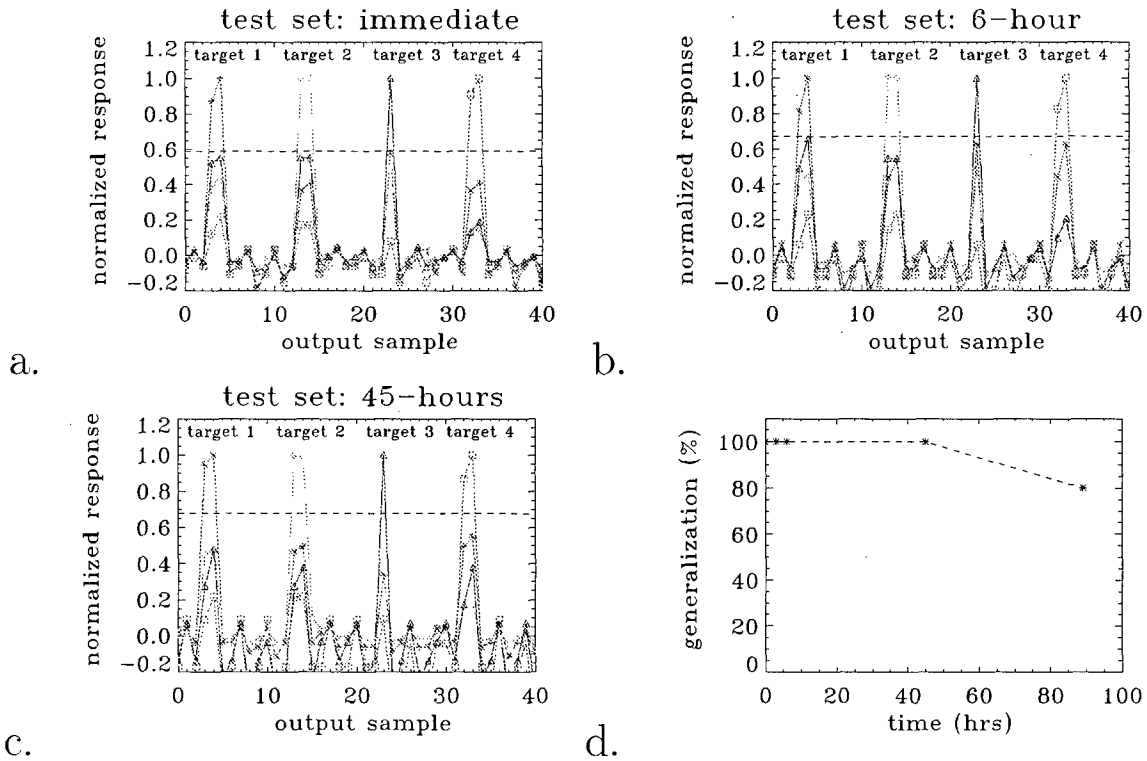
Figure 8: Optical classification of 5.0m profile test set a) immediately; after dark storage: b) 6 hours; c) 45 hours; d) generalization score over decay time.

TARGET IDENTIFICATION IN THE FREQUENCY DOMAIN

S. K. Wong, S. Kashyap, A. Louie, S. Gauthier and E. Riseborough

Defence Research Establishment Ottawa
3701 Carling Ave.
Ottawa, Ontario
Canada K1A 0Z4

ABSTRACT

An alternative approach to the development of an identification algorithm for non-cooperative target recognition (NCTR) is presented. Instead of making use of the features from the conventional range profile of the unknown target, information in the frequency domain is utilized in the identification process. The frequency domain algorithm developed in this paper uses the same High Range Resolution (HRR) based data as in the conventional range profile analysis. A number of preprocessing requirements that are needed in the conventional HRR range profile analysis can be eliminated by working in the frequency domain; for example, range profile localization, alignment with library references, background noise floor determination, Jet Engine Modulation signal removal, I/Q in-phase and quadrature gain and phase imbalance checks and target velocity compensation. Thus the identification process can be made more efficient and has a greater potential to achieve real time operation. A template matching algorithm has been developed for target identification. Highly accurate identification has been obtained even when the input signal to noise ratio is as low as two. An eighty-six percent over-all identification rate has been achieved.

1. INTRODUCTION

The ability to recognize targets quickly, at long distance and under all weather, day or night conditions has the potential to greatly enhance battle or defence capability. To improve identification capabilities and to ensure high confidence in positive air target identification, advanced techniques for non-cooperative target recognition (NCTR) are of great interest to the military. For example, in times of conflict and crisis, a positive identification on what is detected is crucial to determining the appropriate response. Because of the present inability to solve the identification problem, very inflexible airspace control orders are currently invoked which often seriously restrict the full exploitation of the very powerful weapon systems available. Moreover, past experience indicates that there is a need for proper defence of high-value assets such as naval vessels from potential hostile attacks, while at the same time preventing fratricide.

Identification based on High Range Resolution (HRR) range profiles is looked upon as a highly promising technique for NCTR. HRR offers a very simple and rapid way to characterize an air target through the use of radar range profiles; this range profile is essentially a 1-D radar image of the target. It has an all aspect capability. The signal-to-noise ratio requirement is moderate; positive identification may be performed at maximum detection range and only a very short dwell time is required. This technique is applicable to a wide range of a new generation of ground, naval and airborne radars.

Virtually all HRR-NCTR identification analysis found in the open literature uses range profiles. Since the frequency domain is complementary to the range (time) domain in the HRR analysis, we propose to investigate NCTR identification

algorithms in the frequency domain as an alternative to the conventional range profile approach. Moreover, HRR-based in-phase and quadrature data are already in the frequency domain; thus, it seems natural that NCTR in the frequency domain should be exploited. It has already been recognized that NCTR analysis can be more efficient in the frequency domain (Refs. 1, 2); but there has never been any detailed study reported in the literature.

In this paper, a detailed examination of HRR-based target identification will be given. A background on HRR-based target signatures is given in Section 2. We will discuss some of the problems one could expect to encounter in working with the HRR range profiles and what kind of preprocessing is required to prepare the HRR range profile for target recognition in Section 3. To mitigate, or to eliminate some of these problems, we propose, in Section 4, a more efficient approach to target recognition by working in the frequency domain using the same HRR based data. A detailed description on how the frequency domain analysis can overcome the preprocessing problems encountered in HRR range profiles will be discussed. A target identification algorithm based on analysis in the frequency domain will be given in Sections 5 and 6, and results of the identification analysis will be presented in Section 7.

2. HIGH RANGE RESOLUTION (HRR) STEPPED FREQUENCY WAVEFORM

There are several ways to generate HRR-based target profiles; for example, short temporal pulses, frequency modulated pulse compression, and stepped frequency waveforms. Because of the technology and the flexibility associated with stepped frequency wave-forms (SFWFs), many radar systems are using SFWFs in the HRR imaging process. SFWFs remove the requirements for wide instantaneous bandwidth and high A/D sampling rates. Moreover, SFWFs are particularly well suited to phased array radar systems, which have relatively narrow instantaneous bandwidths.

A SFWF consists of a sequence of temporal radar pulses transmitted with a fixed, uniform change in frequency from one pulse to another. Each pulse within the train of pulses has a relatively narrow bandwidth (< 1 MHz). The total effective radar bandwidth is determined by the product of the frequency step size and the number of frequency steps in the train of pulses; i.e.,

$$\beta = N \Delta f \qquad (1)$$

where N is the number of frequency steps and Δf is the frequency step size between adjacent emitting carrier frequencies. The resulting range resolution of the SFWF HRR range profile is given by,

$$\Delta R = \frac{c}{2\beta} \qquad (2)$$

where c is the speed of light. For example, if the effective bandwidth β = 500MHz, the range resolution of the target is 30 cm.

The SFWF produces a range profile from a phase shift generated by means of a change in the frequency of the transmitting radar pulses. Assuming the velocity of the target is negligible, the range to target from the SFWF process is given by

$$R_0 = \frac{c}{4\pi} \frac{\Delta\theta}{\Delta f} \qquad (3)$$

where $\Delta\theta$ is the phase shift and Δf is the frequency step size of the SFWF. Since the phase change is cyclic, ambiguity will exist for $\Delta\theta = \Delta\theta + m2\pi$; that is to say,

$$R = \frac{c}{4\pi} \frac{\Delta\theta}{\Delta f} + \frac{c}{4\pi} \frac{m2\pi}{\Delta f}$$
$$= R_0 + m \frac{c}{2\Delta f} \qquad (4)$$

where m is an integer (e. g., m=1,2,3 ...). Thus, a HRR target range profile will appear inside an unambiguous range window defined by

$$R_U = \frac{c}{2\Delta f} \qquad (5)$$

The location of the target profile inside the unambiguous window depends on the amount of frequency shift that is produced by the scatterer on the target; this is known as the induced phase shift frequency. Furthermore, the periodic nature of the range profile, which is a consequence of the phase, means that part of the target can "wrap" around the same unambiguous window and the target appears to break up into two pieces; this is known as aliasing. Thus a check has to be performed to correct for any aliasing effect since this creates potential problems in localizing the target range profile within the unambiguous window. This is important because the input HRR target profile has to be aligned with a reference profile in the target identification process (Ref. 3).

3.   PREPROCESSING FOR HRR RANGE PROFILES

In processing the SFWF to obtain a HRR range profile, other problems also emerge; corrections have to be made before the target identification process can proceed. In collecting the I and Q samples from each pulse in the SFWF, coherent detection is employed to extract the relative phase from the target echo. The I and Q in-phase and quadrature signals detected are defined as,

$$\begin{aligned} I &= A\cos\theta \\ Q &= A\sin\theta \end{aligned} \qquad (6)$$

where A is the detected radar echo amplitude of the radar return; θ is the relative phase between the echo return and the outgoing pulse reference and is given by,

$$\theta = \frac{4\pi f}{c}\left(R - vt - \frac{1}{2}at^2\right) \qquad (7)$$

where $4\pi fR/c$ is the phase delay due to the range target; $4\pi fvt/c$ and $2\pi fat^2/c$ are the phase delays due to the radial velocity and radial acceleration of the target along the line of sight of the radar receiver respectively. The phase information is obtained by mixing the received echo with a reference sample of the transmitted signal (in difference frequency mode) on a pulse to pulse basis because of the change in frequency from pulse to pulse. This restricts the PRF operation of the SFWF-HRR operation by allowing only one pulse "in the air" at any one time. The PRF depends on the maximum radar detection range desired; for example, to obtain a maximum detection range of 75 km, the SFWF operation would be limited to a maximum PRF of 2 KHz. A limited PRF operation has a couple of consequences. A low PRF means an increase in radar dwell time in collecting the HRR data. Moreover, a lower PRF increases the ramp repetition interval (RRI), demanding a more stringent velocity compensation. For example, if the target's velocity is significant, broadening of the HRR range profile will occur as a result. Figure 1 shows a computer-model generated range profile of a F16 aircraft with radial velocities v=0, 20, 300 m/s respectively. The shifting and broadening of the target's range profile as a result of the target's velocity are quite evident. The results shown in Figure 1 suggest that velocity compensation to within at least 20 m/s is required to restore the fidelity of the range profile sufficiently for identification processing.

Problems may also arise from the generation of the I,Q in-phase and quadrature data. The HRR profile may be distorted if there is any imbalance present in the I,Q quadrature phase and/or gain caused by the I,Q network being off calibration. In addition, if there is a d.c. offset in the quadrature network, another error may be introduced. Figure 2 shows the error introduced to the F16 range profile due to gain imbalance; spurious peaks appear in the profile as a result of gain imbalance. Similar distortion is produced by phase imbalance and these two effects are additive in the range profile. Furthermore, d.c. offset in the I,Q signals also introduces spurious peaks. To summarize, potential

problems in the calibration of the I,Q signals will manifest themselves as spurious scatterers, corrupting the HRR range profile if checks are not made.

Noise constitutes a part of any signal. In the HRR range profile, noise in the signal gives rise to a "noise floor" that can mask the presence of some of the weaker scatterers in the range profile. The noise level has to be determined from the HRR range profile to establish a threshold level for the identification process to "see" above the noise. Rotating parts in an aircraft target such as the compressor blades and the turbine blades of the engines produce extraneous components to the I,Q signal known as JEM (Jet Engine Modulation). The JEM component introduces spurious peaks in the HRR range profile (Ref. 4). Doppler filtering has to be performed to remove the JEM signal from the input to get rid of the spurious JEM lines in the HRR range profile. To summarize briefly, there are a number of preprocessing requirements that must be dealt with before target recognition can proceed when working with the HRR range profile. These are:

1. Localization of target profile in the unamgibuous window.
2. Target radial velocity and acceleration compensation.
3. I,Q phase and gain imbalance checks and corrections.
4. Noise floor determination from the input range profile.
5. JEM signal removal
6. Target profile alignment with library reference.

Furthermore, a practical NCTR system must be able to identify a target in real time. Real time may be loosely defined as the time taken to identify the target between the range when the target is first detected and the maximum weapon system range of the defence platform. Depending on the target's speed, heading and the range where the target is detected, real time can be anywhere from 10-20 seconds to 2-3 minutes. In the context of NCTR, real time is generally considered to be a duration of less than one minute. Thus, there are two parallel requirements for an operational NCTR system, accurate identification and real time operation.

The real time constraint and various preprocessing requirements associated with HRR range profiles provide motivations to look for an alternative method to perform target recognition. However, it must be emphasized that we want to keep the HRR-based data for analysis because they provide an all aspect capability and HRR is compatible with a wide range of radar systems. We are interested in eliminating or mitigating some of the problems in signal processing encountered in HRR range profiles. At the same time, we are looking for a more efficient way to process target recognition in real time. Processing in the frequency domain of the HRR-based data offers solutions to the problems mentioned above. We will discuss in detail how some of the problems encountered in the range profile can be solved by working in the frequency domain.

4. FREQUENCY DOMAIN ANALYSIS

Since the HRR-based data in SFWF are collected in the frequency domain (i.e. I,Q quadrature pair at each frequency), it seems more logical to work directly with the frequency data. The amplitude of the radar echo, detected at a given frequency of the SFWF, is chosen as the working parameter. Unlike in the HRR range profile where aliasing can occur, there is no aliasing in the frequency domain; alignment of frequency spectra between the input frequency profile and library reference profiles is automatically done since the echo amplitude is expressed as a function of frequency. Furthermore, working with the frequency spectrum, there is no need for velocity and acceleration compensation of the target. This is because there is no phase information contained in the frequency spectrum; i.e., the detected echo amplitude

$$A = I^2 + Q^2$$

$$= A^2(\cos^2\theta + \sin^2\theta) \tag{8}$$

where $\cos^2\theta + \sin^2\theta = 1$.

It may be a contentious issue whether phase information is really needed in target identification. Reviewing briefly, the phase information contained in the I,Q in-phase and quadrature data is essential when an inverse Fourier transform is performed to obtain the range profile. This is because it is the phase variations among different scatterers on a target that separate the scatterers along the range axis in obtaining a distinctive range profile. It can be argued that the frequency spectrum also provides a distinctive signature of the target; the absence of phase information is thus irrelevant when working in the frequency domain. To see how a distinctive signature is embedded in the frequency spectrum, let us examine the signal amplitude detected at each frequency. The radar echo amplitude is the sum of all contributions of the reflected radar signal from various parts of the target, i.e.

$$A = \left(\sum_i A_i e^{j\phi_i} \right) \left(\sum_i A_i^* e^{-j\phi_i} \right)$$
$$= \sum_i A_i A_i^* + \sum_{j<i} \sum_i 2A_j A_i \cos(\phi_j - \phi_i) \qquad (9)$$

where A_i is the reflected electric field amplitude from the i-th patch of the target in which the target is divided into many patches to describe the variations of radar return from different locations of the target (see Figure 3). The relative phase difference between the i-th patch and the j-th patch is given by

$$\phi_i - \phi_j = \frac{4\pi f}{c} (R_i - R_j) \qquad (10)$$

where R_i and R_j are the distances of the i-th and j-th patches on the target to the radar receiver respectively. Note that the relative phase difference is a function of frequency and is independent of the target's motion. Thus the detected radar echo is composed of a non-coherent part (the first term in Equation (9)) and a coherent term (the second term of Equation (9)). The non-coherent term is relatively insensitive to frequency; hence it produces a more or less flat spectrum as a function of frequency. The coherent term is a consequence of spatial interference effect due to different path lengths from different parts of the target. Thus the coherent term, which is a function of the relative phase difference, produces distinctive frequency spectra because of the different geometric distributions of the variable R for different target types (see Equation (10)). Moreover, different radar reflectivities from various parts of the target (i.e. the A's in the second term of Equation (9)) also contribute distinctive variations to the frequency spectrum for different target types. Figure 4 shows the computer-model generated frequency spectra of two different aircraft (F-16, F-18) at the same aspect orientation.

Another interesting aspect of working in the frequency domain is that the notion of range resolution no longer has any meaning. Range resolution is only relevant to the HRR range profile for resolving the location of the major scattering centers. Recall that in order to attain a certain level of range resolution in the HRR range profile, a given number of pulses and a given frequency step size are required as given by Equation (1). However working in the frequency domain, the number of frequency data points are flexible and can be adapted to the PRF used and the radar dwell time available. One could have a larger or a smaller piece of the frequency signature of the target; the subsequent identification process would be relatively insensitive to the size of the frequency spectrum. Moreover, the size or length of the target has no role in the frequency spectrum; hence the SFWF does not have to slave to a certain frequency step size Δf to conform to a desired unambiguous "viewing" window (Equation (5)) as in the case of the HRR range profile.

In the real world, any detected or processed signal will be contaminated with noise to some extent. We will examine how much the noise plays a role in the identification process. A random noise waveform can be added to both the I and Q channels of the target signal in the form,

$$s_I(f) = I(f) + K r(f)$$
$$s_Q(f) = Q(f) + K q(f) \tag{11}$$

where r and q are two independent random noise vectors as a function of frequency varying from +1 to -1. K is a scaling factor that gives any desired signal to noise ratio (SNR). In the frequency amplitude parameter,

$$SNR = \frac{A_{rms}}{(Kp)_{rms}} \tag{12}$$

where $A = I^2 + Q^2$, $p = r^2 + q^2$ and the subscript rms denotes root mean square value. In applying a random vector to r and q, we assume that the noise waveform is white and non-Gaussian, i.e. the noise amplitude is random in distribution and uncorrelated in time (frequency here because the SFWF sweeps the frequency in time). It is found that it is much easier to work with noise in the frequency domain than in the range domain. When the noisey I,Q signals are transformed to the range profile, it can be shown that even at a modest noise level (in I,Q), some of the less prominent scatterers in the range profile are already overwhelmed by the noise floor; but in the frequency domain, the spectrum is still quite distinctive. This is illustrated in Figure 5.

JEM signal can also present a problem in the HRR range profile; it shows up as spurious scattering peaks. Thus the JEM signal has to be removed from the range profile so that it will not corrupt the signature and degrade the identification process. In the frequency domain, the JEM signal resembles scintillation noise superimposed on the target signal (Ref. 4). Treating JEM signal as noise in our identification algorithm, we will show later that the presence of JEM and noise would not adversely affect the identification of the target in the frequency domain.

5. TARGET IDENTIFICATION ALGORITHM

To decide which classification method would be the best one for an operational NCTR system, there are two major issues that must be considered, identification accuracy and real time operation. As a general rule of thumb, the more computationally intensive the algorithm, the better the identification accuracy tends to be. However, in order for the NCTR system to be operational, it must function in real time. Depending on the number of target types, the number of permutations of configuration for each target type, the sizes of the azimuth and elevation angle ranges in a search, the number of signatures that have to be searched can be quite substantial (approximately on the order of 10^4 to 10^5). Under the two simultaneous requirements of high accuracy and real time operation, we believe that cross correlation may offer the best solution to the identification problem. Cross correlation is a template matching technique. It is simple and has an intrinsic parallel algorithmic structure; hence it is very efficient and can readily meet the real time criterion. In relating to the Bayesian analysis, the cross correlation function is essentially the likelihood function. A more detailed discussion on how the cross correlation emerged from the Bayesian formalism is given by Smith and Goggan (Ref. 5).

6. CROSS CORRELATION FUNCTION

The cross correlation between two functions F and G is defined by,

$$C_{FG}(m) = \sum_i [F(i) \ G(i-m)] \tag{13}$$

where i and m are the abscissa coordinates. We sum over all i components within the domain of the translated template. Thus, the cross correlation is used as a measure of the similarity between the template and the region of the unknown input in the vicinity of m. It should be noted here that both the functions F

and G are normalized functions. We define the normalization of a function f as,

$$F(i) = \frac{f(i)}{\sum_{j} f(j)} \qquad (14)$$

such that

$$\sum_{i} F(i) = \sum_{i} \left(\frac{f(i)}{\sum_{j} f(j)} \right) = 1 \qquad (15)$$

i.e., the area under the normalized function is 1. We choose to normalize the functions in the cross correlation function defined in the manner above instead of using the conventional Cauchy-Schwarz inequality definition (Ref. 6). Normalization in this manner is intended to accomplish two purposes. First, in order to identify a given target, the detected signature of the target should be independent of the range at which it is detected, the transmitted power of the radar pulses and the sensitivity (i.e., dynamic range) of the receiver. We look for a normalized waveform that is invariant to the "radar equation" given by, $P_r \propto P_e / R^4$, where P_r is the received power, P_e is the transmitted power and R is the distance to target. Second, the normalization definition given in Equation (15) gives the average value of function F as,

$$F_{avg} = \frac{\sum_{i=1}^{N} F(i)}{N} = \frac{1}{N} \qquad (16)$$

where N is the number of data points. It is important to note that all functions F, regardless of target types, will have the same average value given by Equation (16); that is to say, signatures of different target types fluctuate about the same average value. Hence, template matching using cross correlation of the normalized signatures defined above is effectively a measure of the deviation from a common average value from both the input and the library reference. It turns out empirically that normalizing the

functions in this manner makes the template matching process very sensitive to pattern changes and provides rather good identification accuracy.

7.   NUMERICAL RESULTS OF THE IDENTIFICATION ALGORITHM

A survey of the literature indicates that the most practical approach to target recognition would be a system in which the unknown target signature is matched against reference signatures generated by computer model computations. There are at least two reasons why the computed signatures are needed to serve as library references:

1.   It will not be possible to establish a database by real measurements that satisfy the needs for sufficient data under all possible aspect and elevation angles and for all possible target types.
2.   Hostile targets are not normally available for measurements.

In this paper, we have generated target signatures using the XPATCH electromagnetic code. HRR-based data were generated for representing different target types such as the F16, F18, F4 and F14. A total of 570 signatures were computed at different aspect angles from 0 to 180 degrees, spanning the frequency range from 10.0 to 10.6 GHz. These have been stored as library reference templates. Each of the model-generated signatures takes a considerable amount of time to generate; thus it takes a sizeable effort to compile a very large set of signatures. To generate a large number of signatures in the library, an alternative means of generating pseudo target signatures quickly was employed. A further 6200 "bogus" signatures were added to the library database to simulate a large file search environment for the algorithm. These bogus signatures were generated for a dummy target with a random parameter for the number of scattering centers (i.e. target may have 5 to 15 scattering centers) and a random length parameter (i.e. 10 to 30 meters). The larger library database provides a more stressing search environment to test the algorithm. To test the identification

rate, the algorithm was required to identify correctly the target type and aspect angle; the algorithm must pick out a correct match from a database of 6750 reference profiles. Since we do not have any real target signature available as input at present, we use some of the computed signatures as unknown inputs. Some of the signatures were already in the database; some were not in the database but required the algorithm to come up with the closest match from the database. Non-Gaussian white noise was added to the test input signatures giving SNR as small as 2 (i.e., 3 dB). Figure 6 shows an example of the signatures before and after the addition of noise.

Ad hoc factors are added to the cross correlation function in Equation (13). The ad hoc factors are designed to measure the relative change between the input and the reference signatures with respect to the common average given by Equation (16) and to track any prospective large random fluctuation from the noise. These factors help to improve the template matching accuracy in the identification process. The cross correlation C_{FG} is modified as,

$$C_{FG}(m) = \sum_i \frac{[F(i) \ G(i-m) \ Q(F(i), G(i-m))}{R(\sigma^2(F), \sigma^2(G))]}$$ (17)

where Q and R are metric relations between F and G and σ^2 is the variance. Although the ad hoc factors can be perceived as parameters without any clear underlying rationale in the view of orthodox or conventional statistics, this approach is frequently applied in practice (Refs. 6,7).

Over 100 different test target signatures at various aspect angles with various amounts of noise added were tried as inputs. Results from the identification algorithm indicate that 100% correct identification was achieved (i.e., 100 out of 100 tries) as long as there was already a signature in the library database. Correct identification was achieved even if the input signature had a SNR as low as 2. For example, the noisy inputs similar to the one shown in Figure 6 were identified correctly.

However, if the input signature did not already have a reference in the library, the identification rate depended on whether the library database was adequate. It would be helpful to expand on what is meant by having an adequate library. The library contained target signatures with a given aspect angle increment size; initially, an aspect increment of 0.2^0 was used. This angle increment seemed to be satisfactory, for most aspect angles, to achieve a high identification rate. But at some target aspects (for example, near nose-on for the F16), the 0.2^0 increment in the reference library was too coarse; the correct identification rate suffered considerably and was only ~50% (9 out of 20 tries).

Intuitively, the problem of high mis-identification rate using a 0.2 degree aspect increment in the library can be attributed to having too many similarly correlated matches between the library reference templates and the input signature. It seems reasonable to believe that subtle differences in the target matching can be further differentiated by using a finer angular increment in the library templates. When we reduced the aspect increment in the library to 0.1 degree, the correct identification rate increased back up to 90% (9 out of 10 tries) in the aspect regions where the identification rate was zero before. This confirms our conjecture that better discrimination in the target matching may be possible by refining the aspect angle increment in the library. However, there is a penalty we have to pay for reducing the angle increment; with a two times finer angle increment, the computational and memory requirements increase by a factor of four. This is because both the aspect and elevation angles must be refined in a real system. Although from the example above, refined increments are needed only at some aspect angles; it is anticipated that different target types would behave differently at different aspect angles. Hence, the angle increment refinement must be applied uniformly at all angles for all target types.

Increases in the amount of computation and memory required to accommodate finer angular resolution are substantial; this makes real time operation

become much more difficult to realize. Any increase in computational time has a negative impact on the effectiveness of an operational NCTR system; the time taken to identify a target is just as critical as the accuracy of the identification process from a practical point of view. This dilemma motivates us to look for an alternative approach. Instead of decreasing the size of the aspect angle increment to further discriminate subtle differences, it can be argued that increasing the aspect angle increment size in the library can also help to reduce the number of similarly correlated matches by simply having fewer templates to compare. We embark on increasing the angular increment of the library templates to 0.5 degree between signatures and we force the input signature to match the closest template in a coarser set of library templates. As described previously, the frequency amplitude profile is a sensitive function of the aspect angle change due to the speckle effect. From Equation (10), it is noted that the relative phase is a function of both the frequency and the geometrical location of the scatterer relative to one another on the target. We may interpret that a small aspect change corresponds to a slight shift in the relative locations of the scatterers. It can be argued intuitively that for a small aspect rotation (say less than 0.5 degree), the relative phase can be kept relatively unchanged by shifting the frequency slightly to compensate for any change in the geometrical orientation of the target. This is in fact largely confirmed to be the case from examining the computed frequency spectra.

Making use of this fact to force a best match, the input signature was shifted 5 frequency bins in both the left and right directions with respect to each of the library templates in computing a correlation value (i.e. $-5 \leq m \leq 5$ in Equation (17)). The algorithm then computed the most likely target that gave the best match with the input. Computed results indicate that 30 out of 35 tries (86%) were correctly identified. When the input signature was not frequency shifted (m=0) to maximize the correlation, the identification rate fell dramatically.

The positive results above using a coarser aspect increment in the library template files indicate that there could be a significant impact on an operational NCTR system. By increasing the library angular increment size from 0.1 degree to 0.5 degree but still retaining reliable accurate identification, there is a corresponding saving in computational time and memory capacity requirements by a factor of about 25. With this scale of reduction in computing requirements, a real time (less than one minute) NCTR system is within reach. To illustrate with an example, consider that an unknown target has to be searched in a 5 degree (azimuth) by 5 degree (elevation) sector. Using the 0.5 degree increment in the library, this corresponds to 100 searches per target type. Suppose there are 20 different target types and each target type has 5 different possible configurations; a modest size NCTR system thus has to search through 10^4 library templates to make an identification. The current test algorithm described here searches through 6750 library templates and takes 190 seconds to compute the most probable identification on a SUN sparc 1000 computer. This includes the reading of 6750 library profiles from external memory which takes up 80 of the 190 seconds. All the computations in the algorithm are done sequentially. By reprogramming the algorithm in a parallel structure and running it on a faster machine, a factor of 5 in reduction in computing time should be attainable without much technical difficulty with current computing technology.

The tolerance of the algorithm to high noise level in the input signature also has another benefit. JEM signals embedded in the frequency spectrum display characteristics that are very similar to those of scintillation noise. In our approach, we treat the JEM signal as if it is another source of noise in the input spectrum. No additional processing is required to remove the JEM signal; hence this represents an extra level of efficiency in the identification algorithm.

8. CONCLUSION

We have proposed an alternative approach to the development of target identification by analyzing the frequency domain of the HRR-based data. There are many advantages in taking this approach:

1. It eliminates signal pre-processing, thus reducing error and distortion introduced to the data before identification processing.
2. This approach simplifies the system hardware; i.e. the possibility of eliminating the quadrature network. It allows an incoherent mode of radar operation, hence offering more flexibility in the radar waveform, e.g., number of pulses transmitted per SFWF scan, size of the frequency step size, higher PRF operation.
3. It tolerates high noise level and JEM signal contamination; this is important in an operational environment.
4. It permits an efficient parallel structured algorithm that can be implemented both in the hardware and software of the computing processor and has potential for meeting the real time requirement.
5. It could permit rapid target insertion capability in the field to support a flexible and sustained deployment of the NCTR system; i.e., the library needs only I,Q in-phase and quadrature data (coherent mode) or frequency amplitude data (non-coherent mode) without any preprocessing or training of the library set.

The numerical simulations conducted in this paper have demonstrated a high identification rate can be achieved using the cross correlation method in the frequency domain. Real time operation may also be attainable.

9. REFERENCES

1. C. Stewart, V. Larson and J. D. Halsey, "Comparison of classification approaches for high range resolution radar", SPIE Vol.1700, "Automatic Object Recignition II", p.146, 1992.

2. K. B. Eom, "Non-cooperative target classification using hierarchical modeling of HRR radar signatures", Proc. SPIE, Vol.2757, pp.194-205, 1996.

3. D. Iny and M. Morici, "Quantitative analysis of HRR NCTR performance drivers", Proc. SPIE, "Radar Sensor Technology", pp144-152, April, 1996.

4. M. Moruzzi, M. Fuentes and J. P. Henry, "Experiment of high range resolution techniques with a long range multifunction radar", International Conference on Radar, PP257-262, Paris, France, May 1994.

5. C. R. Smith and P. M. Goggans, "Radar Target Identification", IEEE Antennas and Propagation Magazine, Vol.35, No.2, pp.27-38, April 1993.

6. R. O. Duda and P. E. Hart, "Pattern Classification and Scene Analysis", John Wiley and Sons, New York, 1973.

7. D. S. Sivia, "Data Analysis, a Bayesian Tutorial", Clarendon Press, Oxford, 1996.
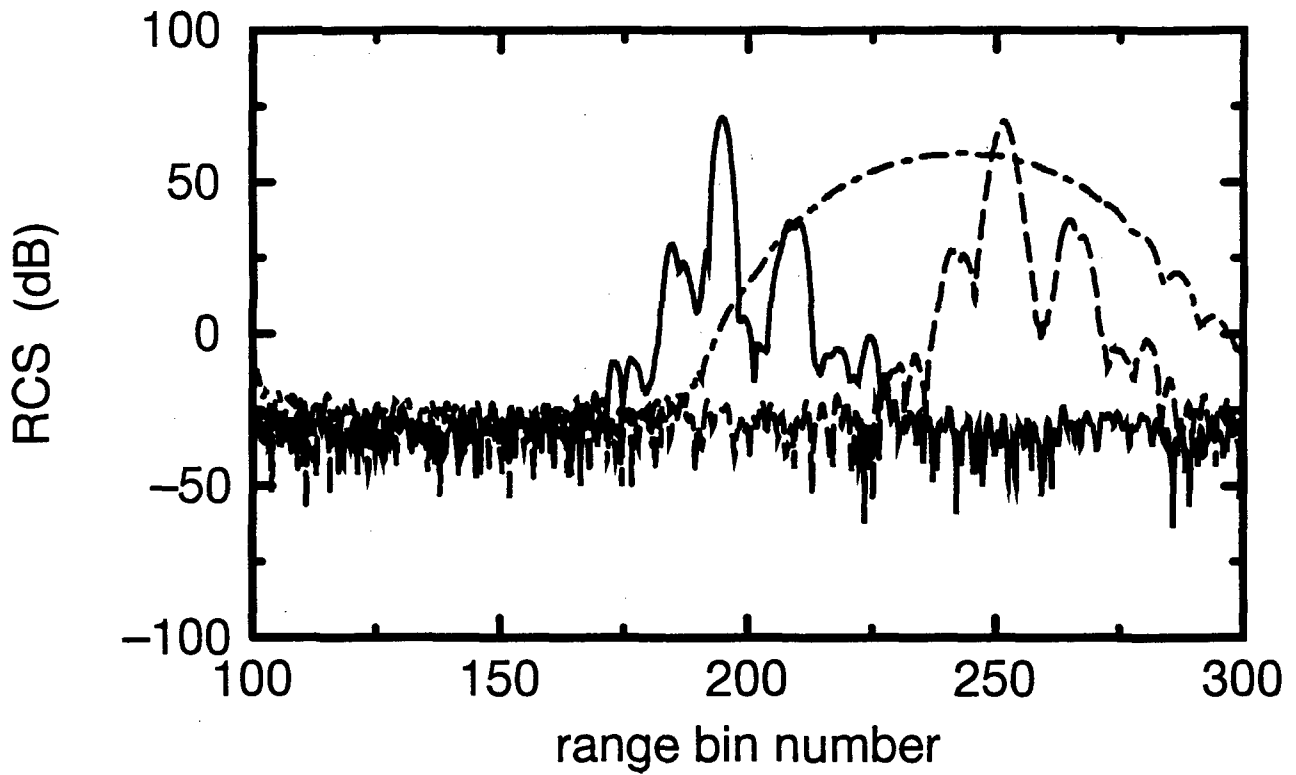
Figure 1   The HRR range profile of a F-16 target with different radial target velocities along
the radar's line of sight. (Target aspect = 0 degrees).
solid: v=0 m/s; dashed: v=20 m/s; dot-dashed: v=300 m/s.
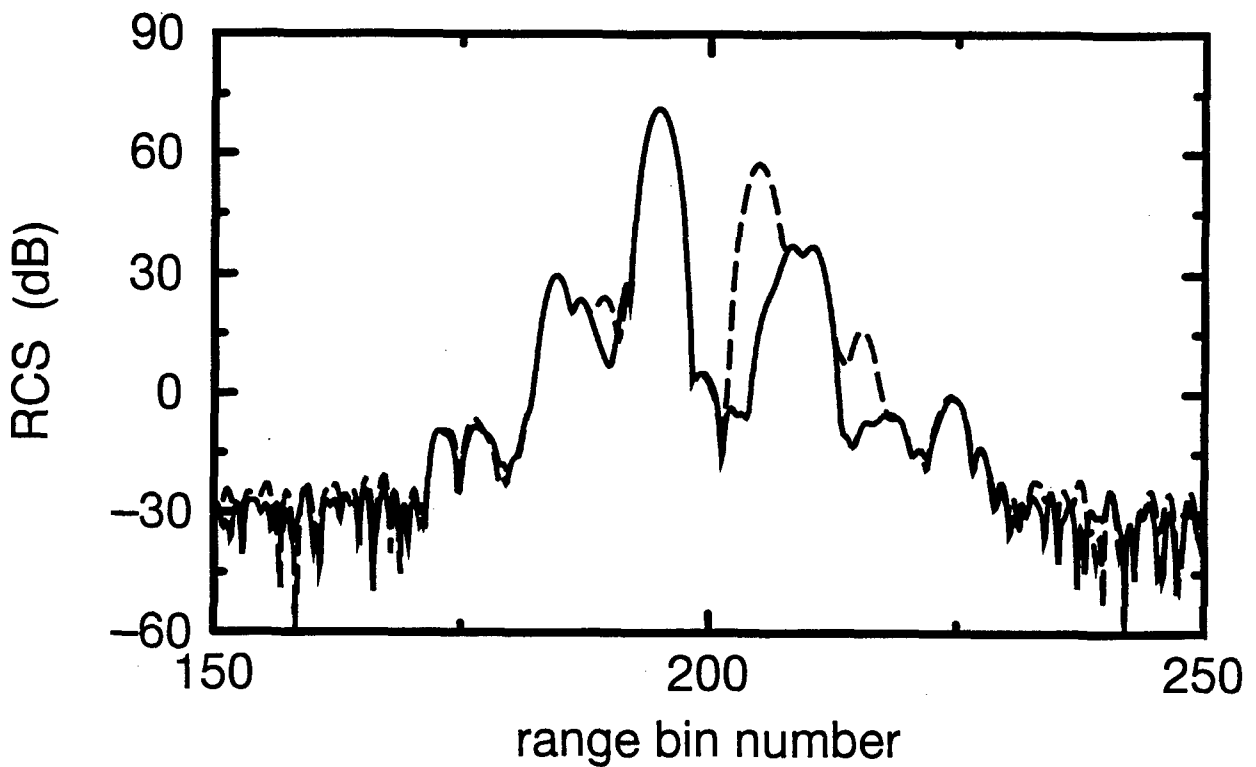
Figure 2   The effect of I,Q gain imbalance on the F-16's HRR range profile.
Gain ratio, $G = A_I / A_Q$
solid: G=1 (no gain imbalance), dashed: G=1.5.
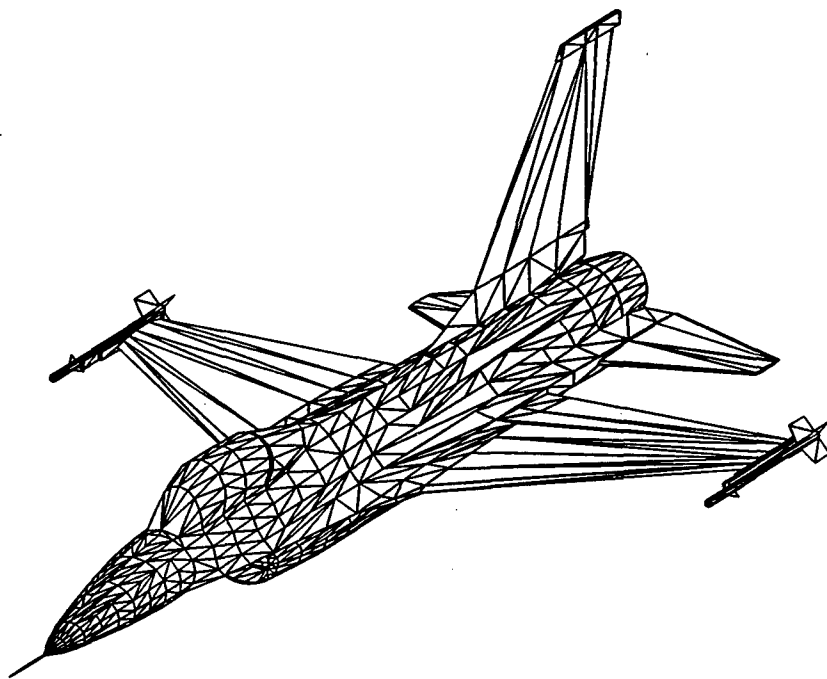
Figure 3   Model of the F-16 target for computing the scattering return from the aircraft.
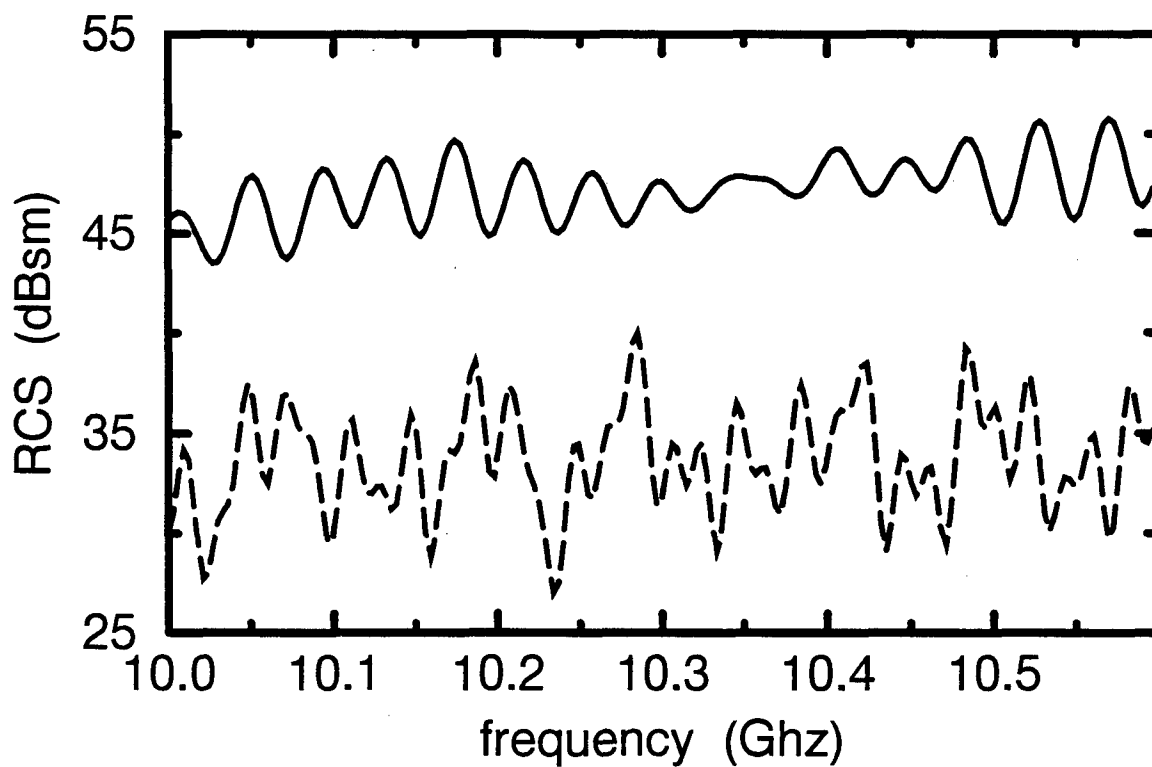
Figure 4   Frequency spectra of two different aircraft at 0 degree aspect.
                solid: F-16; dashed: F-18.
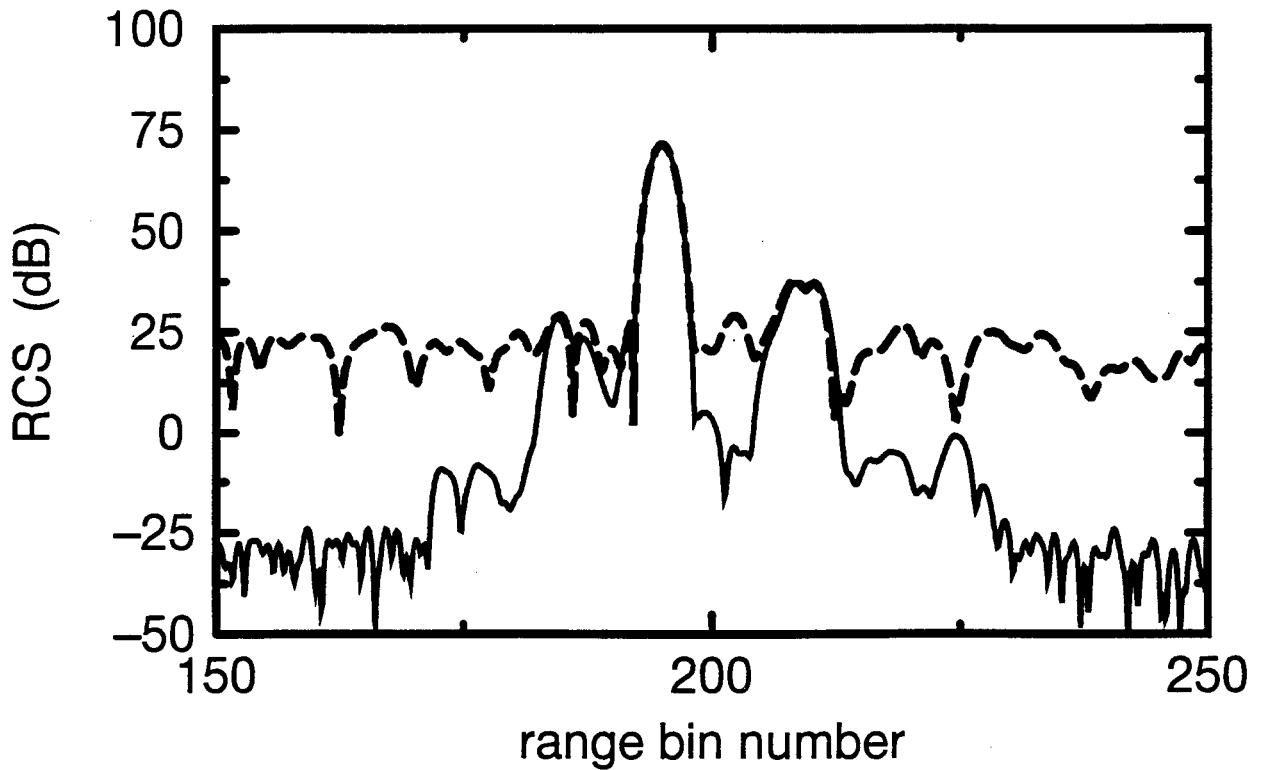
Figure 5a   HRR range profile of the F-16 target (aspect = 0 degrees).
             solid: no noise included; dashed: signal with noise added, SNR≈25.
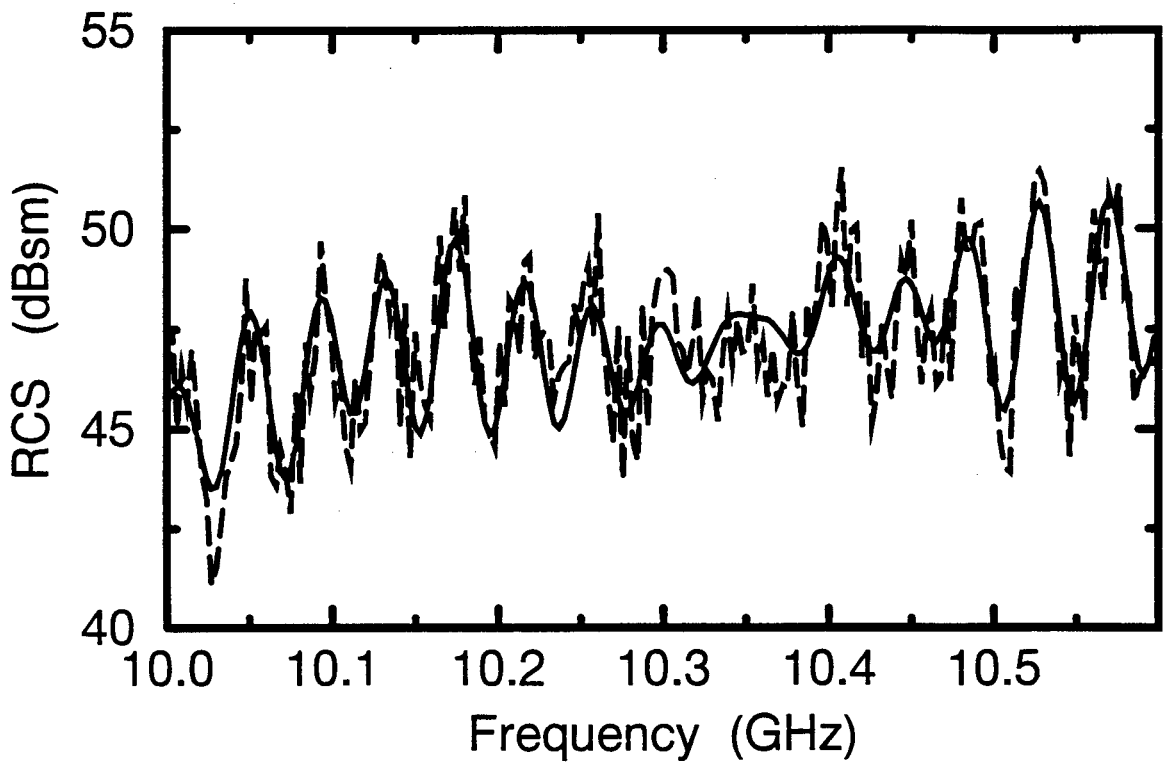
Figure 5b   Frequency spectra of the F-16 target (aspect = 0 degrees).
             solid: no noise included; dashed: signal with noise added, SNR≈25.
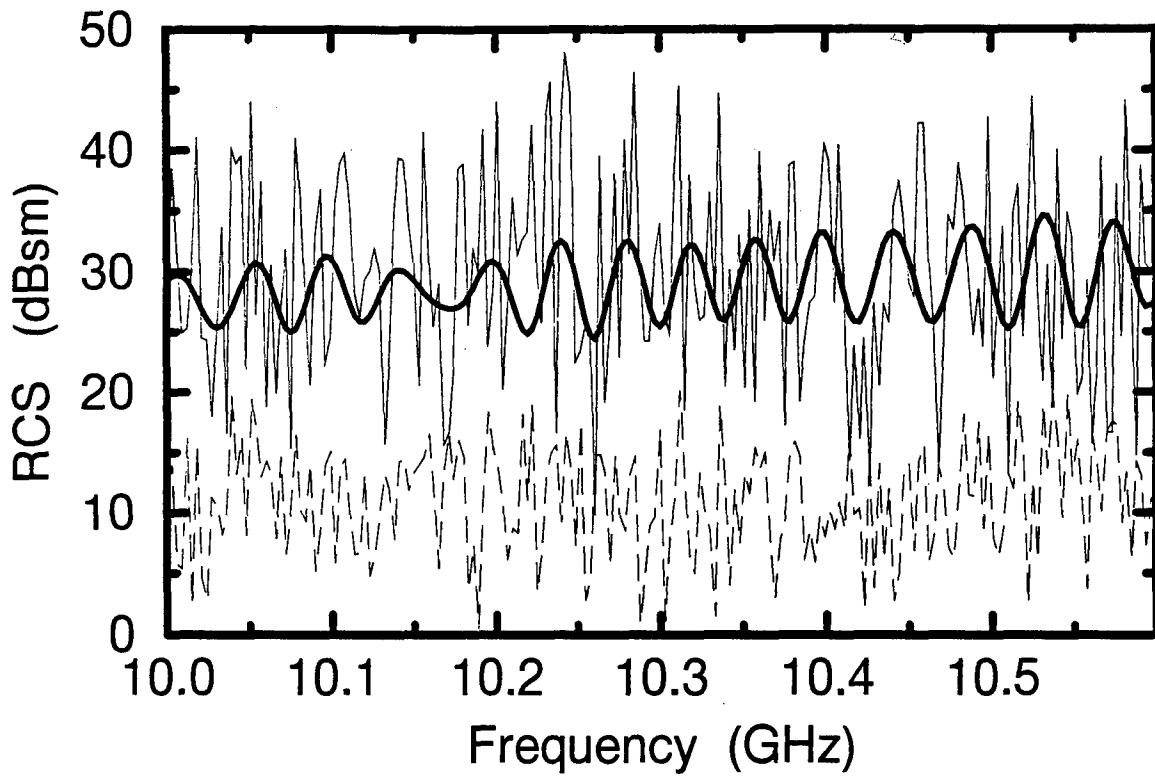
Figure 6   Frequency spectra of the F-16 target with and without noise added (aspect = 4
            degrees).
            solid (thick): signal, dashed (thin): noise; solid (thin): signal+noise, SNR≈2.

Gamma Mixture Models for Target Recognition

Andrew R. Webb

Defence Evaluation and Research Agency,
St Andrews Road,
Malvern,
Worcestershire WR14 3PS.
E-mail: webb@signal.dera.gov.uk

1. SUMMARY

This paper considers a mixture model approach to automatic target recognition using high resolution radar measurements. The mixture model approach is motivated from several perspectives including requirements that the target classifier is robust to amplitude scaling, rotation and transformation of the target.

Latent variable models are considered as a means of modelling target density. These provide an explicit means of modelling the dependence on angle of view of the radar return. This dependence may be modelled using a nonlinear transformation such as a radial basis function network.

A more simple model with separate components is considered. Estimation of the model parameters is achieved using the expectation–maximisation (EM) algorithm. Gamma mixtures are introduced and the EM re-estimation equations derived. These models are applied to the classification of high resolution radar range profiles of ships (where results are compared with a previously–published self–organising map approach) and ISAR images of vehicles.

2. INTRODUCTION

This paper develops work in [16] and addresses the problem of automatic target recognition using mixture models of radar target density and applies these models to the classification of radar range profiles of ships and ISAR images of vehicles. Our aim is to obtain an estimate of the posterior probability of class membership, $p(j|x)$, for class j and measurement vector x. We seek to achieve this via Bayes theorem,

$$p(j|x) = \frac{p(x|j)p(j)}{\sum_j p(x|j)p(j)} \qquad (1)$$

where $p(x|j)$ are the class–conditional densities and $p(j)$ are the class priors. The reason why we seek direct estimates of $p(j|x)$ rather than to design a classifier with class decisions as the output (for example,

a nearest neighbour classifier) is that the classifier will in general form part of a hierarchical decision making process. Classification is not an end in itself and will lead to some actions. Cost of making decisions will need to be considered. Also, supplementary domain–specific information (such as intelligence reports) may need to be combined with sensor–derived results in the decision making process. Therefore it is important that a classifier gives some measure of confidence that a pattern belongs to a particular class. This is provided by the probability of class membership.

The most common measure of the performance of a classification rule is misclassification rate or error rate. Error rate suffers from several disadvantages [17]. Error rate is deficient in that it treats all misclassifications equally and does not distinguish between $p(j|x) = 1$ and $p(j|x) = 0.51$, which for a two–class case results in the same classification; that is, it does not distinguish between estimates of the probabilities of class membership that are close to the threshold of 0.5 and those far from 0.5. Also, error rate does not distinguish between a rule that is bad because classes heavily overlap in data space or a rule that is bad because probabilities of class membership are poorly estimated. Discussion of classifier performance assessment is beyond the scope of the current paper and has been treated elsewhere [17].

However, estimation of the posterior probabilities, $p(j|x)$, through estimation of the class–conditional densities, $p(x|j)$ and Bayes theorem (1) is not without its difficulties. The main difficulty is in the estimation of target densities for data lying in a high-dimensional space. For the range profile data considered later in this paper, the data vectors x_i lie in a 130–dimensional space ($x_i \in \mathbb{R}^{130}$) and nonparametric methods of density estimation (for example, kernel methods) are impractical due to the unrealistic amounts of data required for accurate density estimation. An alternative approach is to trade flexibility for robustness and to use some simple parametric forms for the densities (for example, normal distributions) for which good estimates of the parameters may be obtained. Yet these may impose too much

rigidity on the allowable forms of the density.

The variance in the estimates of the parameters of a simple model may be lower than that of a more complex model, but it would be expected to yield biased probability estimates for much of the x space. However, if simple classification is the main aim, then bias may not be relevant: the best achievable classification results will be obtained provided $\hat{p}(i|x) > \hat{p}(j|x)$ whenever $p(i|x) > p(j|x)$ (see, for example, [7]).

Alternatively, we may estimate the posterior probabilities of class membership directly through a discriminative function approach such as a neural network. These models provide approximations asymptotically to the probabilities of class membership [9]. However, the amount of data required is excessive for high–dimensional data problems. There are several ways to circumvent this problem including linear projections (such as principal components analysis) and nonlinear projections [14, 15] to a lower dimensional subspace.

The approach considered in this paper is to model the density as a mixture of simple parametric forms whose parameters are estimated through some optimisation procedure. The advantage of such an approach, as we see in Section 3, is that it may be used to incorporate desirable features such as robustness to translation of a test image with respect to some centroid position (due to uncertainty in the true centroid) and robustness to scale. Further, angular dependence of the target return can naturally be expressed as a mixture, and different scattering models may also be incorporated into the same framework.

The basic distribution that we use at the heart of our model is a gamma distribution whose use may be motivated from physical arguments and results of empirical investigations.

The outline of the paper is as follows. Section 3 describes the mixture model approach to target classification and how robustness of the model may be incorporated into the mixture model framework. A nonlinear latent variable models for density estimation is introduced as a means of modelling target density (section 3.1) and a special case of independent mixture components considered. Section 4 derives the re–estimation procedure for the mixture model parameters. Section 5 presents results of applying the basic mixture model approach to the classification of radar range profiles; section 6 presents results of applying the approach to ISAR image data. The paper concludes with a summary of the main results and discussion of ways forward.

3. MIXTURE MODELS

In constructing the target probability density function, we wish to exploit expected structure in the data, without making assumptions that are too restrictive or unrealistic, such as normal distributions.

We do this through mixture distributions.

We shall assume that data are gathered on each of C target types as a function of aspect angle. For simplicity, we assume a single angle coordinate (data gathered as a function of azimuth at a fixed elevation) although in principle azimuth and elevation may be considered. The data comprise radar cross section range profiles and a set of d measurements corresponding to d range gates encompassing the target is extracted[1]. Thus, for each class, j, the training data set is $\{x_i, i = 1, \ldots, N_j; x_i \in \mathbb{R}^d\}$, where N_j is the number of patterns in class j. The x_i are usually ordered by angle. On test, we cannot assume that we know the physical position of the target precisely. Therefore, we must have a strategy for extracting an appropriate set of d range gate measurements from the range profile.

We start from the premise that we wish to model the probability density function of the target return, $p_c(x), c = 1, \ldots, C$, where x is a set of target measurements. We choose to model this density as a finite mixture [6, 13]. Mixture models have been used with success in a wide variety of applications and here we consider their application to radar target modelling. We motivate their use by addressing, in turn, several important issues concerning the properties of the probability density function. We drop the suffix c since we are not concerned with a specific class.

3.1 Latent Variable Model

We assume that the distribution of radar returns is characterised by a latent variable θ,

$$p(x) = \int p(x|\theta)p(\theta)d\theta$$
$$= \int p(x|\Psi(\theta))p(\theta)d\theta$$

where $\Psi(\theta)$ are parameters characterising the distribution and are functions of the variable θ. In the case of the gamma distribution (discussed in section 3.6), they are the mean and the order parameters. For the radar target data, θ is univariate and can be interpreted as angle.

Figure 1 illustrates the basic model. The latent space is represented by an angle θ. This is mapped to a parameter space, $\Psi(\theta)$, by a nonlinear model (for example, a radial basis function network (RBF)). Data is generated according to the probability distribution $p(x|\theta)$. In the data space, the data can be viewed as perturbations from a closed–loop contour.

If we suppose that $\Psi(\theta)$ does not vary too rapidly with θ, then we may approximate the integral above by a finite sum,

$$p(x) = \sum_{i=1}^{g} p_i p(x|\Psi(\theta_i)) \qquad (2)$$

[1] For the ISAR data, the d measurements correspond to the d cells in the ISAR image. However, the discussion in this section is confined to radar range profiles.
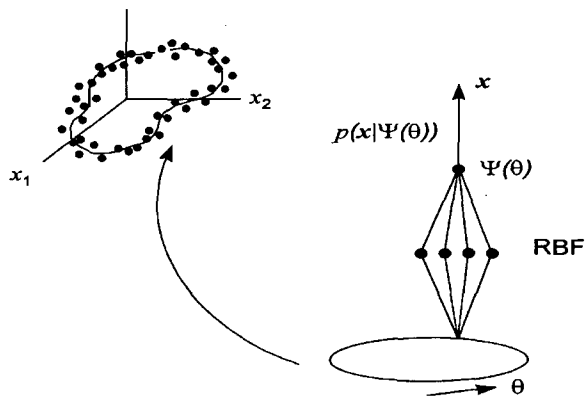
Figure 1. Latent variable model.

where the θ_i are samples on a regular grid. Equation (2) is a *finite mixture distribution* and the problem of calculating $p(x)$ is replaced by one of calculating, or specifying, the component distributions, $p(x|\Psi(\theta_i))$, the parameters associated these distributions, and the component distribution weights, p_i. Given a data set, and some simple parametric form for each of the $p(x|\Psi(\theta_i))$, a maximum likelihood approach, perhaps based on the EM algorithm, may be employed.

Here, we shall regard the variable θ as angle of view of the target. This may be a multivariate quantity comprising azimuth and elevation, but in the examples of section 5, we consider azimuth only. Thus, Equation (7) states that for a given angle of look, θ, the target return, x, is a sample from a distribution, $p(x|\theta)$, and the total distribution is an integral over all angles of look.

For the gamma mixture model, there are two sets of parameters: the component means, μ and the order parameters, m (both $\in \mathbb{R}^d$). For g components, we wish to re-estimate $\{m_k, k = 1, \ldots, g\}$ and the means, $\{\mu_k, k = 1, \ldots, g\}$, which we regard as functions of underlying variables, θ (in the ship and vehicle data θ is univariate),

$$\mu = \mu(\theta) = \sum_{i=1}^{h} v_i \phi_i(\theta)$$
$$m = m(\theta) = \sum_{i=1}^{h} s_i \phi_i(\theta) \tag{3}$$

where ϕ_i is a set of h specified basis functions (for example, radial basis functions) defined on the space characterised by θ and $\{v_i, i = 1, \ldots, h\}$ and $\{s_i, i = 1, \ldots, h\}$ are sets of weights to be determined.

The means and order parameters of the kth group are

$$\mu_k = \sum_{i=1}^{h} v_i \phi_i(\theta_k)$$
$$m_k = \sum_{i=1}^{h} s_i \phi_i(\theta_k)$$

or in matrix form

$$U = V\Phi$$
$$M = S\Phi$$

where $V = [v_1|\ldots|v_h]$, $S = [s_1|\ldots|s_h]$ and $\Phi = [\phi(\theta_1)|\ldots|\phi(\theta_g)]$ and $\phi(\theta_k)$ is the h-dimensional vector with ith component $\phi_i(\theta_k)$. Thus, the parameters of each component, μ_k and m_k, depend on the same set of underlying parameters, V and S.

The distribution, $p(x)$, may now be regarded as depending on two sets of vectors that characterise the means and order parameters: the $d \times h$ matrices V and S,

$$p(x) = p(x|S, V)$$

Given a data set $\{x_i, i = 1, n\}$, we seek to maximise the log likelihood

$$L = \sum_{j=1}^{n} \ln[p(x_j|S, V)]$$

with respect to the parameters of the model S and V. We shall not present the details of parameter estimation for latent variable models here, but note that

1. A radial basis function provides a flexible model for the nonlinear transformation from latent space to data space.

2. An EM scheme may be derived for the model parameters, but unless simplifications are made, the update equations for the means and order parameters are coupled, thus requiring some nonlinear optimisation scheme for their solution.

3. For normal mixtures, Bishop *et al* [1, 2] have derived EM update equations.

4. Smoothness may be ensured through incorporation of a suitable prior on the models.

3.2 Using Angular Information

Knowledge of the angle at which measurements are made is not necessary as part of the latent variable model, but if it is available, how would we use it during training and test? During training, we would use θ_i as part of the maximum likelihood re-estimation. Suppose that the training data comprise radar range profile (or ISAR) measurements together with the angle of look. Thus, we are given the data $\{(x_i, \theta_i), i = 1, \ldots, n\}$. We may write the joint distribution as

$$p(x, \theta) = p(x|\theta)p(\theta) \tag{4}$$

where the conditional density $p(x|\theta)$ depends on parameters that describe the density. If we assume a

gamma mixture with mean and order parameters being a nonlinear function of angle, then

$$p(x|\theta) = p(x|\theta, S, V)$$

The log likelihood, L, is given by

$$L = \sum_{i=1}^{n} \ln \{p(x_i|\theta_i, S, V)p(\theta_i)\}$$

which we maximise as a function of S and V. We may use a simple gradient scheme. The resulting parameters are used to characterise $p(x, \theta)$ (4) for each class.

On test, we may have the measurement x only; that is, we assume that we do not know the heading of the target. Alternatively, we may have an estimate $\hat{\theta}$ of the heading θ, from which we are able to obtain a distribution for the true aspect θ, $p(\theta|\hat{\theta})$.

If we have a measurement x and an estimate of angle $\hat{\theta}$, then we require $p(x, \hat{\theta})$ given by

$$p(x, \hat{\theta}) = \int p(x|\theta)p(\theta|\hat{\theta})d\theta p(\hat{\theta}) \qquad (5)$$

If the estimate is very close to the true angle, we may make the approximation

$$p(x, \hat{\theta}) = p(x|\hat{\theta})p(\hat{\theta}) \qquad (6)$$

otherwise, we must approximate the integral by summing over a range of θ. Our training procedure has given S and V and hence $p(x|\hat{\theta})$. We then use these as our estimates of density in Bayes rule to obtain posterior probabilities.

If we do not have an estimate of angle in the test conditions then we must use the radar measurements, x only,

$$p(x) = \int p(x|\theta)p(\theta)d\theta$$

$$\approx \frac{1}{n} \sum_{i=1}^{n} p(x_i|\theta_i)$$

where the summation is over the training samples, and we have taken a uniform prior on θ.

In (5) and (6) we are using our estimate $\hat{\theta}$ of the heading as part of our decision making; that is, we may use angular information to improve performance of the classifier. Alternatively, if we know target type (or have an estimate) we may use it to get a better estimate of heading – in a tracking situation for example. As an illustration, suppose that target type is known. We require $p(\theta|\hat{\theta}, x)$, the distribution of true angle given an estimate of angle and the radar measurements (for example, the range profile). This may be written, using Bayes theorem, as

$$p(\theta|\hat{\theta}, x) = \frac{p(x|\theta)p(\theta|\hat{\theta})}{\int p(x|\theta)p(\theta|\hat{\theta})}$$

where the integral may be approximated by a finite sum. Thus, the radar image is used to refine target orientation estimates.

3.3 A Special Case

In section 3.1, dependence of the target probability density function on angle was used to motivate a mixture model approach to modelling the radar returns from targets. This dependence was achieved by modelling the distribution parameters as a nonlinear function of a latent variable, with the interpretation of angle. Sampling this distribution gave rise to a mixture model, whose components shared parameters. We now make a simplification. We model each component separately.

We express the overall distribution for a given target, $p(x)$, as

$$p(x) = \int p(x|\theta)p(\theta)d\theta \qquad (7)$$

for some variable θ, notionally an angle coordinate. A finite sample approximation to (7), based on g components, is

$$p(x) = \sum_{i=1}^{g} p(x|\theta_i)p(\theta_i) \qquad (8)$$

where $\sum p_i = 1$ and $p_i = p(\theta_i)d\theta_i$.

This is a finite mixture model of the form (2), but differs from (2) in that the parameters of each component do not depend on the parameters of the function $\Psi(\theta)$, but are independent.

The interpretation of θ as angle allows a simple scheme to be employed for obtaining the parameters of the mixture (8), as follows. Suppose that we have data gathered as a function of azimuth. Partition the data set according to angle into g equal–sized sectors. Use the data within each sector to estimate the parameters (maximum likelihood estimation) of each component distribution separately (assuming a simple parametric form, such as exponential or gamma). The component distribution weights are set to $p_i = 1/g$. This scheme does not maximise the likelihood of the data given the mixture model (8), but provides an approximation in which the likelihood of the data within each sector, given the local model is maximised.

Thus, a mixture model arises naturally if we consider the target density to be a function of angle. Initialisation of the mixture components can be achieved using a data set labelled by angle. Refinement of the mixture components using a full maximum likelihood approach is described in Section 4.

3.4 Robustness to Shifts

If we gather our training data[2] by positioning a vehicle on a turntable, then we know the range gate in which the physical centre of the target lies. Given a test range profile, then ideally we need to extract

---

[2] We assume that the training data comprise measurements on a fixed number of range gates that span the target.

the test image x so that the centre of the target lies in the same range gate. We then evaluate $p(x)$ for each class. However, in practice, we do not know the physical centre of the target (we may not know it for the training data if the target translates as it rotates – see Section 5), but we can calculate a centroid using the test range profile. We then need to extract d range gates around this centroid by deciding which range gate (1 to d) to position the centroid in.

Consider a single component of the mixture, $p(x|\theta_i)$. Suppose that we generate data from this component by random sampling. For each sample generated calculate its centroid. The centroid positions will not necessarily be in the same range gate as the centroid of the distribution mean. There will be a distribution, $p(s_n)$, of centroid positions, $s_n \in \{1, \ldots, d\}$.

We may partition the distribution, $p(x|\theta_i)$, according to the centroids of the generated data,

$$p(x|\theta_i) = \sum_{s_n} p_i(s_n) p(x|\theta_i, s_n) \qquad (9)$$

where $p(x|\theta_i, s_n)$ is the probability distribution of samples whose centroids are in cell s_n.

The quantity $p_i(s_n)$ is the probability that the centroid occurs in s_n from data generated by $p(x|\theta_i)$. It is determined by the distribution, $p(x|\theta_i)$ and may be estimated from that distribution through Monte Carlo simulation, by generating data and noting the distribution of centroid positions. The probabilities, $p_i(s_n)$, depend on i, the mixture component.

Therefore, the overall target distribution may be written as the mixture,

$$p(x) = \sum_{i=1}^{g} p_i \sum_{s_n=1}^{d} p_i(s_n) p(x|\theta_i, s_n) \qquad (10)$$

To evaluate the above equation for a test sample x, we may position the centroid of x over each allowable centroid position (that is, each possible centroid position permitted by the distributions, $p(x|\theta_i)$) in turn, then

1. sum over centroid positions (many may not contribute since $p_i(s_n) = 0$, the centroid position is not allowable for that component)

2. sum over components.

Thus, we have expressed the robustness to pattern translation problem as a mixture formulation (Equations (9) and (10)). In theory, the particular algorithm used to calculate the centroid position is unimportant. Although the distribution of centroid positions depends on this algorithm, we integrate over all possible centroid positions. In practice, however, it may be preferable to have an estimate of centroid position with a narrow distribution, $p_i(s_n)$. This would reduce computational costs since for many values of s_n, $p_i(s_n) = 0$ – samples with that centroid do not occur for $p(x|\theta_i)$.

3.5 Robustness to Amplitude Variation

We may need to scale the test image to normalise the data (the test samples may be measured at a different signal–to–noise ratio that the training data). In the above analysis, we partitioned the data generated by a component according to the centroid position. We may also partition according to the overall amplitude level of the test pattern. Let A denote some overall amplitude measurement of a pattern.

$$p(x|\theta_i) = \sum_A p(x|\theta_i, A) p_i(A)$$

where $p(x|\theta_i, A)$ is the probability distribution of samples whose overall amplitude is A, assumed to take discrete values.

To evaluate for a given x, we scale it to have amplitude A and substitute into

$$p(x) = \sum_{i=1}^{g} p_i \sum_A p(x|\theta_i, A) p_i(A)$$

Thus, in a similar manner to robustness to shifts, we can treat robustness to amplitude scaling by formulating a mixture model.

For computational convenience, we need to discretize A. Also, we need to define a scheme for calculating the amplitude of a pattern. As in the centroid situation, in principle it does not matter how we calculate A, given x, since we integrate over the distribution of A. In practice, it may be important. If our estimator of amplitude has a narrow distribution, then we could take the one extreme that the amplitude distribution is approximated by one cell at the distribution mean. Thus, all test images are scaled to the distribution mean.

3.6 Target Distribution

We still need to specify the forms of the mixture component distributions. For example, we may again take an exponential distribution, although gamma distributions may be more appropriate. The gamma distribution

$$p(x) = \frac{m}{(m-1)!\mu} \left(\frac{mx}{\mu} \right)^{m-1} \exp\left(-\frac{mx}{\mu} \right)$$

has as special cases the Swerling 1 and 2 models ($m = 1$, Rayleigh statistics), Swerling 3 and 4 ($m = 2$) and the non–fluctuating target ($m \to \infty$), although other values of m have been observed empirically [12].

A simple multivariate form is to assume independence of range gates so that the component distribution is given by

$$p(x|\theta_i) = \prod_{j=1}^{d} \frac{m_{ij}}{(m_{ij}-1)!\mu_{ij}} \left(\frac{m_{ij}x}{\mu_{ij}} \right)^{m_{ij}-1} \times$$
$$\exp\left(-\frac{m_{ij}x}{\mu_{ij}} \right)$$

where m_{ij} is the order parameter for range gate j of component i and μ_{ij} is the mean.

We may of course represent the component distribution itself as a mixture in order to model different scattering distributions. Further, we may partition it into two basic components,

$$p(\boldsymbol{x}|\boldsymbol{\theta}_i) = p_t t(\boldsymbol{x}) + p_n n(\boldsymbol{x}) \qquad (11)$$

where $t(\boldsymbol{x})$ is a target distribution, $n(\boldsymbol{x})$ a noise or clutter distribution and p_t and p_n are prior probabilities ($p_t + p_n = 1$). This allows the presence of noise to be taken into account.

3.7 Summary

In this section we have described several different ways in which mixture models may arise in a target modelling situation.

1. to incorporate angular dependencies.

2. to ensure robustness to uncertainty in target centroid position.

3. to ensure robustness to overall amplitude variation.

4. to model different types of target behaviour.

5. to incorporate both noise and target models to reduce sensitivity to noise on test.

The advantage of the mixture model approach is that it provides a simple flexible model for the distribution of target returns, while also incorporating into the same framework features such as robustness that are important in a practical implementation.

How do we use it in practice? In training a model, we specify the form of the component distributions, $p(\boldsymbol{x}|\boldsymbol{\theta}_i)$ (either as single component exponential or gamma, or as a mixture), the number of component distributions in the mixture (ideally, this is determined from the data) and use a maximum likelihood approach to determine the model parameters for each class in turn. The training model is depicted schematically in Figure 2. In the figure, $p(\boldsymbol{x}|\boldsymbol{\theta}_i)$ is expressed as a sum of a noise distribution and a target distribution, which itself is modelled as a sum of two distributions. In the examples of Section 5, we simply use a single component multivariate gamma distribution for $p(\boldsymbol{x}|\boldsymbol{\theta}_i)$.

Once the parameters of the component distributions have been obtained, we consider each component in turn to estimate (perhaps through Monte Carlo simulation) the distribution of centroid positions and amplitudes.

On test, we need to extract a test image from a set of range gates and scale appropriately. For each component, we extract the image so that its centroid lies in each of the allowable centroid positions for that component. Similarly, we scale it to each possible
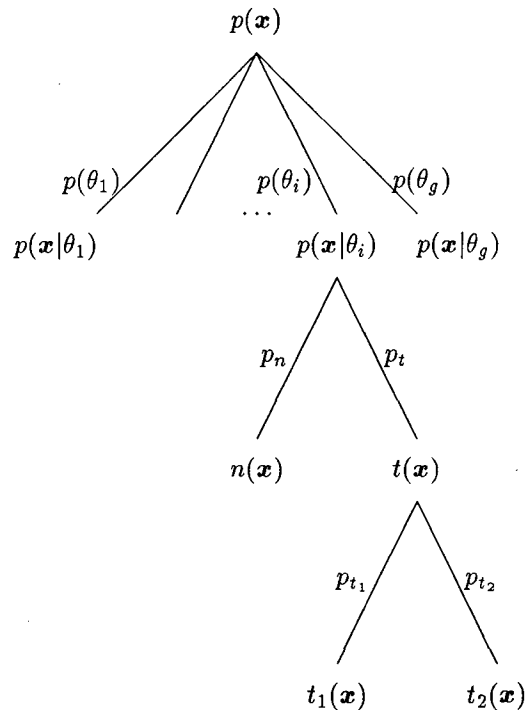
Figure 2. A representation of a target mixture model trained using gathered data for each target separately.

amplitude (suitably quantised). We then evaluate the probability density function for the component and sum over all amplitudes and centroid positions. This is shown in Figure 3 for a model where component i gives rise to three centroid positions and two amplitude values.

4. PARAMETER ESTIMATION

We now address the problem of estimating the parameters of the mixture components. We shall adopt a maximum likelihood approach and derive update equations for the model parameters for gamma mixture models.

Given a set of n observations $(\boldsymbol{x}_1, \ldots, \boldsymbol{x}_n)$, the likelihood function is

$$L_0(\boldsymbol{\Psi}) = \prod_{i=1}^{n} \sum_{j=1}^{g} p_j p(\boldsymbol{x}_i|\boldsymbol{\Psi}_j) \qquad (12)$$

where $\boldsymbol{\Psi}$ denotes the set of parameters $\{\boldsymbol{\Psi}_1, \ldots, \boldsymbol{\Psi}_g\}$ and $\boldsymbol{\Psi}_j$ are the parameters associated with component j. In general, it is not possible to solve $\partial L_0/\partial \boldsymbol{\Psi} = 0$ explicitly for the parameters of the model and iterative schemes must be employed. One approach for maximising the likelihood $L_0(\boldsymbol{\Psi})$ is to use a general class of iterative procedures known as EM (Expectation–Maximisation) algorithms, introduced in the context of missing data estimation by Dempster, Laird and Rubin [5], though it had appeared in many forms previously.
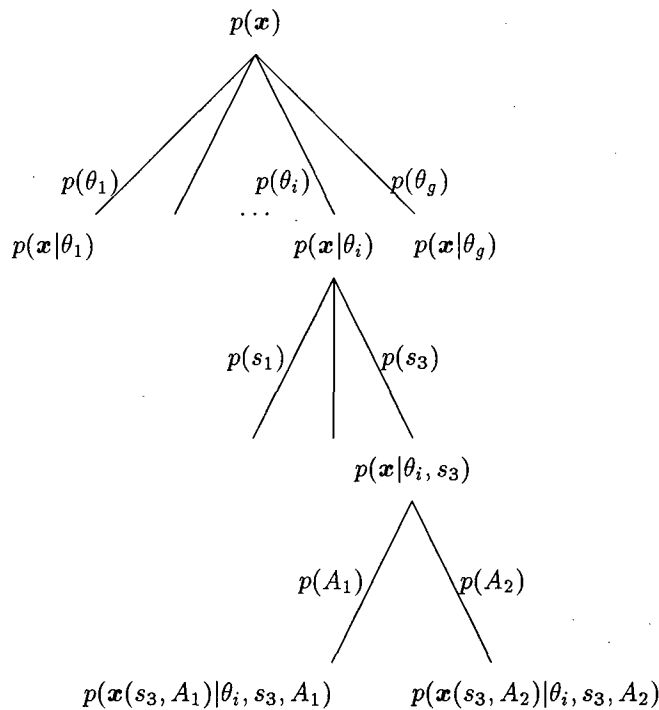
Figure 3. Evaluating the probability density function for a test range profile, x. $x(s_i, A_j)$ is the test image extracted so that its centroid is at s_i and amplitude is A_j.

The EM procedure is well known (for example, Titterington *et al* [13]) and we do not present the stages in the derivation of the re–estimation equations here, simply quoting results.

Let $\Psi_k^{(m)}$ be the estimate of the parameters of the kth component at the mth stage of the iteration. Let w_{ij} be the probability of group j given x_i and $\Psi^{(m)}$, given by

$$w_{ij} = \frac{p_j^{(m)} p(x_i | \Psi_j^{(m)})}{\sum_j p_j^{(m)} p(x_i | \Psi_j^{(m)})} \qquad (13)$$

The the re–estimate of the component weights, p_j, is given by

$$\hat{p}_j = \frac{1}{n} \sum_{i=1}^{n} w_{ij} \qquad (14)$$

We assume that each range gate has a mixture of gamma distributions, with components given by the distribution (independence assumption)[3]

$$p(x | \Psi_k) = \prod_{j=1}^{d} \left[\frac{m_{jk}}{(m_{jk}-1)! \mu_j^k} \left(\frac{m_{jk} x_j}{\mu_j^k} \right)^{m_{jk}-1} \times \right.$$
$$\left. \exp\left(-\frac{m_{jk} x_j}{\mu_j^k} \right) \right]$$

where $x = (x_1, \ldots, x_d)^*$, the vector of measurements; the parameters of the kth group, Ψ_k are $\{\mu^k, m_{jk}\}$ where $\mu^k = (\mu_1^k, \ldots, \mu_d^k)^*$ and m_{jk} is the value of m for the kth group and jth range gate.

The re–estimation of the mean vector of the kth mixture component is

$$\mu^k = \frac{\sum_{i=1}^{n} w_{ik} x^i}{\sum_{i=1}^{n} w_{ik}} \qquad (15)$$

and the m_{jk} satisfy

$$\nu(m_{jk}) = -\frac{\sum_{i=1}^{n} w_{ik} \log\left(\frac{x_{ij}}{\mu_j^k} \right)}{\sum_{i=1}^{n} w_{ik}} \qquad (16)$$

where $\nu(m) = \log(m) - \psi(m)$ and $\psi(m)$ is the digamma function.

The function $\nu(m)$ satisfies the property that

$$\nu(m) \approx \frac{1}{2m} + \frac{1}{12m^2} + \ldots \quad \text{as } m \to \infty$$
$$\nu(m) \approx \frac{1}{2m} + const. \qquad \text{as } m \to 0$$

Therefore, there is at least one solution $m > 0$ for which $\nu(m) = \delta$ for $\delta > 0$. A simple gradient scheme should be sufficient to obtain a solution.

Thus, the operations in the maximisation of the EM procedure are to estimate μ^k using (15) and then to solve (16) for the m_{jk}, using an iterative gradient procedure.

5. APPLICATION TO RADAR RANGE PROFILES

5.1 Ship Data

The data consist of range profiles of ships of seven class types. There are 19 files, each of which contains

---

[3] We are assuming that each mixture component can be represented by a product of univariate gamma distributions. This does not imply that we are making the independence assumption for the mixture distribution, but only for each component. Thus, interpreting i as an angle indicator, we are assuming that locally the range gates are independent, but not globally since scatterers move from one range gate to another as the target rotates.

range profiles of a ship which are recorded as the ship turns through 360 degrees. The aspect angle of the ship varies smoothly as one steps through the file and the centroid of the ship drifts across range gates as the ship turns. Each range profile consists of 130 measurements on radar returns from 130 range gates. These data sets have been used by Luttrell [10] and details are given in Table 1. The data sets are divided

Target Class	no of profiles	
	Train	Test
1	3334	2085
2	2636, 4128	2116
3	2604, 2248, 2923	2476, 3619
4	8879, 3516	4966, 2560
5	3872	3643
6	1696	2216
7	1839	

Table 1. Details of data files

into 11 training files and 8 test files. As we can see from the table, there is no test data available for class 7. Several other classes have more than one rotation available for training and testing.

In each of the experiments below, 1200 samples over 360 degrees from each of the training set files were used in model training. This enables comparison to be made with the results of Luttrell [10].

5.2 Implementation Details

In each experiment, a mixture model density was constructed (using the basic approach described in section 3) for each file and those densities corresponding to the same target type are combined with equal weight. For a mixture model with g components, the parameters of the mixture model were initialised by dividing the data into g equal angle sectors and for each sector separately calculating the maximum likelihood estimate of the mean and order parameters of the gamma distribution. The EM algorithm was run on the whole training data set and the final value of the log likelihood, $\log(L)$, at convergence recorded.

There has been considerable research into model selection for multivariate mixtures. We adopted a simple approach and took our model selection criterion to be

$$AIC2 = -2\log(L) + 2N_p$$

where N_p is the number of parameters in the model,

$$N_p = 2(d+1)g - 1$$

This has been considered by Bozdogan and Sclove [3]; other measures are described and assessed be Celeux and Soromenho [4].

Once the components of the mixture model have been determined, samples form the component distributions were generated and the distribution of the

centroids measured for each mixture component. It was found that most samples ($> 99\%$) lay within two range gates of the position of the centroid of the component mean. Therefore on test, a test pattern was shifted to all positions within 2 range gates of the component mean.

The amplitude of the test pattern was scaled to the amplitude of the component mean.

5.3 Ship Profiles

Below we give results of the method applied to the ship data. We report confusion matrices despite their limitations as measures of classifier performance. Ideally we would like to say how well the estimate of the posterior density, $\hat{p}(j|x)$, approximates the true density $p(j|x)$. A measure of this discrepancy is the reliability of the classifier [11] or imprecision [8]. However, $p(j|x)$ is unknown in practice and techniques for evaluating bounds on imprecision are currently under investigation.

5.3.1 Experiment 1

In this experiment, the classifier is trained with 40 components per file and tested on the test data files with the ship orientated so that it is in the range ±40 degrees bow-on or stern-on to the radar. This restriction is applied so that the results may be compared with those given by Luttrell [10], where a classifier based on a self-organising network was designed. Table 2 reproduces the results of Luttrell [10] and gives the mixture model results alongside.

		True Class					
		1	2	3	4	5	6
	1	84.4	8.9	8.5	4.2	2.3	10.3
	2	12.6	86.1	5.8	6.0	0.5	10.7
Predicted	3	0.6	0.2	68.9	3.4	5.5	23.2
Class	4	1.0	2.0	5.5	73.1	17.0	11.4
	5	0.8	0.0	5.3	8.8	57.1	0.9
	6	0.3	0.0	2.9	1.7	11.3	37.7
	7	0.3	2.9	3.1	2.8	6.3	5.8

		True Class					
		1	2	3	4	5	6
	1	72.0	4.4	2.9	5.2	1.7	6.0
	2	11.3	70.7	10.1	4.8	2.8	8.5
Predicted	3	9.3	10.0	67.7	10.0	24.6	20.2
Class	4	0.6	3.0	1.8	59.6	4.4	0.7
	5	0.2	2.3	3.3	9.0	57.9	2.3
	6	2.5	5.9	9.8	4.5	6.2	59.7
	7	4.2	3.6	4.4	6.7	2.3	2.5

Table 2. Gamma mixture results (top) and self-organising network results (bottom) [10] for a test set pattern ±40 degrees bow-on or stern-on to the radar.

The average classification performance on test of the mixture model approach is 67.9% compared to 64.6% given by Luttrell [10]. There are some notable differences in performance: there is much better clas-

sification rate on classes 1 and 2 and much poorer performance on class 6.

5.3.2 Experiment 2

In this experiment, mixture models were trained with varying numbers of components and tested on the whole of the test set (there is no angle restriction). Again, 1200 samples per file were used and Figure 4 plots the model selection criterion $AIC2$ as a function of the number of components for each of the training files. Figure 5 plots the classification rate as a function of the number of components, where each model has the same number of components. The minimum of $AIC2$ occurs for each of the 11 files when the number of components is given by (80, 80, 70, 70, 60, 80, 70, 70, 50, 70, 100). Thus, each model requires a different number of components. The classification performance for this model is given in table 3.

The overall classification rate is 64% for the selected model. This is about the level of the plateau region in Figure 5. Thus the $AIC2$ criterion has provided a model that is close to the best test set performance over the range of model sizes considered.
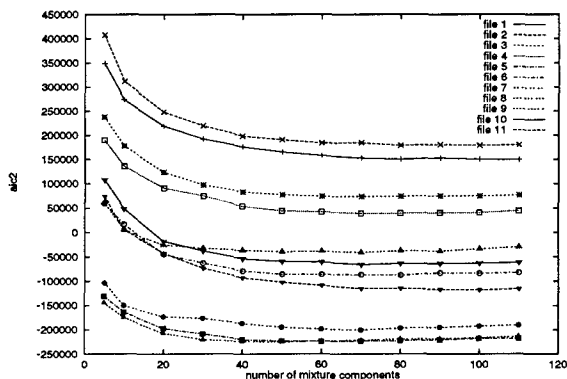
Figure 4. $AIC2$ as a function of the number of mixture components for each file in the training set.

		True Class				
		1	2	3	4	5	6
	1	59.1	5.6	6.5	5.7	0.5	10.0
	2	12.1	67.2	3.2	1.7	0.0	5.3
Predicted	3	5.7	8.9	64.2	5.5	3.4	28.9
Class	4	9.9	10.5	11.0	72.5	25.2	20.7
	5	0.1	4.3	8.3	12.9	67.3	3.1
	6	12.8	2.8	4.0	1.0	2.3	30.7
	7	0.2	0.7	2.9	0.6	1.3	1.2

Table 3. Gamma mixture results for the whole test set for a model chosen according to minimum values of $AIC2$.
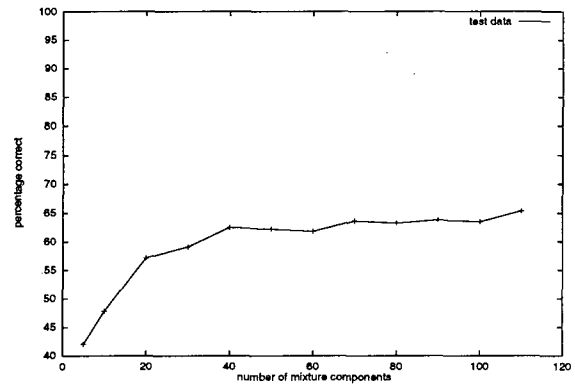
Figure 5. Classification rate as a function of the number of mixture components for the ship data.

6. APPLICATION TO ISAR IMAGES

6.1 Vehicle Data

The data comprise single polarisation ISAR images of three vehicles measured on a turntable. There are two rotations of each vehicle. For each vehicle and each rotation, there are 2000 patterns. The image size is 16 × 20.

A third data set of 'similar' vehicles, but not the same measure type, was also considered as part of an experiment into classifier robustness – see the paper by Britton in these proceedings

6.2 Results

Results for the training set, the second rotation and the separate 'test' set (that differed in some detail from the training data) are given in Figure 6. Each data set was modelled using a gamma mixture model in which the means and order parameters were re–estimated. Again, the criterion $ACI2$ was used to control the complexity of the model. In terms of modelling the data on the second rotation, performance is still increasing at 70 components per class. The $AIC2$ measure has not reached a minimum at this point.

7. SUMMARY AND DISCUSSION

In this paper we have developed a gamma mixture model approach to the classification of radar range profiles and ISAR images. A latent variable model was introduced as one means of modelling the smooth variation of the underlying distribution with angle. EM update equations for the model parameters of a basic mixture model were derived. Robustness to amplitude scaling of the test pattern and unknown orientation and location of the target can be taken into account in the mixture model framework. The approach has been applied to the classification of ship
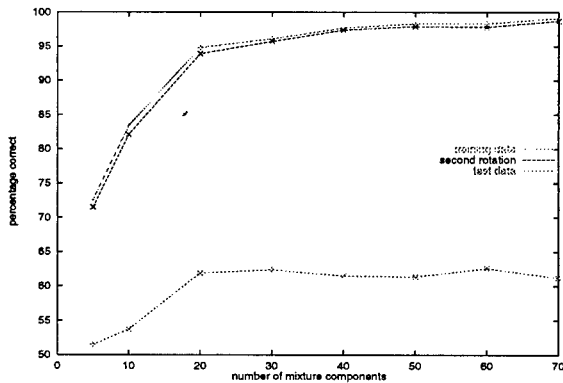
Figure 6. Classification rate as a function of the number of mixture components for the vehicle data.

profiles (giving improved performance, *in terms of error rate*, achieved compared with previously published results) and to ISAR images of vehicles.

However, error rate is only one measure of performance. It does not tell us how good the classifier is. We may get an error rate of 40% say, but if the classes are indeed separable (for the given features), then we could improve performance by better classifier design. Yet, if the Bayes error rate is itself 40%, then we are wasting effort trying to improve classifier design. We must seek additional variables or features. This is one of the motivations behind the work in this paper: to provide estimates of the posterior probabilities that may be combined with other information (for example, misclassification costs, domain–specific data, intelligence reports) in a hierarchical manner for decision making.

Thus, we have developed a *semi–parametric* density estimator that incorporates robustness features and makes use of physical/empirical scattering distributions. The approach may not give better performance in terms of error rate than some other classifiers (although it is clearly better than single component parametric distributions), but hopefully better approximations to the true posterior probabilities. This is difficult to assess and remains an issue for continuing study. Initial work is reported by Yu *et al* [17]. Other areas for further work include further assessment on two–dimensional (SAR/ISAR) images, development of the latent variable models and sensitivity to noise and clutter.

References

[1] C. Bishop, M. Svensén, and C. Williams. EM optimization of latent–variable density models. In D. Touretsky, M. Mozer, and M. Hasselmo, editors, *Advances in Neural Information Processing Systems 8*, pages 465–471. MIT Press, 1996.

[2] C. Bishop, M. Svensén, and C. Williams. GTM: a principled alternative to the self–organizing map. In M. Mozer, M. Jordan, and T. Petsche, editors, *Advances in Neural Information Processing Systems 9*, pages 354–360. MIT Press, 1997.

[3] H. Bozdogan and S. Sclove. Multi–sample cluster analysis using Alaike's information criterion. *Annals of Institute of Statistical Mathematics*, 36:163–180, 1984.

[4] G. Celeux and G. Soromenho. An entropy criterion for assessing the number of clusters in a mixture model. *Journal of Classification*, 13(2):195–212, 1996.

[5] A. Dempster, N. Laird, and D. Rubin. Maximum likelihood from incomplete data via the EM algorithm. *Journal of the Royal Statistical Society B*, 39:1–38, 1977.

[6] B. Everitt and D. Hand. *Finite Mixture Distributions*. Monographs on Statistics and Applied Probability. Chapman and Hall, London, 1981.

[7] J. Friedman. On bias, variance, 0/1 loss, and the curse of dimensionality. *Data Mining and Knowledge Discovery*, 1:55–77, 1996.

[8] D. Hand. *Construction and Assessment of Classification Rules*. John Wiley, Chichester, 1997.

[9] D. Lowe and A. Webb. Optimized feature extraction and the bayes decision in feed–forward classifier networks. *IEEE Transactions on Pattern Analysis and Machine Intelligence*, 13(4):355–364, 1991.

[10] S. Luttrell. Using self–organising maps to classify radar range profiles. In *4th International Conference on Artificial Neural Networks*, pages 335–340, Cambridge, 1995. IEE, IEE.

[11] G. McLachlan. *Discriminant Analysis and Statistical Pattern Recognition*. John Wiley, New York, 1992.

[12] M. Skolnik. *Introduction to Radar Systems*. McGraw–Hill Book Company, New York, second edition, 1980.

[13] D. Titterington, A. Smith, and U. Makov. *Statistical Analysis of Finite Mixture Distributions*. John Wiley and Sons, New York, 1985.

[14] A. Webb. Multidimensional scaling by iterative majorisation using radial basis functions. *Pattern Recognition*, 28(5):753–759, 1995.

[15] A. Webb. An approach to nonlinear principal components analysis using radially-symmetric kernel functions. *Statistics and Computing*, 6:159–168, 1996.

[16] A. Webb. Gamma mixture models for target recognition. 1997. (submitted for publication).

[17] K. Yu, D. Hand, and A. Webb. Evaluating the imprecision of classification rules. 1997. (submitted for publication).

RCS Determination for DLR Stealth Design F7

E. Kemptner, D. Klement, H. Wagner
German Aerospace Center DLR - NE/HF
Institute for Radio Frequency Technology
Postfach 1116, D-82230 Wessling, Germany

1. SUMMARY

The paper presents the current state of work at DLR to analyse a generic airplane design with stealth characteristics using theoretical and experimental tools. The theories implemented in the computer codes and the measurement facilities are described. The procedures to produce scale models are discussed. The results of a mono- and bistatic analysis over a wide frequency band are presented. In addition, implications for the detection probability and an analysis of the target fluctuations relevant for radar detection are shown. The steps pursued in further investigations are outlined.

2. INTRODUCTION

The visibility of an object for radar systems depends on the magnitude of the received radar power P_r, which can be calculated using the radar equitation:

$$P_r = \frac{P_t G_t}{4\pi R^2} \sigma \frac{1}{4\pi R^2} A_r \qquad (1)$$

The transmitted Power P_t, the gain of the transmitting antenna G_t, the effective area of the receiving antenna A_r and the distance R are the most important parameters of the radar system and of the wave propagation in free space. The scattering characteristic of the object is defined by the radar cross section σ. This parameter has the dimension of an area and is usually given in logarithmic scale relative to one square meter (dBsm). In **Fig. 1** the estimated values of σ are given for a number of significant objects. The greatest values of σ can be found for the specular reflection of flat discs or

panels. Cylindrical structures or spheres with the same dimensions have significant lower values of radar cross section, because only a small region around the specular point contributes to the back-scattered field. The field incident to the other regions of the vaulted surface is scattered into other directions. The circular disc with the radius of 1 m has 10 dB respectively 20 dB higher levels than the frigate or the airplane. The front view of the stealth airplane has a very low cross section like a bird. Therefor the demands in accuracy and sensitivity to the experimental as well as to the theoretical tools are very high.
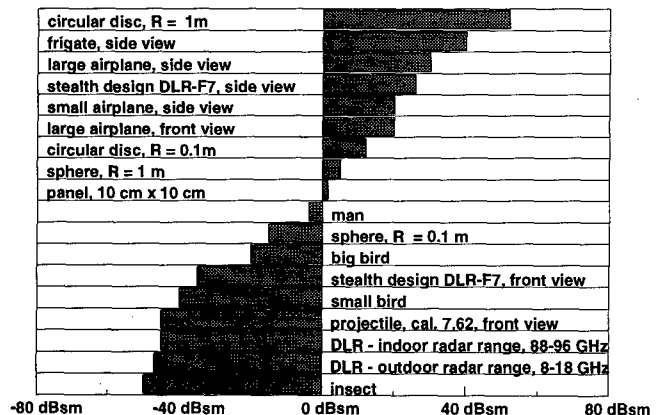
Fig. 1: Typical values for the radar cross section of some targets at 10 GHz.

Two computer codes (SIGMA for the monostatic and BISTRO for the bistatic case), both based on Physical Optics Method (PO) [1, 2], have been and will still be developed at DLR. These codes are applied together with the well-known computer code NEC-2 [3], based on the Integral Equation Method (IEM), to analyse the monostatic and bistatic scattering behaviour of the generic airplane F7 (internal designation) with

stealth characteristics over a wider range of frequencies. Since also mono- and bistatic measurements have to be carried out to validate the theoretical predictions, at least at certain frequencies, the complete analysis will result in a comprehensive work.

This paper reports the present state of the RCS-analysis. Since criteria are needed to estimate the efficiency of this and future configurations the radar data of the F7 further are submitted to a recently established radar range model DORA (Detection of Objects by Radar) to predict the range for a special radar system.

The following section outlines the theories used in the above-mentioned RCS codes as well as of the radar range code. Special attention is given to evaluate the overlapping region between the code SIGMA that is based on high-frequency methods and NEC-2 based on low frequency methods.

These tests were carried out with basis structures like an ogival cylinder. The third section deals with the design and production of scale models adequate for measurements in the X- and W-band. Section four describes the bistatic scatter field test range operating in the W-band that recently was modified to carry out monostatic measurements.

The data of this test range were used for comparison with the predicted values. In section five the results for the F7 collected by the several tools are presented and discussed. For a special radar system the efficiency of different fluctuation models is estimated by determining the radar range. In the conclusion the essentials of the analysis are summarized and the future work is indicated.

3. BASIC THEORIES USED IN SIGMA, BISTRO, NEC-2 AND DORA

3.1 RCS Calculations

The computer codes SIGMA and BISTRO, both developed at DLR, are based on the PO theory. As a high frequency approximation PO is very well suited for the calculation of the scattered field of electrically large structures. SIGMA is conceived for the monostatic case only while BISTRO is applicable in the bistatic case too. Both codes use a procedure to sort out the illuminated panels. In contrast to BISTRO, whose simple Hidden Surface Algorithm is only applicable for convex objects until now, SIGMA can be used for non-convex surfaces including double reflections. In SIGMA the contribution of the edge diffracted field is implemented using the Method of Equivalent Currents (MEC). So SIGMA can optionally be used as a Physical Theory of Diffraction (PTD) code for arbitrary aspects of observations.

As PO and PTD are high frequency methods they are only applicable down to a minimum ratio of the object dimensions to the wavelength. For a long time this minimum was thought to be several wavelengths. Detailed investigations in the last years [4] have shown that for much lower ratios very good results can be achieved. This extension of the wavelength domain to higher values for a given object is of great importance because the area of application of IEM now joins to this of PO and PTD. Therefore the development of a special hybrid method for this transition area seems to be unnecessary.

To use IEM the well-known computer code NEC-2 was applied for the investigated objects. For wire-grid models the Electric Field Integral Equation is chosen. The Method of Moments is used to calculate the currents along the wires. As the interactions of all segments are considered in the impedance matrix it takes a long CPU time and great storage requirements to solve the complex linear system of equations.

In order to compare the PO, PTD and IEM results an ogival cylinder (**Fig. 2**) with dimensions $4\,\lambda$ x $2\,\lambda$ x $4\,\lambda$ was modelled with flat panels for PO and PTD and with wires for IEM. The size of this object compared to the wavelength is already large for IEM and quite small for PO and PTD. **Fig. 3** shows the RCS for the horizontal polarization. Nevertheless the correspondence between the three results is quite good.
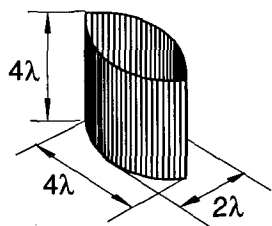
Fig. 2: Sketch of an ogival cylinder
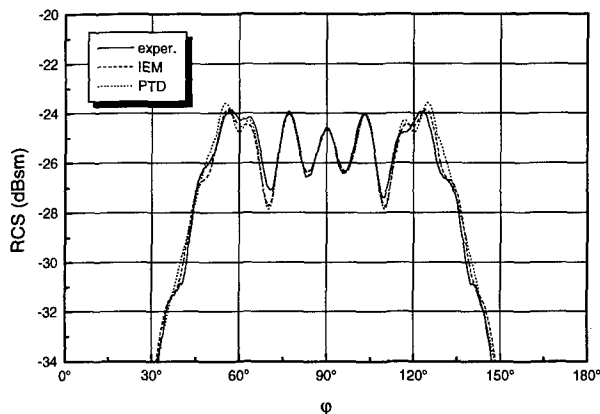
Fig. 3: RCS (HH-polarization) of the ogival cylinder by experiments, IEM and PTD

3.2 Design of a Stealth Airplane

The demand for the design of a stealth airplane is a low radar cross section in order to prevent the detection by radar. **Fig. 4** presents a computer model of the design DLR-F7 which actually is under test in the Institute of Radio Frequency Technology in Oberpfaffenhofen with respect to its stealth characteristics and in the Institute of Design Aerodynamics in Braunschweig with respect to aerodynamic features.

The plane is a generic structure to test the tools. It is fully metallized; the jet inlets are closed and further details are neglected at present. The radar cross section is designed to be less than 30 dBsm for a cone of ±15° around the flight direction. The design was carried out under high frequency considerations for monostatic radars. As mentioned above, flat surfaces and parts of curved surfaces which are oriented perpendicular to the incident radar waves cause high cross sections. It was the concept of the proposal to avoid all those surfaces including cylinders and spheres.

The actual airplane arrangement completely consists of flat panels . In the case of a monostatic radar which is positioned in flight direction most of the energy of the radar pulses is reflected to the sides and only a very small amount is reflected due to edge effects to the radar system.The length of the plane is 15 m and the wingspan of 10 m. For the electromagnetic calculations the computer models BISTRO and SIGMA are used. Both models use the approximation of Physical Optics (PO). Since SIGMA and BISTRO use a panel model of the object there is no deviation from the real shape.
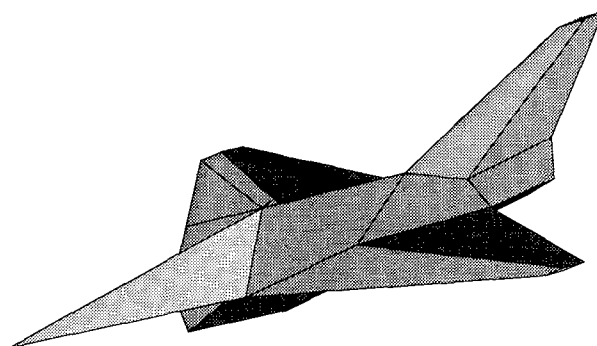
Fig. 4: Computer model of the DLR-F7 stealth design

3.3 Determination of Detection Range

As an extension to the RCS calculations, a tool to determine detection probabilities was developed and the distance, in which the object under investigation can be detected by a radar with the given properties. The starting point is the radar equation for the signal to noise ratio (S/N) for a target at distance R

$$\frac{S}{N} = \frac{P_t nK\tau G^2 \sigma(\vartheta,\varphi)\lambda^2}{(4\pi)^3 R^4 k_B T_{sys}} \frac{1}{\prod_i L_i} \qquad (2)$$

with P_t as peak transmitter power, $K\tau$ the uncompressed pulse width, G the antenna gain, $\sigma(\vartheta,\varphi)$ the polar and azimuth angle dependent RCS, n the number of integrated pulses, k_B as Boltzmann's constant, T_{sys} as system noise temperature and various additional losses L_i.

A signal corresponding to S/N is now fed into a detector which is able to detect the object with probability P_d (S/N), respectively P_d (R) via (3). It is known since the early work of Swerling [5] that

RCS fluctuations diminish the detection probability; the correct form to describe these fluctuations in the case of airplanes has been subject of discussions in the past [6]. So the RCS fluctuations were investigated and the consequences on detection probability in detail using calculated RCS data for the F7, which agree reasonably well with experimental results (see section 6.3). For the calculations "scan to scan" fluctuations were assumed, which are realized for example in the case of a typical airport surveillance radar, for which the scan rate is large compared to the target fluctuation time constant. For a quadratic detector and incoherent integration of n pulses, P_d is then given by

$$P_d = \int_0^\infty P_x(x) P_{d,Marcum}^{(n)}(x) dx \qquad (3)$$

where P_d is the detection probability for a target with constant signal to noise ration x, which was originally found by Marcum [5], and X = S/N a random variable distributed with a probability density function $P_X(x)$.

The probability density function results from the random variation of the aspect angle (ϑ, φ) due to rolling and yawing motion of the airplane via the $\sigma(\vartheta, \varphi)$-dependence. To obtain $P_X(x)$ a statistical analysis of $\sigma(\varphi)$ around a certain azimuth were therefore performed. The computer code allows currently only one-dimensional data analysis; so airplane rolling has to be neglected - with unknown implications on the results. The probability density function obtained is then available as a histogram; P_d can be calculated from (3). In order to generalize the treatment to unknown targets and to decrease computer effort to calculate P_d, it can be advantageous to find a parametric form for $P_X(x)$. Several distributions have been investigated, and are implemented in the computer code: Swerling's models 1 and 3 [5], generalized Chi-squared, lognormal, and Weibull distributions. Their parameters are found as the maximum likelyhood estimators. Detection probabilities are calculated using Shnidman's algorithm [7].

Finally a tool is needed to judge the quality of the different representations. Dowdy [8] proposed a statistical goodness-of-fit test; he applied Chi-squared and Kolmogorov-Smirnov tests. The latter is a parameter free test and is implemented in the program, too. Nevertheless since the detection probability and finally the radar range is in the center of interest, another more powerful method is used for discrimination: the description of the data which is best capable of reproducing P_d calculated from (3) with the (exact) histogram distribution, or the range R_{max} determined from it, is to be preferred.

4. DESIGN AND PRODUCTION OF SCALE MODELS

In order to verify the calculated results of the F7-design measurements had to be planned at scaled frequencies with scale models. To prepare the necessary datasets and technical drawings Auto-CAD-12 was used. Starting with the volume model of the F7 a surface model was created in the first step. Using a simple conversion program outside AutoCAD a panel model dataset for SIGMA and BISTRO was generated. In a second step this dataset was converted into a wire-grid model for NEC-2. In order to produce a scale model with factor 1:10 (**Fig. 5**) in a mechanical workshop technical drawings of all panels including the angles to the connecting panels have been produced. The fuselage was manufactured from a honeycombed material covered with plywood and the wings from a compact foam material. Finally the model was covered with silver.
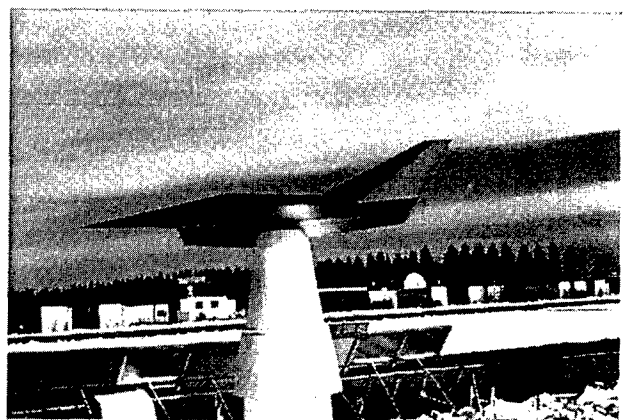
Fig. 5: Manually manufactured model of DLR-F7 (1:10)
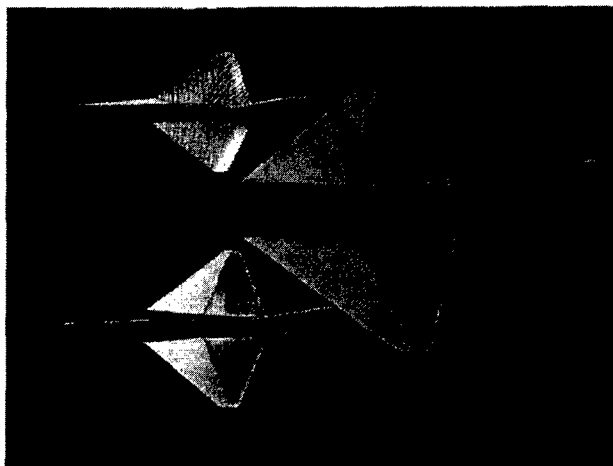
Fig. 6: Models manufactured in Stereo Lithography Technique (1:100; 1:200)

Smaller scale models with factor 1:100 and 1:200 were produced using stereolithography (STL) (**Fig. 6**). This technique is based on a special kind of synthetic resin that is hardened by focused laser light. The laser itself is positioned automatically corresponding to the data in a special STL dataset. This contains the triangular surface model of the object and was exported by AutoCAD starting from the volume model of the F7. Finally the resin model was covered with gold in a galvanic process. The 1:200 model was measured at a frequency of 94 GHz. For the measurement of the 1:100 model the test range has to be arranged with other antennas to satisfy the far field condition.
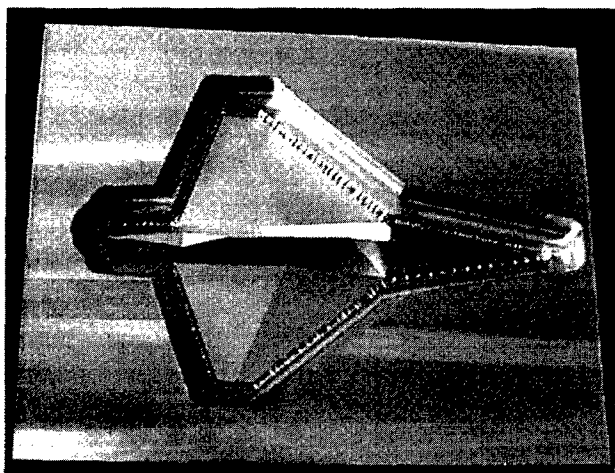
Fig. 7: First step of manufacturing by a CAD milling machine

The STL technique is very fast and inexpensive,

but the quality of the models has not been sufficient. The material did not hold the geometric forms during the process of hardening. Especially the thin structures of the wings have vaulted. Following a thumb rule the accuracy of the surface of the structure should be better than $\lambda/16$ or 0.2 mm for 94 GHz. To fulfil these demands we now make the models with the CAD milling machine. The data for the input are also directly obtained from the AutoCAD data set. **Fig. 7** shows an aluminium model after milling the upper surface. The first models are obviously much more accurate then the STL models. Measurements to compare the models with different accuracy are planned for the near future.

5. MEASUREMENT FACILITY

For monostatic and bistatic RCS measurements at 94 GHz ($\lambda = 3.2$ mm) a full polarimetric indoor range in an anechoic chamber was constructed (**Fig. 8**). The distance from the transmitter and the receiver to the center of the investigated object is 3.2 m. The object (maximum diameter 64 mm) is positioned on a styrene column. In the monostatic case the object is rotated (0° - 360°), in the bistatic case the receiver is moved at a swivel arm (bistatic angle: 8° - 180°). In order to make coherent measurements the local oscillators of receiver and transmitter are locked to a common reference source. Reliable bistatic measurements are possible excluding ±4° around the forward scattering angle. The noise level is at -50 dBsm and the dynamic range is 50 dB.

Fig. 8: Indoor test range for mono- and bistatic RCS measurements at 94 GHz.
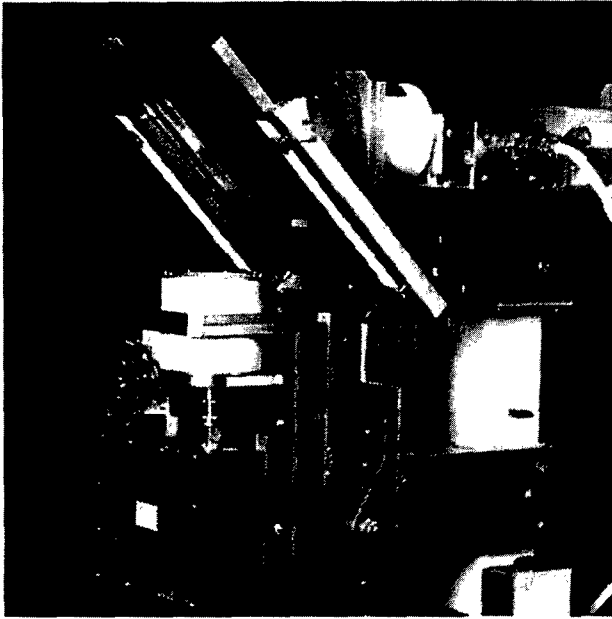
Fig. 9: Frontends of the 94 GHz test range in the set-up for monostatic measurements.

Fig. 9 shows the equipment for monostatic measurements. The scalar lens antennas are mounted directly on the receiving and transmitting front-ends. A layer of glass between the antennas (45° to the axis of radiation) is used as optical power divider for the transmitted and received signal. By this arrangement the centers of radiation of both antennas are in the same position, which is necessary for real monostatic measurements. The crosstalking between transmitting and receiving channel is very low and an easy change from monostatic to bistatic measurements is possible.

6. RESULTS

6.1 Monostatic RCS Results by SIGMA, NEC-2 and Measurements

The monostatic results of the measurements using the 1:200 scale model have been compared with the calculated results. Therefore SIGMA has been applied without using the equivalent edge currents (PO) as well as with them (PTD). As most of the edges at F7 are horizontal **Fig. 10** shows the monostatic RCS values for the more interesting horizontal case for an aspect angle range from 0° (nose of F7) to 120°. For levels under -50 dB only noise could be measured. At 50° the influence of the front edge of the wing is obvious. At this maximum the correspondence between the measured value and the PTD result is very good whereas PO yields no maximum. The high level from 90° to 100° is founded in the rudder and the correspondence of all methods is very good.

In **Fig. 11** the results of PO and PTD are compared with those of the IEM for the 1:200 model at a frequency of 10 GHz for horizontal polarization. NEC- 2 was applied using a wire-grid model of F7. Investigations with NEC-2 using a panel model have also been done but the Magnetic Field Integral Equation, which is applied in NEC in the case of a panel model, fails for the F7 because of the thin wings. For low and high aspect angles the difference between the SIGMA and NEC results is quite high. This is not remarkable because for this aspect angles the F7 has a geometric cross

Fig. 10: Monostatic RCS results by SIGMA (PO, PTD) and experiments for the 1:200 scale model at 94 GHz
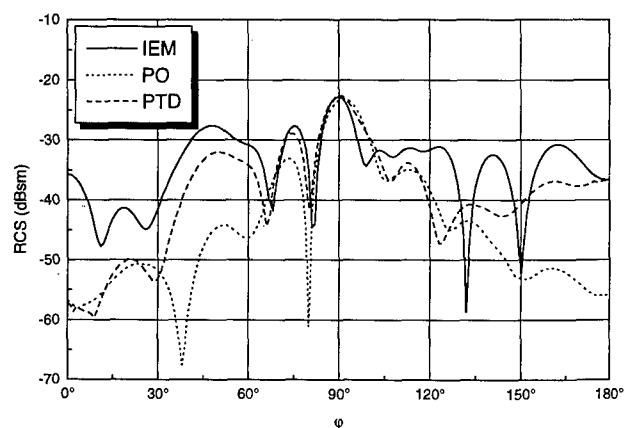
Fig. 11: Monostatic RCS results by SIGMA (PO, PTD) and NEC-2 (IEM) for the 1:200 scale model at 10 GHz

section in the order of λ^2 and therefore is outside the application area of high frequency approximations as PO and PTD. The very good correspondence at the absolute maximum is surprising and again shows that PO and PTD are applicable to objects that have diameters of just a few wavelengths.

Fig. 12 shows an overview of a wide frequency range that can be treated without a gap with the IEM and the PTD. For the 1:200 scale model the RCS levels for both polarizations have been calculated with the IEM (1 GHz, 10 GHz) and the PTD (100 GHz, 1000 GHz). An interesting fact is that the low RCS level at approximately 0° for high frequencies rises dramatically with decreasing frequency. This means that for metallic aircrafts a stealth design is only effective for high frequencies whereas for lower frequencies other methods have to be used.
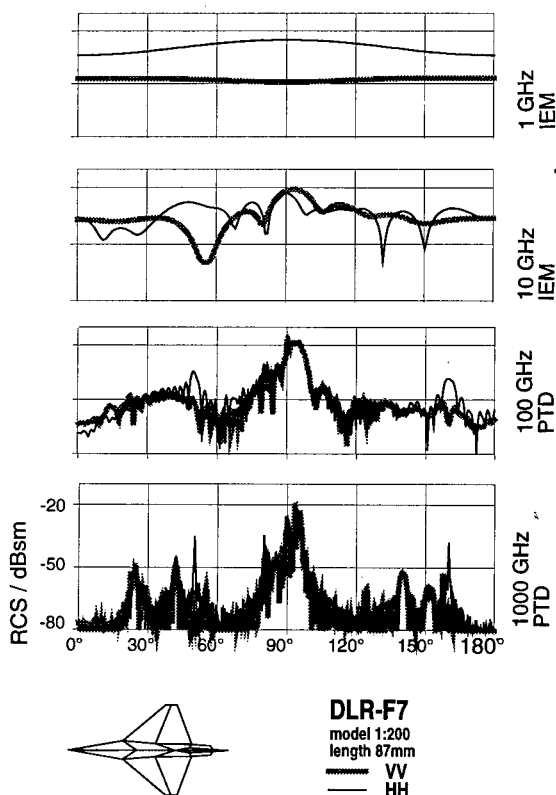
Fig. 12: Overview of the calculated σ over a wide frequency range for the 1:200 scale model

Especially in stealth-applications a strong fre-

quency dependence of the signature exists. This is illustrated by the pattern shown in **Fig. 12**. The thin black curves show the RCS for HH-polarization and the thick grey curves for VV-polarization. One realizes that the stealth characteristics are nearly lost at lower frequencies.

Based on experimental or theoretical RCS results further simulations can follow. Estimations of the radar range with the computer code DORA (see 6.3) or generating radar images by SAR-processing can be done.
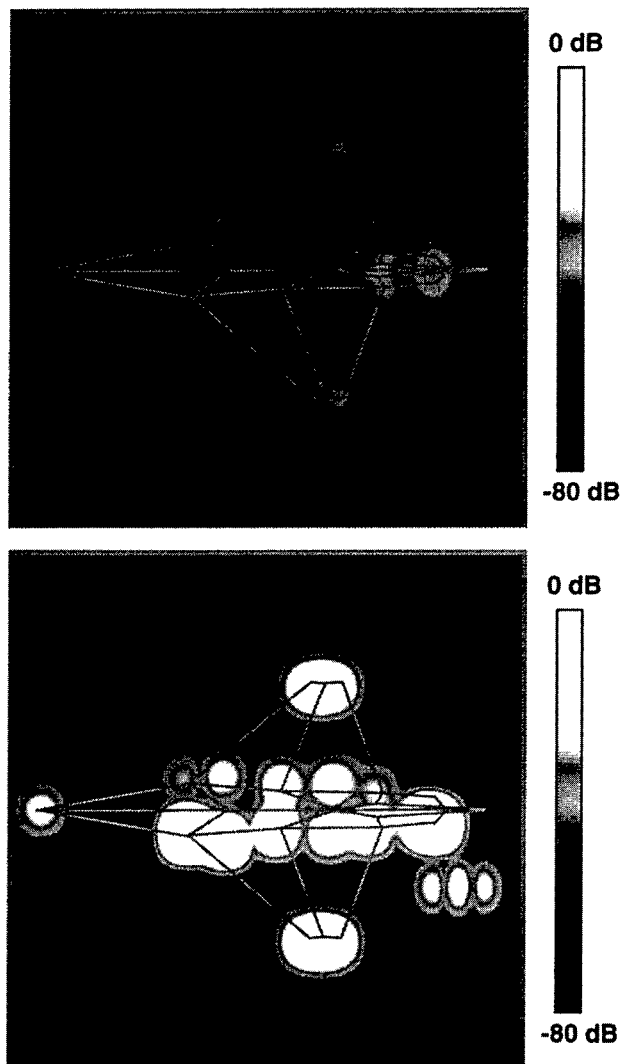
Fig. 13: Radar image of the DLR-F7 from the front (upper picture) and from broad side (lower picture)

Fig. 13 shows the SAR-images of the DLR-F7 observed from top under 45° for nose-on-view and broadside-view, respectively. The RCS data

have been simulated with SIGMA. The resolution in range and azimuth can be obtained by the analysis of the Doppler shift and the dependency of the frequency. It is obvious that the good stealth properties around the flight direction cannot be maintained for broadside view. From such and similar pictures it is possible to decide between more or less favorable flight paths.

6.2 Bistatic RCS Results by BISTRO and Measurements

Bistatic measurements using the 1:200 scale model of the F7 have been carried out for horizontal and vertical polarization and the results have been compared with the PO results of BISTRO. **Fig. 14** shows σ for both polarizations for the case that the transmitter is located 45° from the axis of the aircraft. For both polarizations the correspondence between calculated and measured results is quite good with the exception that for the horizontal polarization the measured values at 10° and at 68° are essentially higher

than the calculated ones. The reason for this difference is that at these angles the horizontal edge of the wing and the horizontal edge behind the nose respectively cause a higher level of the scattered field and that no edge correction currents have been incorporated into BISTRO up to now.

6.3 Prediction of the Radar Range

In **Fig. 15** there is shown an example of detection range analysis described in section 3.3. Radar data typical for an airport surveillance radar are assumed (scan to scan fluctuations, incoherent integration of n = 10 pulses, quadratic detection). Starting from RCS data calculated with PTD for a horizontal cut through the F7 (in 1:1 scale, for $\lambda = 30$ mm) the detection range as a function of the central azimuth φ is shown for the F7 treated exactly and approximated as Swerling 1, Swerling 3 and Chi-squared target. Further an angular weighting function of $\exp(-z^4)$-shape with a full
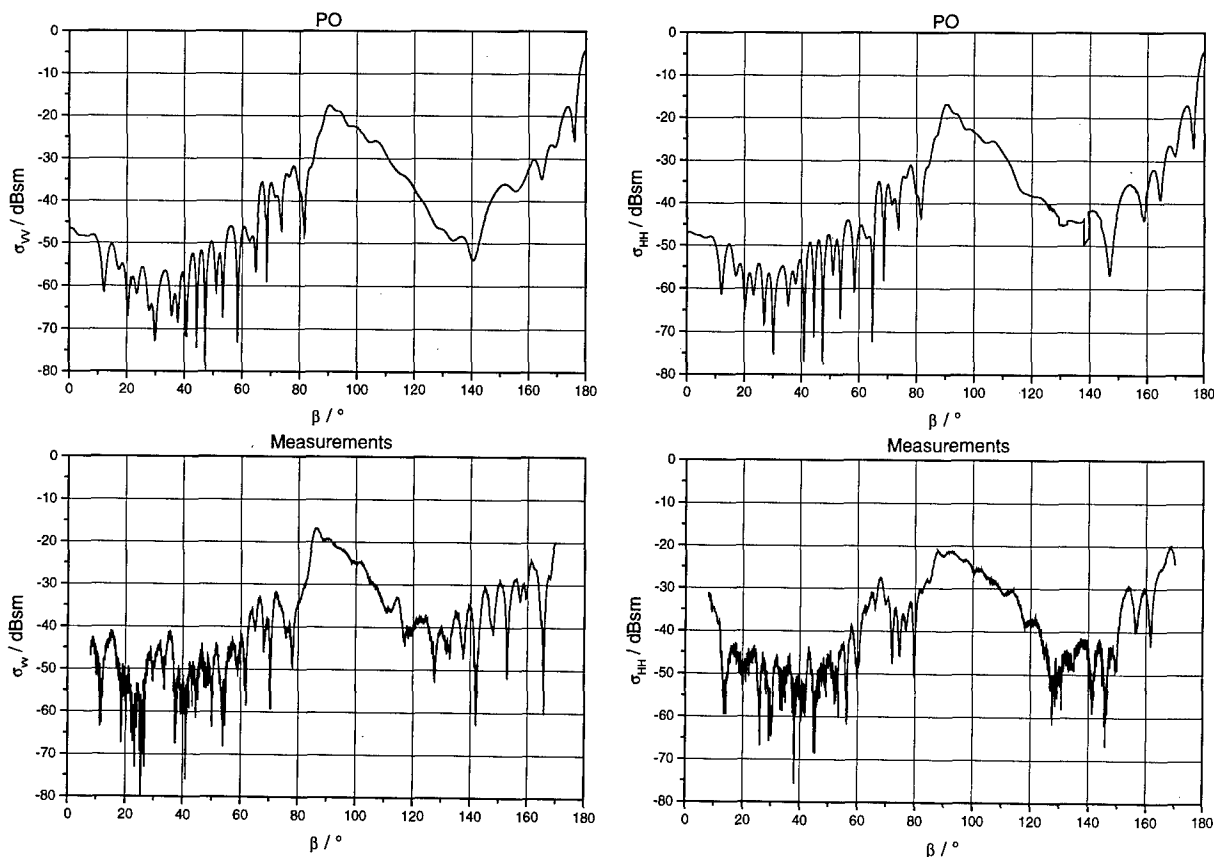
Fig. 14: Bistatic RCS results by BISTRO and measurements for the 1:200 scale model for VV-polarization (left pictures) and HH-polarization (right pictures)
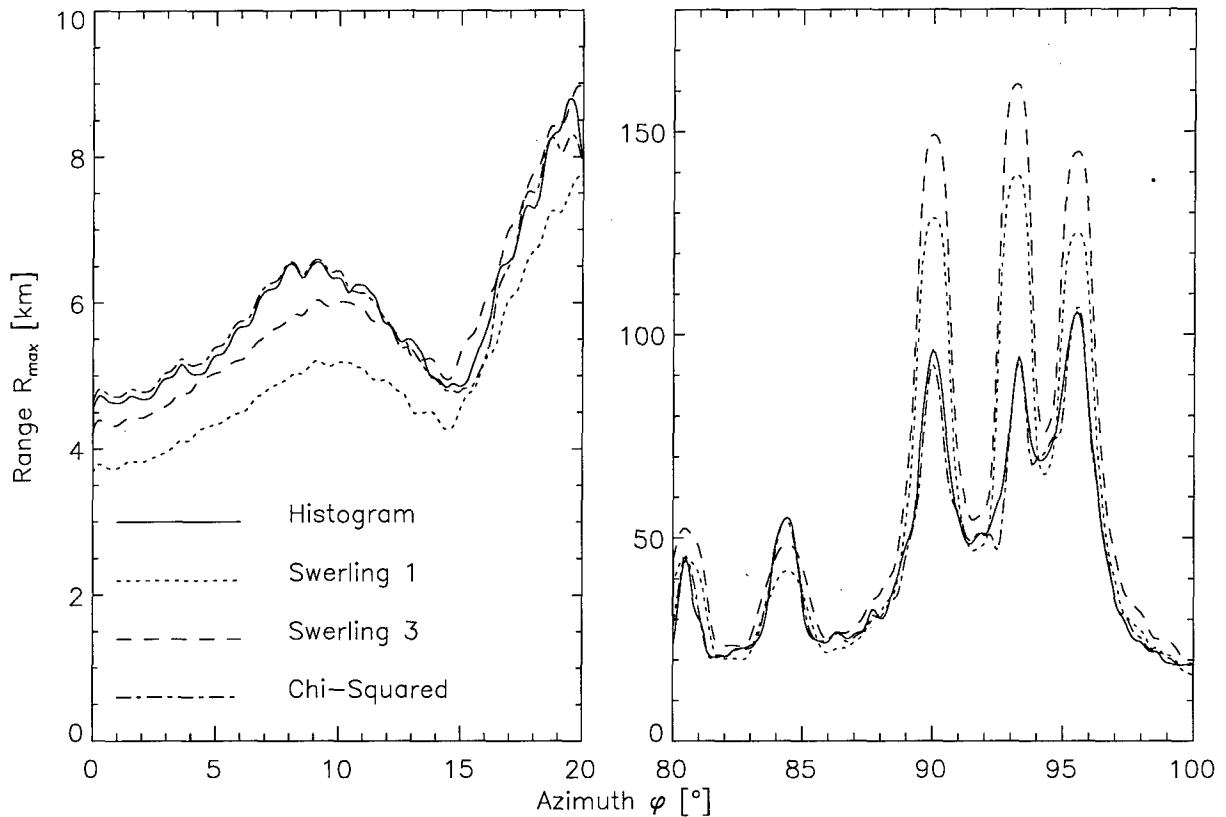
Fig. 15: Predicted radar range for the F7 seen in two aspect angles - nose (left) and broad side (right) view, solid Histogram, dotted Swerling 1, dashed Swerling 3, dash-dotted Chi-Squared

width at half maximum of 1° [6] was used. The two selected aspect angles shown in **Fig. 15** correspond to nose on (at 0° - left diagram) and broad side view (around 90° - right diagram).

It can be seen that the two-parameter Chi-squared distribution is far better in predicting R_{max} than the one-parameter Swerling models. The maximum absolute deviation amounts to 63.8 km for the Swerling 1 target and even 85 km for Swerling 3 at $\varphi = 92.8°$. Thus the error is comparable with the exact value of R_{max} (histo) = 68.4 km at this aspect. As a global measure of the capability to predict R_{max}, the relative deviation from the reference value R_{max} (histo), averaged over the whole azimuth range [0°, 180°], can be taken. It is 3.7% for Chi-squared compared to 13.3% and 18.3% for Swerling 1 and 3, respectively. Both other (two parameter) models - lognormal and Weibull - reproduce the range with approximately the same quality as the Chi-squared model with mean relative deviations of 4.1% and 4.6%. At the moment a comparison between the three two-

parameter-models cannot be performed in detail.

In order to judge the F7 construction under electromagnetic considerations an analysis of the detection range over a wide angular area around the nose-on view (**Fig. 16**) was performed. The result is a map in the (ϑ, φ)-plane as shown in **Fig. 17**. The underlying RCS calculations include edge diffraction. A cone of 45° half width has been evaluated.

The RCS has to be calculated on a mesh which is narrow enough to reproduce relevant structures without loss of information. Since the width of RCS peaks varies linear with the frequency the number of points at which the RCS has to be calculated within a given 2-dimensional angular cone varies with the square of the frequency. In order to save both computer CPU time and disk space the wavelength had to be increased to $\lambda = 100$ mm. With that the RCS-data for one quadrant of the present range map of 45° half

width and a linear mesh spacing of 0.04° could be obtained with four hours CPU time on an IBM RS/6000-990 workstation or about 12 hours on a Pentium 133 PC.
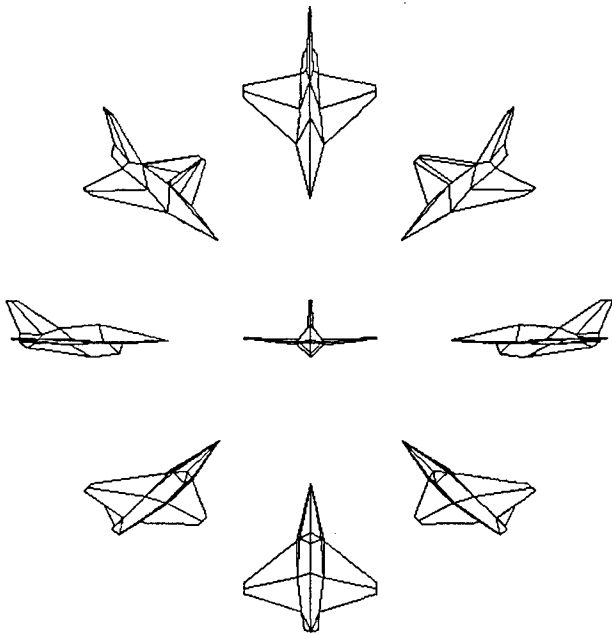
Fig 16: Airplane views corresponding to the range maps in Fig.17

Radar parameters are assumed as in section 3.3 and the wavelength dependent parameters (e.g. antenna gain) scaled to $\lambda = 100$ mm. To explain **Fig. 17**, the corresponding airplane views are indicated in **Fig. 16**. The center of the maps corresponds to nose on aspect; in the upper or lower part of the picture the airplane is seen from above or below, respectively, with elevations between -45° and +45° and in the right/left part from the right /left side, again in a cone -45° to +45°. Light colouring stands for large detection ranges as indicated by the bars in the pictures. The displayed range is $0 \le R \le 162$ km.

Both pictures in **Fig. 17** reveal several structures which have to be explained; their interpretation in turn leads to consequences for the airplane design. For both polarizations the maximum RCS and therefore detection range lies in the lower half and is visible as broad spots right at the edge of the investigated range. These spots arise from specular reflection by the small triangular panels which close the engine inlets (see **Fig. 4**). For a real airplane, the engine inlets would certainly be realized differently. So deviations from the displayed behaviour in that region would be expected. The broad lines starting at these spots end at a triangular structure in the central upper half, which appears dark in the case of HH-polarization **(Fig. 17** left). In that region the complete engine inlet structure becomes invisible and the signal is mainly caused by the upper nose panels of the airplane.

The other dominating features in **Fig. 17** are caused by edge diffraction. For HH-polarization **(Fig. 17** left) the two vertical lines at azimuth
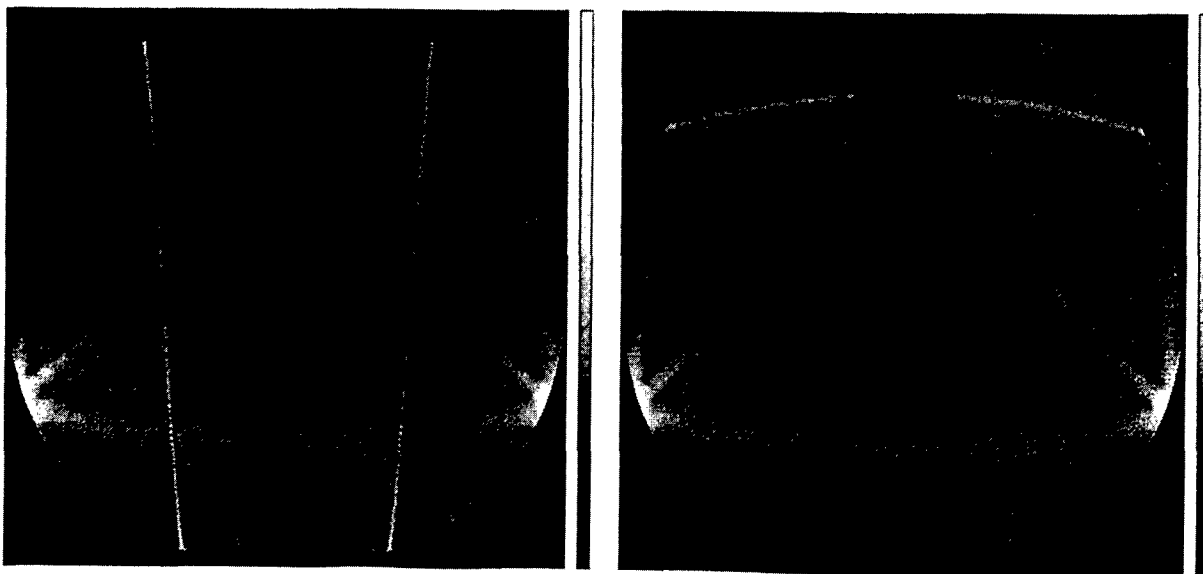
Fig. 17: Detection range maps for HH- (left) and VV- polarizations (right). Display range: 0 - 162 km in linear scale

$\varphi \approx \pm 20°$ which are broken in the middle (elevation $\vartheta = 0°$) arise from the signature of the wing back edges.

The breaks are caused by the shading of the wing's back edges by the wings themselves. The front edges of the wings appear at an azimuth of $\varphi \approx \pm 50°$, outside the range of that image.

Corresponding to the wing back edges for HH-polarization a strong effect can be seen for VV-polarization caused by the back edge of the rudder unit as the broken horizontal line in the top part of **Fig. 17** (right) at $\vartheta \approx 30°$. Again, the back edge is shaded by the rudder around azimuth $\varphi = 0°$.

These figures demonstrate the importance of the consideration of edge effects in calculating RCS and detection range, and consequently the importance of efforts to reduce this edge contribution by coating with radar absorbing materials or constructive measures, e.g. rounding of the edges.

Given the large detection ranges at the maxima of **Fig. 15** for example, one could be sceptical about the potential of this construction in view of stealth requirements. There are nevertheless several aspects which have not yet been taken into account: first of all, the large ranges at broadside aspect angles will be reduced for a real radar by Doppler filtering (which is not modelled here), since the Doppler shift at $\varphi = 90°$ is zero.

Another feature not yet implemented is tracking. Since the angular regions of large detection widths are narrow, in general there is little time for the radar to initiate a track. As an example the maximum at $\varphi = 81°$ in **Fig. 15** for an airplane in 40 km distance would lead to possible detection during an interval of a few seconds; after that interval, a new track would be lost again.

At this point it has to be taken into account that there are mostly monostatic radars detecting an approaching airplane in front view. So the F7 stealth airplane is optimized around this angle. And as it can be seen in **Fig. 15** (left) the detection range for an angle of $\varphi = \pm 5°$ is about 5 km.

7. CONCLUSIONS AND FUTURE WORK

Future efforts will concentrate to complete the analysis and improve the theoretical and experimental tools. The computer code BISTRO for instance has to be extended by an edge diffraction contribution. The deviations in the values predicted by different codes must be clarified as well as the differences between predicted and experimental results. The surface accuracy of the scale models should also be taken into consideration. One option implemented in SIGMA is the capacity to treat non-metallic structures. At this time however there are no reliable validations. For this purpose not only the theory but also the experimental setups to evaluate material parameters must be completed.

8. ACKNOWLEDGEMENT

REFERENCES

[1] D. Klement, J. Preissner, V. Stein
"Special Problems in Applying the Physical Optics Method for Backscatter Calculations of Complicated Objects",
IEEE-A&P, Vol. 36, No. 2, 1988, p. 228-237.

[2] E. Kemptner, M. Ruppel
"Vergleich bistatischer Streufeldmessungen mit Rechenergebnissen nach der Integralgleichungsmethode und der physikalisch-optischen Näherung"
Frequenz, Vol. 49 No. 3 - 4, 1995, p. 90 - 95

[3] G.J. Burke, A.J. Poggio
"Numerical Electromagnetics Code (NEC-2)-Method of Moments."
Technical Document 116, Naval Ocean System Center, San Diego, California, Jan. 1981.

[4] E. Kemptner, D. Klement, V. Stein
"Validation of the PO-Based RCS-Code SIGMA by Using IEM and Experiments",
Proceedings of ACES 1996', Monterey, California, USA, 2.-2.3.1996, p. 719-724.

[5] P. Swerling
"Probability of detection for fluctuating targets",
IRE Trans. Information Theory, vol. 6, pp. 269 - 308, 1960; J.I. Marcum, "Mathematical appendix", ibid., pp. 145 - 267. Originally published as RAND Res. Memo. RM-1217 (1954) and RM-753 (1948), resp.

[6] L. Peters Jr. and F.C. Weimer
"Reply to comments by R.H. De Lano"
IRE Trans. Antennas and Propagation, vol. 9, pp. 228, 1961.

[7] D.A. Shnidman
"Evaluation of probability of detection for several target fluctuation models"
Technical note 1975-35, MIT, Lincoln Labaratory, Lexington, Massachusetts, 1975.

[8] P.C. Dowdy
"RCS probability distribution function modeling of a fluctuating target"
Proceedings of the 1991 IEEE National Radar Conference, New York, 1991, IEEE, pp. 164 - 168.

RADAR MEASUREMENTS ON SCALED MODELS

Jürgen Kruse, Manfred Hochmann, Dirk Bringmann
Daimler-Benz Aerospace AG
Military Aircraft
Hünefeldstr. 1-5, D-28183 Bremen
Tel.: +49 421 538 3291
Fax: +49 421 538 3449
e-mail: Juergen.Kruse@m.dasa.de

1. SUMMARY

Within the scope of the development of military aircraft with reduced radar cross section (stealth), radar signature measurements on scaled models play an important part. Their significance can be compared to that of model measurements in wind tunnels. In addition, radar signature measurements of this type could also be envisaged for the future generation of basic data for non-cooperative target identification.

This paper serves to discuss the prerequisites for this type of model measurements and to illustrate them with the help of examples.

Coherent radar signature measurements on models are carried out at Daimler Benz Aerospace at frequencies of up to a maximum of 100 GHz. This means that the models have to be manufactured with utmost care and that the measuring techniques and set-ups used have to be implemented with the highest precision. This paper presents examples of a series of different aircraft models, discusses the scope of their equipment and the way they are manufactured.

Coherent radar signature measurements are subject to special requirements with regard to constancy as measurements for this purpose extend over several hours. The main task consists in compensating influences through induced vibrations, thermal expansion, angular accuracies of the rotary stand and the phase drift of the measuring equipment. Owing to the extensive measurement range, polarimetric radar signatures are obtained over wide frequency bands (up to 30 GHz) with a high degree of detail with regard to radar scatter centers. It is shown how such scatter center measurements could be subjected to further processing, permitting the additional assessment of details with regard to their signature properties. Also polarimetric signatures are presented with the help of examples.

On the basis of the data obtained, radar signature characteristics can be determined which are distinguishable by aspect angle, frequency polarization and pulse response. In addition, precise scatter center resolution also permits the simulation of stealth measures that might have been implemented on individual components so that also modified radar signatures can be entered into appropriate databases (stealth retrofit). In this way, radar signature measurements on scaled models constitute a valuable means for analyzing also external aircraft types in different equipment conditions.

2. INTRODUCTION

In current aircraft development, reduced signature has become one of the primary aspects. This design criterium has recently joined the other ones such as flying characteristics, design, armament, etc. Aircraft design is particularly influenced by considerations concerning a reduced radar signature. This is illustrated by the example of the F117 or B2 aircraft types. Sharp rounded leading edges or internal loading of weapon systems are quite recent developments and for their implementation it was necessary to achieve an optimum between the different design criteria. It is to be expected that, in future, attention will have to be paid not only to reduced aircraft signature but also to signature characteristics because of non-cooperative target identification.

Since all of these criteria play a decisive role already in the early stages of aircraft design, these properties are investigated by means of model measurements and signature calculations.

As there is still a lack of sufficiently powerful computers which could be used for exact determination of signatures by means of calculation procedures, signature measurements are often performed with the help of scaled models.

3. AIR VEHICLE MODELS FOR RADAR SIGNATURE MEASUREMENTS

Both dielectric materials and metals are used for manufacturing aircraft models for signature measurements. Although metallic bodies permit a highly accurate reproduction of details such as flap slots, air data sensors, etc. by appropriate machining, extensive use of plastic materials has been made in the past for the manufacture of aircraft models. This is mainly explained by the important weight of metallic bodies. At Dasa, objects for signature measurements which exceed the size of approx. 1 meter are mainly made from dielectric materials. In the aerodynamic area, these models are made from metal so as to be able to support the high mechanical loads exercised by the airflow in the wind tunnel [Fig. 1]. After certain modifications (suspension), these models can also be used for radar signature testing. The costs entailed by the implementation of these models amount to approx. 600,000 Deutschmarks for the configuration model and another 700,000 Deutschmarks for the associated external loads including pylons.

An alternative possibility consists in the manufacture of scaled models made from dielectric materials which are either directly conductive (e.g. carbon fibers) or have to be provided with an add-on "metallization". In the case of add-on metallization, either low-resistance conductive varnishes are applied or the model is covered with appropriate conductive foils. When using these procedures, special attention has to be paid to the low resistance of the coating or foil as unsatisfactory implementations can be detected only by means of imaging methods. Fig. 2 shows a surface where the conductivity of the conductive foil used is insufficient. The imaging procedure shows clearly how the different webs have been laid. In this context it should also be seen to it that also the adhesive of the foil is sufficiently conductive.

Other models used at Daimler-Benz-Aerospace have been coated with nickel-, silver- or copper-based conductive varnish. Fig. 3 shows the 1:10 model of the F117 stealth aircraft. Also details such as the four air data sensors or the serrated frame of the IR window in the front area have been modeled here.

Also stereolithographic methods have been used recently for the manufacture of this type of models, permitting scaled modeling of complicated geometries such as engine air inlets. Fig. 4 shows the engine air inlet model constructed to 1:20 of the B2 aircraft. This model had been manufactured by this procedure and was then integrated into the overall model.

With this type of models and with the help of measuring methods still to be described it is possible to determine the radar signature and also to detect any possible modifications of the radar signature that might have been introduced, e.g. by additionally mounted radar absorbers. Fig. 5 shows a rudder fitted with a suitably scaled radar absorber whose absorption effect corresponds to that of a real absorber. In this way it becomes possible to predict forms of radar signatures without any prior possibility of their observation or detection.

4. COHERENT RADAR SIGNATURE MEASUREMENTS

For determination of radar signatures on scaled objects it is, at first, necessary to comply with the known scaling laws.

This means that the measuring frequency f_m is increased with regard to the original frequency f in accordance with the scaling factor k so that the following equation applies:

$$f_m = k \cdot f.$$

In a concrete measuring situation this means that the result achieved with a 1:10 model subjected to a measuring frequency of 100 GHz would be the reflection of an original aircraft at 10 Ghz. From these figures it becomes evident that excessively reduced model scales (e.g. < 1:10) will not lead to any meaningful measuring results. As regards measurements above 100 GHz, it can be said that the financial and technical effort required for the performance of wideband coherent measurements would be entirely out of proportion.

However, in order to provide solutions also in this kind of situations, an extrapolation procedure has been developed for the measurement of ship models. The frigate shown in Fig. 6 was built as 1:33 RCS model (4 m long) and would thus have required a measuring frequency of 330 Ghz to reproduce the original frequency of 10 GHz. Therefore the wideband response of the RCS at 8 to 18 GHz was extrapolated to 330 GHz, using support points in the 26 to 40 GHz and 70 to 100 GHz range [Fig. 7]. The comparison between the results obtained in this manner and RCS measurements on the original frigate presented a satisfactory agreement (Δ = 2.2 dB). Nevertheless it should be said that procedures of this type should be used in exceptional cases only as the reproduction of particular reflection conditions will always furnish a somewhat distorted picture. As a general rule, scaled measurements are performed with the help of an appropriate increase of the measuring frequency, as described in the foregoing.

The results obtained with model measurements are of interest for a number of users. The following analyses can be generated:

o   Distribution of radar scatter centers
o   Scatter center concentration point, glint
o   Simulation of stealth measures
o   Pulse response
o   Polarimetric signature
o   Low-frequency signature

These data require high-precision measurements. In the following, the various measures will be described which have been introduced into Dasa's radar signature measurement (RaSigma) systems in order to ensure compliance with requirements. For performance of radar signature measurements, three measurement chambers are available in Bremen (two at Dasa, one at STN ATLAS Elektronik). All of them operate in accordance with the same measuring principle and are handled by the same Dasa team. This measuring and analysis team is backed by an overall experience of 42,000 measuring hours.

The wideband measuring systems used (0.5 to 100 GHz) are based on the equivalence of complex scatter amplitudes which are measured over a wide band and of short pulses resulting through Fourier transform. Measurement data are obtained by scanning the test object within a discrete frequency raster with high frequency stability. The portions reflected by the test object are recorded via the network analyzer which calculates amplitude ratio and phase difference. The maximum distances between the frequency support points result from the unambiguous range of the Fourier transform in longitudinal direction and those of the angular support points (object rotation) from the unambiguous range in transverse direction (extension of the test object in transverse direction). This means that, the bigger the test object and the measurement chamber, the smaller the frequency and angular measurement steps and the longer the measuring time. By contrast, the resolution of the radar scatter centers (separability of two scatter centers) is determined, in longitudinal direction, by the frequency band width used and, in transverse direction, by the adopted angular range. The maximum value of the resolution reached in the longitudinal direction Δy is determined in accordance with the equation

$$\Delta y = \frac{c}{2B}$$

where c stands for the velocity of light and B for the frequency band width.

The entire measurement process is computer-controlled which permits selective elimination of measurement errors. This includes, among other items, the substraction of the empty room (without test object), calibration of frequency responses and phase drift as well as far-field correction.

For substraction of the empty room, its reflection characteristic is measured with regard to amount and phase and subtracted from the test object measurement. As the time elapsed between empty room and object measurement may vary and phases may become subject to variations in the meantime through temperature fluctuations or equipment drifting, room reflections are not fully eliminated upon empty room subtraction - a small amount of empty room noise will remain as measurement error. In order to reduce these errors to a minimum in practical measurement procedures, the Dasa measurement chambers and equipment racks are air-conditioned and the rotary stand, the measurement chamber and the antenna supports are seismically decoupled. In addition, a defined fixed target is used to check and, if required, compensate residual phase drifts at regular intervals during the measuring phases.

These special efforts are required in order to obtain a coherent radar image which will serve as a basis for the performance of additional analyses concerning the characteristics of the different scatter centers and the overall signature.

This set-up also permits the performance of a far-field correction of the electromagnetic field aimed at correcting the measuring distance between antenna and object which is generally too short. Fig. 8 shows the effect of this far-field correction. The object measured here is a cylinder which is 5 meters long. The radar image is shown with and without correction. The effect can be observed in the RCS response, i.e. in those cases where no correction has been made, the peak as plotted against the angle becomes significantly wider especially in the case of extensively distributed scatter centers (cylinder across antenna).

5. ANALYSIS OF HIGH-RESOLUTION RADAR IMAGES

Radar signature measurements are conducted in the described manner for different aspect angles with regard to the test object. The test object is measured on the rotary stand within the relevant angular range using defined angular measurement steps. The RCS values thus obtained depend on frequency and aspect angle. They can be represented not only as one-dimensional but also as two- or three-dimensional scatter center distribution.

Reconstruction of a two-dimensional radar image is achieved by means of conventional tomographic procedures: The scatter response calculated for a constant aspect angle is distributed via a rear projection algorithm within the imaging area over all matrix elements along the relevant phase fronts (wave fronts) [cf. Fig. 9]. The coherent superposition for all aspect angles provides a microwave image where the test object is represented without distortions. Due to the equivalence between local scatter center distributions and the spatial frequency domain resulting from a two-dimensional Fourier transform it now becomes possible to determine a far-field RCS which depends on frequency and aspect angle. The spatial frequency domain corresponds to a polar coordinate system where the length of a vector starting from the origin of the coordinate system corresponds to the frequency and where the angle with regard to the x-axis corresponds to the aspect angle [cf. Fig. 10]. This means that a radial section through the spatial frequency domain corresponds to the well-known polar diagrams. All other polar diagrams shown have been taken from the relevant spatial frequency domains.

With the help of a spatial filter function (two-dimensional low-pass filtering) local partial areas or individual scatter centers can be filtered from the two-dimensional radar image [Fig. 11] and transformed into the spatial frequency domain so that their frequency- and aspect-angle-dependent backscatter can be investigated in depth [Fig. 12]. Thanks to the filtering which is exactly matched to the local scatter area, it is possible to suppress, to a large extent, all those interference effects which cannot be eliminated through the travel time of the incoming wave alone. This permits, for example, to filter out not only undesired residual reflections of the rotary stand but also the residual empty space error which is not superimposed on the test object. This error is produced by the fact that the test object masks certain areas of the measuring chamber and thus produces an empty room shadow.

Fig. 11 shows the image of an air vehicle with airbreathing engines. The individual scatter centers can be clearly identified. From the K-space, an important backscatter in the side aspect can be clearly distinguished whereas, from the front, the air vehicle's backscatter is somewhat less. This RCS has been subjected to a far-field correction. A concentric section through the K-space will then yield the well-known RCS polar diagram which, however, does not supply any information on signature anomalies. By contrast, such information is provided with the help of the K-space. From Fig. 11 the potential offered by such K-space visualizations becomes quite obvious. An even better illustration of this fact is provided by the polarimetric RCS investigations conducted on air vehicles and aircraft models.

Fig. 13 shows the K-space of an aircraft model across the original frequency range comprised between 0.376 and 2.175 GHz. Fig. 13a illustrates the RCS resulting with an HH polarization. Reflections in the front aspect which are caused by the engine inlet are clearly visible. The maximum linear RCS has been plotted in Fig. 13b whereas Fig. 13c shows the associated polarization angle α. The same type of evaluation is illustrated in Fig. 14 for a dispenser, with application of the same original frequency range that has been mentioned above. A noticeable feature of this image is the heavily pronounced formation of signature islets which is due, on the one hand, to the smaller quantity of individual scatter centers and, on the other, also to the smaller size of the object. The emphasis in Figs. 15a to c lies on the associated polarization signatures for the frequency range comprised between 0.025 and 0.625 GHz. In this frequency range, stealth measures on air vehicles will be without effect as their size as compared to the wave length is too small. Gains which can be achieved by means of optimum choice of polarization can be clearly seen in all cases.

In addition to polarization analyses of this type, Dasa also generates pulse responses with the help of model measurements. These analyses could also be simulated with variable pulse forms. Fig. 16 shows the pulse response of two different air vehicles. With the RaSigma analysis software, stealth measures on defined scatter centers can be simulated and the effects on the pulse response or the 2-D image analyzed.

With the help of scatter center analyses, it is easy to simulate stealth measures from the signature database on an air vehicle to be camouflaged. For this purpose, defined reflection areas to be camouflaged, e.g. fuselage or air vehicle nose, are filtered from the radar image and transformed into the complex spatial frequency domain. Here the scatter amplitudes are attenuated in accordance with the frequency-dependent absorption behaviour of a fictitious absorber and coherently superimposed on the non-camouflaged reflection portions which had also been previously transformed into the spatial frequency domain.

CONCLUSION

Radar signature measurements on scaled models can be used for a variety of analyses. It has been demonstrated that, in spite of the reduced dimensions of the air vehicles, images of scatter centers could be produced and signature anomalies detected. The associated procedures are extremely important not only for the design of new systems but also for the assessment of existing ones. The decisive importance of controlling the measuring situation especially in the case of imaging radar procedures has been explained. Scatter center responses, pulse responses and polarimetric signatures have been illustrated by a series of examples.
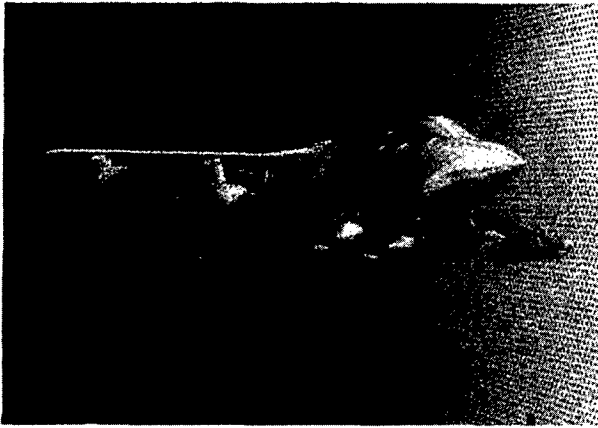
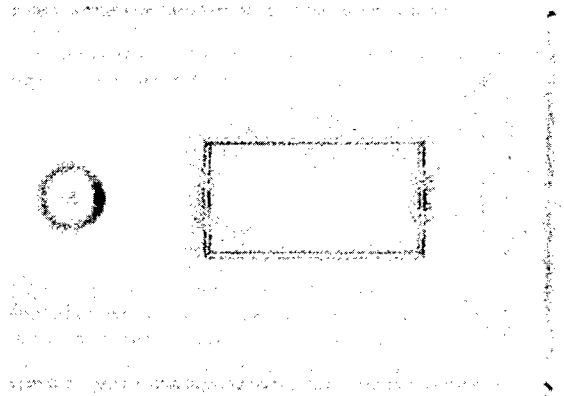Fig. 1: 1:11 scaled metallic model
of TORNADO aircraft

Fig. 2: Radarsignature measurement on
a large plate covered with foils
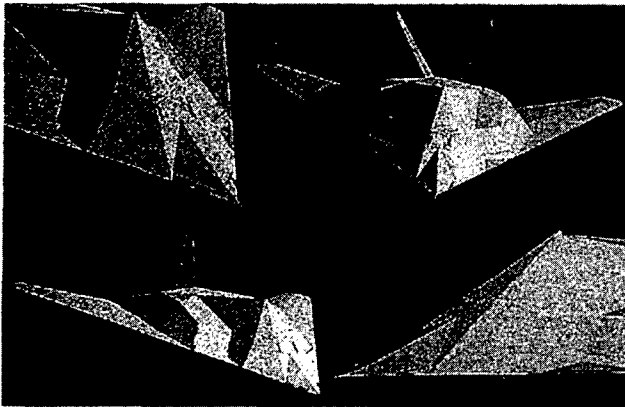of insufficient electrical
conductivity
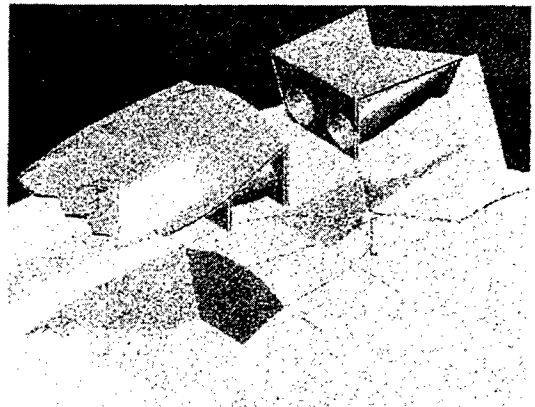

Fig. 3: 1:10 scaled model of F117 aircraft

Fig. 4: Scaled engine inlet model of B2
aircraft manufactured by means of
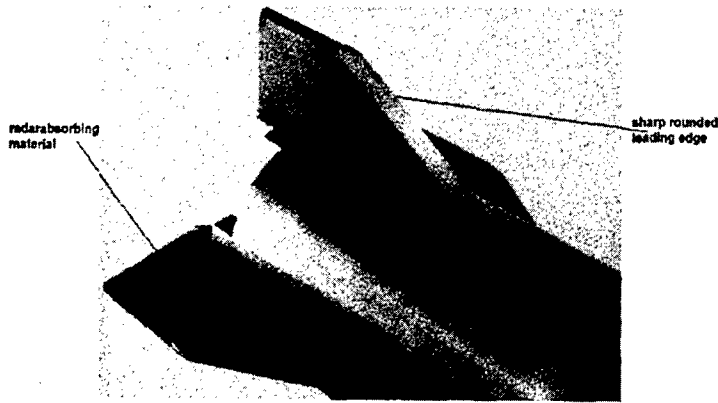stereo-lithographic methods

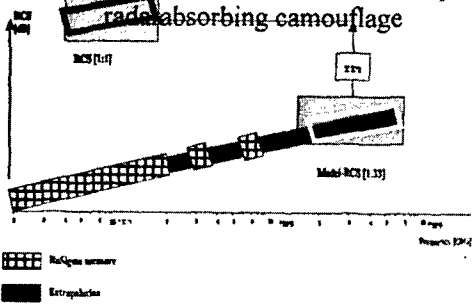Fig. 5: Scaled rudder with adapted radarabsorbing camouflage
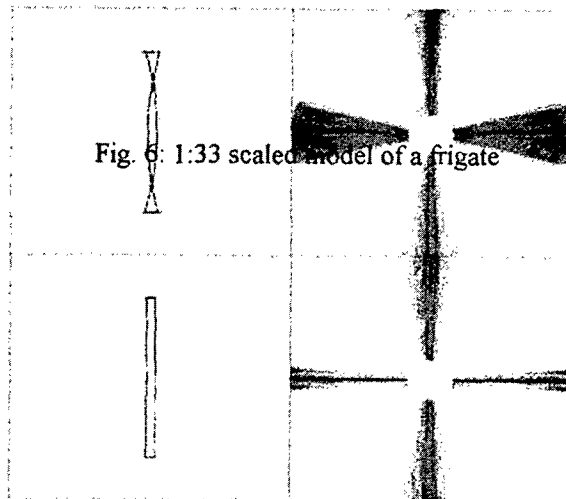
Fig. 6: 1:33 scaled model of a frigate

Fig. 7: Procedure for Extrapolation of measurements at scaled models

Fig. 8: Far-field correction on a cylinder of 5m length
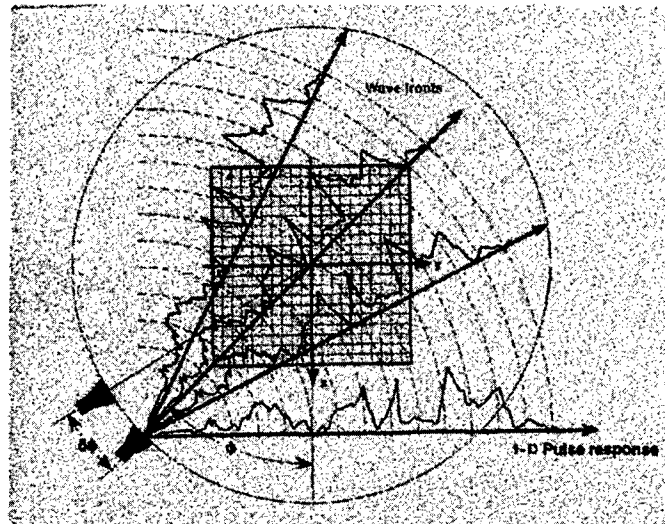
Fig. 9:   1-dimensional imaging and 2-dimensional
          image reconstruction
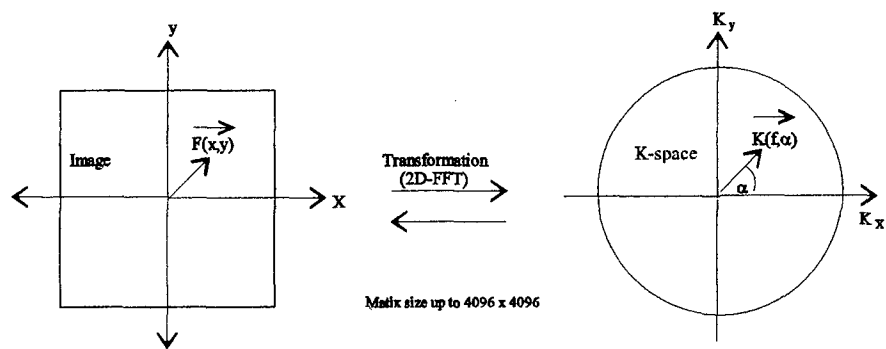
Fig. 10: Relation between image and k-space
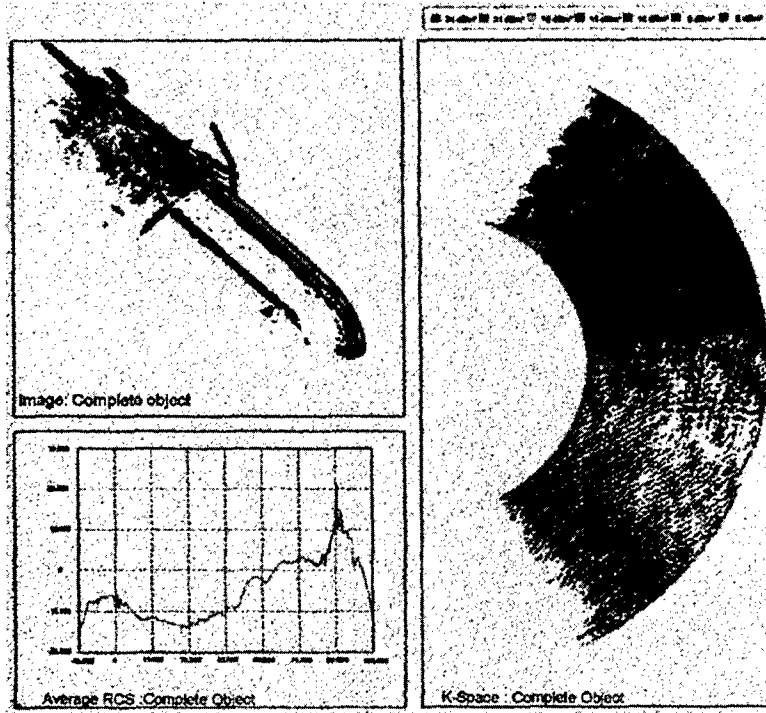
Fig. 11: 2-D Image, k-space and RCS-diagram of an air vehicle
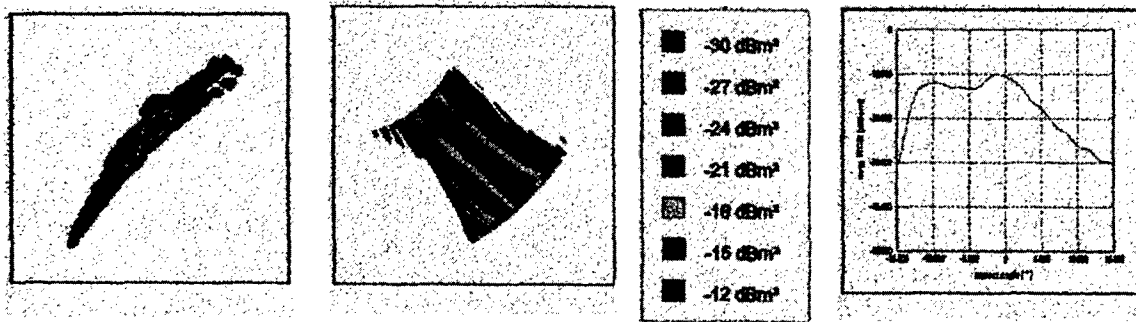
Fig. 12: Filtered single scattering center (forward section of engine inlet)
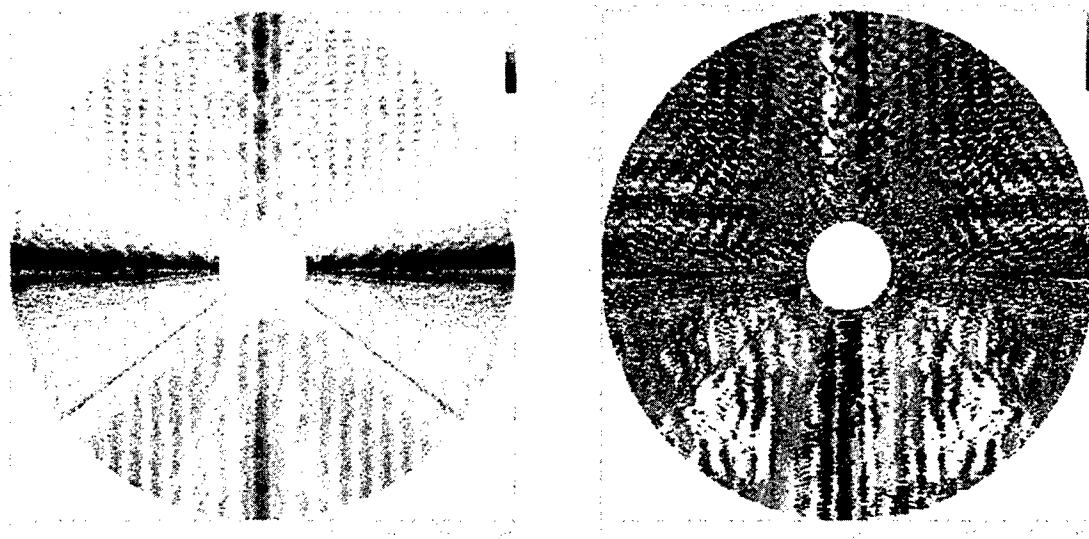
Fig. 13: Polarimetric signatures of an aircraft model (elevation angle 0°, original frequency range 0.376 ... 2.175 GHz)
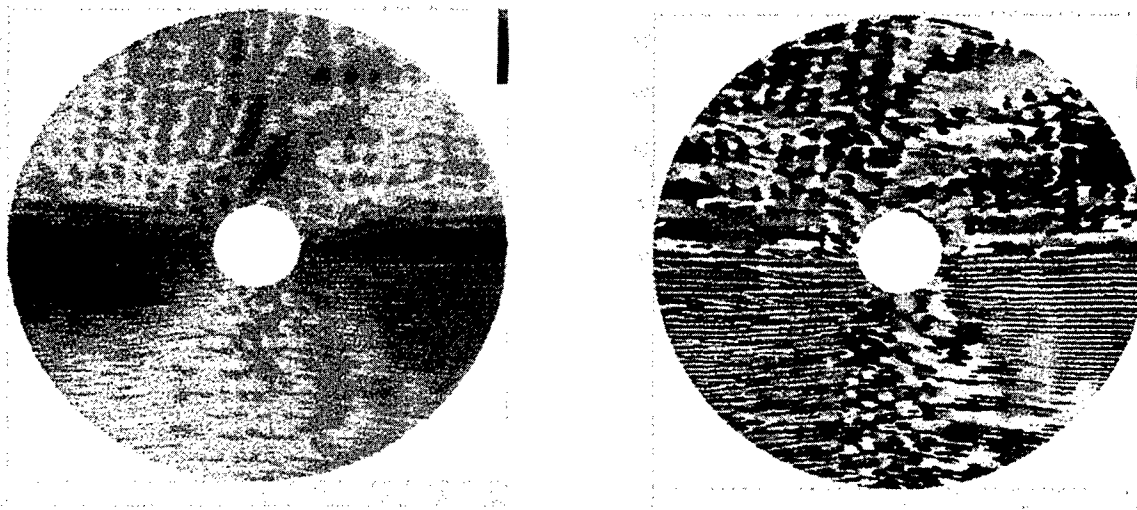
Fig. 14: Polarimetric signatures of a dispenser model (elevation angle 0°, original frequency range 0.376 ... 2.175 GHz)
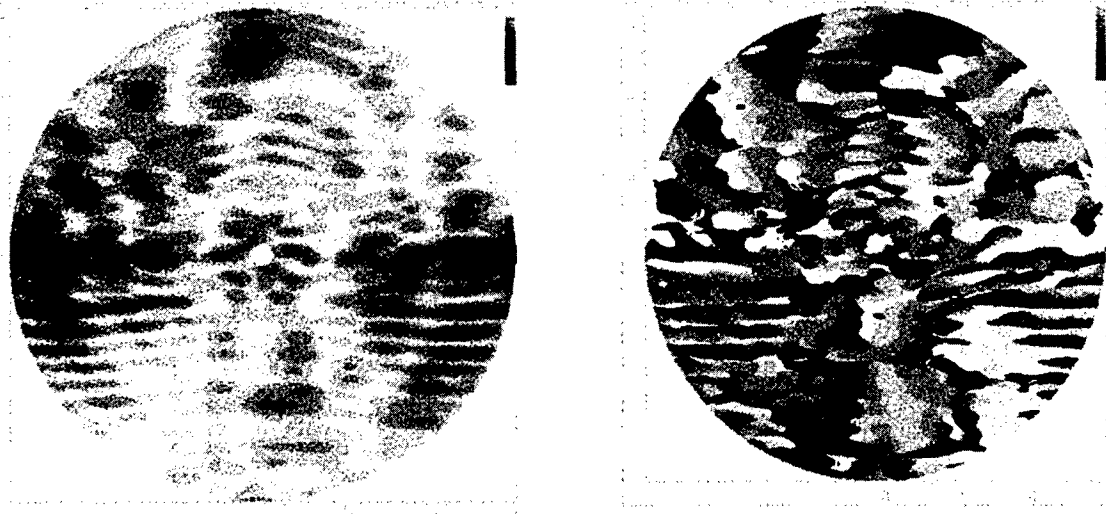
Fig. 15:   Polarimetric signatures of a dispenser model (elevation angle 0°, original frequency range 0.025 ... 0.625 GHz)
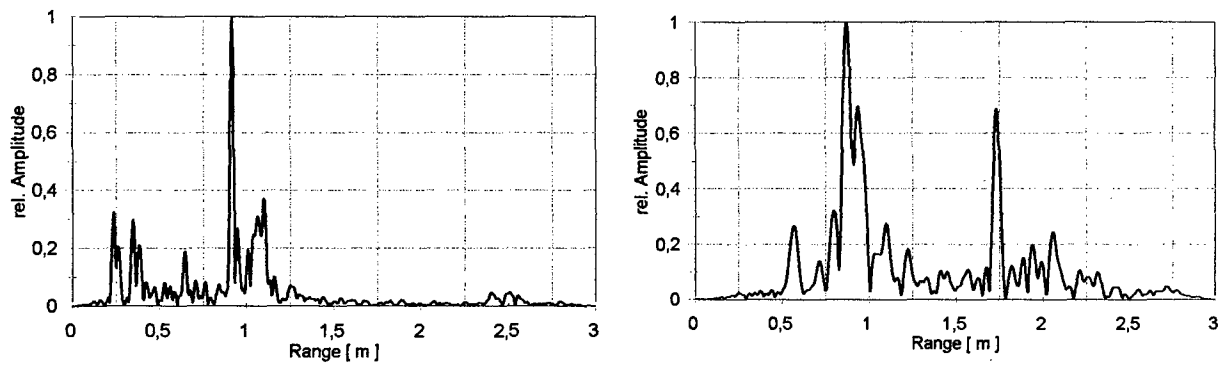
Fig. 16:   Pulse response of two different flight vehicle models

A comparison on radar range profiles between in-flight measurements and RCS-predictions

R. van der Heiden, L.J. van Ewijk
TNO Physics and Electronics Laboratory
PO Box 96864, 2509 JG The Hague, The Netherlands

F.C.A. Groen
University of Amsterdam, Faculty of Mathematics and Computer Science
Kruislaan 403, Watergraafsmeer, 1098 SJ Amsterdam, The Netherlands

ABSTRACT

The validation of Radar Cross Section (RCS) prediction techniques against real measurements is crucial to acquire confidence in predictions when measurements are *not* available. In this paper we present the results of a comparison on one-dimensional signatures, i.e. radar range profiles. The profiles were measured from a target of opportunity, a Boeing 737. At the same aspect angles and frequencies, profiles were predicted using a high-frequency RCS-prediction code in conjunction with a digitised model of the Boeing. Despite the assumptions and simplifications in both the prediction code and the aircraft model, a fairly good agreement is observed on head-on and tail-on aspect angles. The correspondence on broad-side aspect angles is seen to be much better: despite differences in peak amplitudes, normalised correlation coefficients up to 0.9 are observed.

I. INTRODUCTION

For a few decades, RCS-prediction techniques have been under development for predicting the total amount of radar reflection of an object at a certain frequency and seen under a particular aspect angle. When the target dimensions are much larger than the wavelength (high-frequency approximation) the combination of *Physical Optics* and *Geometrical Optics* has shown to be a fruitful approach for predicting the RCS of the target [1, 2, 3].

Prediction techniques can be used to compute radar range profiles - these signatures are essentially one-dimensional 'images' of aircraft. They are promising candidates for the recognition of targets because they depend on the target geometry [4, 5, 6]. We want to be able to *predict* profiles using an RCS-prediction method and an accurate geometrical description of the target. For future use, predicted profiles can be used to build a target library for aircraft recognition.

In a short, earlier paper [12] the results of a comparison between predicted range profiles and profiles measured at broad-side aspect angles only were shown. This report additionally includes: 1) profiles from near tail-on and nose-on aspect angles, 2) an assessment of range profile variability as a function of aspect angle and 3) an approach to improve the estimate of aspect angle using the predicted and measured radar data.

The organisation of this paper is as follows: in the next section, we will briefly treat high-frequency prediction codes and the implementation that has been chosen for our program, named *RAPPORT*. Section III will depict the background of radar range profiles, followed by a description of the range profile acquisition in the subsequent section. Section V describes which predictions are made. Subsequently, section VI shows the comparison between the measurements and the predictions, followed by a discussion in section VII. The final section draws the conclusion.

For the remainder of this paper we will use the abbreviations PRP and MRP for 'predicted range profile and 'measured range profile', respectively.

II. HIGH-FREQUENCY RCS-PREDICTIONS CODES

Most high-frequency electromagnetic scattering codes are based on a combination of *Physical Optics* (PO) and *ray tracing* (related to GO, that is, *Geometrical Optics*) as was first suggested by Knott [1] and further described by Knott [2] and Zolnick [3].

Methods based on PO and GO can be used in the high frequency region of electromagnetic scattering. Here, 'high frequency' means that the object needs to be larger than, typically, five wavelengths.

In the Geometrical Optics or GO-approximation it is assumed that the radar energy propagates along *ray paths*, governed by Fermats principle. It is determined which part of the object is visible to the radar and provides thereby the incident field on an object (ray tracing). If an obstacle is encountered, the reflected field is determined using the theory of Physical Optics (PO) [7].

The combination of PO and GO also enables us to calculate the scattering due to *multiple* bounces, likely to occur in corners and cavities [3]. This is an important property, as these multiple bounces are known to be major contributors to the total RCS of complex, man-made objects like aircraft, vehicles and ships.

When the incident field is reflected by the object, the contribution to RCS is computed by PO. Additionally, GO is used to compute the direction of the reflected field towards other parts of the object. This result is then used as incident field for further reflections and is treated identically to the procedure for the first reflection.

In most techniques the ray-tracing implementation is based upon (a variant of) the *shooting and bouncing ray* (SBR) technique [8]: a dense grid of rays is shot from the incident direction towards the target. Rays are traced according to the

law of Geometrical Optics as they bounce around the target. At the exit point of each ray, an integration is performed to sum up the contribution to the total scattered field. A well-known example of a such a code is XPATCH [9]. The SBR method has the disadvantage that a sampling density of ten rays per wavelength has to be used to obtain accurate results. RAPPORT, acronym for *Radar signature Analysis and Prediction by Physical Optics and Ray-Tracing*, is an RCS-prediction code developed at TNO-FEL. It is similar to most other high-frequency electromagnetic scattering codes; see Brand [10] for a description.

RAPPORT contains however a fundamental advantage compared to most other codes that lies in the ray-tracing implementation. In RAPPORT the illuminated area on the object is reconstructed explicitly with a certain accuracy, using a non-uniform or *backward* ray tracing algorithm. Once the area is known for a certain aspect angle and object, the RCS can be calculated for any desired frequency. RAPPORT is computationally more efficient than SBR techniques as the ray density to obtain the same accuracy is far less.

The objects used by RAPPORT must be described by a combination of flat polygonal plates. All plates are subdivided into triangular patches called *facets*, with a maximum size that is user controlled. The procedure is to step-wise decrease the patch sizes until convergence is achieved.

The number of multiple reflections that has a significant contribution to the RCS is determined by a similar refinement procedure, i.e., take an increasing number of reflections into account until the total RCS converges.

Features that are not implemented in RAPPORT, but will certainly result in an improved estimate of the actual range profiles, are edge diffraction and the reflection on dielectric materials. Currently, all facets are assumed to be perfectly conducting.

III. RADAR RANGE PROFILES

A range profile can be viewed as a one dimensional 'image' of an aircraft, where the parts of the aircraft that reflect the radar radiation, that is, the *scatterers*, are projected onto the line of sight. See figure 1.
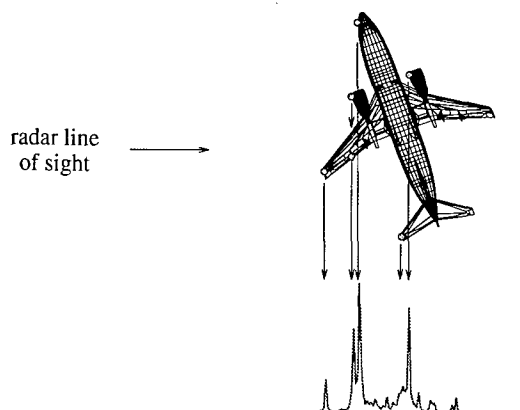
radar line of sight

Fig. 1: A range profile of an aircraft viewed from the left hand side. Responses from the aircraft scatterers (circles) are projected onto the line of sight, resulting in a radar range profile (bottom). (Geometrical data by Viewpoint Datalabs International.)

We produced the range profiles by emitting a bandwidth B using N pulses with linearly increasing frequencies, called a *stepped frequency waveform* [11]. The coherent responses (N complex numbers) are, after optional windowing and/or zero-padding, Fourier transformed and from the resulting sequence the phases are discarded - only the magnitudes are considered. The *target aspect angle* can be expressed as a coordinate pair (α, θ) where α is the *aspect azimuth* and θ is the *aspect elevation*. See figure 2. We define the aspect elevation θ as the angle between the radar line of sight and the plane through the wingtips and nose of the aircraft. The elevation is positive if the aircraft is viewed from underneath. We define the aspect azimuth α as the angle between

* the direction of the nose of the aircraft and
* the direction of the radar line of sight projected on the plane through nose and wingtips.
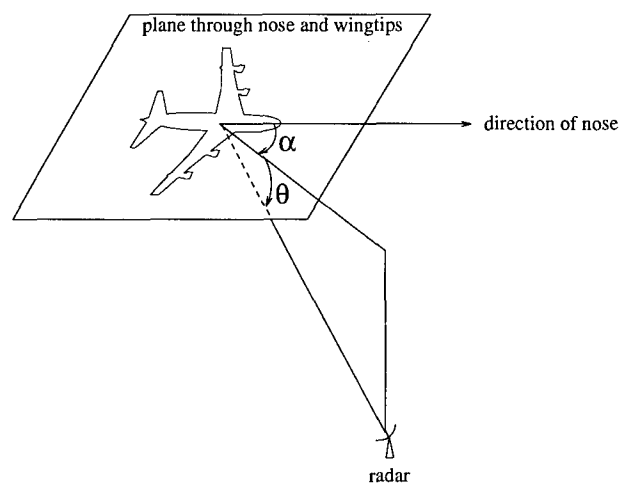

Fig. 2: Definition of aspect elevation, θ, and aspect azimuth α. In this particular orientation both α and θ are positive.

Thus, the aspect azimuth is zero if the aircraft is viewed from nose-on and 180° degrees if viewed from tail-on. Finally, the aspect azimuth is chosen positive if the target is viewed from the starboard side and negative if viewed from the port side. We will assume, however, that the aircraft is symmetric such that a range profile measured at aspect azimuth -α is the same as a range profile measured at α.

The range resolution of a profile can be described in terms of its capability to resolve point targets that are separated in range. The fundamental relationship for the inherent range resolution ΔR associated with radar bandwidth B is [11]

$$\Delta R = \gamma \frac{c}{2B} \qquad (1)$$

Where c is the speed of light.

Usually, a windowing function is applied before Fourier Transforming to reduce spectral leakage. The price to pay is a reduction in resolution, expressed in the factor $\gamma \geq 1$. For both our measurements and the predictions we applied a Hamming weighting which lowers the first sidelobe to -43 dB. For this window, $\gamma \approx 1.3$.

Range profiles depend strongly on the aspect angle. If an aircraft rotates over a large azimuth angle, such that the

outermost scatterers move from one resolution cell to the other, the measured range profiles during this rotation suffer from *Rotational Range Migration* (RRM) [4].

See figure 3. Suppose we look at an aircraft at broad-side, and consider the outermost point left (tip of the nose) and right (end of the tail). Let L be the distance between these points. Now, these points do not change their relative position in range over more than a resolution cell if the change in aspect azimuth $\Delta\alpha$ is less than

$$\Delta\alpha < \Delta\alpha_{RRM} \equiv \frac{\Delta R}{L} \ [rad] \qquad (2)$$

Thus, a range profile measured at (α,θ) does not differ due to Rotational Range Migration from a range profile measured at $(\alpha+\Delta\alpha,\theta)$ if $\Delta\alpha<\Delta\alpha_{RRM}$.

Rotational range migration also occurs if the aspect *elevation* changes. See figure 4. Points on the aircraft that are maximally separated in vertical direction change their relative path length to the radar with $V\sin(\Delta\theta)$ while rotating over an angle of $\Delta\theta$. Similarly, scatterers that are maximally separated in horizontal direction change their relative path length with $2\times L(1-\cos(\Delta\theta))/2$. Note that we have taken the maximum possible separation of scatterers on the wing tips also equal to L as most civil aircraft, including the target under consideration, are nearly 'square'. Thus, we may write for the change in aspect elevation $\Delta\theta$ that does not imply a difference due to rotational range migration:

$$\Delta\theta < \Delta\theta_{RRM} \equiv \min(\arccos(1-\frac{\Delta R}{L}),\arcsin(\frac{\Delta R}{V})) \ [rad] \qquad (3)$$

Another effect, *speckle*, causes range profile variability for much smaller changes in aspect angle. It is caused if in a single resolution cell two distinct scatterers are present - then, only a slight rotation of the aircraft in aspect azimuth or elevation is enough to change the differential path length to the radar over half the wavelength. This causes the sum of the two scatter contributions to turn from constructive to destructive interference within tiny changes of aspect angle; generally between one and two orders of magnitude smaller than the aspect angle changes associated with Rotational Range Migration.
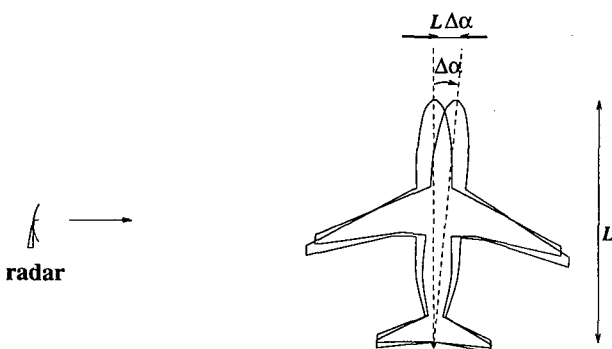
Fig. 3: The differential path of the outermost scatterers due to a small change in aspect elevation of $\Delta\alpha$ equals $L\Delta\alpha$.

The effect of speckle is that the amplitudes of the range profile elements may vary rapidly if a sequence of consecutively measured range profiles is considered - the change in aspect angle is due mainly to small aircraft yaw motions during the recording time. The peak positions, however, do not alter. Thus the following view may be adopted: during the measurement of a sequence of range profiles in real flight, the aircraft rotates with respect to the radar. Over large rotations the profiles decorrelate due to Rotational Range Migration. A small sector may be defined where RRM does not occur, which is called an *RRM-sector*.
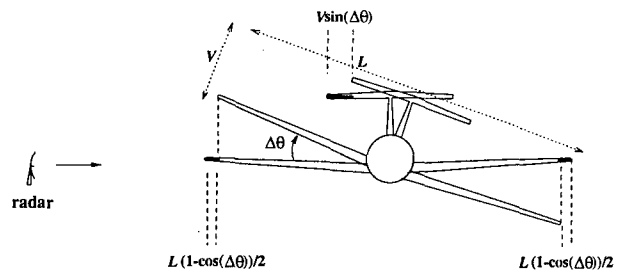
Fig. 4: Differential path length due to change in aspect elevation. In this geometry, the aircraft has its nose pointed perpendicular on the paper (towards the reader) and makes a rotation in elevation of $\Delta\theta$.

It is unfeasible to measure, and computationally very expensive to predict, range profiles at the dense sampling interval that is required to follow all speckle variations - we would typically need several hundreds of profiles per square degree. We therefore settle for a lower sampling density required to avoid RRM, thereby assuring that the *positions* of the scatterers are well-determined. Then, in the comparison of MRPs with PRPs, it should be kept in mind that the amplitudes of range profile elements that contain multiple scatterers will not be accurately predicted as it cannot be determined precisely what the relative phases of the individual scatterers are. Note, however, that most range-cells will *not* contain multiple scatterers if the resolution is high.

Let us now make a final remark on the sampling of range profiles in aspect angle. For L and V usually the aircraft length (or wingspan) and the aircraft height are taken. These are, however, the maximum dimensions of the aircraft. Therefore, equations 2 and 3 give in practice a smaller RRM-sector than they will be in reality because radar scatterers are not necessarily present on the outermost parts of the aircraft.

IV. IN-FLIGHT RANGE PROFILE MEASUREMENTS

In this paper we consider three legs of fifty range profiles each, acquired in the autumn of 1995 from three Boeings 737. During the measurements information from a secondary radar was available, which identified the aircraft as a Boeing 737 from either the 300- or the 500 series. The secondary radar uses the same code-name for both series, therefore it is not possible to tell which of the types was actually measured. The two aircraft types are identical apart from the length of the fuselage, being 33.4 m and 31.0 m for the 300 and the 500 series, respectively. The geometrical model we have available for our comparison is a Boeing 737-500. We must be aware,

therefore, that the MRP-PRP-correlation may be poorer if the measured target was actually a Boeing 737-300.

The range profiles were measured with the FELSTAR S-band radar located at TNO-FEL in the Hague, the Netherlands. A bandwidth of just over 450 MHz was emitted in 324 steps of 1.4 MHz each.

From these parameters and the maximum target length (L=33.4 m) and height (V=11 m, landing gear stowed) we find that the range resolution is 43 cm, and the aspect angle changes associated with Rotational Range Migration are 0.74 and 2.2 degrees for the aspect azimuth and aspect elevation, respectively.

The MRPs used in this paper were calibrated for system errors, virtually free of influences of radial velocity and acceleration and two-fold oversampled to (partly) reveal spectral contributions that are within grid-points. As mentioned before, the comparison was done on the magnitudes of the profiles only. An MRP thus consists of 648 real numbers.

For each range profile, we estimated the target aspect angle (α,θ) from the tracking data, taking into account the target position, motion and roll-angles. Figure 5 shows the aspect angles of the range profiles we use in this comparison. We unfortunately have no firm estimate of the errors in the aspect angle coordinates. The differences in aspect angles will be fairly accurate - a bias on both aspect azimuth and elevation for the whole leg could nevertheless be present. We are confident, however, that the bias for a particular leg will be within 5 degrees for both α and θ.
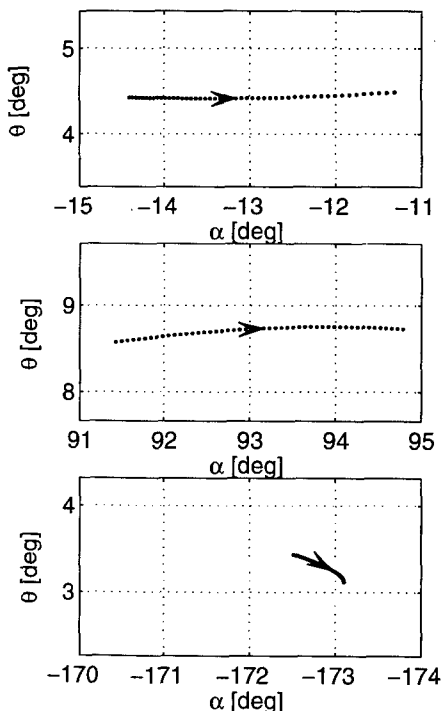
Fig. 5: Aspect angles of measured range profiles used in comparison.

Figure 6 shows for each of the legs how the aircraft is seen by the radar.

V. RAPPORT RANGE PROFILE PREDICTIONS

The aircraft model used in this report is a commercially available Boeing 737-500 (manufactured by Viewpoint Datalabs International, Orem, Utah, USA.); figure 6 shows the model at a few aspect angles. The object description compares very well with the real object with respect to the external dimensions. The engines, however, are closed near the front entrance. This will clearly have influence on the computed range profiles, because the engine is a cavity; such structures are known to have a large RCS [3]. Also, there are no arrangements, nor in the model nor in the RCS-prediction code to produce contributions from the rotating parts in the engine.
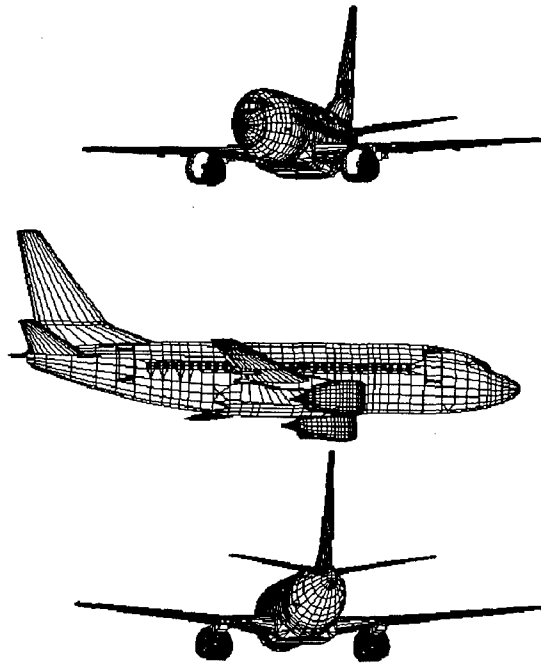
Fig. 6: The Boeing 737-500 model. The topmost figure corresponds to the average viewing angle of leg *i*, the second to leg *ii* and the third to leg *iii*. (Geometrical data by Viewpoint Datalabs International.)

The geometrical description of the aircraft consists of 8,361 polygons. Subdivision by RAPPORT until convergence was reached, led to an internal geometry description consisting of 27,248 facets. Making the number of reflections larger than three did not add significantly to the total RCS, therefore the maximum number of reflections was chosen to be three.

We used RAPPORT for the prediction at exactly the same 324 frequencies as at which the measurements were performed, and at each of the estimated MRP aspect angles shown in figure 5. We thus mimicked the measurement of a stepped frequency waveform. The predicted radar data was processed in the same fashion as the real data, i.e. Hamming weighting, zero-padding, Fourier Transforming and taking the absolute values. We thus produced 150 PRPs.

For a further experiment on leg *ii*, we computed range profiles on a grid around the estimated aspect angles. As discussed earlier, we settle for a sampling in order to avoid Rotational Range Migration. We chose steps of 0.6 degrees in aspect

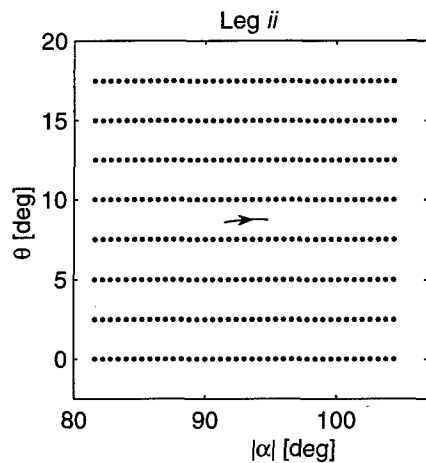azimuth and steps of 2.5 degrees in aspect elevation. See figure 7.

Fig. 7: Grid at which additional range profiles were computed (dots) around the aspect angles of leg *ii* (solid).

VI. COMPARISON RESULTS

To quantify the similarity between a predicted and a measured range profile we chose a straightforward measure: the Maximum Correlation Coefficient η. This number is the peak value of of the normalised correlation function. If $\underline{x}$ is a vector representing the MRP and if $\underline{y}$ is a vector representing the PRP, this similarity measure is defined as

$$\eta = \max_i (\underline{x}^{(i)} \cdot \underline{y}) \qquad (4)$$

Here '·' denotes the inner product of the two vectors and $\underline{x}^{(i)}$ is the original vector $\underline{x}$, but circularly shifted over i positions to the right. For example, if $\underline{x}^{(0)} \equiv \underline{x} = {}^1\!/\sqrt{30}\,[1\ 2\ 3\ 4]$ then $\underline{x}^{(2)} = {}^1\!/\sqrt{30}\,[3\ 4\ 1\ 2]$. Both $\underline{x}$ and $\underline{y}$ are normalised: it means that the sum of squares of the elements (=total energy) equals one. Therefore, if the PRP and the MRP are identical apart from a discrete shift, η equals unity.

The resulting MRPs and PRPs at the same aspect angles are shown in figure 8 in the two topmost diagrams and the bottom left diagram. They show ten measured range profiles (thin lines), each of them aligned with the predicted profile at the same aspect angle (thick lines). The aircraft contour is aligned with the PRP's. From the fifty profiles we show only the five that have the poorest correlation (the downmost five profiles) and the five that show the best correlation (the topmost five profiles). For all profiles the *magnitudes* are shown. The average Maximum Correlation Coefficients are 0.72, 0.80 and 0.69 for leg *i*, *ii* and *iii*, respectively.

In figure 9, another representation of the data is shown: stacks of the predicted and measured profiles are displayed as imager.

Comparing an MRP to a PRP at exactly the same aspect aspect angles disregards the possiblity that there are likely to be errors in the aspect angle estimates of the MRPs. For leg *ii* we therefore carried out the following procedure using the PRPs computed at the grid of aspect angles.

1. Shift the entire leg over a chosen angle in both aspect azimuth and aspect elevation.
2. Consider the aspect angle of a shifted MRP. Find the PRP in the grid of aspect angles that is closest in aspect angle.
3. Perform step 2 for all MRPs, such that for each MRP a PRP is found. (Note that for several MRPs the same PRP can be found, as neighbouring MRPs differ less in aspect angle than the neighbouring PRPs in the grid.)
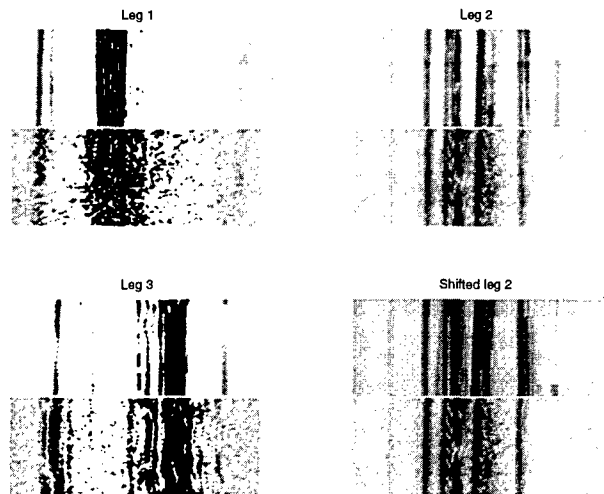4. Compute η for each MRP-PRP pair and average.

Fig. 9: For each of the three legs hundred range profiles are shown as a grey scale image (white: lowest, black: highest amplitude). The fifty predictions are shown at the top and the fifty measurements at the bottom of each sub-figure. The profiles in the bottom-right show the results of optimal shift from leg 2. The horizontal extend is 35 m for all images.

If the procedure is repeated for several shifts in aspect azimuth and aspect elevation, figure 10 is the result. It shows that the average correlation coefficient increases from 0.80 to 0.85 if a proper shift is chosen.
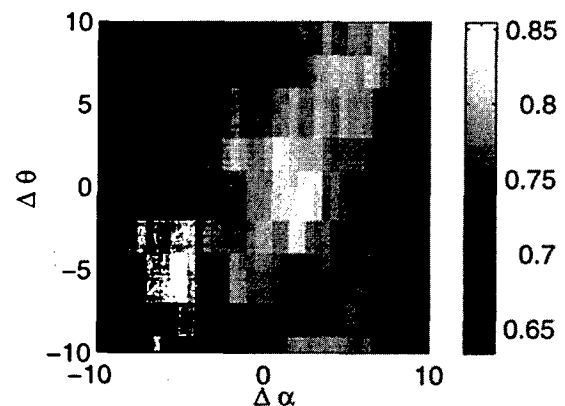

Fig. 10: Average Maximum Correlation Coefficients <η> as function of the shift over aspect azimuth and aspect elevation for leg *ii*. The maximum <η> is found at a shift of Δα = 2.5 and Δθ = -2.
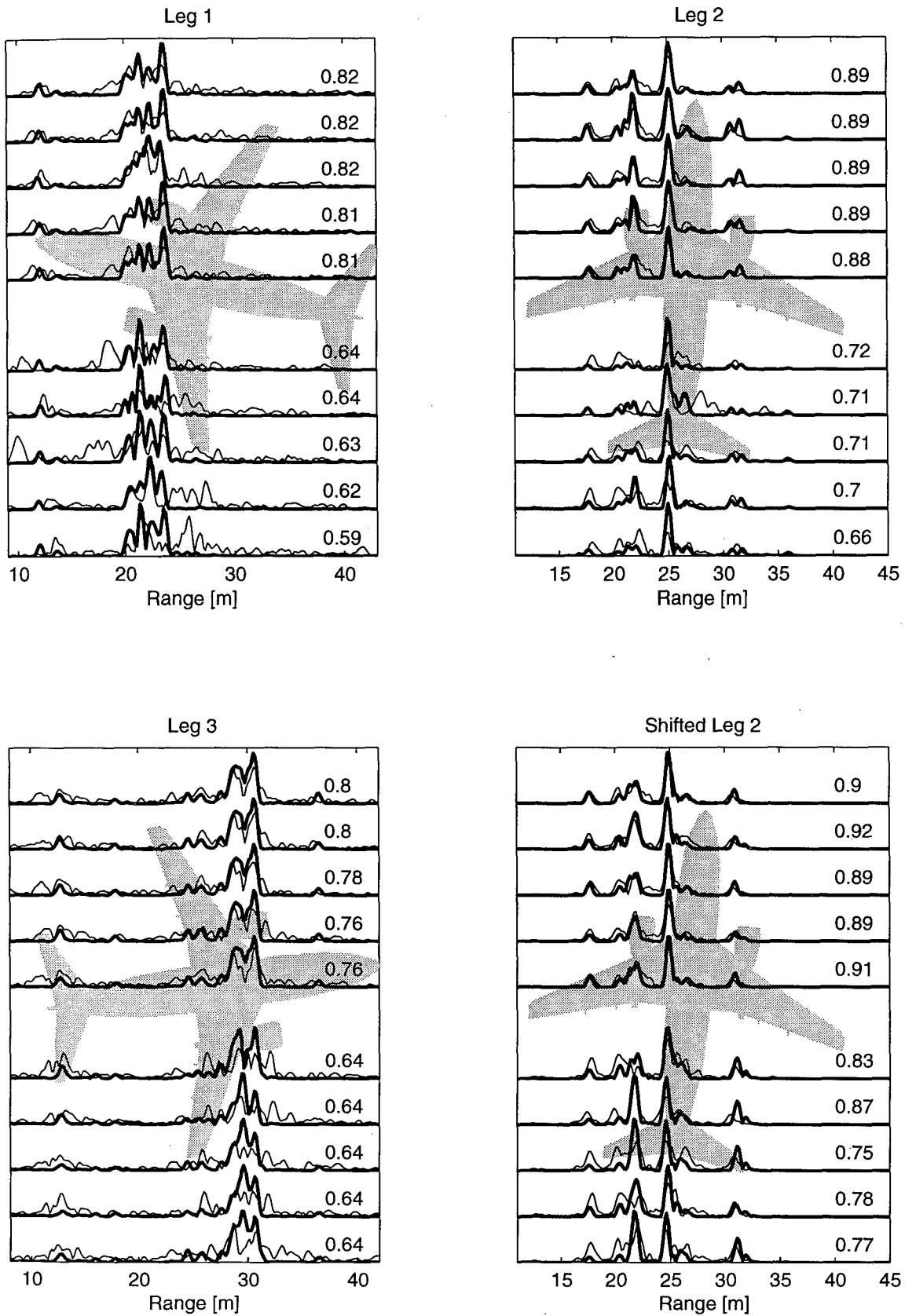
Fig. 8: For each of the three legs ten range profiles are shown. The measurements are shown by thin, the predictions by thick lines. The radar is situated at the left-hand side. The numbers in the figures display η. Only the five profiles in the leg with lowest correlation (bottom five) and the five profiles with highest correlation (top five) are displayed. For the two topmost figures and the bottom left figure, the PRP's are computed at the estimated aspect angles. The profiles in the bottom-right show the results of optimal shift from leg *ii*. In the top-left corner of each figure a bar shows the projected difference in fuselage length between the 300 and 500 series of the Boeing.

The profiles in the bottom right diagram of figure 8 show the same ten MRPs of leg *ii*, but now aligned with profiles that were searched for in the grid. A slightly better match is observed. We have thus found a better estimate of the target attitude, i.e. (α, θ), with respect to the radar.

VII.   OBSERVATIONS AND DISCUSSION

1. Viewing figures 8 and 9 we observe for leg *i* (near nose-on) and for leg *iii* (near tail-on) a fairly good agreement between MRPs and PRPs. The correspondence for leg *ii* (near-broad side) is much better. Even for the MRP-PRP pairs with lowest η, the correspondence is quite good for leg *ii* and still present for leg *iii*.
    These results are very encouraging for the use of RCS-prediction codes for computing radar range profiles of complex targets.

2. The convincing correspondence for the broad-side case, leg *ii*, is clearly favoured by the aspect angle under which we see the aircraft: we do not have reflections from cavities or turbines as we have at head-on and tail-on aspect angles. Also, at these aspect angles not many range cells contain multiple scatterers that give rise to inaccurate amplitudes.

3. For leg *iii*, we may have actually measured a Boeing 737-300 instead of the somewhat smaller Boeing 737-500 as we do see extra signal in the MRP left from the leftmost scatterer in the PRP.

4. Viewing the same figures again, it is seen that, although the peak positions are quite well predicted, the amplitudes match less well. One of probable causes is speckle: to predict the amplitudes of range cells that contain multiple scatterers, the model and the real target should have the same aspect angle within a few hundredths of a degree. Also, the target approximation by small flat patches (instead of round surfaces) and a perfectly conducting surface (instead of dielectric surfaces) is only a first approximation to the actual scattering mechanisms, and is therefore likely to produce inaccuracies in amplitude. One of the obvious causes of amplitude mismatch is the normalisation. As no noise-power is present in the PRPs its normalisation pushes the signal components to higher values compared to the MRPs. This is mainly seen in the first and the last leg, where the signal-to-noise ratio of the MRPs is significantly poorer compared to leg *ii*. Another observation is that the spaces between the profile peaks are 'filled' for the MRPs and are much less filled for the PRPs. This influences the amplitudes as the profiles are normalised.

5. Several reflective processes that occur in reality are presently not accounted for in the RCS-prediction code. We mention the modelling of edge-diffraction, creeping waves, cavities and rotating engine parts.
    Possible scatter contributions not modelled on the geometrical model are: antennas, dielectric materials, transitions between dielectric materials, surface roughness, rotating engines and features that differ from aircraft to aircraft from the same type.
    As the results show, for broad-side views the aircraft range profiles can very well be modelled by Physical Optics and Raytracing only. The main difference is that the MRPs have a clear signal component between the main peaks in the profile. For nose-on and tail-on aspect angles, the Physical Optics and Raytracing approximation predicts the most prominent scatterers, but more reflective processes and better models need to be utilised to account for the other contributions in the range profile. Apparently, most of the extra non-explained signal in these profiles is due to the engines: cavities and rotating fans and turbines.

6. We also observe that for leg *ii* the main features on the aircraft, like the fuselage, the engines and the *flap tracks* (the two dihedral-like structures on each of the wings) can well be seen in the range profiles.

7. We used the Maximum Correlation Coefficien η as a measure of similarity between MRPs and PRPs. This parameter can however be quite low, even if a correspondence between the peaks is observed. As an example, see figure 8, bottom-most profile in the bottom-right figure. For this MRP-PRP pair, a low η is found even though most peaks in the PRP are also present in the MRP. The reason is that η is sensitive to differences in the relative amplitudes of scatterers - unfortunately these are the features that are difficult to predict accurately (see point 5). It is therefore of interest to investigate a better measure of similarity that is less sensitive to amplitude. Such a measure will also benefit a future direction of research, the classification of MRPs with PRPs.

VIII.   CONCLUSION

In this paper we have demonstrated that RCS-prediction codes can be used to mimic the measurement of radar range profiles of complex targets at three different aspect angles. For broad-side aspect angles it was shown to be possible to improve the estimate of target attitude.
Even though several reflective processes are not included in the prediction code and the model is a simplified representation of the true target, the correspondence is convincing.

IX.   ACKNOWLEDGEMENTS

REFERENCES

[1]   E.F. Knott. A tool for predicting the radar cross section of an arbitrary trihedral corner. IEEE *SOUTHEASTCON*, pages 17-20, April 1981.

[2]   E.F. Knott, J.F. Shaeffer, and M.T Tuley. *Radar Cross Section. Its prediction, measurement and reduction.* Artech House inc., 1985. ISBN 0-89006-174-2.

[3]   D.A. Zolnick. Calculating the radar cross section from multiple-bounce interactions. In *IEE International Conference on Computation in Electromagnetics*, pages 193-196. IEE London, Conference Publication 350, 1991.

[4]   S. Hudson and D. Psaltis. Correlation filters for aircraft identification from radar range profiles. *IEEE Transactions on Aerospace and Electronic systems*, 29(3):741-748, July 1993.

[5]   A. Zyweck and R.E. Bogner. Radar target classification of commercial aircraft. *IEEE Transactions on Aerospace and Electronic systems*, 32(2):598-606, April 1996.

[6]   H.-J. Li, Y.-D. Wang, and L.-H. Wang. Matching score properties between range profiles of high-resolution radar targets. *IEEE Transactions on Antennas and Propagation*, 44(4):444-452, 1996.

[7]   G.T. Ruck, D.E. Barrick, W.D. Stuart, and C.K. Krichbaum. *Radar Cross Section Handbook*, volume 1. Plenum Press, New York, 1970. ISBN 0-306-30343-4.

[8]   H. Ling, R. Chou, and S.W. Lee. Shooting and bouncing rays: calculating the rcs of an arbitrary shaped cavity. *IEEE Transactions on Antennas and propagation*, 37:194-205, 1989.

[9]   D.J. Andersh, M. Hazlett, S.W. Lee, D.D. Reeves, D.P. Sullivan, and Y. Chu. XPATCH: A high-frequency electromagnetic-scattering prediction code and environment for complex three-dimensional objects. *IEEE Antennas and Propagation Magazine*, 36:65-69, 1994.

[10]   M.G.E. Brand. Radar signature analysis and prediction by physical optics and ray tracing. The RAPPORT code for RCS prediction. FEL-95-A097, TNO-FEL, 1995.

[11]   D.R. Wehner. *High-Resolution Radar, 2nd edition.* Artech House, 1994. ISBN 0-89006-727-9.

[12]   R. van der Heiden, L.J. van Ewijk, and F.C.A. Groen. *In-flight measurements and RCS-predictions: a comparison on broad-side radar range profiles of a Boeing 737.* IEE conference RADAR 97, Edinburgh, 14-16 October 1997, pp 444-448.

A HIGH-FREQUENCY ELECTROMAGNETIC SCATTERING PREDICTION CODE USING SHOOTING AND BOUNCING RAYS

D. J. Andersh
S. W. Lee
DEMACO, Inc.
100 Trade Centre Drive Suite 303
Champaign, IL 61820

J. Hughes
Air Force Research Laboratory
2010 Fifth Street, Building 23
Wright-Patterson AFB, OH 45434

H. Ling
University of Texas
Department of Electrical & Computer Engineering
The University of Texas at Austin
Austin, TX 78712-1084

SUMMARY

This paper describes an electromagnetic computer prediction code for generating radar cross section (RCS), time-domain signatures and synthetic aperture radar (SAR) images of realistic 3-D vehicles. The vehicle, typically an airplane or a ground vehicle, is represented by a computer-aided design (CAD) file with triangular facets, IGES curved surfaces (NURBS or B-Splines), or solid geometries. The computer code, Xpatch, based on the shooting-and-bouncing-ray technique (SBR), is used to calculate the polarimetric radar return from the vehicles represented by these different CAD files. Xpatch computes the first-bounce Physical Optics (PO) plus the Physical Theory of Diffraction (PTD) contributions. Xpatch calculates the multi-bounce ray contributions by using Geometric Optics (GO) and PO for complex vehicles with materials. It has been found that the multi-bounce contributions are crucial for many aspect angles of all classes of vehicles. Without the multi-bounce calculations, the radar return is typically 10 to 15 dB too low. Examples of predicted range profiles, SAR imagery, and RCS for several different geometries are compared with measured data to demonstrate the quality of the predictions. The comparisons are from the UHF through the Ka frequency ranges for simple and complex targets. One of the powers of Xpatch is the traceback feature, where it is possible to see the cause and effect of different target features. Examples of these features are also presented in this paper. Recent enhancements to Xpatch include improvements for millimeter wave (MMW) applications and hybridization with Finite Element Methods (FEM) for small geometric features and augmentation of additional IGES entities to support trimmed and untrimmed surfaces.

1   INTRODUCTION

Xpatch is a general-purpose radar signature prediction code and environment for calculating high-frequency electromagnetic scattering from complex objects described by several different computer-aided design (CAD) representations. Xpatch has been developed by DEMACO in Champaign, Illinois under the joint Tri-Service sponsorship of Air Force Research Laboratory at Wright-Patterson AFB, Ohio and Kirtland AFB, New Mexico; the Army Research Laboratory at Ft. Belvoir, Virginia; and the Naval Air Warfare Center at Pt. Mugu, California. The X-Window Motif™ Graphical User Interface (GUI) combines CAD geometry pre-processing and analysis tools, along with the Xpatch prediction codes, and post-prediction analysis tools. This GUI allows the user to perform end-to-end predictions analysis all in one package.

Xpatch is based on the high-frequency SBR technique[1,2,3] that is capable of calculating the fully polarimetric radar return from complex geometries represented by different CAD geometry types. Both the first-bounce PO plus the PTD contributions and the multi-bounce geometric optic ray contributions are included in the computation. For the first-bounce calculations, the most time-consuming aspect is shadow and blockage checks on the geometry. A hardware and software Z-buffering technique is used in Xpatch for highly accurate and fast calculations. Once the geometry's blocked and shadowed surfaces are determined, the first-bounce contribution is calculated using PO. The first-bounce PO calculation can be accomplished using a fast frequency-domain integration[4] or by a time-domain technique developed by Sheppard, et. al[5]. An option exists to include the first order metal edge diffraction by

using the Ufimstev-Mitzner incremental diffraction coefficients. Although blockage on edges is taken into account by ray tracing, higher order edge diffractions due to multiple interactions is not included. Plans exist to incorporate higher order diffraction's in future releases.

To calculate the multi-bounce effects, a set of parallel rays are launched from the incidence plane towards the geometry. Each ray is traced as it bounces from one part of the geometry to another, until it exits the geometry. The field on the ray-tube at each bounce point is calculated by the theory of GO and the associated backscattered field is calculated by PO if the bounce point is visible to the observer. The multi-bounce calculations include the effects of polarization, ray divergence factor, and material reflection coefficients for frequency-dependent, multi-layered materials, and for semi-transparent materials such as radomes and dielectric covered cavities or objects. At each bounce point the blockage to the observation point is checked and then a frequency-domain or a time-domain physical optics integration[6] of the induced surface currents are performed to calculate the far-field contribution at each bounce point. Contributions from all rays are then summed up at a far-field observation point to give the final scattered field.

Given the geometry and incident angle, rays are launched from a shooting window determined by the bounding box of the geometry. As an example, consider a typical fighter airplane (F-15 in Figure 1) illuminated at an incidence elevation of -15° and azimuth of -15°. The shooting window is 674 λ by 397 λ at 10 GHz. Accuracy using a SBR type technique RCS and range profile (time-domain) calculations requires a minimum ray density of 10 rays per linear wavelength. Using this minimum ray density, 23 million rays are launched at the 3-D CAD representation of the F-15 shown in Figure 1, of which 4 million rays actually hit the geometry. The minimum required ray density for SAR imagery can also be reduced to two or three rays per linear wavelength, depending upon geometry complexity and the amount of multi-bounce contributions required to accurately calculate the backscattered field from the geometry. An interesting display of the multi-bounce effect is presented in Figure 2 for near broadside incidence of a tank. This figure clearly illustrates the necessity of using the SBR technique to capture all of the multiple bounce effects in backscattering predictions. There was a limit of 15 bounces used for the multi-bounce calculation in Figure 2. The first-bounce calculation was done using the Z-buffer technique[4] and the geometry was represented using triangular facets.

Presently, a typical frequency-domain range profile computation with 1,024 frequencies (50 bounces, 10 rays/λ, X-band, 200,000 facet vehicle) takes approximately 40 minutes on an HP 720 workstation. Performing the same calculation directly in the time-domain on the same HP 720 workstation takes approximately 20 minutes[6]. This technique is currently valid only for perfect electric conducting targets. Computation times for the narrow angle (3°) X-band SAR imagery of a tank, using the direct time-domain approach, takes approximately four minutes on an HP 720 workstation. Similarly, using IGES surface representations increases the frequency-domain run time for the same 200,000 facet vehicle to about 160 minutes on an HP 720 workstation. For this reason, a new technique has been developed in Xpatch that incorporates the surface curvature into a flat-faceted geometry file and can be used as an optional prediction method if curved surface computations become too time intensive. This hybrid geometry file provides fast computation associated with flat-facet targets and accounts for the surface curvature to improve the amplitude calculations by including the ray divergence factor. One drawback of this hybrid approach, depending on the surface curvature, is that 200,000 plus facets are required to represent a typical fighter class vehicle and this means larger core memory requirements. Work is ongoing to develop a hybrid ray tracer that combines facets and NURBS into one geometry representation of the vehicle to optimize computational speed, memory, and accuracy requirements.

The Xpatch codes have been parallelized on the Intel Paragon, IBM SP2, and Cray T3E using MPI. Current production capacity is 14,000+ (1024 X-band frequency points) signatures or images per day on the 480-node Intel paragon. Research is proceeding in several areas to improve performance and accuracy. Optimization of the ray tracer and associated electromagnetic calculations in Xpatch is also an ongoing effort. Research to augment Xpatch with low-frequency codes such as finite elements, finite difference time-domain, and MoM solutions is underway. Hybridization is being pursued to improve the Xpatch prediction code suites' accuracy for cavities, antennas, and vehicle details less than 10 linear wavelengths in size. Hybridization of Xpatch with a FEM code is complete and can now be used to perform calculations on small features of a vehicle such as cracks and gaps[7].

2   CODE CAPABILITIES

The electromagnetic part of Xpatch consists of roughly 50,000 lines of FORTRAN and C, the other parts of the package consist of over 250,000 lines mostly in C and C++. Xpatch consists of three parts:

1) Electromagnetics: XpatchF, Xpatch.
2) CAD and visualization tools: Cifer, XEdge, XYplot, McRange, and McImage.
3) GUI.

Typical output files from electromagnetic computations:
1) Complex scattered far-field or RCS in dBsm (0-D signature).
2) Range profile (1-D signature).
3) Synthetic radar image SAR (2-D signature).

A summary of Xpatch electromagnetic capabilities is given in Table 1. Any code in Xpatch can be used individually as an independent unit, or it can be used as a component in the integrated GUI package. The GUI consists of multiple pre- and post- prediction analysis tools: Cifer, XEdge, XYplot, McRange, and McImage. Cifer is a file translator package that translates CAD formats from one CAD system to another and also translates data into the required formats for the Xpatch electromagnetic codes and the related tools. XEdge is a CAD processing and analysis tool for evaluating geometry fidelity and provides a limited toolset for simple CAD modifications.

XEdge is a visualization tool allowing the user to display the CAD geometry and evaluate the physical integrity of the geometry to determine if the proper material assignments have been made, if normals are correct, and if the surfaces are properly modeled. XYplot is a plotting package for producing xy-plots of the data. McRange allows the user to display the CAD file with measured and predicted time-domain signatures to evaluate the cause and effect of scattering. McImage allows the user to overlay a CAD file with a predicted or measured SAR image and also allows the user to evaluate the cause and effect of the scattering. All of these tools have been integrated into one package with the GUI to allow the user to perform a seamless analysis of a complete electromagnetic prediction task. An example of the GUI is shown in Figure 3. The GUI provides access to file management, Cifer, geometry display and analysis tools, computational settings, job control and status, results displays, signal processing tools, and an on line help system.

The complex object geometry representation for Xpatch radar scattering predictions can be either triangular flat-facets, BRL-CAD™ constructive solid geometries, or IGES·114 surface formats. By far, the most popular format is the triangular facet file because the computation time is about four times faster than the time for curved surface or solid geometry representations. Figure 1 is a facet model of a fighter aircraft, and Figure 4 is a view of a solid model for a typical tank.

One of the most important aspects of radar prediction is the integrity of the CAD geometry file. To analyze the CAD geometry, tools such as XEdge, have been developed. These tools visualize, rotate, evaluate geometry normals, and inspect geometry surface integrity and connectivity (Figure 1). After the geometry has been visualized and evaluated for integrity the next step is to set up the run parameters to compute the electromagnetic scattering from the CAD geometry. The run parameters for Xpatch have all been integrated into a GUI that allows for easy input and assignment of the run parameter. An example input file for Xpatch is illustrated in Figure 5. After the computations with

Xpatch, insight into scattering causes and effects on targets is provided through another tool, McRange. McRange displays the CAD geometry with its corresponding range profile in the same range coordinate system (Figure 6). User-defined vertical solid lines on the plots illustrate the tie of scatter location to a physical attribute on the geometry. These GUI tools are very useful to evaluate the fidelity of CAD geometries, set up the run parameter, monitor the computational run, and analyze the causes and effects of scattering.

3   VALIDATION RESULTS

Xpatch has been extensively validated against primitive objects and full scale complex vehicles[8,9,10]. The results for different geometries are shown in Figures 7 through 13 with a comparison of measured and predicted data. The results in Figure 7 are for a perfect electric conducting (PEC) trihedral with two hemispheres embedded into the sides of the trihedral. As Figure 7 illustrates, the predictions for this complex object are good except at the low RCS levels and at aspect angles of 10 and 80 degrees. The poorer agreement at 10 and 80 degrees is due to higher order multiple diffraction;'s from the edges of the trihedral and the surfaces of the trihedral. These higher order effects are currently not modeled in Xpatch. For the cylindrical duct in Figure 8, 30λ in diameter by 100λ in length, the agreement for this large complex cylindrical cavity is very good. The discrepancies in Figure 8 are also due to higher order interaction terms that are not currently modeled in Xpatch. The comparison of results in Figure 9, between measured and predicted data for an almond shaped object, are also in very good agreement except for the higher order interaction scattering taking place at the tip of the almond. Figure 10 is a comparison of measurements and predictions using the hybrid SBR technique for the object body and the finite element method (FEM) for the gap. Figure 11 is a comparison of exact solution and predicted data for a bulk material loaded rectangular waveguide. Agreement here is also very good. Figure 12 is the comparison of Xpatch and a MoM code. Figure 13 is a comparison of an actual aircraft time-domain response and an Xpatch predicted response. As is illustrated in Figures 13 and 14, the agreement between measured and Xpatch predicted data is excellent. Figure 15 is a McImage rendering of a predicted SAR image of an actual aircraft. This image was computed with the SBR technique using the direct time-domain method and required a computation time of four minutes on a Silicon Graphics workstation. Imagery such as this can be used as a diagnostic tool to study the cause and effect of scattering.

4   CONCLUSIONS

Xpatch provides realistic RCS, range profiles, and 2-D SAR imagery calculations for complex geometry types from 500 MHz to 100 GHz. Deficiencies in the existing CAD models contribute major errors in the predictions.

Model deficiencies include poor or missing detail, inaccurate surface curvature, and improper modeling of small features and materials. The result is incomplete and inaccurate RCS, range profiles, and 2-D SAR images. More accurate CAD geometries can correct the deficiencies, but modeling is time-consuming and difficult. Additionally, the ultimate level of fidelity required for a CAD geometry is unknown. Research is ongoing to quantify the level of fidelity required from CAD models for different frequency ranges and applications.

The code, Xpatch, is providing accurate signatures for the many different targets at all aspects. Xpatch currently does not perform calculations for semi-transparent radar materials, antenna scattering and some of the higher order scattering effects such as traveling waves, and creeping waves. The major conclusion, thus far, is that the range profiles created with Xpatch and flat-faceted CAD files are adequate to use in generating a signature data base for target identification algorithm testing, development, and radar testing.

Xpatch does not currently perform calculations for some of the higher order scattering effects such as traveling waves, surface waves, resonant effects, and creeping waves. Ongoing research to augment Xpatch for these scattering phenomena is currently in progress, with emphasis on new methods and hybridizing the predictions with low-frequency methods. The Xpatch prediction code suite is being upgraded to perform full vehicle in scene predictions from UHF through Ka band. The major conclusion thus far is that the predictions created with Xpatch are adequate to use in studying the radar signatures of complex 3-D objects over a wide range of frequencies.

5   REFERENCES

1. H. Ling, R. Chou, and S. W. Lee, "Shooting-and-Bouncing-Rays: Calculating the RCS of an Arbitrarily Shaped Cavity," *IEEE Trans. Antennas & Propagation.*, vol. 37, 194 : 205 (1988).

2. S. W. Lee, "Electromagnetic reflection from conducting surfaces: geometric optics solution," *IEEE Trans. Antennas & Propagation.*, vol. AP 37, 184 : 191 (1975).

3. G. A. Deschamps, "Ray Techniques in Electromagnetics ," *Proceedings of IEEE.*, vol. 60, 1022-1035 (1972).

4. J. M. Rius, M. Ferrando, and L. Jofre, "GRECO: Graphical Electromagnetic Computing for RCS prediction in real-time," *IEEE Antennas and Propagation Magazine*, vol.35, No.2, pp.7-17, 1993.

5. R. A. Sheppard, T. D. Olson, and C. S. Liang, 1992 *IEEE Antennas and Propagation's Society International Symposium*, Chicago Illinois: 1992 Digest, Volume III, page 1311.

6. J. Jin, S. Ni, and S. W. Lee, "Hybridization of SBR and FEM for scattering for large bodies with cracks and cavities," EM Lab Report for NASA NAG 3-1474, University of Illinois, Urbana, Nov. 1994.

7. H. Ling and R. Bhalla, "Time-Domain Ray-Tube Integration Formula for the Shooting-and-Bouncing-Ray Technique," *Technical Report NASA Grant NCC 3-273*, The University of Texas, Austin Texas (1993).

8. E. M. Miller, D. J. Andersh, and A. J. Terzuoli, Jr, *IEEE Antennas and Propagation's Society International Symposium*, Ann Arbor Michigan: 1993 Digest, Volume III, page 1404.

9. D. J. Andersh, S. W. Lee, *et al.*, "Xpatch: a high-frequency electromagnetic scattering prediction code and environment for complex three-dimensional objects," *IEEE Antennas and Propagation Magazine*, Vol. 36, No. 1, February 1994, pp. 65 - 69.

10 J. Bauldauf, S. W. Lee, L. Lin, S. K. Jeng, S. M. Scarbourgh, and C. L. Yu, "High-Frequency Scattering from Trihedral Corner Reflectors and Oter Benchmark Targets: SBR vs Experiment," *IEEE Trans. Antennas & Propagation.*, vol. 39, 1345:1352 (1991).
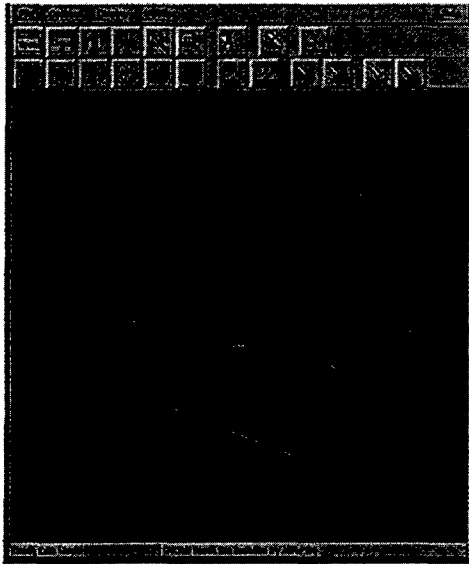
6   ILLUSTRATIONS

Table 1. Xpatch Radar Prediction Code

FEATURE	XpatchF	XpatchT
Frequency / Time-Domain	frequency	time
Target geometry	CSG / NURB / Facet	CSG / NURB /Facet
Coating/Radome	yes	approximate
Divergence factor	yes	yes
First-bounce	PO / SBR z-buffer	z-buffer / SBR
Higher-bounce	SBR	SBR
Edge diffraction	metal	metal
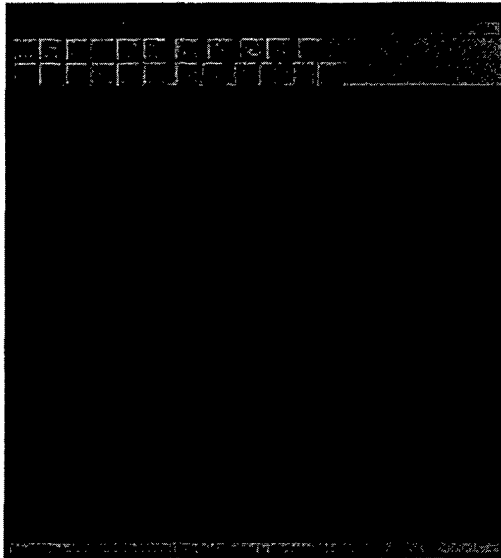
a)

b)

Figure 1. Example of visual ray tracer (a) and faceted aircraft CAD model (b) using visualization tools (XEdge) available in Xpatch.
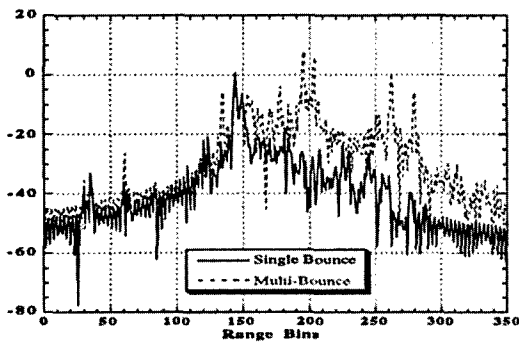

Figure 2. Range (time-domain response) profile plots as a function of range for single bounce (solid line) po calculations versus multi-bounce (dashed line) for a tank at an off cardinal angle of 45° Az and depression of 45° at 10 GHz.
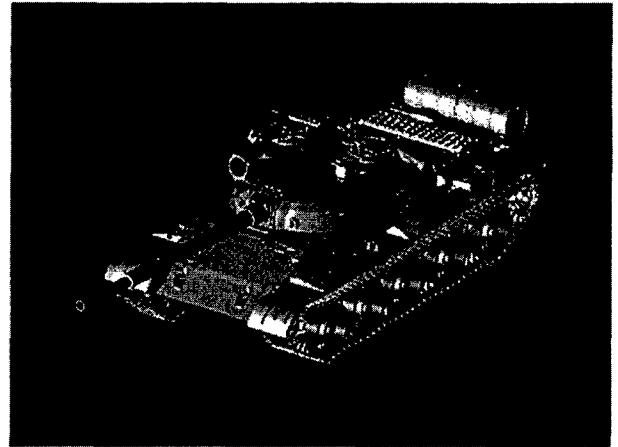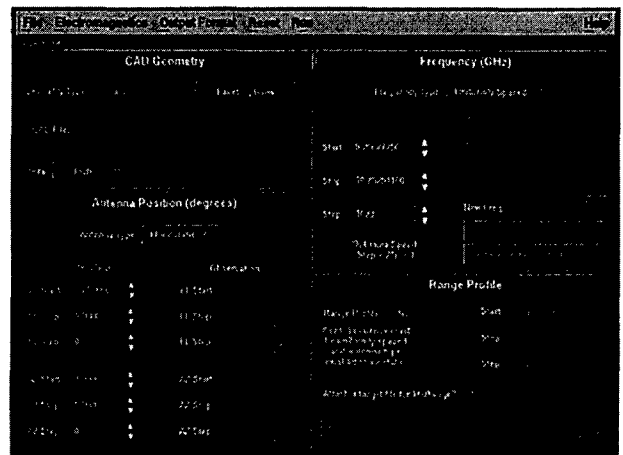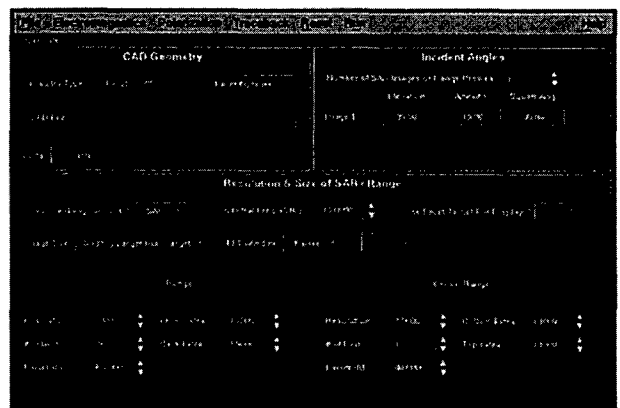

Figure 3. Xpatch GUI menu bar.

Figure 4. Solid model CAD (BRL-CAD) geometry of a tank used with Xpatch.

a)

b)

Figure 5. Xpatch GUI electromagnetic input control pages: a) XpatchF input page; b) XpatchT input page
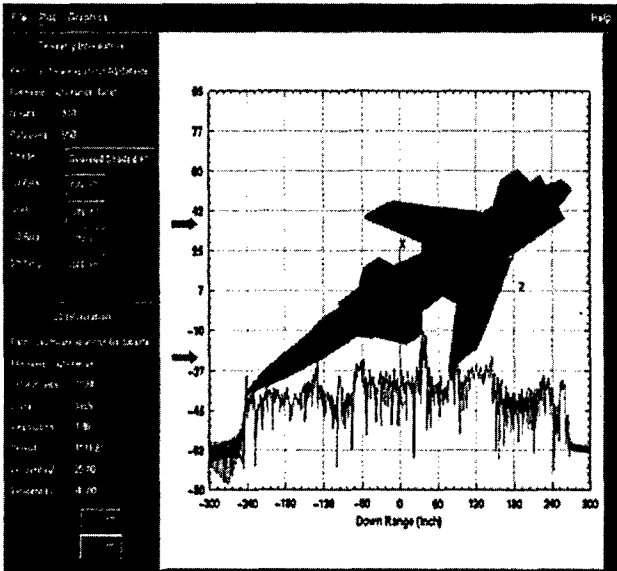
a)
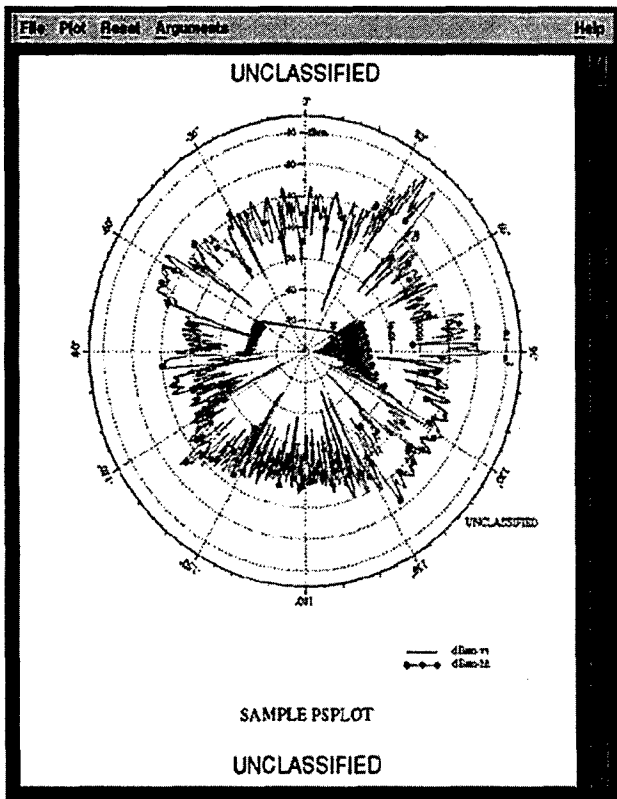
b)

Figure 6. a) Predicted range profile of the X-29 from an aspect of Az = 0 and El = - 15.8 at a center frequency of 10 GHz illustrating the post prediction tool (McRange) (Note solid lines can be drawn from the bottom plot connecting to the upper CAD file showing scattering cause and effect). b) RCS using Psplot for 360 degree RCS display.
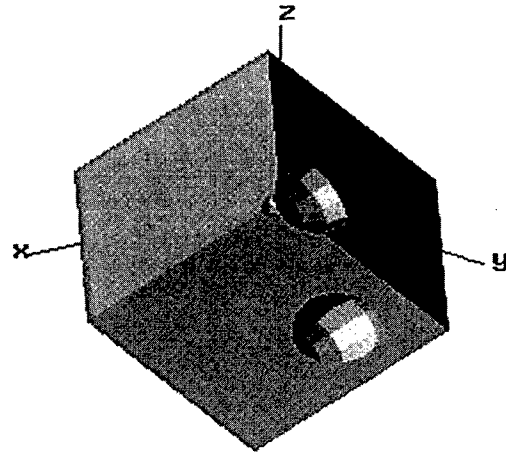
a) Geometry description.
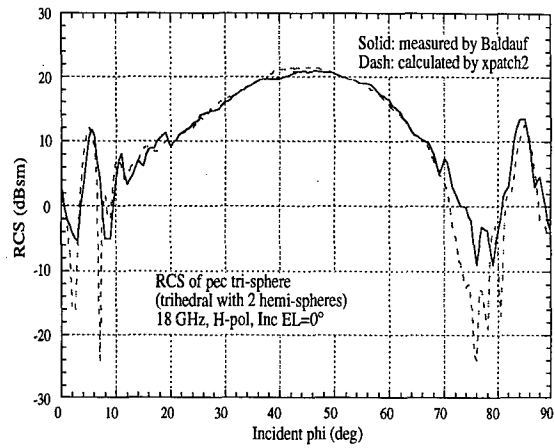
b) Data comparison.

Figure 7. Comparison of predicted data to measured data for a PEC trihedral (a) with two hemispheres, f = 18 GHz, HH Pol, φ = 0°.
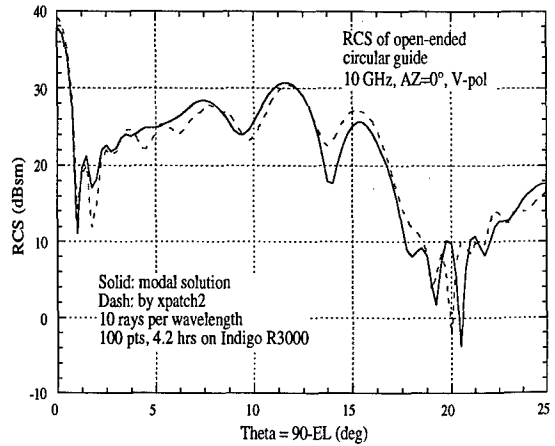
Figure 8. Comparison of predicted data to a modal solution for a shorted cylindrical duct, f = 10 GHz, VV Pol, φ = 0°, diameter = 95.9 cm, length = 254 cm.
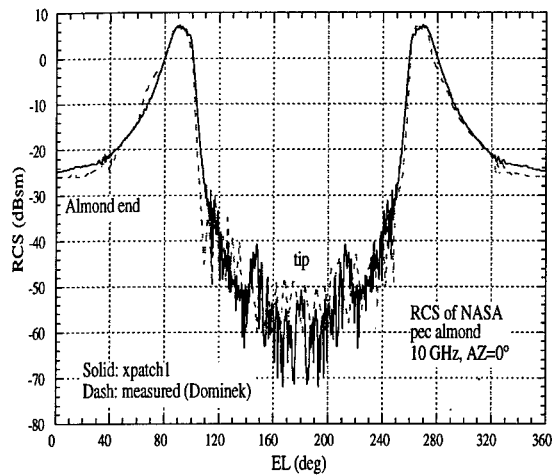
Figure 9. Comparison of measurements and predictions for a PEC almond, VV polarization, f = 10 GHz, NASA 1 meter almond.
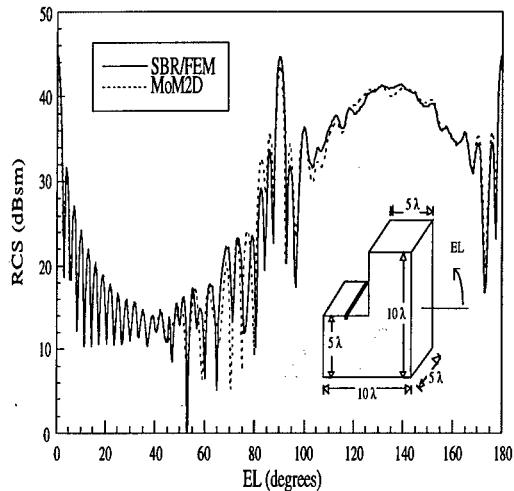
Figure 10. Calculated RCS by XpatchF with the hybrid FEM method and that by the exact Moment Method for a dihedral with a crack for the incident HH polarization[7].
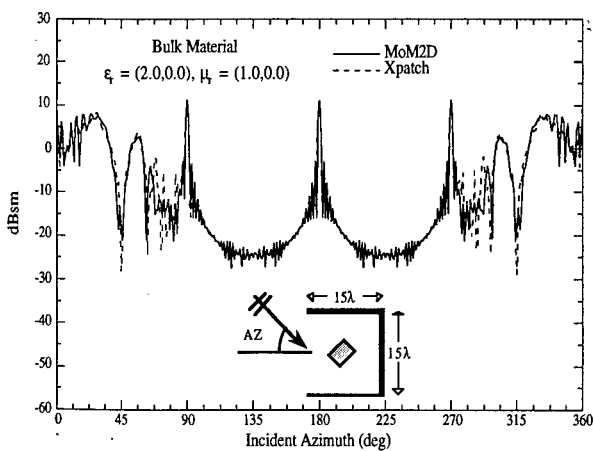
Figure 11. RCS of a rectangular guide with a diamond shaped bulk dielectric material inside at 10 GHz. The incident E-field is in Z-direction.
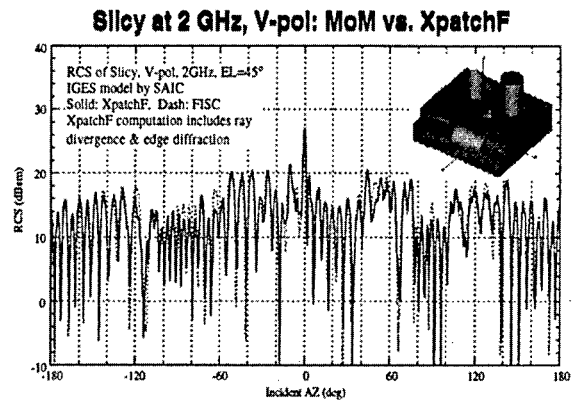
Slicy at 2 GHz, V-pol: MoM vs. XpatchF

Figure 12. Comparison of the MoM and the Xpatch predicted RCS pattern of a primitive target called Slicy at 2 GHz.
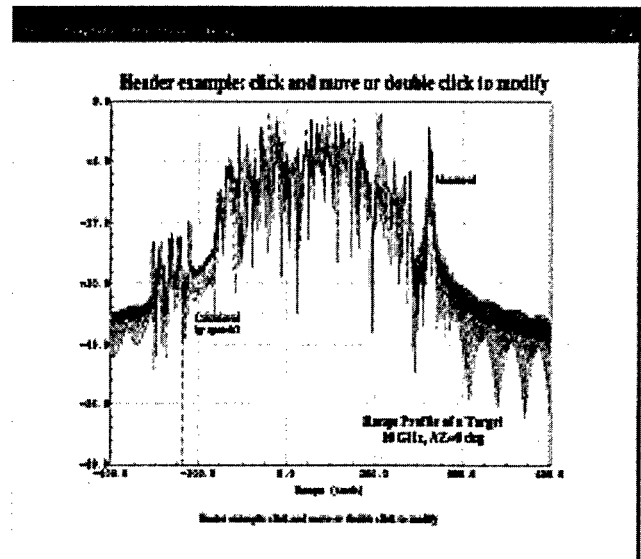
Figure 13. Comparison of Xpatch range profile predictions to measured results for an actual vehicle, VV Pol. f = 10 GHz.
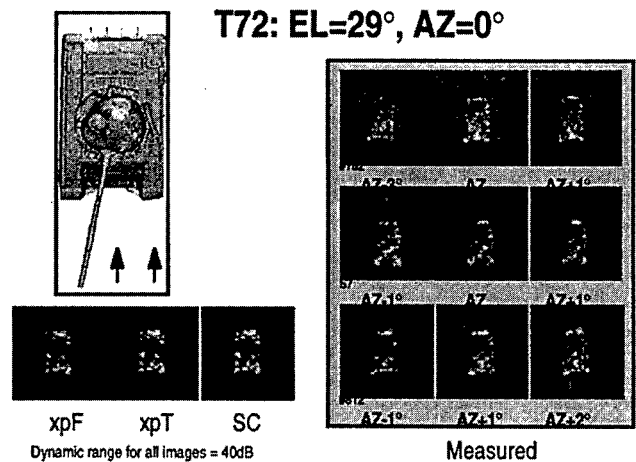
T72: EL=29°, AZ=0°

Figure 14. Prediction XpatchT and XpatchF SAR images of an T72 tank at X-band and compared to measured data at multiple aspect angle.
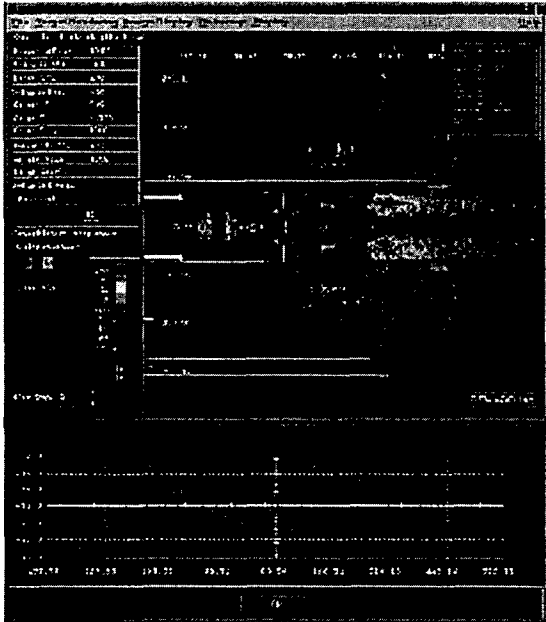
Figure 15. Prediction of an SAR image of an aircraft at X-band and displayed with CAD geometry using the McImage analysis tool.

7   ACKNOWLEDGMENTS

FACETS Prediction Code

J. G. Gallagher
Defence Evaluation and Research Agency
St Andrews Road
Malvern
Worcs WR14 4JY
U.K.

1.   Summary

This paper describes the main high frequency electromagnetic prediction code for generating radar target signature data used in DERA. The FACETS code was developed by Racal-Thorn over a thirteen year period and is a state-of-the-art RCS prediction code based on physical optics, geometrical optics and physical theory of diffraction algorithms. It is an extensively validated code and is supported on a wide range of computer architectures, both serial and parallel.

A large number of resources have been used in developing this capability and in order to maximise the return on our investment we have developed ways of using this software to define radar target models that can be used in larger synthetic modelling environments. In particular, we have developed two different target signature fluctuation models for use in radar system assessment modelling. One of these is based on the standard Swerling model and the other is a new stochastic model that does not need to make any assumption about the distribution function of the target. This new method is superior to the traditional Swerling description of target characteristics and offers a more accurate representation of target RCS. Both methods that we have developed provide the ability to model target glint as well as target RCS levels.

2.   Introduction

The FACETS code (Frequency Asymptotic Code for Electromagnetic Scattering) is a radar cross-section (RCS) prediction program for large complex targets. It has been developed for DERA by Racal-Thorn continuously over this last thirteen years. The code is based on a sequence of high-frequency asymptotic techniques, which are physical optics, geometrical optics and the physical theory of diffraction. FACETS is wrapped up in a system process called the FACETS Electromagnetic Analysis System (FEMAS) that translates the engineering description of the target geometry into a form suitable for the FACETS electromagnetic analyses algorithms. The target geometry description is based on PATRAN, a commercial CAD software package, which describes the target surface through a set of bicubic patches.

FEMAS consists of eight software packages:
- PACT, a program to check the CAD description and translate the data format to the FACETS data format;
- GRANIES, nominates electromagnetic attributes to the CAD target geometry model;
- PRISM, automatic pre-processor for identifying multiple scattering surfaces;
- MESH, modifies the bicubic patches to flat faceted surfaces to user-specified wavelength criteria;
- PIES, produces complex engine models;
- GROUND, program to account for ground plane interactions;
- FACETS, the electromagnetic program containing all the scattering algorithm software;
- FCL, the command language for setting up prediction runs.

A range of post-processing software provides a number of signature visualisation options and ISAR imaging capabilities. The software system can run on a wide range of computer architectures, both serial and parallel, and although originally written in FORTRAN it has now been restructured in C and C++.

The target surface is represented as a mesh of planar quadrilateral facets and this representation enables a closed-form evaluation of the physical optics integral to be calculated efficiently. This flat-faceted target representation is obtained from the bicubic surface patch description generated by the CAD model. A shadowing

algorithm is used to account for target self-shadowing where one part of the target obscures the surface at another part of the target. At shadow boundaries the physical optics surface currents can be modified to propagate energy into the shadow region of the target. If the surface is rough the effect of surface roughness on the scattered fields is also accounted for.

Multiple scattering on the target is modelled by a combination of geometrical and physical optics for surface to surface interactions and reflection to diffraction scattering incorporates the physical theory of diffraction. The surfaces of the target may have a number of different electromagnetic characteristics. For example, some surface patches may be perfectly conducting and others may be coated with radar absorbing material, RAM. Scattering from the RAM surface may be calculated through specification of the material parameters of the RAM material or by using a look-up table for the material coating.

Trailing and leading edge diffraction is modelled using the physical theory of diffraction. Diffraction scattering may be direct, indirect or from hidden edges lying within the shadow region of the target. Sharp or blunt edges can be calculated or obtained through a look-up table. Diffraction from slots or gaps can be obtained from a look-up table.

The code is capable of predicting scattered fields from cavities, such as engine ducts. This is achieved by using first order ray tracing, also known as the shooting and bouncing ray method, SBR. First order ray tracing accounts for ray beam divergence effects where the curvature of each ray bundle is modified by the curvature of the reflecting surfaces that intersect the energy flux of the ray. Physical optics is used at the exit aperture to calculate the cavity signature. Engine duct scattering involves modelling the engine detail and any other internal objects, such as vanes and splitter plates normally found in engine ducts. Ducts may be bifurcated and contain RAM surfaces. Both direct and indirect duct illumination are modelled.

FACETS also deals with the situation where the target signature is modified by the proximity of a ground-plane. The ground-plane gives rise to additional scattered fields and these fields are evaluated and added to the direct scattered fields from the target.

The wide range of scattering mechanisms available in the FACETS code provides a range of output scattering options. Monostatic or bistatic RCS can be selected; near-field or far-field scattering calculations are possible; full vector polarisation scattering matrix data are available; and a frequency sweep option allows the generation of RCS imagery through a two-dimensional Fourier transform giving cross-range and down-range scattering centres.

3. Target Radar Signature Representation

3.1 The target modelling problem

There are many RCS prediction codes in existence and some of these offer a significant and validated capability for determining radar signature characteristics. Initially, the challenge for the radar signature prediction modellers was to provide tools that were able to assist the electromagnetic design of military platforms and weapons systems. This challenge has been successfully completed and there are several prediction codes in existence that are used for the design of military vehicles. The new challenge, now that these codes exist, is the question of whether there are better ways to use the results generated by these codes so that radar engineers and system designers can develop enhanced products.

The radar cross-section of complex targets is a complicated function of target aspect, radar frequency and polarisation. There are large numbers of scattering centres on these targets, not all of which are independent from one another. Energy scattered in the direction of the radar receiver is a coherent summation of these scattering centres and for radar targets of any significant size the radar typically sees a strongly fluctuating signal. Consequently, the radar senses the target as a scintillating signal and we need to consider the best way to describe the target signature characteristics to the radar if we are to provide effective target modelling for the purpose of radar performance assessment. Although the prediction process is deterministic, the target aspect is not known precisely, target dynamics are not known, structural deformations are unknown and so on. So we conclude that a

statistical or fluctuating representation of the target signature is necessary for the evaluation of radar performance.

3.2 The standard fluctuating target model

The traditional method of specifying the fluctuations in target cross-section is the Marcum-Swerling model. This model permits a mathematical analysis of several important radar performance parameters and we can use predictive modelling techniques to determine the most appropriate fluctuation model for a given target.

We describe here a process of target representation by means of a measure of the average RCS together with a Swerling characteristic. We have assumed a simple airframe target representation and have used this to demonstrate our modelling process. RCS data are predicted and analysed at each elevation angle using a sliding azimuth window. Mean RCS as shown in figure 1 is clearly seen to be dependent on the window width and is distorted by peak values. The median RCS characteristic in figure 2 is clearly less sensitive to window size and we conclude that the median is a more appropriate representation of average RCS.

These RCS data were fitted to a gamma distribution so that we can determine the best Swerling model for the target.

$$p(\sigma) = \frac{v^v \sigma^{v-1} e^{-v\sigma/\mu}}{\mu^v \Gamma(v)} \qquad (1)$$

σ the RCS value
v the gamma order parameter
        (v=1 Swerling cases 1 and 2)
        (v=2 Swerling cases 3 and 4)
μ mean RCS

Analysing the data we found that the Swerling prescription is inappropriate when narrow RCS maxima are present. When the statistics are insensitive to window size the μ parameter is large and the mean RCS is close to the median. We conclude that, when the mean RCS is replaced by the median value, we must specify the Swerling 3 or 4 cases. For this simple test

target we found that an azimuth window of 10^0 was appropriate.

The standard model for describing glint statistics is a normal probability density function,

$$p(\sigma) = \frac{e^{-\frac{(\sigma-\mu)^2}{2s^2}}}{\sqrt{2\pi s}} \qquad (2)$$

μ mean glint
s standard deviation

Glint data were analysed for each elevation angle using a sliding azimuth window. Figure 3 shows an example of one azimuth cut of predicted glint data with mean and median curves for a sliding 5^0 window. The mean and median curves are always close and we found it necessary to use small windows to be sufficiently representative of the glint fluctuation. From the evaluation of this simple target we found that the glint data fits a normal probability density function and that mean and standard deviation values, obtained after smoothing the data with a 5^0 azimuth window, are sufficient to describe the glint characteristics.

3.3 A stochastic RCS target model

We now address the question, posed earlier, of whether there are better ways to use the results generated by our radar signature prediction codes to obtain an improved representation of a radar target signature. The method that we have developed applies to both RCS and glint characteristics. It is superior to the traditional Swerling model and requires more data storage than the single parameter description of the Swerling model. However, the data storage requirements are insignificant and make the model easy to implement.

The method makes no assumption about the statistical distribution of the RCS data. The simple target representation is used to illustrate the benefits of the target signature model. Data were generated by the FACETS code for full azimuth coverage over a range of elevation angles from -60^0 to $+60^0$. This data is sub-divided into a number of sectors and average RCS values determined for each sector. The glint characteristics of each sector are described

through mean and standard deviation values. The sector data are offset and scaled to give a pool of normalised data values and a subset of this data is chosen to represent the target signature parameters. On completion of this process we obtain a set of numbers, typically five hundred, which we use to reconstruct the target signature characteristics.

Figure 4 illustrates the result of applying this process to our simple target. The top graph shows the original predicted RCS data plotted as a function of azimuth and the lower graph shows the reconstructed RCS data. Clearly, the reconstruction process has been successful. The glint data have been reconstructed and are shown in figure 5. This process has been equally successful in providing a model of glint.

So this new stochastic approach is capable of reconstructing radar target signatures from a pool of data that has been reduced in size from a large number of predicted values to a relatively very small data pool.

5. Conclusions

The FACETS RCS prediction code has been described in this paper and we have taken this code and applied it to generating target RCS and glint data. We have argued that the capabilities of this code and other high quality signature prediction codes are such that they can provide detailed signature characteristics of radar targets. However, this is a deterministic approach and we described the nature of radar target signatures as seen by a radar system as fundamentally statistical.

Consequently, we have posed the question as to the best way to represent target signature information generated by sophisticated prediction software, such as FACETS. Backscattered electromagnetic fields from targets are sensed as fluctuating signals and it is inappropriate to select a single value for use in radar system analysis.

We have described two approaches to generating radar target signature models using RCS predictive modelling software. The first method uses the traditional Swerling model and we have shown that RCS signature characteristics can be obtained through software modelling processes.

We have also demonstrated that target glint information is readily obtained and modelled b prediction methods.

The second method of representing fluctuating radar target signature characteristics that we have developed is a new stochastic method. Unlike the Swerling model the method makes no assumption about the statistical distribution of RCS data. The method that we have developed applies to both RCS and glint characteristics and it is superior to the traditional Swerling model. It does require more data storage than the single parameter description of the Swerling model. However, the data storage requirements are insignificant and the model is easy to implement.
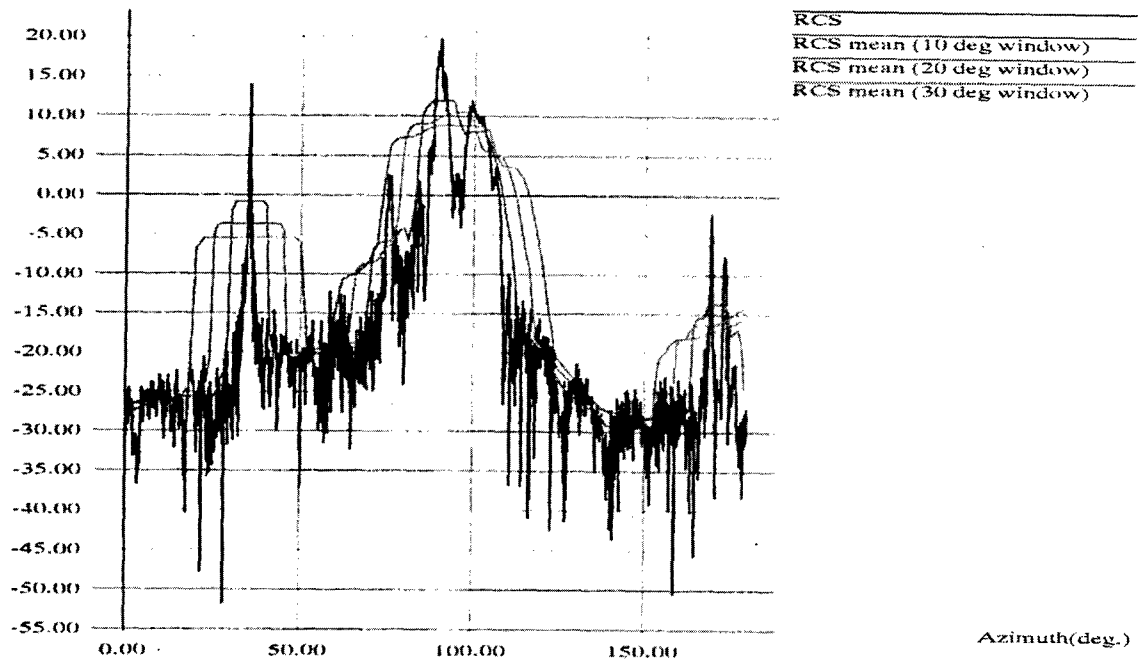
5. Acknowledgements
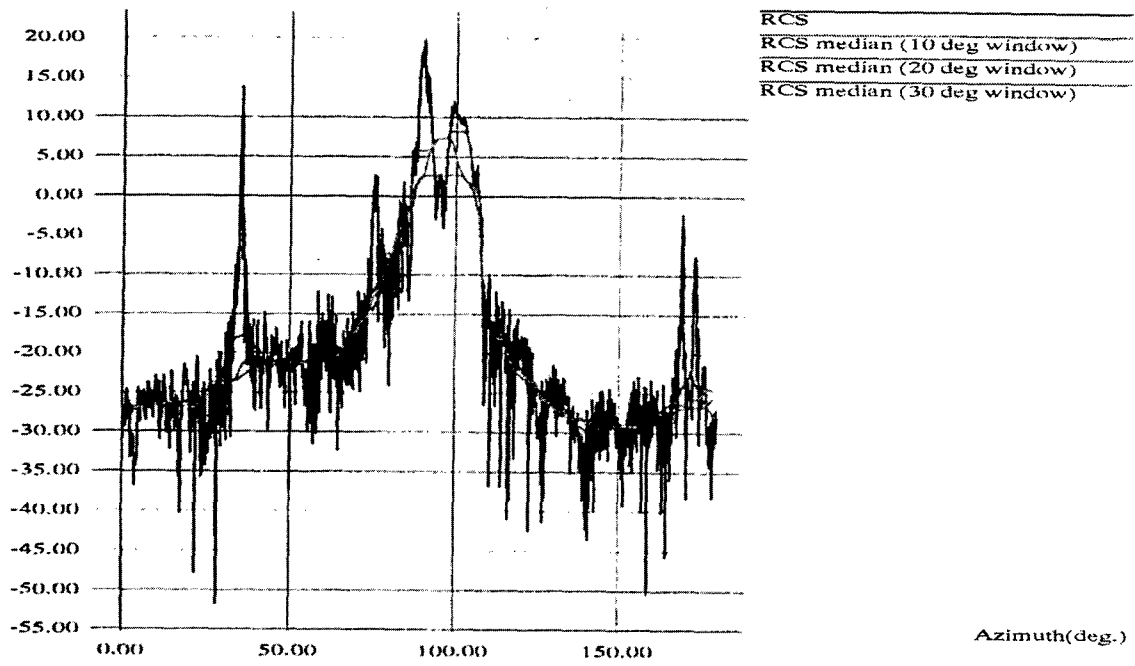
Figure 1. Mean smoothing window
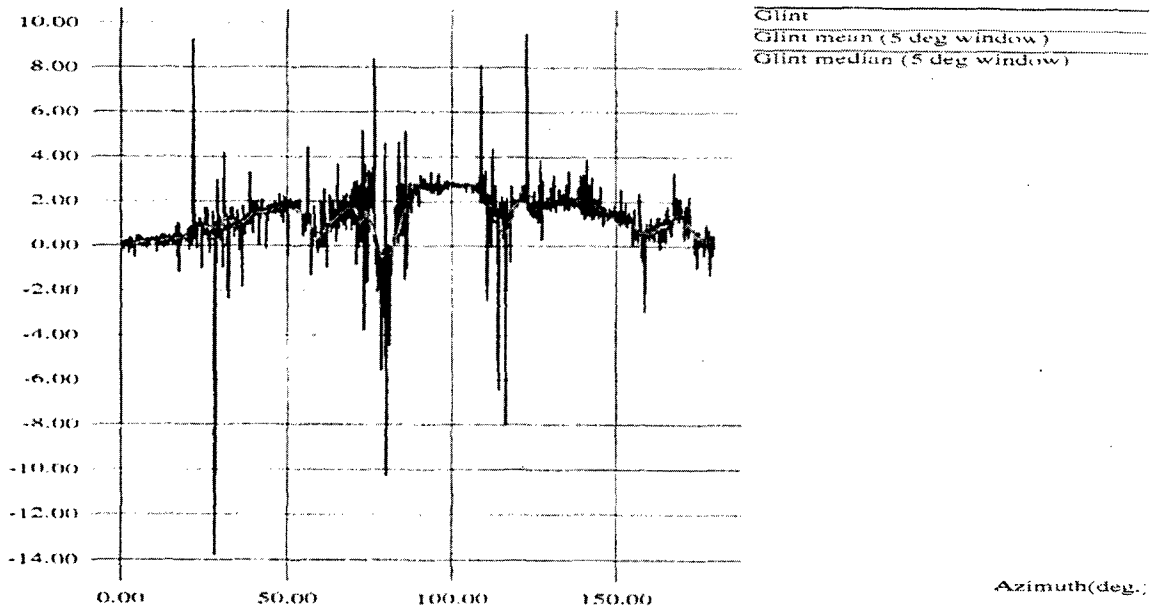

Figure 2. Median smoothing window

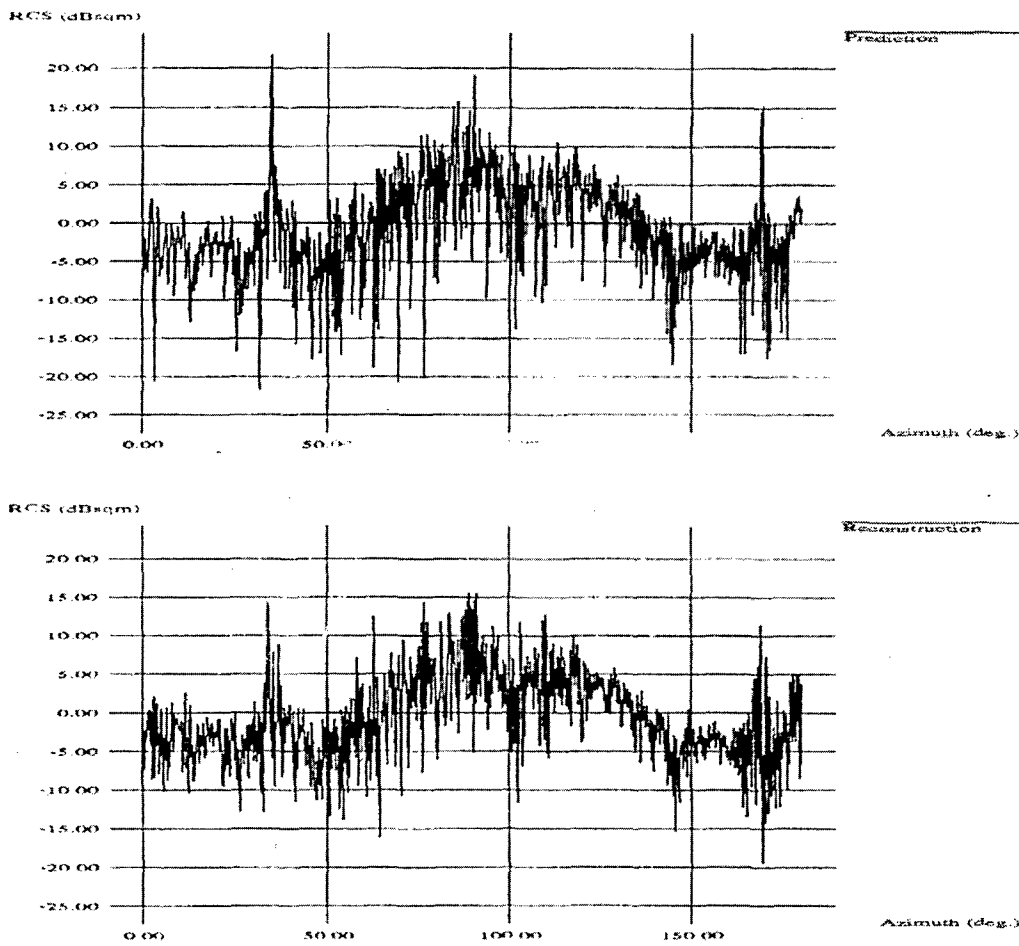Figure 3. Mean and median glint smoothing
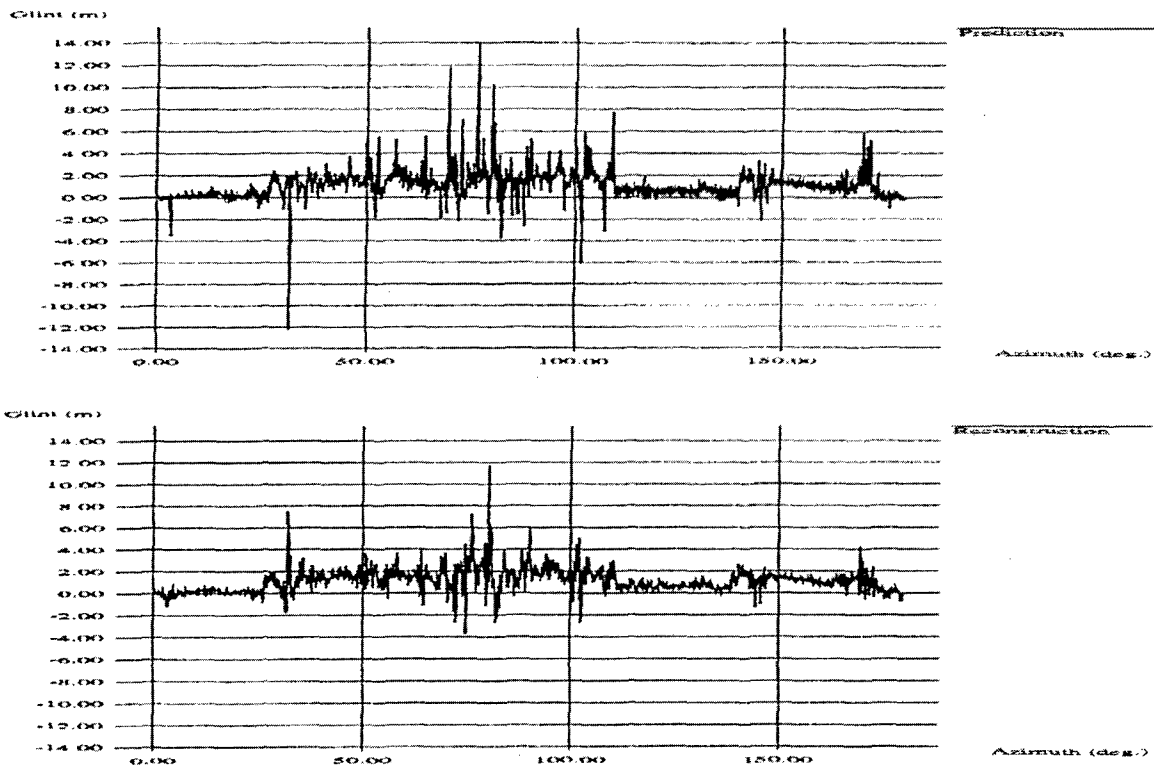

Figure 4. Stochastic model RCS reconstruction

Figure 5. Stochastic model glint reconstruction

Alenia Aerospazio Electromagnetic Tools to Evaluate Radar Signature of Complex Target

V. Volpi
Senior Engineer
Alenia Aeronautica
C.so Marche 41
10146 TORINO - ITALY
E-mail: Volpi@liat.alenia.polito.it

1. SUMMARY

The aim of the proposed paper consists in describing the main current capabilities in the electromagnetic scattering prediction techniques available at Alenia Aeronautica.

Two simulation codes have been developed devoted to the prediction of the radar cross section (R.C.S.): RADSAI (RADar Signature And Imaging) and STASME (STAtionary Solution of Maxwell Equation). RADSAI is based on Physical Optic (PO) and Incremental Length Diffraction Coefficient (ILDC) to evaluate the radar signature of a scatterer on high frequency problems (target much larger than one wavelength). STASME solves directly the Maxwell equations and is based on the Finite Difference Time Domain (FD-TD) method: it allows to calculate the radar signature particularly in the resonance region (target dimension comparable to few wavelengths). Both codes have a close link with a standard CAD system (CATIA) for the correct definition of the geometry of the considered target.

Dedicated Pre Processor and Post Processor tools had been developed to generate the suitable mesh of the object and for visualising the computed results. Typical available outputs consist not only in the estimated R.C.S., but also in parameters able to give electromagnetic information on the target certification such as the reflection coefficients, the currents distribution, the near field, amplitude, phase, etc.. STASME and RADSAI had been validated by the comparison with measurements and other analogous simulation codes referring to standard test cases.

Presently these tools are used in all the Alenia Aeronautica programs that require low observability analysis and detailed electromagnetic field evaluations reducing the costs of the alternative very expensive measurements.

2. LIST OF SYMBOLS

E^i	Incident electric field
E^t	Total electric field
E^s	Scattered electric field
H^i	Incident magnetic field
H^t	Total magnetic field
k	Wave number
λ	Wavelength
Ψ_0	Green potential in far field
Z_0	Vacuum impedance
$\bar{r}$	position vector of a generic point on the object surface
$\bar{n}$	normal versor to the surface
$\bar{s}$	versor in the reflected radiation direction
$\bar{i}$	versor in the incident radiation direction
$\hat{e}_r$	electric polarisation of the receiver
ε	electric permittivity
μ	magnetic permeability
$\bar{w}$	$\hat{i} - \hat{s}$
c_{max}	maximun wave velocity in the media

3. INTRODUCTION

During the past few decades, research in electromagnetic scattering by a variety of targets assumed more importance because of its direct relevance to all radar applications and, in particular, to radar used for military and space operation where the main objectives are to locate, identify and classify unknown targets. A typical radar accomplishes the objectives by processing the received signals, which generally consist of the radiation scattered by the target containing the information distinctive for its identification. The received scattered signal power is directly proportional to the R.C.S. of the target from which the importance of this parameter follows for its classification.

Aeronautical Division of Alenia Aerospazio has achieved the capability to evaluate the radar signature of complex targets, in particular of aircraft, by in house development of two electromagnetic scattering simulation tools.

For the users, the most important difference between two tools consists in the geometry modellisation and in the operative frequency range of the associated solvers (high frequency and resonance frequency range respect to the target main dimension). Globally the two solvers allow to analyse a wide range of scattering problems of aeronautical interest.

Each tool takes into account all phases needed for a complete EM analysis:

1. Pre Processing phase: including CAD modellisation of the target, its electromagnetic characterisation and mesh generation suitable for the chosen solver.

2. Computation phase: for the evaluation of the physical behaviour of the target subjected to an external EM field by a simulation solver.

3. Post Processing phase: associated to the visualization and manipulation of the computed data.

For some analysis it is possible to utilize the output obtained using a tool like input data for the other one.

In the following, each tool, named like the associated solver, will be described in more detail. In the last part of the paper an example of interaction between the tools will be illustrated.

4. STASME TOOL

4.1 Pre Processing

This phase foresees different steps that lead to:

- the definition of the CAD model of the considered target;
- the generation of a CAD output file suitable for grid generator;
- the mesh generation;
- the definition of the electromagnetic parameters necessary for the computation.

For all Alenia Aeronautica applications Dassault System CATIA is utilized as CAD system. For EM scattering analysis it is possible to hold of all the CATIA models of the aircraft developed inside the company. Figure 1 shows the CATIA model of a previous aircraft study.
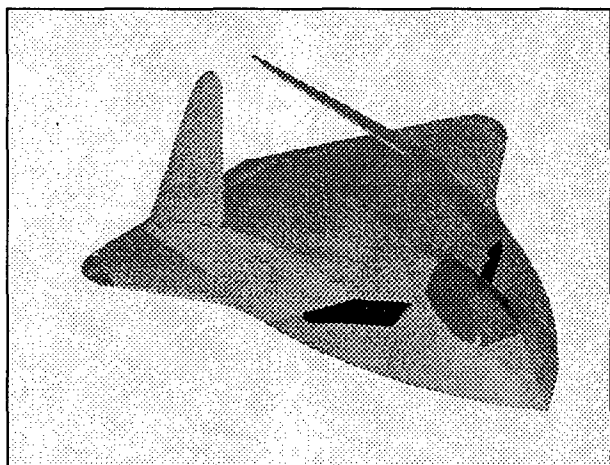

Figure 1: CATIA model

CATIA has a Geometry Interface package that allows to read the model and write it on a legible neutral file. In the CATIA system the model can be described by surfaces and curves; surfaces are composed by patches. Neutral file contains information on the surfaces that defines the CATIA model: for each surface the number of patches, the material index, the occupied volume and the coefficients that describe the single patch polynomial are given. In Table 1 an example of a neutral file is shown.

A suitable software had been developed to be able to read these information and generate the mesh for STASME solver. As it will be described in the following paragraph 4.2, the solver needs of a cartesian mesh of cubic cells to perform its analysis. Besides the neutral file by CATIA, the mesh generator needs like an input the number of grid points for each spatial direction, X,Y,Z, and the dimension of the cubic cell. The software developed to generate the orthogonal mesh is written using FORTRAN 77 language. It can run on all machines that support a FORTRAN compiler. Actually it works both on Silicon Graphic (SGI) workstations and on CRAY J90 4 cpus machine.

In Figure 2 the mesh obtained starting from the CATIA model of Figure 1 is shown: it includes 280x180x66=3326400 cubic cells of 5 cm length. For the considered example, mesh generator required 2371s on CRAY J90 to create the shown mesh.

```
NI NJ   9  1 *SUR42  1
VOL  8474.801 9125.199  749.800 1150.200   49.800  850.200
NTAB NU NV   29   4   2
NPU NPV   22  34
VOL  8474.900 9125.100 1008.059 1150.100  823.904  850.100
TAB XYZ .9125000000E+04 .1150000000E+04 .8500000000E+03
TAB XYZ -.1102307579E-08 .1450066865E+03 .6604034098E-01
TAB XYZ .5162291927E-08 .4769969014E-01 -2663076119E+02
TAB XYZ -.3648892744E-08 .3117961244E+01 .5687696871E+00
TAB XYZ -.6500000000E+03 .0000000000E+00 .1136868377E-12
TAB XYZ .4420144251E-09 .0000000000E+00 .0000000000E+00
TAB XYZ -.2024535206E-08 .0000000000E+00 .0000000000E+00
TAB XYZ .1480657374E-08 .0000000000E+00 .0000000000E+00
```

Table 1: neutral file example

Mesh generator is able to take into account of different materials (conductor, dielectric and dispersive materials) by the indexes that characterize the surfaces in the neutral file: media index is associated to the vertices of the cubic cell.

Two algorithms had been developed to visualize and modify the obtained geometry: the first shows the comprehensive studied volume using different colours to characterize the material (see Figure 2), and the second is able to visualize and modify single section of the created mesh. The last allows to do little modification of the starting model without generating a new CATIA model.
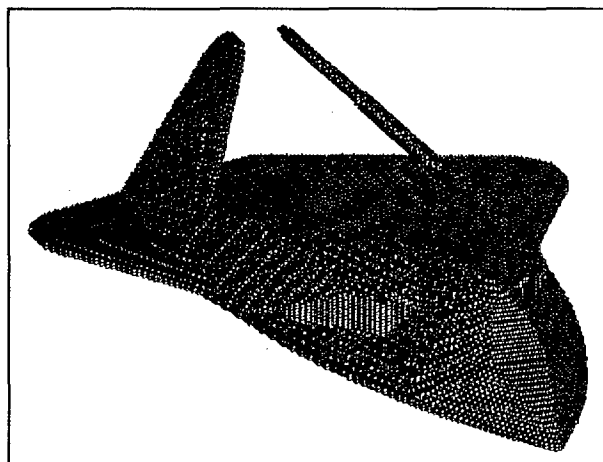

Figure 2: cartesian mesh

The visualization softwares had been written in FORTRAN 77 using graphical libraries of UNIRAS package available on the SGI workstations.

Before performing the computations it is necessary to define the electromagnetic parameter suitable for the analysis, such as:

- source: plane wave, pulse, etc.;
- azimuth and elevation of the incident wave;
- frequency;
- electromagnetic characterisation of media:
  for each index: $\varepsilon = \varepsilon' - i\varepsilon''$, $\mu = \mu' - i\mu''$
- chosen output: near fields, far fields, R.C.S., etc...

4.2 Solver Theoretical Background

The analysis of electromagnetic fields generated in the scattering of waves by complex objects presents many difficulties, especially if such scatterers include openings or parts having characteristic dimensions comparable to the incident radiation wavelength. In many cases the only alternative to experimental measurements is the direct solution of Maxwell's Equations by numerical analysis methods.

As a numerical modelling approach for these purposes the Finite Difference Time Domain solution of Maxwell's time dependent curl equations was chosen. The starting point are Maxwell's curl equation:

$$\frac{\mu \partial \vec{H}(\vec{r},t)}{\partial t} = -\vec{\nabla} \times \vec{E}(\vec{r},t) - \sigma_m \vec{H}(\vec{r},t)$$

$$\frac{\varepsilon \partial \vec{E}(\vec{r},t)}{\partial t} = \vec{\nabla} \times \vec{H}(\vec{r},t) - \sigma_e \vec{E}(\vec{r},t)$$

(1)

where $\vec{E}(\vec{r},t)$ and $\vec{H}(\vec{r},t)$ are the electric and the magnetic field, ε the local electric permittivity, μ the magnetic permeability, σ_e the electric conductivity and σ_m the magnetic conductivity. The solution is uniquely determined by the initial conditions $\vec{E}(\vec{r},0)$ and $\vec{H}(\vec{r},0)$. If the considered domain is finite, using numerical techniques the initial conditions can be replaced by the simulation of all incoming waves [1],[2]. Let us suppose:

$$\vec{E}(\vec{r},t) = \vec{E}_w(\vec{r},t) \bullet e^{iwt}$$

$$\vec{H}(\vec{r},t) = \vec{H}_w(\vec{r},t) \bullet e^{iwt}$$

(2)

Substituting in the (1), we obtain:

$$\frac{\partial \mu \vec{H}_w(\vec{r},t)}{\partial t} = -\vec{\nabla} \times \vec{E}_w(\vec{r},t) - (iw\mu + \sigma_m)\vec{H}_w(\vec{r},t)$$

$$\frac{\partial \varepsilon \vec{E}_w(\vec{r},t)}{\partial t} = \vec{\nabla} \times \vec{H}_w(\vec{r},t) - (iw\varepsilon + \sigma_e)\vec{E}_w(\vec{r},t)$$

(3)

The time dependency of the terms $\vec{E}_w(\vec{r},t)$ and $\vec{H}_w(\vec{r},t)$ takes into account of transient variations.

Equations (3) represent the starting formulation for FD-TD.

It does not employ potentials, instead it applies second order accurate central difference approximations for time and space derivatives of the electric and magnetic fields directly to the differential operators of the curl equations: for an accurate description of the central

difference approximation see [3]. Electric and magnetic field components are interleaved in space to allow a natural satisfaction of tangential field continuity conditions at media interface. The study volume is represented by cubic cartesian lattice. Figure 3 illustrates the positions of the electric and magnetic field components inside a unit cell of the FD-TD lattice: each electric field component is surrounded by four circulating magnetic field components, and vice versa. Electromagnetic characteristic of the local media (ε, μ, and σ) are assigned at each of them.
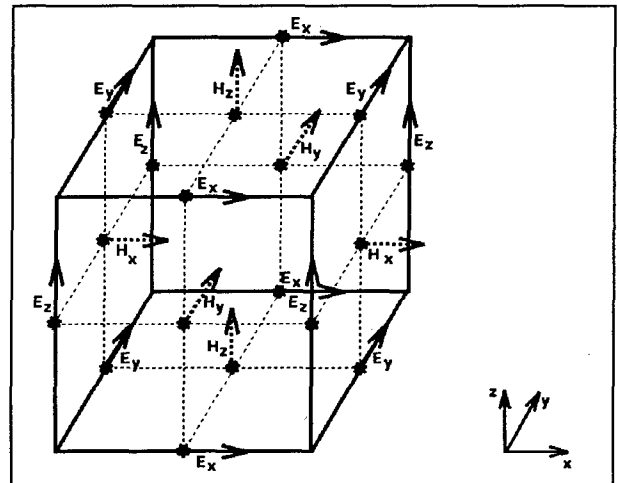

Figure 3 : lattice unit cell in cartesian coordinates

For a simulation, a region of space including the object is selected for field sampling in space and time. The method assumes that at the time t=0 an incident plane wave enters in the study volume where all fields are placed equal to zero. Propagation of the incident wave is simulated by the repeatedly implementation of the finite difference analog of the Maxwell's curl equations. This procedure, named time-stepping, continues until the desired late-time response or steady-state (for R.C.S. analysis) behaviour is achieved.

At each time step, the system of equations to update the field components is fully explicit, so that it is not necessary to solve a system of linear simultaneous equations: as a consequence the required computer storage and running time are proportional to N, where N is the number of the unknown electromagnetic fields in the modelled volume.

All outgoing scattered waves analogs ideally propagate through the lattice truncation planes with negligible reflection to exit the sampling region: for incident plane wave problem, a very efficient boundary method, that will be described in the following paragraph 4.2.1, was developed. For problem considering internal domain sources, a perfectly matched layer method [4] was adopted to solve boundary conditions.

Using FD-TD method to solve Maxwell's equations, phenomena such as induction of surface currents, scattering and multiple scattering, penetration through apertures, cavity excitation, creeping and travelling waves are modelled in an automatic way time step by time step. Self-consistency of the modellisation is assured if the spatial discretisation δ and the temporal variation Δt are well resolved by the space and time

sampling process. The values of δ and Δt are achieved by reasons of accuracy and stability of the algorithm. To assure the accuracy of the computed spatial derivative in (3), δ had to be small compared to the wavelength: δ should be small enough to allow resolution of the main surfaces or volumetric details of the model. Anyway to obtain an uncertainty of near field less than $\pm 2\%$ it needs $\delta \leq \lambda/20$. While to ensure the time-stepping algorithm stability, Δt has to satisfy:

$$\Delta t \leq \frac{\delta}{c_{max}\sqrt{3}} \qquad (4)$$

or, in other words, the temporal variation has to be at least less than the time necessary to go through the unit cell by the main diagonal to the maximum wave velocity c_{max} within the model.

For each iteration time fields components are updated and the near-fields values are available. Starting from near field values is possible to derive every parameters of electromagnetic interest.

For radar cross section computation, the near field values are transformed into the corresponding far field values by mean of free-space Green's function using [5] methodology. From far field values the RCS is so defined:

$$\sigma = \lim_{r \to \infty} 4\pi r^2 \left|\frac{E^s}{E^i}\right|^2 = \lim_{r \to \infty} 4\pi r^2 \left|\frac{H^s}{H^i}\right|^2 \qquad (5)$$

where r represents the distance between the scatterer and the observer. R.C.S. has the dimension of an area and is expressed in m^2, but generally it is possible to refer to R.C.S. as dBsm using the following expression:

$$\sigma_{(dBsm)} = 10\log_{10}\sigma_{(m^2)} \qquad (6)$$

4.2.1 Boundary Condition

The solver is based on Yee's algorithm that requires the knowledge of the fields a half-cell to each side of the point on which the difference approximations are applied. Hence central differences cannot be implemented on the outer boundary of the domain, the information a half-cell outside the boundary is missing. Many techniques had been employed in computing codes to absorb the outgoing waves and solve boundary conditions, such as the "radiating boundary", the "matched layer" and the "one-way approximation". None of these techniques is faultless and a small amount of numerical reflections occurs in practical computations. In this paragraph a simple procedure will be described, suitable to simulate electromagnetic scattering problem in stationary conditions using an incident plane wave.

It consists in placing the boundary to a quarter of wavelength from the scatterer and implementing the Yee algorithm in all the integration domain except on the outer border.

To analyse numerically the boundary condition by the proposed procedure, let us consider a bidimensional TE

case ($\vec{E} = E_x \vec{i} + E_y \vec{j}$; $\vec{H} = H_z \vec{k}$). Based on Yee's scheme, the location of H_z, E_x and E_y field components within the unit cell is shown in Figure 4, while Figure 5 illustrates fields components nodal location in correspondence of boundary layers.
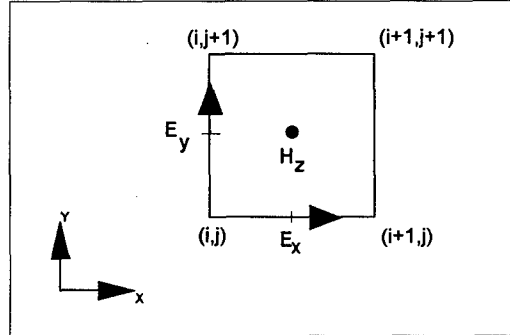

Figure 4: EM fields components location within unit cell

Referring to Figure 5 if we suppose to have to evaluate the E_y component related to the points along the boundary 2 (NI;J), we should know, for the central difference discretisation of the partial derivatives, the H_z values at (NI-1,J) and at (NI,J) grid points. As H_z(NI,J) values are not evaluated by FD-TD method, the following procedure has been developed:

- For each time iteration of the algorithm the scattered Ey component is evaluated for every points of the boundary:

$$E_y^s = E_y^t - E_y^i \qquad (7)$$

where E^t, E^s and E^i represent the total, the scattered and the incident field respectively.
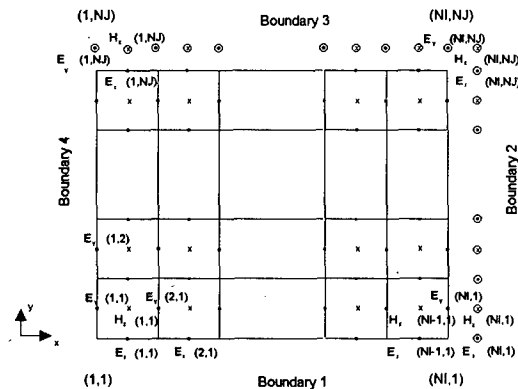

Figure 5: fields components nodal location in correspondence of a boundary layer

- Then the finite-difference approximation of Maxwell's equation is used for the scattered field:

$$\frac{\partial E_y}{\partial t} = \frac{1}{\varepsilon}(\frac{\partial H_z}{\partial t}) - iwE_y \qquad (8)$$

which, using FD-TD analog, becomes:

$$\frac{E_y^{n-1}(NI,J) - E_y^n(NI,J)}{\Delta t} \tag{9}$$

$$\frac{1}{\epsilon\delta}\left[H_z^{n-\frac{1}{2}}(NI-1,J) - H_z^{n-\frac{1}{2}}(NI,J)\right] - i\frac{\omega}{2}\left[E_y^{n+1}(NI,J) - E_y^n(NI,J)\right]$$

Because $H_z(NI,J)$ is unknown, instead of doing an central difference approximation of the spatial partial derivative $\partial H_z/\partial y$ as in (9), it is profitable to do a left approximation around the point (NI,J). In this way the second member of (9) becomes:

$$\frac{1}{\epsilon}\frac{\left[H_z^{n+\frac{1}{2}}(NI-1,J) - H_z^{n+\frac{1}{2}}(NI-\frac{1}{2},J)\right]}{\frac{\delta}{2}} - i\frac{\omega}{2}\left[E_y^{n+1}(NI,J) - E_y^n(NI,J)\right] \tag{10}$$

- Since we use an incident plane wave and we put the scatterer far from the boundary, we can suppose the scattered wave is nearly plane near the boundary. Based on this assumption, we can utilize the expression, proper in free space:

$$H = \pm\sqrt{\frac{\epsilon_0}{\mu_0}}E \tag{11}$$

Then (10) becomes:

$$\frac{2}{\epsilon\delta}\left[H_z^{n+\frac{1}{2}}(NI-1,J) - \sqrt{\frac{\epsilon_0}{\mu_0}}\frac{E_y^{n+1}(NI,J) + E_y^n(NI,J)}{2}\right] +$$

$$-i\frac{\omega}{2}\left[E_y^{n+1}(NI,J) - E_y^n(NI,J)\right] \tag{12}$$

that, utilized in (1), gives:

$$E_y^{n+1}(NI,J) = \frac{1 - i\frac{\omega\Delta t}{2} - \frac{c\Delta t}{\delta}}{1 + i\frac{\omega\Delta t}{2} + \frac{c\Delta t}{\delta}}E_y^n(NI,J) +$$

$$+\frac{2\frac{\Delta t}{\epsilon\delta}}{1 + i\frac{\omega\Delta t}{2} + \frac{c\Delta t}{\delta}}H_z^{n+\frac{1}{2}}(NI-1,J) \tag{13}$$

- When, added to the incident field E_y^i (NI,J), it represents the total field along the boundary 2.

An analog procedure is utilized along all the boundary layers in which it is not possible to evaluate the fields using central difference approximation. Apart from the other boundary conditions the procedure is simple to implement and gives good results. A literature test [6] has been executed to verify the occurring numerical reflection [7] and many testcases, solved using this technique, have been submitted to international workshops obtaining a validation. Also the Alenia solver, that is based on this methodology to solve boundary condition, has been validated [8] by the Electromagnetic Code Consortium benchmark [9].

4.3 Post Processing

The output values provided by the solver consist in the near field components of the electric and magnetic field in correspondence of each vertex of the considered mesh.

Post Processing algorithms are able to manipulate the near field data in a way to obtain the desired output such as: far field, radar cross section, antenna radiation diagram, current distributions, phase data, reflection coefficients and so on. Graphical programs allow to display the different computed values using the more suitable visualization. The programs created for visualization are written in FORTRAN 77 language using graphical library of UNIRAS package and run on SGI workstation.

Globally it is possible, for example, to display: polar or linear diagram for R.C.S. and antenna radiation diagram, shaded or contour map images for near field in correspondence of defined geometry sections, current distribution on geometry surface, etc.

Figures 6 shows a 2D section of the near field obtained for a two NACA profiles geometry (binaca) at steady state condition using a contour map visualization.
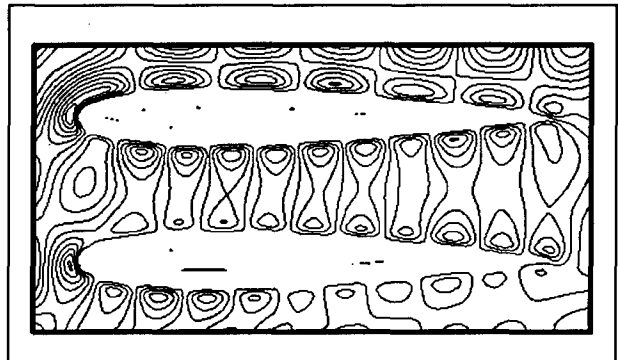

Figure 6: near fields contour map for a binaca geometry

Figure 7 displays the induced current distribution on an aircraft surface due to an external incident plane wave. Figure 8 illustrates the radiation pattern obtained for a $\lambda/4$ monopole antenna.
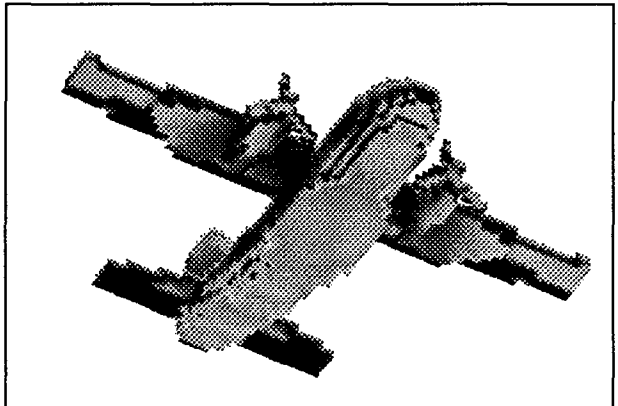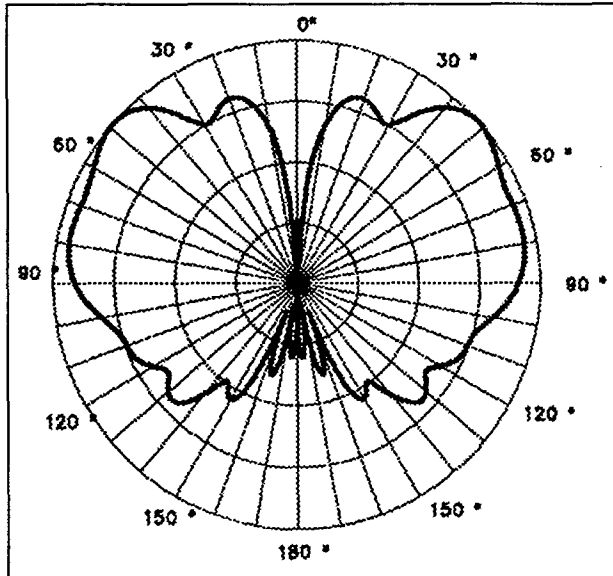

Figure 7: surface induced current distribution

Figure 8: radiation pattern of a λ/4 monopole antenna

5. RADSAI TOOL

5.1 Pre Processing

RADSAI tool needs the same steps as STASME to reach the desired solution.

Also in this case the used CAD models are generated by CATIA system. For RADSAI grid generator the suitable CATIA output has to include the curves that describe the object at fixed section (for examples sections to constant values of X for the fusolage, to constant values of Y for the wing and to constant values of Z for the vertical tail plane). Mesh generator uses these information to create a geometrical model made by oriented triangular plane panels. Figure 9 shows an example of RADSAI geometry. The side dimension of each panel needs to be greater than five times the considered wavelength to satisfy high frequency conditions. Electromagnetic characteristics (thickness, ε and μ) can be associated to each panel to include absorbing material: by default the panels represent conductive media. The grid generator had been developed in Alenia Aeronautica and it is a Fortran 77 code that utilizes graphical library (UNIRAS package) to create interactively the scatterer geometry. The code runs on a SGI workstation.

For each analysis it is necessary to define the characteristics of the incident radiation, such as frequency, polarisation, direction of illumination, and output typology (monostatic R.C.S. or bistatic R.C.S.).

Last step before the computation foresees the definition of the scattering elements, surface or wedges, visible respect to the direction of illumination : an hidden lines numerical techniques had been developed to perform this aim. Some elements can be oriented in the same direction of the incident radiation or can be placed in the shadow cone of other portions of the analysed object: for the computation only visible parts are considered.

5.2 RADSAI theoretical background

RADSAI solver is devoted to the computation of the radar cross section of an aircraft and to the definition of its main scattering centers.

The principal scattering phenomena that contribute to the radar cross section of an object are:

• surface reflection;
• vertices and wedges diffraction;
• multiple reflections;
• creeping and travelling waves.

RADSAI solver has been developed to consider only the first two phenomena in a way to obtain a robust and fast code for the preliminary design phase.
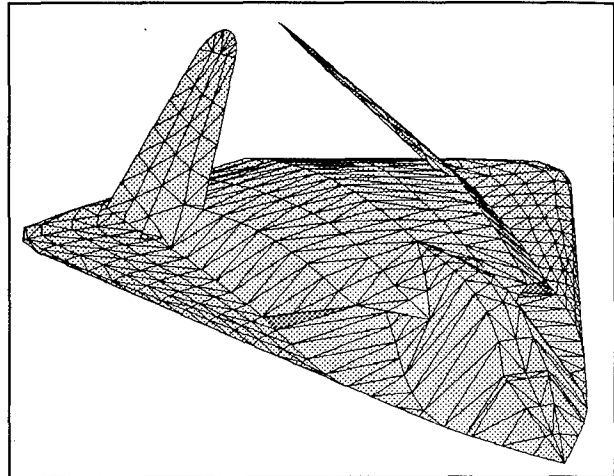
Figure 9: triangular plane panels geometry

Surface reflections represent the predominant contribution to the radar cross section from a quantitative point of view. Its theoretical prediction had been based on Physical Optic (PO) method. This method allows to evaluate the scattered electromagnetic field by the approximate evaluation of the induced field on reflective surfaces. In far field condition the scattered electromagnetic fields due to PO can be expressed by [10]:

$$\vec{E}^s = ik\Psi_0 \int \hat{s} \times \left[\hat{n} \times \vec{E} - Z_0 \hat{s} \times \left(\hat{n} \times \vec{H} \right) \right] e^{ik\vec{r}\cdot(\hat{i}-\hat{s})} dS \qquad (14)$$

$$\vec{H}^s = ik\Psi_0 \int \hat{s} \times \left[\hat{n} \times \vec{H} + Z_0 \hat{s} \times \left(\hat{n} \times \vec{E} \right) \right] e^{ik\vec{r}\cdot(\hat{i}-\hat{s})} dS \qquad (15)$$

The surface electromagnetic field can be evaluated by the approximation of the tangent plane that is to consider each elementary surface as perfectly plane and smooth. For perfectly conductive surfaces it is possible to consider:

$$\hat{n} \times \vec{E} = 0 \quad ; \quad \hat{n} \times \vec{H} = 2\hat{n} \times \vec{H}^i \qquad (16)$$

that, substituted in (14), gives:

$$\vec{E}^s = -2ikZ_0 H^i \Psi_0 \int_S \hat{s} \times \left[\hat{s} \times \left(\hat{n} \times \hat{H}^i \right) \right] e^{ik\vec{r}\cdot(\hat{i}-\hat{s})} dS \qquad (17)$$

This expression is implemented in RADSAI solver to evaluate the R.C.S. of the target computing the integral

only for the illuminated surfaces. Substituting (17) in (5), it is possible to obtain the R.C.S. square root like:

$$\sqrt{\sigma} = -i\frac{k}{\sqrt{\pi}}\int_S \left(\hat{n} \cdot \hat{e}_r \times \hat{H}_i\right) e^{ik\bar{r} \cdot (\hat{i}-\hat{s})} dS \qquad (18)$$

Generally the surface integral in (18) can be solved analytically only for simple geometry. Gordon analysis [11] allows to simplify the computation by transforming the surface integral in (18) into a linear integral on the outline of each surface element. For conductive material and normal incident plane wave on a plane panel, the (18) reduces to simple wellknown expression:

$$\sigma = \frac{4\pi A^2}{\lambda^2} \qquad (19)$$

where A represents the plane panel area.

The solver is also able to consider the contribution to the reflection due to dielectric material by an extension of classical PO method due to an Alenia Aeronautica development in collaboration with the Electronic Engineering Department of Genova University [12].

The diffraction contribution by vertices and wedges is computed by the implementation of the ILDC method in the solver. It was proposed by Mitzner [13] in 1974 and it allows to widen the achievable Physical Theory of Diffraction (PDT) solution to the diffraction directions outside the Keller cone [14]. A more detailed description of the implemented method is available in[15].

Globally the R.C.S. computation is obtained by the application of the suitable technique to the different scattering elements that characterized the object. For each visible element respect to the illumination direction and obtained by hidden lines procedure, the contribution to the comprehensive R.C.S. is evaluated as follows:

$$\sqrt{\sigma} = \sqrt{\sigma_{rifl}} + \sqrt{\sigma_{diff}} = \left|\sqrt{\sigma}\right| \cdot e^{i\varphi} \qquad (20)$$

where φ represents the phase difference between the terms. Then the comprehensive R.C.S. of the target is the sum of the different N contributions:

$$\sigma = \left|\sum_{n=1}^{N} \sqrt{\sigma_n} \cdot e^{i\varphi_n}\right|^2 \qquad (21)$$

RADSAI solver had been validated by the comparison of computed results with experimental data: the validation had demonstrated a good agreement in the frequency range for which the adopted numerical techniques are devoted. The solver is written in Fortran 77 language and uses double precision variables on 32 bit computer. It can run on SGI workstation or on CRAY J90 machine. The solver is very profitable by the time consuming point of view: for example to obtain the global R.C.S. map (-180°≤azimuth≤180°,-90°≤elevation≤90°, 0.2° step) of a transport aircraft for

10 different frequency it needs about 2 cpu hours on CRAY J90.

The main limits of the code are due to the neglected scattering phenomena, such as travelling and creeping waves, that does not allow to consider the effects produced by discontinuities, apertures, cavities and etc.. In presence of cavities and apertures in the considered geometry, they are generally closed by panels for the computation.

Anyway the simulated physical phenomena, surface reflection and wedge diffraction, permit to evaluate with good approximation the R.C.S. of a given configuration requiring limited computation time and memory storage.

5.3 Post Processing

RADSAI is able to give different output results: comprehensive monostatic or bistatic R.C.S. of the target, complex R.C.S. values associated to each geometry elements. The outputs can be graphically visualized in such a way to choose among linear or polar visualization of the R.C.S.: see Figg. 10 and 11.
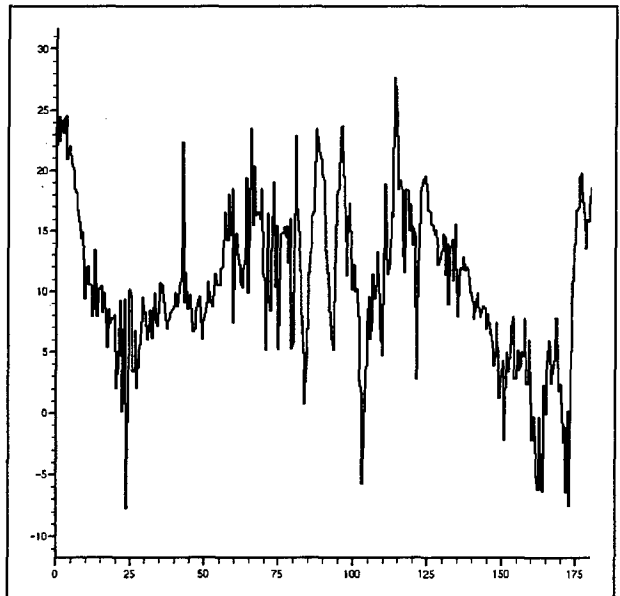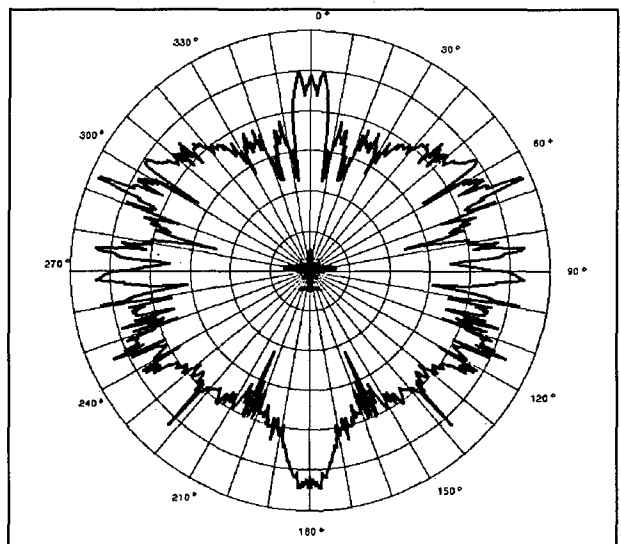

Figure 10: R.C.S. linear plot (a.u.)

Figure 11: R.C.S polar plot (a.u.)

It is also possible to obtain a shaded image of the signature related to each panels as shown in Figure 12.
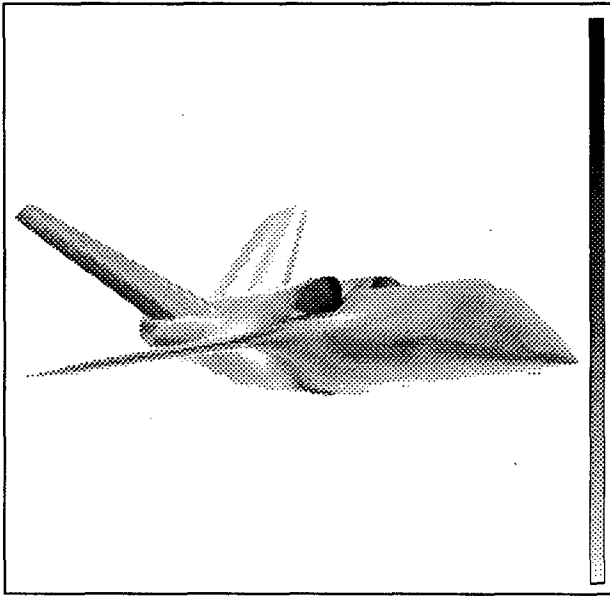

Figure 12: shaded image of single panel R.C.S.

Starting from the complex R.C.S. values associated to each visible element of the geometry it is possible to derive an indication of the scattering centers, 'hot spots', of the considered configuration by a tridimensional exploitation of the signature in function of Range and Cross Range parameters. Range represents geometrical coordinates related to the geometry evaluated along the incident direction, while Cross Range is associated to coordinates in the normal direction respect to the incident radiation.
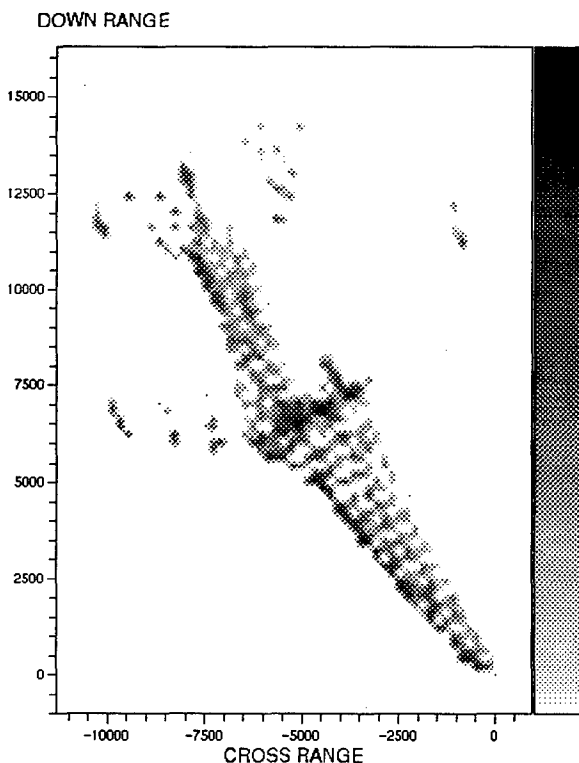

Figure 13: scattering centers representation

This output elaboration allows to individuate, in the preliminary design phase, the main scattering sources for the incident directions considered critical. In Figure 13 an example is shown for an incident wave to -20° in azimuth and 0° in elevation.

All post-processing programs are written in Fortran 77 language using graphical library included in a UNIRAS package available on SGI workstation.

6. APPLICATION

As we declared in the previous paragraphs, RADSAI tool is not able to consider cavities, ducts and apertures, that are indeed very important in an aircraft radar cross section definition. To overcome this limit and to enhance the tools application field, STASME and RADSAI capabilities are integrated by a closed link procedure.

Let us consider the case of an intake duct. The adopted procedure foresees to close the aperture using panels with electromagnetic characteristics equivalent to the media that generates the same reflected power observed to the cavity aperture. STASME tool allows to execute a detailed analysis of the electromagnetic behaviour of the duct when subjected to an external electromagnetic field for different incident angles. STASME is able to evalute the E and H fields in correspondence of the aperture and to derive the equivalent ε and μ. If we suppose $\varepsilon = \varepsilon' \varepsilon_0$ and $\mu = \mu_0$ and:

$$Z = \frac{E}{H} = \sqrt{\frac{\mu}{\varepsilon}} = \sqrt{\frac{\mu_0(\mu' - i\mu'')}{\varepsilon_0(\varepsilon' - i\varepsilon'')}} = \sqrt{\frac{\mu_0}{\varepsilon_0 \varepsilon'}} = \frac{\eta_0}{\sqrt{\varepsilon'}} \qquad (20)$$

it follows:

$$\varepsilon' = \left(\frac{\eta_0}{Z}\right)^2 \qquad (21)$$

By STASME analysis a matrix containing the equivalent ε and μ at each incidence angle is derived for the desired frequencies. Using these ε and μ values in RADSAI, it is possible to include apertures in the R.C.S. computation to high frequency range. STASME capabilities to evaluated correct values of the equivalent electromagnetic characteristics had been tested by considering measured data.

A schematisation of the illustrated procedure is shown in Figure 14.

CONCLUSION

In this paper an overview of Alenia Aeronautica capabilities in electromagnetic scattering simulation has been proposed.

Particularly two simulation codes, devoted to the prediction of the radar cross section, have been described: RADSAI, for high frequency problems, and STASME, for resonance problems. Solver dedicated Pre Processor and Post Processor tools had been

developed to generate the suitable mesh of the object and for visualising the results. In the paper they have been illustrated and some examples have been shown.
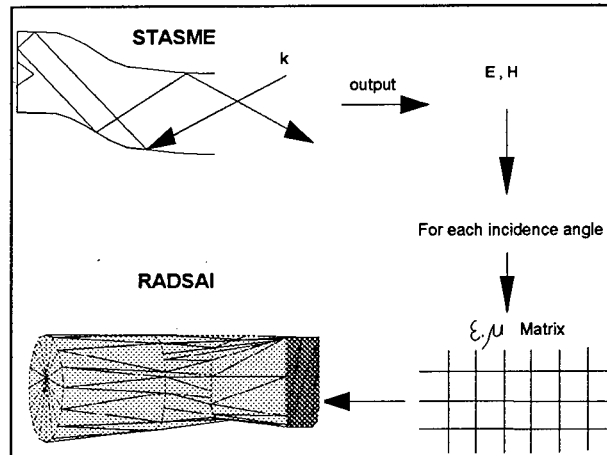

Figure 14: procedure schematisation

The typical available outputs consist not only in the estimated R.C.S., but also in parameters able to give electromagnetic information on the target characterisation such as the reflection coefficients, the current distributions, the near field, amplitude, phase, etc...

Presently these tools are used in all the Alenia Aeronautica programs that require low observability analysis and detailed electromagnetism evaluations reducing the costs of the alternative very expensive measurements.

Future objectives are related to the upgrade of the available tools in such a way to spread their applicability range and to improve computational performance.

REFERENCES

1 A.Taflove and K. Umashankar, 'A Novel Method to Analyse Electromagnetic Scattering of Complex Objects', IEEE Trans. Elect. Comp., EMC-24, pp. 397-405, 1982

2 A. Taflove and K. Umashankar, 'Review of FD-TD Numerical Modelling of Electromagnetic Wave Scattering and Radar Cross Section', Proc. IEEE, 77, pp. 682-699, 1989

3 K.S. Yee, 'Numerical Solution of Initial Boundary Value Problems Involving Maxwell's Equation in Isotropic Media' , IEEE Trans. Ant. Prop., AP-14, pp.302-307, May 1966

4 Berenger, 'A Perfectly Matched Layer for the Absorption Electromagnetic Waves', Journal of Comp. Physics, 114, pp.185-200, 1994

5 A. Taflove, K. Umashankar, 'Radar Cross Section of General Three-Dimensional Scatteres', IEEE Trans. Elect. Comp., EMC-24, n° 4, pp. 433-440, November 1983

6 K. Mei, J. Fang, "Superabsorption - a Method to Improve Absorbing Boundary Conditions", IEEE Trans. Ant. Prop., vol. 40, n 9, September 1992

7 V. Volpi, 'Simple Boundary Conditions for Plane Wave Scattering Problems Using FD-TD Method', ICEAA Conf., pp.321-324, 12-15 Sept. 1995

8 V. Volpi, "Benchmark di Validazione Codice STASME", Alenia technical report, 65/RT/T302d/94.036, April 1994

9 Woo, Wang, Schuh, Sander, "Benchmark Radar Target for the Validation of Computational Electromagnetic Program", IEEE Ant. Prop. Magazine, Vol. 35, n° 1, pp. 84-89, February 1993

10 E.F. Knott, J.F. Shaffer, M.T. Tuley, 'Radar Cross Section', The Artech House Radar Library, Ch. 5

11 W.B. Gordon, 'Far Field Approximation of the Kirchoff-Helmholtz Representation of Scattered Fields', IEEE Trans. Ant. Prop., Vol. AP-23, n° 1, pp. 864-876, July 1975

12 B. Bianco, 'Metodi di Calcolo di Diffusione e Riflessione di Onde Elettromagnetiche', Tech. Report, Dipartimento di Ingegneria Biofisica ed Elettronica, Università di Genova, March 1988

13 K.M. Mitzner, 'Incremental Length Diffraction Coefficients', Tech. Report N° AFAL-TR-73-296, Northrop Corporation, Aircraft Division, April 1974

14 P. Ufimtsev, 'Approximate Computation of the Diffraction of Plane Electromagnetic Wave at Certain Metal Bodies: Pt.1 Diffraction Patterns at a Wedge and a Ribbon', Zh. Tekhn. Fiz. (URSS), Vol . 27, n° 8, pp. 1708-1718, 1957

15 A. Nappi, 'Calcolo della RCS: Contributo della Diffrazione da Spigoli', Tech. Report 99/RT/T308/89.015, March 1989

Automatic Recognition of Air Targets for Future SHORAD Radars

Michel MORUZZIS, Nathalie COLIN
Thomson-CSF/ AIRSYS
7-9 rue des Mathurins, BP 10, Bagneux, France

ABSTRACT

For fulfilling the needs of future SHORAD (SHORt Range Air Defence), new radar concepts are being studied for both forces escort and area defence. NCTR (Non Cooperative Target Recognition) is required for these new systems especially for improving their performances in terms of situation assessment, ECCM (Electronic Counter-Counter Measures) optimisation and weapon assignment.

This paper gives an overview of the studies currently under progress for specifying the NCTR function.

The operational objectives and the full NCTR process design are presented in the first part of this paper. The following section is dedicated to radar waveforms and signal processing attributes.

Then one introduces the method used for target class estimation from measured attributes; this method being based on Fuzzy Logic and Theory of Possibility, one emphasises the main mechanisms of this method and one illustrates how reference data (membership function and density of possibility) are managed.

The last part of the paper highlights the simulation tools and models used for the evaluation of the function; performances are illustrated by typical results.

In conclusion, future works and perspectives are outlined and one shows how one can extrapolate the designed method to achieve a more precise target recognition level. In this last perspective, constraints and needs in terms of target modelling are discussed.

1. INTRODUCTION

Target Recognition is a function which is now required for future radars. As such, it must be considered in the early design phases because main radar characteristics such as coverage, waveforms and processing capabilities are driven by the NCTR objectives.

For future battlefield short range radars, several projects are being studied for forces escort and for area defence. All these projects take in account the NCTR needs at different levels; specific developments are undertaken for the detailed definition of their NCTR function and are related hereafter.

2. NCTR REQUIREMENTS

The term "NCTR" covers several aspects, all complementary to the detection and localisation of an unknown target. This function is aimed at giving some additional information regarding the nature of the target (number, identity, class, intention, nationality,..) and even its change in nature (patrol splitting, ordnance delivering, kill assessment,..). On a technical point of view, one often uses the following terms:

- *numbering*; which aims at giving the number of target within a given domain (in general the radar resolution cell),
- *classification*; which allows to give a coarse class label to the target (for instance, air targets main classes are: aircraft, helicopters, missiles, UAVs; sometimes one may refine some classes -for instance the "aircraft" class can be split into "jet aircraft" and "propeller aircraft"-),
- *recognition*; whose objective is to give the type of target within its class (for instance "F16" or "Grippen" within the "jet aircraft" class),
- *identification*, which is more an operational than a technical level in the sense that it gives the target intention (friend, foe, neutral,..); this last level is strongly dependant on the tactical environment and is in general evaluated at an upper operational level in the decision chain.

On a technical point of view only the three first levels are considered. They correspond to an increasing hierarchy in the requirements regarding both the necessary knowledge and the measurement techniques.

2.1 SHORAD operational needs

Regarding the air threat, the organisation of modern battlefield defence relies on two major components:
- *Air Defence*, whose main missions are Close Air Support, Tactical Air Intelligence, Interception and Suppression of Enemy Air Defence,
- *Anti-Aircraft Artillery*, which is mainly involved in Own Forces Escort and Area Defence.

The overall efficiency of this system relies on sensors which must detect the threat as soon as possible in order to:
- provide the concerned units a real time alert,
- trigger the counter-measures,
- neutralise the threat at a secure range.

2.1.1 Radar concepts

Previous studies showed that one must define two categories of radars adapted to two different operational missions (Own-Force Escort and Area Defence).

The radar corresponding to the first mission must be compact enough to be integrated within a highly mobile weapon system. Its primary targets are hovering helicopters. The possible candidates are 2D or 3D radars.

The second mission (Area Defence) requires a smarter surveillance radar to be fit in a mobile shelter and providing detection at a longer range. Its primary targets are missiles and hovering helicopters. It is required that the radar has a 3D dual-band capability. Several antenna concepts are candidates including fixed antenna or rotating antenna with a possible staring mode. In all cases this radar has a multifunction capability for spatially managing several waveforms dedicated to search and target recognition.

2.1.2 NCTR Requirements

For Short Range Area Defence applications it is required that the NCTR function provides the following classification:
- Helicopter,
- Aircraft,
- Missile,
- UAVs.

Apart from the kinematics, the following radar features can be used for this level of classification:
- RCS (narrowband or wideband),
- Doppler Spectrum -DS-,
- High Resolution Down-Range Profiles -HRDR-,
- High Resolution Cross-Range Profiles -HRCR-,
- 2D imagery (DS+HRDR or DS+HRCR or HRDR+HRCR),
- Polarimetry.

A first selection of features was made according to a trade-off analysis in which one considered the following criteria:
- permanence (as much as possible the information must be obtained independently of the target behaviour -HRCR and imagery using HRCR is not a prime candidate according to this criterion because they need a variation of the target aspect angle-),
- potential (which covers both the a priori capacity of the feature to separate the classes and the capacity to supply more refined information for future improvements),
- feasibility (regarding the type of radars which will be used),
- maturity (which consists to prefer the features for which some experience was gained in an operational environment -according to this criterion, the polarimetry was downgraded in our analysis-).

This analysis resulted in the following list of features:
- RCS (narrowband and wideband),
- Doppler spectrum purity,
- Doppler spectrum width,
- Range profile length,

2.2 Design of NCTR function

The recognition of targets by radars is a specific task, far more complicated than other pattern recognition problems. It is mainly due to the following characteristics:
- the number of possible objects to analyse is very large,
- the available knowledge on their characteristics is rapidly limited (when one looks for detailed information) and often uncertain,
- the discriminating power of any measurement is highly variable with the target behaviour (for instance the EM signature, including the Doppler spectrum, is highly variable with the target aspect angle),
- some characteristics may be discriminant but fugitive (for instance a blade flash, a sudden acceleration,..),
- radar measurements are sometimes difficult to analyse (for instance because of spectral ambiguities, propagation,...)
- radar measurements are always contaminated by interferences (thermal noise, clutter, jamming, internal limitations such as stability,...),
- measurement errors may be highly variable.

The consequence is that in general there is no unique discriminant feature and that strong false alarm (false decision) may occur if one does not take care of the measurement errors.

This can be translated in terms of function architecture in which one finds several feature sources (coming from both signal and data processing), and a recognition processing able to:
- merge these different features together,
- time integrate,
- evaluate and provide the (current) target ID and its confidence level,
- decide of the best measurement (waveform) to make for the next step (burst, scan,...).

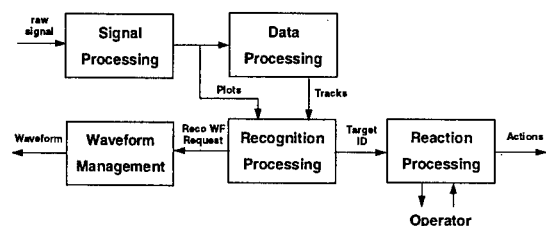A scheme for such an architecture is shown on Figure 1.

Figure 1

3. SYSTEM SPECIFICATIONS

In terms of system specifications the definition of features to be extracted from the signal processing are the most critical because it puts requirements on the radar design (waveforms) and cost (processing power). This chapter is dedicated to this analysis.

3.1 NCTR waveforms

NCTR waveforms can be split into two categories:
- standard waveforms, which are designed for search and track and which are used for the kinematics part of the NCTR function. In addition they can be used for giving an estimate of the target RCS (in general in narrowband) provided that the processing is able to estimate the parameters included in the radar range equation,
- specific waveforms, which are scheduled on request by the recognition processing.

For the purpose of our application, one defined two categories of specific waveforms (Doppler and High Range Resolution), whose duration vary from 2 ms to 250 ms depending on their objective and environment.

3.1.1 Doppler waveforms

For helicopters one can define two types of waveforms:
- long; dedicated to the measurement of blade flashes period, with a PRF compatible with the blade flash duration,
- short; dedicated to the analysis of the flash spectrum when it occurs, having the same PRF requirement.

For jet and propeller aircraft, one defined an intermediate waveform able to separate the spectral lines of propeller engines which is the most important constraints in terms of frequency resolution. In order to minimise the Doppler ambiguities (JEM Doppler line foldover), the PRF is the highest compatible with the constraints of radar energy (duty cycle) and detection performance (ground clutter in range ambiguity).

3.1.2 HRR waveforms

For this study we defined a Synthetic Bandwidth HRR using a burst to burst Stepped Frequency waveform. This kind of waveform is the less demanding in terms of hardware constraints (its uses a conventional narrowband mono channel transmit/ receive front end); its counterpart is that it needs a dwell time proportional to the desired bandwidth.

The total dwell time is given by the following relationship:
$$T = NB_{Pulse/Burst} * NB_{Burst} * T_R$$

The Doppler resolution is:
$$R_D = 1 / (N_{Pulse/Burst} * T_R)$$

The total bandwidth is:
$$B = N_{Burst} * \Delta F$$

The range ambiguity is:
$$R_R = C / (2. \Delta F)$$

The range resolution is:
$$R_R = C / (2.B)$$

When no Doppler processing is required (no clutter, no spectral component to filter out) and for a limited range resolution (for instance 1m), one can use a high PRF short waveform (for instance with a 2 ms duration).

For a cluttered environment requiring a Doppler processing and a better range resolution, that can lead to a total dwell time of about 250 ms.

One finds that the necessary dwell times for both Doppler and HRR waveforms are of the same order of magnitude and can both vary from 2 ms to 250 ms.

3.2 NCTR attributes at Signal Processing level

Each attribute already defined (see 2.1.2 above) is detailed hereafter:

3.2.1 Narrowband RCS

It is based on the radar range equation and a calibrated reference. It takes in account the following real time estimations:
- Propagation factor
- Losses (transmitter, receiver, propagation)
- Antenna beam losses,
- Processing gains and losses (pulse compression, Doppler filtering),

Among these, the most difficult estimation is the propagation factor which must make some assumption onto the environment conditions.

The RCS measurement accuracy is computed from the different elementary accuracies occurring in its estimation. It must be noted that it requires a specific (higher order) CFAR (Constant False Alarm Ratio) estimator.

3.2.2 Doppler spectrum purity

Performed after Doppler processing, it is based on an estimation of the contrast between the airframe Doppler line and the remaining of the target spectrum. It is aimed at detecting any spectral component revealing some rotating part on the target.
It uses an estimation of the clutter level based on a CFAR circuit and an estimation of the Doppler transfer functions.

Its accuracy is estimated by using the same inputs and by making some assumptions regarding the probability distributions of interference signal (thermal noise, clutter, stability).

3.2.3 Doppler spectrum width

Also performed after Doppler processing, it is based on a detection procedure and on an estimation of the extreme Doppler components. Basically it relies on the following relationship:

$$B = N . b$$

where N is the number of consecutive detected Doppler filters and b their elementary width. As for range CFAR it can be necessary to eliminate the Doppler filters in the vicinity of the airframe line to prevent errors due to the helicopter hub signature.

Its accuracy is based on both the Doppler transfer function and on the CFAR levels.

3.2.4 Wideband RCS

Performed after HRR processing it is based on the summation of every component included in the range profile.
Each component is processed in the same way as for the narrowband RCS estimation.

The accuracy is computed from the accuracy of each elementary component which is itself estimated in the same manner as for the narrowband RCS estimation.

3.2.5 Range profile length

It is basically the same process as for the Doppler width estimation, and uses the same kind of inputs for the estimation of its accuracy (transfer functions and CFAR levels)

4. EXTRACTION OF TARGET CLASS

Among the different techniques able to manage the specificities of radar target recognition (see 2.2 above), one chose the Fuzzy logic because it provides a smart way to handle the most important requirements:

- explicit and simple description of uncertainties on both knowledge and measurement errors,
- simple computations,
- easy multi-feature merging and time integration.

It is reminded here that the first point is mandatory for mastering the false alarm (taking in account the measurement errors in such a recognition procedure is a direct extension of the CFAR method for the detection purpose).

More details concerning the different techniques and their relative advantages can be found in [2], [3], [4], [5].

4.1 Fuzzy logic principles

They can be summarised by four main elements:

4.1.1 Representation of classes

For a given parameter X (for instance the RCS), each class C (for instance the "missile" class) is represented by a "Membership Function" $M_c(X)$ whose value (ranging in [0,1]) indicates the degree of membership to the class.
This function summarises the available knowledge about the class C for the parameter X. It does not take in account the measurement process.
This is simply an extension of the classical Boolean logic for which only 0 or 1 values or used.
It must be noted that any shape of the function may be used, including discrete ones.

Figure 2 gives 4 examples of Membership Functions.
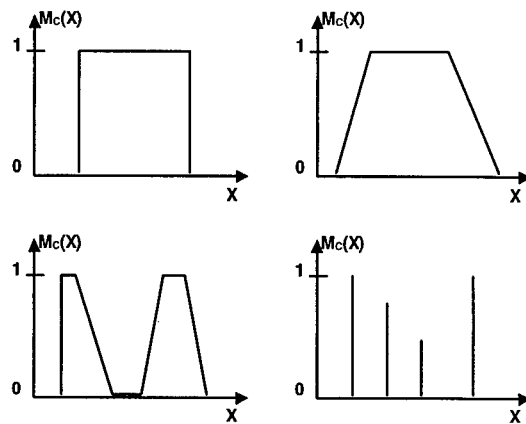
Figure 2

4.1.2 Representation of measurements

In order to represent the measurement process one uses another function called "Density of Possibility" D(X) which gives the degree of Possibility of the parameter X.
This function is highly dynamic because it is a representation of the measurement itself.

A simple example is given by a measurement corrupted by a Gaussian noise. Let X be the actual (unknown) value, x the measured value and σ the standard deviation of the measurement error.
Given an estimation σ' of σ, one can define D(X) in a simple way (see Figure 3) such as:

- $D(X) = 0$ if $|X-x| > k2.\sigma'$,
- $D(X) = 1$ if $|X-x| < k1.\sigma'$,
- linear interpolation otherwise.

Figure 3

It can be noted that this function does depend only on the radar and is independent of the classes. Furthermore it is well suited to the representation of fugitive behaviour because one can easily express the fact that some values of the parameter X are still possible (D(X)=1). This is the case for instance if X represents the Doppler contrast as long as, even if one measured a strong contrast, one can express that it may be small for another target aspect angle (but not conversely) -see Figure 4-.

Figure 4

4.1.3 Correspondence between classes and measurements
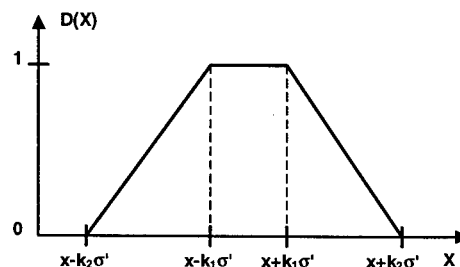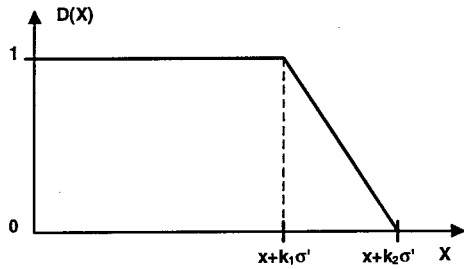
The degree of matching between a measurement (represented by a Density of Possibility D(X)) and a class (represented by a Membership Function $M_c(X)$) is represented by two values called "Possibility" P_{cx} and "Necessity" N_{cx}.

They are given by the following relationships (see Figure 5)

$$PC_x = Max_x \{ Min [M_c(X), D(X)] \}$$

$$NC_x = Min_x \{ Max [M_c(X), 1\text{-}D(X)] \}$$

The Possibility gives the degree of overlapping between the class and the measurement. It is null only if there is not any common parts between $M_c(X)$ and D(X).

If the Possibility is 0 then one can reject the assertion "according to X, the class is C".

The Necessity gives the degree of inclusion of D(X) into $M_c(X)$. It is equal to 1 only if D(X) is totally included into $M_c(X)$.

If the Necessity is 1 then one may accept the assertion "according to X, the class is C".
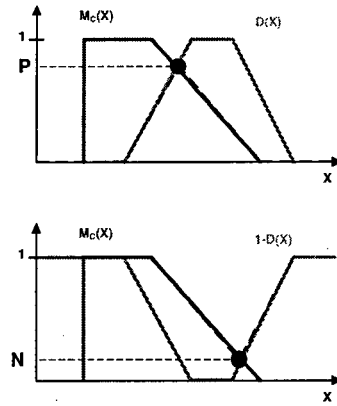
Figure 5

The complete process for a parameter X and a class C is illustrated on Figure 6.
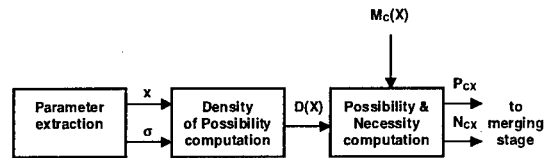
Figure 6

4.1.4 Merging

Several methods can be used for merging the results (P_{cx_i} and N_{cx_i}) coming from different parameters (Xi) for a given class (C).
The simplest ones come from the classical "and" and "or" operator and are easy to interpret in terms of target behaviour.

The basic relationships are as follows:

for a "and" merging:

$$P_c = Min_i \{ Max [1\text{-}Wi , P_{cx_i}] \}$$
$$N_c = Min_i \{ Max [1\text{-}Wi , N_{cx_i}] \}$$

for a "or" merging:

$$P_c = Max_i \{ Min [Wi , P_{cx_i}] \}$$
$$N_c = Max_i \{ Min [Wi , N_{cx_i}] \}$$

In the above equations Wi represents the weight attached to the parameter Xi. (Max (Wi) =1).

The above mechanism can be used for time integration. Furthermore, it may be implemented in a recursive way thus avoiding the drawback of memory size. Figure 7 illustrates a complete generic merging/ integration structure for a given class.
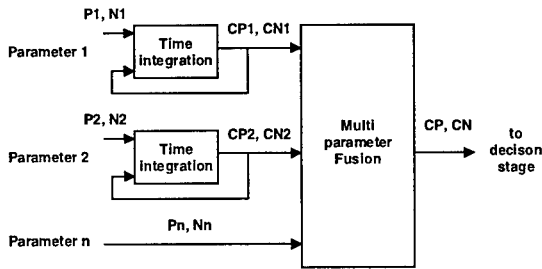
Figure 7

Figure 8

4.2 Illustration

For the SHORAD application one defined:

- the 20 (more) Membership functions corresponding to the four main classes (missiles, aircraft, helicopters and UAVs), and the five parameters (RCS narrowband, RCS wideband, Doppler spectrum purity, Doppler spectrum width, Range profile length), -in fact one defined more membership functions for some parameters such as the RCS which is a function of the target aspect angle-
- the 5 Densities of Possibility corresponding to the measurements performed on each parameter.

It is not intended here to give all these results but it was thought interesting to illustrate the reasoning for one example concerning the RCS of aircraft and missile in front view (0° aspect angle). The elaboration of these membership functions was based on the following:

- specialised literature (see [6], [7]) which gives some synthesis and models concerning the average RCS values for aircraft and missiles,
- application of existing models giving a coarse relationship between the target dimensions and its RCS; for these models we used a database containing a description of physical characteristics for almost all existing aircraft,
- these synthesis were completed by considering the RCS fluctuation (it is reminded that the measured RCS is an instantaneous value which may fluctuate according to the radar frequency and to the target aspect angle),
- furthermore the results were checked with existing measurements obtained during live trials (see [8], [9], [10]).

The resulting Membership functions are illustrated on Figure 8 (it is reminded that these functions are for C-Band, front view and covers all types of aircraft - including liners and small private aircraft- and all air to surface missiles.

On a practical point of view, small values of RCS which can be used for discriminating missiles are of limited interest because they often correspond to situations where the SNR is low then the accuracy is bad. The main interest of this parameter will then be for large RCS values thus allowing to discriminate aircraft.
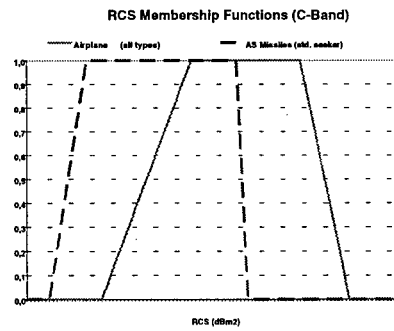
5. SIMULATION TOOLS AND MODELS

In order to evaluate the complete process one designed a simulation based on existing modules (target models, front end and processing simulations) on which one adapted the specific waveforms, signal processing, parameter extraction and classification.
At this stage, merging and time integration was not yet implemented; the results are thus given for each parameter before fusion.

5.1 Simulation framework

Figure 9 illustrates the complete simulation framework.
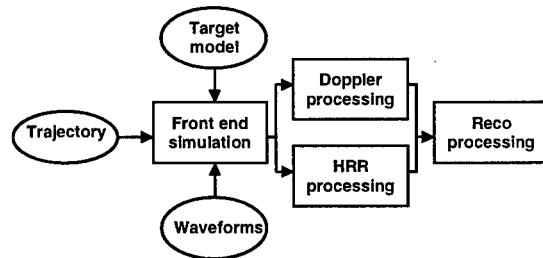
Figure 9

5.2 Target models

5.2.1 Principles

The main requirements regarding the target signature model was as follows:

- capability of generic modelling (aircraft, helicopter, missile, UAV, ...) with no CAD (Computer Aided Design) digital database
- capability to represent the signature as a function of:
  - aspect angle,
  - frequency,
  - time (rotating parts, random component)
- high frequency modelling (the application was in C-band for targets of several meters -up to several tens of meters-),
- computation time compatible with Monte-Carlo performance assessment.

One used a discrete scatterer model based on physical optic for determining the main characteristic (maximum RCS, directivity) of each contribution. The number, location and physical characteristics of each scatterer was defined from external characteristics of actual targets and the resulting signature was tuned with actual data.

Several types of generic scatterers are taken into account in this model:

- stationary, for representing the reflection of fixed element of the target (cockpit, fuselage, wing leading and trailing edges, fins,...); they are defined by their location, maximum RCS, backscatter direction and width,
- modulated, for representing the small rotating elements (such as jet engine rotors); they are defined as the stationary scatterers but in addition they have a modulation frequency and initial phase,
- mobile, for representing the large rotating elements (such as helicopter blades); they are defined by their centre and period of rotation, dimension and reflectivity. The RCS of such elements is computed as a function of aspect angle which is itself a function of time,
- random, to take in account high frequency components such as vibration or multiple reflections on small parts of the target.

5.2.2 Illustration

Figure 10 illustrates the RCS of a simulated helicopter as a function of aspect angle (azimuth from 90° -side view- to 100°) for a fixed frequency (6 GHz) and with no time contribution (blade or tail rotor). One can see the specular reflection occurring on the rear part of the fuselage (around 95°) and the fast RCS variations generated by the different amplitude/ phase combination of elementary contributors when the aspect angle changes.
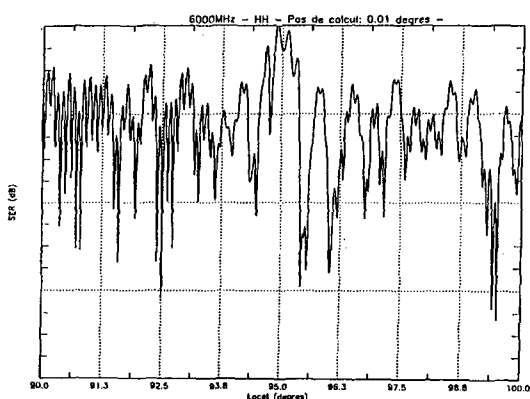
Figure 10

Figure 11 shows an example of a front view (0° aspect angle) Doppler spectrum corresponding to a (receding) blade return. One clearly sees the airframe line and the blade echo.
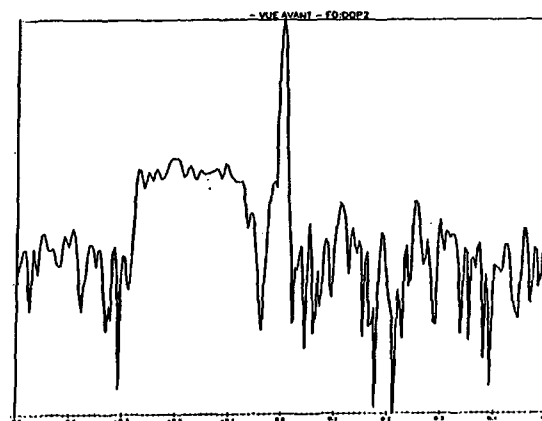
Figure 11

For comparison one shows on Figure 12 an actual measurement obtained during live trials on the same helicopter as the simulated one.
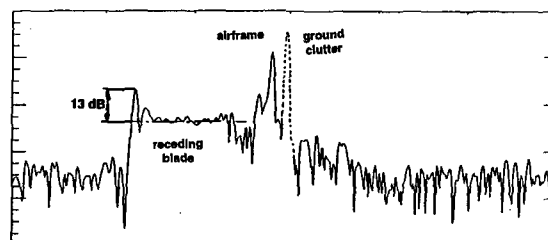
Figure 12

Figure 13 is an example of a front view (0° aspect angle) HRR profile. The different echoes correspond to the simulated scatterers having a contribution in the forward direction (cabin, engine air intake, engine compartment, hub, landing structure, rear stabiliser, random discontinuities).
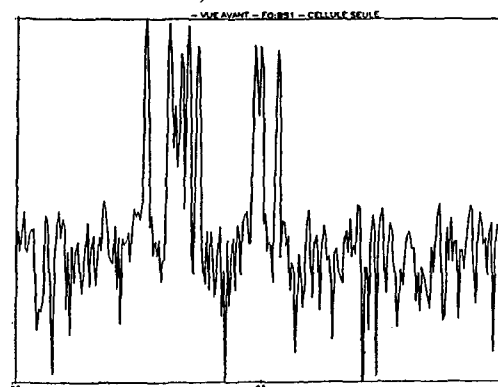
Figure 13

5.3 Scenarios for test

Several scenarios were defined for testing the method. Four targets were defined (helicopter, jet aircraft, missile and UAV) and located at a range where the average SNR is about 20 dB for the search mode. For each target one defined several aspect angles according to the following table:

	Front (0°)	Side (90°)	Rear (180°)
Helicopter	✓	✓	
Aircraft	✓	✓	
Missile	✓	✓	
UAV	✓	✓	✓

Table 1

5.3 Typical results and analysis

The UAV in front view is chosen to illustrate the different results. For each parameter one presents the Possibility and Necessity corresponding to each class. It is reminded that one can use these results as follows:

- when the Possibility is 0 one must reject the assertion "according to the parameter P the target class is C",
- when the Necessity is 1 then one may accept the assertion "according to the parameter P the target class is C".

5.3.1 Narrowband RCS

Figure 14 shows that possible classes could be either UAV or missile. However one may not reject the aircraft and helicopter classes because the measured RCS is in a region where all classes overlap. For this case the RCS is not a discriminant feature.
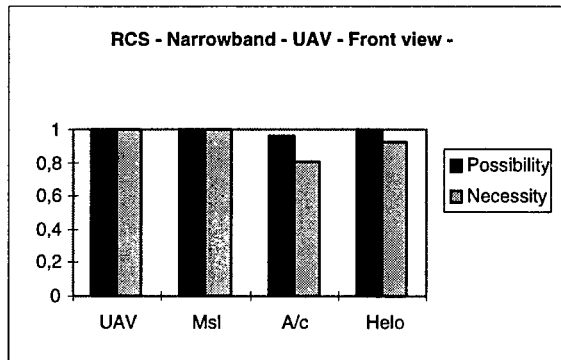
Figure 14

5.3.2 Doppler spectrum purity

This parameter was measured with a long Doppler waveform. Propeller modulation was detected. Figure 16 shows that, because the spectrum is not a single line one must reject the missile class (Possibility=0). All other classes (aircraft, helicopter and UAV) are possible (Necessity =1).
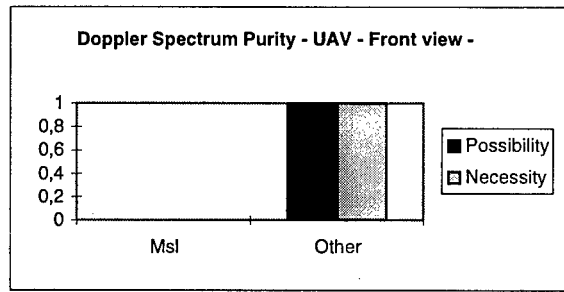
Figure 15

5.3.3 Doppler spectrum width

By using a shorter Doppler waveform (which could be the result of a sliding window applied onto the previous long Doppler waveform) one increases the SNR of a possible wide spectrum (representative of an helicopter blade return). On Figure 16 one sees that the measured width is not compatible with an helicopter; one must then reject the helicopter class (Possibility=0). All other classes (aircraft, missile and UAV) are possible (Necessity=1).
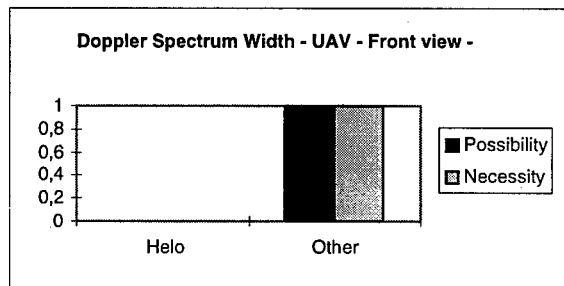
Figure 16

5.3.4 Wideband RCS

Although the measured value is slightly different from the Narrowband RCS, the same conclusion can be drawn -see Figure 17-.
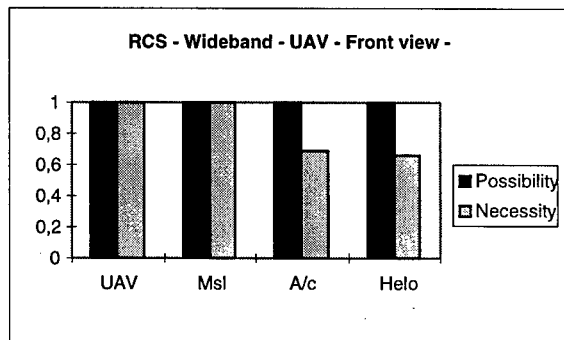
Figure 17

5.3.5 Range profile length

The estimated length is close to the simulated target one. The difference is due to the presence of propeller modulation residue which was not filtered out by a Doppler pre-processing. Figure 18 shows that the

aircraft and helicopter classes should be rejected by this parameter (Possibility=0). UAV and missile classes can be accepted (Necessity=1).

HRR Profile Length - UAV - Front view -
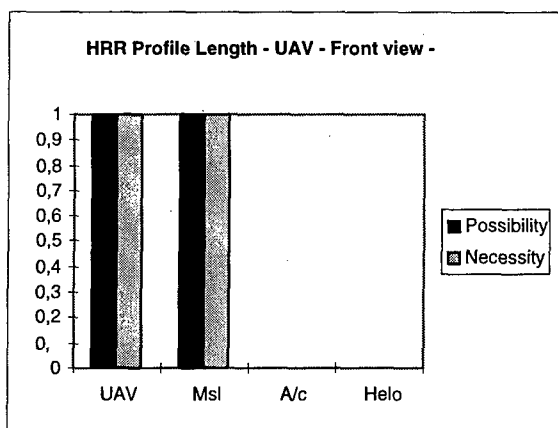
Figure 18

5.3.6 Synthesis

Table 2 summarises the conclusion which can be drawn from the different measurements. In this table one put:
- "Yes" if the Necessity is 1,
- "No" is the Possibility is 0,
- "?" otherwise.

We added a last line corresponding to the result of a "and" merging process. From this merging one would decide with no ambiguity that the target is a UAV.

However one must point out that this would be obtained thanks to:
- the spectrum purity which rejected the "missile" class,
- the spectrum width which rejected the "helicopter" class,
- the profile length which rejected the "aircraft" class.

It must also be mentioned that, for this case (but this must not be generalised), the RCS measurements are not discriminant.

	H	A	M	U
Narrowband RCS	?	?	Yes	Yes
Spectrum purity	Yes	Yes	No	Yes
Spectrum width	No	Yes	Yes	Yes
Wideband RCS	?	?	Yes	Yes
Profile length	No	No	Yes	Yes
"And"	**No**	**No**	**No**	**Yes**

Table 2

6. CONCLUSIONS

6.1 NCTR: a key function for future SHORAD

This paper which summarises some works undertaken for the definition of future SHORAD systems intends to show that:

- NCTR is one of the most important function of future radars,

- it is required to (at least) make the following discrimination: Helicopters, Aircraft, Missiles, UAVs,

- in order to achieve these objectives and according to a trade-off analysis the following parameters are recommended:
  - from conventional waveform: RCS (and kinematics -to be further analysed-),
  - from specific Doppler waveform: spectrum purity and width (at least)
  - from specific HRR waveform: RCS, profile length (at least).

- Fuzzy logic is a smart method for handling the whole recognition process:
  - knowledge description and uncertainty,
  - measurement accuracies,
  - simple computations with real time confidence assessment,
  - multi-parameter merging and time integration.

- according to preliminary tests already performed it appears that:
  - on-line estimation of parameters accuracies is mandatory for NCTR false alarm control,
  - attention is to be paid to interference (clutter) estimation for mastering robustness,
  - range profiles can be distorted by Doppler modulations such as JEM (Jet Engine Modulation) or HERM (HElicopter Rotor Modulation); a Doppler pre-processing is required to filter out these components,
  - not any proposed parameter can be removed at this stage of the developments.

6.2 Future works

These works will be carried on thanks to the MILORD project (see [1]). In particular it will allow the definition of kinematics and fusion procedures.

Furthermore MILORD will also give important conclusions regarding the possibilities of a more detailed NCTR analysis, at the "recognition" level. It will incorporate first results and recommendations regarding the methodology to be used for managing the necessary knowledge using models, anechoic chamber measurements and live trials data.

However additional activities will be required for specific applications such as SHORAD. In particular it is thought that performance assessment in cluttered environment would require complementary trials and that studies should be undertaken for defining real time waveform selection procedures.

Acknowledgements

Bibliography

[1] "MILORD: a Technical Demonstrator for Long Range Radar Identification"
C. DELHOTE, M. MORUZZIS
NATO RTO Symposium on "Non-Cooperative Air Target Identification using Radar"
Mannheim, April 1998

[2] "Probabilités et incertitude en fusion de données multisenseurs"
A. APPRIOU
Revue scientifique et technique de la Défense
1er trimestre 1991

[3] "Applications of Multisensor Data Fusion to Target Recognition"
M. MORUZZIS, N. COLIN, G. MILHEM
NATO AGARD MSP Panel 3rd Symposium on "Tactical Aerospace C3I in coming years"
Lisboa, October 1995

[4] "Radar Target Recognition by Fuzzy Logic"
N. COLIN, M. MORUZZIS
US National Radar Conference
Syracuse, May 1997

[5] "Fusion methods for multisensor classification of airborne targets"
A. BASTIERE
Aerospace Science and Technology
1997, n° 1, 83-94

[6] High Resolution Radar, Second Edition
D.R. WEHNER
Artech House 1995

[7] Radar Engineer's Sourcebook
W. MORCHIN
Artech House 1993

[8] Rapport final du groupe d'étude 12 pour la "Recherche sur l'identification radar des objectifs aériens non coopératifs"
AC/243 (Comission 10/ RSG. 12) D/7
Septembre 1987

[9] Rapport final sur les techniques de modulation des signaux radar
OTAN AC/243 (Comission 10) TR/5, RSG12
30 Mars 1992

[10] "Analysis of experimental data for NCTR target modelling"
M. MORUZZIS, J.C. GUILLEROT, C. LESTRADE
NATO AGARD SPP Symposium on "Radar Signature Analysis and Imaging of Military targets"
Ankara, October 1996

MICRODOPPLER CLASSIFICATION OF NON-COOPERATIVE TARGETS AND ITS APPLICATION TO FORWARD AREA AIR DEFENSE

J.A. Eck
J.F. Takacs
The Boeing Company
5301 Bolsa Ave.
Huntington Beach, CA 92647-2099
United States
H.L. Pratt
U.S. Army AMCOM
C. Shen
NAWC-AD
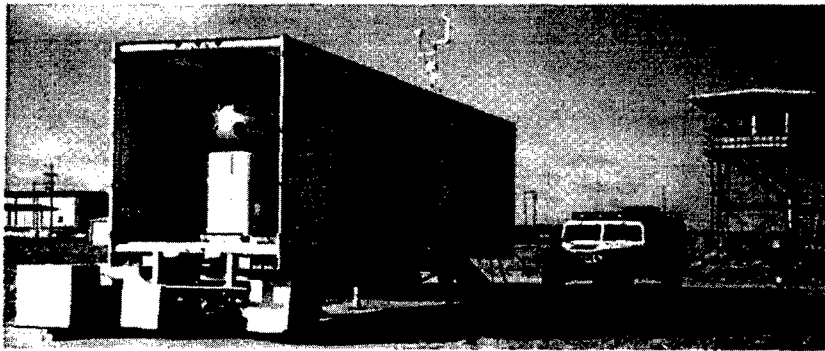
SUMMARY

This paper describes a Multi-Functional Optical System (MFOS) which contains passive imaging cameras and an active microDoppler Ladar. The imaging cameras cover visible, mid-wave infrared (MWIR), and long-wave infrared (LWIR) wavelength bands. The Ladar is a CO_2 based Ladar that is capable of measuring the macroDoppler (velocity) of a moving target and the microDoppler (vibration signature) of the target. Imaging cameras provide a capability for close-in classification/identification of targets by target size and/or shape at ranges where target images can be resolved. At longer ranges (>10 km), where target images cannot be resolved to provide clear classification, the Ladar provides a classification/identification capability using microDoppler (vibration) signatures. The Ladar's macroDoppler signal gives target velocity along the Ladar's line of sight. Its microDoppler gives a spectrum of vibrations present on the surface of the target. Target vibrations, whether structural resonance or direct engine vibrations are unique to the type of target. MicroDoppler signals can be exploited for non-cooperative classification/identification.

As part of an Advanced Concept & Technology II (ACT II) program, rotary-wing, fixed-wing jet, and fixed-wing propeller aircraft were flown against the MFOS in simulated Forward Area Air Defense (FAAD) scenarios. MFOS Ladar microDoppler results are presented for each of these aircraft.

A coherent detection Ladar, which was developed by Boeing North American (formerly Rockwell) for the Naval Air Warfare Center - Aircraft Division, Patuxent River, was integrated with a Multi-Functional Optical System testbed, which was developed, maintained, and operated by Boeing (formerly McDonnell Douglas). The combined system, referenced as MFOS in this paper, was provided to the Army by Boeing and the Naval Air Warfare Center (NAWC) in support of this ACT II program.

Field tests were conducted at the Ft Bliss Air Defense Battle Lab Support Element's (AD BLSE) Short Range Air Defense (SHORAD) range. Fixed-wing jet aircraft, fixed-wing propeller aircraft, and rotary wing aircraft were provided as airborne targets by the AD BLSE and engaged by the MFOS. The targets flew typical operational patterns for attack and surveillance missions. A portable search radar, provided by the Army, detected and tracked these targets. The angular bearings of all targets being tracked by the radar were sent over a digital radio network to selectively cue MFOS. After performing slew-to-cue, the MFOS acquired, tracked, and classified all of these targets at Beyond Visual Range (BVR).

The results of this test demonstrated how an integrated coherent detection Ladar on a stabilized gimbal can provide an adjunct to the FAAD SHORAD elements for BVR classification and identification.

INTRODUCTION

A continuing problem of the modern battlefield is that the range performance of existing weapons exceeds the range performance of existing sensors with identification capability. The inclination of defensive systems is to shoot first and then identify what has been shot. However, this leads to fratricide - the destruction of friendly resources. There is a strong need for a long range aircraft classification/identification capability so that friendly forces will not be engaged by fire units.

Current cooperative Identification Friend/Foe (IFF) systems provide positive identification of friendly targets that respond to interrogation signals. They do not positively identify hostile targets since no response is given to interrogations. There is a need for a non-cooperative classification/identification system. The microDoppler system discussed in this paper provides such a capability.

The Boeing Company recently demonstrated a CO_2 based microDoppler Ladar system during the Army's Live Experiment II (Live Ex II) field tests. The demonstration was funded as an Advanced Concept & Technology II (ACT II) program. This paper presents an overview of the ACT II program, the microDoppler system, the Live Ex II test results, and it gives a description of the applicability to non-cooperative target identification/classification.

BACKGROUND

The Army's ACT II program was established to encourage application of technologies that are mature or nearing maturity in the commercial sector to address Army concerns. The ACT II program provides funding to demonstrate the technical feasibility of such technologies that, if successful, can either become a part of the regular funded Army research and development program, be selected for entry into the Army Warfighting Rapid Acquisition Program, or transition directly to an end item.

The basic objective of this ACT II program was to demonstrate the capability of a coherent detection Ladar microDoppler system to perform Beyond Visual Range Identification (BVRID) against rotary wing, fixed wing, unmanned aerial vehicle (UAV), and cruise missile type targets.

Current Army air defense doctrine requires that FAAD SHORAD fire units have visual verification of threat targets to eliminate fratricide. This requirement limits the effective range of SHORAD fire units to distances shorter than the maximum range of their weapons. A long range identification capability such as microDoppler can increase the effective range of weapon systems by allowing early engagement of targets.

The Boeing Company, with the cooperation of the Army AD BLSE, demonstrated the utility of advanced passive and active Electro-Optic (EO) technology enhancements to the Army's FAAD. These EO enhancements, which are based on existing developments by industry, will provide a significant combat identification capability to FAAD and other situations where target classification/identification is needed. Boeing has developed a Multi-Functional Optical System testbed for long range target detection, track, and classification of low-observable cruise missiles, unmanned air vehicles, fixed wing aircraft, and rotary wing aircraft. The MFOS testbed, a derivative of Boeing's Army Mast Mounted Sight (MMS) product which is used on the OH-58D Kiowa Warrior, consists of advanced next-generation, passive infrared cameras and a state-of-the-art active, coherent detection Ladar. These sensors have been integrated onto the upgraded MMS gimbal in the MFOS testbed. The gimbal is a highly stabilized, two-axis compound gimbal system with improved payload size and weight capacity over the production MMS.

Objectives

The objective of this funded effort was to evaluate the existing MFOS testbed in the Army's FAAD engagement scenario and to demonstrate the capability of this technology to detect, track, and classify evolving threats to the close battle area.

A Multi-Functional Optical System testbed developed, maintained, and operated by Boeing, was provided as contractor furnished equipment. The coherent detection Ladar was provided as Government Furnished Equipment (GFE) by the Naval Air Warfare Center - Aircraft Division, Patuxent River for the Army's Live Experiment II field tests.

Approach

The approach that Boeing took to meet this objective was to use hardware and software from its existing Non-Cooperative Target Classification program. This equipment is jointly owned by Boeing and the U.S. Navy. This hardware was used to classify and/or identify airborne targets in a realistic Forward Area Air Defense scenario.

The goal was to demonstrate the long range Non-Cooperative Target Classification (NCTC) capability of a Multi-Functional Optical System and to develop cost-effective operational concepts for integrating this enhanced combat identification capability into Forward Area Air Defense . The incorporation of a NCTC capability will make it possible for FAAD rules of engagement to be changed , and it will permit Beyond Visual Range engagements allowing FAAD weapons to be used to their full potential.

MFOS uses optical cameras (visible and infrared) that can detect and track unresolved targets out to about three times BVR. MFOS then utilizes a coherent detection Ladar, which measures target vibration signatures, to classify targets within two seconds after detection allowing weapon commit well before the range of visual identification.

The imaging cameras are utilized to acquire and track unidentified air targets. Once a target is in passive IR track, the MFOS Ladar, which is boresighted with the cameras, illuminates the target for a few seconds and classifies the target using microDoppler signature returns. Target position and closing speed are also measured and displayed. Target classification and identification are accomplished through comparison of the microDoppler signature with known target signature characteristics stored in a computer database. Since these are audible signatures, they can be fed into headphones for operator-assisted identification much like Navy anti-submarine warfare systems.

A functional sketch of the system operating in conjunction with a search radar is shown in Figure 1. MFOS can be cued by radar for target detection, track, and classification or it can perform an independent sector search. In addition, using high resolution IR camera measurements, MFOS can detect low radar cross section air targets or threats that have sophisticated radar jamming equipment that elude radar. Since the search mode is passive, detection of MFOS's location is difficult.
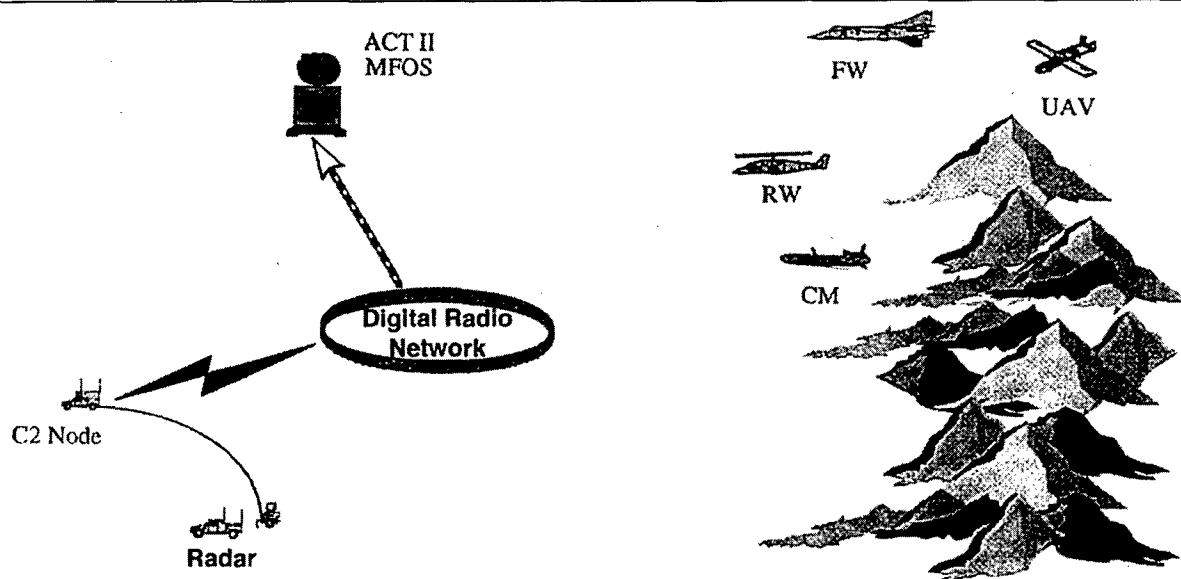
Figure 1. Search Radar Cues MFOS to Target Using Digital Data Link.

The existing MFOS testbed is shown in Figure 2. This testbed is currently configured for field operation and is the same testbed that has been successfully tested at low power at the Naval Command, Control, and Ocean Surveillance Center, Point Loma, CA, where it engaged surface and air targets out to 20 kilometers.

SYSTEM CONFIGURATION

The MFOS, as an integrated system, consists of: sensors, stabilized gimbal, Off-Gimbal Optical Transfer System (OGOTS), support electronics box, controls and display console. Each of these components is described in detail in the following paragraphs. Photographs of the major physical components are shown in Figure 3.

Sensors

The MFOS sensors, which are mounted on the gimbal and housed within shrouds, consist of passive cameras (visible, MWIR, and LWIR) and an active Ladar. The passive electro-optic cameras transform the optical scene into electrical signals for the tracker and display monitors. The Ladar provides target range, 2-dimensional (angle/angle/range) image data, and Doppler (i.e., velocity and vibration) measurements. Table 1 shows the specifications of the passive cameras and the Ladar.

Gimbal and Stabilization

A two-axis compound gimbal system controls the direction of the optical line of sight of the turret. Figure 2 shows the gimbal with MFOS sensors installed and shrouds removed. The coarse gimbals are driven by high efficiency, brushless, permanent magnet, gear motors. The fine gimbals are driven by Boeing's proprietary "paddle torquers." These torquers are

flat, open-frame, magnetic positioners, which have high bandwidth and two-axis motion. The gimbal system is capable of azimuth coverage of $\pm 190°$ and elevation coverage of $\pm 30°$. During Live Ex II tests, the gimbal was mounted within Boeing's 40 foot trailer. Azimuth coverage was limited by the trailer walls to $\pm 40°$. The slew and acceleration rates of the gimbals are 45°/sec and 45°/sec^2, respectively.
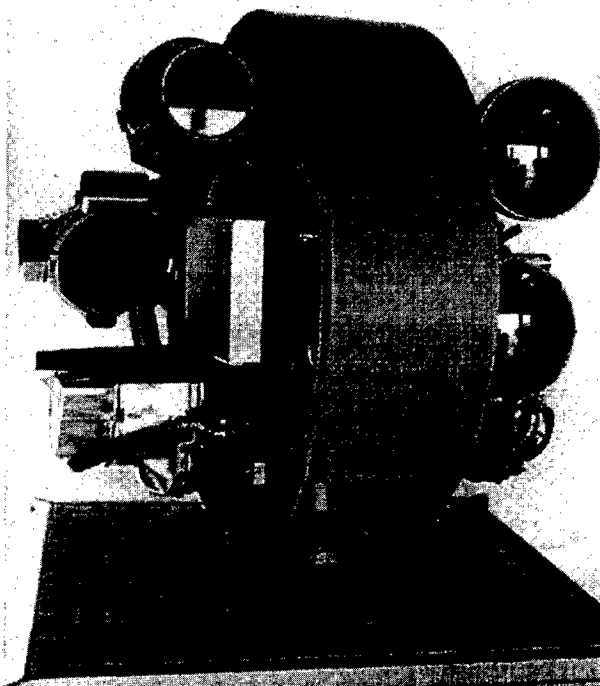
Figure 2. Two-Axis Gimbal Supports Multiple Sensors

L50549
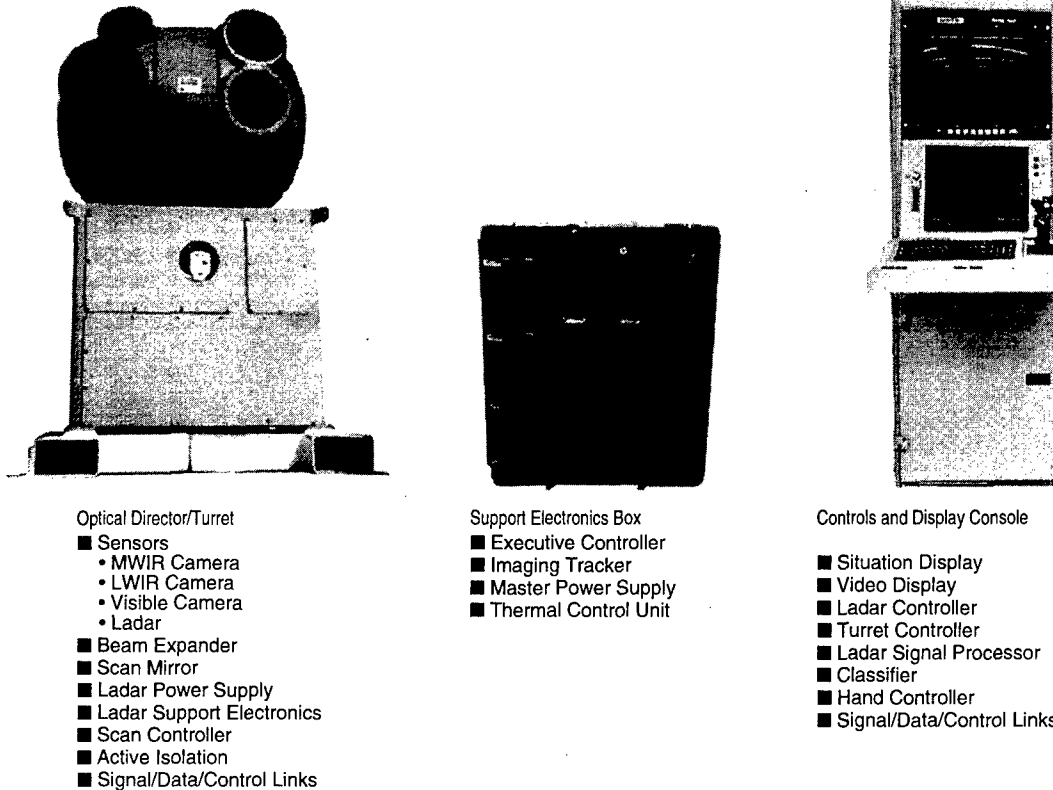
Optical Director/Turret
- ■ Sensors
  - • MWIR Camera
  - • LWIR Camera
  - • Visible Camera
  - • Ladar
- ■ Beam Expander
- ■ Scan Mirror
- ■ Ladar Power Supply
- ■ Ladar Support Electronics
- ■ Scan Controller
- ■ Active Isolation
- ■ Signal/Data/Control Links

Support Electronics Box
- ■ Executive Controller
- ■ Imaging Tracker
- ■ Master Power Supply
- ■ Thermal Control Unit

Controls and Display Console
- ■ Situation Display
- ■ Video Display
- ■ Ladar Controller
- ■ Turret Controller
- ■ Ladar Signal Processor
- ■ Classifier
- ■ Hand Controller
- ■ Signal/Data/Control Links

Figure 3. MFOS Equipment Forms a Self Contained MicroDoppler Test and Evaluation System.

The active stabilization system is the same gyro-stabilized system presently used on Boeing's MMS. This Boeing proprietary stabilization system controls the sensors' optical line of sight to better than 20 microradians, thus providing highly stabilized viewing and reliable tracker operation. Together, the gimbal and its mounting pedestal weigh 500 lbs and they are capable of supporting and additional 200 lbs of sensor payload weight on gimbal. Total size of the complete gimbal and pedestal is 57 inches x 30 inches x 30 inches.

The range coverage of the system is limited on the long end by the sensitivity of the Ladar (30 km) or earth curvature and on the short end by look angle to target and azimuth/elevation limitations.

Table 1. MFOS Sensor Specifications		
Sensor	Performance Area	Specification
Visible CCD Camera	FOV (narrow)	2°
	Resolution	50 microradians
	Aperture	4.0 inch diameter
	Illuminance Range	1 to 100 lm/m^2
MWIR Camera (320 x 240 HgCdTe array)	FOV (narrow)	2°
	Resolution	122 microradians
	Aperture	6 inch diameter
	NEI	1E-15 W/cm^2
LWIR Camera (Scanned 120 element linear array Common Module FLIR)	FOV (narrow)	2.22°
	Resolution	170 microradians
	Aperture	6.6 inch diameter
	NEI	1E-13 W/cm^2
Ladar	Aperture	6 inches
	Power	<20 Watts
	Weight	<100 lbs.
	Beam Control Accuracy	3 microradians
	Noise	<10 mm per second
	Range Resolution	1 foot

Off-Gimbal Optical Transfer System (OGOTS)

The OGOTS transfers laser energy from the laser source located in the base of the gimbal mounting pedestal to a beam expander and scan mirror located on the stabilized gimbal. The unique requirement is to transfer the laser beam in such a way that the beam is not misaligned or obstructed as the gimbal rotates to track a target.

The OGOTS satisfies this requirement by transferring the laser beam along the rotation axes of the gimbals. A CO_2 laser is mounted in the base below the gimbal. The laser beam enters the OGOTS vertically along the azimuth axis of the coarse gimbal. The beam continues upward, independent of a rotation in azimuth, to the axis of the fine elevation gimbal where another folding mirror reflects the beam along the elevation axis. The beam is then folded upward toward the secondary mirror of the beam expander telescope. From there, the beam expands downward to the 6-inch diameter primary mirror where it is recollimated before proceeding to the scan mirror. Since this is a monostatic transceiver, the reflected energy from the target follows the reverse path.

Support Electronics Box

The Support Electronics Box (SEB) is enclosed and located near the gimbal and sensors to minimize the length of critical signal paths. The SEB controls sensor selection and gimbal functions and contains the power supply hardware as well as the Integrated Mission System Processor (IMSP), which operates at 1.4 GFLOPS. The IMSP provides overall system control and tracking functions. The SEB includes the interfaces for the IMSP, the video distribution electronics, the power control/distribution assembly, and other equipment, cables, and controls necessary to perform mission operations.

The SEB also contains a thermal control system, which consists of two chillers. One chiller is the fine control of the temperature of the Ladar's master oscillator; the other chiller removes bulk heat from the Ladar power amplifier and the electronics in the MFOS gimbal and pedestal.

Controls and Display Console

The Controls and Display Console (CDC) allows an operator to control MFOS manually or automatically by computer. The CDC displays sensor images, range, speed, target classification, and general system status information.

The CDC controls Ladar functions for target ranging, imaging, and Doppler measurements.

A Situation Display presents system status and a graphical representation of the target in relation to the MFOS location. A 1553 interface allows the operator to cue the direction of the gimbal with data from the Army's search radar and to transmit target data to the weapon fire control system or a C2I network.

SYSTEM OPERATION

There are two major hurdles that must be overcome in order to classify/identify airborne targets. First, the MFOS must acquire and track targets before it can classify targets. A flow diagram (Figure 4) shows the steps that must be performed to classify targets. Detection can occur by using the infrared cameras to scan the horizon for targets. The field-of-view (FOV) for the IR cameras is limited to 8° in wide FOV setting. A better (more systematic) approach to detection uses the Azimuth and Elevation outputs from a scanning radar to cue the MFOS to within the 8° wide FOV or 2° narrow FOV windows of the imaging cameras. Once a target is detected, the MFOS operator puts it under automatic track. MFOS Azimuth and Elevation angles can be compared with radar angles to confirm that the correct target is being tracked. Once a target is being tracked, the microDoppler Ladar can be used to give positive non-cooperative classification/identification. A flow diagram of the Ladar processing is shown in Figure 5. The laser beam reflected from the target is Doppler shifted from the outgoing beam. The Doppler shifted difference frequency is proportional to the speed of the target and is called macroDoppler. It appears as an FM carrier signal. Target vibrations give an FM modulation (i.e. microDoppler signal) and can be detected using FM demodulation techniques.

Radar Cue

The MFOS was connected to the Forward Area Air Defense Command and Communication (FAAD C2) system through the Enhanced Position Location Reporting System (EPLRS) which was provided GFE by the AD BLSE. Radar cue information was sent to MFOS over the EPLRS network. EPLRS provided velocity, range, azimuth, and altitude of the target. Using this information MFOS performed a Slew to Cue (STC) and acquired targets. MFOS only received target information through EPLRS and did not provide information back onto the EPLRS network.

Data Recording

Video from the visible CCD, LWIR, and MWIR cameras was recorded on VHS tape along with IRIG time. Also, the Ladar output with IRIG time was recorded on a digital data recorder for additional post processing analysis. Target position data versus IRIG time was recorded during flights for post test correlation of microDoppler signals versus target range.

Handover

The Army search radar detected and tracked airborne targets and sent targets metrics (range, angular position, and velocity) to MFOS via the EPLRS network. MFOS used the target cueing information as an input for its prepoint capability. MFOS, with its wide field of view (FOV) of 8 degrees or narrow FOV of 2, was slewed to the calculated angular direction of the target and performed a search to detect the target. As targets were detected in the angular handover window, the Ladar performed range and velocity measurements to correlate to the FAAD C2 target metrics. Once the range and velocity were correlated, a microDoppler measurement was performed to quantify the targets' vibration signature for BVRID.

| Detect | Track | Classify |

❏ Wide Are Surveillance
• Radar Detection and Track
• Radar Handover to MFOS
• Manual/Automated MFOS
  Passive IR Reacquisition

Automated
Passive IR
Tracking

Automated Ladar
Doppler Tracking

❏ Limited Sector Search
• Manual/Automated MFOS
  Passive IR Acquisition
  at Weapon System

Outputs

Outputs

❏ Azimuth and Elevation
Bearings and their Rates

❏ Range
❏ Velocity
❏ Vibration Classification

❏ Target Flight Trajectory
❏ Target Classification
❏ Target Selection Prioritization
❏ IFFN

Figure 4. Target Engagement Procedure

Laser — Amplifier — Transfer/Receiver Optics — Infrared (IR) Camera / Stabilized, 2-Axis, Beam Director

IR Tracking
Laser Beam

Doppler-Shifted Laser
Return and Target
Vibration Signature

Target to Be Classified

Detection

Signal Extraction and Processing

Output
■ Target Image
■ Target ID
■ Target Range
■ Target Speed
■ Target Bearing

FM Signal

FFT

Signature
Database → Comparison

Figure 5. Non-Cooperative Targets are Classified using Coherent Ladar MicroDoppler Signature Measurements.

LIVE EXPERIMENT II

The ACT II Enhanced Combat ID engagements were integrated into AD BLSE's Live Experiment II field tests which were conducted from 1 - 12 December 1997 at the SHORAD Range, New Mexico.

Test Configuration

As part of the Live Experiment II, a search radar was connected to FAAD C2 which was connected through the Enhanced Position Location Reporting System (EPLRS) network to the MFOS as shown in Figure 1.

Data Link

The MFOS was connected to the Forward Area Air Defense Command and Communication (FAAD C2) system through the Enhanced Position Location Reporting System (EPLRS) that was provided GFE by the AD BLSE . The radar tracks and target metrics were displayed on a Handheld Terminal Unit (HTU) providing target range, speed, azimuth angle, elevation angle, and altitude. Using this information, MFOS performed a slew to cue to acquire and track the target. MFOS did not provide any information back onto the EPLRS network.

Test Results

Live Ex II tests provided the following MFOS data outputs: visible video, MWIR video, LWIR video, macroDoppler plots, digitized microDoppler data versus IRIG time, and target position versus IRIG time.

Video

Video from visible, MWIR, and LWIR cameras was recorded for test review and validation of microDoppler signatures. IRIG time was recorded on an available audio channel on the video tape.

MacroDoppler Signatures

Figure 6 is a sample macroDoppler plot. Frequency (MHz) is on the x-axis, time (sec) is on the y-axis, and signal intensity is shown by pixel shading (black is higher amplitude than white). The black line in the figure is the macroDoppler signal from an airborne target. The macroDoppler frequency corresponds to the target's velocity along the Ladar's line-of-sight (LOS). Variations in this frequency (wavy line) occur when the target speed changes or when the target changes its heading relative to the Ladar.
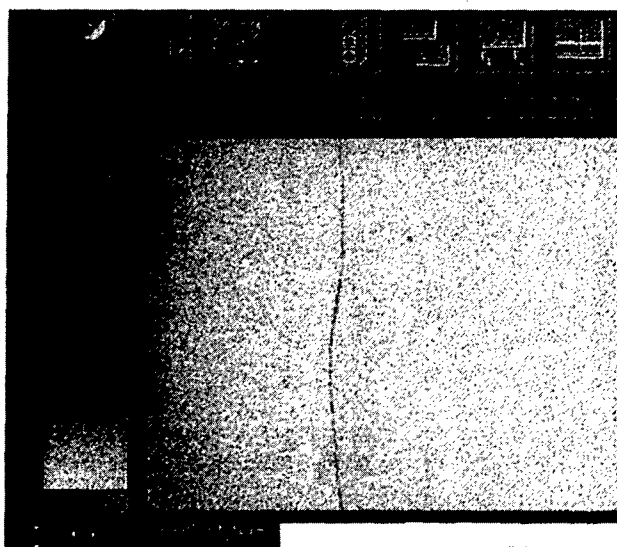
Figure 6. MacroDoppler Signal Indicates Target Velocity and Speed/Direction Variations.

MicroDoppler Signatures

Live Ex II provided realistic, target engagement scenarios against multiple airborne threats. These threats included

rotary and fixed-wing targets. The microDoppler signatures of these targets were measured and documented during the airborne engagements. The following figures show LOFAR Grams of the microDoppler signatures for each of the targets observed during the Live Ex II tests. The LOFAR gram is a representation of signal strength versus frequency and time. For the following plots, frequency is plotted along the x-axis in Hertz and time is plotted along the y-axis in seconds. Signal intensity is given by the darkness of the lines.

The LOFAR gram of Figure 7 shows the spectrum from a rotary-wing target's microDoppler. The main rotor passing frequency of 24.5 Hz is clearly visible.
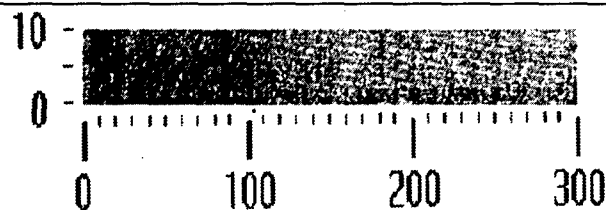
Figure 7. LOFAR Gram of Rotary-wing Target

The microDoppler signature shown in the LOFAR gram of Figure 8 is that from a fighter aircraft with jet engines. Distinct lines occur at 187 and 257 Hz. Broadband energy is also present from DC out to 40 Hz.
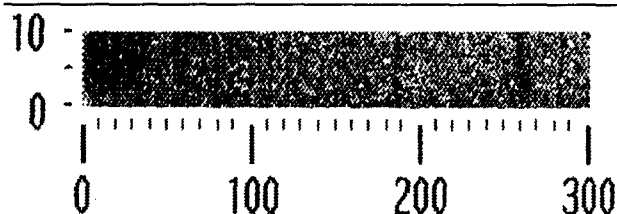
Figure 8. LOFAR Gram of Fixed-wing Jet

A Bi-Plane's microDoppler signature (Figure 9) shows engine vibration energy at 31, 62, and 93 Hz. A structural noise frequency is seen at 150 Hz. This aircraft contains many structural components made of wood and its wings and fuselage are covered with canvas.
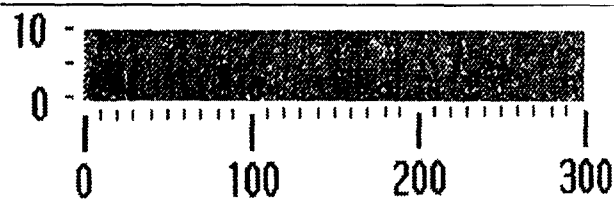
Figure 9. LOFAR Gram of Fixed-wing Bi-Plane

Figure 10 is the LOFAR gram for a Piper Cherokee aircraft. This aircraft is used during most system verification exercises and it provides a common target for "calibrating" performance. Its engine vibration frequencies show up in the microDoppler signature at 75, 150, and 225 Hz.
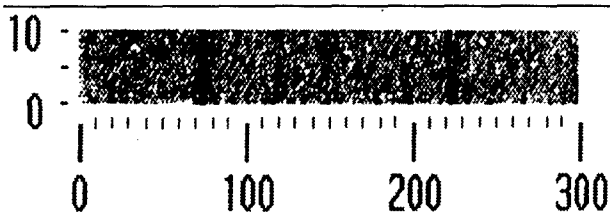
Figure 10. LOFAR Gram of Fixed-wing Piper Cherokee

A Long EZ aircraft was used to simulate a UAV. This "homemade" aircraft is a push prop design with composite structure. The simulated unmanned air vehicle (UAV) microDoppler signature, (Figure 11), shows the main rotor frequency at 82 Hz, with structural and noise lines at 29, 56, and 109 Hz.
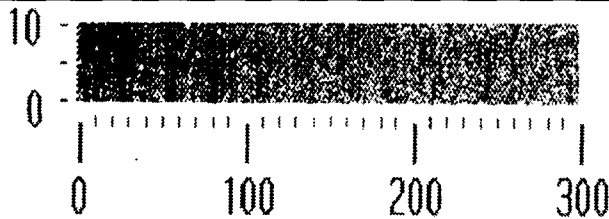
Figure 11. LOFAR Gram of Fixed-wing Surrogate UAV

FAAD Results

The results of this field test demonstrated the capability of a microDoppler LADAR system to provide non-cooperative target classification/identification at beyond visual range.

The Live Ex II tests demonstrated the capability of MFOS to perform a slew-to-cue using data from an existing radar. The key to MFOS' operational effectiveness is the minimized time (latency) between radar detection and microDoppler classification. This latency can be minimized by reducing the coverage of each microDoppler Ladar to selective threat corridors.

Prioritizing of threats based on the threat's classification, range, direction, and speed will determine the engagement sequence used by the weapon systems.

Participation in the next All Service Combat Identification and Evaluation Team (ASCIET) Exercise is planned to evaluate the MFOS microDoppler classification/identification of airborne targets under more realistic operational conditions.

DYNAMICAL NETWORKS FOR ATR

N.Farhat, G.H.Lee, and X.Ling
University of Pennsylvania D-2
Electrical Engineering Dept.
200 S. 33rd St.
Philadelphia, PA 19104, USA
email: farhat@pender.ee.upenn.edu

1. SUMMARY

A new class of networks for the classification of spatio-temporal signals (signatures) of the kind that can be generated in automated target recognition (ATR) and other remote sensing applications are described. The networks consist of parametrically and nonlinearly coupled bifurcation processing elements and are biologically inspired in that they incorporate several known or plausible organizational attributes of the cortex. The cortex is that part of the brain that is the seat of higher-level brain functions including the classification, recognition, and learning of sensory data that is usually not static but continually changing in time. The networks described are shown to: (a) employ *compact dynamical attractors* to classify spatio-temporal inputs, (b) exhibit *ultrastability* through multiple state-determined bifurcations, (c) compute with diverse attractors, i.e., not only with static (fixed-point) attractors as in conventional neural net models but also with dynamic (periodic and chaotic) attractors, and (d) exhibit behavior reminiscent to that seen in *functional magnetic resonance imaging* (fMRI) of brain activity. As such, dynamical networks, offer a new setting for studying the way the brain handles dynamic patterns and for using the knowledge gained to design artificial brain-like recognition systems.

2. INTRODUCTION

In automated recognition of aerospace objects using radar, it is frequently possible to generate a sequence of target signatures rapidly at regular time intervals that convey information about the nature and the way the signature depends on aspect. The signatures can be range-profiles of the target, Doppler spreads, or sets of suitably extracted features. The possibility of using such target signatures as training sets for neural networks has attracted much interest. The motivation was that a trained network may be able to identify a target from a single look (echo), obviating thereby the more involved and difficult task of forming an image in order to recognize the target (see for example [1] and references therein). One can intuitively appreciate that the design and performance of neural based ATR systems can be enhanced by incorporating in the recognition process detail about the way target signatures change in time. This requires the development of neural networks that can naturally accept and handle dynamic input patterns , and not only static ones as has been the case in the past [1].

In this paper, we describe a new class of biologically inspired dynamical networks that are naturally suited for handling (accepting and classifying) dynamic input patterns. The networks described incorporate attributes of critical networks and are shown to possess functional properties that make them potentially useful for the design of a new generation of intelligent recognition systems.

3. PARAMETRICALLY COUPLED LOGISTIC NETWORKS

There is considerable evidence that the basic functional unit for higher-level processing in the cortex is the *netlet* or *neuronal assembly* (neuronal pool or group) [2]-[11]. This evidence includes extensive analytical and modeling work of netlets carried out independently by several groups in the past. Nearly all that body of work points to the possibility that netlet dynamics, may be adequately described by the discrete time evolution of the activity $A(n)$, which is the percentage of neurons in the netlet active at time n. Plots of $A(n+1)$ vs. $A(n)$, called return maps, obtained under a range of circumstances and assumptions are found to invariably resemble a distorted version of the *quadratic or logistic map*, a nonlinear irreversible iterative map on the unit interval that exhibits complex orbits (fixed-point, period-m, or chaotic) depending on the value of a nonlinearity (control or bifurcation) parameter [12]. The similarity between the netlet's return map $A(n+1)$ vs. $A(n)$ and that of the logistic map has also been noted by Harth [11] who also mentions that complex and unpredictable sequences $A(n)$ were observed in some of their early simulations of netlets suggesting that certain regions of the netlet's parameter space can lead to observation of chaos in addition to the periodic and fixed point modalities they usually observed.

In light of this evidence we have conjectured that cortical networks can be mathematically modeled and numerically studied in an efficient way by means of parametrically coupled populations of logistic processing elements [13]. To test this conjecture we have studied the dynamics of such a network when it is subjected to dynamic input: external stimulus patterns that changed in time. The networks we study differ from coupled map lattices (CMLs), [14]-[15], in several ways: (a) The networks described here employ parametric rather than the diffuse coupling used in CMLs, (b) The coupling is nonlinear to represent the possibility that the interaction between cortical netlets can depend on the activity of the netlets and on the density of active fibers connecting one netlet to another, (c) Parametrically coupled logistic nets (PCLNs) can be externally driven by dynamic or static patterns, or by composite patterns that are partially time varying and partially stationary, (d) In the PCLN, control over network dynamics is gradually handed over from initially entirely extrinsic control to eventually intrinsically dominated control. This gradual transfer of control over network dynamics from extrinsic to intrinsic is biologically plausible and is inspired by the remarkable biophysical observation made by Freeman and coworkers [16] regarding gradual disappearance of the trace of a sensory stimulus applied to the olfactory bulb of rabbit as it was followed deeper in the sensory cortex where it was found to eventually vanish in a sea of intrinsically dominated activity. Similar behavior has apparently been observed by Freeman's group in other sensory modalities.

The argument for the handing-over of control over dynamics is reinforced by another view, held by brain scientists (see for example [17] and [18]), namely that an animal or

organism surviving in a complex uncontrolled environment is constantly buffeted by energy and forces created by the environment that act on its sensory organs where they are converted into sensory data from which information and meaning are extracted by the cortex. More simply: information and meaning are created in the brain and not in the environment. To do so effectively, the cortex must be unhampered by steady influences of sensory data while it is making sense of the trace of sensory data it has already received. This implies that the cortex receives transient (gradually fading) influences of sensory data rather than steady ones. The above view, considering that the cortex is a high-dimensional nonlinear dynamical system whose behavior can be described in a state-space of suitable dimension, agrees with the picture of the transient or decaying trace of the sensory data serving to guide the state-space trajectory of the system, in its initial stages, towards a "loss region" of the state space. While this is happening, control over the dynamics (trajectory) by intrinsic influences such as memory (reflecting its past learned experience), context, and other factors steadily increase to enable them to play a maximum role in the interpretation and "making-sense", so to speak, of the sensory data through the system convergence to an attractor within the loss region that would classify the original input stimulus. We expect this intriguing view of biological information processing, and how it distinctly differs from standard approaches to the processing of information, to have an increasing impact on the design philosophy of future brain-like artificial intelligent systems including ATR systems.

The preceding remarks suggest that networks of parametrically coupled logistic maps may offer an effective way to study the functional complexity of cortical networks in order to understand the way they perform higher-level functions, including the handling (classification, recognition, and generation) of spatio-temporal patterns. Such higher-level functions are beyond the capabilities of present day sigmoidal networks, and incorporating them in artificial network offers a possible means for increasing their functional repertoire, processing power, and widening their scope of application into ATR and other areas.

The network studied is shown in Fig.1. For simplicity and ease of displaying its state evolution in time, a one-dimensional topology is chosen. It consists of a one-dimensional array of N parametrically coupled logistic maps $L_i, i = 1,2,...N$. Parametric coupling means the nonlinearity, (control or bifurcation parameter) $\mu_i(n)$ of the i-th map is not fixed but is modulated in time. In the network, $\mu_i(n)$ is modulated by both extrinsic and intrinsic influences according to

$$\mu_i(n) = \varepsilon(n) g_i^s(n) + \frac{1-\varepsilon(n)}{2N_i} \sum_{j=i-N_i}^{i+N_i} g_{ij}(n), \qquad (1)$$

$$\varepsilon(n) = \varepsilon_0 \exp(-\alpha n)$$

In eq.(1) $i = 1,2,...,N$, the first term represents the extrinsic (sensory) input to the i-th logistic processing element or cell, the second term represents the net intrinsic input to the i-th cell through feedback from all other cells connected to it including itself (self-feedback), n is discrete integer time, $2N_i$ is the number of logistic cells connected to the i-th cell i.e. the number of cells falling within a "connection radius R_c" that is taken to be identical for all cells,

$g_i^s(n) = 4(u_i(n))^{c_i^s}$ is the extrinsic (sensory) input to the i-th

cell with state variable $u_i(n) \in [0,1]$ being produced in the simulation conveniently by a stimulus generating logistic map according to: $u_i(n+1) = \mu_i^s u_i(n)(1-u_i(n))$ with $u_i(0) = 0.5$ and μ_i^s being a fixed control parameter of the i-th stimulus generating logistic map. Selecting μ_i^s in [0,4] enables the production of a wide range of stationary, periodic (period-m) or chaotic patterns $u_i(n)$ or any desired mix of such patterns on i depending on the values one selects for μ_i^s. Thus by adjusting the control vector $\bar{\mu}^s$ of the N stimulus generating logistic cells, a wide variety of spatio-temporal driving signals can be conveniently produced and applied to the network. The coupling factor c_i^s ranges between 0 and ∞. For example $c_i^s = 0$ produces $g_i^s(n) = 4$ which means the extrinsic contribution into eq.(1) tends to make $\mu_i(n)$ high with the result that the i-th processing cell is more prone to exhibit a chaotic orbit. On the other hand $c_i^s = \infty$ yields $g_i^s(n) = 0$, because the state variable u_i of the logistic map is in [0,1]. This means that small values of c_i^s introduce disorder while larger values introduce inhibition. Similarly, the quantity $g_{ij}(n)$ in eq.(1) represents the input from the j-th processing cell to the i-th processing cell; it has a form similar to $g_i^s(n)$, namely

$$g_{ij}(n) = 4[x_j(n)]^{c_{ij}} \text{ with } c_{ij} \text{ being in } [0,\infty] \text{ and } x_j(n)$$

being the state variable of the j-th logistic processing cell of the network governed by: $x_j(n+1) = \mu_j(n)(1-x_j(n))$ where $\mu_j(n)$ is given by eq.(1) and $x_j(n)$ is also in $[0,1]$.

Note the nonlinear dependence of $g_i^s(n)$ on $u_i(n)$ and of $g_{ij}(n)$ on $x_j(n)$ serves two purposes. One, it confines their combined contribution to $\mu_i(n)$ to the allowable range $[0,4]$, and second, the values of c_i^s and c_{ij} provide control over the level of excitation/disorder on the one hand and inhibition on the other, that are injected into the dynamics of the i-th cell, and hence into the network as a whole, by the i-th sensory cell or by the j-th processing cell respectively. The parameter α in eq.(1) is a positive real constants whose value determines the speed with which control over the dynamics of the network is handed over from initially entirely extrinsic control to eventually dominantly intrinsic control. A value of $\varepsilon_0 = 1$ means that initially the dynamics of the network are totally controlled by the extrinsic (sensory) pattern and $\alpha = 0$ means there is no fading of the effect of extrinsic input.

The handing-over of control over dynamics from extrinsic to intrinsic control, together with the fact that $\mu_i(n)$, $i = 1,2,...N$, the control parameters of the processing elements(PEs) in the network, are state-dependent, lead to ultrastability of the PCLN. Ultrastability means that the network's parameters can always be chosen in a range where every applied stimulus always leads to a stimulus specific static or dynamic compact attractor in the state space of the network via multiple bifurcations (rapid switchings of behavior at critical points). The compactness of the attractors is explained below.

4. SIMULATION RESULTS

The behavior of the PCLN was numerically studied for $N = 100$ under a variety of conditions and parameter values and rich behavior was observed. Particularly interesting was the behavior when local connectivity was used where $N_i \ll N$ to reflect the dominance of presumably short-range interconnection between netlets of the cortex. When self-connection of cells was allowed and the following parameters were used: R_c randomly selected in $[0,1]$, $\varepsilon_o = 1$, $\alpha = 0.1$, $c_i^s = 0.5$, $u_i(0) = 0.5$, random coupling coefficients i.e., c_{ij} randomly and uniformly selected in $[a,b]$, and random initial state vector $\bar{x}(0)$ i.e. $x_i(0)$ randomly and uniformly selected in $[0,1]$, the network exhibited isolated clusters of activity for values of the constants a ranging in $[0,0.3]$ and $b \approx 3$ which furnished a mix of chaos and order inducing coupling functions. Examples of the behavior of the network are shown in Figs.2, 3, and 4 for different forms of the stimulus generating vector $\bar{\mu}^s$, i.e. for different spatio-temporal inputs. Detailed descriptions of these figures are given in the figure captions. The form of isolated clustering, and the orbits of cells within clusters seen in these figures are stimulus specific and independent of initial state of the network, as would be desired. The clustering was relatively rapid occuring usually within the first tens to hundreds of iterations depending on the value of α. Cell orbits of different type i.e., fixed-point, period-m (m-cycle that repeat), intermittent, and chaotic can coexist within a cluster and often the period-m orbits of cells within well separated clusters were not only phase-locked but synchronized. This latter behavior conforms with synchronized oscillations of local field potentials observed by several workers in the brain of cat and monkey and with Eckhorn's modeling of that behavior in networks of spiking neurons [19]-[24].

Most interesting is the isolated clustering which is reminiscent to the isolated clusters of brain activity seen *in functional magnetic resonance imaging* (fMRI) *and positron emission tomography* (PET) images of brain activity in individuals subjected to sensory stimulus or when performing an assigned cognitive or motor task.

The conceptual similarity of the isolated clustering behavior in PCLNs and the clustering of brain activity seen in fMRI and PET raises an interesting scientific question: if PCLNs are valid models of cortical nets then the clusters of brain activity "hot-spots" seen in fMRI and PET should also exhibit analogous temporal activity. Unfortunately the time resolution of fMRI and PET at present is too coarse to discern any temporal activity within the "hot spots" because both measure the change in blood flow to active brain regions. An increasing number of studies employing PET and fMRI show however that different sensory stimuli or assigned cognitive tasks can "light-up" the same brain spots. This strongly suggests a role for temporal encoding to enable differentiation. It would be interesting to see if future technological advances in functional brain imaging could provide the needed temporal resolution to verify the prediction of the PCLN.

5. DISCUSSIONS

The generally rich behavior we observe with PCLNs including the remarkable specific behaviors described above have no parallel in sigmoidal neural network, and apparently also in coupled map lattices and cellular automata. Therefore we believe that the use of PCLNs to model cortical networks and higher-level brain functions provide a unique tool and opportunity for the development of intelligent systems that can operate in natural and artificial environments where time varying signatures are the norm and not the exception.

In particular the following functional characteristics and attributes of networks of parametrically coupled bifurcation (here logistic) processing elements are noteworthy:

- Ability to accept spatio-temporal inputs (dynamic input patterns). This expands the repertoire of neural based signal processing systems, which is presently confined to stationary inputs because of inherent limitations of the networks used, to dynamic inputs.

- The characteristic convergence of network activity to a small number of isolated active cells (PEs), or groups (clusters) of cells, in a large background of inactive cells (see examples in Figs 2-4) means these networks can be made to produce trajectories in their N-Dimensional state-space that are confined to limited or compact "volumes" of their state space, i.e., to compact dynamic attractors. Such dynamic attractors can be composed of combinations of fixed-point, periodic, and chaotic orbits. As such they combine levels of order and chaos that are under the designer's control.

- The convergence to such compact dynamic attractors is relatively fast and controlled occuring, typically, within the first few tens or hundreds of iterations, depending on the value of the parameter α which determines the speed with which control over network dynamics is handed over from extrinsic to intrinsic control.

- Compact dynamic attractors are stimulus specific. Distinct input patterns produce distinct attractors and similar input patterns converge to the same compact dynamic attractor. This latter property suggests that compact dynamic attractors can possess *basins of attraction* analogous to the attraction basins in conventional neural networks which exhibit however only static (point) attractors and not dynamic ones.

- The compact dynamic attractors the network converges to are also dependent on the coupling factors c_{ij} of the network. In the simulations presented here, c_{ij} are selected randomly because the goal at present was to probe and understand the network dynamics. In the future however we expect that structured (nonrandom) c_{ij} matrixes, arrived at via suitably developed algorithm for adaptation and learning, would be utilized in these networks. It is worth noting that clustering into a small number of small isolated pockets of activity can be desirable and beneficial in the study of adaptation and learning algorithms based on *mutual information* for example because of the sparsity of the resulting mutual information matrix and the greatly reduced computational effort needed to generate it from the orbits of the few active cells in the network that characterize the input.

- Ability to exhibit ultrastability which means that network parameters can always be suitably selected so that every dynamic input pattern applied to the network causes the network to converge to an associated compact dynamic attractor. This occurs through repeated bifurcations of the network because the control parameters $\mu_i(n)$ of the network is state-dependent, in addition to being inflenced by the extrinsic stimulus (see eq.(1)).

- The behavior of the network under extrinsic stimulus is independent of the initial state vector $\bar{x}(0)$ (i.e. $x_i(0), i = 1,2,...N$) of the network. Note however the initial states $u_i(0), i = 1,2,...N$, of the input stimulus generating logistic cells (see Fig.1) are fixed to guarantee repeatability and coherence of the spatio-temporal input patterns used to drive the network.

- In the absence of extrinsic input, i.e. when the network is undriven, the response of the network was seen, in simulations not reported here, to depend on the initial state of the network in a manner analogous to that in conventional recurrent networks (Hopfield-type networks) that compute with static (point) attractors. The behavior here would be similar but with both dynamic in addition to static attractors occuring. Basins of attraction delineated by probing with different initial states are also present just like conventional point attractor network.

- We have been able to conceive of networks that can be made to exhibit all three types of attractors found in dynamical systems, i.e., networks that "compute" with diverse attractors. This is significant because cortical network can be viewed as high-dimensional dynamical systems that are known o exhibit all three types of attractors in their state-space depending on the location in parameter space. Because conventional neural networks exhibit point attractors only, they can not be used in the modeling and study of cortical networks and the higher-level brain functions they produce. The dynamical networks presented here are however quite suited for this modeling task.

5. ACKNOWLEDGEMENT

6. REFERENCES

1. H. Babri, *Neurodynamic Networks for Recognition of Radar Targets*, PhD dissertation, University of Pennsylvania (1992).

2. E.M. Harth, et. al., J. Theor. Biol., vol.26, pp.93-120, (1970).

3. P.A. Annios, et. al., J. Theor. Biol., vol.26, pp.121-148, (1970).

4. M. Usher, H.G. Schuster and E. Neibur, Neural Computation, vol.5, pp.370-386, July, 1993.

5. G.M Edelman, *Neural Darwinism: The Theory of Neuronal Group Selection*, Basic Books, Inc., Publishers, New York, (1987).

6. C. van Vreeswijk and H. Sompolinski, Science, vol. 274, pp. 1724-1726, Dec. (1976).

7. T. Wennekers and F. pasemann, International Journal of Bifurcation and Chaos in Applied Science and Engineering, vol. 6, pp. 2055-2067, (1996).

8. T. Wennekers, F. pasemann and G. Palm, in *Supercomputing in Brain Research: From Tomography to Neural Networks*, H. Hermann, D. Wolf and E. Poppel (Eds.), World Scientific, Singpore, (1995).

9. G.L. Shaw and D.J. Silverman, in *Computer Simulation in Brain Science*, R. Cotterill (Ed.), Cambridge Univ. Press, Cambridge, (1988), pp.189-209.

10. M. Shadlen and W. Newhouse, Opin. Neurobiology, vol. 14, pp. 569-579, (1994).

11. E. Harth, "Order and Chaos" in IEEE Trans. on Systems Man and Cybernetics, vol. SMC-13, pp. 48-55, (1983).

12. R.C. Hilborn, *Chaos and Nonlinear Dynamics*, Oxford Univ. Press, New York (1994).

13. N. Farhat and E. del Moral Hemandez, "Recurrent nets with recursive processing elements: Paradigm for dynamical computing," SPIE, vol. 2324, SPIE, Bellingham, Wash. (1996), p. 158-170.

14. K. Kaneko, in *Theory and applications of Coupled Map Lattices*, K. Kanako (Ed.), J. Wiley, New York, (1993), pp. 1-49.

15. J. Crutchfield and K. Kanako, in *Directions in Chaos*, vol. 1, World Scientific Publishing Co., Singapore, (1987), pp. 272-353.

16. W.J. Freeman, *Societies of Brains*, LEA Associates Publishers, Hillsdale, N.J., (1995).

17. S. Franklin, *Artificial Minds*, MIT Press, Cambridge, MA (1995).

18. W. Ross Ashby, *Design For A Brain*, J. Wiley and Sons, London (1960).

19. C.M. Gray and W. Singer, "Stimulus specific neuronal oscillations in the cat visual cortex: a cortical functional unit," Soc. Neurosci. abstr., 404, (1987).

20. _____,"Stimulus dependent neuronal oscillations in the cat visual cortex area 17," Neuroscience, vol. 22, [suppl.], (1987).

21. C.M Gray, P. Konig, A.K. Engel and W. Singer, "Oscillatory responses in cat visual cortex exhibit inter-columnar synchronization which reflect global stimulus properties," Nature, vol. 338, pp. 334-337, (1989).

22. C.M. Gray and W. Singer, "Stimulus specific neuronal oscillation in orientation columns in cat visual cortex", Proc. Natl. Acad. Sci., USA, vol.86, pp.1698-1702, (1989).

23. R. Eckhorn, M. Arndt and P. Dike, "Feature linking via synchronization among distributed assemblies: simulation results from cat visual cortex," Neural Computation, vol. 2, pp. 293-307, (1990).

24. R. Eckhorn and H.J. Reitboeck, "Stimulus-specific synchronization in the cat visual cortex and its possible role in visual pattern recognition," in *Synergetics of Cognition*, H. Haken and M. Stadler (Eds.), pp. 99-111, Springer-Verlag, Berlin, (1990).

FIGURE CAPTIONS

Fig. 1.   Parametrically coupled logistic network (PCLN) consisting of N bifurcation (logistic) processing elements or cells. The network employs (a) novel biologically plausible nonlinear (activity) dependent coupling functions between cells each representing a netlet and (b) a biologically plausible gradual transfer of control over network dynamics from initially totally extrinsic (sensory) control to nearly totally intrinsic control. The network can be driven externally by spatio-temporal inputs provided by the stimulus generating network that employs an array of uncoupled logistic maps to conveniently produce a variety of static, time-periodic, chaotic, or composite signals made of any mix of these three-types of signals. The quantized versions of the coupling functions are useful for studying the coarse-grain dynamics of the PCLN.

Fig. 2(a).   Example of the behavior of the driven parametrically coupled logistic net of $N = 100$ cells. Cells are numbered vertically from $i = 0$ to 99. Each cell has self-connection and is connected to its adjacent cells with probability of ½. The stimulus generating vector $\overline{\mu}^S$ is shown in the leftmost panel, the spatio-temporal pattern $u_i(n)$ produced by the i-th stimulus generating logistic element is shown in the next panel for the last ten ($n = 90$ to $n = 99$) iterations. The central large panel shows the temporal evolution of the state vector $\overline{x}(n) = \{x_i(n), i = 0,1,..., N = 99\}$ for the first hundred iterations ($n = 0,1,2,...,99$). The next panel to the right of the central panel is the power spectrum of $\exp(2\pi j x_i(n))$ where the variable $x_i(n)$ is regarded as a phase variable. The last panel to the right is the color code used to represent $x_i(n)$. The initial states $x_i(0)$ for iterating the logistic processing cells was selected randomly in $[0,1]$ and the control parameter $\mu_i(n)$ was that of eq. (1) of the text. Note the rapid emergence of clusters and convergence into "steady state" i.e., persistent types of orbits: for example period-4 orbit for $i = 9$, fixed point for $i = 22$ period-2 for $i = 51$, chaotic orbit for $i = 29$. Cells with fixed point orbits, encoded by uniform color line, are easily identified in the central panel. The pattern of isolated clusters shown is specific to the stimulus vector $\overline{\mu}^S$. It is independent of the initial state vector $\overline{x}(0)$ but depends as expected and desired on the matrix of coupling coefficients c_{ij} which was selected randomly in $[0,3]$ in order to allow the appearance of some chaotic orbits within the isolated clusters. (Changing the range of c_{ij} to $[0.3,3]$ eliminates chaos in the orbits and results in isolated clusters containing cells with period-m and/or fixed-point orbits only). Other parameters of the network were $\alpha = 0.1$ and $\varepsilon_o = 1$. The convergent pattern of isolated clusters shown in this figure was extended to iteration $n = 100-199$ as shown in Fig. 2(b) which shows clearly the three types of orbits: fixed-point, period-m, and chaotic. Note the sparse isolated clusters of activity in a large background of silent cells in this figure, which are typical, indicate the orbits occupy a compact region of the 100-dimensional state-space of the network i.e., a *compact dynamic attractors* that can combine order and chaos..

Fig. 2(b).   Same as Fig. 2(a) but for iterations 100-199 to show persistence of the convergent state after it emerges at about the 60-th iteration (see Fig. 2(a)).

Fig. 3.   Same conditions as in Fig. 2(a) but with a different stimulus generating vector $\overline{\mu}^S$ to show that the associated compact dynamic attractor is stimulus specific by way of appearance of three new active cells as compared to the orbits diagram in Fig. 2(b).Note the three new orbits are sufficient to place the compact dynamic attractor associated with Fig. 3 at different location in state-space in the network that does not overlap with the location of the compact dynamic attractor associated with Fig. 2(b).

Fig. 4.   Same condition as in Fig. 2(a) but with stimulus generating vector $\overline{\mu}^S$ that differs slightly from that shown in Fig. 2. This illustrates that similar spatio-temporal inputs are classified by the same compact dynamic attractor and that compact dynamic attractors possess basins of attraction.
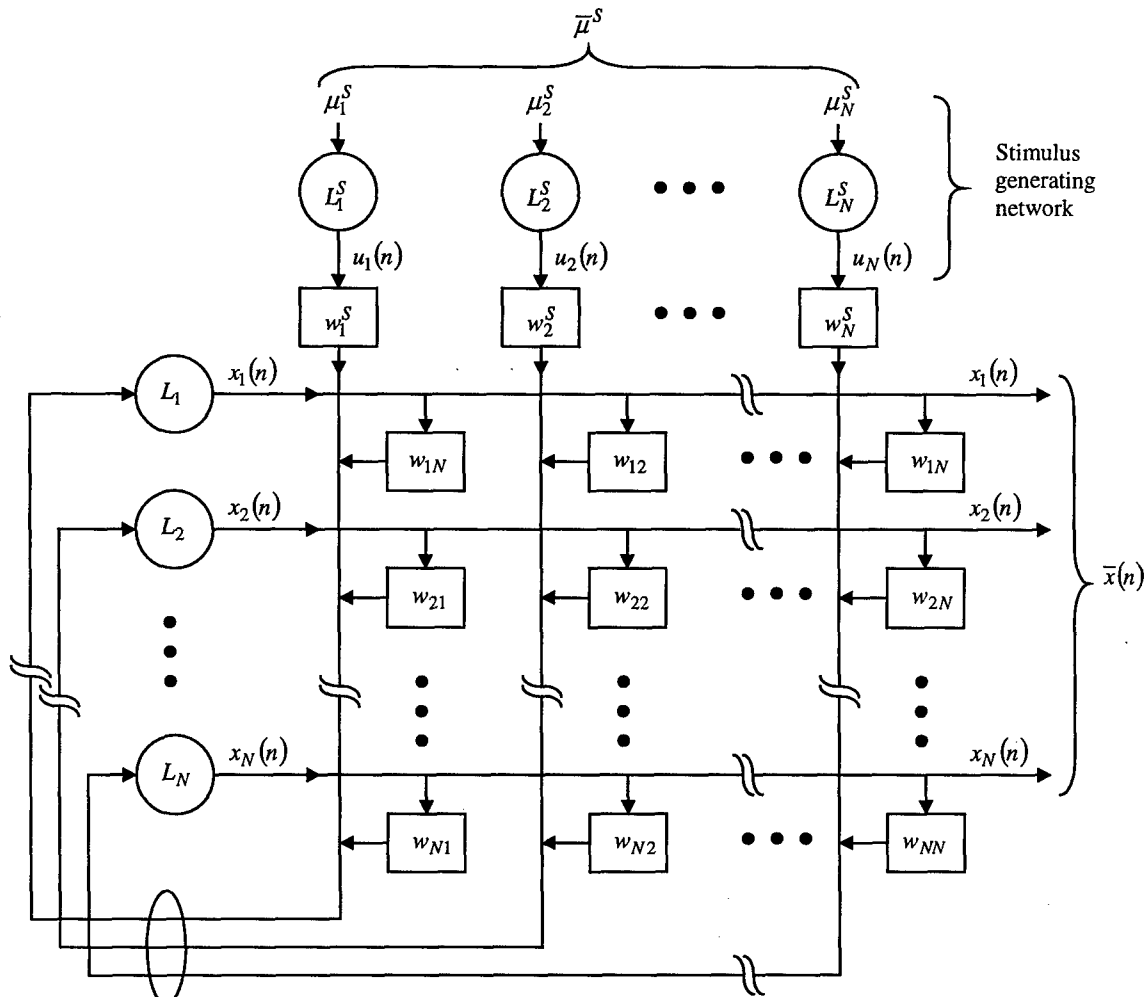
$$\mu_i(n) = \varepsilon(n)w_i^S(u_i) + \frac{1-\varepsilon(n)}{2N_i}\sum_{j=i-N_i}^{i+N_i}w_{ij}(x_j)$$

$$\varepsilon(n) = \varepsilon_o \exp(-\alpha n)$$

where ε_o is in $[0,1]$ and $\alpha \geq 0$ is positive real number.

w_i^S and w_{ij} are nonlinear activity dependent coupling functions with two possible forms each:

$$w_i^S = \begin{cases} g_i^S(u_i) = 4[u_i(n)]^S_i \\ B_i^S(u_i) = \text{quantized version of } g_i^S(u_i)(N_b \text{ levels}) \end{cases}$$

$$w_{ij} = \begin{cases} g_{ij}(x_j) = 4[x_j(n)]_{ij} \\ B_{ij}(x_j) = \text{quantized version of } g_{ij}(x_j)(N_b \text{ levels}) \end{cases}$$
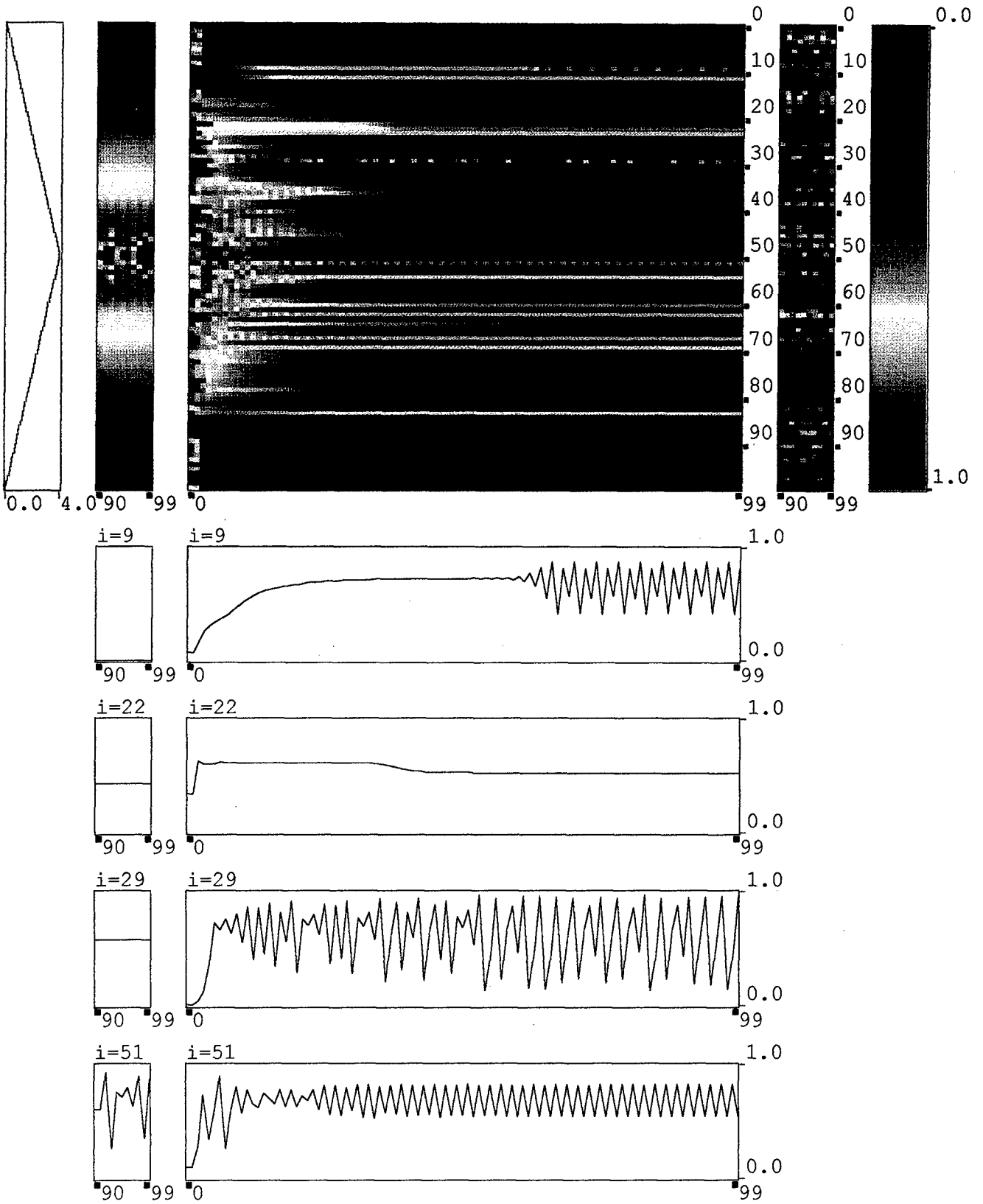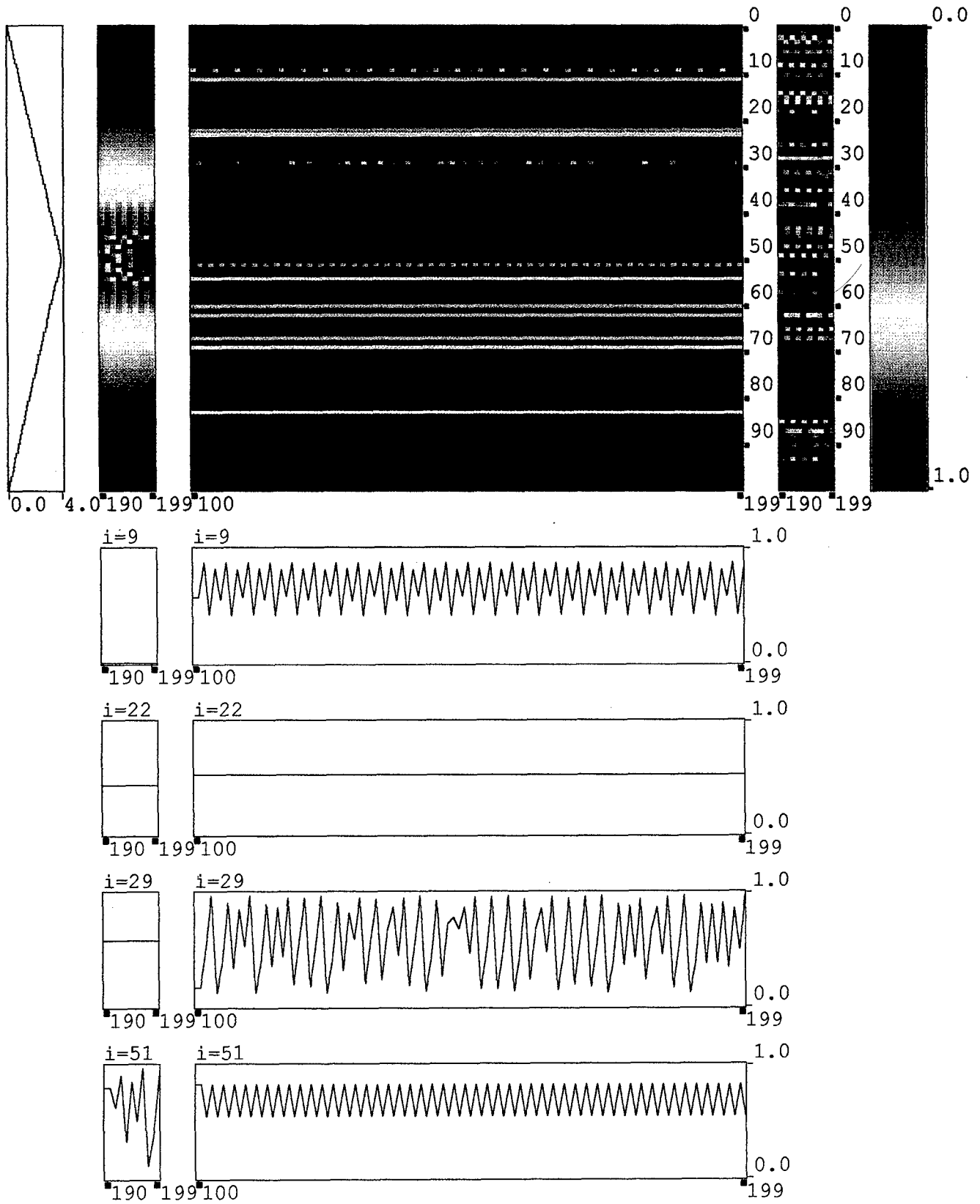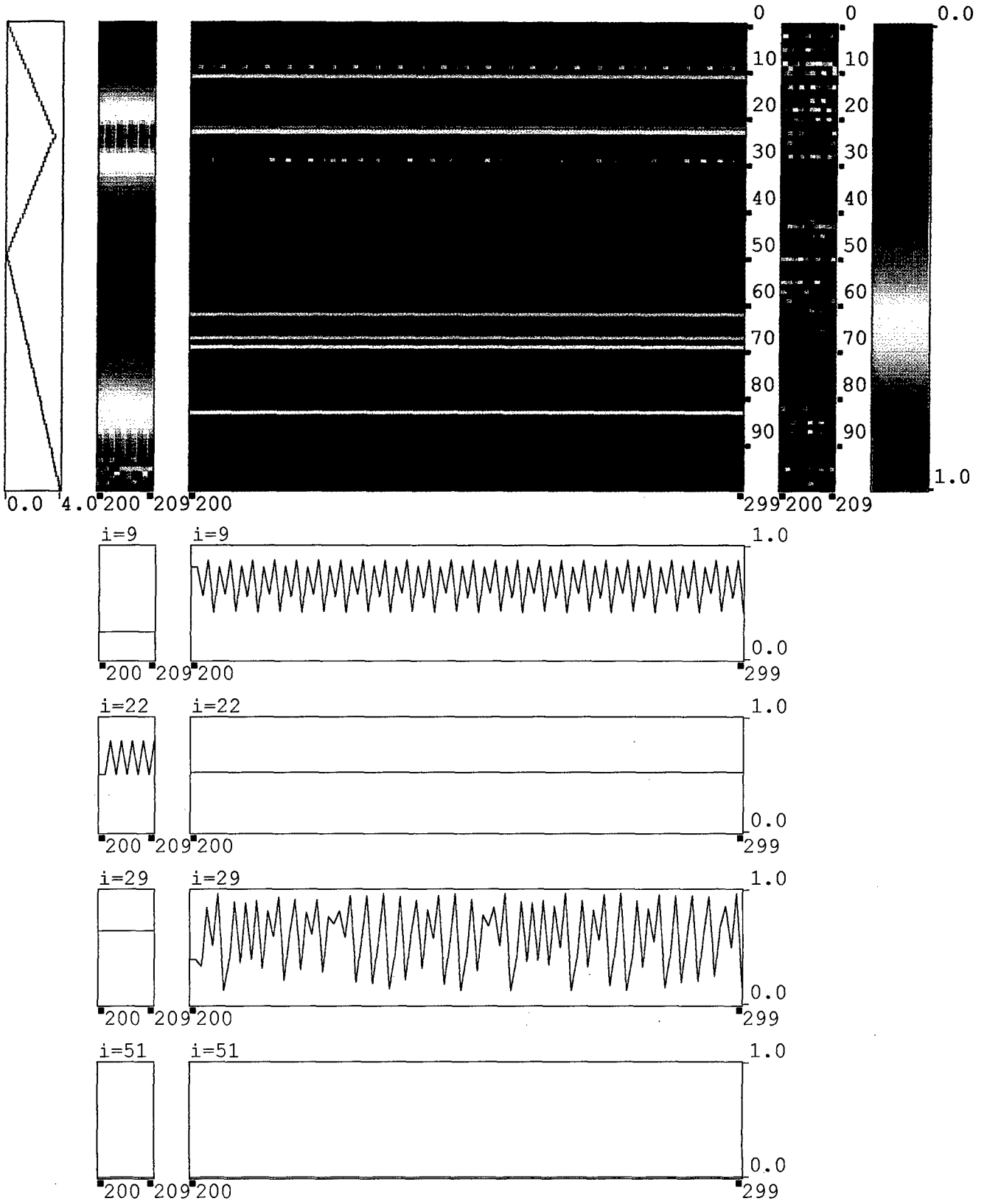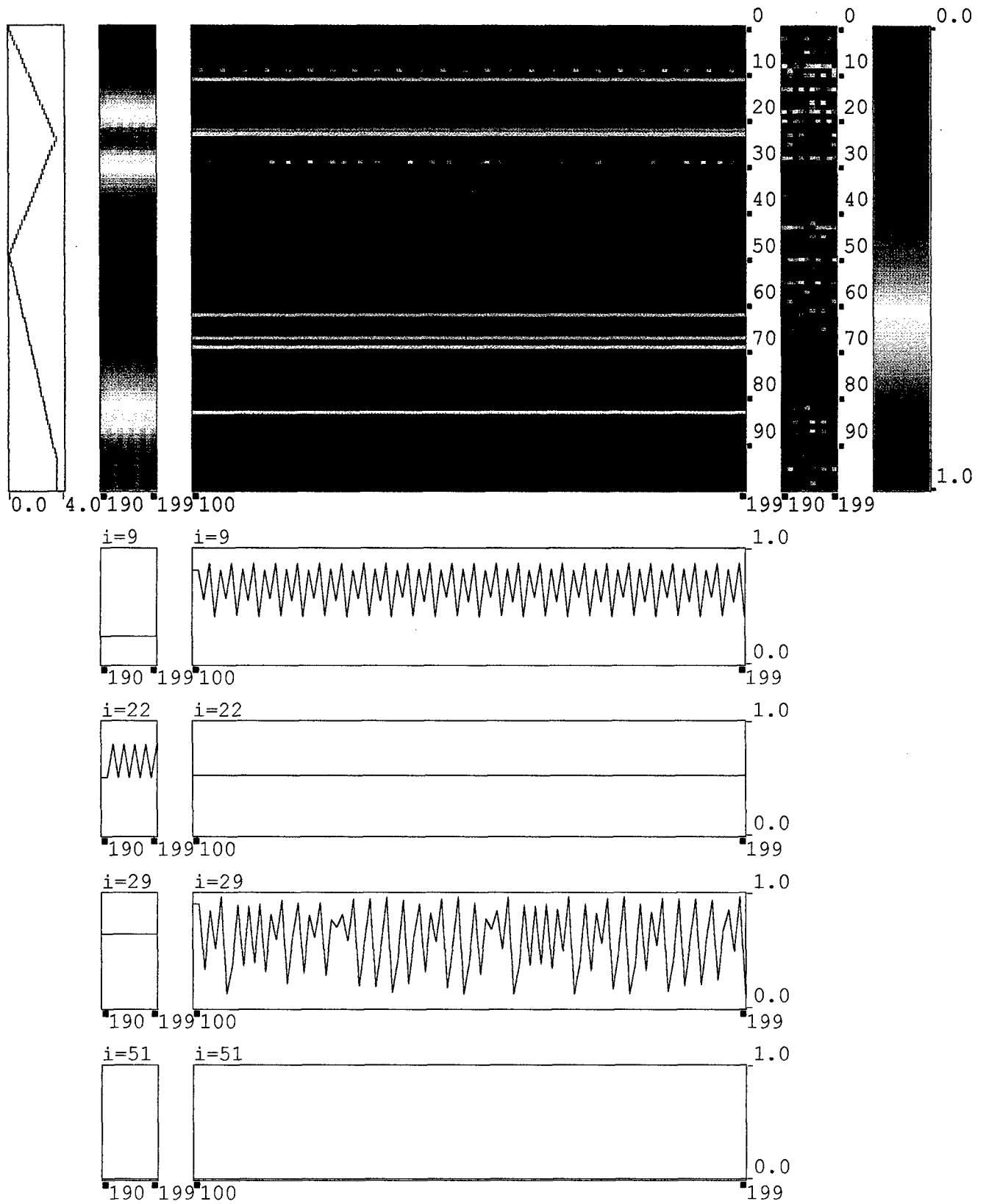
Fig. 2(a)

Fig. 2(b)

Fig. 3

Fig. 4

Non-Cooperative Helicopter Detection by Acoustical Sensors

Gunnar R. Becker

STN ATLAS Elektronik GmbH, Dept LFE5
Land and Airborne Systems Division
Sebaldsbruecker Heerstr.235
28305 Bremen, Germany

Abstract

This paper discusses the potential of acoustic sensors and arrays for non-cooperative air target detection. Acoustic sensors, i. e. microphones, are passive and make use of the sound emitted by the targets themselves. It is shown that acoustic systems can provide valuable information such as detection, tracking and classification of air targets. The paper mainly focuses on low flying combat helicopters, because they are difficult to detect by other means. It turns out that Radar and acoustics are sensors with complementary performance.

1. Introduction

Any air target emits sound which can be detected by acoustical sensors. Signal processing is able to analyze the sound and give valuable information for the military, e.g. azimuth of target and class of target. In contrast to Radar acoustics offers some interesting features:

- Acoustic systems are designed as passive systems, i. e. they do not radiate energy themselves but use the energy emitted by the targets itself.

- Acoustic systems cover the full azimuth at once but are still able to bear target direction.

- Acoustic systems do not require line-of-sight conditions to operate.

- The hardware requirements are much lower for acoustic systems. The processing can easily be done on a PC or DSP in realtime. Typical overall bandwidth is 50 kHz.

- Extreme low power consumption can be achieved by specific wake-up circuitry, resulting in operation times of typically up to four weeks.

In this paper we will describe the main key modules of such an acoustic system for the detection and tracking of helicopters. We are focussing on helicopters since they are a severe problem in surveillance. Combat helicopter usually fly nap-of-the-earth, masked by terrain or vegetation, and are hardly to detect by other means.

2. Detection of Helicopters

The acoustic signature of helicopters is characteristic for this class of targets. The main contributions are spectral lines due to blade passing frequencies of main and tail rotor. Similar features can be found in Radar signatures of helicopters. An example of a typical signature is presented in Fig. 1. In the lower right you can see the acoustic spectrogram of the helicopter approaching the microphone. The spectral lines are clearly visible and detectable. At the left hand you find the sound pressure in the analyzed frequency band and the broad band noise level, respectively. This broad band noise is removed in the spectrogram to enhance the contributions of the spectral lines and yield an estimate of the signal-to-noise-ratio (SNR). As can be seen from the averaged spectra in the top two windows of Fig. 1, there is a significant broadband noise contribution (upper: with broad band noise, lower: broad band noise removed).

In order to obtain a reliable measure for the early detection of approaching helicopters the spectrograms are analyzed. Spectral lines are detected and extracted automatically. The result of such an analysis is shown in Fig. 2. for the same run as above. In addition a confidence measure ('Konfidenz') is deduced, given at the left hand of the sketch.

This confidence measure serves as detection measure. As can be seen the confidence increases significantly as soon as the spectrogram exhibits target features, i. e. the harmonics of the blade passing frequencies and thus allows for an

early detection of the helicopter.

Since acoustics is not that much effected by obstacles it is possible to detect targets even though they are not visible from the sensor position. This is demonstrated in Fig. 3. It shows a measurement, where microphones have been deployed across a hillside from one base to the other. The hill rised the surrounding site by about 25 m. The signatures of an approach of a helicopter flying nap-on the-earth are measured at both base positions and presented at the bottom of the sketch. As can be seen, the signature of the helicopter can even be detected with the microphone deep in the shadow of the hillside, whereas a Radar would have no chance.

This example clearly demonstrates the superority of acoustics in situations, where line-of-side-conditions are hardly to expect.

2. Acoustic Bearing and Tracking

It is well known from Sonar that the directions to sound emitting targets can be evaluated. This has been the most powerful sensor system in anti submarine warfare (ASW) so far.

Instead of using a single microphone a number of omnidirectional microphones are used to build a so called acoustic array. Such an array is presented in Fig. 4, being integrated into a mine prototype. The array shown comprises of seven microphones, six of them are located on a circle with a diameter of approximately one meter. The seventh microphone is located in the centre. As sound propagates across the array phase shifts occur between the different microphone positions. There exist various algorithms to invert these phase shifts in order to obtain the bearing of the sound source. These algorithms are summarized under the term 'beamforming'.

STN ATLAS has implemented time-delay- and frequency-domain-beamformers on PC's and DSP's. They allow for the estimation of the bearing in realtime. Fig. 5 shows the evolution of the bearing estimates during a fly-by of a helicopter. The horizontal axis covers 360°. The energy is plotted over angle for a number of subsequent evaluations. It turns out that the bearing estimates are much better than one might expect from the 3-dB-beamwidth of the arrays mainlobe.

Using more sophisticated algorithms even the bearing of e. g. two targets at the same time is possible. This is demonstrated with Fig. 6. During this run a tank drove on a nearby track while a helicopter was passing the array.

Combining two or more acoustic arrays to a distributed sensor network furthermore allows to localize and track targets in an area under observation. Typical distances between the arrays are in the order of hundreds of meters.

3. Classification

The acoustic signatures of different classes of targets (e. g. ground targets, helicopters, fixed wing aircraft) vary, while they are very similar within the classes itself. This offers the potential to discriminate the different classes. In addition the acoustic 'fingerprint' of helicopters is strongly related with the blade passing frequencies. Identifying these frequencies in the acoustic spectra at least allows to reduce the types of helicopters possible. Both classical and neural net approaches have been succesfully applied to the problem.

4. Military Relevance

In the previous sections the potential for non-cooperative air target detection and classification by acoustic means has been discussed and demonstrated. Since acoustic systems make use of the targets sound they are especially suited for the observation of low flying air targets, such as helicopters, drones, etc.

Acoustic devices can be used in unattended, autonomous systems, because of their low power consumption. They therefore can operate for weeks with batteries only. Signal processing will be integrated on board the systems, including detection, classification and tracking. The more complex processing, however, will only be switched on as long as a potential target is detected.

Radar and acoustics are complementary sensors. While Radar is the better solution for long range and unmasked targets, acoustics is superior for 360° surveillance, unattended and covert operation as well as the detection of masked targets.

The combination of both principles will result in

a new type of multisensor. In that case the acoustic subsystem will cue Radar and provide information such as detection and bearing. Radar then will operate only if a relevant target is present.

5. Conclusion

This paper discusses the potential of acoustics for non-cooperative air target detection, tracking and classification. It has been shown that acoustic sensors and arrays offer a great potential, especially for low flying targets, e. g. helicopters. Unattended operation is possible. Radar and acoustics may be combined to exploit the complementary features of the sensors.

Fig. 1 Acoustic spectrogram of a helicopter passing a microphone
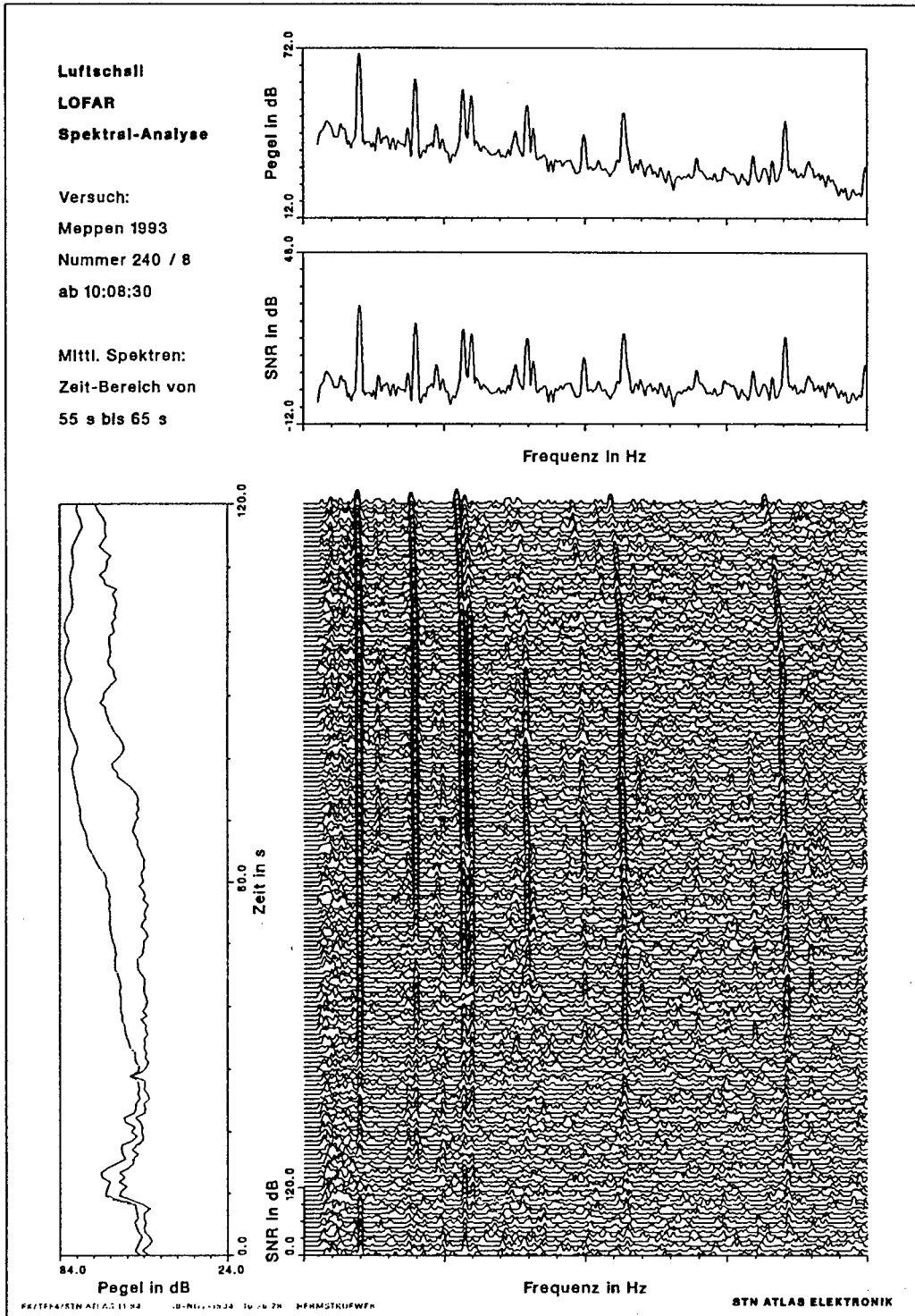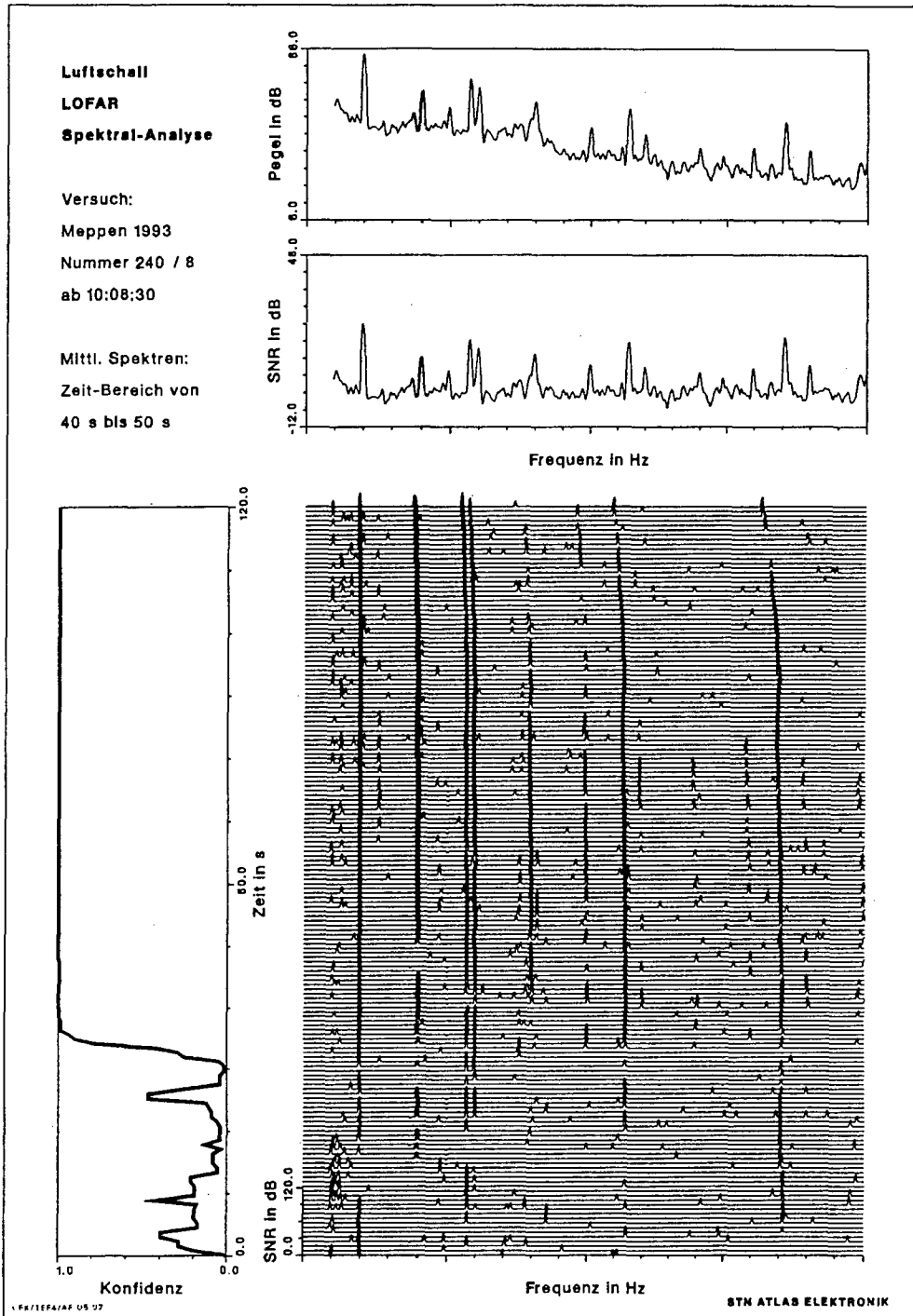
Fig. 2 Confidence measure indicating detection of a target
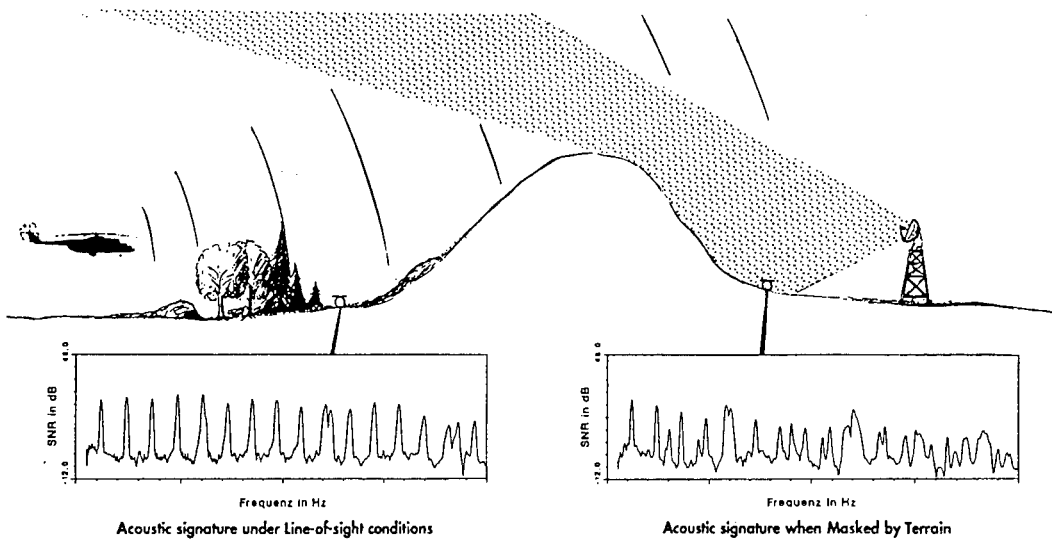
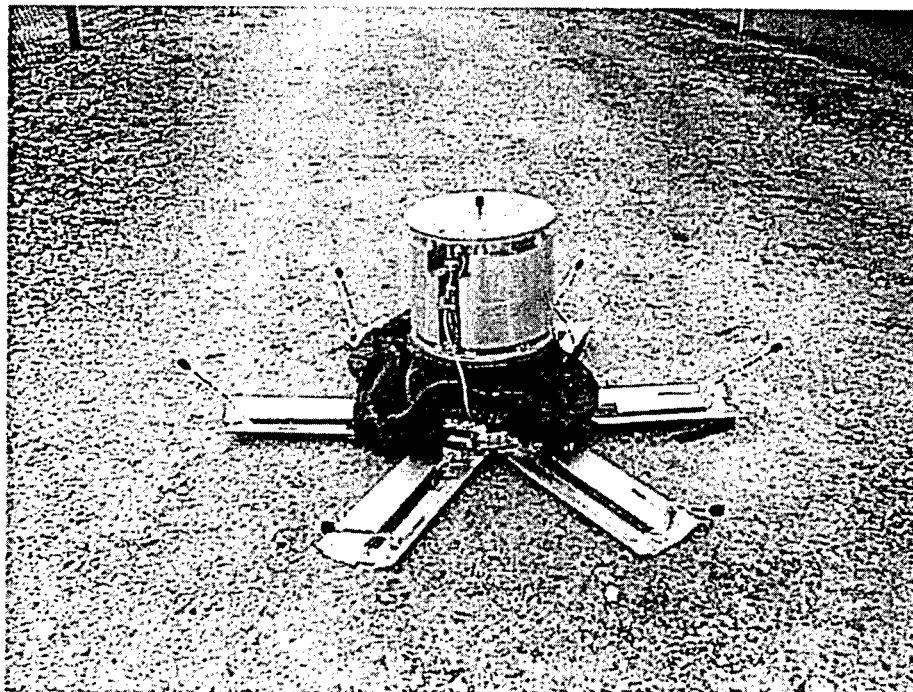Fig. 3 Acoustic signature measured under LOS conditions and in the shadow

Fig. 4 Example of a compact portable acoustic array, aperture appr. 1 m
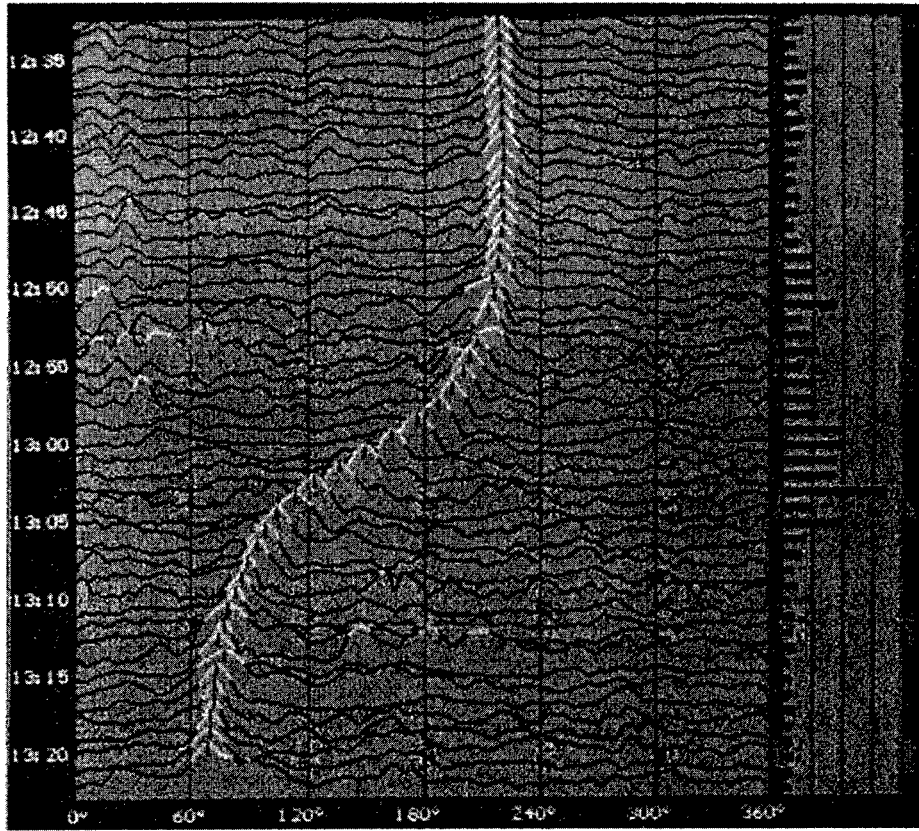
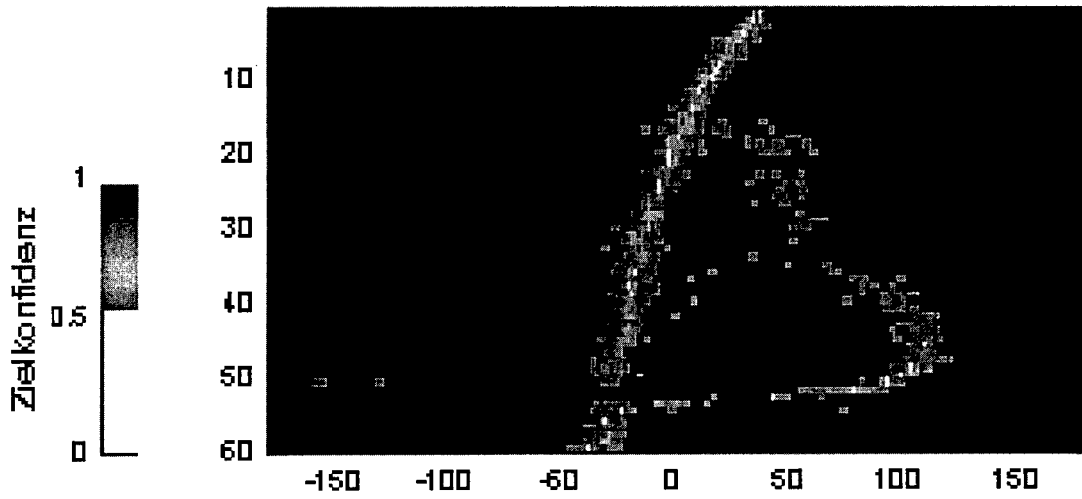Fig. 5 Acoustic bearing of a passing helicopter, arriving from 210° and departing to 70°

Fig. 6 Acoustic tracking of multiple targets with a single antenna

THE CLASSIFICATION OF VEHICLES IN MMW IMAGERY

William Denton and Dr Adrian Britton

DERA(M)
St Andrews Rd
Malvern
Worcs WR14 3PS
UK

SUMMARY

In this paper we exploit high resolution millimetre wave radar ISAR imagery to develop a vehicle classification algorithm, which is robust to orientation and position of the vehicle in the scene. A statistical model of the aspect dependent fluctuations of the radar signatures of a variety of vehicles is developed and is then used to define the Maximum Likelihood (ML) classification algorithm. The performance of this algorithm is compared with that achieved using a number of alternative sub-optimal classification tests, again utilising the statistical model. It is shown that the statistical model can provide a fairly accurate representation of the fading characteristics of the vehicle and that the performance of the ML algorithm is very high under conditions of perfect knowledge of the position and orientation of the vehicle in the scene. However, in real applications in which these parameters have to be estimated, some performance degradation is observed. In comparison, the sub-optimal tests are shown to offer increased robustness to uncertainties in the vehicle location. The models and techniques reported here provide a robust approach for general radar classification problems.

1. INTRODUCTION

This paper presents a vehicle classification algorithm for ISAR imagery, which classifies vehicles into three classes. The algorithm utilises a statistically derived model of the vehicles to account for the changes in ISAR imagery as vehicle rotates on a turntable.

The paper is structured in the following way; section 2 describes the design of the classification algorithm and summarises the range of classification tests evaluated. The performance of the algorithm is presented in section 3 and discussed in section 4. Conclusions are then presented.

2. ALGORITHM DESCRIPTION

2.1 Introduction

The classification of the vehicle signature under test involves it's comparison with representations of the three different class types, and therefore requires 'class templates' to be identified. These were constructed by averaging ISAR images of typical vehicles belonging to each class over adjacent 5° windows as they rotated around 360°, thus producing seventy two templates for each class type. This model is referred to as the Angular Decomposition (AD) model and is explained in section 2.2.

The algorithm described below consists of two main parts. The first part is the alignment of the vehicle with the templates representing the classes under consideration, and the second part is the mathematical tests used to classify the vehicles.

2.2 Statistical model

A general rule in classification is that the separation of classes is best exploited when the maximum a priori knowledge of the statistical behaviour of the classes is utilised in the classifier [1, 2]. Therefore, the most promising way of developing effective radar classification algorithms is to devise accurate statistical models of objects, which can then be used as the basis for the application of statistical pattern classifiers.

It is often recognised that the radar signature of an object is very sensitive to changes in viewing angle. In general, the vehicles of interest, are complex structures with a combination of odd and even bounce scatterers, and a single profile could not be expected to adequately describe such a vehicle at all aspects. Clearly, the model must contain more than one template.

A typical vehicle can be modelled for radar signature purposes as a large number of distinct scattering centres. Given this model the variation in the vehicle signature then arises from two effects. Firstly, as the viewing angle changes the distance of each of the scatters in the range gate to the radar changes. This results in a change in the coherent addition of the backscattered signal from each of the scatterers as measured at the radar giving a changes in the measured radar cross section (RCS). Secondly, changes in the viewing angle lead to changes in the number and strength of scatterers in each range bin contributing to the backscattered signal which also results in changes in the measured RCS.

The approach adapted for model described in this paper exploits a two-scale statistical model to describe the fluctuations of the RCS. The application of such a model is based upon the assertion that the above two mechanisms giving rise to the RCS fluctuations operate on different rates of change in angle from which the vehicle is viewed.

To determine the appropriate statistical model for vehicle ISAR images, the normalised moments of the value of each pixel where examined over a range of azimuth windows (5°, 10°, 20°). This allowed the appropriate statistical model to be selected together with size of azimuth window over which the model held. When the angle swept exceeds this window, obviously, a different set of model parameters is required.

The values of the second, third and fourth normalised moments found with the vehicle ISAR data matched those expected for an exponential distribution when a 5° azimuth window was used. The exponential distribution has particular significance because it is the distribution of RCS expected of a radar cell containing a large number of randomly interfering scatterers. As

the size of the angular window was increased the values of the normalised moments were found to increase. This is characteristic of a two-scale process and reflects the impact of different scatterers contributing to the RCS fluctuations in the two halves of the angular window. A change in scatterer population across the angular window implies that the RCS fluctuation has a different mean value in the two halves of the window. Therefore, although locally the RCS distribution may be exponential, combination of the RCS fluctuations from two processes with different mean values will not maintain the exponential form in the composite distribution. Generally the normalised moments of the combined distribution will be higher than those of the two components, which was found when larger azimuth windows were used. This analysis therefore indicates that a two scale process can be used to model the fluctuations in the radar signature of vehicles. Within this two-scale process the RCS fluctuations due to the interference of the scatterers within a resolution cell occurs on a smaller scale of angular change than the RCS fluctuations due to changes in the number and strength of the scatterers.

The analysis of normalised moments has suggested that over angular windows of 5° the RCS in each pixel conforms to the exponential distribution. The exponential distribution is defined by a single parameter, its mean value. Consequently, a complete description of the statistics of the RCS signature of the vehicle can be expressed by the average of the ISAR images obtained over a 5° window.

The statistical model derived above does not constitute a complete description of the vehicle signature needed for the development of an algorithm. This is because any correlation between the RCS fluctuations in one pixel with those in other pixels needs to be accounted for within the modelling of the signature. However, analysis of the vehicle signature indicates that there are not large correlations between the RCS fluctuations of any pair of pixels. Therefore, for the purposes of algorithm development, the vehicle will be considered as completely described by the above statistical model. This approach to the statistical modelling of the RCS signatures of vehicles in which the angular coverage of the vehicle is decomposed into a number of angular windows will be referred to as the angular decomposition (AD) approach.

To facilitate the classification, the algorithm utilises 3 statistical models - one for each class of vehicle. Each model was constructed from approximately 2000 radar 'snapshots' of a typical vehicle as it rotated on a turntable. These 3 models comprise 72 templates each, and each template represents the mean of all snapshots (about 27) in a 5° rotation of a vehicle typical of the class.

The above statistical analysis used to generate angular decomposition model has recently been supported by a data driven approach to modelling the angular variation. In this approach, the data was clustered using a k-means clustering [2] into 72 classes. It has been found that with 72 classes data groups into approximately 5° windows.

2.3 Alignment of vehicle signature with class templates

The position of the vehicle within the radar image has to be determined in order to register it accurately with the templates.

The process developed to achieve this initially median filters the radar image and applies a threshold to give a binary image. After this binary morphological opening and closing are used to clean-up the image by removing isolated regions, amalgamating adjacent regions and smoothing region outlines. In order to isolate the vehicle region, the centre of mass of this binary image is found and isolated by region growing from this point. This should remove any regions which are not associated with the vehicle. The centre of mass of the remaining region is then used as the centre of the vehicle. Obviously, the radiometric centre of the image is unlikely to correspond to the geometric centre of the vehicle. Consequently, it is necessary to apply the same centre estimation process to the templates, so that the similar offsets, between the estimated centre and actual geometric centre, are applied to the test data and the templates which will then bring them into better alignment.

As the position estimate is solely dependent on the signature under test which can vary significantly over small changes in azimuth angle, the estimate will have some uncertainty associated with it. The magnitudes of these uncertainties have been estimated empirically to be ± 1 pixel in cross-range and ±2 pixels in down-range. Within the classification algorithm, these are accommodated by allowing a range of possible alignments between the signature under test and the templates. At each position considered within the estimated error bounds, the vehicle region within the radar image is extracted using a mask of vehicle dimensions. It is then positioned over each of the templates so that the vehicle and template pixels with corresponding co-ordinates can be compared. In order to account for the vehicle orientation, the signature under test is extracted using a mask at all possible orientations and compared with the corresponding template. For each distance metric, the best value resulting from this comparison over the range of possible alignments and orientations is used for classification.

2.4 Classification Tests

Once the vehicle signature has been aligned with the templates, six classification tests are used. These tests are essentially measures of the distance in a multi-dimensional space of the signature under test from each of the templates. The differences between the tests reflect different weights associated with amplitudes of pixels in the test and template signatures. The classification tests were appropriately normalised with respect to the number of pixels measured, which varies with the vehicle orientation. The number of pixels measured varies because the mask used to extract the test data is a rectangular in shape and is projected onto a discrete rectangular grid at a number of orientations. The six classification tests evaluated were:

Test 1: A negative log likelihood discriminant based on the statistics of the AD model. The AD model assumes that the resolution cells in each vehicle image have an exponential distribution with mean values given by the corresponding average templates. Within this model the statistical likelihood that an observed image, $\underline{x}$, originated from the ith class is given by:

$$p(\underline{x}|i) = \prod_{j=1}^{a} \frac{1}{\mu_{ij}} \exp\left(-\frac{x_j}{\mu_{ij}}\right) \tag{1}$$

where,

x_j - amplitude of the jth resolution cell in the test image,

μ_{ij} - amplitude of the jth resolution cell in the average template of class i,

a - all pixels contained in vehicle region.

x is assigned to the class for which $-\ln(p(\underline{x}|i))$, the negative log likelihood, is a minimum. The negative log likelihood value is given by:

$$-\ln(p(\underline{x}|i)) = \sum_{j=1}^{a}\left(\frac{x_j}{\mu_{ij}} - \ln(\mu_{ij})\right) \tag{2}$$

Test 2: The gamma distribution was evaluated as an empirical attempt to reduce the effect of noise contained in erroneously extracted vehicle regions on the classification result. Instead of assuming an exponential distribution for the negative log likelihood test, a 2nd order gamma distribution was assumed. A description of the reasons for using this distribution and its impact is given later in this paper. The negative log likelihood equation for a gamma distribution of order 2 is given by:

$$-\ln(p(\underline{x}|i)) = \sum_{j=1}^{a}\left(2\frac{x_j}{\mu_{ij}} - \log\left(\frac{2x_j}{\mu_{ij}}\right) + \log\left(\frac{\mu_{ij}}{2}\right)\right) \tag{3}$$

Test 3: Correlation. When the vehicle signature and the templates representing the three classes are correlated, the maximum correlation coefficient indicates the best match. The correlation coefficient, C, is given by:

$$C = \frac{\sum_{j=1}^{a}(x_j - \bar{x})(\mu_{ij} - \bar{\mu_i})}{\sqrt{\sum_{j=1}^{a}(x_j - \bar{x})^2 \sum_{j=1}^{a}(\mu_{ij} - \bar{\mu_i})^2}} \tag{4}$$

Test 4: Nearest neighbour using the city block distance metric. For nearest neighbour metrics, the smaller the distance, d, between the vehicle image and the templates, the closer the match between the two. The city block distance metric is given by:

$$d = \sum_{j=1}^{a}|x_j - \mu_{ij}| \tag{5}$$

Test 5: Nearest neighbour using the Euclidean distance metric. This metric distance takes the form of:

$$d = \sqrt{\sum_{j=1}^{a}(x_j - \mu_{ij})^2} \tag{6}$$

Test 6: Nearest neighbour using the Mahalanobis distance in which an exponential distribution of the vehicle pixel amplitudes is assumed with means given by the corresponding pixel amplitudes in the average templates. In addition, it is assumed that there is no correlation between pixels with the templates, which has been verified empirically. As an exponential distribution is assumed the variance is equal to mean and hence the Mahalanobis distance is given by:

$$d = \sum_{j=1}^{a}\frac{(x_j - \mu_{ij})^2}{\mu_{ij}^2} \tag{7}$$

3. ALGORITHM PERFORMANCE

A series of experiments are described below which were designed to investigate the performance of the algorithm when classifying vehicles into one of the three classes. The algorithm was presented with a complete rotation of each vehicle under test. For each image, each of the classifiers assigned the vehicle to the class which gave the best match between the vehicle and one of the templates.

Examples of three classes of vehicles were used to train the classifiers by constructing the templates through angular averaging. These vehicle images were also used to test the classifiers. For test set 4, the training vehicle for test set 1 was imaged at a different depression angle. For test set 5, the same vehicle as test set 1 was imaged under the same conditions, but with the engine running. The engine causes the vehicle to vibrate and hence changes the reflected Doppler frequency which then potentially has an impact on the ISAR imagery. For test set 6 & 7, a vehicles of the same class as test set 1, but physically different, were imaged. The vehicles used are summarised in the following table.

Test set number	Description
1	Training - example of vehicle type 1
2	Training - example of vehicle type 2
3	Training - example of vehicle type 3
4	Test - same vehicle as test 1, but imaged at a different depression angle
5	Test - same vehicle as test 1, but imaged with the engine on
6	Test - a vehicle of the same class as test 1, but physically different
7	Test - a vehicle of the same class as test 1, but physically different

Table 1; Test vehicle descriptions.

When the test vehicles and the templates are perfectly aligned the maximum performance for the training data should be obtained with all the distance metrics. The results obtained under these conditions are shown below in table 2.

Test set number	Distance metric					
	1	2	3	4	5	6
1	99.7	100.0	99.9	100.0	99.9	100.0
2	100.0	100.0	99.9	100.0	99.9	100.0
3	100.0	100.0	99.8	99.9	99.2	100.0
4	39.3	57.2	51.6	62.8	71.7	70.5
5	98.4	100.0	99.7	100.0	99.9	100.0
6	71.0	84.5	66.9	95.0	89.9	88.7
7	33.4	55.8	55.4	75.1	76.8	75.1

Table 2; Classification rate when the test data and templates are perfectly aligned.

When the centre of the vehicles and templates are estimated using the techniques described earlier the results shown in table 3 were obtained.

Test set number	Distance metric					
	1	2	3	4	5	6
1	89.0	94.4	84.7	92.2	90.9	95.8
2	92.9	94.7	89.6	93.6	89.7	91.4
3	92.0	94.2	88.9	92.8	84.6	89.8
4	71.3	84.3	63.6	83.5	83.6	89.0
5	76.0	87.4	72.0	87.9	88.5	92.7
6	64.0	65.0	52.0	66.6	71.6	74.3
7	54.8	57.8	48.4	58.5	65.4	75.6

Table 3; Classification rate when the position of the vehicles and templates are estimated.

When the centre of the vehicles and templates are estimated and the alignment between them allowed to slip the results shown below in table 4 were obtained.

Test set number	Distance metric					
	1	2	3	4	5	6
1	94.4	99.8	98.5	100.0	99.1	99.9
2	98.6	99.9	99.5	100.0	99.5	100.0
3	94.2	99.8	99.2	99.9	98.8	99.8
4	67.1	90.2	72.1	92.6	87.6	95.8
5	86.1	99.1	95.6	99.5	98.1	99.7
6	48.3	51.0	46.1	62.0	71.3	67.3
7	42.5	44.3	38.3	43.0	56.2	67.9

Table 4; Classification rate when the position of the vehicles and templates are estimated and the alignment is allowed to slip.

4. DISCUSSION

The results presented in section 3 show that ISAR imagery potentially contains enough signature information to allow the effective classification of vehicles into three distinct groups. If the vehicle position can be located exactly, allowing the precise extraction of the vehicle from it's background, all the tests can achieve very good performance on training vehicles. Even on test vehicles, which are imaged at a different depression angle or are physically different, good performance can be achieved with some of the distance metrics.

Table 3 shows that when the position of the vehicle is estimated, the classification rate is still good for the training vehicles. However, as expected there is a slight reduction in performance compared to the perfect alignment case which will be due to inaccuracies in the position estimation causing an incomplete vehicle to be extracted. This will lead to an area of the mask used to extract the vehicle containing background.

To overcome the inaccuracies in the position estimation, the alignment between the test data and templates was allowed to slip by up to ±2 pixels in down-range and ±1 pixel in cross-range. This arrangement gave the results shown in table 4. These results represent a more realistic assessment of the performance as the vehicle position is estimated and slipping is used to minimise the effects of errors in the position estimation.

The results show that very good performance can be achieved with the training vehicles. In addition, generalisation to different depression angles and different vehicles can be achieved using some of the distance metrics.

On the training vehicles, there is little difference between the performance of the different distance metrics. However, it should be noted that the maximum likelihood classifier based on the exponential statistics of the AD model has a lower performance than all of the other distance metrics. This reduction in performance can be understood by considering equation 2. This shows that pixels with low values give small contributions to the overall value of test 1, supporting a close match between vehicle and template. This reflects the fact that low values are very likely when the signal is exponentially distributed. However, where the test signature has not been extracted accurately (due to poor estimation of the vehicle's position) some of the pixels will contain low level background, which when equation 2 is applied will give small response indicating a good vehicle/template match. This effect is believed to reduce the performance of the classifier by causing misclassification when the test signature is not extracted accurately.

To reduce the effect of background pixels biasing the negative log likelihood classification, a more general 2nd order Gamma distribution was assumed rather than the exponential distribution. This assumption leads to the distance metric given in equation 3. The difference between the exponential and Gamma distributions can be seen below in figure 1.
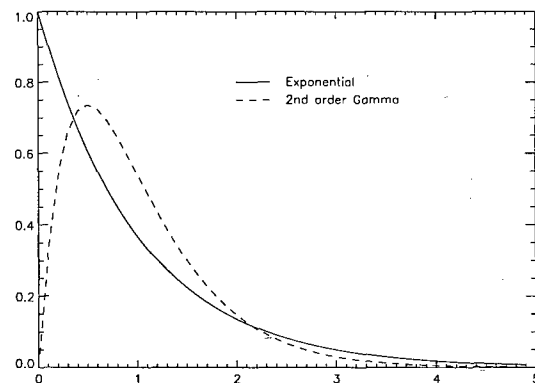
Figure 1; Exponential and Gamma distributions with means of one.

When the Gamma distribution is used, the biasing effect is vastly reduced as pixels with low values have a reduced contribution to the test. Therefore, low level pixels in inaccurately extracted vehicle regions have less effect on the test. The benefits of this change can be seen in improvement in performance between test 1 and 2 in table 4 for the training vehicles. Similarly, the performance of the Gamma based test is better on the test vehicles.

With the training vehicles it is difficult to separate the performance of the different distance metrics. However, with the test vehicles it is possible to make a limited assessment of

the generalisation of the distance metrics. To make a more detailed assessment it would be necessary to use more test vehicles. With the available test data it can be seen that on average the Mahalanobis distance metric (test 6) performs better than any of the other distance metrics. In particular, it obtains an average performance on the test data of 83% which is considerably better than the maximum likelihood classifier's (test 1) average performance of 61%.

A key issue in the design of the classification algorithm is the selection of the training data used to generate the templates. In the analysis reported here, the test vehicles are completely new to the algorithm, and therefore a very high level of performance might not be expected when the classifier is using the complete radar signature. This is because the high spatial resolution radar imagery has a large amount of fine detail that may be masking the more global aspects of the signatures that are characteristics of each of the classes. There are two approaches for future algorithm development; simply widen the data set used in the training of the algorithm, or investigate in more detail the principal characteristics of the radar signature of the vehicles and their variation with vehicle configuration.

The first approach would include data in the training process that covers a wider range of vehicle conditions. In practice, this would be expected to reduce the classification levels for the training vehicles, but increase the performance on test vehicles as the average vehicle representation becomes more general.

A second approach would be to review the generation of the templates. At present these are defined by the rigid 5^0 angular windows identified by the AD analysis. Although these windows are likely to be appropriate on average, it would be sensible to devise the templates in a more data dependent manner that would allow statistically similar signatures from a wider range of viewing angles to be combined into a single template if appropriate. This may reduce the number of templates, and allow a more natural representation of the fluctuations in the vehicle signature. Depending on the sensitivity of the performance of the improved algorithm on the vehicle configuration, this could then be followed by an investigation of the detailed vehicle signature to try and identify principal characteristics that are invariant to the changing conditions of the vehicle. Such analysis could comprise either a data dimension reduction analysis or a wavelet analysis to identify scales at which the vehicle signature is stable to changing configuration. The results reported here show that the basic information within vehicle signature can support effective classification, and that the future problem is to identify the 'essential' vehicle representation that maintains the classification performance, but adds the required robustness to vehicle configuration and vehicle type.

In addition to changing the templates, it may be possible to improve the performance by combining the information from different distance metrics by another classifier such as a neural network. This combined classifier could use information from all the distance metrics and all the classes. This would include both measures of similarity and dissimilarity in the decision making process.

5. CONCLUSIONS

A number of distance metrics were evaluated as classification tests. On training data there was little difference in performance between the distance metrics. However, it is evident that the maximum likelihood classifier based on exponential statistics of the vehicle model, although having good performance in perfect conditions, does not perform as well as the other classifiers in a more realistic situation. In the more realistic situation where the position of the vehicle has to be estimated, the Mahalanobis distance metric offers better performance than any of the other distance metrics. More ISAR measurements of different vehicles of each class would be desirable, allowing the robustness of the algorithms to be tested more thoroughly.

The results presented in this paper have shown that the classification is sensitive to errors in vehicle location and configuration, and techniques need to be developed to improve it's robustness. Currently, the templates used are defined rigidly over 5^0 windows. Alternative templates derived directly from the combination of signatures from a wider range of aspects may be integrated into a statistical mixture model that better describes the natural fluctuations in the vehicle signature. More advanced classification techniques can then be developed by using these mixture models in a Bayesian framework by comparing vehicles with all templates from all classes within classification decision. This model could also be used to incorporate robustness to inaccuracies in the vehicle region position and the vehicle configuration.

6. REFERENCES

1. Fukunaga, K., "Introduction to Statistical Pattern Recognition", Electrical Science Series, 1972.

2. Duda, R.O. and Hart, P.E, "Pattern Classification and Scene Analysis", John Wiley & Sons Inc., 1973.

3. Gonzalez, R.C. and Woods, R.E., "Digital Image Processing", Addison-Wesley Inc., 1993.

A Maximum Likelihood Range-Profile Classifier for Maritime Targets

Jim P. Ballard
Tom P. Leonard
Defence & Evaluation Research Agency
St Andrew's Road, Malvern
WR14 3PS, UK

SUMMARY

Traditional approaches to range-profile classification of ship targets have been feature-based, where the features are chosen directly by the algorithm designer or indirectly by the inherent bias of the mathematical algorithm; the correlation classifier being an example of the second type of classifier. Feature-based classifiers are naturally biased and often do not use all the data. Hence, not surprisingly, these classifiers have all had mediocre performance.

Maximum likelihood classifiers are optimal under certain assumptions, and now that the computational power is available to implement them, they are a better place to start than feature-based classifiers. Maximum likelihood classifiers are not biased and use all of the data available. In addition, they naturally lend themselves to data fusion with the output of other sensors and intelligence information.

However, there are a number of difficulties with implementing a maximum likelihood classifier on real data, some of which are also common to other classifiers. The most common problem is aligning or registering a template with the as yet unclassified target. This problem may be partly overcome by brute computational power, but more satisfactory solutions are required. Other problems related to target end detection, slight changes in aspect, range-cell independence, distribution selection and physically different targets are also discussed, together with some suggested solutions.

A maximum likelihood classifier has been constructed using a number of the solutions to the problems described and has given promising results on real data. The limitations and advantages of the classifier are discussed together with possible solutions and improvements. The improvement in classifier performance with respect to its mis-classification rate is investigated when the minimum likelihood algorithm is implemented to overcome a set of the aforementioned problems.

The importance of confidence in a classifier's prediction is also explained together with the results of using confidence levels in the maximum likelihood classifier to further boost performance.

1. INTRODUCTION

The primary role of high-resolution airborne maritime radar is to detect small targets. However, a useful spin off of this technology is that when a high-resolution radar illuminates a large maritime target like a ship, the resulting high-resolution range-profile can be used as a means to classify the target. The recognition of a target by its range-profile is currently performed manually, but with the advent of powerful computational facilities the opportunity to classify targets automatically presents itself.

Much of the early work in the area of ship range-profile classification was performed with a view to solving the problem in a quick and simple fashion so that the capability could be put into military service as soon as possible. In addition, the complexity of the early algorithms was limited by the computational power available at the time. Now that it has been realised that the problem is much more difficult than originally anticipated and with the huge increase in computational power becoming available, more complex algorithms can be investigated.

From a study of simple algorithms, attention has been drawn to the possibility of optimal algorithms. As the range-profile of a target varies from pulse to pulse, the optimal method to discriminate between candidates for the target's true identity is to model the range-profiles that these candidates would produce using probability density functions and then invoke the maximum likelihood criterion.

The maximum likelihood criterion states that, when there are several models that may lead to the observed outcome, the model that has the highest likelihood of generating the observed outcome is the one that should be selected. This involves calculating the likelihood function, $L(\theta)$:

$$L(\underline{\theta}) = f(x_1, x_2, ..., x_n; \underline{\theta}) \tag{1}$$

For values of $\underline{\theta}$ within a given domain, where x_1, $x_2, ..., x_n$ is the value of a random sample from a

multivariate population with the parameter vector $\underline{\theta}$ and $f(x_1, x_2,..., x_n)$ is the value of the joint probability density of the multivariate random variable $X=\{x_1,x_2,..., x_n\}$ [1]. [2] gives an easy-to-follow description of how a maximum likelihood classifier functions together with a worked example.

For ship range-profile classification the joint probability density is the multivariate probability density function of the values occurring in the range-cells of the range-profile. Once the likelihood has been calculated for each of the ship classes, the target is classified as the class with the highest likelihood.

The range-profile of a target varies with aspect-angle. Hence, the probability density functions that describe the range-cell fluctuations also vary with aspect-angle thus requiring different aspect-angles of the same target to be considered as different classes at the classifier training stage. Since there are a continuum of aspect-angles the domain of aspect-angle is divided up into discrete aspect-angle bins. The aspect-angle range covered by each of these aspect-angle bins will be determined by a trade-off between the rate of change observed in the range-profile as the aspect-angle varies, processing time, classification performance and the amount of training data available.

This paper is structured as follows. Section 2 describes the pre-processing schemes that must be performed. Section 3 describes a mid-processing scheme that can be used to boost performance. Section 4 describes a post-processing scheme that can be used to boost performance. Section 5 gives results of the classifier's performance using different pre and post-processing schemes. Section 6 describes the planned direction of future work. Section 7 is the conclusion.

2. PRE-PROCESSING ALGORITHMS

Three types of pre-processing tasks must be performed to enable the classifier to perform its task. Further, the accuracy with which these pre-processing tasks are performed directly influences the performance of the classifier. The first of these three types of task is to align one range-profile with another. This type of task must first be performed on each set of training range-profiles during the training stage of classification. Thus all of the range-profiles representing a target at a certain aspect-angle must be aligned with each other. This alignment ensures that the returns in a range-cell, to which a probability density function is subsequently matched, all come from the same set of scatterers [3], [4]. After the classifier is trained, and during the classification stage, this alignment process must be performed on the trained template and the profile-undergoing-classification, so that the test-profile range-cell value is compared to the correct template probability density function. This alignment during classification process is known as

localisation [5] and is vital for all types of classifiers that do not use position-invariant feature-vectors.

The classifier used to generate the results presented in this paper uses a sophisticated alignment algorithm. The algorithm makes use of the cross-correlation coefficient to make an initial alignment and then uses a focusing metric and a shift of phase in the Fourier domain to achieve alignment to a fraction of a range-cell.

The second type of task is to find the probability density function that best matches the fluctuations, which nominally come from the same set of scatterers, observed in a range-cell. The optimum method of determining the best fit distribution is to use the maximum likelihood criterion again, both for the type of distribution [6] and for the distribution's parameters [1]. The calculation of the distribution's parameters can be quite involved, often involving an iterative process [7]. Thus, a more practicable approach is to use the method of moments [1] to determine the parameters of a finite list of candidate distribution types and then find the best fit using the maximum likelihood method.

The values that appear in each of the range-cells are assumed to be independent so that the multivariate probability density function can be constructed as the product of a number of univariate probability density functions. It has been shown that the gamma distribution provides a good fit to the range-cell fluctuations [6] and so it has been used here. The parameters of the gamma distribution that best describes the fluctuations of a range-cell are recorded for each range-cell, of each class of ship, at the training stage of the classification process. They are then used to evaluate the likelihood that each class would have generated the value observed in the corresponding range-cell of the range-profile under test. The likelihoods generated for each range-cell are then multiplied together to determine the overall likelihood that a class would have generated the ship range-profile under test. These overall likelihoods are then normalised by their length in range-cells to provide a fair comparison between ship classes of different lengths.

When a previous attempt was made to use the maximum likelihood criterion for ship range-profile classification, the likelihood of a class generating the entire range-profile was calculated. As can be seen in figure 1, some of the range-cells in the range-profile do not represent reflections from the target of interest but instead from the surrounding environment. The dominant contribution to the values of these off-target range-cells is from thermal noise within the receiver. Hence the data contained in these range-cells contain no information about the target and hence are of no value in attempting to classify the target. Further, it was found that the component of the overall likelihood generated from these sea-surface range-cells dominated the overall likelihood calculation and hence resulted in poor classification performance.

Figure 1. Typical Range Profile
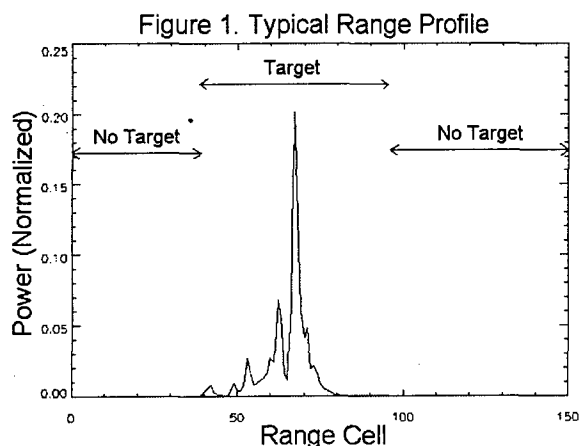
The classifier, used to generate results for this report, uses only range-cells that contain scatterers located on the target of interest. It does this by using a thresholding and correlation process to locate the ends of the target and only using range-cells between the two ends. This end-determination task comprises the third and final pre-processing task.

3. MID-PROCESSING SCHEMES

This mid-processing scheme provides a useful compromise between a rigorous theoretical approach and a more practical application based approach. Although it is not required to allow the main part of the classifier to function correctly and by using this scheme the overall classifier is no longer a true maximum likelihood classifier, there are good theoretical reasons for using the scheme and it has been shown to increase classifier performance significantly.

It has been assumed that the target undergoing classification is physically identical to the target of the class that was used to train the classifier. However, this is clearly not the case for ship targets. Ships of nominally the same class are often built in batches, so that ships within a batch are theoretically the same, but may be significantly different to other ships within the same class but from a different batch. Furthermore, even different ships within the same batch have often undergone slightly different modifications during their lifetime. This problem is further compounded by the different physical configurations that a target can take over a few hours: hangar doors can be open or closed, helicopters may be present or absent, weapon systems may change orientation independent of the target as a whole etc. If there are physical differences between test and training targets then the values returned in the test range-cells will not obey the probability density functions recorded in the database, yielding a very low likelihood and possible misclassification.

However, most of these differences affect only a small part of the target, and thus only a few range-cells. Hence most of the range-cells behave as recorded in the database. If the influence of the changed range-cells can be limited then the overall likelihood may remain relatively high and correct classification should result.

One method of limiting the influence of these changed range-cells is to assign a minimum likelihood to any range-cell. In this way, if the value in a range-cell is near the value expected then a high likelihood results, the closer the value the higher the likelihood. But if it is further than a specified amount then it is considered to be from a physically different set of scatterers than those used to generate the probability density function for that range-cell and it is assigned a pre-determined low likelihood. There are two reasons behind using a minimum value. The first is to 'fine' the candidate-class for having a different set of scatterers occupying the range-cell no matter whether they are slightly different or very different: it only matters that they have been judged to be different. The second reason is to allow the likelihood of the entire range-profile to remain relatively high even if one range-cell is radically different to expectation. The use of this minimum likelihood improves classification performance, but the performance increase is a function of the value chosen. The setting of this minimum likelihood is investigated in section 5.

4. POST-PROCESSING SCHEMES

One of the purposes of an automatic classifier is to perform the classification function currently performed by a radar operator, but faster and with greater accuracy. Direct comparison of the capabilities of an automatic classifier with a radar operator is however, often overlooked. Most automatic classifiers calculate which class stored within their database provides the best match to the test range-profile. However, this is quite different to deciding if a range-profile has come from one of the targets in the radar operator's memory, which is the process actually performed by radar operators. There are two significant differences between these two processes.

Firstly, the radar operator may know through prior information that a certain class of ship is not operating in the vicinity and so will know that although the, say, 'A' class provides the best match to the test-profile the target cannot be from the 'A' class. This demonstrates the use of prior knowledge in the classification decision. Secondly, none of the targets stored in the database (or memory) may provide a good fit to the observed test profile. The radar operator would then classify the target as 'unknown' or wait for more range-profiles to be collected by the radar before a classification decision was made. However, most classifiers would classify the target as the class that provided the least-bad fit.

Both of these differences may be directly incorporated into a maximum likelihood classifier. Prior knowledge may be incorporated into a maximum likelihood classifier, thus making the classifier a Bayes classifier.

This is achieved by multiplying the likelihood generated for each class of ship by the prior probability of encountering a ship of that class and then using the maximum likelihood criterion on the new Bayes likelihood values generated for each class. Thus if the prior probability of encountering a class of ship is zero then so is the Bayes likelihood, hence this class cannot have the maximum likelihood and so will not be selected. The classifier's response to the previous range-profile can be used to adjust the prior probability for the current range-profile. Spatial prior information can also be used when there are multiple targets, a fishing fleet for example, to affect the posterior classifications of the targets based on other classifications in the group. However, care has to be taken not to set up a positive feedback effect [8]. Equation 2 shows how to calculate the Bayes likelihood.

$$Bayes\ Likelihood_i = PP_i \times ML_i \qquad (2)$$

In equation 2, i denotes the ith class, PP_i the prior probability of encountering a target of class i and ML_i is the maximum likelihood generated by class i [2].

The second difference, the potential for declaring poor-fit targets as unknown can be incorporated by calculating a confidence value and assigning a confidence threshold. The confidence value is a measure of how confident a radar operator would be in the classification decision. If the confidence value is below the threshold value then the range-profile is either put in the 'unknown' class or merely left unclassified. The confidence value should be some function of the maximum likelihood of all classes. Thus if the range-profile is a poor match to all classes they will all yield low likelihoods resulting in a low maximum likelihood and hence a low confidence. The confidence threshold should be set according to the estimated costs and benefits of misclassifying targets compared to leaving them as unknown or unclassified. These costs and benefits should also be used to weight the class likelihood before the maximum likelihood criterion is used. Equation 3 demonstrates how to calculate this weighted likelihood.

$$Weighted\ likelihood_i = (Bayes)\ L_i \times T^1_i \times B_i\ /\ T^2_i \qquad (3)$$

In equation 3, i denotes the ith class, L the maximum likelihood generated by the class or the Bayes likelihood if prior probabilities have been included, T^1 the cost of making a type 1 error, T^2 the cost of making a type 2 error and B the benefit from a correct classification for this class. A type 1 error occurs when a target of this class is classified as something else. A type 2 error occurs when a target from another class is classified as belonging to this class.

The correct-classification to misclassification ratio will also rise as the confidence threshold rises as misclassifications tend to have low maximum

likelihoods. This is because occasionally a range-profile will not be similar to the range-profiles of that class used to train the classifier and so yield a low likelihood from its true class, thus the maximum likelihood will be distributed randomly among all the classes in the database. This relationship between confidence threshold and correct-classification to misclassification ratio is investigated in section 5.

5. RESULTS

The maximum likelihood classifier was trained on a set of 7 ships. The radar was cliff-mounted and each ship in turn circled in front of the radar so that the ships' characteristic range-profiles could be recorded at all aspect-angles. The circles were divided up into approximately 2° bins, and then for each aspect-angle bin the probability density functions that best described the fluctuations in each range-cell were recorded.

Six of the targets performed a second circle. These second circles were used to test the classifier. The classifier had a high correct classification rate when tested on 6 test classes and 7 training classes using the pre-processing schemes described in section 2.

The effect of using the minimum likelihood described in section 3 was investigated for a variety of minimum likelihood values. The results of this investigation are shown in figure 2. The error rate per class is defined as the percentage of misclassifications per class. The mean of these gives the overall absolute error rate. The relative error rate is defined as the overall absolute error rate for a certain minimum likelihood expressed as a percentage of the overall absolute error rate for the classifier when no minimum likelihood is used. Hence, when the minimum likelihood is zero, which is equivalent to having no minimum likelihood, the relative error rate is one hundred per cent.

Figure 2. Relative error rate vs minimum likelihood
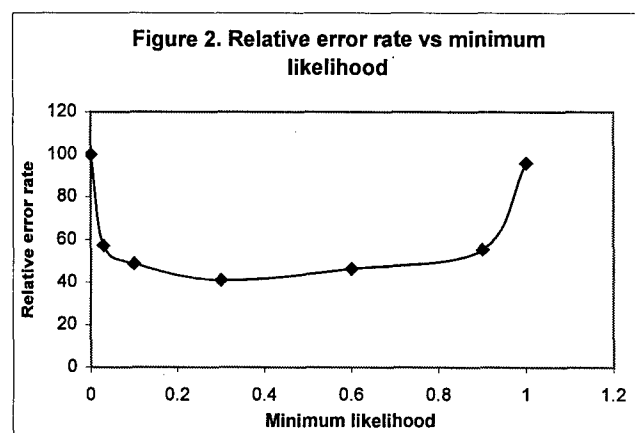
It can be seen that when the mid-processing scheme of a minimum likelihood is used the relative error rate approximately halves. This means that the number of misclassifications also halves. Hence the use of a minimum likelihood drastically improves the

performance of a ship range-profile, maximum-likelihood classifier.

It can also be seen that the setting of the value of the minimum likelihood also affects performance. If set too low it will have little or no effect. If set too high the performance gain will be reduced. If set extremely high performance will actually fall until classification is essentially random. Note that the values of the y-ordinate as a function of the x-ordinate are specific to this data set. For other data sets the behaviour of the curve will be similar but the minimum error rate may occur at a radically different minimum likelihood.

The use of the confidence threshold described in section 4 was investigated on the maximum likelihood classifier. The classifier was trained and tested as described above for the minimum likelihood investigation, but the minimum likelihood was fixed at the value 0.3. The maximum likelihood generated by any of the training classes for a single test profile was compared to the confidence threshold. If the maximum likelihood exceeded the confidence threshold then the test range-profile was classified as the class that generated the maximum likelihood, as before. However, if the maximum likelihood was lower than the confidence threshold the test profile was left unclassified. Unclassified profiles were considered neither correctly-classified nor misclassified.

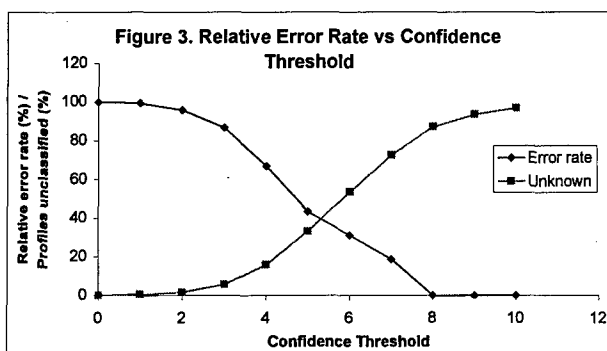Figure 3. Relative Error Rate vs Confidence Threshold

Figure 3 shows the error rate relative to the percentage of misclassifications if no confidence threshold is used. Hence when the confidence threshold is zero, which is equivalent to not using a confidence threshold, the relative error rate is one hundred per cent. Figure 3 also shows the number of unclassified test profiles as a percentage of all the test profiles.

It can be seen that as the confidence threshold rises so does the number of unclassified profiles and since these low confidence profiles contain a higher percentage of misclassifications, the relative error rate falls. There are slight kinks in the error rate curve. This is because the rise in the number of profiles unclassified gives fewer classifications from which to calculate the error rate, leading to a drop in the accuracy with which the error rate for the classifier is estimated. If the number of

profiles classified increased then these kinks should disappear.

Note that if the confidence threshold is greater than or equal to 8 no misclassifications occur, thus at this point all classifications made are correct, however, most profiles are left unclassified.

The values of the y-ordinate as a function of the x-ordinate are particular to this data set. For other data sets the same behaviour of the two curves is expected but it will occur at a different position along the x-ordinate. It can be seen that the use of a confidence threshold is a powerful tool in that a classifier can increase its performance in terms of misclassifications, in exchange for allowing a number of range-profiles to go unclassified. If the results of the classifier were passed onto a further intelligence, whether human or artificial the confidence should be passed on too. Then the human or machine can decide how to use the classifier's decision based upon the classifier's confidence in that decision and the costs and benefits of making the right or wrong decision based upon the classification. The confidence can be used to fuse the classifier's decision directly with that of other maximum likelihood classifiers which have different sensory inputs, by multiplying the confidences of each together.

6. CONCLUSIONS

It has been suggested that the maximum likelihood criterion should be used to classify ship targets using radar range-profiles. There are a number of pre-processing schemes that must be employed to enable a classifier to work on real range-profiles; these pre-processing schemes include range-profile alignment and finding the best fit distribution to range-cell fluctuations. Real targets are not identical to others in their class and this causes misclassifications to occur. A mid-processing scheme using a minimum likelihood can be used to reduce the number of misclassifications. Use of a minimum likelihood has been investigated and found to be highly effective.

Radar operators performing manual classification do not classify every range-profile. If a classifier is allowed to only classify those that it considers to be good matches to its database then its number of misclassifications falls.

7. ACKNOWLEDGEMENTS

8. REFERENCES

[1] Freund J E, 'Mathematical Statistics', Prentice Hall, 1992.

[2] Strahler A H, 'The use of prior probabilities in maximum likelihood classification of remotely sensed data', Remote Sensing of Env, 10, pp135-163, 1990.

[3] Holden M H, 'An Investigation into range-profile alignment', DERA internal report, Sept 1997.

[4] Kosir P, DeWall R, 'A multiple measurement approach to feature alignment', Proc IEEE Nat Aerospace & Electronics Conf, 1995.

[5] Zyweck A, Bogner R E, 'Radar target classification of commercial aircraft', IEEE Trans Aerospace & Elec Sys, 32, 2,pp598-606, 1996.

[6] Ballard J P, 'Optimum solutions in range-profile classification and finding the best fit distribution to range-cell fluctuations', IEE Radar 97 Conf, Edinburgh UK, Oct 97.

[7] Harter H L, Moore A H, 'Maximum-likelihood estimation of the parameters of gamma and Weibull populations from complete and censored samples', Technometrics, 7, 4, pp639-643, 1965.

[8] Liu G et al, 'Bayesian classification of multi-look polarimetric SAR images with a generalized multiplicative speckle model and adaptive a priori probabilities', Int J. Remote Sensing, 19, 1, pp161-170.

REPORT DOCUMENTATION PAGE

1. Recipient's Reference	2. Originator's References	3. Further Reference	4. Security Classification of Document
	RTO-MP-6 AC/323(SCI)TP/2	ISBN 92-837-0000-7	UNCLASSIFIED/ UNLIMITED

5. Originator Research and Technology Organization
North Atlantic Treaty Organization
BP 25, 7 rue Ancelle, F-92201 Neuilly-sur-Seine Cedex, France

6. Title
Non-Cooperative Air Target Identification Using Radar

7. Presented at/sponsored by
The Symposium of the RTO Systems Concepts and Integration Panel (SCI)
held in Mannheim, Germany, 22-24 April 1998.

8. Author(s)/Editor(s)	9. Date
Multiple	November 1998

10. Author's/Editor's Address	11. Pages
Multiple	308

12. Distribution Statement There are no restrictions on the distribution of this document.
Information about the availability of this and other RTO
unclassified publications is given on the back cover.

13. Keywords/Descriptors

JEM (Jet Engine Modulation)	NCTI (Non-Cooperative Target Identification)
Aerial targets	Polarimetry
Target acquisition	Radar images
Fighter aircraft	Waveform recognition
Radar detection	Aircraft detection
Doppler effect	Target classification
Acoustic signatures	Algorithms
Calibrating	Target recognition
Inverse synthetic aperture radar	Radar cross sections
High resolution radar	Air defense

14. Abstract

Contains the unclassified papers presented at a Symposium on Non-Cooperative Air Target Identification using Radar organised by the Systems Concepts and Integration Panel (SCI) of RTO, in Mannheim, Germany, 22-24 April 1998.

Novel solutions to the Non-Cooperative Target Identification (NCTI) Problem, using radar are proposed. The papers are presented under the following headings:

- System requirements
- Target characterisation
- Radar measurements and feature extraction
- Target classification
- Scattering techniques, target modelling and validation

RT

RESEARCH AND TECHNOLOGY ORGANIZATION

BP 25 • 7 RUE ANCELLE

F-92201 NEUILLY-SUR-SEINE CEDEX • FRANCE

Télécopie 0(1)55.61.22.99 • Télex 610 176

DIFFUSION DES PUBLICATIONS

RTO NON CLASSIFIEES

L'Organisation pour la recherche et la technologie de l'OTAN (RTO), détient un stock limité de certaines de ses publications récentes, ainsi que de celles de l'ancien AGARD (Groupe consultatif pour la recherche et les réalisations aérospatiales de l'OTAN). Celles-ci pourront éventuellement être obtenues sous forme de copie papier. Pour de plus amples renseignements concernant l'achat de ces ouvrages, adressez-vous par lettre ou par télécopie à l'adresse indiquée ci-dessus. Veuillez ne pas téléphoner.

Des exemplaires supplémentaires peuvent parfois être obtenus auprès des centres nationaux de distribution indiqués ci-dessous. Si vous souhaitez recevoir toutes les publications de la RTO, ou simplement celles qui concernent certains Panels, vous pouvez demander d'être inclus sur la liste d'envoi de l'un de ces centres.

Les publications de la RTO et de l'AGARD sont en vente auprès des agences de vente indiquées ci-dessous, sous forme de photocopie ou de microfiche. Certains originaux peuvent également être obtenus auprès de CASI.

CENTRES DE DIFFUSION NATIONAUX

ALLEMAGNE
Fachinformationszentrum Karlsruhe
D-76344 Eggenstein-Leopoldshafen 2

BELGIQUE
Coordinateur RTO - VSL/RTO
Etat-Major de la Force Aérienne
Quartier Reine Elisabeth
Rue d'Evere, B-1140 Bruxelles

CANADA
Directeur - Gestion de l'information
(Recherche et développement) - DRDGI 3
Ministère de la Défense nationale
Ottawa, Ontario K1A 0K2

DANEMARK
Danish Defence Research Establishment
Ryvangs Allé 1
P.O. Box 2715
DK-2100 Copenhagen Ø

ESPAGNE
INTA (RTO/AGARD Publications)
Carretera de Torrejón a Ajalvir, Pk.4
28850 Torrejón de Ardoz - Madrid

ETATS-UNIS
NASA Center for AeroSpace Information (CASI)
Parkway Center, 7121 Standard Drive
Hanover, MD 21076

FRANCE
O.N.E.R.A. (Direction)
29, Avenue de la Division Leclerc
92322 Châtillon Cedex

GRECE
Hellenic Air Force
Air War College
Scientific and Technical Library
Dekelia Air Force Base
Dekelia, Athens TGA 1010

ISLANDE
Director of Aviation
c/o Flugrad
Reykjavik

ITALIE
Aeronautica Militare
Ufficio Stralcio RTO/AGARD
Aeroporto Pratica di Mare
00040 Pomezia (Roma)

LUXEMBOURG
Voir Belgique

NORVEGE
Norwegian Defence Research Establishment
Attn: Biblioteket
P.O. Box 25
N-2007 Kjeller

PAYS-BAS
RTO Coordination Office
National Aerospace Laboratory NLR
P.O. Box 90502
1006 BM Amsterdam

PORTUGAL
Estado Maior da Força Aérea
SDFA - Centro de Documentação
Alfragide
P-2720 Amadora

ROYAUME-UNI
Defence Research Information Centre
Kentigern House
65 Brown Street
Glasgow G2 8EX

TURQUIE
Millî Savunma Başkanliği (MSB)
ARGE Dairesi Başkanliği (MSB)
06650 Bakanliklar - Ankara

AGENCES DE VENTE

NASA Center for AeroSpace
Information (CASI)
Parkway Center
7121 Standard Drive
Hanover, MD 21076
Etats-Unis

The British Library Document
Supply Centre
Boston Spa, Wetherby
West Yorkshire LS23 7BQ
Royaume-Uni

Canada Institute for Scientific and
Technical Information (CISTI)
National Research Council
Document Delivery,
Montreal Road, Building M-55
Ottawa K1A 0S2
Canada

Les demandes de documents RTO ou AGARD doivent comporter la dénomination "RTO" ou "AGARD" selon le cas, suivie du numéro de série (par exemple AGARD-AG-315). Des informations analogues, telles que le titre et la date de publication sont souhaitables. Des références bibliographiques complètes ainsi que des résumés des publications RTO et AGARD figurent dans les journaux suivants:

Scientific and Technical Aerospace Reports (STAR)
STAR peut être consulté en ligne au localisateur de ressources uniformes (URL) suivant:
    http://www.sti.nasa.gov/Pubs/star/Star.html
STAR est édité par CASI dans le cadre du programme
NASA d'information scientifique et technique (STI)
STI Program Office, MS 157A
NASA Langley Research Center
Hampton, Virginia 23681-0001
Etats-Unis

Government Reports Announcements & Index (GRA&I)
publié par le National Technical Information Service
Springfield
Virginia 2216
Etats-Unis
(accessible également en mode interactif dans la base de données bibliographiques en ligne du NTIS, et sur CD-ROM)

NATO's Research and Technology Organization (RTO) holds limited quantities of some of its recent publications and those of the former AGARD (Advisory Group for Aerospace Research & Development of NATO), and these may be available for purchase in hard copy form. For more information, write or send a telefax to the address given above. **Please do not telephone**.

Further copies are sometimes available from the National Distribution Centres listed below. If you wish to receive all RTO publications, or just those relating to one or more specific RTO Panels, they may be willing to include you (or your organisation) in their distribution.

RTO and AGARD publications may be purchased from the Sales Agencies listed below, in photocopy or microfiche form. Original copies of some publications may be available from CASI.

NATIONAL DISTRIBUTION CENTRES

BELGIUM
Coordinateur RTO - VSL/RTO
Etat-Major de la Force Aérienne
Quartier Reine Elisabeth
Rue d'Evere, B-1140 Bruxelles

CANADA
Director Research & Development
Information Management - DRDIM 3
Dept of National Defence
Ottawa, Ontario K1A 0K2

DENMARK
Danish Defence Research Establishment
Ryvangs Allé 1
P.O. Box 2715
DK-2100 Copenhagen Ø

FRANCE
O.N.E.R.A. (Direction)
29 Avenue de la Division Leclerc
92322 Châtillon Cedex

GERMANY
Fachinformationszentrum Karlsruhe
D-76344 Eggenstein-Leopoldshafen 2

GREECE
Hellenic Air Force
Air War College
Scientific and Technical Library
Dekelia Air Force Base
Dekelia, Athens TGA 1010

ICELAND
Director of Aviation
c/o Flugrad
Reykjavik

ITALY
Aeronautica Militare
Ufficio Stralcio RTO/AGARD
Aeroporto Pratica di Mare
00040 Pomezia (Roma)

LUXEMBOURG
See Belgium

NETHERLANDS
RTO Coordination Office
National Aerospace Laboratory, NLR
P.O. Box 90502
1006 BM Amsterdam

NORWAY
Norwegian Defence Research Establishment
Attn: Biblioteket
P.O. Box 25
N-2007 Kjeller

PORTUGAL
Estado Maior da Força Aérea
SDFA - Centro de Documentação
Alfragide
P-2720 Amadora

SPAIN
INTA (RTO/AGARD Publications)
Carretera de Torrejón a Ajalvir, Pk.4
28850 Torrejón de Ardoz - Madrid

TURKEY
Millî Savunma Başkanliği (MSB)
ARGE Dairesi Başkanliği (MSB)
06650 Bakanliklar - Ankara

UNITED KINGDOM
Defence Research Information Centre
Kentigern House
65 Brown Street
Glasgow G2 8EX

UNITED STATES
NASA Center for AeroSpace Information (CASI)
Parkway Center, 7121 Standard Drive
Hanover, MD 21076

SALES AGENCIES

NASA Center for AeroSpace Information (CASI)
Parkway Center
7121 Standard Drive
Hanover, MD 21076
United States

The British Library Document Supply Centre
Boston Spa, Wetherby
West Yorkshire LS23 7BQ
United Kingdom

Canada Institute for Scientific and Technical Information (CISTI)
National Research Council
Document Delivery,
Montreal Road, Building M-55
Ottawa K1A 0S2
Canada

Requests for RTO or AGARD documents should include the word 'RTO' or 'AGARD', as appropriate, followed by the serial number (for example AGARD-AG-315). Collateral information such as title and publication date is desirable. Full bibliographical references and abstracts of RTO and AGARD publications are given in the following journals:

Scientific and Technical Aerospace Reports (STAR)
STAR is available on-line at the following uniform resource locator:
    http://www.sti.nasa.gov/Pubs/star/Star.html
STAR is published by CASI for the NASA Scientific and Technical Information (STI) Program
STI Program Office, MS 157A
NASA Langley Research Center
Hampton, Virginia 23681-0001
United States

Government Reports Announcements & Index (GRA&I)
published by the National Technical Information Service
Springfield
Virginia 22161
United States
(also available online in the NTIS Bibliographic Database or on CD-ROM)